Submarine landslides in the Northern Tyrrhenian Sea and relationship with the turbiditic and contouritic deposits: morphology, stratigraphy, geotechnics and modelling

Elda Miramontes

UBO
université de bretagne occidentale

UNIVERSITE BRETAGNE LOIRE

THÈSE / UNIVERSITÉ DE BRETAGNE OCCIDENTALE
sous le sceau de l'Université Bretagne Loire

pour obtenir le titre de
DOCTEUR DE L'UNIVERSITÉ DE BRETAGNE OCCIDENTALE
Mention : Géosciences Marines
École Doctorale des Sciences de la Mer

présentée par

Elda Miramontes García

Préparée à IFREMER, Unité Géosciences Marines, Laboratoire Aléas géologiques et Dynamique sédimentaire

Glissements sous-marins en Mer Tyrrhénienne septentrionale et relations avec les dépôts contouritiques et turbiditiques : morphologie, stratigraphie, géotechnique et modélisation

Thèse soutenue 22 novembre 2016
devant le jury composé de :

Marc DE BATIST
Professeur, Université de Gand, Belgique, Rapporteur

Katrin HUHN-FREHERS
Professeur, MARUM, Brême, Allemagne, Rapporteur

Eric CAUQUIL
Expert aléas géologiques, TOTAL, Paris, Examinateur

Jacques DEVERCHERE
Professeur, IUEM-UBO, Brest, Examinateur

Laurence DROZ
Chargé de Recherche CNRS, IUEM-UBO, Brest, Examinateur

Nabil SULTAN
Chercheur, IFREMER, Brest, Directeur de thèse

Antonio CATTANEO
Sébastien GARZIGLIA
Gwenael JOUET
Chercheurs, IFREMER, Brest, Encadrants scientifiques, Invités

Ifremer

PAMELA
PAssive Margins Exploration LAboratories

TOTAL

Remerciements
Agradecimientos
Acknowledgements

www.jluisgarcia.com Modified colours

Sueños de ingravidez

Gracias a mis padres por haberme mostrado que los sueños pueden hacerse realidad, sólo hay que salir a buscarlos.

Je voudrais remercier mes encadrants Antonio Cattaneo, Nabil Sultan, Gwenael Jouet et Sébastien Garziglia pour leur soutien, pour m'avoir accordé leur confiance et pour m'avoir donné une formation d'aussi haute qualité. Ce travail a été possible grâce au financement d'Ifremer et de TOTAL dans le cadre du projet PAMELA et grâce au soutien de l'Unité de Géosciences Marines.

I would like to thank the members of the jury for having accepted to judge my work and for their advices that helped me improve this manuscript. Thank you Katrin Huhn-Frehers, Marc De Batist, Eric Cauquil, Jacques Déverchère and Laurence Droz.

Merci à Ricardo Silva Jacinto pour m'avoir mis en contact avec ce project, à Angélique Roubi, Michael Rovere, Sandrine Cheron et Audrey Boissier pour leur aide dans l'analyse des carottes, à Arnaud Gaillot pour l'aide avec la bathymétrie et à l'équipe sismique Bruno Marsset, Estelle Théreau, Pauline Dupont et Yannick Thomas pour l'excellente qualité des données sismiques auxquelles j'ai pu avoir accès, ainsi que pour m'avoir donné l'opportunité d'apprendre à traiter la sismique multitrace d'haute résolution. Merci aussi à Romain Pellen pour avoir partagé ses données de Minorque, ainsi qu'à Pierre Garreau et à Matthieu Caillaud pour leur collaboration et pour nous avoir donné l'opportunité d'utiliser le modèle hydrodynamique afin de mieux comprendre la formation de contourites. Je voudrais aussi remercier CINES pour l'accès à la machine Occigen (projet ode7663).

Merci aussi aux institutions et personnes qui ont permis mes deux séjours à l'étranger. Mon séjour d'un mois à Bologne (Italie) a été possible grâce à une bourse de mobilité de l'Université Européenne de Bretagne. I would like to thank Marzia Rovere for helping me during my stay at ISMAR-CNR, as well as Fabio Trincardi, Claudio Pellegrini, Vittorio Maselli and Marco Taviani for the interesting scientific discussions, Andrea Gallerani and Patrizia Giordano for their help with the grain size measurements, and Marco Ligi for helping with the processing of the seismic data. Mon séjour de trois mois en Angleterre a été financé par deux bourses de mobilité, du LabexMER et de l'Ifremer, et j'ai été accueilli par FJ Hernández-Molina à la Royal Holloway University of London. Gracias Javier por todo tu apoyo, por hacerme sentir como en casa, por todos tus buenos consejos, por las súper discusiones, por hacerme pensar y por pensar conmigo. I would also like to thank Michael Clare for providing new data for this project and for the interesting discussion, as well as Brian Docherty for being such a nice mate during these three months in England.

Un remerciement spécial à Martin pour m'avoir accompagné dans cette aventure et à ma famille brestoise pour avoir partagé ces trois dernières années avec moi : Ruth, Marta, Ewan, Gwendoline, Julien, Kevin, Solène, Julia, Romain, Guillaume, Carl, Grégory, Lyvane, Sophie, Steven, Iván. Merci aussi au Dojo Brestois et à tous les judokas pour m'avoir accueillie aussi bien depuis le premier jour et pour me donner de l'énergie chaque soir pour une nouvelle journée de travail au labo.

CONTENTS

Submarine landslides in the Northern Tyrrhenian Sea and relationship with the contouritic and turbiditic deposits: morphology, stratigraphy, geotechnics and modelling

The Corsica Trough is an asymmetric confined basin located in the Northern Tyrrhenian Sea between the Corsica Island and the Tuscan Archipelago, with the western flank dominated by turbiditic and hemipelagic processes and the eastern flank (Pianosa Ridge) by mass transport and contouritic processes. This is thus an ideal setting to study the interactions between the different sedimentary processes. The Corsica Trough has been poorly studied in terms of geohazards and impact of bottom currents on sediment dynamics. The present PhD project aims to develop our understanding of the mechanisms that control the formation of submarine landslides within muddy contourites (sediment deposits related to bottom currents) in the Corsica Trough during the Plio-Quaternary. The broad data set available for this PhD project includes: multibeam bathymetry, seismic reflection data, sediment cores, *in situ* geotechnical measurements, current ADCP measurements and results of a hydrodynamic model.

The contourites of the Corsica Trough are mainly composed of mud with sandy layers formed by enhanced bottom currents during periods of sea level fall. The contourite drifts grow slowly during sea level high-stands and rapidly during sea level low-stands due to the high sediment availability provided by an active turbidite system. Bottom currents control the seafloor morphology and generate plastered drifts on the slope. This is a convex-shaped contourite with steep slope gradients in the lower part limited by a moat (incision created by bottom currents). The Pianosa Slump, which is the largest submarine landslide found in this area, was initiated in this lower part of the plastered drift. Hydrodynamic modelling of the present-day oceanic circulation showed that contouritic moats may be under erosion during winter but not during summer. The present-day cold season is used as an analogue for past cold periods and therefore it is expected during cold periods the occurrence of continuous erosive processes that could undercut the slope and trigger submarine landslides.

Another predisposing factor for slope instability identified in the Pianosa Ridge is the presence of a potential weak layer with a post-peak strain softening behaviour (strength loss with increasing strain), high moisture content, compressibility and permeability. These particular properties are caused by the presence of zeolites (product of the alteration of volcanic rocks). This layer originated the basal failure surface of the Pianosa Slump. 2D slope stability modelling showed that a strength reduction of the zeolitic layer created by erosion could be at the origin of the Pianosa Slump.

In summary, the two main factors predisposing the formation of submarine landslides in the Pianosa Ridge are: the morphology of the plastered drift with steep slopes in the lower part and a potential weak layer composed of zeolitic muddy sediment. The main triggering factor seems to be undercutting by bottom currents.

Glissements sous-marins en Mer Tyrrhénienne septentrionale et relations avec les dépôts contouritiques et turbiditiques : morphologie, stratigraphie, géotechnique et modélisation

Le Canal de Corse est un bassin confiné asymétrique localisé en Mer Tyrrhénienne septentrionale entre l'Île de Corse et l'Archipel de la Toscane, dont le flanc ouest est dominé par des processus turbiditiques et hémipélagiques et le flanc est (Ride de Pianosa) par des mouvements en masse et des processus contouritiques. Les aléas géologiques et l'impact des courants de fond sur la dynamique sédimentaire ont été peu étudiés dans cette zone alors que ce site présente un cas idéal pour l'étude des interactions entre les différents processus sédimentaires observés. Le présent projet de doctorat a pour objectif de comprendre plus précisément les mécanismes contrôlant la formation des glissements sous-marins dans les contourites vaseuses (dépôts sédimentaires formés par les courants) du Canal de Corse pendant la période Plio-Quaternaire. Le vaste jeu de données disponible pour ce projet de doctorat inclut : la bathymétrie multifaisceaux, la sismique de réflexion, les mesures géotechniques *in situ*, les mesures de vitesse de courant et les résultats d'un modèle hydrodynamique.

Les contourites du Canal de Corse sont principalement composées de vase avec la présence de couches de sable formées par de forts courants de fond pendant les périodes de baisse du niveau marin. La croissance des dépôts contouritiques dépend de la disponibilité de sédiment fourni par le système turbiditique. Ainsi, cette croissance est lente pendant les périodes interglaciaires de haut niveau marin et rapide pendant les bas niveaux marins. Les courants contrôlent la morphologie du fond et génèrent les plastered drifts de forme convexe avec des pentes plus raides dans la partie avale, limités par une incision créée par les courants (*moat*). Le glissement de Pianosa (*Pianosa Slump*) qui est le plus grand glissement trouvé dans cette zone a été initié dans cette partie basse du plastered drift. La modélisation hydrodynamique de la circulation océanique actuelle (périodes hivernales) suggère que les *moats* pourraient être érodés préférentiellement pendant les périodes froides passées déclenchant ainsi certains glissements observés.

Un autre facteur prédisposant l'instabilité de pente sur la Ride de Pianosa est la faiblaise d'une couche dont le comportement mécanique se caractérise par du radoucissement (perte de résistance avec le cisaillement), une compressibilité et une perméabilité importantes pour une forte teneur en eau. Ces propriétés particulières sont dues à la présence de zéolites (produit de l'altération des roches volcaniques). Cette couche a formé la surface basale de rupture du *Pianosa Slump*. La modélisation 2D de la stabilité de pente a également confirmé que la réduction de la résistance de la couche zéolitique provoquée par l'érosion basale pourrait être la cause de la formation du *Pianosa Slump*.

En conclusion, les deux principaux facteurs prédisposant la formation de glissements sous-marins sur la Ride de Pianosa sont : la morphologie du *plastered drift* avec une pente plus raide en avale et la couche faible composée de sédiment vaseux riche en zéolites. Le principal facteur déclenchant semble être l'érosion basale.

Deslizamientos submarinos en el Mar Tirreno septentrional y relación con los depósitos contorníticos y turbidíticos: morfología, estratigrafía, geotecnia y modelización

El Canal de Córcega es una cuenca confinada asimétrica que se localiza en el Mar Tirreno septentrional, entre la Isla de Córcega y el Archipiélago de la Toscana, y que se caracteriza por tener el flanco oeste dominado por procesos turbidíticos y hemipelágicos y el este (Cresta de Pianosa) por inestabilidad de talud y procesos contorníticos. Los riesgos geólogicos y el impacto de las corrientes de fondo en la dinámica sedimentaria han sido poco estudiados en el Canal de Córcega, a pesar de ser un sitio ideal para estudiar la interacción entre los diferentes procesos sedimentarios. El presente proyecto de doctorado tiene como objetivo mejorar los conocimientos sobre los mecanismos que controlan la formación de deslizamientos submarinos en contornitas fangosas (depósitos creados por las corrientes de fondo) en el Canal de Córcega durante el periodo Plio-Cuaternario. El amplio conjunto de datos disponible para este proyecto de doctorado incluye: batimetría multihaz, sísmica de reflexión, testigos de sedimento, medidas geotécnicas *in situ*, medidas de corriente ADCP y resultados de un modelo hidrodinámico.

Las contornitas del Canal de Córcega están compuestas principalmente de fango con capas de arena formadas por corrientes de fondo fuertes durante periodos de bajada del nivel del mar. Los depósitos contorníticos crecen despacio durante periodos del nivel del mar alto y rápido durante periodos del nivel del mar bajo, gracias al sedimento aportado por un sistema turbidítico activo. Las corrientes de fondo controlan la morfología del fondo y crean *plastered drifts* en el talud. Estos son contornitas de forma convexa que tienen una pendiente más importante en la parte baja y que están limitados por un *moat* (incisión creada por las corrientes). El *Pianosa Slump* es el deslizamiento más grande de la zona y se inició en la parte baja del *plastered drift*. La modelización hidrodinámica de la circulación actual muestra que los *moats* pueden erosionarse en invierno pero no en verano. La estación fría actual se usa como análogo de los periodos pasados fríos y, por lo tanto, se espera que durante los periodos fríos haya procesos erosivos continuados que puedan socavar el talud y desencadenar deslizamientos submarinos.

Otro factor que predispone la inestabilidad de talud en la Cresta de Pianosa es la presencia de una capa débil potencial con un comportamiento de strain softening (pérdida de resistencia al aumentar la cizalla), una densidad baja y contenido en agua, compresibilidad y permeabilidad altos. Estas propiedades particulares son provocadas por la presencia de zeolitas en el sedimento (producto de la alteración de las rocas volcánicas). Esta capa originó la superficie de ruptura del *Pianosa Slump*. La modelización 2D de la estabilidad de talud mostró que una reducción de la resistencia de la capa zeolítica provocada por la erosión podría ser el origen del *Pianosa Slump*.

En resumen, los dos principales factores que predisponen la formación de deslizamientos submarinos en la Cresta de Pianosa son: la morfología del plastered drift con pendientes escarpadas en la parte baja y una capa débil potencial compuesta de sedimento fangoso zeolítico. El principal factor desencadenante parece ser la socavación generada por las corrientes.

List of figures

Chapter 1

Chapter 2

Chapter 3

Chapter 4

Chapter 5

Chapter 6

Chapter 7

Chapter 8

Appendices

List of tables

Chapter 2

Chapter 3

Chapter 4

Chapter 5

Chapter 6

Chapter 7

List of symbols

A	Area of the sediment column in the falling head permeability test
a	Permeability parameter obtained from the expression k=exp(ae+b)
a_{max}	Maximum horizontal acceleration at the ground surface
ADCP	Acoustic Doppler Current Profiler
AW	Atlantic Water
β	Slope angle
b	Permeability parameter obtained from the expression k=exp(ae+b)
BP	Before Present in ages/ Back Pressure in triaxial tests
CAUC	Consolidated Anisotropic Undrained Compression (triaxial tests)
c	Cohesion
c'	Effective cohesion
C_c	Compression index
CDS	Contourite Depositional System
CPTU	Cone Penetrometer Test with pore pressure measurements
CRR	Cyclic Resistance Ratio
CSR	Cyclic Stress Ratio
CU	Consolidated Undrained (triaxial tests)
Δd	Axial displacement in oedometer tests
Δe	Change in void ratio
Δh	Change in thickness of the sediment in compaction correction
Δl	Change in height of water in the burette in the falling head permeability test
$\Delta\sigma'_v$	Increment of the vertical effective stress in compaction correction
Δu	Excess pore pressure (in CPTU)
d	Sample heigh in oedometer tests
e	Void ratio
e_i	Initial void ratio in oedometer tests
e_0	Reference void ratio for compaction correction
EMDW	*E*astern Mediterranean Deep Water
FOS	Factor Of Safety
f_s	Sleeve friction
γ_s	Unit weight of the sediment
g	Gravity acceleration
h	Thickness of the sediment in compaction correction
h_d	Decompacted thickness of the sediment
κ	Von Karman constant
k	Permeability
K_0	Lateral earth pressure
kyr	Kiloyears
λ	Compression index (C_c/2.3)
LIW	Levantine Intermediate Water
l_0	Initial height of water in the burette in the falling head permeability test
l_1	Final height of water in the burette in the falling head permeability test
L	Length of the sediment column in the falling head permeability test
LL	Liquid Limit
mbsf	Meters below the seafloor
MSCL	Multi-Sensor Core Logger
MTD	Mass Transport Deposit

Myr	Million years
n	Porosity
n_0	Initial porosity
N_{kt}	Specific factor of the soil to calculate *Su* from q_t
$N_{\sigma t}$	Specific factor of the soil to calculate σ'_p from q_{net}
OCD	Overconsolidation Difference
OCR	Overconsolidation Ratio
PGA	Peak Ground Acceleration
PI	Plasticity Index
PL	Plastic Limit
q_c	Cone resistance
q_{net}	Net cone resistance
q_t	Corrected cone resistance
ρ_s	Density of the sediment
ρ_{solid}	Density of the sediment solid fraction
ρ_{water}/ ρ_w	Density of water
r_d	Stress reduction factor
σ_1	Axial stress (in triaxial tests)
σ_3	Cell pressure, also called radial stress or confining pressure (in triaxial tests)
σ_v	Total vertical stress
σ'_H	Horizontal effective stress
σ'_p	Preconsolidation effective stress
σ'_v	Vertical effective stress
σ'_{v0}	Reference vertical effective stress for compaction correction
S_t	Sensitivity
SBP	Sub-bottom profiler
Su	Undrained Shear Strength
Su_p	Peak Undrained Shear Strength
Su_r	Residual Undrained Shear Strength
SYSIF	*Système Sismique Fond* (Deep-towed seismic system)
τ	Bed layer shear stress/ Bottom shear stress (also BSS)
τ_{av}	Average cyclic shear stress
TDW	Tyrrhenian Dense Water
φ	Internal friction angle
φ'	Effective internal friction angle
u_2	Pore pressure (in CPTU measurements)
uh	Hydrostatic pressure (in CPTU measurements)
w	Moisture content
w.d.	Water depth
w_d	Dry sediment mass
w_w	Wet sediment mass
WIW	Western Intermediate Water
WMDW	Western Mediterranean Deep Water
XRD	X-Ray Diffraction
XRF	X-Ray Fluorescence
u^*	Friction velocity
υ	Poisson ratio
ψ	Angle of dilatancy
z	Depth below the seafloor (in CPTU measurement) or water depth (in the hydrodynamic model)

CHAPTER 1. Introduction

CHAPITRE 1. Introduction

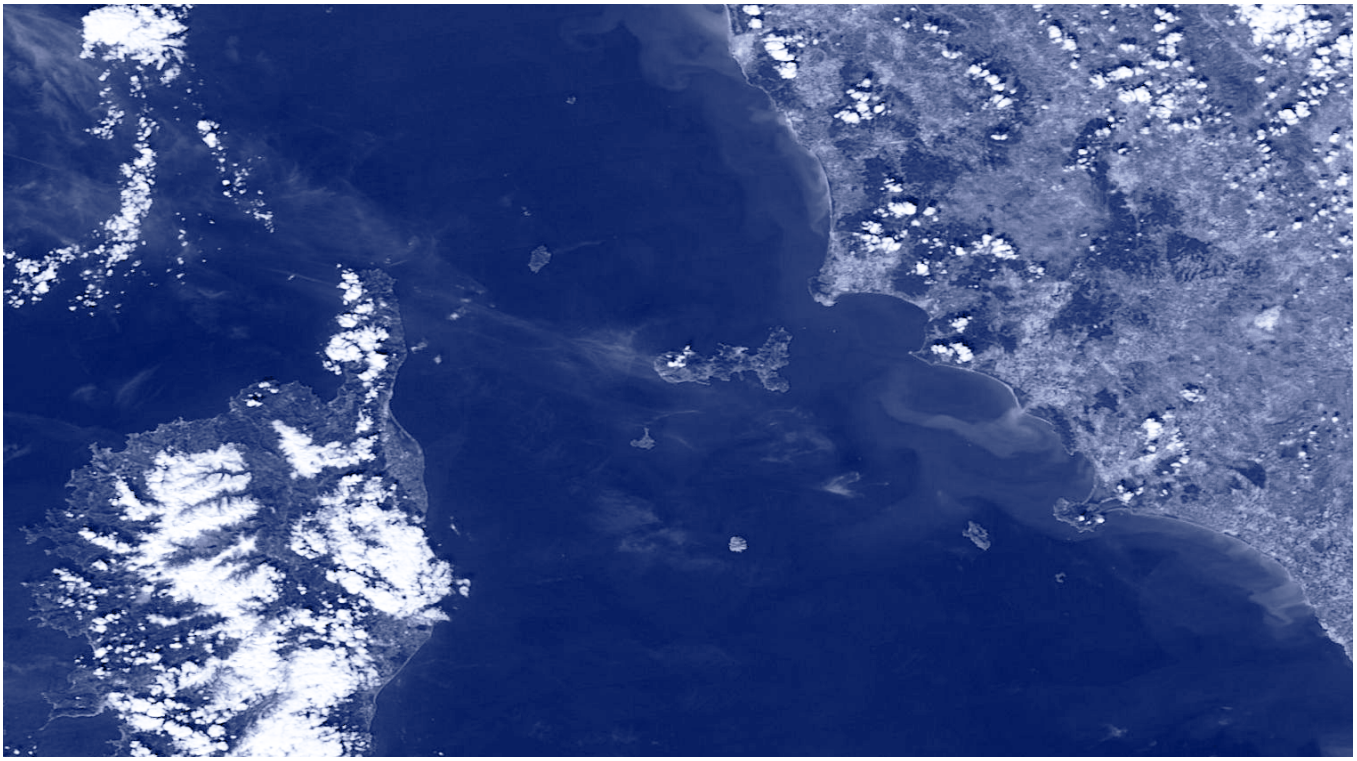

NASA worldview 2013-03-13. Modified colours

1.1. General background and purpose of the PhD thesis

The northern Tyrrhenian Sea has been poorly studied in terms of marine geohazards, even if the presence of repeated submarine landslides along tectonic structures, such as the Pianosa Ridge (between Corsica and the Tuscan Archipelago), was already known. The study of marine geohazards in the Mediterranean Sea and the study of the association of submarine landslides with turbidites and contourites are two reasons why the oceanographic surveys PRISME2, PAMELA-PAPRICA and PRISME3 were carried out in the area in 2013. The data obtained during these cruises were available for the present PhD project in order to achieve the following objectives:

1. Identify the morphological and sedimentological characteristics of the submarine landslides and the contourites present in the Corsica Trough and along the Pianosa Ridge (Northern Tyrrhenian Sea).
2. Determine the chronostratigraphic framework of the submarine landslides and establish stratigraphic relations with the contourites.
3. Determine the evolutionary setting and the factors controlling the formation of the contourites.
4. Identify the possible presence of weak layers in the sedimentary record and reconstruct the mechanisms that control the formation of submarine landslides, using geotechnical measurements and numerical modelling.

The present study is based on an integrated and complete approach, necessary for fully understanding the processes involved in slope instability. The study is based on geophysical data (multibeam bathymetry and high resolution seismic reflection data), sediment cores that followed a sedimentological and a geotechnical analysis, geotechnical in situ measurements, slope stability modelling, as well as the integration of oceanographic circulation modelling in the seafloor analysis.

Previous studies in the Corsica Trough were mainly focused on the analysis of the turbidites from the Golo Turbidite Network, first only offshore (Gervais, 2002; Gervais et al., 2004; Gervais et al., 2006; Deptuck et al., 2008), and some years later also onshore in a source-to-sink approach (Sømme et al., 2011; Calvès et al., 2013; Freslon, 2015). In addition, other studies in paleoceanography (Toucanne et al., 2012; Mintoʻo et al., 2015) and paleoclimatology (Toucanne et al., 2015) were done in the Corsica Trough providing a good stratigraphic and paleoceanographic framework. The GDEC4-2 is a borehole drilled on the western flank of the Corsica Trough during the GOLODRILL cruise by the R/V 'Bavenit' (FUGRO) in 2009. It has a very well constrained chronostratigraphy that covers the last 547 kyr (Toucanne et al., 2015). It has been used for correlation with the newly acquired data on the eastern flank of the Corsica Trough (i.e. on the Pianosa Ridge), a zone not studied in detail in the past, although the presence of submarine landslides and contourites had already being recognised with the previous data sets (Gervais et al., 2006; Cattaneo et al., 2014). The present study permits to complete the comprehension of this area of the western Mediterranean Sea in a way that is rarely achieved in other sedimentary basins.

1.2. Scientific questions

Hereby we expose the main scientific discussions that inspired the present project. They are summarised in final scientific questions, that led us to the development of the present manuscript:

1.2.1. On the importance of studying submarine landslides

Submarine landslides are much larger than landslides on land (Hampton et al., 1996; Vanneste et al., 2006) and they transport large amounts of sediment to the deep ocean (Masson et al., 2006). The Storegga Slide offshore Norway is one of the largest submarine landslides in the world with a surface three times larger than Brittany (Haflidason et al., 2005). The amount of sediment involved in the Storegga slide could cover the whole surface of France with 5 m of sediment. This volume is 300 times the sediment flux transported every year to the ocean by all the rivers of the world (Talling et al., 2014). Submarine landslides can have an important economical and societal impact since they may damage seafloor infrastructures, such as offshore platforms, pipelines, telecommunication cables... (Carter et al., 2014), and may generate devastating tsunamis (Bondevik et al., 2005; Tappin et al., 2001). Nowadays more than 95 % of the global internet traffic goes through seafloor telecommunication cables (Urlaub et

al., 2013) and it is thus important to know the risks at the sites where they are deployed. Even small slope failures can have catastrophic consequences when they take place near the coast. In 1979 part of the Nice airport collapsed into the sea and generated a 2-3 m high tsunami wave (Gennesseaux et al., 1980). This landslide caused the loss of human lives and important material damages. The coasts of the Mediterranean Sea have a dense population with many buildings and infrastructures close to the sea. Therefore, they are very vulnerable to submarine and coastal geological hazards. The present study is focused in the eastern margin of the Corsica Trough in the Northern Tyrrhenian Sea, an area poorly studied until present off the eastern coast of Corsica and west of the Tuscan Archipelago.

- What is the size of the submarine landslides along the Pianosa Ridge?
- Is there a high geological risk for the Corsica Island and the Tuscan Archipelago?

1.2.2. External factors controlling slope instability

A particularity of submarine landslides compared to terrestrial landslides is that they can develop in low seafloor gradients of less than 2° (Urlaub et al., 2013). The mechanisms that control submarine slope failure are still not well constrained, despite being the key to solve the problem of future prediction. Some of the factors that precondition slope failure can be rapid accumulation of impermeable sediment that generates excess pore pressure (Leynaud et al., 2007; Masson et al., 2010), the presence of free gas in the sediment (Wheeler, 1988; Lafuerza et al., 2012), steep slope gradients (Fell et al., 2008), the presence of sediment layers susceptible to liquefaction (Robertson, 2004; Boulanger and Idriss, 2006) or the presence of weak layers within the sediment column (Locat et al., 2014). These factors make the slope susceptible to failure in the long term, but they do not initiate the mass movement. Earthquakes are often invoked as a triggering factor, but some recent large earthquakes did not generate widespread slope failures (Sumner et al., 2013; Völker et al., 2011) and submarine landslides tend to be smaller in tectonically active margins (Urgeles et al., 2013). Other factors at the origin of slope failures can be tectonic movements such as folding (Morley, 2009) or faulting (Wright and Rathje, 2003), basal erosion or undercutting (Sultan et al., 2007) and gas hydrate dissociation (Hühnerbach and Masson, 2004).

A good understanding of the timing and frequency of submarine landslides can help determine the controlling factors of slope instability and also try to predict geohazards in the context of the present and future global warming. Some authors propose that the frequency of large submarine landslides may increase due to gas hydrate dissociation (Maslin et al., 1998; Tappin, 2010). Sea level changes have been considered to play a role in preconditioning or triggering mass-wasting processes (Lee, 2009). It has been suggested a higher occurrence of slope failures during periods of sea level low-stand and sea level rise (Maslin et al., 2004; Owen et al., 2007; Lee, 2009; Leynaud et al., 2009; Urgeles et al., 2013). However, most recent analyses that take into account the age uncertainties in a global (Urlaub et al., 2013) and a regional (Clare et al., 2014) data set suggest that the distribution of landslides is temporally random. Pope et al. (2015) pointed out that there are not enough well-dated large submarine landslides to determine if they are random and also that global studies that include different preconditioning and triggering factors result in a random combined data set. Therefore, it is very important to do an effort in dating, mapping and analysing the size and controlling factors in all known submarine landslides, so that a more complete and detailed data base can be constructed in the future that help better understand the formation of slope failures.

- What are the predisposing and triggering factors of submarine landslides in the Corsica Trough?
- Is there a climatic control of slope instability along the Pianosa Ridge? What is the frequency of the submarine landslides?
- Is the size and frequency of submarine landslides related to the slope gradient?

1.2.3. The role of contourites in slope instability

The analysis of the sedimentological and geotechnical properties is essential to identify possible weak layers, where the failure surface may focus. Bryn et al. (2005a) and Laberg et al. (2002) reported that the basal failure surfaces of the Storegga and the Trænadjupet Slides (offshore Norway) were located within contourite deposits. Contourites are the sediments deposited by the action of bottom currents (Stow and Faugères,

2008). The fine-grained contourites offshore Norway were found to be weaker and more sensitive (with a decrease in shear strength with increasing strain) than the glacigenic sediments (Baeten et al., 2014; Laberg et al., 2016). The development of contourite drifts and slope instabilities are common processes along continental margins (Laberg and Camerlenghi, 2008). Multiple cases of destabilised contouritic deposits have been also identified in the Mediterranean Sea: along the Pianosa Ridge (Cattaneo et al., 2014), in the Gela Basin (Minisini et al., 2007; Minisini and Trincardi, 2009) and in the Central Adriatic Basin (Dalla Valle et al., 2013; Dalla Valle et al., 2015; Pellegrini et al., 2015).

Laberg and Camerlenghi (2008) argued that contourites have particular properties that make them susceptible to slope instability because:

5. They are well-sorted sandy sediments that may liquefy under cyclic loading due to an earthquake.
6. They often present higher sedimentation rates than pelagites and hemipelagites, resulting in high water content, underconsolidation and thus low shear strength.
7. In high-latitude margins they can be sandwiched between glacigenic sediment that was deposited very fast, generating excess pore pressure within the contourites.
8. There may be a strength reduction due to the presence of gas in the contourites, since contourites develop along continental margins, zones with relatively high organic carbon content that can potentially form gas.

However, these arguments are not very convincing since similar characteristics and processes could be applied to hemipelagic sediments (formed by vertical particle settling and thus not under the influence of currents) that are also commonly present along continental margins. More effort needs to be done in comparing the sedimentological and geotechnical properties of contourites and hemipelagites to demonstrate if they really present distinctive mechanical behaviours. To better understand how contourites may influence slope instability, it is very important to characterise the oceanographic processes related to their development, the origin of the sediment that forms the contourites, the sedimentation rates and their variability in time, as well as the morphology and distribution on the slope of the contourite drifts and their associated erosive features.

- Do contourites have intrinsic or inherited properties that make them susceptible to slope failure?
- What are the sedimentation rates in contourites? What is the origin of the sediment? How is the morphology and geological evolution of contourites?
- What is the intensity and variability of the currents that control the formation of the contourites?

1.3. Geological context

The Corsica Trough is a narrow basin located in the Northern Tyrrhenian Sea, flanked to the west by the Corsica Island and to the east by the Tuscan Shelf and the Pianosa Ridge (also known as Elba Ridge or Elba-Pianosa Ridge; Fig. 1.1). This basin connects the Ligurian and Tyrrhenian Seas. It is a N–S trending basin, about 100 km long and 10–35 km wide at depth

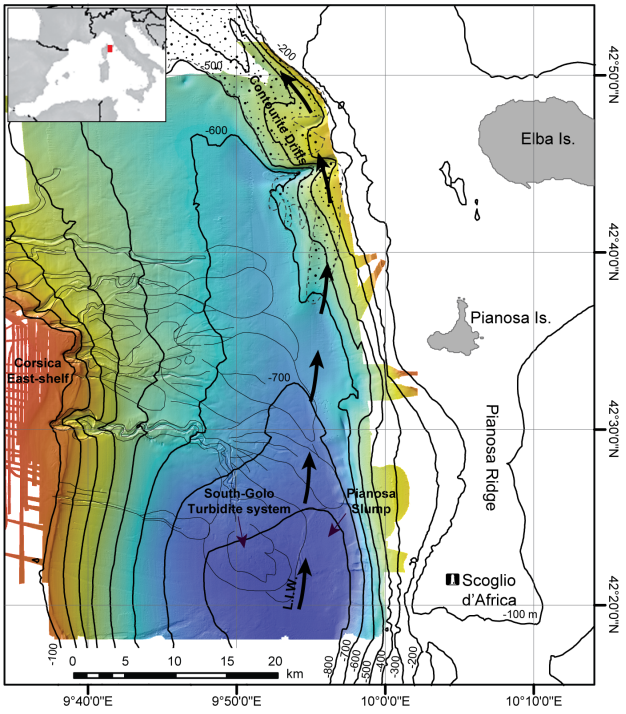

Fig. 1.1. Bathymetric map of the Corsica Trough after Cattaneo et al. (2014) showing the steep morphology of the Pianosa Ridge with contourites (polygons with dots from Roveri, 2002) in contrast with the western side dominated by turbidite systems (outlined in grey from Deptuck et al., 2008). The arrows represent the Levantine Intermediate Water (LIW) flowing northwards.

of the shelf edge. It has a maximum depth of 900 m in the southern part, becoming shallower towards the north (Fig. 1.1).

The Corsica Trough is an asymmetric in morphology and Plio-Quaternary sedimentary processes (Fig. 1.1). The western flank of the basin has a gentle slope (mean values between 2° and 3°), while the eastern flank, formed by the Pianosa Ridge, has steeper slopes (between 3° and 10°, reaching 20° locally). The western part of the Corsica Trough is dominated by downslope gravity-driven depositional processes that resulted in the formation of the Golo turbidite network (Fig. 1.1; Gervais et al., 2004; Gervais et al., 2006; Deptuck et al., 2008; Calvès et al., 2013). On the other side, the Pianosa Ridge is characterised by both alongslope processes, resulting in contourite drifts (Fig. 1.1; Marani et al., 1993; Roveri, 2002; Cattaneo et al., 2014), and downslope mass-wasting processes (Fig. 1.1; Cattaneo al., 2014). The extension of the contourites shown in Figure 1.1 is based on the study done by Roveri (2002). The present PhD project allowed a better characterisation of this contourite system and the identification of contourite drifts further south along the Pianosa Ridge. This topic will be detailed in Chapter 4. The trajectory of the Levantine Intermediate Water (LIW) is also oversimplified in Figure 1.1. Chapter 5 will show a more complex circulation of the LIW near the seafloor.

The Corsica Trough developed during the opening of the Northern Tyrrhenian Sea, between the late Burdigalian and Langhian (Zitellini et al., 1986), resulting in the formation of a half graben (Fig. 1.2; Pascucci, 2002). The Pianosa Ridge, that is a magmatic and metamorphic ridge (Pandeli et al., 2010), corresponds to a tilted block of the half graben, with the master fault located on the Corsican side of the basin (Fig. 1.2; Pascucci, 2002), and separates the Corsica Trough from the Tuscan Shelf (Figs. 1.2; 1.3). Several N–S and NW–SE trending basins can be found in the Tuscan Shelf (Fig. 1.3; Pascucci et al., 2007), trapping a great part of the sediment from Italy (Roveri, 2002). They developed on a thrust substrate locally dissected by normal faults (Bartole, 1995).

The Tuscan Magmatic Province is formed by acidic to mafic intrusive and extrusive zones located in southern Tuscany, northern Latium and the Tuscan Archipelago (Dini et al., 2002). The materials are mainly plutonic granitoid rocks (e.g. in the Elba Island and

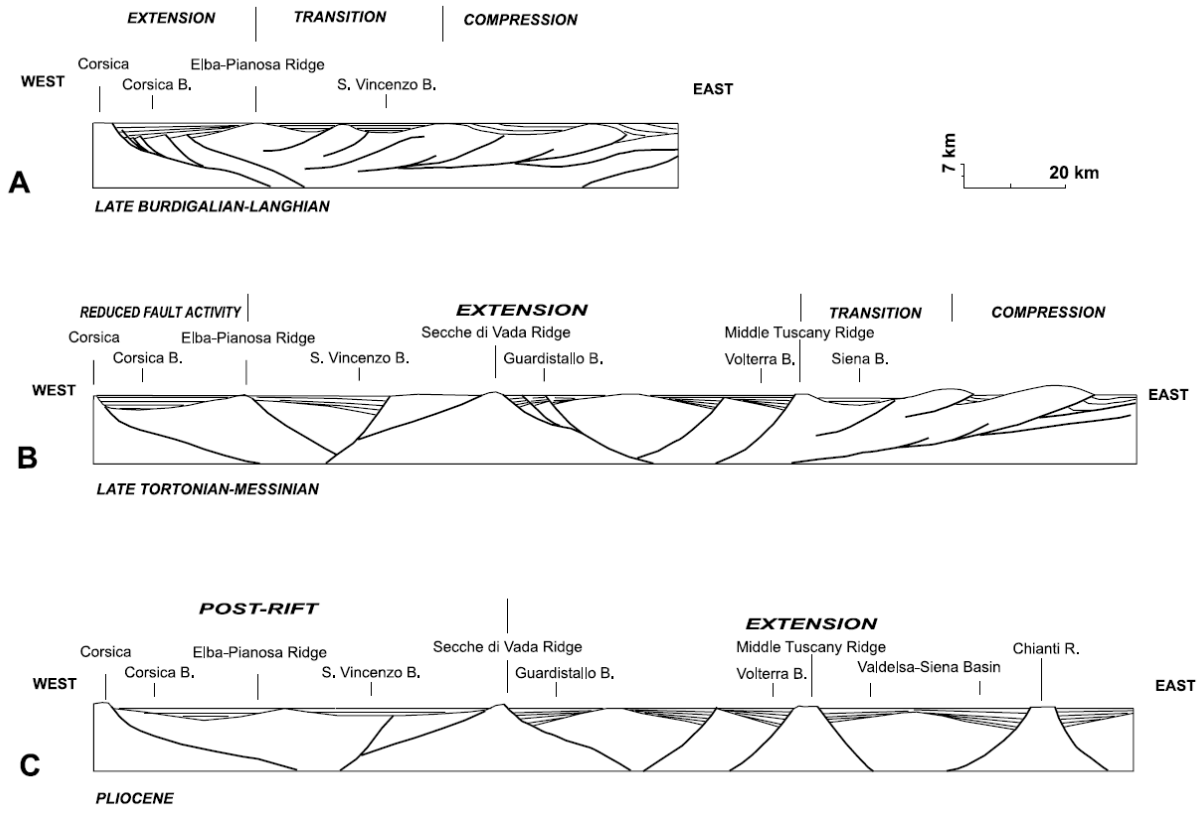

Fig. 1.2. Cross-sections showing the evolution of the Corsica Basin-Tuscan-Shelf-Western-Tuscany system. (A) Late Burdigalian-Langhian, (B) late Tortonian, (C) Early Pliocene (Pascucci, 2002).

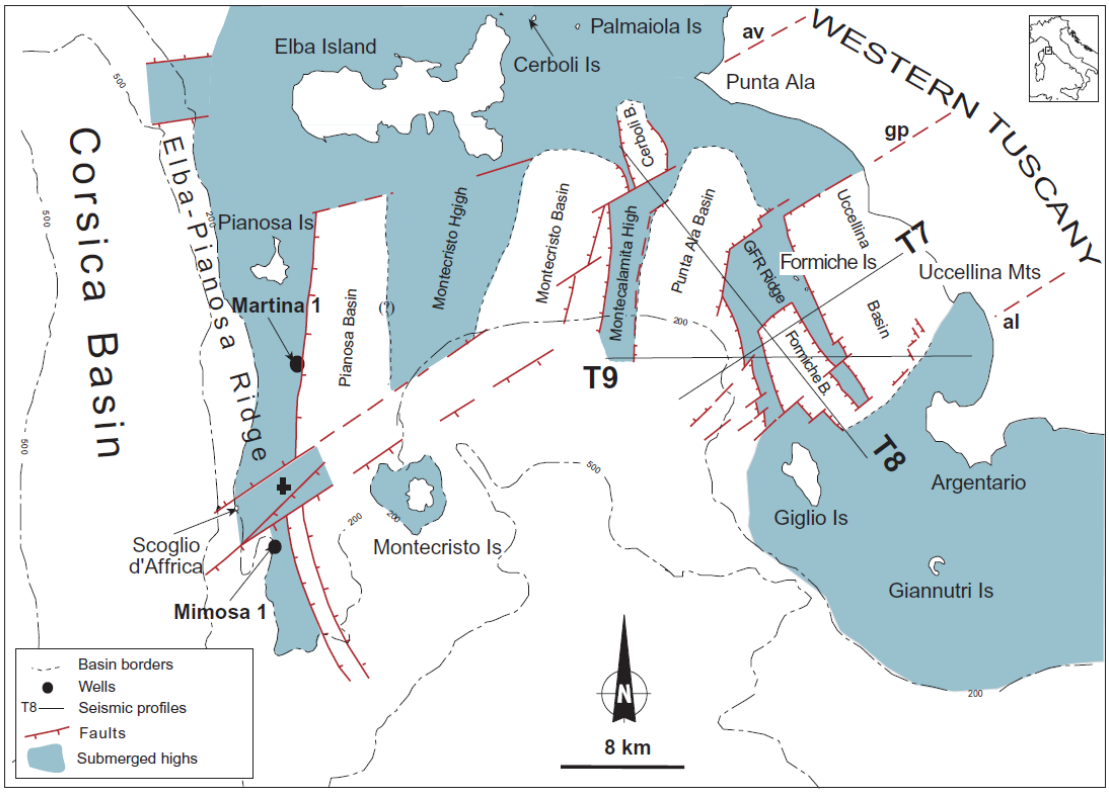

Fig. 1.3. Generalised structural map showing the main faults, basins and submerged highs present in the Tuscan Shelf (Pascucci et al., 2007).

in the Montecristo Island), but also subvolcanic porphyric dykes, sills and laccoliths in the Elba Island and volcanic rocks, for instance in the Capraia Island, in S. Vincenzo, Roccastrada and Amiata (Dini et al., 2002). The magmatic activity started first at the west at 14 Myr in Sisco (northeast Corsica) and moved then eastwards with a phase at the Elba Island, Montecristo Island and Capratia Island at 8.4-5.9 Ma and a final phase onland, in Tuscany, at 1.3-0.2 Ma (Dini et al., 2002).

The present-day seismicity in the Corsica Trough is considered to be very low (Scisciani and Calamita, 2009). The maximum horizontal acceleration (a_{max}) or Peak Ground Acceleration (*PGA*) given for the Corsica Trough for a 475 year return period by the Global Seismic Hazard Assessment Program is lower than 0.4 $m{\cdot}s^{-2}$ (Fig. 1.4; Slejko et al., 1999). Moreover, Pascucci et al. (1999) and Pascucci (2002) argued that the Corsica Trough entered in a post-rift phase from the late Messinian (Fig. 1.2), suggesting that the tectonic activity has been low during the Plio-Quaternary, that is the period of time studied in the present PhD project.

At the end of the Miocene, between 5.97 and 5.33 Myr, the Messinian Salinity Crisis affected the whole Mediterranean area and caused large environmental changes as a result of geodynamic and climatic forcings that lead to major erosion and important evaporitic deposits (Roveri et al., 2014; and references therein). During the Messinian Salinity crisis, the Corsica Trough was a perched lake, isolated from the deeper

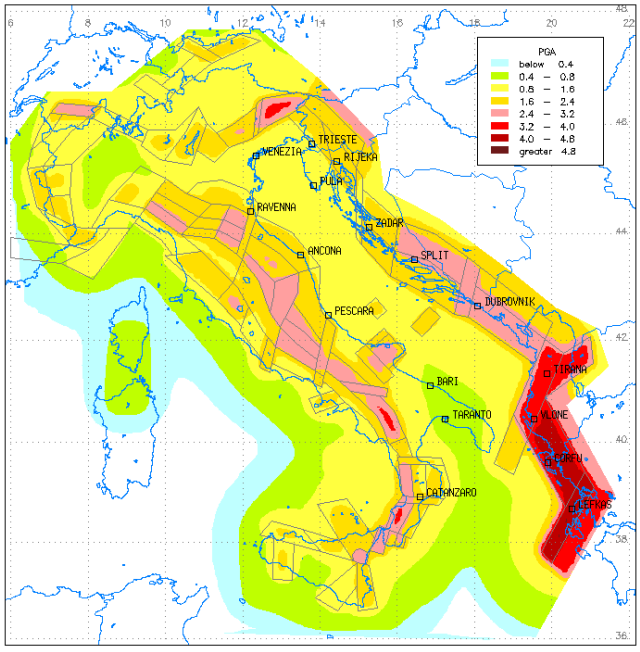

Fig. 1.4. Peak Ground Acceleration (PGA in $m{\cdot}s^{-2}$) with a 475-year return period for Adria (Slejko et al., 1999).

Tyrrhenian basins (Thinon et al., 2016). At the end of the Messinian Salinity Crisis, the Corsica Trough was connected with the Thyrrhenian Basin, generating a network of incised valleys (Thinon et al., 2016). The end of the Messinian Salinity Crisis corresponds to a seismic discontinuity that can be clearly identified in the seismic reflection data due to the high lithological contrast with the Pliocence sediments deposited during the reflooding of the basin (Thinon et al., 2016).

1.4. Structure and contents of the manuscript

The present document is composed of 5 main chapters (Chapters 3-7) that are coherent and complete separately, so that they can be understood independently. A short introduction with the problematic and aims, as well as a geologic and oceanographic context, are provided in every chapter according to the needs of the topic. But to avoid repetitions and for more clarity, the materials and methods used in all the project are combined in a single chapter (Chapter 2). The chapters are distributed in a logic sequence, in order to acquire at each step useful information for the following chapters (Fig. 1.5). First the submarine landslides are identified,mapped, geometrically characterised and we determine their chronology and frequency. Then, the

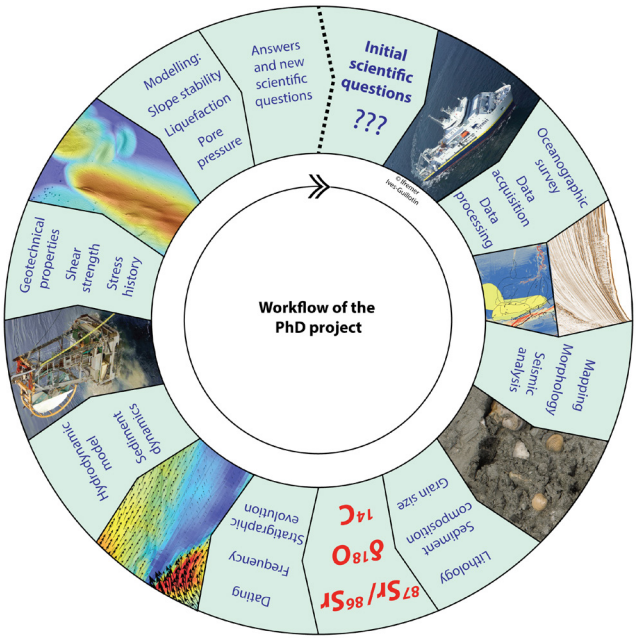

Fig. 1.5. Workflow of the PhD project with the different topics placed in the same order as in the chapters of the manuscript.

contourites are also mapped, we study their morphology, lithology and evolution during the Plio-Quaternary. Afterwards, we analyse the oceanographic processes that control their development to better constrain the erosional and depositional processes. In the following step we study the sedimentological and geotechnical properties of contourites and how they might be related to slope instability, using data and numerical modelling. Finally, we study the properties of a weak layer and we model the formation of a failure surface, also using numerical modelling based on observations from our dataset.

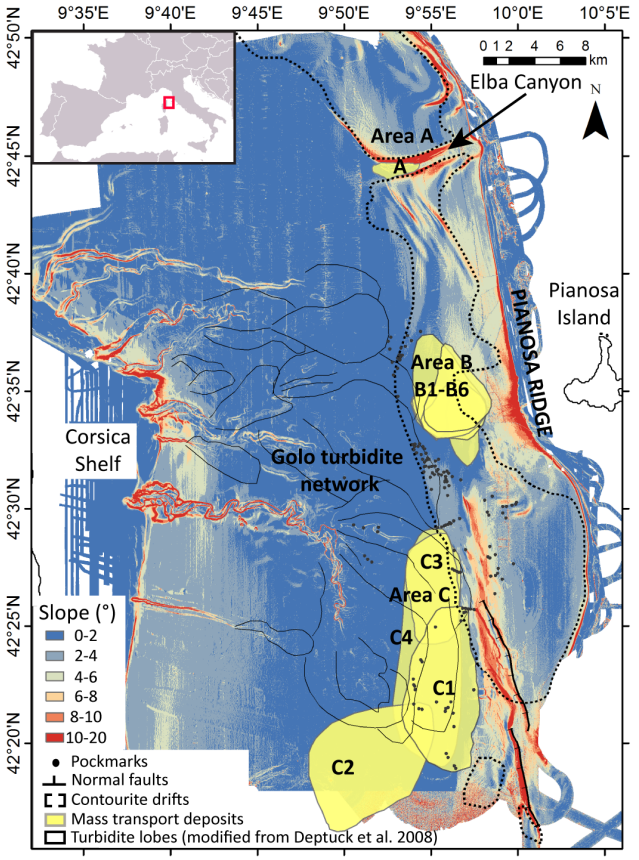

Area	Name	Volume (km^3)	Maximum runout (km)	Maximum length (km)	Maximum width (km)	Width/Length ratio	Age (kyr BP)
A	A	0.10	1.5	1.2	3.6	3.0	<12
B	B1	0.19	7.0	5.7	7.6	1.3	42-59
	B2	0.09	8.0	5.6	4.6	0.8	125-137
	B3	0.26	7.5	5.9	7.2	1.2	420-437
	B4	0.15	4.2	2.5	7.4	3.0	452->542
	B5	0.05	6.0	3.4	4.4	1.3	>542
	B6	0.04	6.2	3.6	4.4	1.2	>542
C	C1	2.62	9.0	6.0	13.5	2.3	42-50
	C2	0.47	16.0	10.0	7.8	0.8	125-160
	C3	0.67	6.0	4.0	8.7	2.2	265-321
	C4	1.86	10.4	5.3	18.6	3.5	321-380

Fig. 1.6. Graphic abstract of Chapter 3 showing the location and extension of the submarine landslides on the slope gradient map, and a table with their size and age.

- *Chapter 2: Materials and methods*

All the materials and methods used in the whole project are explained in detail in Chapter 2. The dataset is composed of multibeam bathymetry, high resolution seismic data, Acoutic Doppler Current Profiler (ADCP), sediment cores and Cone Penetration Tests with pore pressure measurement (CPTU). We also used a hydrodynamic model, a 1D and a 2D slope stability model, a 1D consolidation model and a model for liquefaction potential assessment.

- *Chapter 3: Morphology, spatial distribution and age of submarine landslides*

Chapter 3 focuses on the identification of the submarine landslides, their characterisation and their age (Fig. 1.6). It provides basic information for more detailed further analyses. Part of this chapter has been published with the title *"Implications of Sediment Dynamics in Mass Transport along the Pianosa Ridge (Northern Tyrrhenian Sea)"* in *Submarine Mass Movements and Their Consequences 7th International Symposium*:

Miramontes, E., Cattaneo, A., Jouet, G., Garziglia, S. (2016). Implications of sediment dynamics in mass transport along the Pianosa Ridge (Northern Tyrrhenian Sea). In Lamarche, G., Mountjoy, J., Bull, S., Hubble, T., Krastel, S., Lane, E., Micallef, A., Moscardelli, L., Mueller, C., Pecher, I., Woelz, S. (Eds.), Submarine mass movements and their consequences, Dordrecht, The Netherlands, Advances in Natural Hazard Research, Springer, 30, 301–309.

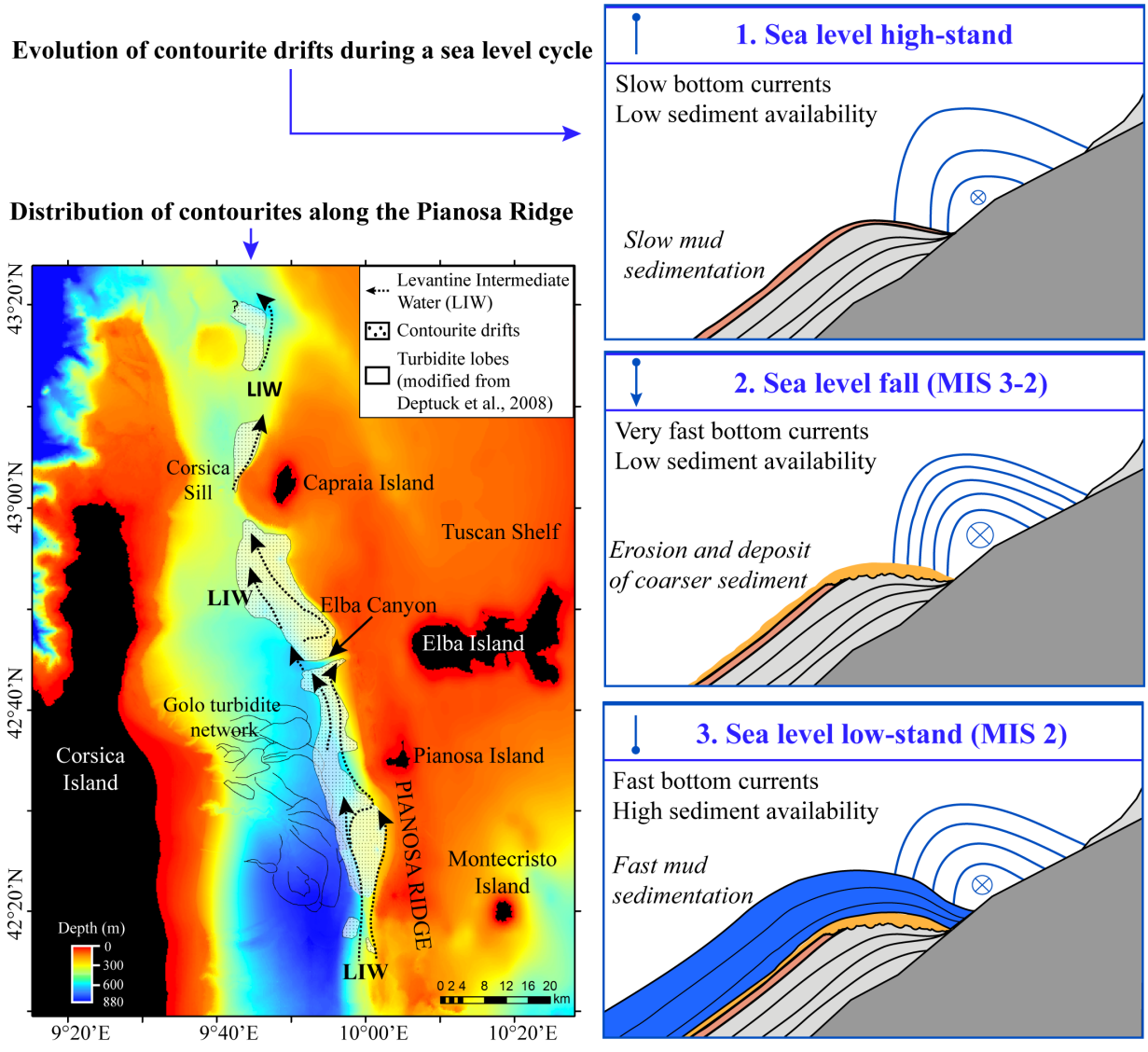

Fig. 1.7. Graphic abstract of Chapter 4 showing the location and extension of the contourites along the Pianosa Ridge, and a scheme explaining the evolution of contourite drifts during a sea level cycle.

- *Chapter 4: The Pianosa Contourite Depositional System (Northern Tyrrhenian Sea): drift morphology and Plio-Quaternary stratigraphic evolution*

For the understanding of slope instability, it is important to characterise the morphology and lithology of the sediment bodies where mass wasting processes were initiated, in this case the contourites. Chapter 4 aims to provide useful information about the morphology, lithology and evolution of the contourites during the Plio-Quaternary (Fig. 1.7). This study on contourites has been developed with the objective of constraining the sedimentological context of submarine landslides in the Corsica Trough, but it may be also useful for other studies focused on sediment transport, contouritic processes and sedimentary evolution of continental margins. This chapter has been published in the journal *Marine Geology* with the same title as the chapter:

Miramontes, E., Cattaneo, A., Jouet, G., Théreau, E., Thomas, Y., Rovere, M., Cauquil, E., Trincardi, F. (2016). The Pianosa Contourite Depositional System (Northern Tyrrhenian Sea): Drift morphology and Plio-Quaternary stratigraphic evolution. Marine Geology, 378, 20-42.

- *Chapter 5: New insights on the formation of contourites from hydrodynamic modelling in the North Western Mediterranean Sea*

Chapter 5 focuses on the oceanographic processes that control the formation of contourites. Since a contouritic environment presents zones of erosion that may generate basal erosion in the slope and thus trigger submarine landslides, it is important to know when and in which zones erosive processes may be enhanced. Moreover, bottom currents are one of the main processes shaping continental margins and they can thus induce the formation of sediment drifts with steep slopes that could be potentially unstable. Therefore, we need to understand how bottom currents control the sediment distribution along continental margins (Fig. 1.8). This chapter is being currently prepared as a manuscript for submission in an international journal.

- *Chapter 6: Morphological control of slope instability in contourites: A geotechnical approach*

Chapter 6 summarises the sedimentological and geotechnical properties of contourites, comparing them to the hemipelagites present in the Corsica Trough. In this chapter we also propose some predisposing factors of slope instability in this margin. We analyse the

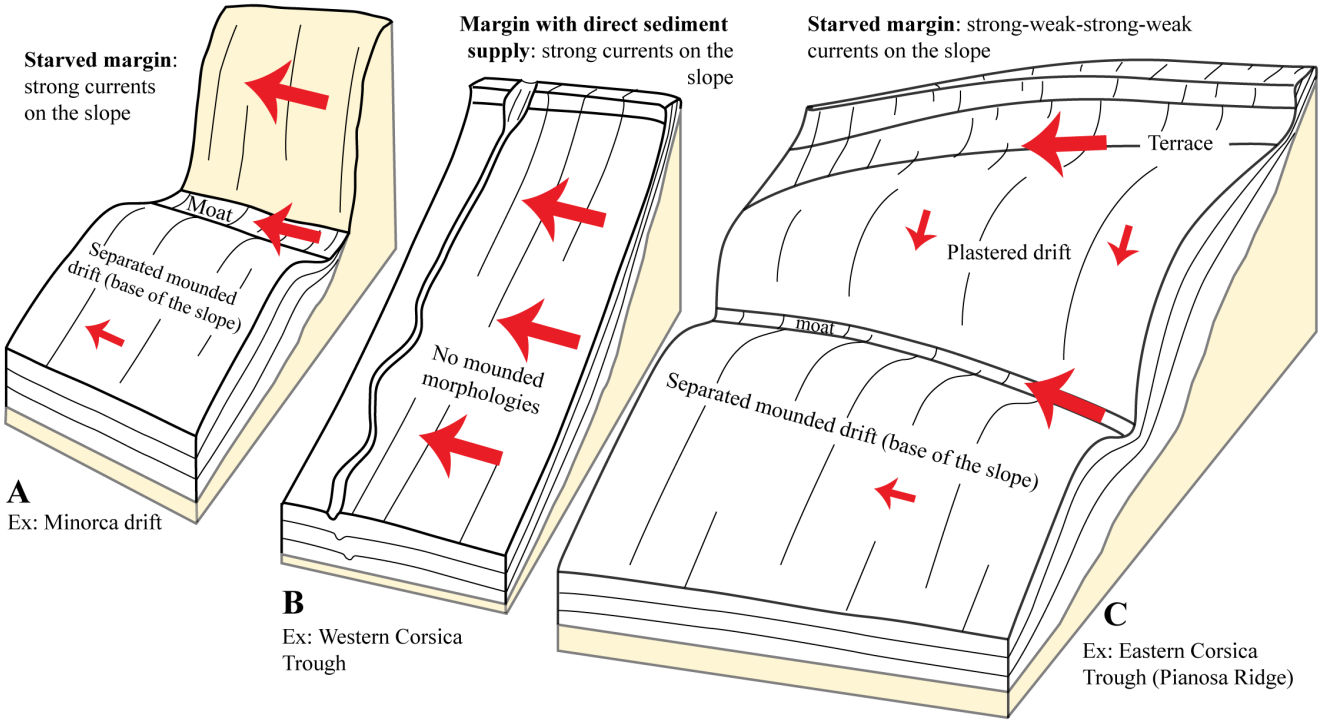

Fig. 1.8. Graphic abstract of Chapter 5 showing a conceptual model that explains the different types of contourite drifts and margin morphologies according to the distribution of bottom-current strength.

effects of sedimentation, seismicity and seafloor morphology on slope instability (Fig. 1.9). This chapter is being currently prepared for submission in an international journal.

- *Chapter 7: Altered volcanic deposits as basal failure surfaces of submarine landslides*

Chapter 7 focuses on the presence of a potential weak layer, on its characteristics, its origin and on the possible triggering factor (Fig. 1.10). This weak layer contains zeolites, product of the alteration of volcanic rocks, and presents a post-peak strain softening behaviour (loss of undrained shear strength with increasing strain). The triggering factor in this case is basal erosion at the foot of the slope. The information contained in this chapter is currently being corrected for the resubmission of the manuscript to *Geology*.

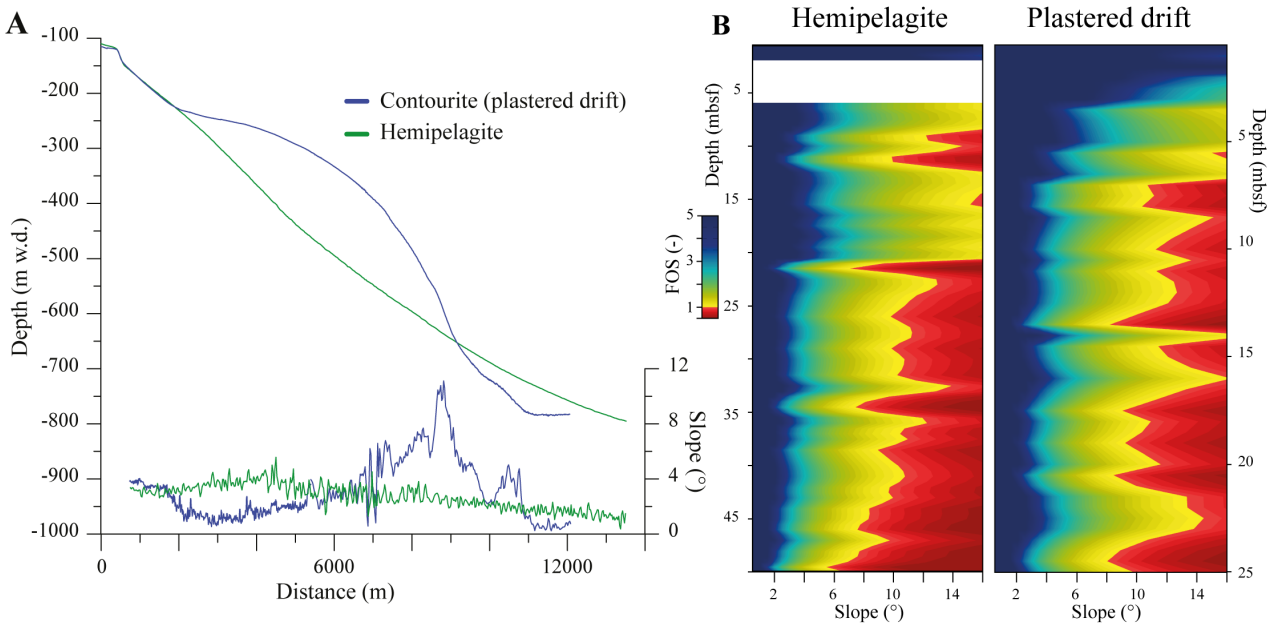

Fig. 1.9. Graphic abstract of Chapter 6 showing **(A)** the bathymetric profiles and slope gradients of a contouritic margin (blue) and a hemipelagic margin (green); and **(B)** the results of the slope stability analysis, with the Factor Of Safety (FOS) in function of depth and slope angle, obtained using the mechanical properties of hemipelagites and plastered drifts.

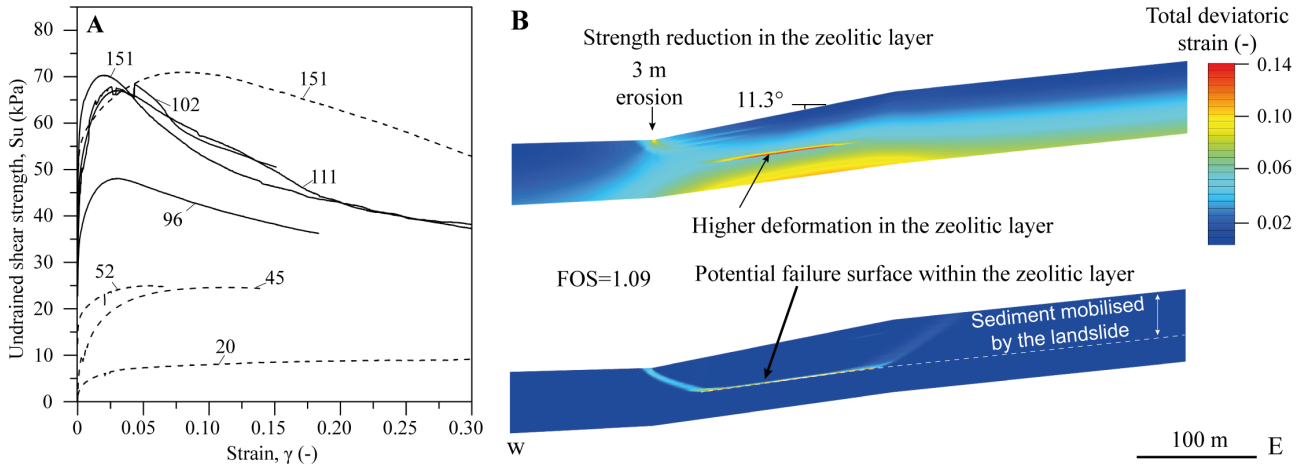

Fig. 1.10. Graphic abstract of Chapter 7 showing **(A)** the strain softening behaviour of the zeolitic layer (with the solid lines), and **(B)** the formation of a potential failure surface within the zeolitic layer due to a higher deformation of this layer caused by erosion.

1.1. Contexte générale et objectif de la thèse de doctorat

La Mer Tyrrhénienne septentrionale a été, jusqu'à maintenant, peu étudiée en termes d'aléas géologiques, même si la présence de glissements sous-marins le long de structures tectoniques, telles que la Ride de Pianosa (entre Corse et l'Archipel de la Toscane), était déjà bien connue. L'étude des aléas géologiques sous-marins en Mer Méditerranée et le lien potentiel entre des glissements sous-marins et la présence de turbidites et contourites ont été les deux principales motivations pour la réalisation en 2013 dans ce secteur de trois campagnes océanographiques PRISME2, PAMELA-PAPRICA et PRISME3. Les données obtenues lors de ces campagnes ont été disponibles au début de ce projet de thèse dont les quatre objectifs complémentaires consistaient à :

1. Identifier les caractéristiques morphologiques et sédimentologiques des glissements sous-marins et des contourites présents dans le Canal de Corse le long de la Ride de Pianosa (Mer Tyrrhénienne septentrionale).
2. Déterminer la chronologie des glissements sous-marins et établir les relations stratigraphiques avec les contourites.
3. Déterminer le cadre évolutif et les facteurs de contrôle de la formation des contourites.
4. Identifier la présence possible de couches de faiblesse dans l'archive sédimentaire et caractériser les mécanismes de contrôle de la formation de glissements sous-marins, à l'aide des mesures géotechniques et de la modélisation numérique.

Pour atteindre ces objectifs, une approche intégrée a été mise en œuvre en se basant sur des données géophysiques (bathymétrie multifaisceaux et sismique haute résolution), des mesures géotechniques *in situ*, des analyses sédimentologiques et géotechniques en laboratoire sur du sédiment collecté par carottage, des modélisations numériques de la stabilité des pentes et de la circulation des masses d'eau.

Les études précédentes dans le Canal de Corse se sont principalement concentrées sur l'analyse du fonctionnement du système turbiditique du Golo, d'abord en mer (Gervais, 2002; Gervais et al., 2004; Gervais et al., 2006; Deptuck et al., 2008), et quelques années plus tard à terre avec une approche de la source au dépôt sédimentaire, « *source-to-sink* » (Sømme et al., 2011; Calvès et al., 2013; Freslon, 2015). D'autres études récentes portant sur la paléocéanographie (Toucanne et al., 2012; Mintoʻo et al., 2015) et la paléoclimatologie (Toucanne et al., 2015) du Canal de Corse ont contribué à fournir un cadre stratigraphique et paléocéanographique propice à l'étude détaillée de la seconde moitié du Quaternaire de cette zone d'étude. Le forage GDEC4-2, réalisé en 2009 sur le flanc ouest du Canal de Corse (campagne GOLODRILL à bord du N/O 'Bavenit'-FUGRO), a permis de définir une chronostratigraphie précise des derniers 547 ka (Toucanne et al., 2015). Ce forage a été utilisé pour corréler les nouvelles données acquises le long du flanc est du Canal de Corse (Ride de Pianosa), une zone très peu étudiée dans le passé, même si la présence de glissements sous-marins avait déjà été reconnue avec les jeux de données plus anciens (Gervais et al., 2006; Cattaneo et al., 2014). Le travail ici présenté permet de compléter la compréhension de la sédimentologie de cette zone de la Méditerranée occidentale d'une façon rarement atteinte dans d'autres bassins sédimentaires.

1.2. Questions scientifiques

Ce paragraphe présente les principales thématiques scientifiques qui ont inspiré ce projet de thèse. Elles sont synthétisées par la suite sous forme de questions scientifiques, qui ont défini la structure et l'organisation du présent manuscrit :

1.2.1. L'importance de l'étude des glissements sous-marins

Les glissements sous-marins sont bien plus étendus que les glissements terrestres (Hampton et al., 1996; Vanneste et al., 2006) et contribuent au transport d'importantes quantités de sédiments vers l'océan profond (Masson et al., 2006). A titre d'exemple, le glissement sous-marin de Storegga, au large de la Norvège, est un des glissements les plus grands du monde avec une surface trois fois supérieure à celle de la Bretagne (Haflidason et al., 2005). La quantité de sédiment qu'il a remobilisé pourrait couvrir la surface de la France sur une épaisseur de 5 m. Ce volume correspond à 300 fois le flux sédimentaire annuel de tous les fleuves du monde vers l'océan (Talling et al., 2014). En outre, les glissements sous-marins peuvent endommager des infrastructures sous-marines servant

à la production de ressources naturelles ou à la télécommunication (Carter et al., 2014) et générer des tsunamis dévastateurs (Bondevik et al., 2005; Tappin et al., 2001). Le fait qu'actuellement plus de 95% du trafic d'internet international est assuré par des câbles sous-marins (Urlaub et al., 2013) souligne l'importance de la caractérisation des risques de glissements sous-marins auxquels ceux-ci peuvent être confrontés. L'effondrement du port en construction au large de l'aéroport de Nice et le tsunami meurtrier qui s'en suivit en 1979 demeurent de tristes exemples des conséquences humaines et socio-économiques que peuvent avoir les glissements sous-marins (Gennesseaux et al., 1980). Au-delà de cet évènement et de ce site, les fortes densités de population et d'infrastructures font des côtes méditerranéennes des zones dont la vulnérabilité aux phénomènes d'instabilité en milieu sous-marin nécessite d'être évaluée. C'est dans cette optique que cette étude a été menée sur la marge est du Canal de Corse, en Mer Tyrrhénienne septentrionale. Le fait que l'aléa glissement de terrain dans cette zone n'avait pas été le sujet d'analyses approfondies jusqu'à présent pose les questions suivantes :

- Quelle est la taille des glissements sous-marins le long de la Ride de Pianosa ?
- Existe-il un risque géologique élevé pour l'Île de Corse et pour l'Archipel de la Toscane ?

1.2.2. Facteurs externes de contrôle de l'instabilité des pentes

Une des particularités des glissements sous-marins est qu'ils peuvent se déclencher sur des pentes inférieures à 2° à la différence des glissements terrestres (Urlaub et al., 2013). Malgré ce constat, les mécanismes contrôlant l'instabilité des pentes sous-marines demeurent peu contraints, d'autant que les forts gradients de pente demeurent considérés comme le facteur principal d'instabilité (Fell et al., 2008). L'accumulation rapide de sédiment argileux peu perméable est donc communément reconnu comme un facteur favorisant la rupture en engendrant le développement de surpressions interstitielles et de fait la préservation de niveaux anormalement peu résistants (Leynaud et al., 2007; Masson et al., 2010). D'autres auteurs ont mis en évidence le rôle favorisant du chargement en gaz libre qui peut contribuer à réduire la résistance mécanique des sédiments (Wheeler, 1988; Lafuerza et al., 2012). Dans d'autres cas, la faible résistance mécanique peut être attribuée à une susceptibilité à la liquéfaction sous l'effet de séismes (Robertson, 2004; Boulanger and Idriss, 2006). Les séismes sont d'ailleurs fréquemment considérés comme le principal facteur déclenchant, même si de grands évènements récents ne semblent pas avoir eu de large pouvoir déstabilisant sur les fonds marins (Sumner et al., 2013; Völker et al., 2011) et si les volumes glissés ont tendance à être plus faibles sur les marges où la sismicité est élevée (Urgeles et al., 2013). Les autres facteurs communément invoqués comme déclencheur de glissement sous-marin incluent les mouvements tectoniques tels que la déformation plicative (Morley, 2009) ou celle liée aux failles (Wright and Rathje, 2003), l'érosion basale de la pente (Sultan et al., 2007) et la dissociation des hydrates de gaz (Hühnerbach and Masson, 2004).

Une meilleure compréhension de la chronologie et de la fréquence des glissements sous-marins peut aider à déterminer leur facteurs de contrôle et aider à quantifier les aléas associés dans le contexte du réchauffement climatique actuel et futur (Maslin et al., 1998; Tappin, 2010). Au chapitre de l'influence du climat, les variations du niveau marin sont en effet suspectés de pouvoir jouer un rôle important en tant que facteur favorisant et/ou déclenchant des mouvements en masse (Lee, 2009). Certains auteurs suggèrent une occurrence plus élevée des glissements pendant les périodes de bas et de remontée du niveau marin (Maslin et al., 2004; Owen et al., 2007; Lee, 2009; Leynaud et al., 2009; Urgeles et al., 2013). Cependant, des études récentes prenant en compte les incertitudes sur les âges avec un jeu de données global (Urlaub et al., 2013) et régional (Clare et al., 2014) suggèrent que la distribution des glissements dans le temps est aléatoire. Pope et al. (2015) ont de plus remarqué que la rareté des grands glissements convenablement datés ne permet pas de déterminer si leur distribution temporelle est aléatoire. Ce constat milite pour accentuer les efforts de datation, cartographie, analyse géométrique et de caractérisation des facteurs ayant participé au déclenchement de glissements sous-marins connus afin de construire une base de données détaillée. Dans cette perspective, cette étude envisage d'aborder les questions suivantes :

- Quels sont les facteurs prédisposants et déclenchants des glissements sous-marins dans le Canal de Corse ?

- Existe-il un contrôle climatique de l'instabilité de pente le long de la Ride de Pianosa ? Quelle est la fréquence des glissements sous-marins ?
- Est-ce que la taille et la fréquence des glissements sous-marins sont liées au gradient de pente ?

1.2.3. Le rôle des contourites dans l'instabilité des pentes

L'analyse des propriétés sédimentologiques et géotechniques est essentielle pour l'identification de couches de faiblesse où des surfaces de glissement peuvent se développer. Bryn et al. (2005a) et Laberg et al. (2002) ont montré que les surfaces basales des glissements de Storegga et Trænadjupet (au large de la Norvège) étaient localisées dans des dépôts contouritiques. Les contourites sont des sédiments déposés sous l'action des courants de fond (Stow and Faugères, 2008). Il a été démontré que les contourites vaseuses de la marge norvégienne sont mécaniquement moins résistantes et plus sensibles (sujettes à une perte importante de résistance lors de grandes déformations induites par le cisaillement) que les sédiments glaciogéniques (Baeten et al., 2014; Laberg et al., 2016). Le développement des contourites et des instabilités de pente sont des processus communs le long des marges continentales (Laberg and Camerlenghi, 2008). Plusieurs cas de dépôts contouritiques affectés par des glissements ont été identifiés en Mer Mediterranée : le long de la Ride de Pianosa (Cattaneo et al., 2014), dans le Basin de Gela (Minisini et al., 2007; Minisini and Trincardi, 2009) et dans la Mer Adriatique Centrale (Dalla Valle et al., 2013; Dalla Valle et al., 2015; Pellegrini et al., 2015).

Laberg et Camerlenghi (2008) ont argumenté que les contourites ont des propriétés particulières qui les rendent susceptibles de rompre car :

1. Elles sont constituées de sédiments sableux bien triés et donc susceptibles de se liquéfier sous la charge cyclique d'un séisme.
2. Elles présentent fréquemment des taux de sédimentation plus élevés que les pelagites ou hemipelagites, et elles ont donc des teneurs en eau plus élevées, elles sont sous-consolidées et plus faibles mécaniquement.
3. Dans les marges de hautes latitudes, les contourites peuvent se retrouver entre deux couches de sédiment glaciogénique déposé rapidement, ce qui peut générer le développement de surpressions interstitielles dans les contourites.
4. Leur résistance mécanique peut être affaiblie par la présence de gaz dans le sédiment dans les zones où la teneur en matière organique est forte.

Une partie de ces arguments n'est pas complétement convaincante puisque certaines des propriétés évoquées ne sont pas exclusivement caractéristiques des contourites mais peuvent aussi l'être des sédiments hémipélagiques (formés par décantation verticale des particules et donc sans influence des courants). Cette constatation a servi de point de départ à une analyse comparative des sédiments hémipélagiques et contouritiques du Canal de Corse afin de répondre aux questions suivantes :

- Est-ce que les contourites ont des propriétés intrinsèques ou héritées qui les rendent susceptibles à l'instabilité de pente ?
- Quels sont les taux d'accumulation des contourites ? Quelle est l'origine du sédiment? Quelle est la morphologie des contourites et comment évolue-t-elle ?
- Quelle est l'intensité et la variabilité des courants contrôlant la formation des contourites ?

1.3. Contexte géologique

Le Canal de Corse est un bassin étroit localisé en Mer Tyrrhénienne septentrionale, limité à l'ouest par l'Île de Corse et à l'est par le Plateau de la Toscane et la Ride de Pianosa (aussi connue comme Ride d'Elbe ou Ride d'Elbe-Pianosa ; Fig. 1.1). Ce bassin, de 100 km de longueur et 10-35 km de largeur au niveau du rebord du plateau, est orienté N-S et connecte la Mer Tyrrhénienne à la Mer Ligure. Alors que la profondeur maximale de 900 m est atteinte dans la partie méridionale du bassin, cette profondeur devient bien moins importante (~500 m) vers le nord (Fig. 1.1).

Le Canal de Corse est asymétrique en morphologie et en processus sédimentaires Plio-Quaternaires (Fig. 1.1). La pente du flanc ouest est assez faible (valeurs moyennes entre 2° et 3°), alors que le flanc est formé par la Ride de Pianosa présente des pentes plus raides (valeurs moyennes entre 3° et 10°, avec des valeurs localisées de 20°). Alors que la partie occidentale

du Canal de Corse est dominée par des processus gravitaires sont à l'origine du système turbiditique du Golo (Fig. 1.1 ; Gervais et al., 2004 ; Gervais et al., 2006 ; Deptuck et al., 2008 ; Calvès et al., 2013), la Ride de Pianosa se caractérise par l'impact des processus contouritiques (Fig. 1.1 ; Marani et al., 1993 ; Roveri, 2002 ; Cattaneo et al., 2014), et les processus de transport en masse (Fig. 1.1 ; Cattaneo et al., 2014). L'extension des contourites de la Figure 1.1 est basée sur l'étude de Roveri (2002). Le présent projet de doctorat a permis une meilleure caractérisation de ce système contouritique et l'identification des dépôts contouritiques plus au sud de la Ride de Pianosa. Cette thématique sera détaillée dans le Chapitre 4 de ce manuscrit. A noter que la trajectoire de l'Eau Levantine Intermédiaire présentée dans la Fig. 1.1 est trop simplifiée et la circulation complexe de cette masse d'eau près du fond sera détaillée dans le Chapitre 5.

Le Canal de Corse s'est formé pendant l'ouverture de la Mer Tyrrhénienne septentrionale, entre le Burdigalien tardif et le Langhien (Zitellini et al., 1986), résultant en la formation d'un demi-graben (Fig. 1.2 ; Pascucci, 2002). La Ride de Pianosa, qui est une ride magmatique et métamorphique (Pandeli et al., 2010), correspond à un bloc basculé du demi-graben, avec une faille principale localisée sur le côté corse du bassin (Fig. 1.2 ; Pascucci, 2002) séparant ainsi le Canal de Corse du Plateau de la Toscane (Figs. 1.2 ; 1.3). Plusieurs bassins orientés N-S et NO-SE se localisent sur le Plateau de la Toscane (Fig. 1.3 ; Pascucci et al., 2007) et piègent une grande partie du sédiment provenant de l'Italie (Roveri, 2002). Ces bassins se sont développés sur un substrat structuré par des chevauchements et, localement fracturé par des failles normales (Bartole, 1995).

La Province Magmatique de la Toscane, localisée au sud de la Toscane, au nord de Latium et dans l'Archipel de la Toscane, est formée par des zones intrusives et extrusives, composées de roches acides et mafiques, (Dini et al., 2002). Les matériels se composent principalement de roches plutoniques granitoïdes (par exemple dans l'Île d'Elbe et dans l'Île de Montecristo), mais aussi dykes, sills et laccolithes porphyriques subvolcaniques (l'Île d'Elbe), et de roches volcaniques (par exemple dans l'Île de Capraia, en S. Vincenzo, Roccastrada et Amiata; Dini et al., 2002). L'activité magmatique s'est progressivement déplacée depuis l'ouest à 14 Ma à Sisco (nord-est Corse) vers l 'est avec une phase importante au niveau des Îles d'Elbe, Montecristo et Capraia à 8.4-5.9 Ma. La phase finale a eu lieu à terre, en Toscane, entre 1.3-0.2 Ma (Dini et al., 2002).

La sismicité actuelle dans le Canal de Corse est considérée comme très faible (Scisciani and Calamita, 2009). Pour cette zone, l'accélération horizontale maximale (PGA) calculée par le « Global Seismic Hazard Assessment Program » pour une période de retour de 475 ans est inférieure à 0.4 $m{\cdot}s^{-2}$ (Fig. 1.4; Slejko et al., 1999). De plus, Pascucci et al. (1999) et Pascucci (2002) ont montré que le Canal de Corse est rentré dans une phase post-rift à partir du Messinien tardif (Fig. 1.2), ce qui suggère que l'activité tectonique a été faible pendant le Plio-Quaternaire, qui est la période étudiée dans ce projet de doctorat.

A la fin du Miocène, entre 5.97 et 5.33 Ma, la Crise de Salinité du Messinien a affecté toute la Mer Méditerranée et a provoqué des importants changements environnementaux liés aux forçages géodynamiques et climatiques et qui ont provoqué des érosions majeures ainsi que des dépôts évaporitiques (Roveri et al., 2014). Pendant cette Crise de Salinité, le Canal de Corse était un lac perché, isolé des bassins profonds tyrrhéniens. A la fin de la Crise de Salinité du Messinien, le Canal de Corse s'est connecté avec le Bassin Tyrrhénien, en engendrant la formation d'un système de chenaux incisés (Thinon et al., 2016). La fin de la Crise de Salinité du Messinien correspond à une discontinuité sismique qui peut être clairement identifiée sur la sismique de réflexion grâce au grand contraste lithologique avec le sédiment Pliocène déposé pendant la re-inondation du bassin (Thinon et al., 2016).

1.4. Structure et contenus du manuscrit

Ce manuscrit se compose de 5 chapitres principaux (Chapitres 3-7), qui sont cohérents et peuvent être compris de façon indépendante. Un court contexte géologique et océanographique est fourni au début de chaque chapitre selon les besoins de la thématique. Afin d'éviter la répétition et pour plus de clarté, le chapitre 2 présente les matériels et méthodes employés dans ce travail. Les chapitres sont ordonnés avec une séquence logique pour acquérir à chaque étape l'information nécessaire aux chapitres suivants (Fig. 1.5-f). Dans un premier temps, les glissements sous-marins sont

identifiés, cartographiés, leur typologie établie, leur âge et leur fréquence estimés. Par la suite, les contourites sont à leur tour cartographiées, leur morphologie et leur lithologie étudiées afin de définir leur évolution Plio-Quaternaire. Cela donne lieu dans le chapitre suivant à une analyse des processus océanographiques contrôlant actuellement le développement des contourites pour mieux contraindre les processus d'érosion et de dépôt. Cette approche est complétée par l'étude des propriétés sédimentologiques et géotechniques des contourites pour évaluer leur rôle dans le déclenchement d'instabilité de pente. Le dernier chapitre s'appuie sur des données minéralogiques et géotechniques ainsi que sur des modélisations numériques de stabilité de pente pour mettre en évidence le rôle d'une couche de faible résistance dans le déclenchement d'un plan de rupture conformément aux observations sismiques.

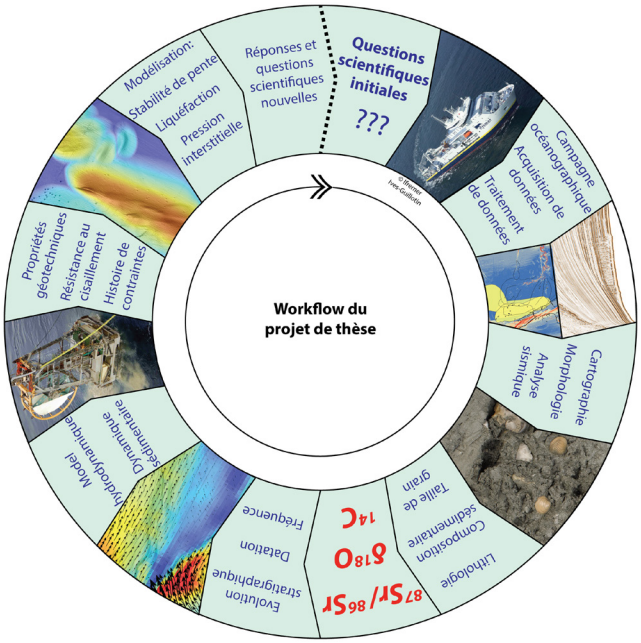

Fig. 1.5-f. Workflow du projet de thèse avec les différentes thématiques présentées en suivant le même ordre que les chapitres du manuscrit.

- *Chapitre 2 : Matériels et méthodes*

Les matériels et méthodes utilisés dans le cadre de ce projet sont détaillés dans le Chapitre 2. Le jeu de données est composé de bathymétrie multifaisceaux, sismique de haute résolution, mesures de vitesse des courants (ADCP), carottes sédimentaires et mesures pénétrométriques (CPTU). On a aussi utilisé un modèle hydrodynamique, deux modèles de stabilité de pente en 1D et 2D, un modèle de consolidation 1D et un modèle pour estimer le potentiel de liquéfaction.

- *Chapitre 3 : Morphologie, distribution spatiale et âge des glissements sous-marins*

Le Chapitre 3 se concentre sur l'identification des glissements sous-marins, leur caractérisation et leur âge (Fig. 1.6-f). Une partie de ce chapitre a été publiée avec le titre: « *Implications de la dynamique sédimentaire dans le transport en masse le long de la Ride de Pianosa (Mer Tyrrhénienne Septentrionale)* » en « *Submarine Mass Movements and Their Consequences 7th International Symposium* » :

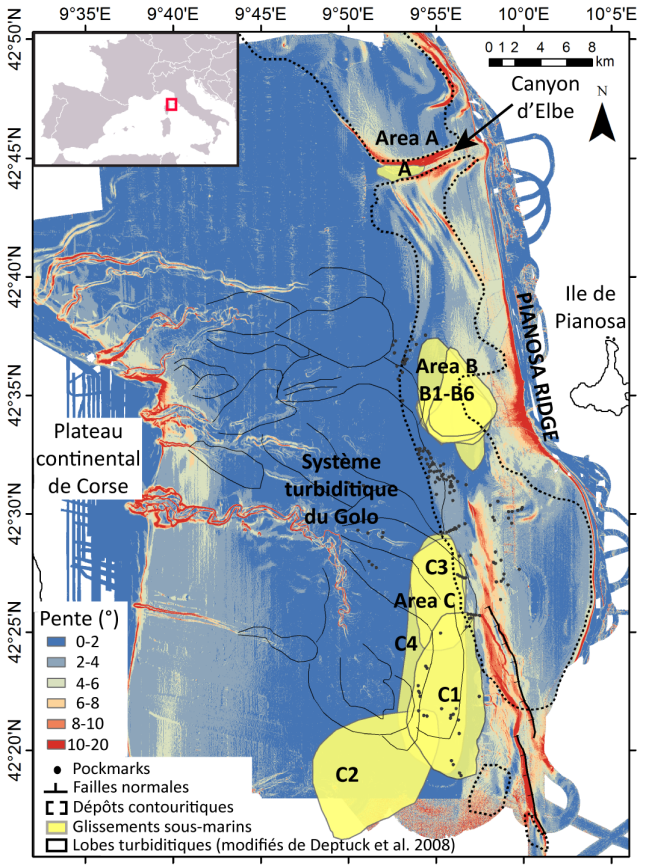

Area	Nom	Volume (km^3)	Runout max. (km)	Longueur max. (km)	Largeur max. (km)	Rapport longueur/largeur	Age (ka BP)
A	A	0.10	1.5	1.2	3.6	3.0	<12
B	B1	0.19	7.0	5.7	7.6	1.3	42-59
	B2	0.09	8.0	5.6	4.6	0.8	125-137
	B3	0.26	7.5	5.9	7.2	1.2	420-437
	B4	0.15	4.2	2.5	7.4	3.0	452->542
	B5	0.05	6.0	3.4	4.4	1.3	>542
	B6	0.04	6.2	3.6	4.4	1.2	>542
C	C1	2.62	9.0	6.0	13.5	2.3	42-50
	C2	0.47	16.0	10.0	7.8	0.8	125-160
	C3	0.67	6.0	4.0	8.7	2.2	265-321
	C4	1.86	10.4	5.3	18.6	3.5	321-380

Fig. 1.6-f. Résumé graphique du Chapitre 3 montrant la localisation et l'extension des glissements sous-marins sur une carte de gradient de pente, ainsi qu'un tableau avec leur taille et âge.

Miramontes, E., Cattaneo, A., Jouet, G., Garziglia, S. (2016). Implications of sediment dynamics in mass transport along the Pianosa Ridge (Northern Tyrrhenian Sea). In Lamarche, G., Mountjoy, J., Bull, S., Hubble, T., Krastel, S., Lane, E., Micallef, A., Moscardelli, L., Mueller, C., Pecher, I., Woelz, S. (Eds.), Submarine mass movements and their consequences, Dordrecht, The Netherlands, Advances in Natural Hazard Research, Springer, 30, 301–309.

- *Chapitre 4 : Le système contouritique de Pianosa (Mer Tyrrhénienne Septentrionale): morphologie des dépôts et évolution stratigraphique Plio-Quaternaire*

Ce chapitre vise à caractériser la morphologie, la lithologie et l'évolution des contourites pendant la période Plio-Quaternaire (Fig. 1.7-f). Cette étude sur les contourites a été menée dans l'objectif de contraindre le contexte sédimentologique des glissements, mais il apporte aussi des informations pertinentes pour l'étude du transport sédimentaire, des processus contouritiques et plus largement de l'évolution des marges continentales.

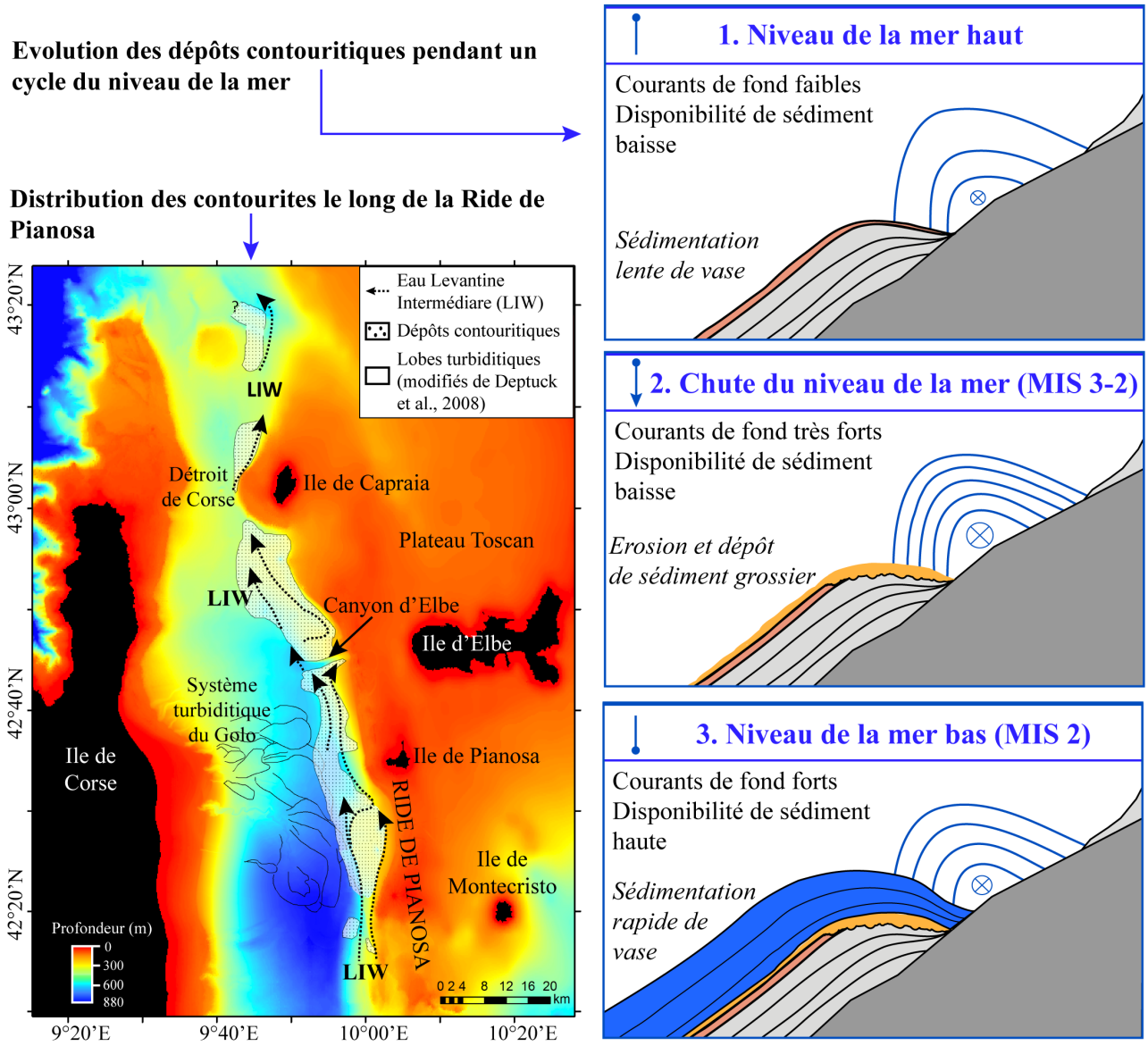

Fig. 1.7-f. Résumé graphique du Chapitre 4 montrant la localisation et l'extension des contourites le long de la Ride de Pianosa, ainsi qu'un diagramme expliquant l'évolution plio-quaternaire des contourites pendant un cycle du niveau de la mer.

Ce chapitre a été publié dans le journal *Marine Geology* avec le même titre que le chapitre :

Miramontes, E., Cattaneo, A., Jouet, G., Théreau, E., Thomas, Y., Rovere, M., Cauquil, E., Trincardi, F. (2016). The Pianosa Contourite Depositional System (Northern Tyrrhenian Sea): Drift morphology and Plio-Quaternary stratigraphic evolution. Marine Geology, 378, 20-42.

- *Chapitre 5 : Nouveaux aperçus sur la formation des contourites à partir de modélisation hydrodynamique en Mer Méditerranée nord-occidentale*

Le Chapitre 5 se focalise sur les processus océanographiques qui contrôlent la formation des contourites. Les résultats de modélisations hydrodynamiques sont confrontés à des données bathymétriques, sismiques et sédimentologiques afin de révéler l'influence de ces processus océaniques sur la localisation de zones d'accumulation et d'érosion (Fig. 1.8-f). Cette approche s'inscrit dans la perspective d'améliorer la caractérisation des forces motrices impliquées dans le déclenchement de glissements. Ce chapitre est en cours de préparation pour être soumis sous forme d'article à une revue internationale.

- *Chapter 6 : Contrôle morphologique des phénomènes d'instabilité de pente dans un système contouritique : approche géotechnique*

Le Chapitre 6 résume les propriétés sédimentologiques et géotechniques des contourites, et présente une comparaison avec les hémipelagites du Canal de Corse afin de mettre en évidence les facteurs ayant favorisé l'instabilité sur cette marge. Une attention particulière est portée à l'évaluation des effets de la sédimentation, de la sismicité et de la morphologie du fond marin (Fig. 1.9-f). Ce chapitre est en cours de préparation pour être soumis sous forme d'article à une revue internationale.

- *Chapitre 7 : Influence de dépôts volcaniques altérés dans la surface de rupture de glissements sous-marins*

Le Chapitre 7 se concentre sur la caractérisation d'une couche de faiblesse mécanique potentielle et sur la détermination de son comportement sous l'effet d'un forçage externe (Fig. 1.10-f). La faiblesse de cette couche est attribuée à la présence de zéolites, minéraux produits de l'altération des roches volcaniques, induisant une perte de résistance au cisaillement sous l'effet d'un forçage tel que celui produit par de l'érosion en pied de pente. L'information de ce chapitre est en cours de révision pour resoumission à la revue *Geology*.

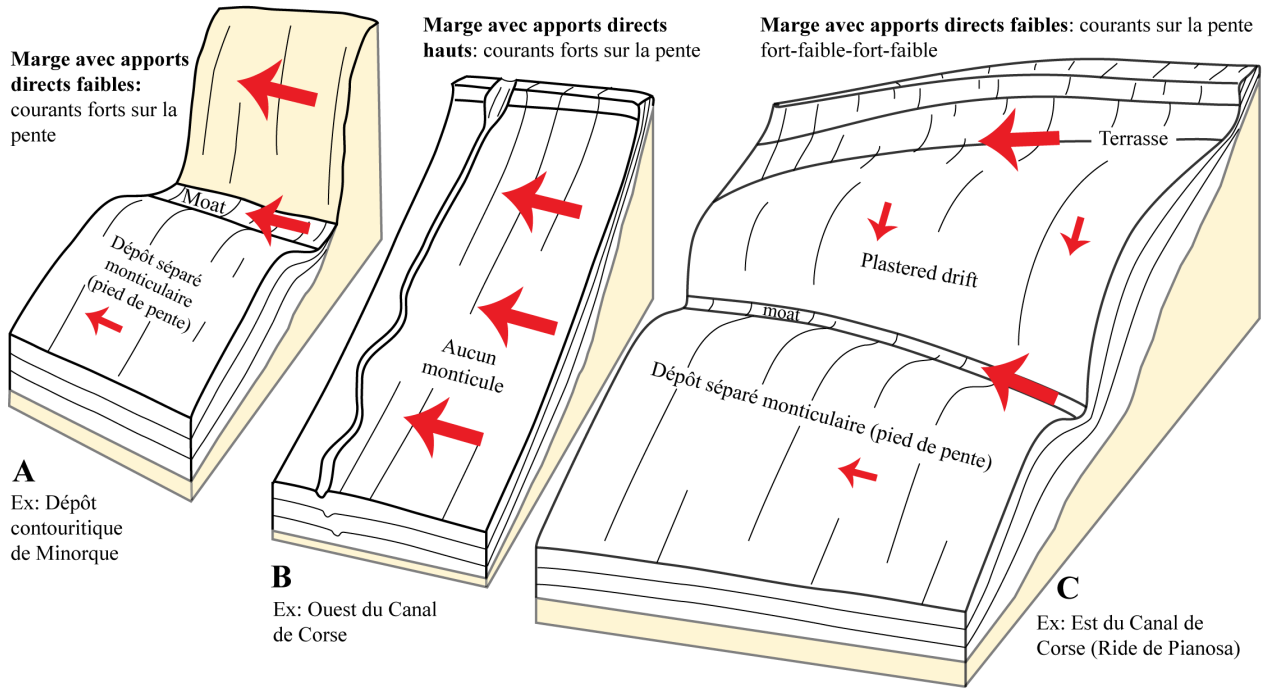

Fig. 1.8-f. Résumé graphique du Chapitre 5 montrant un modèle conceptuel de la formation des différents types de dépôts contouritiques et les morphologies de marges continentales selon la distribution de l'intensité de courants.

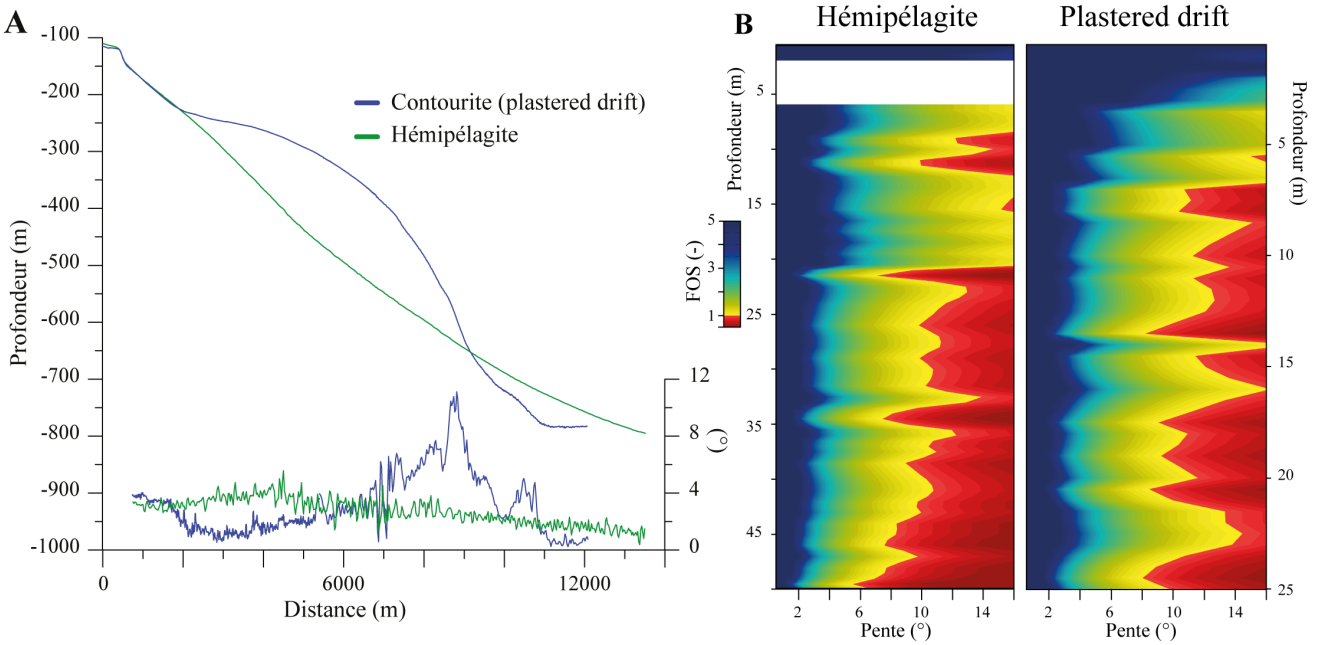

Fig. 1.9-f. Résumé graphique du Chapitre 6 montrant **(A)** les profils bathymétriques et les gradients de pente d'une marge contouritique (bleu) et d 'une marge hémipélagique (vert) ; et **(B)** les résultats de l'analyse de la stabilité de pente, avec le Facteur de Securité (FOS) en fonction de la profondeur et l'angle de pente, obtenus à partir des propriétés mécaniques des hémipélagites et du « plastered drift ».

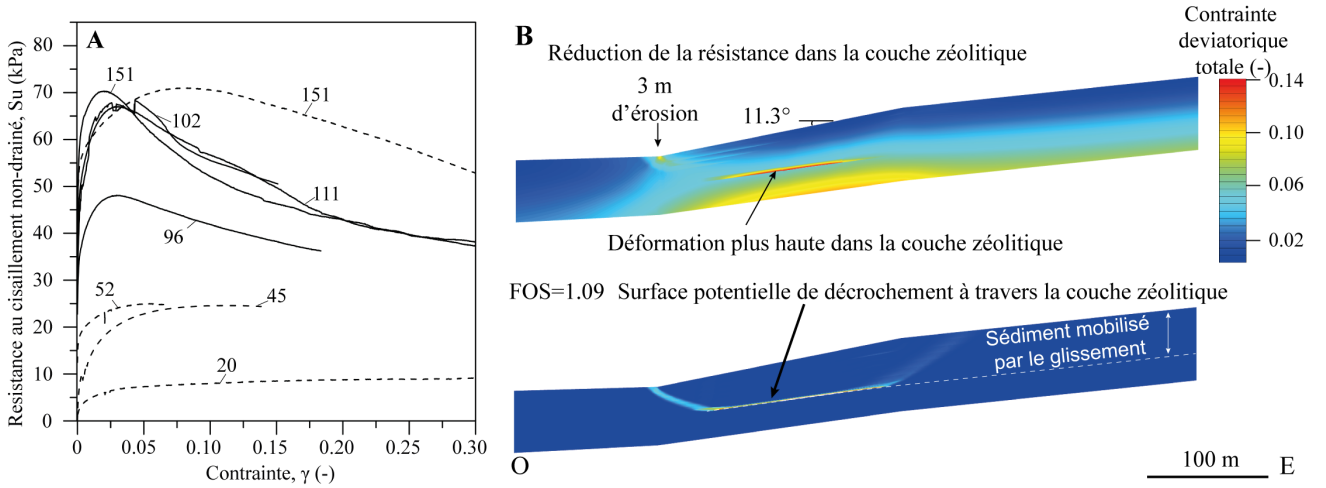

Fig. 1.10-f. Résumé graphique du Chapitre 7 montrant **(A)** la diminution de la résistance avec le cisaillement de la couche relativement riche en zéolites (avec traits solides) et **(B)** la formation d'une surface potentielle de glissement à travers cette même couche.

CHAPTER 2. Materials and methods

The study of submarine landslides requires a good comprehension of the geological context of the margin, its stratigraphy and evolution, and of the sedimentological characteristics: type of sediment, grain size, sedimentation processes, sedimentation rates... In addition, sediment geotechnical properties provide information about the strength and stress history of the sediment, necessary for slope stability modelling. For this purpose, a broad data set was acquired along the Pianosa Ridge, composed of multibeam bathymetry for seafloor geomorpholgy, seismic data (multi-channel high resolution mini GI gun, hull-mounted sub-bottom profiler, deep-towed SYSIF and mono-channel high resolution sparker) for subseafloor stratigraphy, ADCP data to measure current velocity, sediment cores for sedimentological and geotechnical characterisation and measurements with the Penfeld penetrometer for in situ mechanical measurements. The whole data set, as well as the analytical methods used to exploit the data, are presented in detail in this chapter. Here, we also explain the numerical models used in this project: hydrodynamic model (MARS3D-MENOR), 1D and 2D slope stability model (PLAXIS 2D), 1D consolidation model (SeCo) and a model for liquefaction potential assessment.

CHAPITRE 2. Matériels et méthodes

Pour la réalisation d'une étude sur glissements sous-marins, il est nécessaire d'avoir une bonne compréhension du contexte géologique de la marge, de sa stratigraphie et son évolution, ainsi que des caractéristiques sédimentologiques : type de sédiment, taille de grain, processus sédimentaires, taux d'accumulation... De manière complémentaire, les propriétés géotechniques fournissent des informations sur la résistance et l'histoire des contraintes, nécessaire pour la modélisation de la stabilité de pente. Afin de répondre à ces objectifs, un vaste jeu de données a été acquis le long de la Ride de Pianosa ; il est composé de bathymétrie obtenue par des sondeurs multifaisceaux pour l'étude de la géomorphologie du fond, de données sismiques pour la stratigraphie sismique (multitraces haute résolution (mini GI), sondeur de sédiment de coque, SYSIF tracté près du fond et monotrace haute résolution avec une source sparker) pour la stratigraphie sismique, d'enregistrements ADCP pour mesurer la vitesse des courants dans l'eau, de carottes de sédiment (type Calypso) pour la caractérisation sedimentologique et géotechnique et enfin de mesures avec le pénétromètre "Penfeld" pour évaluer les propriétés mécaniques in situ du sédiment. Les types de données qui contribuent à cette étude, ainsi que les méthodes utilisées pour leurs exploitations, sont détaillés dans ce chapitre. Seront également abordés dans cette partie les modèles numériques utilisés dans ce projet : un modèle hydrodynamique (MARS3D-MENOR), deux modèles de stabilité de pente 1D et 2D (PLAXIS 2D), un modèle de consolidation 1D (SeCo), ainsi qu'un modèle pour l'évaluation du potentiel de liquéfaction.

CAPÍTULO 2. Materiales y métodos

El estudio de deslizamientos submarinos requiere una buena comprensión del contexto geológico del margen, de su estratigrafía y evolución, y de las características sedimentológicas: tipo de sedimento, tamaño de grano, procesos sedimentarios, tasas de sedimentación... Además, las propiedades geotécnicas del sedimento proporcionan información sobre la resistencia y la historia de tensión sufrida por el sedimento, necesaria para la modelización de la estabilidad del talud. Con este objetivo se adquirió un amplio conjunto de datos en la Cresta de Pianosa, compuesto de batimetría multihaz para la geomorfología del fondo submarino, datos sísmicos (multicanal de alta resolución (mini GI), perfilador sísmico de casco, SYSIF remolcado cerca del fondo y monocanal alta resolución con una fuente sparker) para la estratigrafía del subsuelo, ADCP para medir la velocidad de las corrientes, testigos de sedimento (tipo Calypso) para la caracterización sedimentológica y geotécnica, y medidas mecánicas in situ con el penetrómetro Penfeld. Todo el conjunto de datos y los métodos utilizados para la explotación de los datos están presentados en detalle en este capítulo. En este apartado también se explican los modelos numéricos utilizados: un modelo hidrodinámico (MARS3D-MENOR), dos modelos de estabilidad de talud 1D y 2D (PLAXIS 2D), un modelo de consolidación 1D (SeCo) y un modelo para evaluar el potencial de liquefacción.

2.1. Bathymetric data

The multibeam bathymetry of the Corsica Trough was acquired during the CORFAN survey (doi 10.17600/98060110) in 1998 onboard the R/V L'Europe, the CORFAN 2 survey (doi 10.17600/1020030) in 2001 and the SIGOLO survey (doi 10.17600/8020110) in 2008 onboard the R/V Le Suroît. The resolution of the compiled DEM is 25 m. The echosounders used during these surveys were Simrad EM1000 (95 kHz) for the shallow area and EM300 (30 kHz) for the deep area. The bathymetry of the Corsica Trough was completed during the surveys carried out by IFREMER in 2013 PRISME2 (doi 10.17600/13010050) and PAMELA-PAPRICA (doi 10.17600/13010300) onboard the R/V L'Atalante (Fig. 2.1 and for more detail Fig. A.1 in the appendices). Two multibeam echosounders were used on the Pianosa Ridge onboard the R/V L'Atalante: Simrad EM122 (12 kHz, resolution of 15 m) for zones deeper than 800 m water depth and Simrad EM710 (100 kHz, resolution of 5 m) for shallower zones (0-800 m water depth).

The multibeam bathymetry of a seamount in the Northern Tyrrhenian Sea is an industrial data set from EM300 multibeam and is binned as 30 x 30 m. Detailed bathymetry was acquired in this zone from AUV with a 1-m resolution. Additional bathymetric data of the Tyrrhenian Sea were retrieved from the EMODnet Bathymetry compilation (http://portal.emodnet-bathymetry.eu/) with a resolution of 1/8 x 1/8 minutes and the bathymetry of the NW Mediterranean Sea from the GEBCO dataset (GEBCO_08, version 2010-09-27, http://www.gebco.net) with a 30 arc-second resolution.

2.2. Seismic data

2.2.1. Hull-mounted sub-bottom profiler (SBP)

Seismic data were acquired using a hull-mounted sub-bottom profiler (SBP, 1800-5300 Hz) by IFREMER in 2013 during the surveys PRISME2, PAMELA-PAPRICA onboard the R/V L'Atalante and PRISME3 (doi 10.17600/13030060) onboard the R/V Pourquoi pas ? (Fig. 2.1 and for more detail Fig. A.2 in the appendices section). The acquisition, the quality control and the processing of the data were carried out using the QC SUBOP software developed by IFREMER.

2.2.2. Multi-channel high resolution

Multi-channel (72 channels) high resolution profiles sourced by a mini GI gun (50-250 Hz) were acquired in 2013 during cruises PRISME2 and PAMELA-PAPRICA (Fig. 2.1 and for more detail Fig. A.2 in the appendices). The penetration below the seafloor was higher than 1 s Two-Way travel Time (TWT) in the deep zones and up to 0.5 s TWT in the continental shelf. The onboard pre-processing was done using Sispeed V5.3 (recently upgraded in SolidQC): due to the shallow depth of the Corsica Trough, a constant source delay was applied.

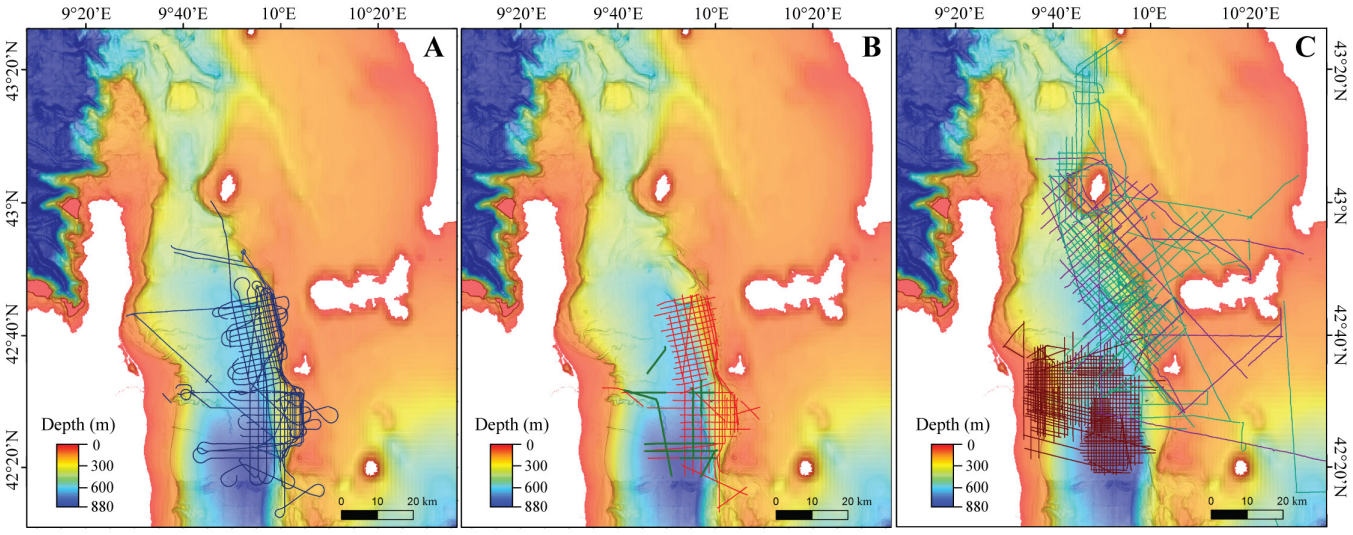

Fig. 2.1. Location of the seismic profiles used for this study displayed over the bathymetric map of the Corsica Trough and the Tuscan Shelf: **(A)** Hull-mounted Sub-Bottom Profiler (SBP) of cruises PRISME2, PAMELA-PAPRICA and PRISME3; **(B)** Multi-channel high resolution mini GI gun (72 channels) in red (PRISME2 and PAMELA-PAPRICA) and deep-towed SYSIF in green (PRISME2). See Fig. A.2 in the appendices for more detail; **(C)** Multi-channel high resolution sparker (48-72 channels) in dark red (SIGOLO), single-channel sparker in green (ET91 and ET95) and in purple (ET95) from ISMAR-CNR.

The conversion into SEGY format was done without applying a bandpass filter. Further processing consisted in a velocity analysis, stack and migration of the seismic data using the ProMAX seismic processing software.

A multi-channel seismic reflection profile of low resolution has been used in Chapter 5 (Figs. 5.2; 5.3). It was acquired in the Minorca basin during the Valsis survey in 1988. In the same chapter we also used a multi-channel ultra high resolution seismic reflection profile acquired from a sleeve gun array in the Northern Tyrrhenian Sea during an industrial survey. See Chapter 5 for the exact location of the profiles.

2.2.3. Deep-towed SYSIF seismic system

The deep-towed SYSIF seismic system was recently developed by IFREMER (Fig. 2.2; Marsset et al., 2014) and it is more efficient in image quality and penetration than older similar systems (Marsset et al., 2010; Ker et al., 2010). The system is usually towed 100-150 m above the seafloor at 2 kn. Towing the source and the streamer near the seabed improves the horizontal resolution, reduces the interferences caused by reflections and diffractions and the relation noise/signal is better due to a less noisy environment and the closer position of the receptor respect to the reflectors. The frequency range used during the cruise PRISME2 is 220-1050 Hz (Fig. 2.1 and for more detail Fig. A.2 in the appendices).

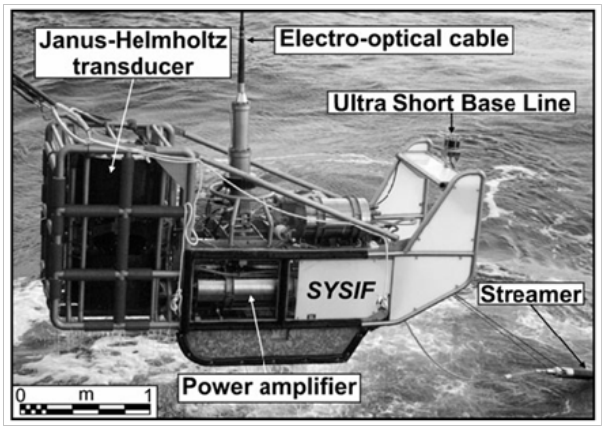

Fig. 2.2. Deep-towed SYSIF seismic system (Ker et al., 2010).

2.2.4. Sparker

Single-channel 1 kJ sparker (50-60 Hz) profiles were collected during cruises ET91 (N/O Bannock), ET 93 and ET95 (N/O Urania) carried out by the former Istituto di Geologia Marina of Bologna of the Italian National Research Council (CNR), now ISMAR-CNR (Fig. 2.1C; Roveri, 2002). Seismic data from surveys ET91 and ET95 were interpreted from analogical profiles and used to map the contourites. ET93 sparker profiles were available in digital format and were processed using the software FOCUS 5.4. We also used multi-channel (48-72 channels) sparker reflection seismic profiles (130-750 Hz) acquired during the SIGOLO survey in 2008 onboard the R/V Le Suroît. These data cover the western and central parts of the Corsica Trough and are used to complete the seismic analysis of the area (Fig. 2.1C).

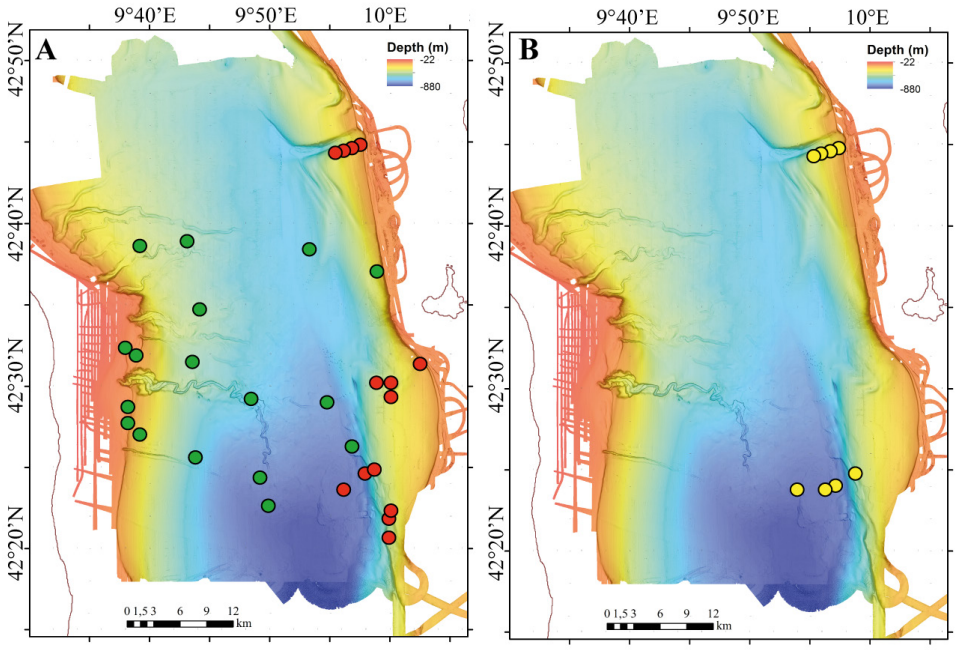

Fig. 2.3. Multibeam bathymetry of the Corsica Trough with the location of: **(A)** sediment cores collected during the PRISME3 cruise in red, that were analysed during the present project, and in green sediment cores analysed in previous studies, whose results have also been used in Chapters 5 and 6; **(B)** CPTU and P-wave velocity measurements acquired with the Penfeld penetrometer during the PRISME3 cruise, represented with yellow dots. See Fig. A.3 in the appendices for the references of cores and Penfeld penetrometer measurements.

2.3. Acoustic Doppler Current Profiler (ADCP)

Current velocity measurements were acquired with the hull-mounted Acoustic Doppler Current Profiler (ADCP) OS38 of R/V L'Atalante during the cruise PRISME2 in August 2013. The data were processed with the CASCADE V6.1 software developed by IFREMER. Tide corrections and a linear filter were applied. The ADCP data are available along the same profiles as the seismic profiles (Fig. 2.1B).

2.4. Sediment cores

Fourteen Calypso piston cores (up to 30-m long) were collected along the Pianosa Ridge in 2013 during the cruise PRISME3 (Table 2.1; see core location and references in Fig. A.3 in the appendices). The cores are of high quality, with no evidences of piston effects. They were used for sedimentological and geotechnical analysis. The systematic analysis of all the cores consisted on the following steps:

1. Cut the core in 1-m long sections.
2. Measure gamma density, P-wave velocity and magnetic susceptibility using a GEOTEK Multi-Sensor Core Logger (MSCL).
3. X-ray radiography using a GEOTEK MSCL-XCT.
4. Using the data obtained from the MSCL and the XCT, some parts of the section are selected for further geotechnical analysis (oedometer and triaxial tests).
5. Split the cores in two half sections: one is the archive section and the other one is the work section used for sedimentological and routine geotechnical analysis (celerimeter for P-wave velocity measurement, vane shear test and moisture content).
6. Visual description of the archive half-section
7. Photography of the archive half-section
8. Analysis of the bulk sediment semi-quantitative geochemical composition with an Avaatech X-ray fluorescence (XRF) core scanner on the archive half-section.
9. Measurement of sediment moisture content on the work half-section.
10. Vane shear test for undrained shear strength determination on the work half-section.
11. Measurement of P-wave velocity with a celerimeter on the work half-section.

We also used two boreholes drilled in the central part of the Corsica Trough (GDEC8-2) and in the western flank of the basin (GDEC4-2) during the 2009 GOLODRILL cruise by the R/V Bavenit (FUGRO; Fig. 2.3). These boreholes were already analysed and processed during the Golo program consortium (Jouet et al., 2012), but their results have been also used to support and complete the present project. In Chapter 5, we used the grain size analyses of the top of fifteen sediment cores collected during the cruises CORFAN2 (doi 10.17600/1020030) in 2001, MD124/GEOSCIENCES2 (doi 10.14600/1200060) in 2001 and CORK (doi 10.17600/99060020) in 1999.

2.4.1. Depth correction of Calypso piston cores

Depth disturbances in piston cores were corrected using the software CINEMA[2] . Based on accelerometer measurements carried out during coring, this software can determine the position of the base of the

Core name	Latitude	Longitude	Water depth (m)	Length (m)
PSM3-CS003	42.741602°N	9.946704°E	245	9.14
PSM3-CS006	42.740227°N	9.938869°E	281	20.91
PSM3-CS009	42.503177°N	9.998834°E	370	21.23
PSM3-CS011	42.492267°N	9.999239°E	349	27.60
PSM3-CS012	42.503334°N	9.983666°E	425	26.96
PSM3-CS013	42.367498°N	9.998666°E	410	23.70
PSM3-CS014	42.363470°N	9.998663°E	434	20.60
PSM3-CS015	42.346669°N	9.998837°E	431	5.04
PSM3-CS016	42.523503°N	10.043666°E	171	9.10
PSM3-CS017	42.411721°N	9.976764°E	534	23.89
PSM3-CS018	42.412231°N	9.970599°E	594	19.83
PSM3-CS020	42.743169°N	9.956997°E	176	21.60
PSM3-CS021	42.738332°N	9.926891°E	342	20.69
PSM3-CS022	42.393883°N	9.941500°E	820	28.09

Table 2.1. Calypso piston cores collected along the Pianosa Ridge during the PRISME3 survey in 2013. See Fig. A.3 in the appendices for core location.

piston and core catcher, being able to estimate the in situ depth of the core (Fig. 2.4; Woerther et al., 2012). The depth correction of sediment cores permits a more accurate estimation of sedimentation rates and correlation with seismic data and *in situ* measurements.

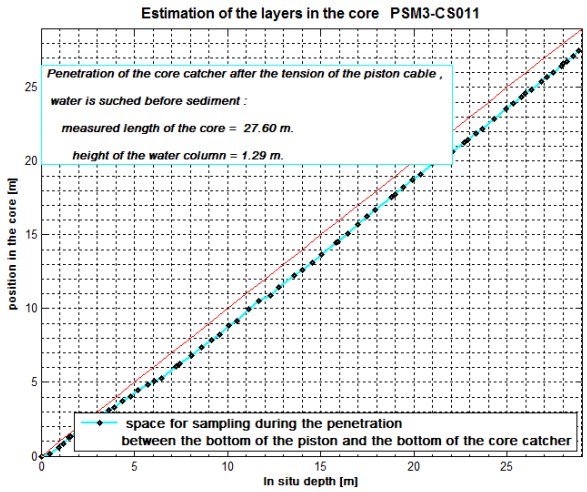

Fig. 2.4. Graph of the position in the core in function of the in situ depth provided by the CINEMA[2] software that allows the correction of depth in the sediment core.

2.4.2. Sedimentological measurements on Calypso piston cores

2.4.2.1. Multi-sensor Core Logger (MSCL)

P-wave velocity, gamma-density and magnetic susceptibility were measured on whole core sections using a Geotek Multi-Sensor Core logger (MSCL) at IFREMER laboratories or directly onboard during campaigns (Fig. 2.5). Measurements were carried out every centimetre. Gamma-density and P-wave velocity values provide information about the lithology, the grain size and the stress history of the sediment. For example, coarse sediment usually corresponds to high P-wave values.

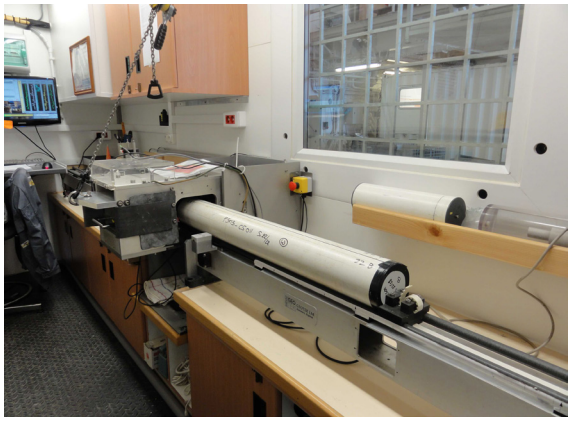

Fig. 2.5. GEOTEK Multi-sensor Core Logger (MSCL) in IFREMER container portable laboratory.

Moreover, when the density and the P-wave velocity increase linearly with depth, it could be argued that the sediments were deposited continuously without big changes in composition and, therefore, they could be expected to be normally consolidated. This first information about the type of sediment present along the core is very useful to choose the sections that will be used for geotechnical analyses on whole sections, such as oedometer and triaxial tests.

2.4.2.2. MSCL-XCT

The X-ray radiography of whole sediment core sections was carried out using a Geotek MSCL-XCT (Fig. 2.6). The radiography was done with planes oriented in three different angles: 0°, 90° and 180° in order to better observe sediment structures, pebbles or shells that are not located in the centre of the core. In the studied cores, neither lamination nor sedimentary structures related to sediment dynamics were identified after the radiography images. But these measurements show very common bioturbation structures and shells.

Fig. 2.6. GEOTEK MSCL-XCT in IFREMER container portable laboratory.

2.4.2.3. X-ray fluorescence (XRF) core scanner

The bulk sediment semi-quantitative geochemical composition was measured with an Avaatech X-ray fluorescence (XRF) core scanner on split cores at the IFREMER container portable laboratory. Measurements were carried out at 1-cm step. The semi-quantitative geochemical composition is a very useful proxy to determine possible changes in sediment composition, sediment provenance, as well as to correlate different cores. The Ca/Fe ratio has been used in cores from the Pianosa Ridge for correlation.

Fig. 2.7. Avaatech X-ray fluorencence (XRF) core scanner in IFREMER container portable laboratory.

2.4.2.4. Quantitative X-ray fluorescence (XRF) and X-ray Diffraction (XRD)

Quantitative geochemical analyses were carried out on twelve sediment samples from cores PSM3-CS012, PSM3-CS017 and PSM3-CS021 in order to obtain the quantitative elemental composition, as well as the mineral and clay composition and check if there were geochemical differences between a sediment layer with specific mechanical properties and the adjacent sediment. For that purpose, the sediment samples were first dried at 65°C and then crushed to make a powder. Part of this powder is compressed to obtain a flat, rounded pellet used for the quantitative X-ray Fluorescence (XRF) analysis, whereas the rest was used for X-ray Diffraction (XRD) analysis. The XRF analysis provides the absolute quantity of the geochemical elements present in the sample, while the XRD analysis provides information about the mineralogical composition and the quantity of the different types of clay minerals present in the sample.

2.4.2.5. Grain size

Grain size analyses were carried out on 4 cores from the Pianosa Ridge (PSM3-CS009, PSM3-CS011, PSM3-CS017 and PSM3-CS021) with variable spacing ranging from 10 cm (in the homogeneous muddy facies) to 2 cm (in the sandy areas and mud-sand transitions). Grain size measurements were performed on cores PSM3-CS009 and PSM3-CS011 using the Coulter LS200 laser microgranulometer of IFREMER laboratories with no chemical pre-treatment of the bulk sediment. Further grain size measurements were performed using a Malvern Mastersizer 3000 laser microgranulometer on the bulk sediment fraction of cores PSM3-CS017 and PSM3-CS021, as well as on the carbonate-free fraction of the upper 6.85 m of core PSM3-

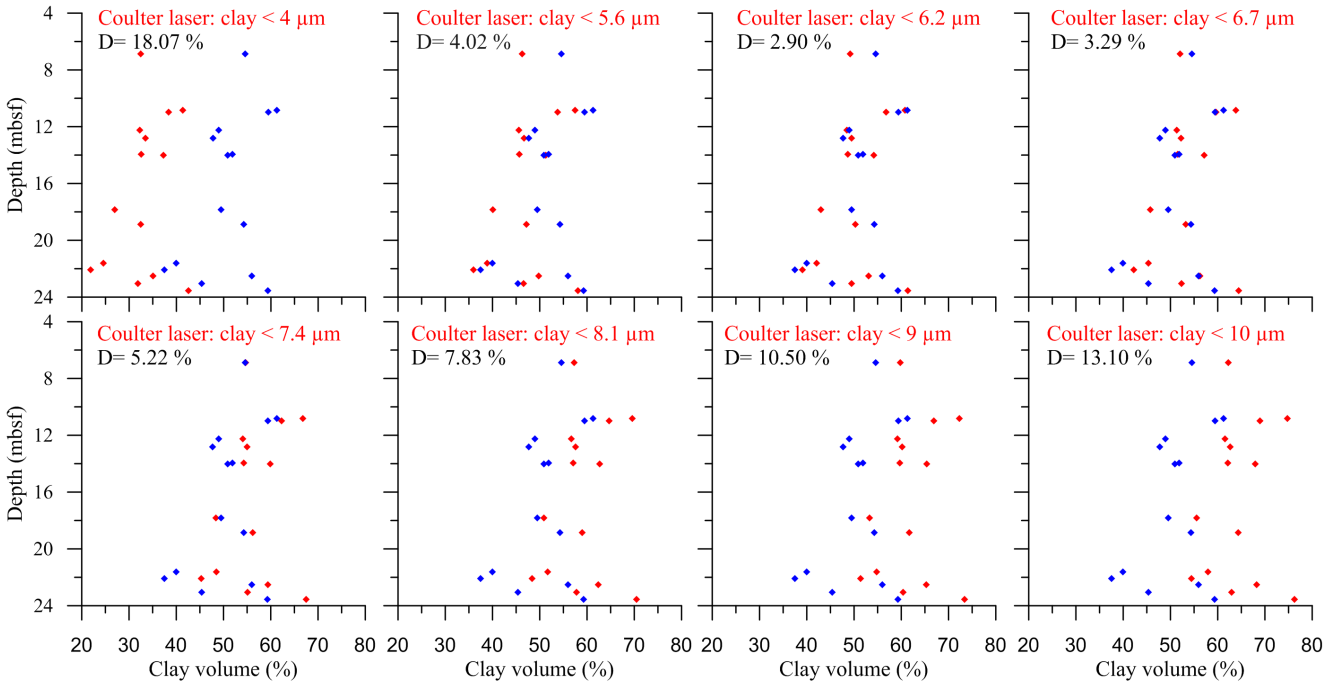

Fig. 2.8. Comparison of clay volumes measured with a Sedigraph 5100 (blue diamonds) and with Coulter LS200 laser microgranulometer with no chemical pre-treatment (red diamonds). Different size boundaries for clay have been compared for the laser grain size measurements in order to establish a more appropriate boundary that provides less differences (D) in clay volume compared to the clay volume obtained from the Sedigraph.

CS011. In order to compare the contourites from the Pianosa Ridge with the hemipelagites of the central and western parts of the Corsica Trough, we also used the results of the grain size measurements carried out previously on boreholes GDEC4-2 and GDEC8-2 with the Couler LS200 laser microgranulometer of IFREMER laboratories. Grain size analysis were also performed on selected muddy samples (<63 μm) with a Sedigraph 5100 (φ 4 to 12) at ISMAR-CNR laboratories and with the Coulter LS200 laser microgranulometer at IFREMER laboratories in order to better determinate the fine fraction below 10 μm. The pre-treatment of the samples for grain size analysis using the Sedigraph consisted in the following steps:

1. Cover the sediment samples with a dilution of H_2O_2 composed of 1 L of 30% H_2O_2 and 3.5 L of distilled water. This step is done in order to remove all the organic matter. The samples stayed 5 days in this dilution, until there were no evidences of release of gas bubbles formed during the process of disintegration of the organic matter.
2. Wet sieve at 63 μm and recover of the fine fraction.
3. Dry the sediment fraction coarser than 63 μm in the oven at 59°C and measure it in a dry sieving column.
4. Fine sediment must settle down before analysis in the Sedigraph. For a faster decantation process, a vacuum filtration technique was applied.
5. 4.5 g of the sediment were mixed with sodium metaphosphate.

The preparation of samples for grain size analyses with the laser microgranulometer is simpler. A very small amount of sediment is sampled directly from the core section, mixed with distilled water and agitated until there is an homogeneous mixture (4-10 min). Then the mixture can be directly used for measurement. Samples of core PSM3-CS011 between 18.7 and 20.6 m below the seafloor (mbsf) presented very strong flocculation that was not destroyed with the common agitation. In order to disperse these samples, $(NaPO_3)_6$ was added and the samples were in a ultrasound bath for few seconds (about 5 s).

The laser microgranulometer is based on the measurement of the diffraction patterns of a laser beam when it passes through the particles in suspension (Agrawal et al., 1991). The Sedigraph is based on the X-ray sedimentation technique, using the settling velocity of the particles that is proportional to particle size and X-ray attenuation that is proportional to mass concentration (Coakley and Syvitski, 1991). The Sedigraph measures more accurately fine sediments than the Coulter laser microgranulometer, since the latter overestimates the amount of fine silt. Therefore, 14 samples from core PSM3-CS012 have been analysed using both methods in order to establish a size boundary between clay and silt that provides more accurate clay and silt volumes obtained using the Coulter laser microgranulometer. The clay volume obtained from the Sedigraph, establishing the clay boundary at 2 μm, is compared with the clay volume obtained from the Coulter laser microgranulometer using 8 different size boundaries: 4, 5.6, 6.2, 6.7, 7.4, 8.1, 9 and 10 μm (Fig. 2.8). The difference (D) in clay volume obtained using the two methods was calculated for each sample. The mean difference at the distinct grain size boundaries is shown in Fig. 2.8. The lowest difference is 2.90 % when the boundary is established at 6.2 μm. This size boundary is thus used in all the clay and silt volumes presented later in this study.

Core number	Depth (cm)	Material	Lab code	Cal BP age (yr)
PSM3-CS006	7	Bulk planktonic	Poz-63394	2,854 ± 75
PSM3-CS006	250	Bulk planktonic	Poz-63395	46,955 ± 3,044
PSM3-CS009	41	Bulk planktonic	Poz-63392	2,730 ± 31
PSM3-CS009	1126	Bulk planktonic	Poz-63393	30,524 ± 636
PSM3-CS009	1400	Bulk planktonic	Beta-394859	29,810 ± 408
PSM3-CS011	104	Bulk planktonic	Beta-394860	17,311 ± 193
PSM3-CS011	380	Bulk planktonic	Beta-394861	21,820 ± 221
PSM3-CS011	709	Bulk planktonic	Beta-394862	26,668 ± 366
PSM3-CS018	60	Bulk planktonic	Poz-63402	4,036 ± 65
PSM3-CS018	1750	Bulk planktonic	Poz-63403	31,408 ± 509
PSM3-CS018	1880	Bulk planktonic	Beta-394863	35,374 ± 487
PSM3-CS021	100	Bulk planktonic	Beta-394864	18,325 ± 187
PSM3-CS021	550	Bulk planktonic	Beta-394865	28,154 ± 313
PSM3-CS022	220	Bulk planktonic	Poz-63398	10,911 ± 220
PSM3-CS022	1080	Bulk planktonic	Poz-63399	25,542 ± 375
PSM3-CS022	1662	Bulk planktonic	Poz-63400	42,326 ± 1,663

Table 2.2. Samples analysed for radiocarbon dating.

2.4.2.6. Age-depth conversion

The chrono-stratigraphic framework was constructed using radiocarbon dating, strontium isotope dating and oxygen isotope analysis in core PSM3-CS011 correlated with borehole GDEC4-2. Furthermore, correlation among cores and with borehole GDEC4-2 was supported by Ca/Fe ratio from XRF measurements and seismic correlation. Carbonates recovered at the bottom of PSM3-CS015 were dated by SEDISOR using Strontium isotopes.

Radiocarbon dating measurements were performed on bulk planktonic foraminifera and were carried out by the Beta Analytic and the Poznan radiocarbon laboratories (Table 2.2). Radiocarbon ages were corrected for a marine reservoir effect of 400 years and calibrated using Calib 7.0.2 radiocarbon calibration software and the IntCal13 calibration curve (Reimer et al., 2013). Stable isotope (oxygen) measurements were carried out on samples from core PSM3-CS011 using specimens of benthic foraminifera (*Uvigerina peregrina* and *Uvigerina mediterranea*) from the size fraction higher than 150 µm. Isotope analyses were done at the laboratories of the Leibniz Institute of Marine Sciences of the University of Kiel. A correction factor of -0.25‰ for $\delta^{18}O$ was applied to the isotope values from *Uvigerina mediterranea* to take into account the common differences in isotope values recorded between *U. peregrina* and *U. mediterranea* related to their different vital and habitat preferences (Schmiedl et al., 2004; Fontanier et al., 2006). The $\delta^{18}O$ curve of borehole GDEC4-2 (western slope of the Corsica Trough; Ange Minto'o, 2014; Toucanne et al., 2015) was used as a reference for the construction of the age model with the $\delta^{18}O$ values of core PSM3-CS011 (eastern slope of the Corsica Trough, Pianosa Ridge). Cores PSM3-CS012 and PSM3-CS009 were correlated with PSM3-CS011 using the Ca/Fe ratio obtained from the XRF.

2.4.2.7. Compaction correction to estimate sedimentation rates

Compression indices obtained from oedometer tests, carried out on cores PSM3-CS009 and PSM3-C012, were used to correct the effect of compaction on the sediment thickness and thus to calculate sedimentation rates, by applying the compressibility equation that links the void ratio (e) with the vertical effective stress (σ'_v) (Lambe and Withman, 1979):

$$e = e_0 - \lambda \ln\left(\frac{\sigma'_v}{\sigma'_{v0}}\right), \quad (1)$$

where e_0 is a reference void ratio at a reference vertical effective stress σ'_{v0} of 1 kPa and λ is the compression index. The e-ln(σ'_v) plots obtained from the oedometer test provide the values of e_0 at the intersection of the virgin compression line and the reference value σ'_v= 1 kPa. The compression index (λ) is the slope of this line. The values used for core PSM3-CS009 are λ= 0.180 and e_0= 1.921; and for core PSM3-CS012 λ= 0.204 and e_0= 2.111. They correspond to the mean λ and e_0 values obtained from 5 oedomenter tests on samples from core PSM3-CS012 and 4 oedometer tests on samples of PSM3-CS009 located in between 2 and 11 mbsf. Decompaction in core PSM3-CS011 was carried out using λ and e_0 values obtained from core PSM3-CS009.

The change in thickness (Δh) of a sediment layer of initial thickness h_0, created by the increment of the lithostatic stress ($\Delta\sigma'_v$), depends directly on the change in void ratio (Δe), according to:

$$\frac{\Delta h}{h_0} = \frac{\Delta e}{1+e_0} = -\frac{\lambda}{1+e_0}\ln\left(\frac{\Delta\sigma'_v}{\sigma'_{v0}}\right) \quad (2)$$

Then, the decompacted thickness h_d can be calculated following the equation:

$$h_d = h_0\left[1+\frac{\lambda}{1+e_0}\ln\left(\frac{\sigma'_v}{\sigma'_{v0}}\right)\right] \quad (3)$$

2.4.3. Geotechnical measurements on Calypso piston cores

2.4.3.1. Vane shear test

The laboratory vane shear test permits to measure the peak and residual undrained shear strength of a sediment (Fig. 2.9A). This test was carried out systematically on all cores used for this study. The measurements were done every 10 or 15 cm. The vane shear test can be only performed in soil composed of fine-grained material, since the results are not reliable if the soil contains sand (ASTM D4648). The test consists on first pushing the vane vertically into the soil, and then the top of the vane is rotated with a constant velocity. The results provided by the machine is the undrained shear strength (Su) in function of the rotation angle (Fig. 2.9B). The peak shear strength (Su_p) corresponds

to the maximum value and the residual shear strength (Su_r) the minimum value at a rotation of 180° reached after the maximum *Su* (Fig. 2.9B). The sensitivity (S_t) of the sediment is then calculated as:

$$S_t = Su_p \cdot Su_r^{-1} \quad (4)$$

2.4.3.2. Celerimeter

In addition to the P-wave velocity values obtained from the MSCL, complementary direct P-wave velocity measurements were carried out at the same time as vane shear tests. This test is done to avoid errors related to a bad contact between the sediment and the tube and they are also useful to test the quality of the MSCL results. The celerimeter is composed of a fork, with source and receiver are separated by 7 cm. P-wave velocity measurements were performed every 15 cm.

2.4.3.3. Natural moisture content, porosity and density

The moisture content (w) is defined as the ratio of the weight of water to the weight of solids in a given volume of sediment. Natural moisture content was systematically measured in all cores every 25 cm. About 30 g of sediment are sampled directly from the core section. First the wet sample is weighted (w_w) and then it is dried in the oven at 105°C during 24 h. Finally, the dry sediment is weighted (w_d) and the moisture content is calculated as:

$$w = \frac{w_w - w_d}{w_d} \quad (5)$$

w is usually expressed in percent.

The porosity (n) is defined as the ratio of the volume of voids to the total volume and it can be obtained from the moisture content, as:

$$n = \frac{w}{w + \frac{\rho_{water}}{\rho_{solid}}} \quad , \quad (6)$$

where ρ_{water} is the density of the water (1 g·cm^{-3}) and ρ_{solid} is the density of the sediment solid fraction (considered equal to 2.66 g·cm^{-3}). The porosity is also commonly expressed in percent. The density of the sediment (ρ_s) can be calculated using the porosity and considering a constant density of the soil solid fraction of 2.66 g·cm^{-3}:

$$\rho_s = n \cdot \rho_{water} + (1\text{-}n)\, \rho_{solid} \quad (7)$$

2.4.3.4. Fall cone test

The fall cone test permits to establish the Atterberg limits:

- Plastic Limit (*PL*): it is the moisture content at the point of transition from semisolid to plastic state.
- Liquid Limit (*LL*): it is the moisture content at the point of transition from plastic to liquid state.

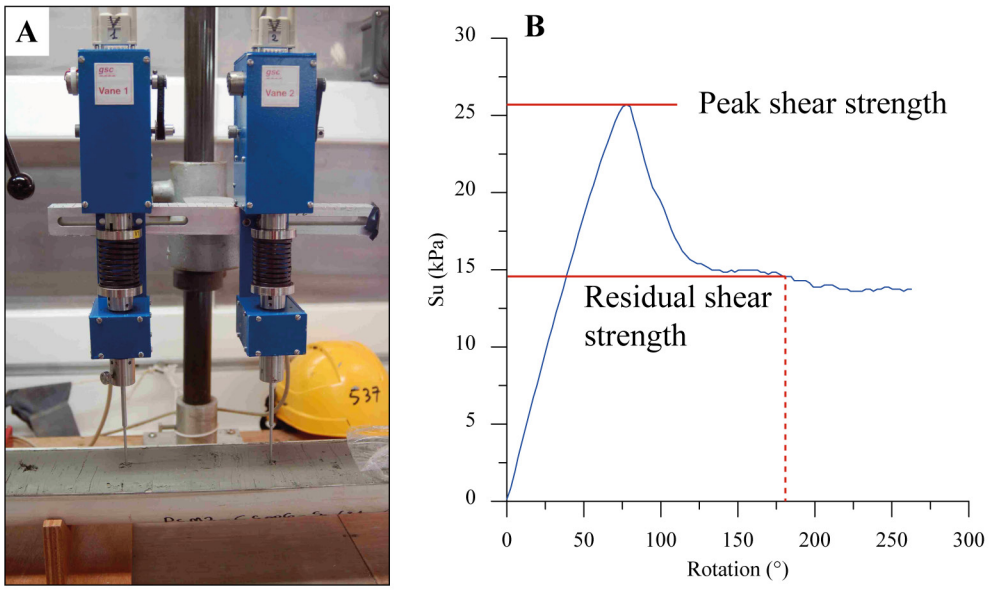

Fig. 2.9. (A) Photo of the IFREMER laboratory vane shear test with the vanes inserted in the sediment. **(B)** Example of an undrained shear strength (*Su*) curve obtained after a vane shear test. The maximum *Su* value corresponds to the peak shear strength and the value at 180° of rotation after the peak corresponds to the residual shear strength.

- The Plasticity Index (*PI*) can be calculated as the difference between the liquid limit and the plastic limit: $PI = LL - PL$ (8)

The Atterberg limits provide information about the consistency of fine grained sediments and permit to classify sediments in function of their plasticity. The fall cone test was carried out on all samples that were also used for further geotechnical analysis (oedometer and triaxial tests).

For the fall cone tests we used the method discribed by Koumoto and Houlsby (2001). It consists on first mixing and remoulding the sediment sample with a spatula in order to break the internal structure. Then we put the remoulded sample in a metal cylinder that is 2 cm high, and finally we use the fall cone and measure the penetration of the metal cone in the sediment (Fig. 2.10A). The measurement is repeated four times, then the results of the first measurement and the mean values are compared. We finally choose the one with the highest correlation coefficient. The fall cone test is repeated at different moisture contents, thus the operation is repeated approximately every one or two hours and the sediment gets drier under normal aerial conditions between consecutive tests. The test is carried out at five different moisture contents, presenting a logarithmic decrease in penetration with a decrease in moisture content (Fig. 2.10B). The plastic limit corresponds to the moisture content at 2 mm of penetration, while the liquid limit is the moisture content at 20 mm of penetration (Fig. 2.10B).

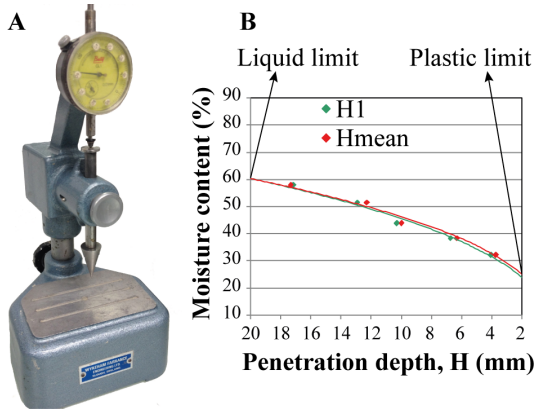

Fig. 2.10. (A) Fall cone of IFREMER laboratory. **(B)** Example of the calculation method of the Atterberg limits.

2.4.3.5. Oedometer test

The oedometer permits to perform a one dimensional consolidation test (Fig. 2.11). The test consists on applying on a sediment sample a vertical stress and measuring the amount of deformation induced by the stress. The sample is contained in a metal ring (5 cm of diameter and 2 cm high) that prevents lateral displacement of the sample. Above and below the sample two paper filters and two porous stone discs permit the drainage of the water. The sample and the porous stone discs are contained in a metal support connected with two tubes: the lower one is connected to a burette with water that keeps the sample saturated, and the upper one is connected to a flask that stocks the excess of water (Fig. 2.11).

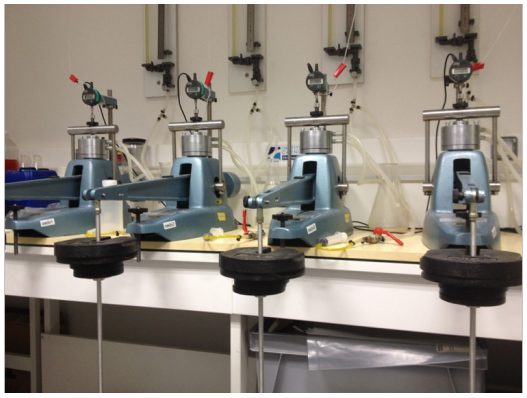

Fig. 2.11. Oedometers of IFREMER geotechnical laboratory.

The stress is originated by putting a weight on an arm lever (10:1 ratio) that will compress the sample in function of the amount of weight. The first measurement is carried out using a weight of 50 g applied during 24 h. After that time the weight is doubled to 100 g and the operation is repeated up to a maximum of 32 kg and every weight is applied during 24 h. All the applied weights are: 0.05, 0.1, 0.2, 0.5, 1, 2, 4, 8, 16 and 32 kg (the vertical effective stress ranges between 1.379 and 1765.12 kPa). Finally a discharge is performed, reducing the weight every one hour down to a minimum weight of 1 kg. The initial void ratio (e_i) is calculated after drying another sample from the same depth of the core at 105°C during 24 h, following the relation:

$$e_i = \frac{n_i}{1 - n_i}, \quad (9)$$

where e_i is the initial void ratio and n_i is the initial porosity.

Then the change in void ratio in function of the applied vertical effective stress (σ'_v) can be obtained using the axial displacement (Δd) of the sample and the following expression:

$$\Delta e = \frac{\Delta d}{d}(1+e) \,, \tag{10}$$

where d is the sample height (2 cm at the beginning of the test).

The preconsolidation stress (σ'_p) is the maximum vertical effective stress that the sediment sample experienced in the past and it can be calculated from the plot e-σ'_v (see Fig. 2.12 for details). In this study the Pacheco-Silva method has been used (Fig. 2.12; Pacheco Silva, 1970) because it is based on more objective steps (Clementino, 2005) that are also not scale dependent like the Casagrande (Casagrande, 1936) or the Onitsuka methods (Onitsuka et al., 1995). This method consists on tracing a vertical line passing through the intersection of the virgin compression line and the initial void ratio (e_i; Fig. 2.12). The virgin compression line is here considered the steepest line formed by the compression curve of the sediment. Where this vertical line crosses the data curve, we draw another horizontal line. The preconsolidation stress (σ'_p) is the value of the x-axis at the intersection point of this line and the virgin compression line (Fig. 2.12). The compression index (C_c) of the sediment can be calculated as the slope of the virgin compression line in a e-log(σ'_p) plot and the swell index (C_s) as the slope of the rebound curve (Fig. 2.12).

The overconsolidation ratio (OCR) can be calculated as the ratio between the preconsolidation stress (σ'_p) and the vertical effective stress (σ'_v). The vertical effective stress can be calculated as:

$$\sigma'_v = \int_0^z (\gamma_s(z) - \gamma_w(z))dz \,, \tag{11}$$

where z is the in situ depth and γ_s is the unit weight of the sediment calculated as the product of the gravity and the sediment density and γ_w is the unit weight of the water calculated as the product of the gravity and the water density.

The OCR provides information about the stress history of sediments which can be classified as normally consolidated, underconsolidated and overconsolidated. Values of OCR are close to 1 in normally consolidated sediments as they display a loading history in which the preconsolidation stress or the maximum prior load is equal to that generated by the present effective overburden stress. Underconsolidated sediments are those for which values of OCR lower than 1 indicate that they remained above the virgin line with high porosity despite increasing burial depth, a situation associated with the development and maintenance of excess pore fluid pressure. Sediments that have been unloaded by erosion or landslides have values of OCR higher than 1 and are said to be overconsolidated.

Oedometer tests were carried out on 8 different sediment cores from the Pianosa Ridge in order to better constrain the stress history of the zone and to evaluate possible erosive processes. The samples were chosen before splitting the cores, based on MSCL and radiography results obtained from measurements on whole cores to avoid the presence of shells on the samples.

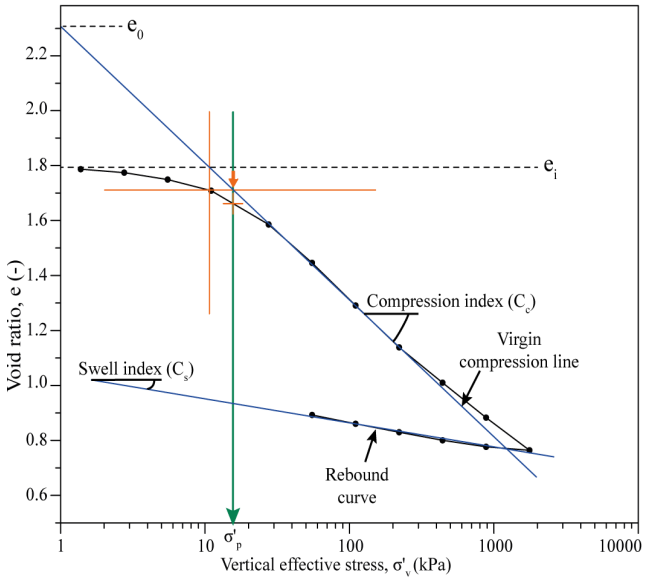

Fig. 2.12. Pacheco-Silva method used to calculate the preconsolidation stress (σ'_p).

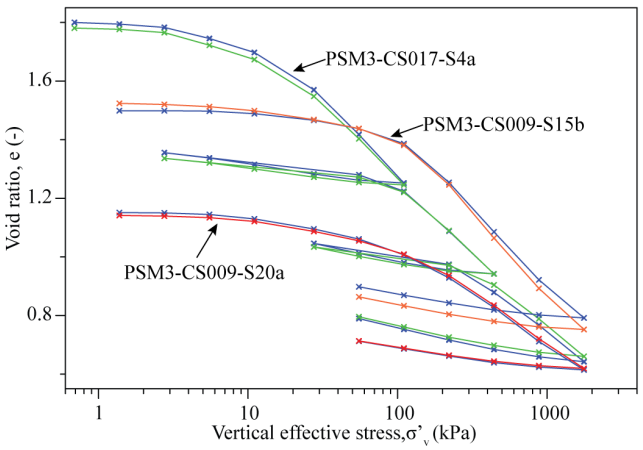

Fig. 2.13. Compression curves obtained from six oedometer tests carried out to check the effects of the pore fluid salinity on the compression behaviour of the samples. Three discharges were done during the test of sample PSM3-CS017-S4a.

Table 2.3. Compression indices obtained from the oedometer tests performed on intact samples using distilled or sea water. Samples from core PSM3-CS017 present 3 compression indices because 3 discharges were carried out during the test Note that the use of distilled water has no influence on the compression behaviour of the samples.

Core sample	Depth (m)	Type of water	Compression index (C_c)
PSM3-CS017-S4a	3.86-3.88	Distilled water	0.53/0.47/0.39
PSM3-CS017-S4a	3.75-3.77	Sea water	0.50/0.46/0.40
PSM3-CS009-S15b	14.12-14.14	Distilled water	0.55
PSM3-CS009-S15b	14.06-14.08	Sea water	0.59
PSM3-CS009-S20a	18.23-18.25	Distilled water	0.36
PSM3-CS009-S20a	18.17-18.19	Sea water	0.36

Once the zone of interest was identified, a 10-cm section was cut and preserved for a future test.

The samples were saturated with distilled water. When distilled water is in contact with marine sediment samples, the salt contained in the sediment is diluted in the water that is incorporated during the test. Yukselen-Aksoy et al. (2008) reported significant sea water effects when the marine clay samples present a liquid limit higher than 110 %, a plastic limit over 70% and a shrinkage limit higher than 104 %. In order to check if the use of distilled water instead of sea water has an influence on the compression behaviour of the sediment from the Pianosa Ridge, we performed oedometer tests on two intact samples of the same core at approximately the same depth, in one test using distilled water and in the other one using sea water. This comparison was done in three different samples from two different cores at depths of 3.8, 14 and 18.2 mbsf (Table 2.3). The sea water used in the test comes from the Atlantic Ocean and has a salinity of about 35 psu. The first charge applied was 12.5 g for the sample PSM3-CS017-S4a and 20 g for the samples of core PSM3-CS009 (Fig. 2.13), then it increased progressively until 32 kg every 24 h, like in the normal protocol.

All the intact samples present very similar compression curves (Fig. 2.13) and compression indices (Table 2.3), in contrast to the lower C_c found by Van Paassen and Gareau (2004) in the samples with sea water. Therefore, we can argue that there is no clear effect of the salinity in the sediment samples from the Pianosa Ridge and we used distilled water in the tests.

Permeability

The permeability of the sediment is measured on each sample placed within the oedometer cell after applying every stress at the end of the 24 h, starting at 55 kPa. Permeability is not measured at lower stresses because they are usually comprised in the swell phase and the permeability has to be measured during the compression phase. For that purpose, the falling head permeability test is applied. The sample is connected to a burette that provides the water head. At the beginning the water level is established at a height of 45 cm. The water can pass through the saturated sample and the change in the water level on the burette is measured every 15 min during a total time of 1 h. Then, the permeability (k) can be calculated as:

$$k = \frac{aL}{At} \ln\left(\frac{l_0}{l_1}\right), \qquad (12)$$

where a is the area of the falling head burette, L is the length of the sediment column, A is the area of the sediment column, l_0 is the initial height of water in the burette, l_1 is the final height of water in the burette ($l_1 = l_0 - \Delta l$) and, t the time required to get head drop of Δl.

2.4.3.6. Triaxial test

The triaxial test permits to determine, among others, the shear strength parameters of the sediment. Bender elements inserted into a triaxial top-cap and pedestal permit to measure P-wave and S-wave velocity in the

Table 2.4. Sediment samples and parameters used for Consolidated Undrained (CU) triaxial tests.

Core	Corrected depth (mbsf)	Confining pressure (kPa)	Back pressure (kPa)	Type of sediment
PSM3-CS012	12.57-12.71	180	100	Muddy sand
PSM3-CS012	12.71-12.86	200	100	Muddy sand
PSM3-CS012	12.86-13.01	220	100	Muddy sand
PSM3-CS018	1.32-1.48	110	100	Mud
PSM3-CS017	4.36-4.55	170	100	Mud
PSM3-CS017	4.55-4.73	120	100	Mud
PSM3-CS017	8.54-8.69	175	100	Mud

sediment specimen during the triaxial test. To prepare the sediment sample for this test, the following steps are performed:

1. The sediment is sampled from the core using a metal cylinder with grease in the inner part in order to minimise the deformation of the specimen while sampling.
2. The sediment and the cylinder are taken out of the plastic tube and a U-channel is prepared in order to obtain a continuous XRF register of the whole core.
3. The sediment left over around the cylinder is sampled every 2 cm and can be used for further analysis.
4. The specimen is taken out of the cylinder and introduced into an impermeable rubber membrane. The final specimen usually has a diameter of 5 cm and a height of 10 cm.
5. Two porous stone discs and two paper filters are put on the pedestal where the specimen will be placed and under the top-cap (placed on the top of the specimen). Then the tubes and porous stones are filled with water and the specimen can be placed. Finally, the cell can be closed and filled with distilled water.
6. The piston is placed in contact with the specimen.
7. First a cell pressure of 5 kPa is imposed in order to keep the specimen stable and then the test can start.
8. All tests start by a saturation phase in order to assure that the specimen is completely saturated and that there is no leak in the membrane. We considered that the sediment was saturated when the Skempton coefficient B was higher than 0.95 (Skempton, 1954).

For the present study, two different type of triaxial tests have been performed: Consolidated Undrained (CU) and Consolidated Anisotropic Undrained Compression (CAUC) triaxial tests.

In the CU triaxial tests the saturated specimen is first consolidated at a determined cell pressure (σ_3, also radial stress or confining pressure), that is homogeneous in all the directions. The effective consolidation pressure is the difference between the cell pressure and the imposed back pressure (i.e. pore pressure at the top of the specimen). When σ_3 increases, the pore pressure at the bottom of the specimen increases, too. Then it will start to decrease because the back pressure transducer drains the pressure to keep it at the fixed level. The consolidation is finished when the pore pressure (at the bottom of the specimen) is equal to the back pressure (at the top of the specimen). Once the specimen is consolidated, it is sheared under undrained conditions at a velocity of 0.01 %·min^{-1}. If after the consolidation the specimen has a height of 9 cm, then the shearing velocity will be 0.009 mm·min^{-1}. Seven CU triaxial test were carried out in order to obtain the internal friction angle of the sediment (Table 2.4): four in muddy samples of cores PSM3-CS017 and PSM3-CS018 and three in muddy sandy samples of core PSM3-CS012.

In the CAUC triaxial test the consolidation is anisotropic to try to reproduce the in situ conditions of the sample. The applied vertical effective stress is the vertical effective stress in situ (σ'_v) according to the depth of the sample. The horizontal stress (σ'_H) is calculated as:

$$\sigma'_H = \sigma'_v \cdot K_0 , \qquad (13)$$

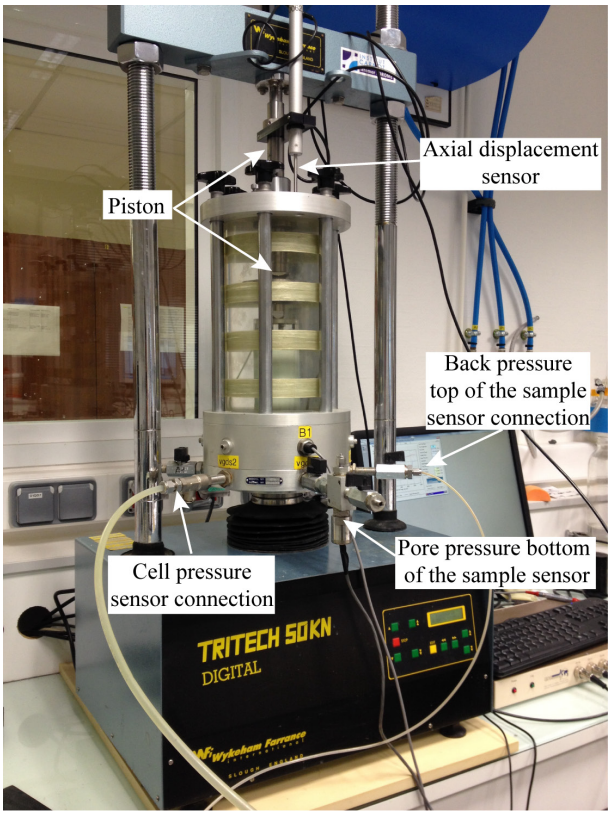

Fig. 2.14. Static triaxial cell filled with water from the IFREMER geotechnical laboratory. The axial displacement is generated by the upwards movement of the whole cell, while the piston remains at the same place. It is composed of a Wykeham Farrance cell and GDS pressure transducers.

Table 2.5. Sediment samples and parameters used for Consolidated Anisotropic Undrained Compression (CAUC) triaxial tests. The test on the sample of core PSM3-CS021 marked in bold was carried out at the *in situ* conditions of the PSM3-CS012 sample in bold characters for comparison.

Core	Corrected depth (mbsf)	Type of sediment	Vertical effective stress (σ'_v)	Horizontal effective stress (σ'_H)	K_0
PSM3-CS021	3.43-3.58	Mud	23	12	0.518
PSM3-CS021	10.97-11.12	Mud	67	44	0.660
PSM3-CS021	17.95-18.10	Mud	114	75	0.660
PSM3-CS021	19.62-19.77	Mud with zeolites	124	82	0.660
PSM3-CS021	20.83-20.98	Mud with zeolites	132	87	0.660
PSM3-CS021	**21.31-21.47**	**Mud with zeolites**	**175**	**104**	**0.597**
PSM3-CS012	22.59-22.73	Mud with zeolites	152	91	0.597
PSM3-CS012	**26.28-26.42**	**Mud**	**175**	**104**	**0.597**

where K_0 is the lateral earth pressure, for a normally consolidated sediment (Jaky, 1948):

$$K_0 = 1 - \sin\varphi', \quad (14)$$

where φ' is the effective internal friction angle.

During the CAUC triaxial test, first an isotropic consolidation is carried out at a cell pressure: $\sigma_3 = \sigma'_H + BP$ (where *BP* is the Back Pressure). Once this consolidation is finished, the next phase is an anisotropic consolidation, keeping the same σ_3 as in the previous phase, but adding an axial stress that is $\sigma_1 = \sigma'_v + BP$. Finally, all the samples are sheared as in the CU tests under undrained conditions at a velocity of 0.01 %·min^{-1}.

2.5. Cone Penetrometer Test with pore pressure measurement (CPTU)

In situ geotechnical measurements have been carried out with the PENFELD penetrometer which is a seabed rig developed by IFREMER to ensure continuous penetration of a rod down to 30 m below seafloor. The rod has a diameter of 36 mm and is coiled around a 2.2 m diameter drum before penetration (Fig. 2.15A). It can push two types of probes into the sediment to carry out CPTU or P wave velocity measurements (Fig. 2.15B). The sonic fork, that measures P-wave velocity, has a source with a frequency of 1 MHz separated 7 cm from the receiver. CPTU measurements were carried out at the standard penetration rate of 2 cm·s^{-1} to simultaneously obtain three independent measurements with depth, the cone resistance (q_c), sleeve friction (f_s) and pore pressure (u_2).

Eight CPTU measurements were acquired along the Pianosa Ridge (Fig. 2.3; Table 2.6; see CPTU location and references in Fig. A.3B in the appendices): 4 on multicrested drifts and 4 in the vicinity of the Pianosa Slump zone (one characterising sediment from the basin, two in the Pianosa Slump deposit and one upslope the Pianosa Slump headwall). In addition, one measurement with the P-wave velocity fork was carried out upslope the Pianosa Slump headwall (Fig. 2.3).

The data obtained from CPTU (q_c, f_s and u_2) were used for deriving geotechnical parameters such as the peak undrained shear strength (*Su*) and overonsolidation ratio (*OCR*) of sediments through semi-empirical cor-

Table 2.6. *In situ* measurements with the PENFELD penetrometer carried out along the Pianosa Ridge during the PRISME3 survey in 2013. See Fig. A.3B in the appendices for location.

Name	Latitude	Longitude	Tool (PENFELD)	Length (m)
PSM3-PFM01-01	42.74317°N	9.95701°E	Mechanic	30
PSM3-PFM01-02	42.7407°N	9.946358°E	Mechanic	30
PSM3-PFM01-03	42.74035°N	9.938228°E	Mechanic	30
PSM3-PFM01-04	42.738166°N	9.927166°E	Mechanic	30
PSM3-PFM02-01	42.393997°N	9.900844°E	Mechanic	23.47
PSM3-PFM02D-01	42.398842°N	9.95168°E	Mechanic	30
PSM3-PFM02D-02	42.393883°N	9.941506°E	Mechanic	30
PSM3-PFM02D-03	42.411723°N	9.976764°E	Mechanic	30
PSM3-PFV04-01	42.41164°N	9.976804°E	Velocity	8.53
PSM3-PFV04-02	42.411582°N	9.976875°E	Velocity	30

relations. This required to first calculate corrected cone resistance values (q_t) from the following expression:

$$q_t = q_c + \Delta u + uh\,, \quad (15)$$

where Δu is the excess pore pressure and uh is the hydrostatic pressure.

Then, using the corrected cone resistance, the net cone resistance can be calculated as:

$$q_{net} = q_t - \sigma_v\,, \quad (16)$$

where σ_v is the total vertical stress in situ which is calculated as:

$$\sigma_v = \int_0^z \gamma_s(z)dz \quad (17)$$

The sediment mass density used in this study to calculate the unit weight of the sediment (γ_s) and the vertical stress is the density calculated from the moisture content obtained from core sediment samples.

The peak undrained shear strength (Su) can be calculated from CPTU data as:

$$Su = q_{net} \cdot N_{kt}^{-1} \quad (18)$$

N_{kt} is a cone factor depending on sediment parameters such as the stress history, stiffness and strength sensitivity. It typically ranges between 10 and 20 with a value of ~14 found to be appropriate for soft clays (Low et al., 2010). Five CAUC triaxial tests were carried out on core PSM3-CS021 in order to obtain site-specific N_{kt} values and thus more accurate Su estimations from CPTU measurements. Unfortunately the results of these CAUC tests could not be used to calibrate CPTU PFM01-04 because we noticed that the undrained shear strength (Su) calculated from the triaxial tests was too high, up to 40% higher than the Su provided by the vane shear tests. After this observation, we realised that the K_0 used for the tests was not appropriate and the samples were thus unintentionally overconsolidated.

The sleeve friction values from CPTU measurements can be a good estimate of the residual undrained shear strength (Lunne et al., 1997). But in the Pianosa Ridge f_s provides lower values than the residual undrained shear strength obtained from laboratory vane shear tests. This might be caused by an inappropriate correction of the sleeve friction values, that caused too low values, reaching even zero in some cases.

Based on statistical studies, Demers and Leroueil (2002) and Mayne (2007) showed that the preconsolidation effective stress (σ'_p) can also be obtained from CPTU measurements using q_{net} and a specific and empiric $N_{\sigma t}$ factor:

$$\sigma'_p = q_{net} \cdot N_{\sigma t}^{-1} \quad (19)$$

In soft clays the $N_{\sigma t}$ factor is usually comprised

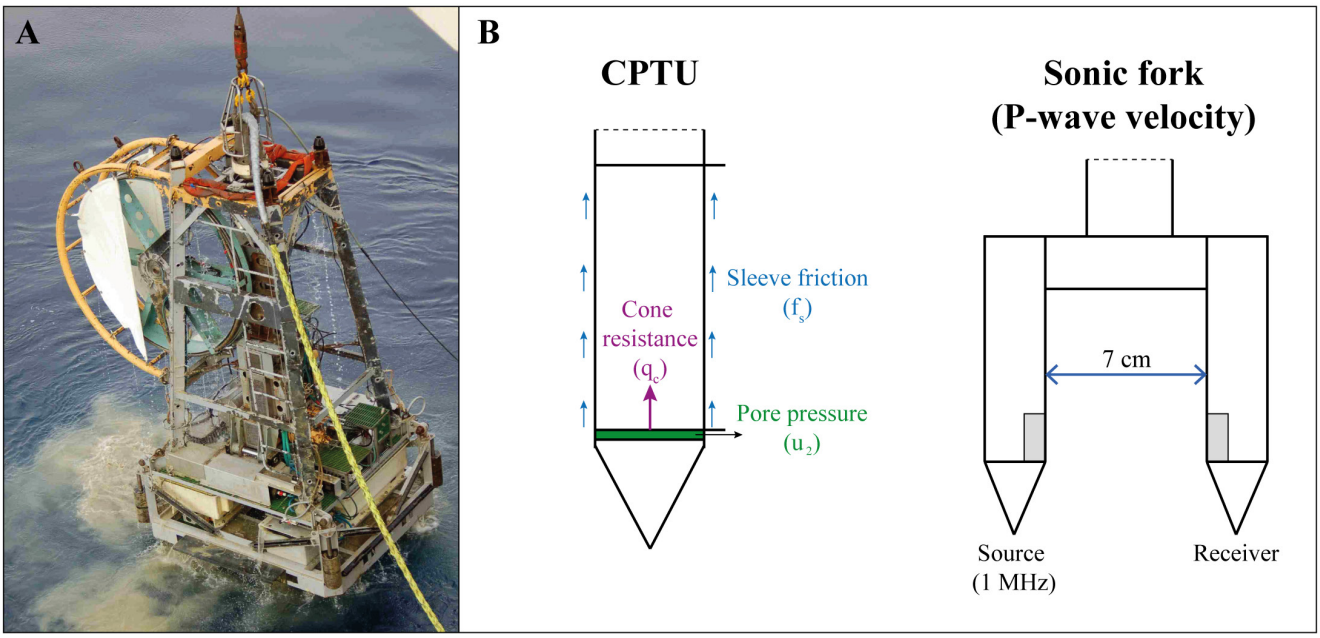

Fig. 2.15. (A) PENFELD penetrometer being deployed in the Pianosa Ridge. **(B)** Scheme of the cone penetrometer with the three different captors to measure cone resistance (q_c), sleeve friction (f_s) and pore pressure (u_2); as well as the sonic fork used to measure P-wave velocity in the sediment.

between 2.9 and 4.5. 3.4 can be a first reliable estimation (Demers and Leroueil, 2002). Specific $N_{\sigma t}$ values were calculated for the Pianosa Ridge using σ'_p values obtained from oedometer tests and q_{net} from CPTU measurements:

$$N_{\sigma t} = q_{net} \cdot \sigma'^{-1}_p \quad (20)$$

More information of the stress history of the site can be obtained using the calculated σ'_p values to estimate the Overconsolidation Ratio (*OCR*) that corresponds to the quotient of the preconsolidation stress (σ'_p) and the vertical effective stress (σ'_v).

2.6. Numerical modelling

2.6.1. MARS3: hydrodynamic model

The coastal and regional circulation model MARS3D (3D hydrodynamical Model for Applications at Regional Scale) of IFREMER was developed by Lazure and Dumas (2008) and uses base algorithm revised by Duhaut et al. (2008). It is an oceanic code with primitive equations and free surface subjected to the Boussinesq and hydrostatic approximation. The turbulent kinetic energy model proposed by Gaspar et al. (1990) is used to compute the vertical turbulent diffusion. The horizontal viscosity is dependent on local mesh dimensions and velocity gradients, and is computed using the formulation proposed by Smagorinsky (1963). The MARS3D code prognostic uses finite differences schemes in a "Arakawa C" shifted grid for the calculations of current, free surface, temperature and salinity. Its originality compared to other similar codes (Symphonie, ROMS, POM, NEMO) is the utilisation of a semi-implicit method to resolve the external or barotropic mode. MARS3D can generate AGRIF zooms (Adaptative Grid Refinement In Fortran; http://www-ljk.imag.fr/MOISE/AGRIF/) and is used for academic research and also for daily operational oceanography through the PREVIMER project.

The MENOR configuration of the MARS3D model extends from the Balearic Islands to the Gulf of Lions and the Ligurian Sea (longitude: 0°E 16°E, latitude: 39.5°N 44.5°N). It has a horizontal resolution of 1.2 km and 60 levels using generalised sigma coordinates system. The open boundaries and initial conditions were obtained from a coarser global circulation model (PSY2V4/Mercator Ocean) at a resolution of 6 km which assimilates SLA, SST and (T,S) profiles. The atmospheric forcing is provided by the ARPEGE-HR model from Météo-France. The grid resolution of this model is 10 km and fields are provided at a time resolution of 1 hour. This is the configuration proposed by the operational system PREVIMER.

To increase resolution in the area of interest, a zoom at 400 m resolution has been embedded in the MENOR configuration, using the AGIRF library. The configuration extends from 9.39°E to 12.33°E and 41.71°N to 43.27°N covering an area from the east Corsican coast to the Italian coast. During the simulation the MENOR grid and the zoom are computed simultaneously. The coarser grid (MENOR, also called mother grid) provides information on the finer grid (the zoom which is also called child grid) boundaries. There is also a feedback from child grid to the mother grid on their common area improving the solution for the coarser grid.

We simulated three months of the winter (January, February and March) of 2013 to represent a period of strong currents and the summer of 2013 to represent a period of weak currents (July, August, September). We chose the year 2013 because it is known that the oceanic circulation was very intense during this winter. For the simulations a spinup of 3 months before the period of interest has been applied (i.e. calculations started in September 2012 to have a better initial solution in January 2013).

For the present project we were interested in the circulation near the seafloor to study the interaction current-seafloor. Therefore we calculated the bottom shear stress generated by currents on the seafloor. In the bed layer the shear stress (τ) is mostly turbulent and can be expressed with the sea water density (ρ) and the friction velocity (u^*) with the relation :

$$\tau = \rho \cdot u^{*2} \quad (21)$$

In the boundary layer with a steady current, the turbulent velocity can be deduced from the current speed near the bottom with the relation :

$$u^* = \frac{\kappa \cdot u(z)}{\ln\left(\frac{z}{z_0}\right)} \quad , \quad (22)$$

where κ is the Von Karman constant (equal to 0.4) and z_0 the bottom roughness length taken here to a constant equal to 0.0035 m. The bottom shear stress is here computed over the thickness of the first layer.

The simulations have been performed by Pierre Garreau (IFREMER, Laboratoire d'Océanographie Physique et Spatiale, Centre de Brest, France) and Mathieu Caillaud (IFREMER, Dynamiques des Ecosystèmes Côtiers, Centre de Brest, France).

2.6.2. SeCo software: 1D consolidation modelling

The SeCo software (Sultan et al., 2004; Leynaud et al., 2007) allows quantification of the evolution of pore pressure over time in one (vertical) dimension. The quantification is done by a back analysis using the sedimentation rate, the porosity and the bulk unit weight of the sediment. During the consolidation processes caused by sediment accumulation, the sediment is compacted and the pore water escapes to other sediment layers. However, low permeability may impede pore water movement with increasing burial depth, thus retarding normal consolidation and leaving the sediment in an underconsolidated state. The objective of using this software for the present study is to analyse if the estimated sedimentation rates and measured sediment characteristics could generate a significant overpressure that may have favoured slope instability. We modelled a single layer with the same parameter of the type of sediment, only sedimentation rates changed in time. The required input parameters for the model are:

- Initial void ratio (e_0) at a reference vertical effective stress (σ'_{v0}) of 0.01 kPa.
- Compressibility of the sediment (λ)
  e_0 and λ are both related to the vertical effective stress (σ'_v) through the following equation:

  $$e = e_0 - \lambda \ln(\sigma'_v \cdot \sigma'^{-1}_{v0}) \quad (23)$$

- The a and b parameters are related with the permeability (k or hydraulic conductivity) of the sediment, and are obtained from the relation between the permeability and the void ratio (e):

  $$k = a \exp(e \cdot b) \quad (24)$$

2.6.3. Liquefaction potential assessment

The approach presented by Robertson (2004) was applied to the CPTU data to evaluate the potential for an earthquake to trigger cyclic liquefaction and to estimate post-earthquake displacements. The method requires an estimation of the Cyclic Stress Ratio (*CSR*) and the Cyclic Resistance Ratio (*CRR*) of the ground. The Factor of Safety (*FOS*) can be calculated as the quotient between *CRR* and *CSR*. When *FOS* is lower than 1, liquefaction may occur. We used the method proposed by Robertson (2004) to estimate CRR using CPTU data, as well as the lateral displacements caused by liquefaction. A site-specific seismicity analysis can be carried out to determine the *CSR* profile with depth. Seed and Idriss (1971) developed a simplified method to estimate *CSR* based on the maximum ground surface acceleration (a_{max}) at the site, using the following equation:

$$CSR = \left(\frac{\tau_{av}}{\sigma'_v}\right) = 0.65\left(\frac{a_{\max}}{g}\right)\left(\frac{\sigma_v}{\sigma'_v}\right) r_d \ , \quad (27)$$

where τ_{av} is the average cyclic shear stress; a_{max} is the maximum horizontal acceleration at the ground surface; g = 9.81 m·s^{-2} is the gravitational acceleration; σ_v and σ'_v are the total and effective vertical overburden stresses, respectively; and r_d is a stress reduction factor which is dependent on depth, that can be estimated using the following function (Robertson, 2004):

$r_d = 1.0 - 0.00765z$ (28)
if $z < 9.15$ m
$r_d = 1.174 - 0.0267z$
if $z = 9.15$ to 23 m

where z is the depth in meters.

The maximum horizontal acceleration (a_{max}) or Peak Ground Acceleration (*PGA*) given for the Corsica Trough for a 475 year return period by the Global Seismic Hazard Assessment Program is lower than 0.04 g (Slejko et al., 1999). The earthquake of the historical record that is the closest to the CPTU sites is located at a distance of about 15 km and has a magnitude of 3.4. Therefore, one of the analysis was done for a 3.4 magnitude and a *PGA* of 0.04 g. Using Idriss' method (Idriss, 1993) and supposing a similar location of the earthquake (distance of 15 km between the epicentre and the CPTU site), *PGA* values were calculated for a magnitude of 4.5 and 6.5.

2.6.4. 1D slope stability modelling

Two slope profiles and two different types of sediment properties were used in a 1D slope stability assessment in order to investigate which factor has a more important role in slope stability in the Corsica Trough: the seafloor morphology (i.e. the slope) or the sediment properties. Since the main studied landslides took place in an open slope with little lateral changes in slope gradient, edge effects can be ignored and we can assume

the slope is infinite in the calculation of the Factor of Safety (FOS). The slope is stable when FOS is higher than 1 and unstable when FOS is lower than 1. The FOS was calculated in static undrained conditions as:

$$FOS = \left(\frac{Su(z)}{\sigma'_v(z)\sin\beta\cos\beta} \right), \quad (29)$$

where Su is the undrained shear strength, σ'_v the effective vertical stress calculated as equation 11 and β is the slope angle.

2.6.5. PLAXIS 2D: slope stability modelling

Plaxis 2D is a commercial finite element program that simulates soil behaviour for geotechnical applications using soil models (Brinkgreve et al., 2012). Plaxis 2D was used in the present study to do a slope stability and factor of safety analysis of the study area that would help to understand the factors and processes that favoured the formation of one of the identified submarine landslides. The geotechnical parameters used for the modelling are specific to the study area and were obtained from laboratory tests carried out on sediment cores.

The soil model used in this study is the Mohr-Coulomb model. It is a linear elastic perfectly-plastic model that can be very useful when the failure behaviour of the soil plays a dominant role. The safety factor is calculated using a "phi-c reduction" approach. The required input parameters are the Young's modulus (E) and the Poisson ratio (υ) for soil elasticity, the undrained shear strength (Su) for soil plasticity under undrained conditions and ψ as an angle of dilatancy. The initial stresses are generated using the K_0 procedure. An approximated approach is used in order to simulate the strain-softening behaviour of some sediment layers by applying the method proposed by Lobbestael et al. (2013), based on Lo and Lee (1973) and Potts et al. (1990). The approach consists in tracking the plastic strains and reducing the shear strength accordingly, using the reference strength-strain curve obtained from a CAUC triaxial test.

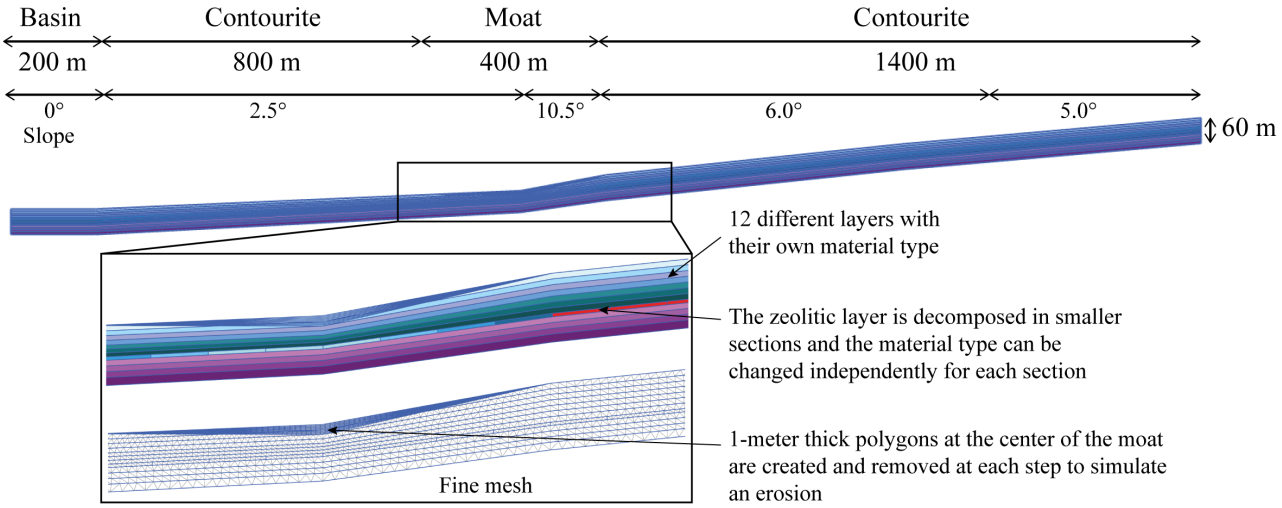

Fig. 2.16. Scheme of the model constructed with Plaxis 2D.

CHAPTER 3. Morphology, spatial distribution and age of submarine landslides

The Pianosa Ridge forms the eastern flank of the Corsica Trough in the Northern Tyrrhenian Sea: it is the site of preferential accumulation of contourites and Mass Transport Deposits (MTDs). Eleven MTDs with a total volume of 6.5 km^3 were identified along the Pianosa Ridge. These MTDs are distributed in three areas: (A) one small MTD associated to canyon flank destabilisation in the northern part of the study area; (B) six intermediate size MTDs in the central area; (C) four MTDs of larger size (up to 2.62 km^3) to the south, including the Pianosa Slump, which is the most recent MTD in this area (dated at 42–50 kyr BP) and analysed in more detail. The main factor controlling the formation of MTDs in areas A and B seems to be steep slopes associated to erosion and heterogeneous sedimentation caused by bottom currents. In contrast, multiple factors may control slope instability in the zone where the largest MTDs took place (area C): the incision generated by contour currents, the convex morphology of the contourite and the presence weak layers in within contourite drifts.

CHAPITRE 3. Morphologie, distribution spatiale et âge des glissements sous-marins

La Ride de Pianosa constitue le flanc est du Canal de Corse en Mer Tyrrhénienne septentrionale : elle se caractérise par l'accumulation de contourites et la formation de glissements sous-marins. Onze glissements, avec un volume total de 6,5 km³, ont été identifiés sur la pente orientale du Canal de Corse. Ces glissements se distribuent en trois zones : (A) un glissement de petit taille lié à la déstabilisation d'un flanc du canyon situé au nord de la zone d'étude ; (B) six glissements de taille intermédiaire dans la zone centrale ; (C) quatre glissements de taille plus importante (jusqu'à 2,62 km³) dans la zone sud. Le glissement de Pianosa (Pianosa Slump), qui est le plus récent de cette zone (daté à 42-50 ka BP) participe au volume des masses glissées de la zone sud et a été analysé de façon plus détaillée. Les facteurs de contrôle principaux de la formation des glissements dans les zones A et B semblent liés aux pentes fortes associées à l'érosion et la sédimentation hétérogène générées par les courants de fond. Concernant les glissements les plus imposants de la zone C, la stabilité de pente pourrait être contrôlée par plusieurs facteurs associés : l'incision générée par les courants sur le fond, la morphologie convexe de la contourite et la présence de couches de faiblesse au sein de l'organisation stratigraphique.

CAPÍTULO 3. Morfología, distribución espacial y edad de los deslizamientos submarinos

La Cresta de Pianosa forma el flanco este del Canal de Córcega en el Mar Tirreno septentrional, lugar de una acumulación preferencial de contornitas y formación de deslizamientos submarinos. Once deslizamientos, con un volumen total de 6,5 km³ pudieron ser identificados a lo largo de la Cresta de Pianosa. Los deslizamientos se distribuyen en tres áreas: (A) un pequeño deslizamiento asociado a la destabilización del flanco de un cañón en el norte de la zona de estudio; (B) seis deslizamientos de tamaño intermedio en la zona central; (C) cuatro deslizamientos de mayor tamaño (hasta 2,62 km³) en el sur, incluyendo el « Pianosa Slump », que es el más reciente de esta zona (datado a 42-50 ka BP) y que ha sido analizado en más detalle. Los principales factores que controlan la formación de deslizamientos en las áreas A y B parecen ser las altas pendientes asociadas a la erosión y a la sedimentación heterogénea creadas por las corrientes de fondo. Sin embargo, múltiples factores podrían controlar la estabilidad de talud en la zona donde se formaron los deslizamientos más grandes (área C): la incisión generada por las corrientes de contorno, la morfología convexa de la contornita y la presencia de capas débiles.

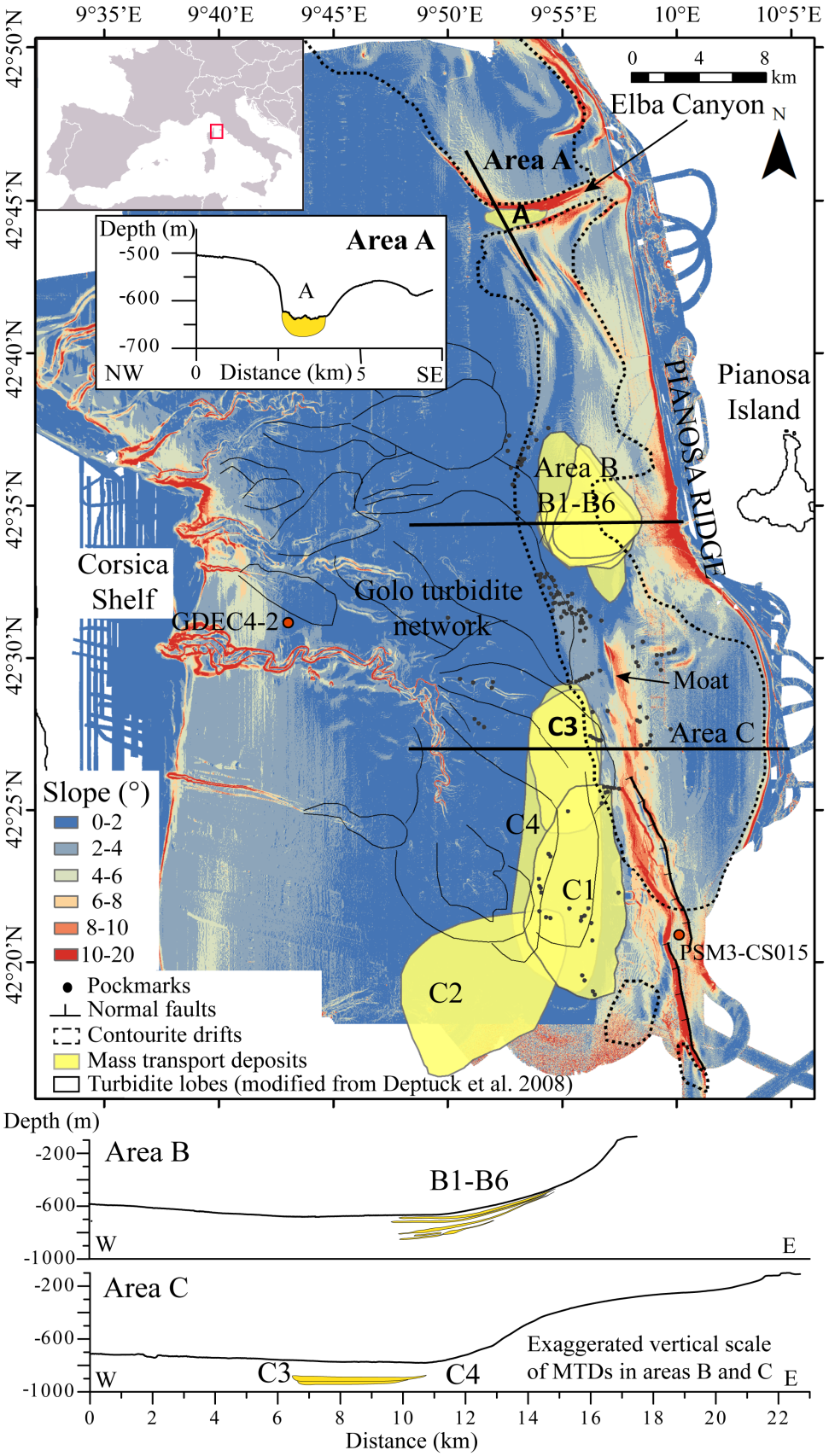

Fig. 3.1. Seafloor gradient map of the Corsica Trough with superposed location of morpho-sedimentary features: Mass Transport Deposits (MTDs), contourite drifts and turbidite lobes (see legend). Three bathymetric cross-sections across areas A, B and C show the location of MTDs.

3.1. Introduction

The Corsica Trough is located between Corsica and the Tuscan Shelf in the Northern Tyrrhenian Sea. It has a maximum depth of 880 m and connects the Tyrrhenian and Ligurian Seas. The eastern flank of the Corsica Trough is formed by the Pianosa Ridge, a tectonic structure with typical slopes between 3° and 10°, reaching 20° locally (Fig. 3.1). This area is characterised by several submarine landslides and contourite deposits (Cattaneo et al., 2014; Fig. 3.1). Contourite drifts are formed by the Levantine Intermediate Water (LIW), flowing northwards along the Pianosa Ridge (Artale and Gasparini, 1990). The sediment input from the Tuscan Shelf is low since sediment from Italian rivers is mostly trapped in the Tuscan Shelf and cannot reach the Corsica Trough (Roveri, 2002). Most of the sediment deposited in the Corsica Trough is transported from the Corsica shelf by the Golo turbidite network (Deptuck et al. 2008; Fig. 3.1).

The aims of this study are to present the size and the stratigraphic distribution of Mass Transport Deposits (MTDs) along the Pianosa Ridge, and to analyse their relationship with the pre-existing seabed morphology.

3.2. Size, chronology, distribution of submarine landslides and relation to the pre-existing slope

Eleven MTDs were identified in the Quaternary sediment record along the Pianosa Ridge (42°15'N-42°45'N; Fig. 3.1), representing a total volume of 6.5 km^3.

The morphological characteristics of the MTDs are summarised in Table 3.1 and have been obtained using the multi-channel high resolution mini GI gun seismic data with the following criteria:

- **Volume**: the volume of the deposit was calculated using Kingdom Suite software by quantifying the time interval between the top and the bottom of the MTD from the seismic profiles.
- **Maximum runout**: the maximum horizontal distance between the headwall scarp and the frontal part of the MTD corresponds to the maximum runout (Fig. 3.2; Finlay et al., 1999). When the buried headwall scarp is not evident in the sediment record, the reference used to estimate the runout is the shelf-edge.
- **Maximum length**: it is the maximum extension of the MTD in the direction perpendicular to the slope (Fig. 3.2).
- **Maximum width**: it is the maximum extension of the MTD in the direction parallel to the slope (Fig. 3.2).
- **Width/length ratio**: it provides information about the confinement of the submarine landslide. The MTD would be more confined when the width/length ratio is higher than 1.

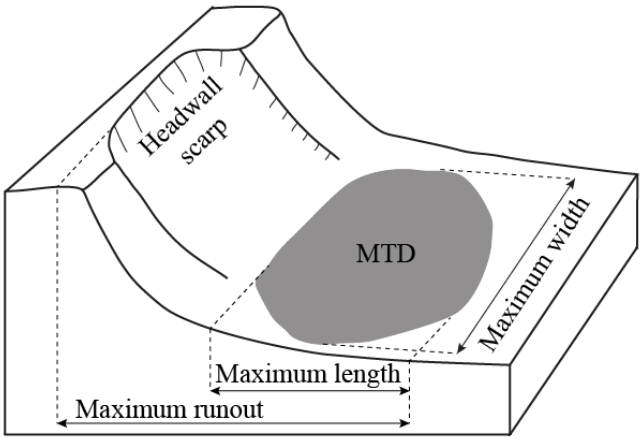

Fig. 3.2. Scheme explaining the criteria followed to determine the maximum runout, length and width.

The differences in location, volume and morphology were used to distinguish three areas of MTDs: A, B and C (Table 3.1).

- **Area A**

Area A is located in the northern part of the study area and shows the presence of a small size submarine landslide (< 2 km long) associated to the destabilisation of the northern flank of the Elba Canyon (west of the Elba Island), where the slope is 8° to 20° (Figs. 3.1 and 3.3). The headwall scarp and the deformation features of the MTD are clear in the local multibeam bathymetry (Fig. 3.3). The slide headwall is located at depths ranging from 380 to 620 m and has a wavy shape (Figs. 3.3 and 3.4). The upper part of the canyon northern flank, which was not affected by the submarine landslide, presents longitudinal incisions (Fig. 3.3). MTD A is of Holocene age, since it disrupts a regional reflector dated at 12 kyr (Fig. 3.4).

Table 3.1. Characterisation of Mass Transport Deposits (MTDs) in areas A, B and C.

Area	Name	Volume (km^3)	Maximum runout (km)	Maximum length (km)	Maximum width (km)	Width/Length ratio	Age (kyr BP)
A	A	0.10	1.5	1.2	3.6	3.0	<12
B	B1	0.19	7.0	5.7	7.6	1.3	42-59
	B2	0.09	8.0	5.6	4.6	0.8	125-137
	B3	0.26	7.5	5.9	7.2	1.2	420-437
	B4	0.15	4.2	2.5	7.4	3.0	452->542
	B5	0.05	6.0	3.4	4.4	1.3	>542
	B6	0.04	6.2	3.6	4.4	1.2	>542
C	C1	2.62	9.0	6.0	13.5	2.3	42-50
	C2	0.47	16.0	10.0	7.8	0.8	125-160
	C3	0.67	6.0	4.0	8.7	2.2	265-321
	C4	1.86	10.4	5.3	18.6	3.5	321-380

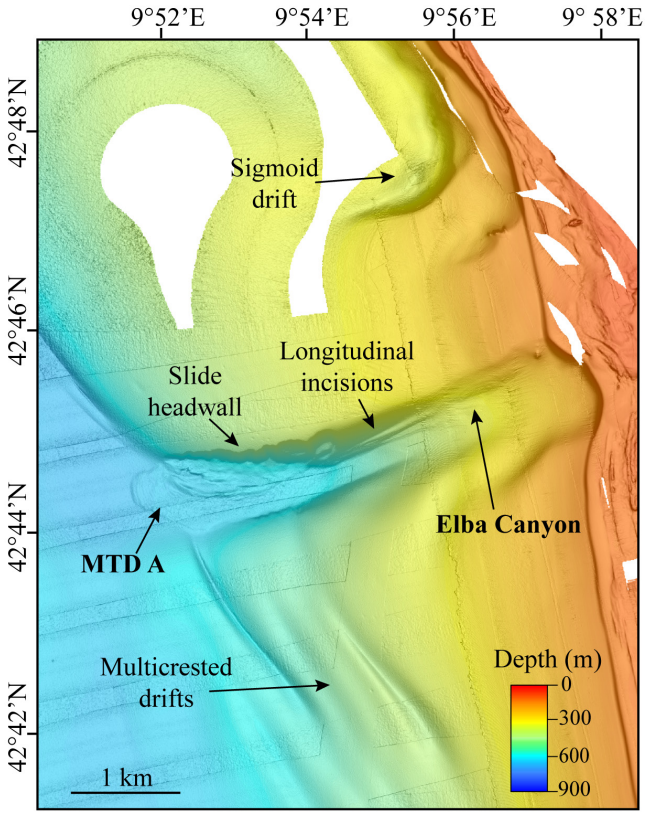

Fig. 3.3. Multibeam bathymetry showing the presence of MTD A in the Elba Canyon.

- **Area B**

Six small to intermediate size (2-6 km long) MTDs (B1 to B6) are observed in area B (Table 3.1). They are located west of the Pianosa Island, where the Pianosa Ridge forms an edge, generating high slope gradients (8-10°; Fig. 3.1). Downslope processes created gullies from the continental shelf edge to the lower slope that are not observed in other zones of the Pianosa Ridge (Figs. 3.5 and 3.6), showing that this zone is under stronger downslope movements. Another evidence of more intense downslope processes, is that the shelf edge prism is absent in the area where the gullies are larger (up to 5 km long in contrast to 1.5 km long gullies in the adjacent zone), probably due to the erosion of the shelf edge prism (Fig. 3.5). Furthermore, the slope presents buried slide scarps and the Plio-Quaternary sediment record is more reduced than in other zones of the Pianosa Ridge (Fig. 3.6). The MTDs of area B have an oval shape in plan view (Fig. 3.2) and their volumes range between 0.04 and 0.26 km^3 (Table 3.1). Their width/length ratio is commonly around 1, except for MTD B4 that is 3.0, suggesting a significant confinement of the submarine landslides that did not allow the preferential growth of the MTD in the direction of the flow.

B1, B2, B3 and B4 have a mean thickness of about 10 m; B5 and B6 mean thickness is 5 m (Fig. 3.7). The continental slope in area B is starved during Pliocene and Quaternary compared to the other areas of the Pianosa Ridge (Fig. 3.7), probably due to the fact that fast bottom currents prevent sediment deposition. The Messinian surface is formed by carbonates that have been sampled by core PSM3-CS015 (Fig. 3.2) and dated through Strontium isotopic stratigraphy at dated at 9.25 ± 0.27 Myr (Tortonian, Late Miocene). Pre-Messinian deposits crop out in patches in the upper slope in area B and at the south of

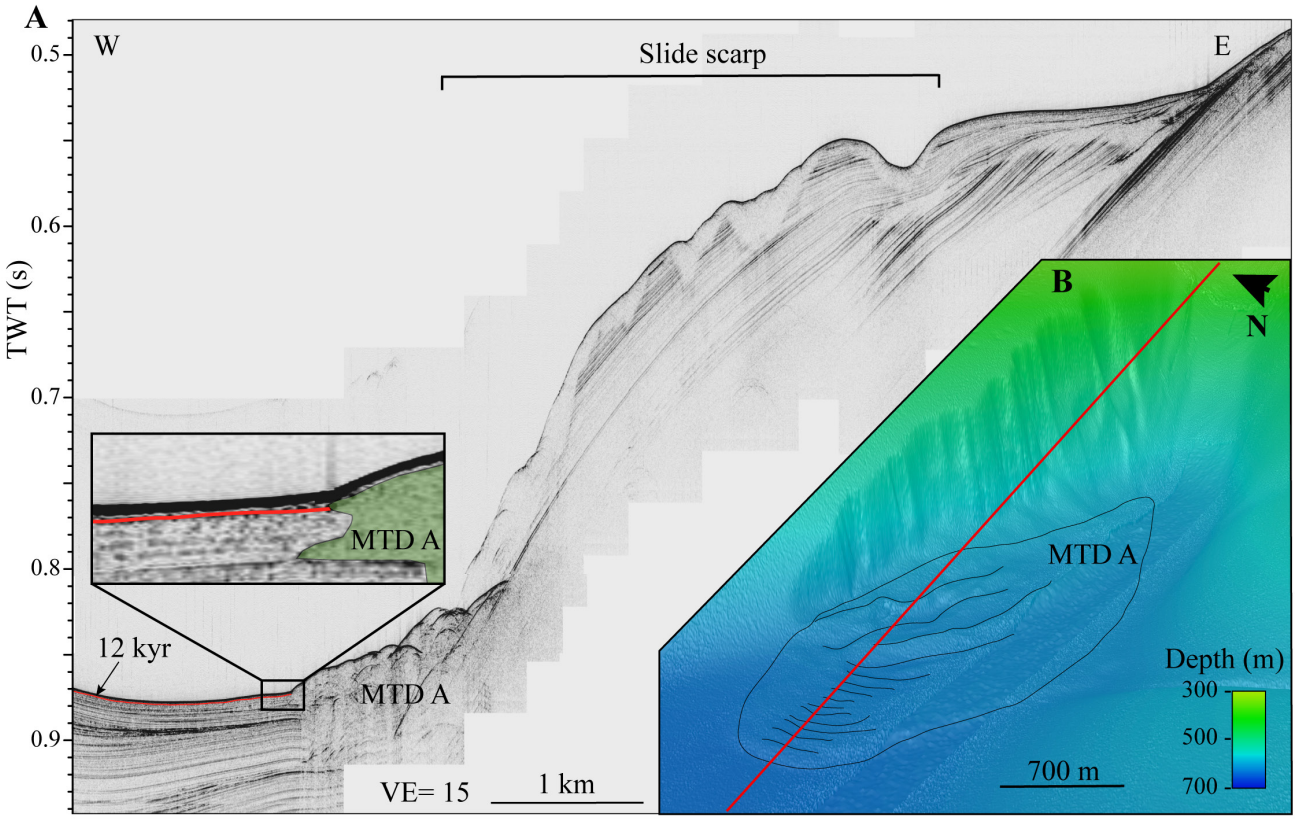

Fig. 3.4. (A) SBP profile crossing MTD A and the northern flank of the Elba Canyon, affected by a slide scarp. MTD A was formed during the Holocene since it disrupts a seismic reflector dated at 12 kyr (red line). **(B)** Multibeam bathymetry of the lower part of the Elba Canyon evidencing the surface morphology of MTD A and the slide scarp on the northern flank of the canyon. The red line shows the location of the SBP profile PSM2-CH-053.

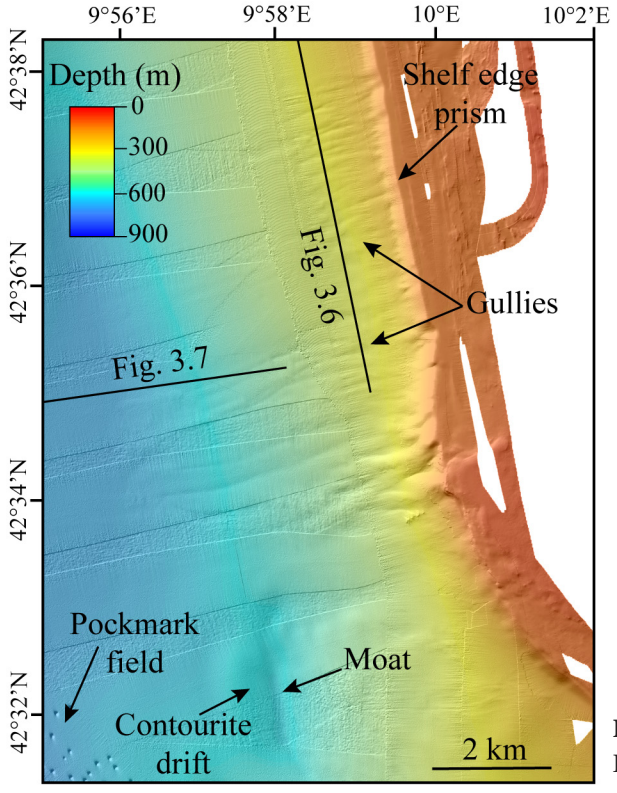

of area C.

Despite the reduced size of these MTDs, their thickness corresponds to about 30% of the Plio-Quaternary deposits in the lower continental slope (Fig. 3.7). B6 and B5 MTDs are older than 542 kyr, while the sediment covering B4 was deposited at 452 kyr, based on correlation to the bottom of borehole GDEC4-2. B3 is close in time to B4 but separated by 300 kyr from B2 (Table 3.1). B1 is the most recent MTD (42-59 kyr) in area B, it took place about 80 kyr after B2. The frequency of the slope failures in area B is irregular and it was higher during the Middle Pleistocene than during the Upper Pleistocene.

Fig. 3.5. Multibeam bathymetry of the area where MTDs of area B were originated. Note that the slope is incised by gullies.

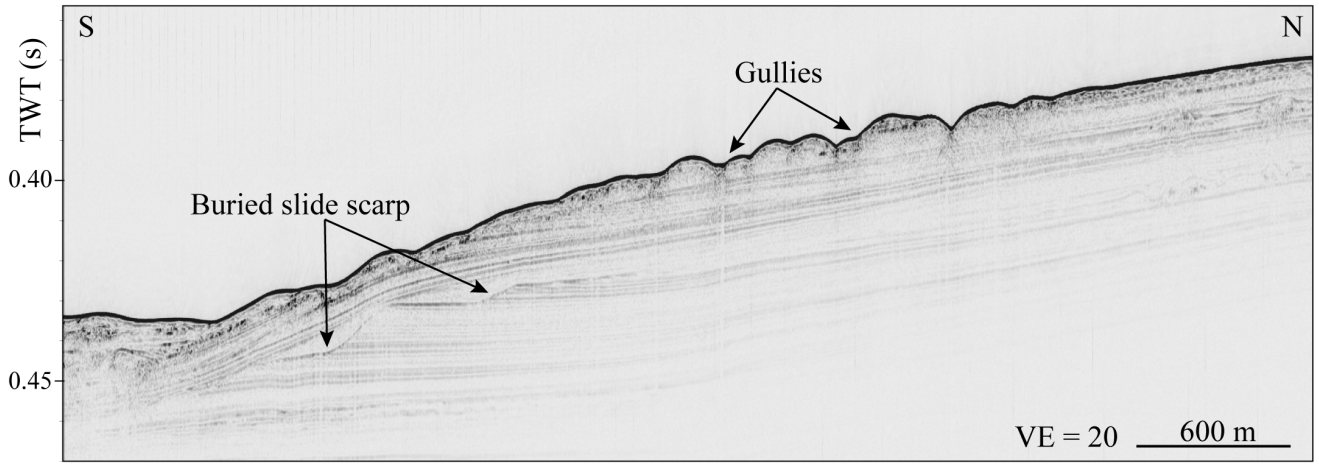

Fig. 3.6. PSM2-CH-015 SBP profile along the upper slope in area B with abundant gullies and a buried slide scarp.

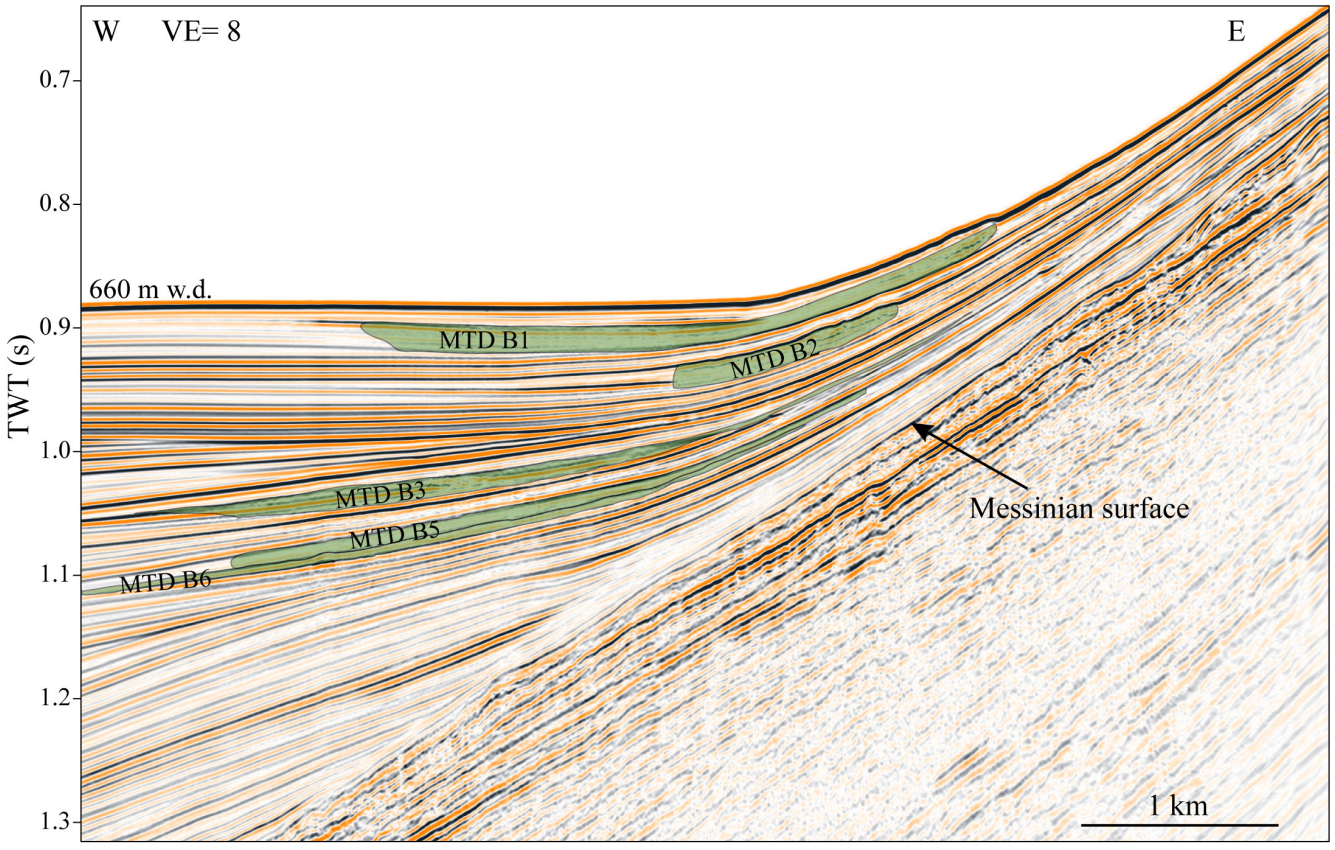

Fig. 3.7. PSM2-HR-058 multi-channel high resolution mini GI gun seismic reflection profile across the slope in area B with the MTDs represented with green polygons.

- **Area C**

Four MTDs (C1 to C4) are found in area C, that is located in the southern part of the study area. These are the largest MTDs identified in the Pianosa Ridge (>4 km long; Table 3.1). The post-Messinian sedimentation in this zone is characterised by the presence of a plastered drift on the upper slope and an elongated separated mounded drift on the lower slope. The mounded drift is absent in the southern-most area, that was affected by the last mass-wasting process (Fig. 3.1). MTDs in area C present volumes that range from 0.67 to 2.62 km^3 and are characterised by a high width/length ratio, except for C2 that has a ratio lower than 1 (Table 3.1), suggesting a high confinement of the deposits. MTDs C3 and C4 were formed between 265 and 380 kyr BP, followed by C2 at 125-160 kyr (Table 3.1). MTDs C2, C3 and C4 present chaotic and transparent seismic facies (Figs. 3.8 and 3.9C). The Pianosa Slump (C1) is the most recent MTD of area C and it presents more diverse seismic facies, providing more information about the internal structure (Figs. 3.8 and 3.9). C1 was analysed in more detail than the other MTDs due to the availability of ground truth data: Calypso piston core PSM3-CS022 and two sites of measurements with the Penfeld Cone Penetration Test with pore pressure measurements (CPTU) PFM02D-01 and PFM02D-02 (Fig. 3.9). The top of C1 (i.e. the bottom of the post-slide hemipelagic sediment; Fig. 3.11) is dated at 42,326 cal yr BP and Cattaneo et al. (2014) reported that the MTD disrupted sediments as old as 50,000 cal yr BP. C1 is overlain by about 17 to 20 m of sediment (Figs. 3.9, 3.10, 3.11). However, various morphological features related to MTD C1 can still be appreciated at the present seafloor (Fig. 3.9).

3.3. Kinematic indicators of the Pianosa Slump (C1)

The headwall domain of C1 has the same lateral extent as the Pianosa Slump deposit. However, the headwall morphology is rather irregular. In the northern part, the headwall is continuous, with a triangular shape, one side parallel to a normal fault (Fig. 3.8). It is connected to the MTD by a sidewall that is up to 30 m high and has an inclination of 20-25° at the present seafloor (Figs. 3.8 and 3.9). The mobilised sediment height was estimated measuring the height of the buried headwall scarps and using a velocity of 1510 m·s^{-1} for the time-depth conversion, resulting in 35 to 39 m. Dragged flow banding can be found on the lateral margin, and is an evidence of strike-slip deformation on the sidewall (Fig. 3.8). On the contrary, south of this zone, the slope is cut by multiple discontinuous headwalls and scarps. Rounded

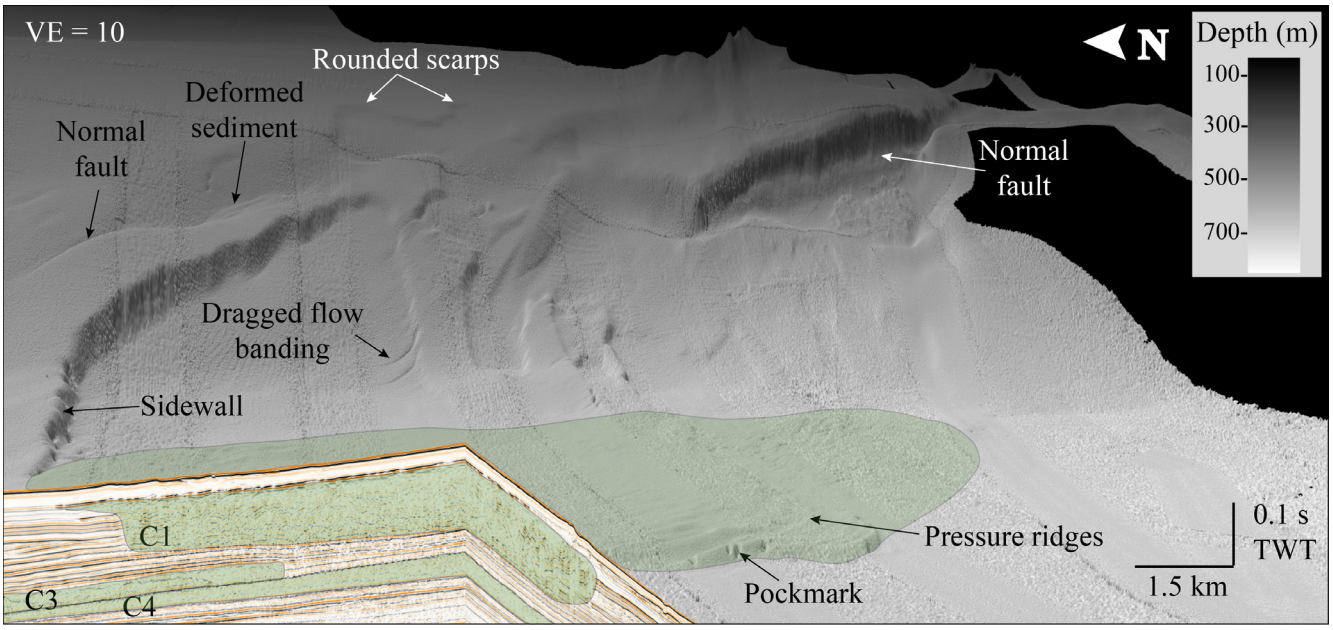

Fig. 3.8. Multibeam bathymetry and multi-channel high resolution mini GI seismic profiles PSM2-HR-009 and PSM2-HR-061 showing the features produced by mass-wasting processes of area C. MTDs are represented by green polygons and the surface of C1 is projected on the seafloor.

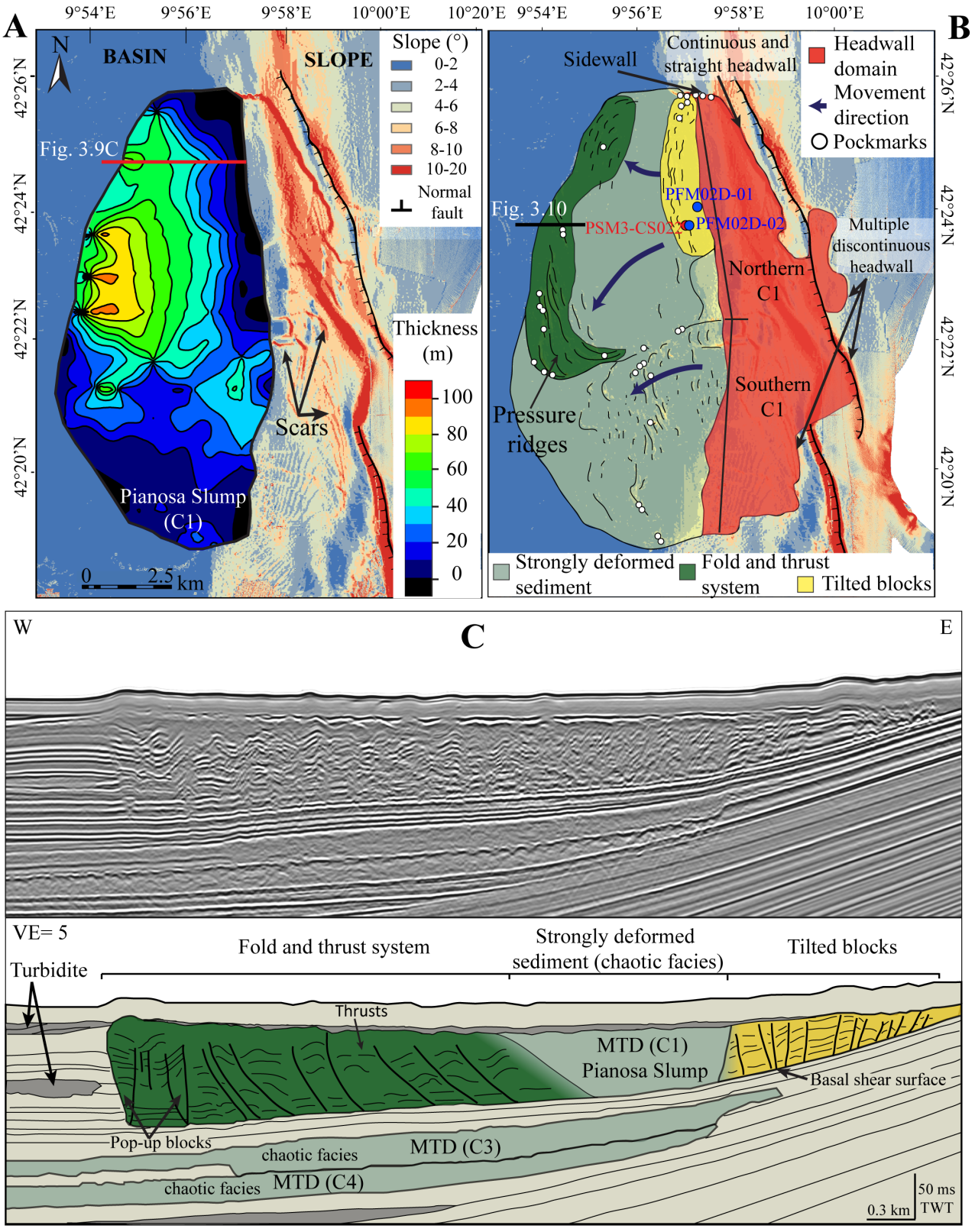

Fig. 3.9. **(A)** Isopach map of the Pianosa Slump (C1) overlaying the present seafloor gradient map with the location of Calypso piston core PSM3-CS022. **(B)** Morphological interpretation of C1. **(C)** PSM2-HR-033 multi-channel high resolution mini GI gun seismic reflection profile across MTDs C1, C3 and C4 and line drawing with the interpretation.

scarps are present upslope the main headwall (Figs. 3.8 and 3.9). MTD C1 is composed of three main parts (Figs. 3.9B and 3.9C) deduced from seismic profiles, bathymetry and Calypso piston core PSM3-CS022:

- Strongly deformed sediment
- Fold and thrust system
- Tilted blocks

The strongly deformed sediment corresponds to chaotic seismic facies that are present in the central northern part and in the southern part of C1, where the headwall is discontinuous. In this area the surface morphology shows lobate shapes and crests that indicate a movement towards the west that turned slightly to the southwest, in the direction of increasing depth (Fig. 3.9B). The MTD thickness of the southern part shows that there is a deposit at the foot of the slope up to 50 m thick and a thicker zone (50-70 m) in the central distal part (Fig. 3.9A).

In the northern part of C1 the internal structure of the deposit is more complex than in the southern part. In the northern part of C1 the toe domain of the MTD is formed by a fold and thrust system. The frontal part of C1 is composed of hemipelagites and turbidites that are deformed and compressed forming a system of thrusts, folds and pressure ridges, with individual pop-up blocks apparent in the frontal part of the MTD (Fig. 3.9C). Turbidites form high amplitude reflections that can be identified in the MTD body as part of the pop-up blocks, folds and thrusts, very clear in the multichannel SYSIF seismic profile, and also evident in the multi-channel high resolution mini GI gun seismic profiles, although with a poorer resolution (Fig. 3.10). The SBP signal does not allow the characterisation of the internal structure of an MTD, since it shows transparent seismic facies with frequent diffraction hyperboles (Fig. 3.10).

The greatest thickness of C1 deposits (up to 100 m) is found in the central zone of C1, where the pressure ridges are the highest (up to 10 m high) and the largest (up to 2 km long) (Fig. 3.9A). The proximal part consists of tilted blocks (Figs. 3.9, 3.11) that become more deformed towards the south. Tilted blocks are identified in seismic profiles where reflectors dip in different directions. Moreover, tilted blocks form crests that are apparent in the seafloor. Groundtruthing evidence of the presence of tilted blocks comes from the bottom of Calypso piston core PSM3-CS022 (Fig. 3.11). This core shows that a 4.7-m-thick debris flow deposit composed of mud with clay pebbles lies on top of the tilted blocks. These distinct seismic and lithological facies correspond to different degrees of deformation, which can be identified in the XRF Calcium curve. When the degree of deformation is very high (debris flow deposit), the Calcium signal is very noisy (Fig. 3.11). The MTD is expressed in the CPTU data as a zone with a higher variability in the corrected cone resistance (q_t), sleeve friction (f_s) and pore pressure (Du). These variations have a lower amplitude in the tilted blocks registered by PFM02D-02 than in the zone of debris flow (Fig. 3.12A) and in the MTD zone registered by PFM02D-01 (Fig. 3.12B). The site of PFM02D-01 is probably composed of debris flow deposits because the CPTU results show high amplitude variability and its position is close to the site of core PSM3-CS022, where the debris flow was identified (Fig. 3.11). Higher variability in CPTU data is probably caused by a higher degree of deformation in the sediment that results in more heterogeneities in the mechanical properties of the sediment.

Between the compressed frontal zone and the zone of tilted blocks, the sediment is strongly deformed and characterised by chaotic seismic facies and by a relatively smooth upper surface (Fig. 3.9). Since the pressure ridges and the crests are perpendicular to the mass movement, they provide information on the direction of the transport. The northern part of the Pianosa Slump comes from the area of the straight headwall parallel to the fault. The northernmost part moved slightly towards the northwest, while most of the sediment was transported in a southwest direction, towards the deepest part of the basin (Fig. 3.9B).

Multibeam bathymetry reveals the presence of many pockmarks located in the contourite drifts between areas B and C and close to MTDs in zone C (Fig. 3.2). The fluid escape paths over the Pianosa Slump are mainly found in the pressure ridges, in the crests and in the sidewall (Fig. 3.9B).

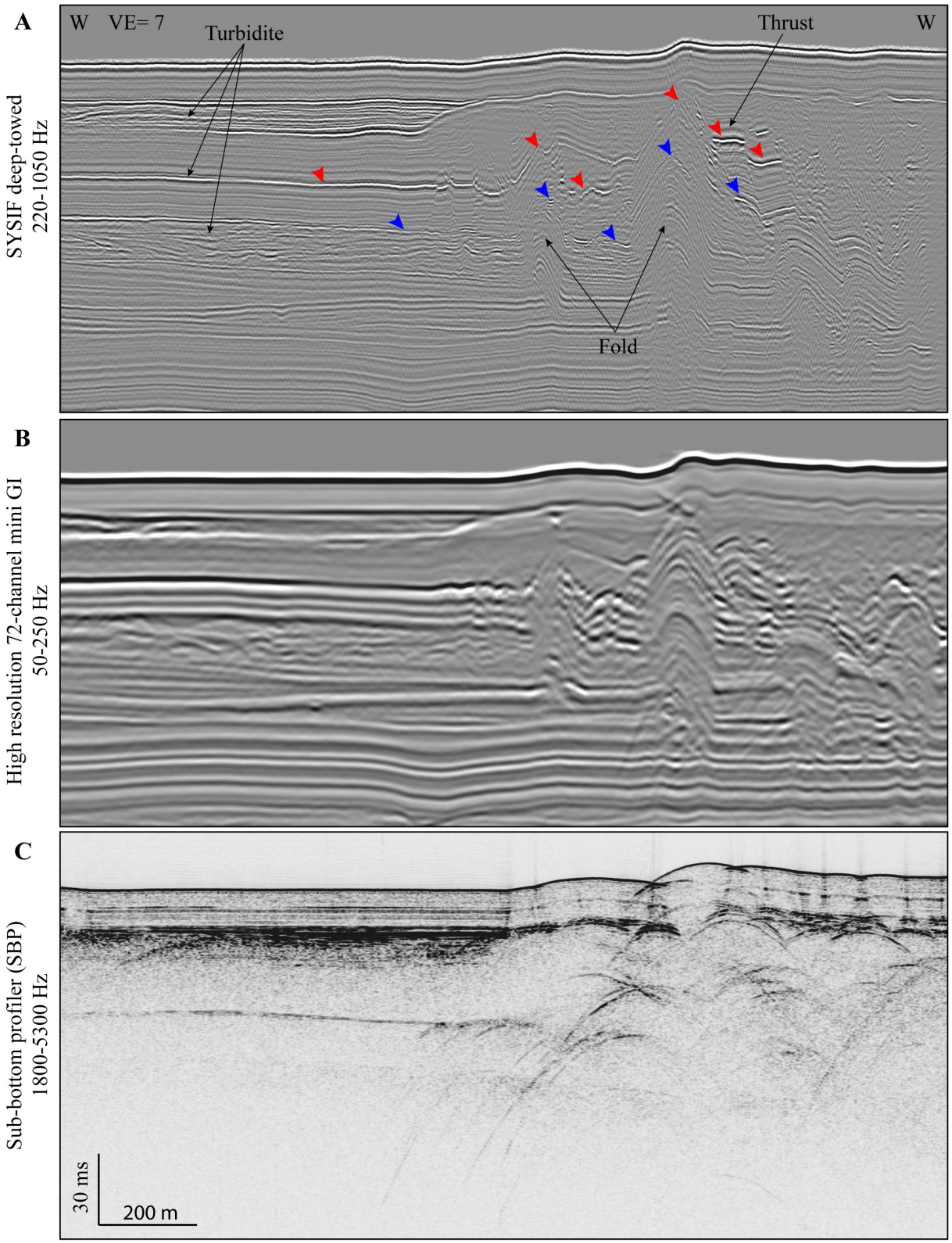

Fig. 3.10. Comparison of the frontal part of C1 imaged by three different seismic systems: **(A)** PSM2-04-PL03-PR03 profile with the SYSIF deep-towed system (220-1050 Hz); **(B)** PSM2-HR-061 profile with the multi-channel high resolution mini-GI (50-250 Hz); **(C)** PSM2-CH-061a profile with the SBP (1800-5300 Hz). The red and blue triangles show reflections that correspond to turbidites, which have been deformed and incorporated into the MTD. Note that the SYSIF is a very effective tool to image the internal structure of MTDs, resolving a system of thrusts and folds invisible for the SBP and poorly imaged by the multi-channel HR mini GI device (Marsset et al., 2014).

3.4. Discussion and conclusions

Slope instability has been a recurrent process along the Pianosa Ridge, although the origin and the control factors could vary according to the location of the submarine landslides. The differences in size and volume between MTDs in areas B and C are likely caused by the combination of an uneven sedimentation along the Pianosa Ridge related to the basement morphology and to bottom currents. Sediment accumulation on the slope in area C is much higher compared to area B. Therefore, more sediment could be potentially mobilised by mass transport during a single event, generating larger submarine landslides. In area B bottom currents may be accelerated due to the higher slope gradient, preventing sediment deposition. Areas B and C present some similarities in the time intervals of slope failure, since B1-C1 and B2-C2 are in similar ranges of age. In contrast, the other MTDs are not synchronous. When C3 and C4 were formed, area B was in stable conditions (Table 3.1).

The main predisposing factor in areas A and B seems to be the steep slopes (8-20° and 8-10°, respectively) (Fig. 3.1). Within the Elba Canyon, due to the Coriolis effect, bottom currents could produce a stronger erosion on the northern flank of the canyon, generating the observed canyon asymmetry with a steeper

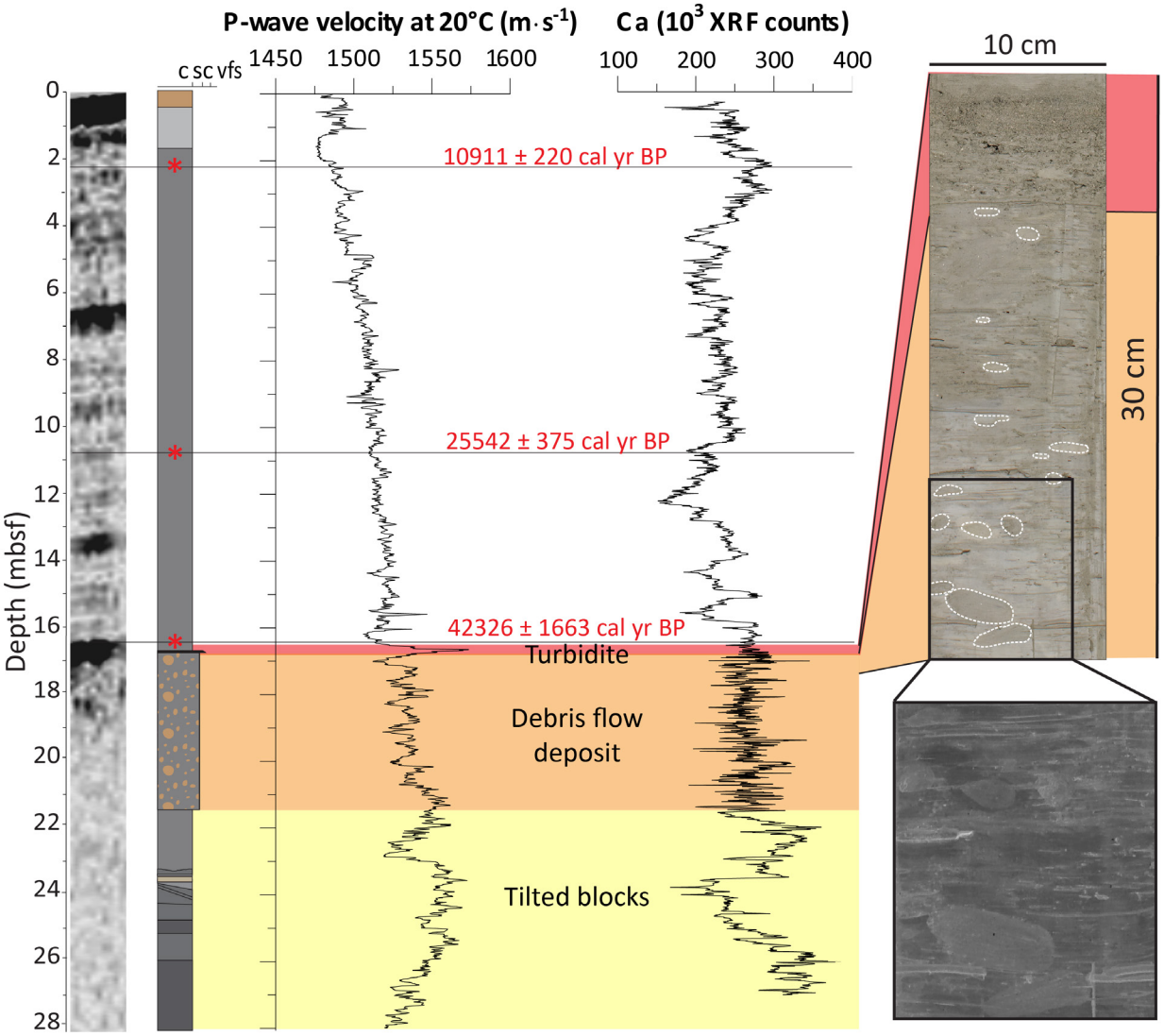

Fig. 3.11. From left to right: SBP seismic facies, core log, P-wave velocity and XRF Calcium curves of Calypso piston core PSM3-CS022. Photo of the core and zoom with inverted colour. The red area shows a turbidite (peak in P-wave velocity), the orange area a debris flow deposit and the yellow area tilted blocks. Three calibrated radiocarbon ages are represented with red stars at 2.2, 10.8 and 16.23 mbsf.

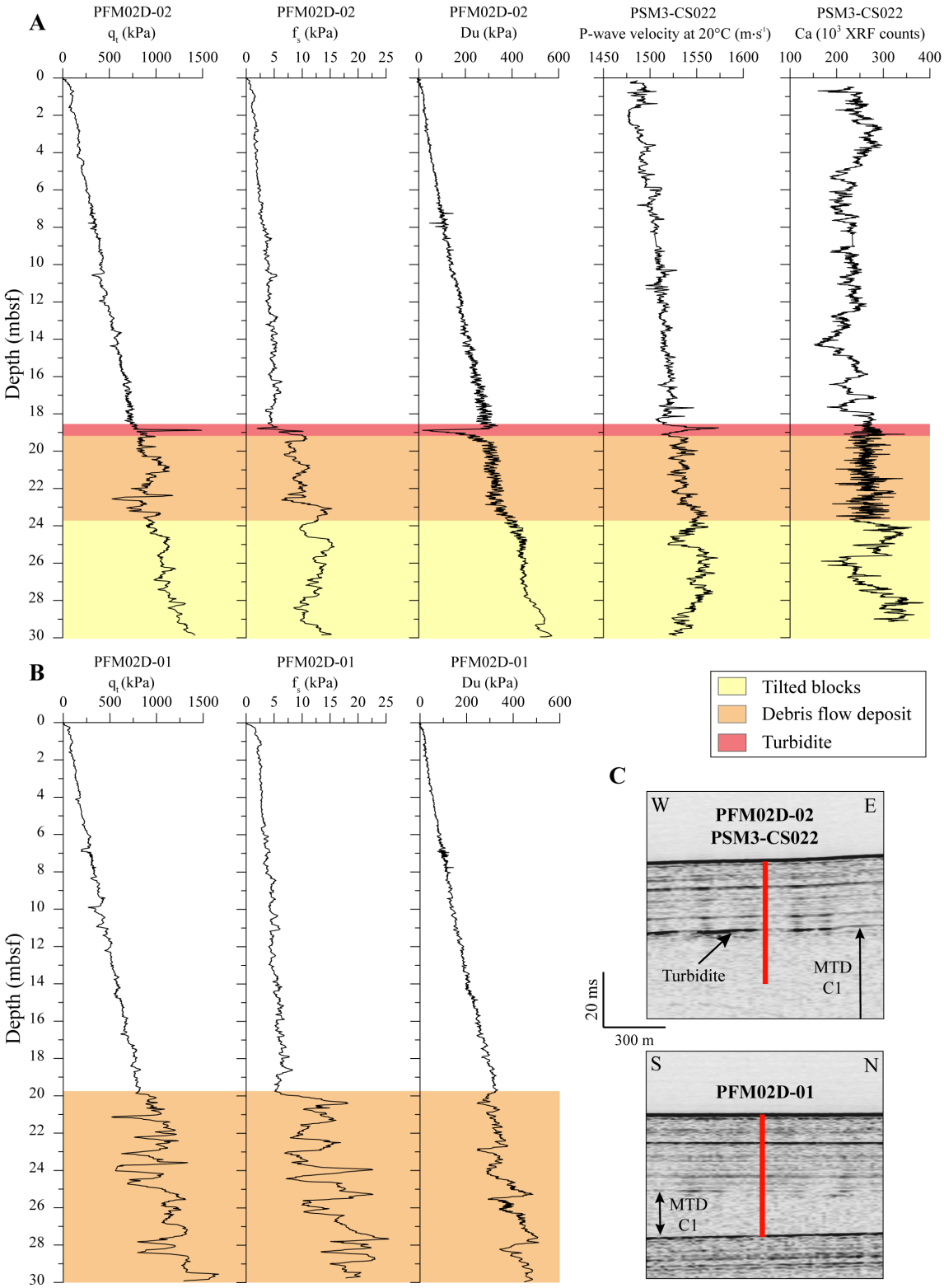

Fig. 3.12. (A) From left to right, corrected cone resistance (q_t), unit sleeve friction resistance (f_s) and pore pressure (Du) from CPTU PFM02D-02; P-wave velocity and Calcium XRF counts from core PSM3-CS022. The depth of the core was corrected to the real *in situ* depth using the CINEMA² software (Woerther et al., 2012). Note that after this correction the position of the sediment core fits perfectly the CPTU in situ measurements. **(B)** From left to right, corrected cone resistance (q_t), unit sleeve friction resistance (f_s) and pore pressure (Du) from CPTU PFM02D-01. **(C)** SBP profiles (PSM2-CH061a upper one and PSM2-CH006 lower one) showing the location of core PSM3-CS022, CPTU PFM02D-02 and CPTU PFM02D-01.

northern flank (Fig. 3.1). Incisions and oversteepening on the northern flank might have contributed to the formation of MTD A, as proven in other canyons such as the Boucart Canyon (Sultan et al., 2007). In area B, six MTDs are stacked, and represent a relevant percentage (30 %) of the Pliocene-Quaternary deposit in the lower slope, suggesting that an important proportion of the sediment accumulated on the middle and upper slope was affected by mass transport.

The formation of submarine landslides in area C (Fig. 3.1) seems to be much more complex and multiple factors may predispose slope instability in this area. Bottom currents may have an important role since they provide sediments and generate incisions with higher slopes, i.e. corridors of non deposition or slight erosion (moat with slope of 15°; Fig. 3.1). The effect of erosion has been modelled and will be presented in Chapter 7. In addition, the continental slope in this area is dominated by a contourite deposit (plastered drift), characterised by a convex shape with much higher sediment accumulation on the central longitudinal axis than on the upper and lower sides. Its special morphology may have important implications on slope instability, since overpressure may be generated in the mid-slope due to higher sedimentation rates. The potential implications in slope instability of the particular morphology of the plastered drift and of sedimentation have been modelled and the results will be presented in Chapter 6. The basal failure planes of the landslides in this area seem to correspond with high amplitude reflectors that present particular properties that will be explained in detail in Chapter 7.

Numerous pockmarks affect the present-day seafloor on top of the MTDs and contourite drifts (Figs. 3.1, 3.9). Some of these pockmarks are clearly rooted on buried MTDs and turbidite lobes.

In the Pianosa Ridge the present-day seismicity is considered to be very low (Scisciani and Calamita 2009), while the area entered in a post-rift phase from the late Messinian (Pascucci et al., 1999). Therefore, we argue that the submarine landslides were probably not triggered by earthquakes.

Taking into account all the exposed factors, a reconstruction of the development of the Pianosa Slump is proposed (Fig. 3.13).

Before the slope instability process was triggered, the continental slope Plio-Quaternary sediment was composed of a plastered drift. This is a type of contourite characterised by a convex shape, with the depocenter situated at the mid-slope and decreasing thickness towards the sides of the deposit, especially towards the south. An elongated separated mounded drift would be located in the lower slope, with a moat separating it from the plastered drift. Both the mounded drift and its associated moat would decrease in size towards the south. This sediment configuration is found in the adjacent zone to the north that was not affected by mass transport. Currents would have created an heterogeneous sediment pattern along the Pianosa Ridge that would influence slope stability, not only by probably acting as predisposing factors as discussed before, but also by conditioning the type and size of the submarine landslide triggered. For instance, the southern part of the Pianosa Slump is thinner and the slide scarps are more irregular than in the northern part of the Pianosa Slump. This is probably related to the fact that the plastered drift was thinner and more patchy in the southern zone.

The mass transport processes took place in two steps. First the main part of the Pianosa Slump (in blue colour in Fig. 3.13) was formed, resulting in a northern thicker deposit associated to a regular triangular-shaped headwall, and a thinner southern deposit associated to an irregular headwall. Then, the downslope process may have weakened the sediment situated upslope the headwall, favouring its destabilisation. As a result, a mass-failure may have happened, resulting in rounded scarps on the slope and a debris-flow deposit (in green colour in Fig. 3.13). The debris flow would have been originated in the zone of the rounded scarps and then would have crossed the main headwall of the Pianosa Slump and finally deposited at the foot of the slope (step 2 in Fig. 3.13). In addition, further deformation would be created upslope associated to a normal fault. The role of this fault is not very well constrained. Its displacement, at least in the Plio-Quaternary section, seems to be small. Therefore, it might not be a source of earthquakes and it could have been generated by heterogeneous compaction. Its size and displacement seem to be more important in the pre-Messinian deposits, reaching 65 m (applying a sound velocity of 1570 $m \cdot s^{-1}$). The role of the fault might have been more important for the older submarine landslides of area C than for the Pianosa Slump because the reflectors present net displacements until the headwall that corresponds to C3 and afterwards

the displacements or deformations seem to be more gradual and diffuse.

In conclusion, bottom currents, and in particular contour currents, control the sediment dynamic and the sediment stacking pattern, shaping mounds and incisions, as well as zones of higher sediment accumulation along the Pianosa Ridge during the Plio-Quaternary. This patchy sediment distribution could generate some zones prone to failure. The area with lower slope gradients and higher sediment accumulation presents larger submarine landslides, while the area with steeper slopes and lower sediment accumulation presents smaller slope failures. However, the frequency of the submarine landslides seems to be similar in both areas.

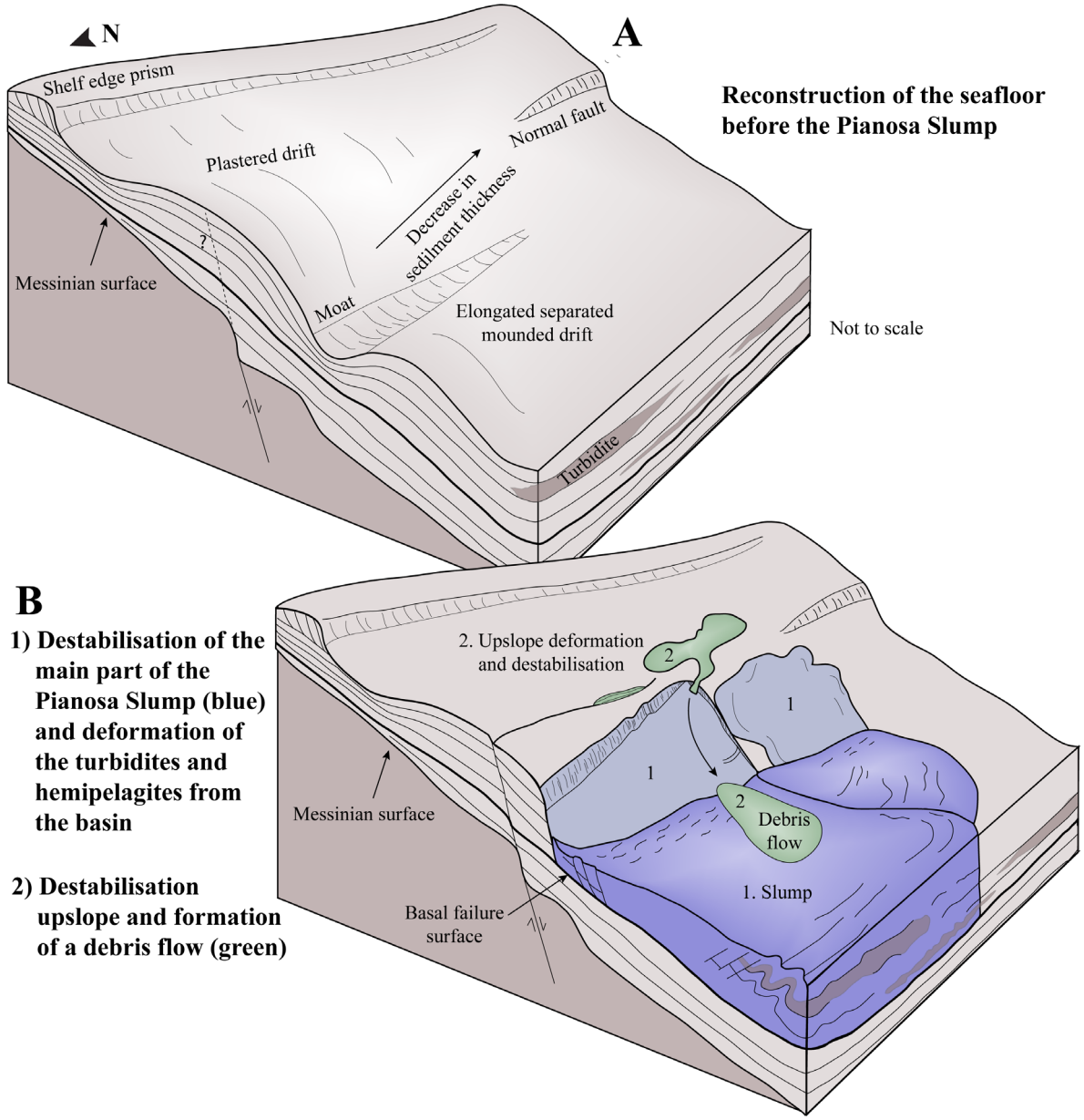

Fig. 3.13. Reconstruction of the Pianosa Slump (C1). **(A)** Suggested pre-slide situation, with the upper slope Plio-Quaternary record formed by a plastered drift on the mid- to upper-slope and an elongated separated mounded drift on the lower slope, both decreasing in thickness towards the south. **(B)** Step 1: main destabilisation of the slope (blue colour), consequently forming a slump that generates a strong deformation of hemipelagites and turbidites present in the basin. Both the slump deposit and the headwall domain are smaller and more irregular in the southern part of the area, where the plastered drift was thinner, and thus less sediment could fall downslope. The thicker black line represents a high amplitude reflection that corresponds to the basal shear surface of C1. Step 2: after the main event, the zone upslope was weakened, generating a debris flow and deformation on a normal fault (green colour).

CHAPTER 4. The Pianosa Contourite Depositional System (Northern Tyrrhenian Sea): drift morphology and Plio-Quaternary stratigraphic evolution

The Pianosa Contourite Depositional System (CDS) is located in the Corsica Trough (Northern Tyrrhenian Sea), a confined basin dominated by mass transport and contour currents in the eastern flank and by turbidity currents in the western flank. The morphologic and stratigraphic characterisation of the Pianosa CDS is based on multi-beam bathymetry, seismic reflection data (multi-channel high resolution mini GI gun, single-channel sparker and hull-mounted sub-bottom profiler), sediment cores and ADCP data. The Pianosa CDS is located at shallow to intermediate water depths (170 to 850 m water depth) and is formed under the influence of the Levantine Intermediate Water (LIW). It is 120 km long, has a maximum width of 10 km and is composed of different types of muddy sediment drifts: plastered drift, separated mounded drift, sigmoid drift and multicrested drift. The reduced tectonic activity in the Corsica Trough since the early Pliocene permits to recover a sedimentary record of the contourite depositional system that is only influenced by climate fluctuations. Contourites started to develop in the Middle–Late Pliocene, but their growth was enhanced since the Middle Pleistocene Transition (0.7–0.9 Myr). Although the general circulation of the LIW, flowing northwards along the eastern margin of the Corsica Trough, remained active all along the history of the system, contourite drift formation changed, controlled by sediment influx and bottom current velocity. During periods of sea level fall, fast bottom currents often eroded the drift crest in the middle and upper slope. At that time the proximity of the coast to the shelf edge favoured the formation of bioclastic sand deposits winnowed by bottom currents. Higher sediment accumulation of mud in the drifts occurred during periods of fast bottom currents and high sediment availability (i.e. high activity of turbidity currents), coincident with periods of sea level low-stands. Condensed sections were formed during sea level high-stands, when bottom currents were more sluggish and the turbidite system was disconnected, resulting in a lower sediment influx.

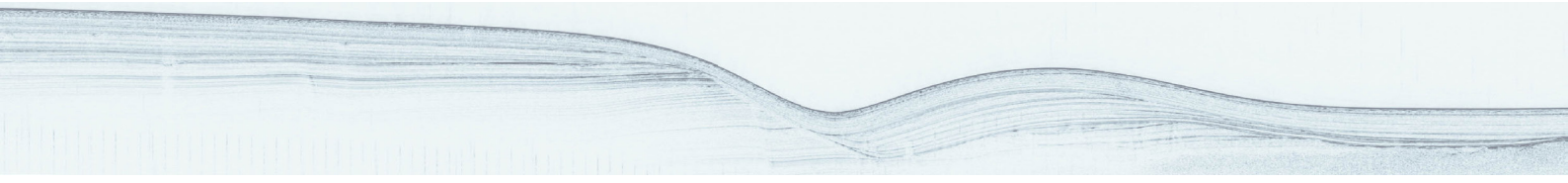

CHAPITRE 4. Le système contouritique de Pianosa (Mer Tyrrhénienne septentrionale): morphologie des dépôts et évolution stratigraphique Plio-Quaternaire

Le système contouritique de Pianosa se situe dans le Canal de Corse (Mer Tyrrhénienne septentrionale), un bassin confiné dominé sur son flanc est par les processus gravitaires en masse et courants de contour, et sur son flanc ouest par courants de turbidité. La caractérisation morphologique et stratigraphique du système contouritique de Pianosa se base sur de la bathymétrie multifaisceaux, de la sismique de réflexion (multichenal haute résolution mini GI gun, sparker monochenal et sondeur de sédiment de coque), des carottes de sédiment et des données d'ADCP. Le système contouritique de Pianosa se situe à des profondeurs entre faibles à intermédiaires (entre 170 et 850 m) et s'est formé sous l'influence de la masse d'Eau Levantine Intermediare (LIW). Avec une longueur de 120 km et une largeur maximale de 10 km, ce complexe contouritique est composé de différents types de dépôts sédimentaires: « plastered drift », « mounded drift », « separated mounded drift », « sigmoid drift » et « multicrested drift ». L'activité tectonique réduite dans le Canal de Corse depuis le Pliocène inférieur permet d'étudier une archive sédimentaire du système contouritique qui est principalement influencé par les fluctuations climatiques et océanographiques. Les contourites ont commencé à se développer pendant le Pliocène Moyen-Supérieur, mais leur croissance a accéléré depuis la Transition du Pléistocène Moyen (0.7-0.9 Ma). Même si la circulation vers le nord des eaux de la LIW, le long de la marge est du Canal de Corse, est restée active durant toute la construction du système, la formation des dépôts contouritiques a été également influencée par le volume des apports sédimentaires et la vitesse des courants. Pendant les périodes de chute du niveau de la mer correspondant à des épisodes de refroidissement global du climat, les courants plus intenses érodaient la crête des dépôts dans la pente continentale moyenne et supérieure. Le rapprochement de la côte avec le rebord du plateau favorisait à cette époque la formation de dépôts sableux bioclastiques vannés par les courants sur le haut de pente. Les accumulations contouritiques de sédiments fins résultent de l'action de courants forts et de la forte disponibilité en sédiment associé à l'activité turbiditique du système sédimentaire du Golo pendant les bas niveaux marins glaciaires. Les intervalles condensés qui scellent ces dépôts contouritiques se sont formés en contexte de haut niveau marin avec les courants plus faibles et des apports sédimentaires plus faibles, conséquence d'un système turbiditique Est-Corse déconnecté du bassin profond.

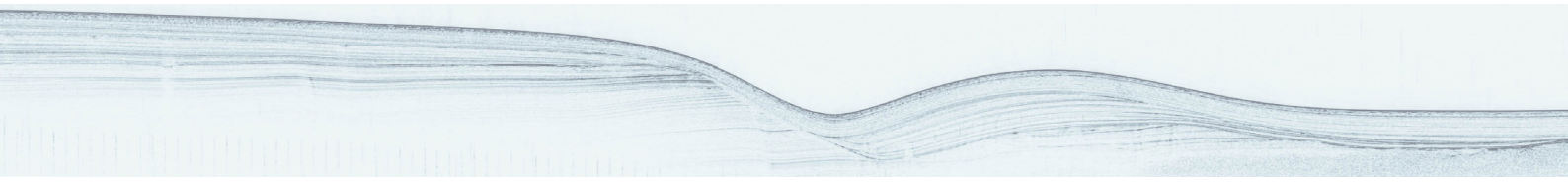

CAPíTULO 4. El sistema deposicional contornítico de Pianosa (Mar Tirreno septentrional): morfología de los depósitos y evolución estratigráfica Plio-Cuaternaria

El sistema deposicional contornítico de Pianosa está situado en el Canal de Córcega (Mar Tirreno septentrional), una cuenca confinada dominada por transporte en masa y corrientes de contorno en el margen este y por corrientes de turbidez en el flanco oeste. La caracterización morfológica y estratigráfica del sistema contornítico de Pianosa se basa en batimetría multihaz, sísmica de reflexión (multicanal de alta resolución mini GI gun, sparker monocanal y perfilador de sedimento), testigos de sedimento y datos de ADCP. El sistema contornítico de Pianosa se encuentra en aguas someras a intermedias (de 170 a 850 m de profundidad) y se forma bajo la influencia del Agua Levantina Intermedia (LIW). Tiene 120 km de largo, un máximo de 10 km de ancho y se compone de diferentes tipos de depósitos: "plastered drift", depósito separado monticular, depósito sigmoidal y depósito multicresta. La reducida actividad tectónica en el canal de Córcega desde el Plioceno temprano permite recuperar un registro sedimentario del sistema deposicional contornítico que solo está afectado por fluctuaciones climáticas. Las contornitas empezaron a desarrollarse en el Plioceno medio-tardío, pero su crecimiento se aceleró a partir de la Transición del Pleistoceno Medio (0.7-0.9 Ma). A pesar de que la circulación general de la LIW, hacia el norte a lo largo del talud este del canal de Córcega, permaneció activa a lo largo de la historia del sistema, la formación de los depósitos cambio, controlada por el aporte de sedimento y la velocidad de las corrientes. Durante los periodos de caída del nivel del mar, las corrientes son más fuertes y suelen erosionar la cresta de las contornitas en el talud medio y superior. Durante estos periodos, la costa estaba situada más cerca del borde de la plataforma continental, lo que favorecía la formación de depósitos arenosos bioclásticos donde el sedimento fino fue transportado por las corrientes. La mayor acumulación de sedimento tuvo lugar durante los periodos de corrientes más fuertes y mayor disponibilidad de sedimento (es decir, cuando las corrientes de turbidez son más activas), coincidiendo con los niveles del mar bajos. Las secciones condensadas se formaron durante niveles del mar altos, cuando las corrientes eran mas débiles y el sistema turbidítico estaba desconectado, resultando en un menor aporte sedimentario.

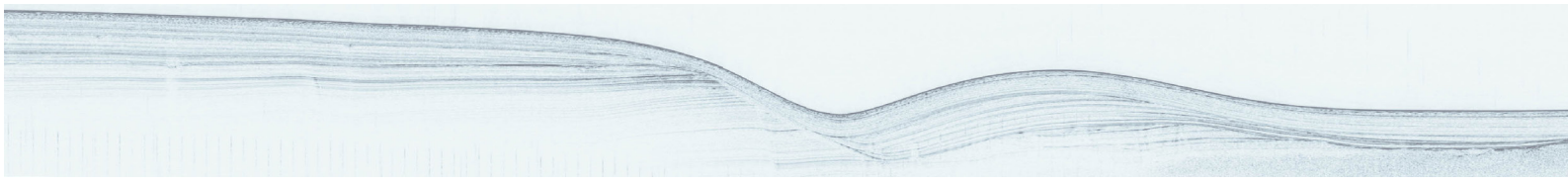

4.1. Introduction

Contour currents are strictly defined as bottom currents flowing alongslope, parallel to a bathymetric contour, and driven by the thermohaline circulation or by the wind (Rebesco et al., 2008). The sediment deposits related to persistent contour currents, named contourites, were first recognised in deep sea environments (Heezen and Hollister, 1964). Numerous cases of contourite drifts controlled by the activity of long-lasting bottom currents have been later identified on the continental shelves (Harris and Beaman, 2003; Harris et al., 1999; Vandorpe et al., 2011) and the upper slope (Marani et al., 1993; Viana et al., 1998; Verdicchio and Trincardi, 2008a) in oceanic settings and along Mediterranean margins. Contourites in the Mediterranean Sea are typically of smaller size compared to drifts found in oceanic settings (Verdicchio and Trincardi, 2008b) and tend to be confined in settings constrained by local morphology such as straits or channels (Pellegrini et al., 2015 and references therein).

Shallow and intermediate depth contourites are more directly affected by sea level fluctuations, since during sea level low-stands, even if they remain in submerged conditions, the sediment flux from the continental shelf is usually enhanced and downslope transport is more frequent. In addition, the upper continental slope may be more influenced by wind-driven currents and the depth range of the superficial and intermediate water masses may change and thus the current regime affecting the seafloor.

Mixed turbidite-contourite systems are common along continental margins where contour currents rework and/or redistribute gravity deposits (Mulder et al., 2008). The interaction between downslope gravity currents and alongslope contour currents is often recognised when both processes take place along the same margin (Rebesco et al., 2002; Hernández-Molina et al., 2006; Marches et al., 2010; Brackenridge et al., 2013). In the Corsica Trough, turbidity and contouritic processes have occurred in opposite margins of the basin. This physical separation of along- and downslope processes avoids problems associated with the identification and differentiation of sediment bodies related to contour or turbidity currents, and permits to better constrain the influence of the activity of turbidity currents on the development of contourites.

The purpose of this study is to present an accurate morphologic and stratigraphic characterisation of the contourite depositional system located on the eastern flank of the Corsica Trough, named here the Pianosa Contourite Depositional System (CDS). Thanks to the confined setting and the available stratigraphic control, the Pianosa CDS provides a unique opportunity to

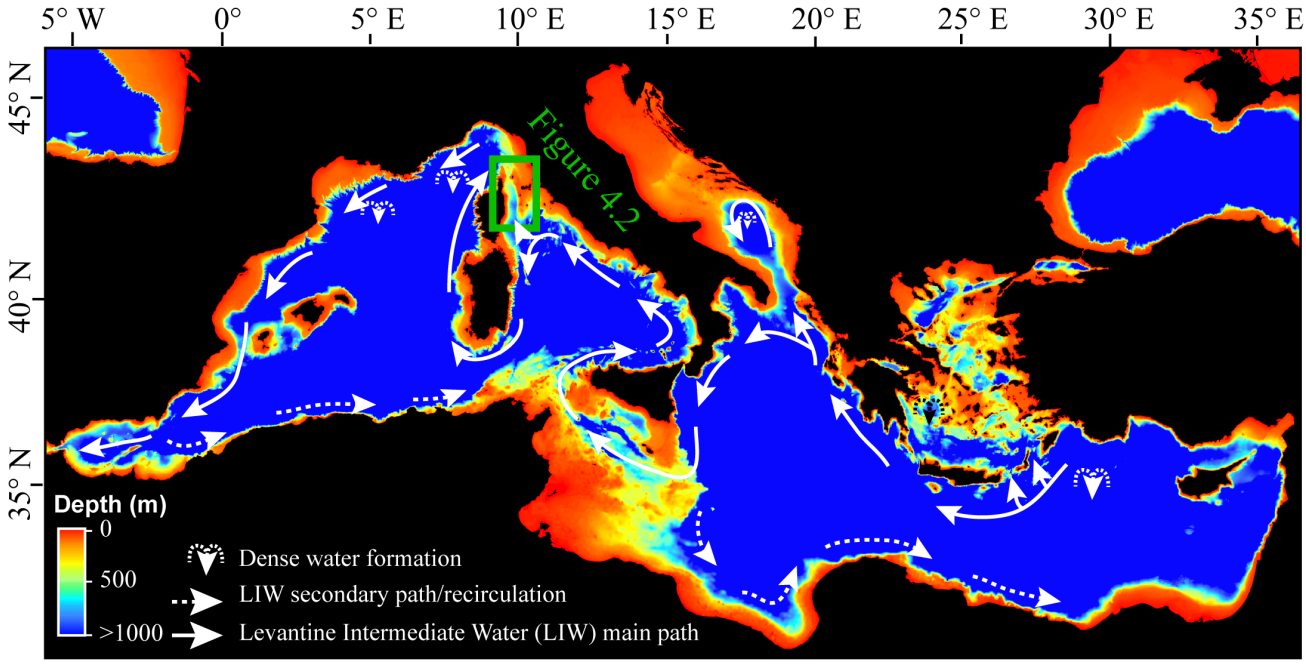

Fig. 4.1. Bathymetry of the Mediterranean Sea with the circulation of the Levantine Intermediate Water (adapted from Millot and Taupier-Letage (2005)).

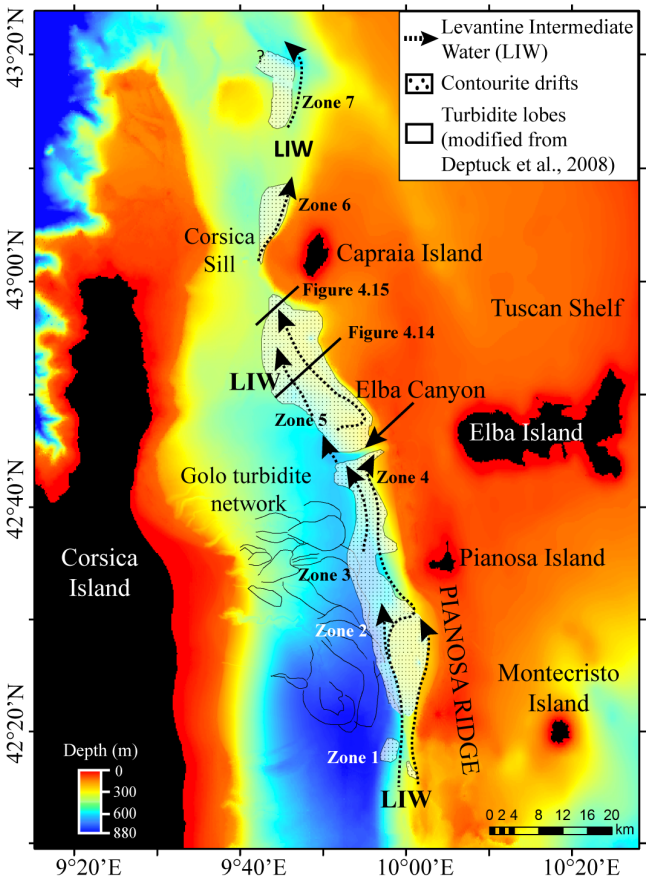

Fig. 4.2. Bathymetry of the Corsica Trough and cartography of the contourite drifts that form the Pianosa Contourite Depositional System and of the turbidite lobes of the Golo Turbidite Network.

achieve a high resolution reconstruction of the spatial and chronological contourite evolution and to infer their relationship to the activity of the turbidite system and sea level fluctuations.

4.2. Regional setting

4.2.1. Geology and morphology

The Corsica Trough is a narrow basin located in the Northern Tyrrhenian Sea (Fig. 4.1), flanked by the Corsica Island to the west and by the Pianosa Ridge and the Tuscan Shelf to the east (Fig. 4.2). It is a N–S trending basin, about 100 km long and 10–35 km wide at depth of the shelf edge. This basin connects the Ligurian and Tyrrhenian Seas. It has a maximum depth of 880 m in the southern part, becoming shallower towards the north. The narrowest and shallowest zone is found offshore the Capraia Island, where the Tuscan and Corsican continental shelves are separated by the Corsica Sill, that is 9.5 km wide between opposite shelf edges.

The Corsica Trough developed during the opening of the Northern Tyrrhenian Sea, between the late Burdigalian and Langhian (Zitellini et al., 1986), resulting in the formation of a half graben (Pascucci, 2002). The Pianosa Ridge corresponds to a tilted block of the half graben, with the master fault located on the Corsican side of the basin (Pascucci, 2002) and separates the Corsica Trough from the Tuscan Shelf. Several N–S and NW–SE trending basins can be found in the Tuscan Shelf (Pascucci et al., 2007), trapping a great part of the sediment from Italy (Roveri, 2002). They developed on a thrust substrate locally dissected by normal faults (Bartole, 1995).

The asymmetry of the Corsica Trough is the result of tectonic processes and is still evident at the present seafloor (Fig. 4.2). The western flank of the basin has a gentle slope (mean values between 2° and 3°), while the eastern flank, formed by the Pianosa Ridge, has steeper slopes (between 3° and 10°, reaching 20° locally). The western part of the Corsica Trough is dominated by downslope gravity-driven depositional processes that resulted in the formation of the Golo turbidite network (Fig. 4.2; Gervais et al., 2004; Gervais et al., 2006; Deptuck et al., 2008; Calvès et al., 2013). On the other side, the Pianosa Ridge is characterised by both alongslope processes, resulting in contourite drifts (Marani et al., 1993; Roveri, 2002; Cattaneo et al., 2014), and downslope mass-wasting processes (Cattaneo et al., 2014; Miramontes et al., 2016a).

4.2.2. Oceanography

The limited depth of the Corsica Trough (max. 880 m) does not allow the transit of the Mediterranean Deep Water, thus the Levantine Intermediate Water (LIW) is the only water mass in contact with the seafloor. The Western Intermediate Water formed in the Liguro-Provençal subbasin is not present in the Tyrrhenian Sea. Therefore, the LIW is in general located just below the Atlantic Water (AW) (Millot, 2013). The AW is found at water depths ranging from 0 to 200 m (Astraldi and Gasparini, 1992; La Violette, 1994; Millot, 1999; Toucanne et al., 2012). The LIW is formed in the Rhodes cyclonic gyre in the NW of the Levantine Basin (Fig. 4.1) by a process of evaporation during the summer, resulting in a warm and salty surface water mass, and a later winter cooling that increases its density. As a consequence, the water sinks inside the Rhodes cyclone during February and March (Lascara-

tos et al., 1999). The LIW formation presents interannual variability: the formation area is enlarged during very cold winters, covering the whole north Levantine Basin (Lascaratos et al., 1999). After its formation, the LIW flows westwards through the Strait of Sicily, then it continues northwards in the Tyrrhenian Sea. A branch of the LIW keeps the same direction crossing the Corsica Trough, while another branch turns to the south and flows along eastern Sardinia (Fig. 4.1; Millot and Taupier-Letage, 2005).

The circulation along the eastern part of the Corsica Trough is characterised by northward flowing currents that change significantly with seasons, it is stronger during the cold seasons (reaching 10–40 cm·s^{-1} from late autumn to early spring) (Astraldi and Gasparini,1992; Vignudelli et al., 1999) and resulting in a higher water transport through the Corsica Trough during this period (Vignudelli et al., 2000).

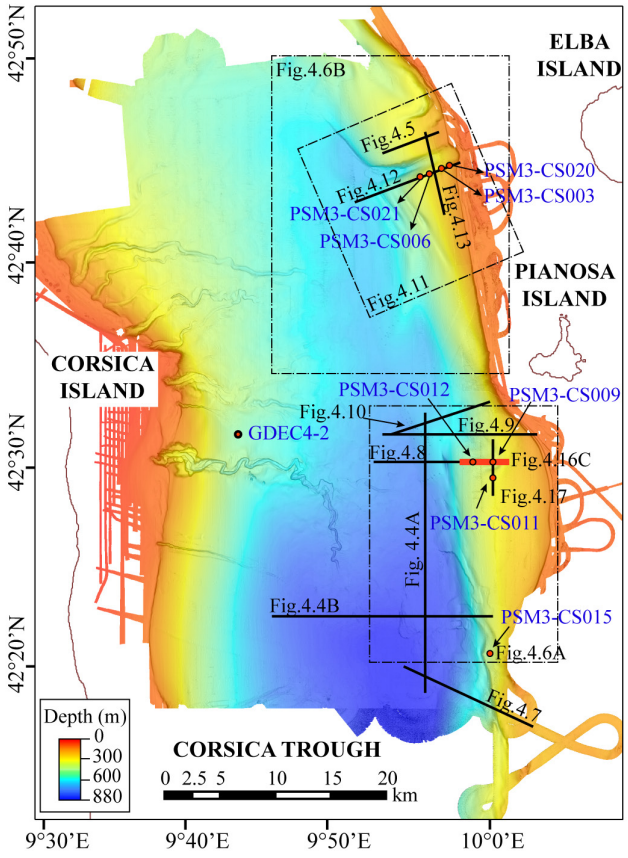

Fig. 4.3. Multibeam bathymetric map of the Corsica Trough with the location of the seismic profiles, sediment cores and the borehole used in this study. Fig. 4.16C location is represented by a red line superposed on the black line of figure 4.8. The location of Figs. 4.6 and 4.11 is represented with dashed squares.

The seasonal variability is in part caused by a climatological steric difference in sea level between the Ligurian and the Tyrrhenian Seas because of the formation of colder and saltier water masses in the Ligurian Sea during the winter (Vignudelli et al., 2000). These changes in circulation are related to large-scale atmospheric patterns, such as the North Atlantic Oscillation (Vignudelli et al., 1999). Similar processes have likely occurred in the past. During cold periods, bottom water masses were better ventilated (Cacho et al., 2000; Mintoʾo et al., 2015) and faster (Toucanne et al., 2012) in the Mediterranean Sea. More arid and cold climatic conditions during cold intervals could favour the production of denser LIW(Cacho et al., 2000).

4.3. Results

4.3.1. Evidences of present-day bottom-current activity

Current velocity obtained from hull-mounted ADCP shows two main zones with northward currents and higher velocities (25-30 cm·s^{-1}), found at 50-200 m and at 700-850 m in the eastern part of the basin (Fig. 4.4A). The whole water column flows northwards in the eastern part of the Corsica Trough at about 10 cm·s^{-1}, while the central-western part of the basin has a preferential velocity of about 5 cm·s^{-1} towards the south, with maximum values of 10 cm·s^{-1} at 100-200 m water depth (Fig. 4.4B).

The coupling of ADCP data and the seafloor reflections provides a better understanding of how currents influence the seafloor morphology. Figure 4A shows a faster (25-30 cm·s^{-1}) pathway of the LIW in northern direction at about 800 m water depth (w.d.) that decreases in velocity towards the north, at the place where the separated elongated mounded drift starts to develop. Higher velocities are found at the lower slope, at the bottom of the Pianosa Slump scar, where the present-day seafloor gradient is 13° (Fig. 4.4B).

The LIW pathway is strongly affected by the presence of a seafloor depression, that we define as the Elba Canyon (Fig. 4.2), in the short-term by inducing an upwelling to the north of the canyon (Fig.5) and in the longterm by forming sigmoid drifts at the north of the canyon (Fig. 4.6B). Although the multi-channel high resolution mini GI seismic data were acquired and calibrated to image the sediment below the seabed, some reflections are apparent in the upper water column

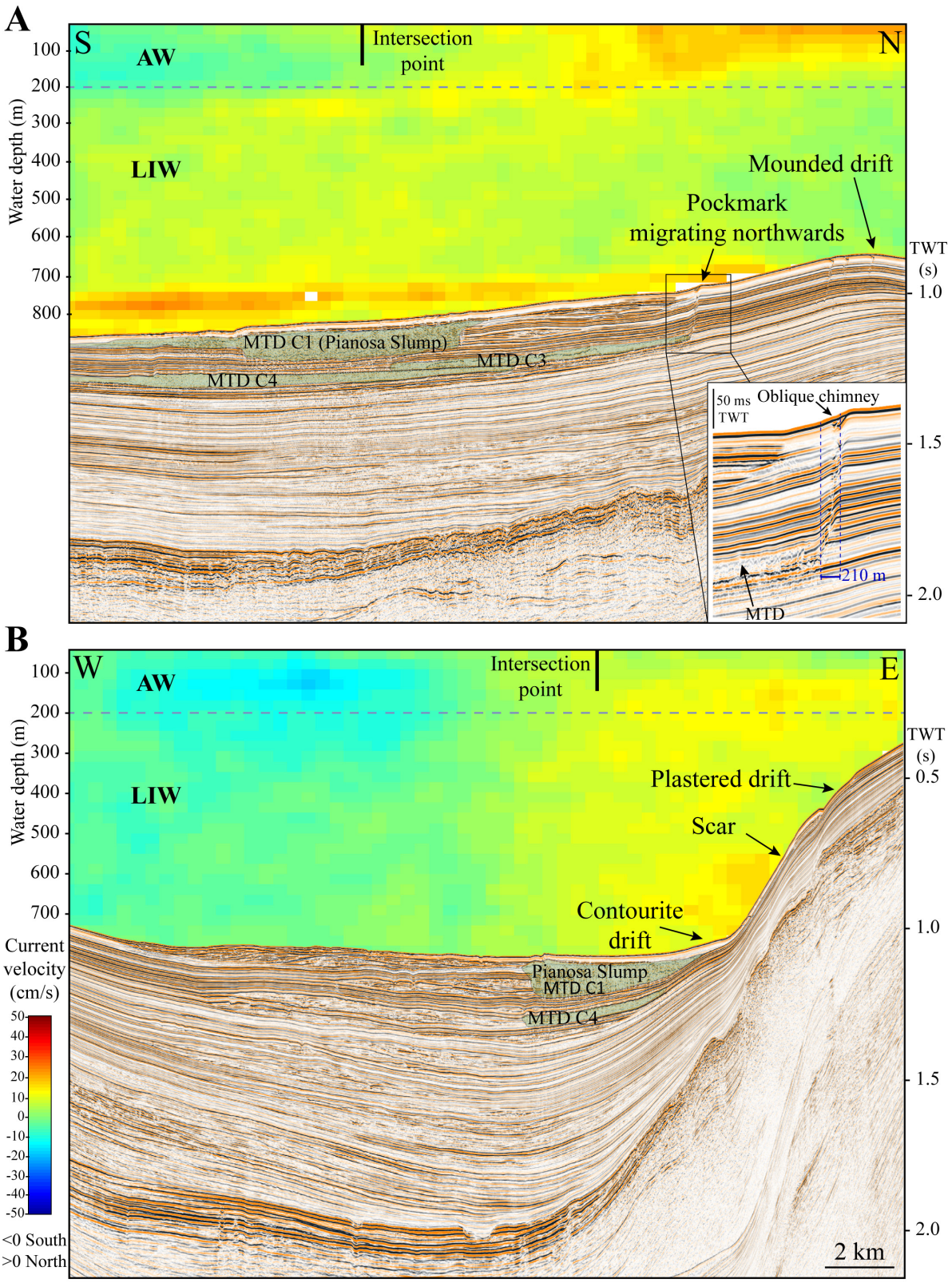

Fig. 4.4. Current velocity in north-south direction (positive towards the north and negative towards the south) from hull-mounted ADCP, coupled with multi-channel high resolution mini GI gun seismic reflection profiles. **(A)** North-South profile PSM2-HR-009 and zoom showing the presence of a pockmark with an oblique chimney rooted in MTD C3. **(B)** East-West profile PSM2-HR-061. The horizontal dashed blue line shows the general interphase between the Atlantic Water (AW) and the Levantine Intermediate Water (LIW) (Astraldi and Gasparini, 1992; La Violette, 1994; Millot, 1999; Toucanne et al., 2012). Mass Transport Deposits (MTDs) are outlined by green polygons. See Fig. 4.3 for seismic profile location.

(Fig. 4.5). The horizontal reflections located at 120–150 m w.d. are interpreted as the mixing zone between the Atlantic Water (AW) and the Levantine Intermediate Water. Other minor changes in salinity and/or temperature of the Levantine Intermediate Water may have formed the deeper reflections found between 225 and 270 m w.d. (Fig. 4.5).

4.3.2. Distribution and morphology of the Pianosa Contourite Depositional System

The Pianosa CDS is 120 km long and has a maximum width of 10 km, extending along the Pianosa Ridge, also known as Elba Ridge (Roveri, 2002) or Elba-Pianosa Ridge (Pascucci et al., 1999), from the southernmost part (west of Montecristo Island; Fig. 4.2) to the north of the Corsica Sill, that connects the Ligurian and the Tyrrhenian Seas at the north of the Capraia Island (Fig. 4.2). The drift size and morphology present remarkable changes along the system due to the variations in depth and physiography of the basin and the Pianosa Ridge. For a better understanding, the system has been divided in seven zones (zone 1 at the south and zone 7 at the north; Fig. 4.2).

Two separated mounded drifts have been identified in the southernmost part of the CDS (zone 1; Fig. 4.2). An escarpment generates a local acceleration of bottom currents, maintaining an abraded surface where the Messinian surface outcrops at the seafloor, and forming adjacent contourite drifts (Fig. 4.7). North of this zone, a plastered drift is found in the continental

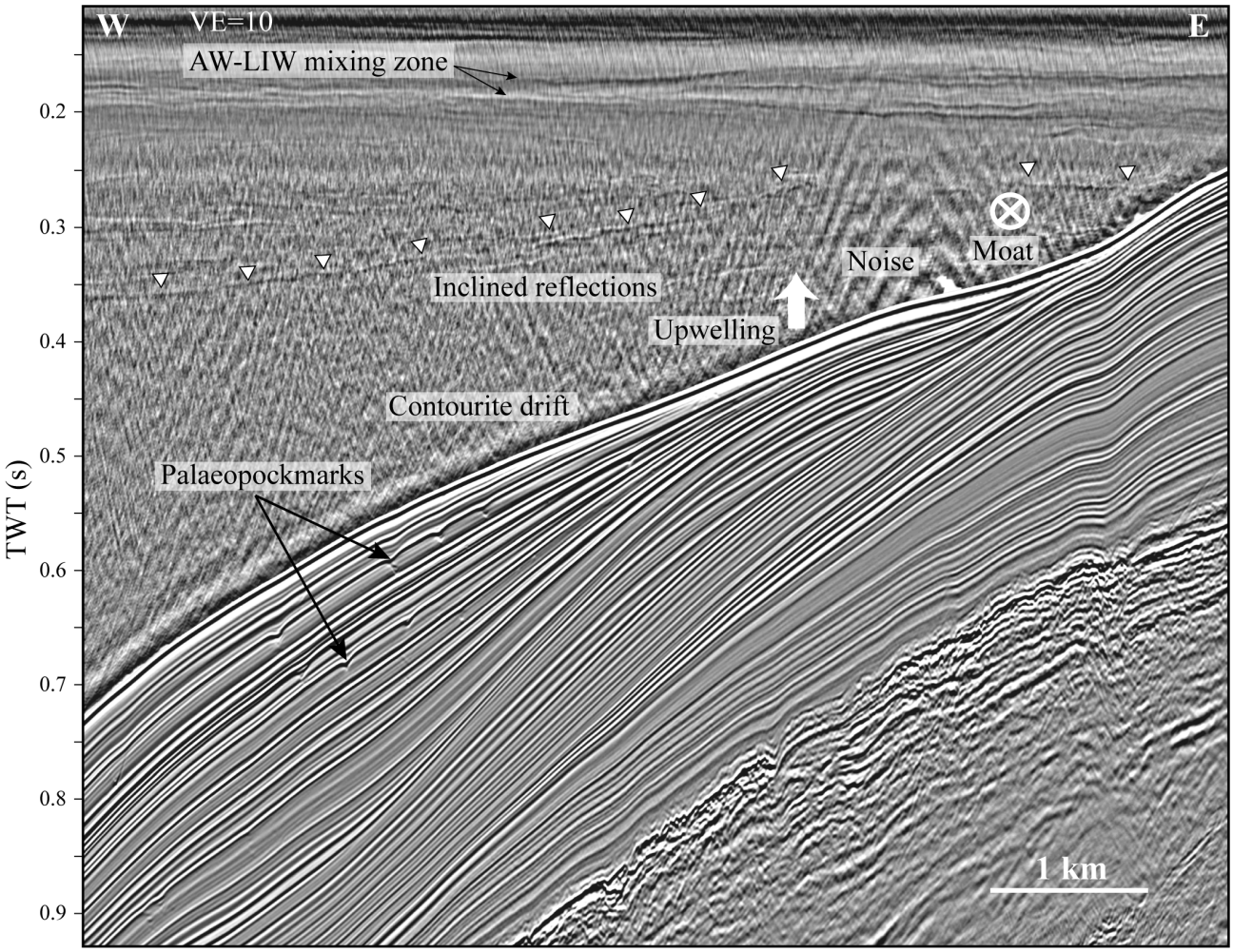

Fig. 4.5. PSM2-HR-043 multi-channel high resolution mini GI seismic reflection profile of the water column and sedimentary succession located at the north of the Elba Canyon. The horizontal reflections located at 0.16-0.20 s TWT (120-150 m w.d.) are interpreted as the mixing zone between the Atlantic Water (AW) and the Levantine Intermediate Water (LIW). Inclined reflections in the water column located at 0.30-0.36 s TWT (225-270 m w.d.) and marked with white triangles show the upwelling of deeper and denser water on the slope, where a moat and a mounded drift are formed. See Fig. 4.3 for seismic profile location.

slope between 230 and 700 m w.d., bounded in the upper part by faster bottom currents formed at the interphase between the AW and the LIW (Fig. 4.4B). The southern part of the plastered drift was affected by multiple mass-wasting processes that formed scars on the slopes and mass transport deposits on the basin (Figs. 4.4B and 4.6A). A small mounded drift was formed at the bottom of the scar of the Pianosa Slump, related to faster bottom currents at the foot of the slope (Fig. 4.4B).

Faster bottom currents present along the lower slope at about 600-650 m depth (Fig. 4.4B) are coincident with the location of a deep moat (up to 56 m deep) in zone 2 (Fig. 4.2), that creates a corridor with steeper slopes, up to 15° (Fig. 4.8). West of the moat, an elongated separated drift is formed, with the western limit marked by an inflexion in the slope: turbidites and hemipelagites dip eastwards, while contourite drifts dip westwards (Fig. 4.8). Offshore the Pianosa Island (zone 2) the Pianosa Ridge is retreated towards the east, forming a bulge on the slope (Fig. 4.6A). This morphological structure induced a change in the LIW pathway. While the mentioned deeper LIW branch continues northwards, another branch of the current flows at about 400 m depth contouring the slope edge and forming sigmoid moats and sigmoid separated mounded drifts (Figs. 4.6A and 4.8).

North of the bulge in the Pianosa Ridge (zone 3; Fig. 4.2), the continental slope is relatively steep with slope values between 8° and 10°. An abraded surface extends from the bottom of the prograding shelf edge prism at 225 m depth, that was formed during the last sea level low-stand, to the mounded drift, until 560 m water depth (Figs. 4.6A and 4.9). In this zone, the moat is flat and the crest is not very well developed. The separated elongated mounded drift presents multiple undulations and a pockmark field (Figs. 4.6A and 4.9).

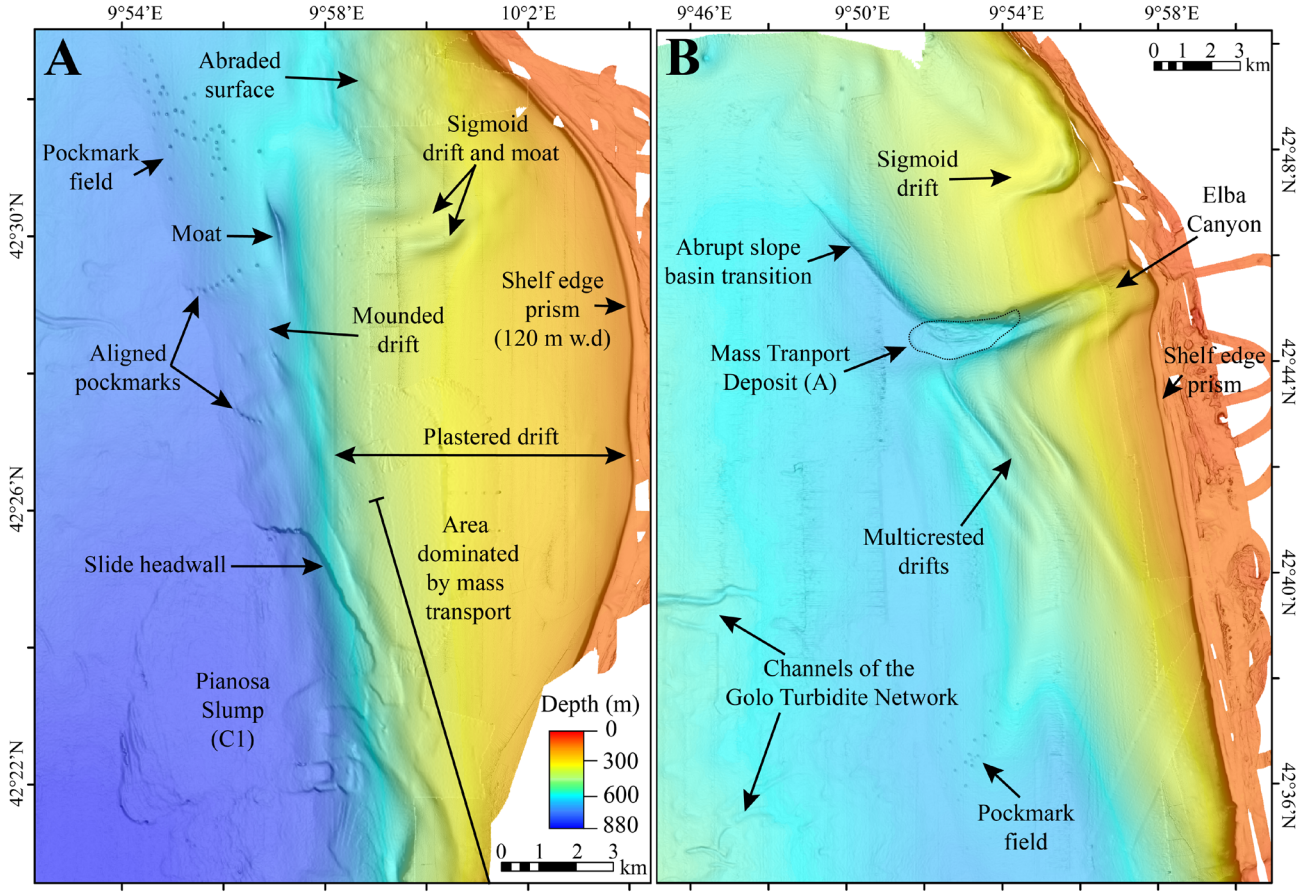

Fig. 4.6. (A) Multibeam bathymetry zoom of the southern area of the system evidencing the presence of sigmoid drifts, a separated mounded drift, a plastered drift, numerous pockmarks, a mass transport deposit (Pianosa Slump, C1) and an area of the slope very affected by mass-wasting processes. **(B)** Multibeam bathymetry zoom of the area around the Elba Canyon revealing the surface morphology of multicrested and sigmoid drifts, a pockmark field and a mass transport deposit (A) at the toe of the Elba Canyon.

Slightly to the north, the same contourite drift has a more developed mounded shape at the crest next to the moat, which is about 1 km wide and was originated by an obstacle created by a buried mass transport deposit (Fig. 4.10).

North of the Pianosa Island (zone 4; Fig. 4.2) the slope becomes gentler (2-6°) and contourite drift develop from 650 to 200 m water depth (Figs. 4.11 and 4.12). The deeper LIW branch flows in northeast direction until it converges with the shallowest branch that flows northwards parallel to the ridge (Fig. 4.2). As a result, and probably also due to the interaction with the Elba Canyon, multiple branches with northeast direction are formed, resulting in the deposition of multicrested drifts (Figs. 4.6B, 4.11 and 4.12).

The Elba Canyon is located offshore the Elba Island and it is the only canyon that crosses the Pianosa Ridge. Neither channel-levee systems nor turbidite lobes have been found associated with this canyon, and a low-stand shelf edge prism was deposited on the top of the canyon head (Fig. 4.11). Bottom currents have modelled its morphology in three different ways:

1. A contourite drift extends into the inner southern flank of the canyon (Fig. 4.13).
2. Downslope bottom currents through the canyon are accelerated towards the north, eroding the northern flank and forming an asymmetric canyon. The slope in the northern eroded flank is steeper (up to 20°) than in the southern flank, that is dominated by drift deposits (up to 15°) (Fig. 4.13).
3. Downslope bottom currents are deflected towards the north when they flow out of the canyon toe, creating an abrupt transition with high seafloor gradients (up to 15°) between the basin and the lower slope (Figs. 4.6B and 4.11).

In zone 5 (Fig. 4.2), the LIW pathway is affected by the presence of the canyon and it is separated in two branches (Fig. 4.2). The first branch continues flowing northwards at about 650 m w.d. The second shallowest branch is deflected towards the east, upwelling until about 150 m w.d. (Figs. 4.5 and 4.6B), where it becomes stabilised and continues flowing northwards, constrained by the steep morphology of the continental slope. The shallowest branch forms a sigmoid separated mounded drift similar to the drift located at the south of the Pianosa Island (zone 2). Northwards, these two LIW pathways run parallel, the shallowest one forms a 30-m-deep moat located parallel to the ridge at about 350 m w.d.; and the deepest pathway forms a 35-m-deep moat at 500 m w.d. (Fig. 4.14). These mounded drifts become flatter towards the north, at the same time that the basin becomes shallower and narrower, favouring erosion and non-deposition (Fig. 4.15).

The northernmost part of the system is characterised by patchy mounded drifts related to obstacles. North of the Corsica Sill, the basin opens in a funnel shape. Consequently, the LIW likely decelerates, favouring the sediment deposition and the formation of a drift (zone 6; Fig. 4.2). Finally, in the middle of the funnel-shaped basin (zone 7), a contourite drift is formed, associated with a mounded elevation (Fig. 4.2).

Table 4.1. Radiocarbon ages of cores PSM3-CS009, PSM3-CS011, PSM3-CS006 and PSM3-CS021. The age dates were corrected for a marine reservoir effect of 400 years and calibrated using Calib 7.0.2 and the IntCal13 calibration curve (Reimer et al., 2013).

Core number	Zone	Depth (cm)	Material	Lab code	Cal BP age (yr)
PSM3-CS009	2	41	Bulk planktonic	Poz-63392	2,730 ± 31
PSM3-CS009	2	1126	Bulk planktonic	Poz-63393	30,524 ± 636
PSM3-CS009	2	1400	Bulk planktonic	Beta-394859	29,810 ± 408
PSM3-CS011	2	104	Bulk planktonic	Beta-394860	17,311 ± 193
PSM3-CS011	2	380	Bulk planktonic	Beta-394861	21,820 ± 221
PSM3-CS011	2	709	Bulk planktonic	Beta-394862	26,668 ± 366
PSM3-CS006	4	7	Bulk planktonic	Poz-63394	2,854 ± 75
PSM3-CS006	4	250	Bulk planktonic	Poz-63395	46,955 ± 3,044
PSM3-CS021	4	100	Bulk planktonic	Beta-394864	18,325 ± 187
PSM3-CS021	4	550	Bulk planktonic	Beta-394865	28,154 ± 313

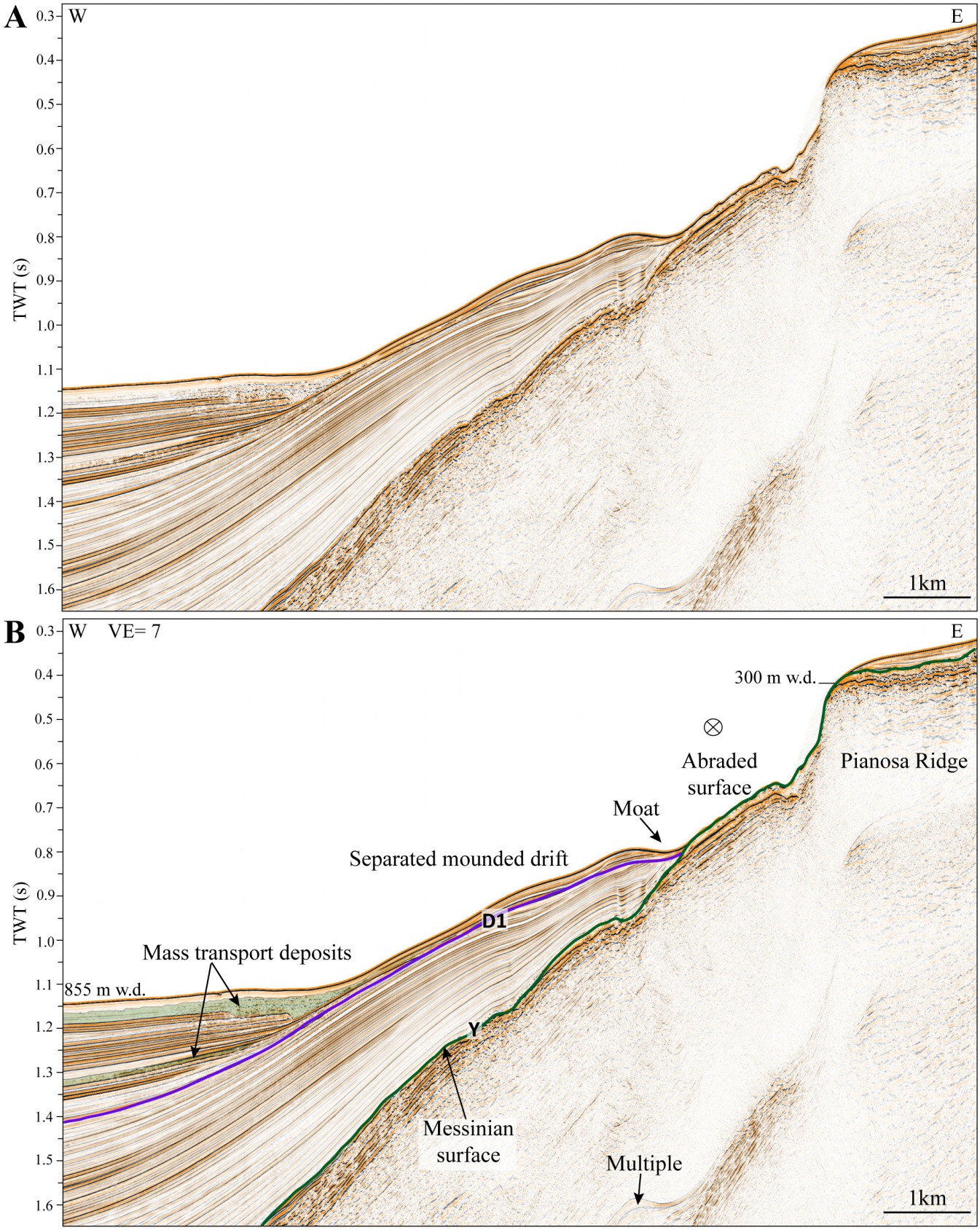

Fig. 4.7. (A) Uninterpreted and **(B)** interpreted PSM2-HR-074 multi-channel high resolution mini GI gun seismic reflection profile showing the main seismic unit boundaries in zone 1 of the Pianosa CDS. The mounded drift is separated from the escarpment by an abraded surface. See Fig. 4.3 for seismic profile location.

4.3.3. Stratigraphy of the Pianosa Contourite Depositional System

4.3.3.1. Seismic stratigraphy and age model

The Corsica Trough entered in a rifting phase during the Middle Miocene (Zitellini et al., 1986). Horizon Z (name used by Zitellini et al., 1986) corresponds to the seismic reflection that marks the lower boundary of the syn-rift deposits (Figs. 4.8, 4.9; Zitellini et al., 1986). Reflection Y (name used by Zitellini et al., 1986) is the erosional surface formed during the Messinian salinity crisis (Table 4.2). It corresponds to a very high amplitude reflection that marks a strong increase in sound velocity, since it separates the Plio-Quaternary sediment from the Miocene carbonates. Core PSM3-CS015 sampled the carbonates that form this surface in the Pianosa Ridge (Fig. 4.3), dated at 9.25 ± 0.27 Myr (Tortonian age, Late Miocene) through Strontium isotopic stratigraphy. This result suggests that no Messinian material is preserved in the Pianosa Ridge. Reflection X (name used by Zitellini et al., 1986) is the base of the post-rift deposits, of Middle Pliocene age (Table 4.2; Zitellini et al., 1986). Unit Y/X was deposited during the early Pliocene and it is mainly located in the deeper part of the basin. It usually onlaps the flanks of the basin, but in some zones it forms a thin layer concordant to the lower slope (Figs. 4.8 and 4.9).

The sediment deposited in the Corsica Trough from the Middle Pliocene (reflection X) to the present-day, is composed of 7 main units: U1, U2, U3, U4, U5, U6 and U7 (Figs. 4.8 and 4.9). Unit 1 is bounded between seismic reflection X (Middle Pliocene) and D1. The seismic discontinuity D1 is proposed to be related to the Middle Pleistocene Transition (MPT, 700-900 kyr) by analogy with the Quaternary stratigraphic pattern suggested by Hernández-Molina et al. (2002) for the Gulf of Cadiz and the Alboran Sea (Table 4.2). Reflections in unit 1 onlap the lower part of the continental slope and are concordant to the middle slope. The upper boundary of Unit 1 is the erosional surface D1. This regional erosion removed most of the sediment deposited on the middle slope, forming erosional truncations on the easternmost part of unit 1 (Figs. 4.7, 4.8 and 4.9). Mounded reflections can be found in Unit 1, evidencing the presence of mounded drifts in all the system, more developed in the vicinity of the Elba Canyon

Table 4.2. Stratigraphic framework of the Pianosa Ridge. MIS: Marine Isotope Stage. MPT: Middle Plesitocene Transition. The name of unit boundaries in red colour is the original name used by Zitellini et al. (1986).

Age (kyr)	Unit boudaries (this study; Zitellini et al. (1986))	Units	Tectonic phases
		U7	Post-rift
MIS 2 (30)	D6		
		U6	
MIS 4	D5		
		U5	
MIS 6	D4		
		U4	
MIS 10	D3		
		U3	
MIS 14-MPT	D2		
		U2	
MPT (700-900)	D1		
		U1	
	X		
Late Messinian to Early Pliocene		Y/X	
Messinian salinity crisis	Y		Syn-rift
Tortonian to Early Messinian		Z/Y	
	Z		
Early to Middle Miocene			Pre-rift

(Fig. 4.12). Unit 2 is bounded by erosional seismic reflections D1 and D2, both characterised by high amplitude (Figs. 4.8, 4.9, 4.12, 4.16C and 17B). D2 is deeper than the bottom of borehole GDEC4-2 (western side of the Corsica Trough) that was dated at 550 kyr BP. Units 3 to 7 are separated by seismic reflections of high amplitude that correspond to coarser sediment layers (Figs. 4.8, 4.9, 4.12 and 4.17). All the units present similar characteristics: they alternate packages of low amplitude reflections with packages of high amplitude reflections (Fig. 4.9). Unit 7 is the most recent one, it is characterised by low amplitude reflections that follow the same morphology as the previous units, but it drapes the shallowest moat in zones 2 and 3, as well as part of the middle slope, thinning upslope (Figs. 4.8, 4.9 and 4.16C). Seismic and oxygen isotope correlation with borehole GDEC4-2 allowed the more precise chronology of units 3 to 7 (Fig. 4.17A). Unit 3 extends until MIS 10, unit 4 from MIS 10 to MIS 6, unit 5 from MIS 6 to MIS 4, unit 6 from MIS 4 to MIS 2 (30 kyr) and unit 7 from 30 kyr to the present (Table 4.2).

Sedimentation rates (SR) were calculated for unit 7 in contourite drifts of zone 2 (Fig. 4.18). The core depths used for the estimation of sedimentation rates

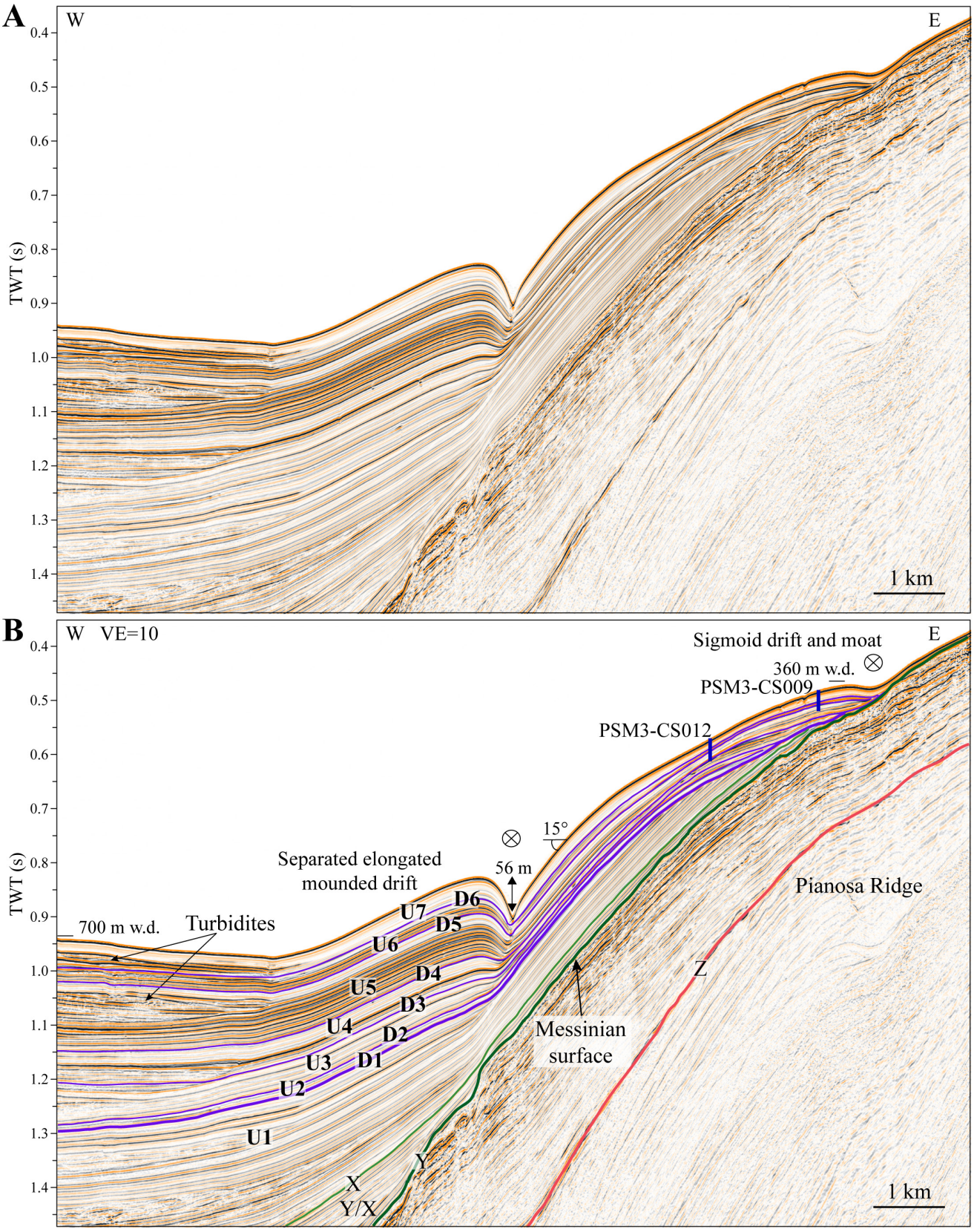

Fig. 4.8. **(A)** Uninterpreted and **(B)** interpreted PSM2-HR-064 multi-channel high resolution mini GI gun seismic reflection profile of zone 2 showing the main seismic unit boundaries and units of the Pianosa CDS. The location of Calypso piston cores PSM3-CS009 and PSM3-CS012 is indicated with blue lines. See Fig. 4.3 for cores and seismic profile locations.

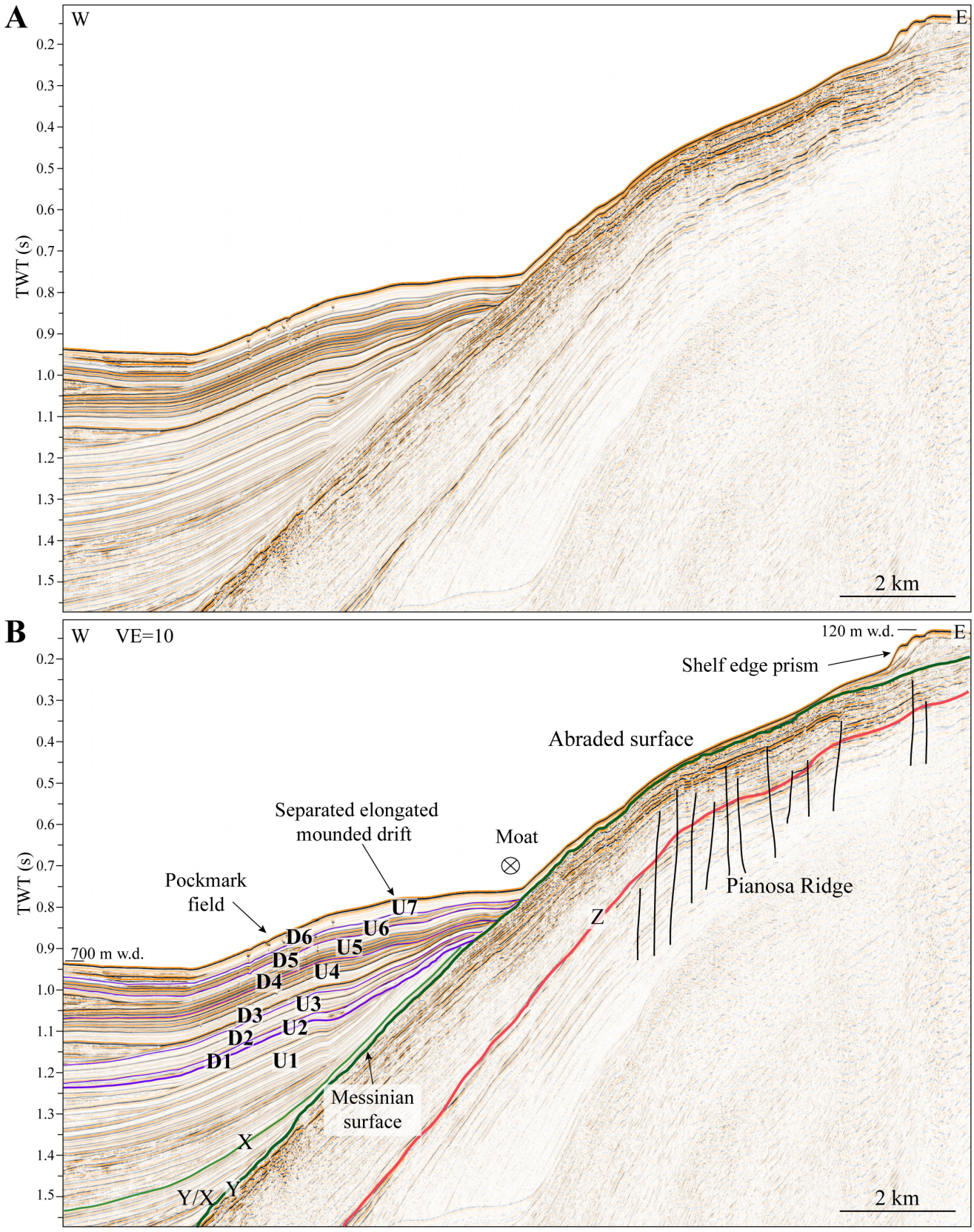

Fig. 4.9. **(A)** Uninterpreted and **(B)** interpreted PSM2-HR-037 multi-channel high resolution mini GI gun seismic reflection profile of zone 3 showing the main seismic unit boundaries and units of the Pianosa CDS. The contourite drift is separated from the shelf edge prism by an abraded surface. See Fig. 4.3 for seismic profile location.

were corrected for coring perturbations (Woerther et al., 2012) and mechanical compaction effects. SR on the crest of the mounded contourite drift in the middle slope from core PSM3-CS009 (Figs. 4.6, 4.14 and 4.15) resulted in a mean SR value corrected for compaction and core sampling perturbations of 13 cm·kyr^{-1} for the last 12 kyr (non-corrected SR would be 9.5 cm·kyr^{-1}) and 81 cm·kyr^{-1} between 12 and 30 kyr (non-corrected SR is 63 cm·kyr^{-1}) (Fig. 4.18). Core PSM3-CS012 is located in a deeper zone of the contourite, farther from the moat, where sediment accumulation is slightly lower, with mean corrected SR values of 11 cm·kyr^{-1} for the last 12 kyr BP (non-corrected SR would be 6 cm·kyr^{-1}) and 70 cm·kyr^{-1} between 12 and 30 kyr BP (non-corrected SR is 47 cm·kyr^{-1}). Core PSM3-CS011 shows a similar pattern in sedimentation rates, with lower values during the last 17.3 kyr (9 cm·kyr^{-1}, 6 cm·kyr^{-1} non-corrected) and higher SR between 17.3 and 26.7 kyr (88-111 cm·kyr^{-1}, 61-68 cm·kyr^{-1} non-corrected).

4.3.3.2. Sedimentological characterisation

Contourite drifts in the Pianosa CDS are mainly composed of bioturbated mud without lamination, although it is also common to find layers of bioclastic muddy sand. The abundance, grain size and bed thickness of these sandy layers changes along and across the Pianosa Ridge. Three Calypso piston cores sampled the sigmoid drift of zone 2: PSM3-CS011, PSM3-CS009 and PSM3-CS012, recovering information from units 2 to 7. In general, contourites are muddy with sand contents around 10 % of the total bulk volume (Figs. 16B and 17A). The sand is mainly composed of bioclasts. Decarbonated samples of core PSM3-CS011 (between 0 and 6.85 mbsf) present sand contents between 0.2 and 3% of the total volume in the range 63-150 μm. Bulk grain size analysis of the same samples showed sand volumes oscillating between 5 and 45 % of the total volume in the range 63-1000 μm (Fig. 4.19). Some layers have higher sand contents (up to 70 %; Figs. 16B and 17A) and correspond to high amplitude reflections in the multi-channel and SBP seismic profiles and to increased P-wave velocities (Figs. 4.16 and 4.17B). The granulometry of PSM3-CS009 shows that D6 corresponds to a sandy layer coarsening-up until it reaches a maximum sand content of 70 % and then fining-up (Fig. 16B). Two radiocarbon analyses were carried out on planktonic foraminifera in core PSM3-CS009 on the muddy sediment over the sandy layer (at 11.26 mbsf)

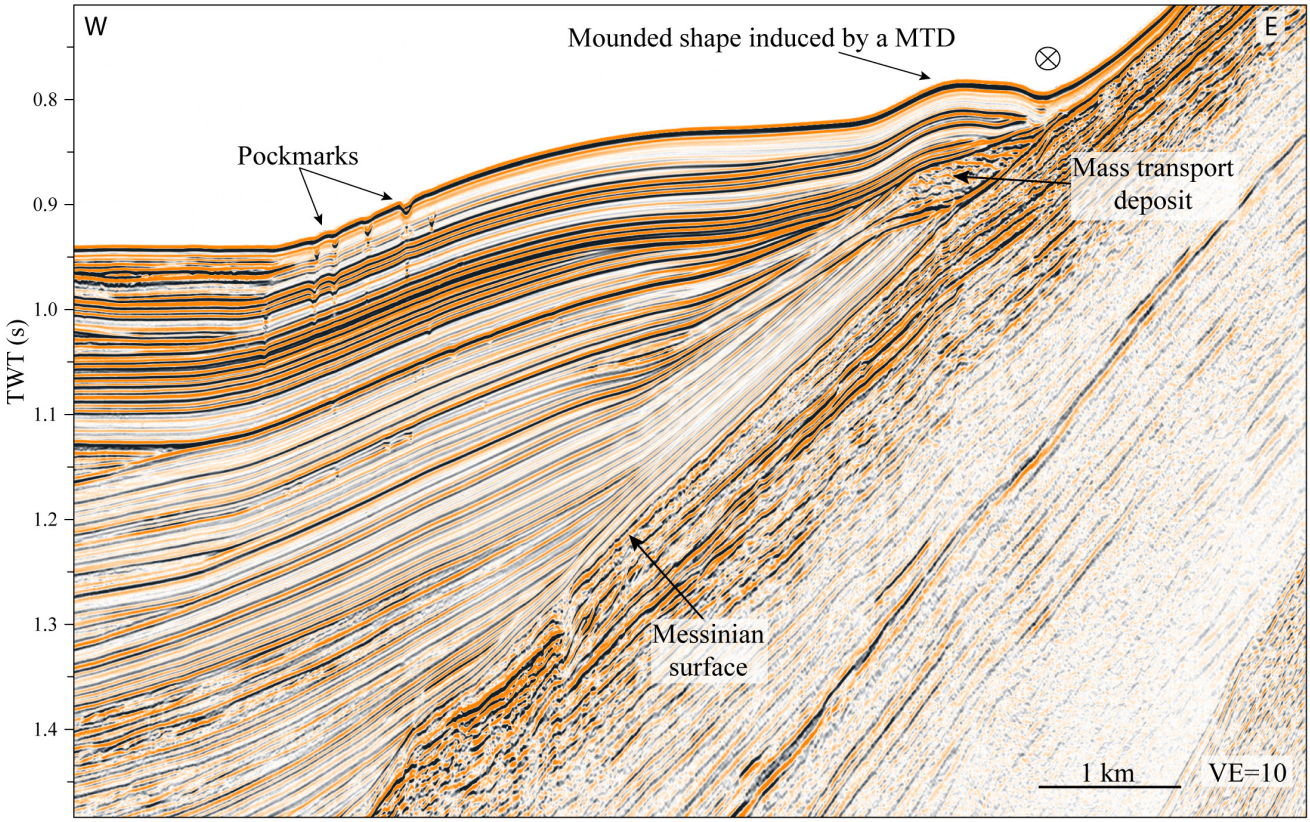

Fig. 4.10. PSM2-HR-063 multi-channel high resolution mini GI gun seismic reflection profile, showing the formation of a mounded shape induced by a mass transport deposit. See Fig. 4.3 for seismic profile location.

and under it (14.00 mbsf), resulting in approximately the same age: 30,000 cal yr BP (Table 4.1). Sand content in the contourite drift decreases with depth and with the distance to the moat. Therefore, PSM3-CS012 has a finer grain size than PSM3-CS009, especially remarkable in the coarser layers. For instance, the peak in P-wave velocity that corresponds to D6 in PMS3-CS012 (Fig. 4.16A) is less marked than in PSM3-CS009 (Fig. 4.16B). Another layer of coarser material can be found at 1.14 mbsf in core PSM3-CS009 and at 0.76 mbsf in core PSM3-CS012 that was deposited during the Younger Dryas (Fig. 4.16). PSM3-CS011 also shows coarser grain size at D6 and the Younger Dryas (Fig. 4.19A) and finer sediment during MIS2 (between YD and D6). Mean sortable silt values obtained from decarbonated samples of PSM3-CS011 between 0 and 6.85 mbsf increase during Heinrich Event 2 (HE2) and then a decrease during Dansgaard-Oeschger Event 2 (DO2; Figs. 4.17A and 14.9B). During MIS 2, mean sortable silt values tend to increase, reaching higher values in the Younger Dryas and, finally decreasing during the Holocene (Figs. 4.17A and 4.19B).

The multicrested mounded drifts of zone 4 were sampled by four Calypso piston cores along an east-west profile located at the south of the Elba Canyon (Figs. 12 and 20): PSM3-CS021, PSM3-CS006, PSM3-CS003, PSM3-CS020 (from the deepest to the shallowest core in water depth). These cores are between 9 and 22 m long and penetrated sediment from units from 1 to 7. In zone 4, there is an evident decrease in grain size with water depth, sandy layers become less abundant, thinner and finer grained with depth (Fig. 4.20). The coarser layers are mainly composed of coarse grained bioclasts and mud, with abundant shells of bivalves, brachiopods (*Gryphus vitreus*) and fragments of the bryozoan *Myriapora truncata*. Some of the transitions between the sandy and the muddy layers are gradual, while others form sharp contacts (Fig. 20). The gradual transitions and the muddy layers located between two proximal sandy areas are commonly mottled mud with silty patches. The sandy layers are easily identified in the P-wave velocity and in the Ca/Fe curves since they correspond to faster P-wave velocities in sand and higher calcium content because of the bioclastic content.

4.4. Discussion

4.4.1. Influence of seafloor morphology on contourite drift structure

The evolution of contourite deposits is directly linked to water circulation influenced by the seafloor mor-

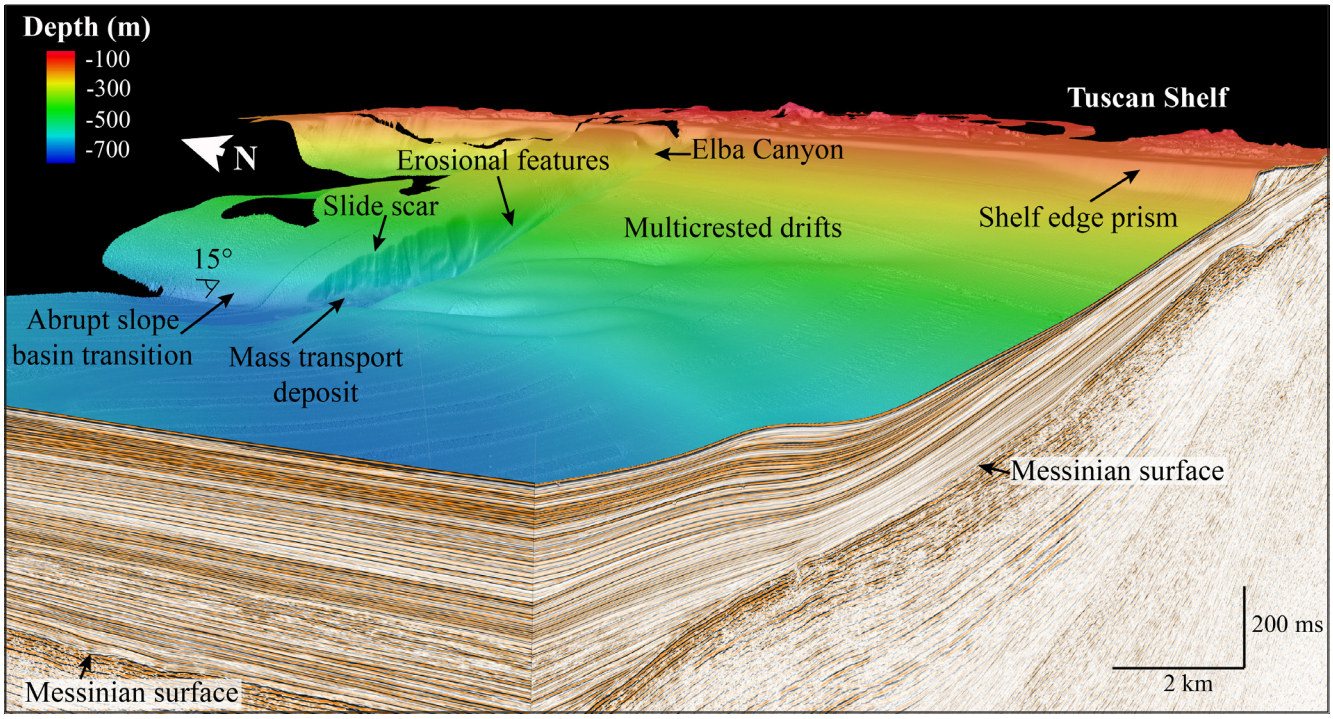

Fig. 4.11. 3D-rendered image composed of PSM2-HR-046 (E-W) and PSM2-HR-004 (N-S) multi-channel high resolution mini GI gun seismic reflection profiles and multibeam bathymetry of zone 4 in the Pianosa CDS showing the Elba Canyon and multicrested drifts. Note that the number of crests of the contourite drifts increases towards the north, while the size of the crests decreases in the same direction. See Fig. 4.3 for location.

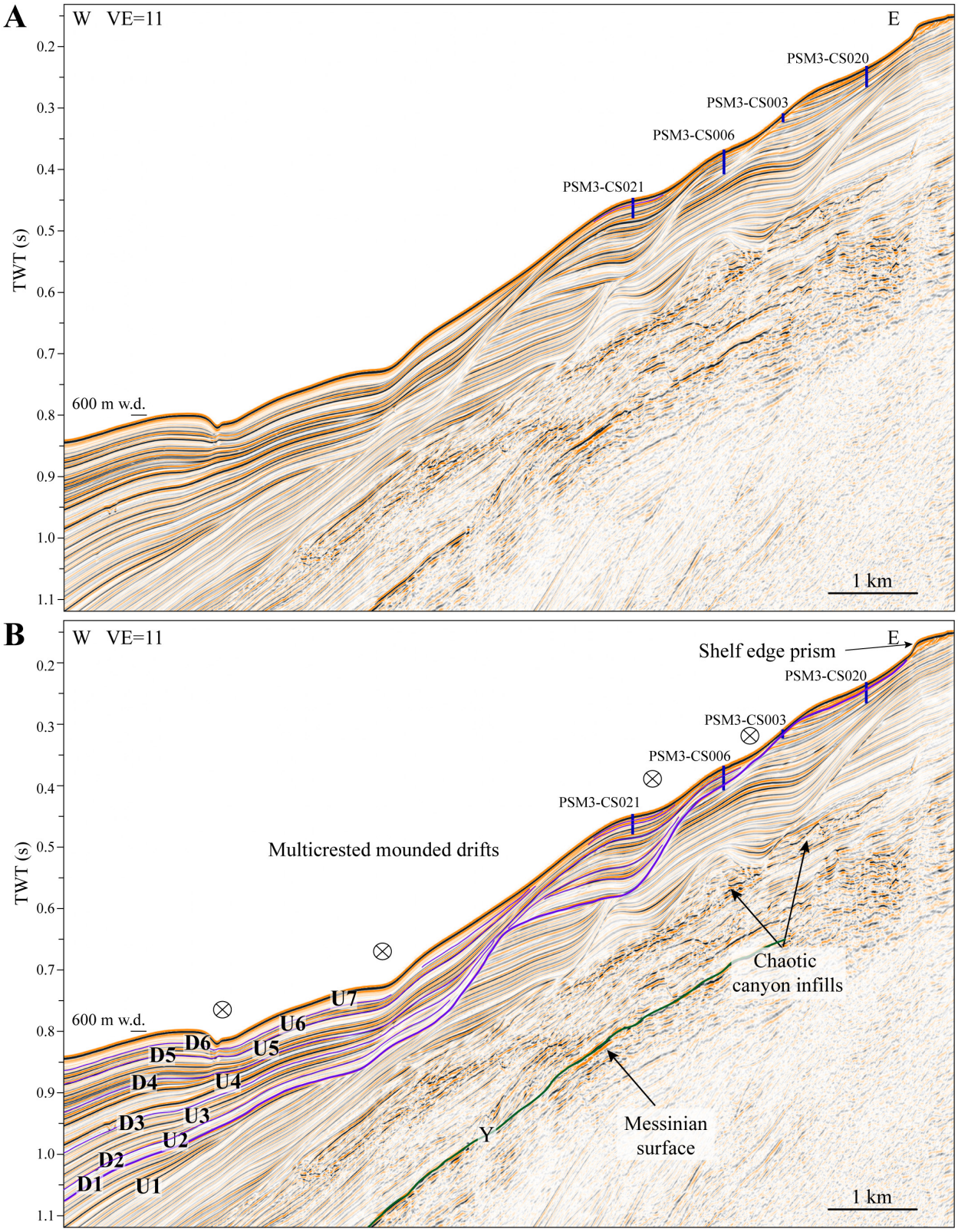

Fig. 4.12. **(A)** Uninterpreted and **(B)** interpreted PSM2-HR-054 multi-channel high resolution mini GI gun seismic reflection profile of zone 4 showing the main seismic unit boundaries and units of the Pianosa CDS in the zone of multicrested drifts. See Fig. 4.3 for seismic profile location.

phology. In the Pianosa CDS, the effect of locally increased slopes and the occurrence of bulges clearly impacts the bottom-current pathways, and consequently the growth of the sediment drifts. For instance, a sigmoid drift is related to a bulge in the Pianosa Ridge at the south of the Pianosa Island (Fig. 4.6A).

The Elba Canyon seems to be a morphological depression originated as a graben in the pre-Messinian deposits and developed by sedimentation altered by bottom currents (Figs. 4.13 and 4.21). There is no evidence of active turbidity activity through this canyon since neither channel-levees system nor turbidite lobes have been observed related to this canyon. In addition, a shelf edge prism blocks the head of the canyon. This prism extends almost all along the Pianosa Ridge. Downslope processes probably exist all along the margin. They may transport coarser bioclastic material from the Tuscan Shelf to the contourite drifts. However, they do not seem to be high density flows saturated of sediment recurrent in time that result in the formation of turbidite lobes in the basin. The Elba Canyon does not seem to be a typical canyon of mixed turbidite-contourite processes that can be found for example in the Gulf of Cadiz (Brackenridge et al., 2013; Hernández-Molina et al., 2006; Marches et al., 2010) or in Antarctica (Rebesco et al., 2002). It is most probably a depression modelled mainly by bottom currents, by processes of differential erosion and deposition. It is an important difference because this is a continuous process, while in mixed turbidite-contourite canyons the effect of turbidity currents is only caused by discrete events separated in time.

Bottom-current circulation is more dynamic in the zone around the Elba Canyon. Firstly, the branches of the current are slightly deflected towards the NE and enter into the canyon. Secondly, part of the water may flow downslope along the canyon, eroding the northern flank and forming longitudinal incisions on it (Fig. 4.6B). At the end of the canyon, bottom currents may turn to the right and erode the bottom of the slope (Fig. 4.6B). Thirdly, the inclination of the reflections in the seismic profile of the water column located at the north of the Elba Canyon (Fig. 4.5) suggests the upwelling of deeper denser water to the upper slope that could be induced by the effect of the canyon on an alongslope current (Hickey, 1997; Klinck, 1996; Sobarzo et al., 2001).

The development of the multicrested contourite drifts (Fig. 4.12), located at the south of the Elba Canyon at the present-day seafloor, is strongly subjected to the migration and evolution of the latter. Figure 4.12 registers the first aggradation in the centre of the

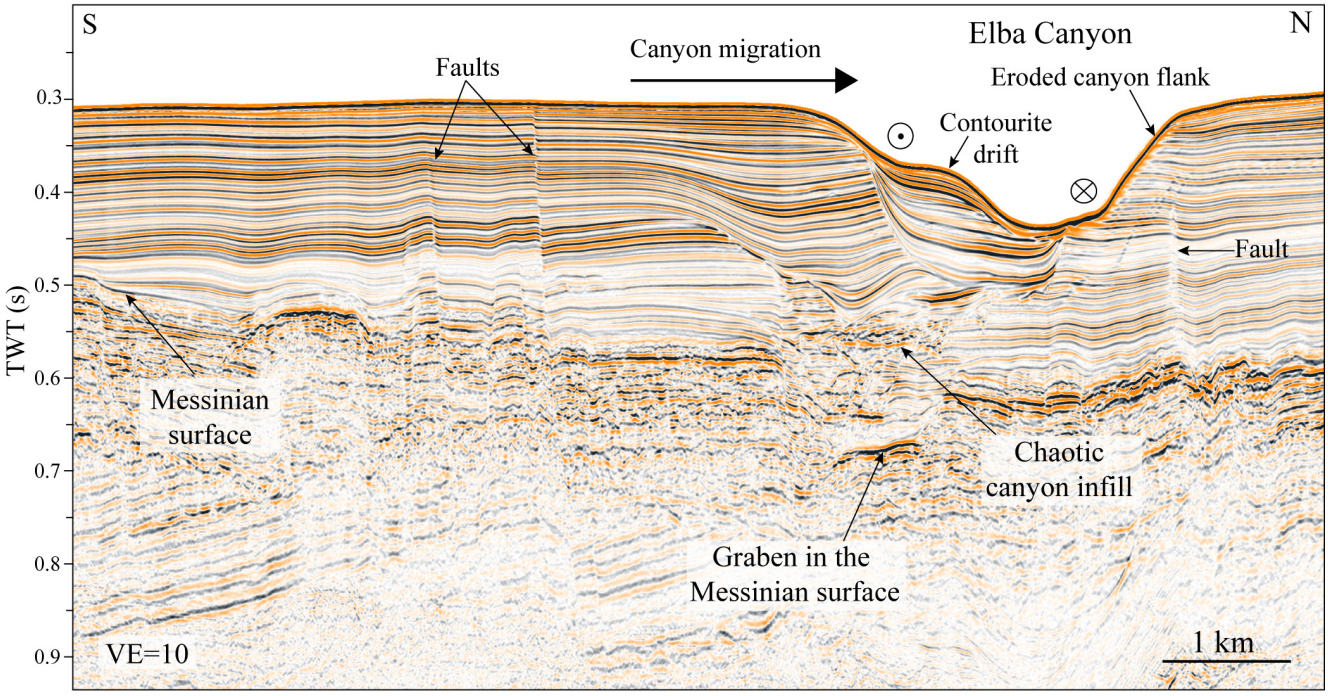

Fig. 4.13. PSM2-HR-015 multi-channel high resolution mini GI gun seismic reflection profile across the Elba canyon showing the northwards migration of the canyon and the formation of a contourite drift on the southern flank. See Fig. 4.3 for seismic profile location.

canyon (step 2 in Fig. 4.21), followed by multiple destabilisations of the canyon flanks deposited on the axis of the canyon (steps 3-4 in Fig. 4.21). During this period, the canyon starts to migrate towards the north; later, a contourite drift is formed in the centre of the canyon (step 5 in Fig. 4.21). Afterwards, the canyon migrates farther north and contourites grow in its southern flank (step 6 in Fig. 4.21). Finally, a drift enters from the south into the canyon axis (steps 7-8 in Fig. 4.21). In summary, Fig. 4.12 documents the apparent complicated morphology of the sediment drifts because it was positioned in the middle of the canyon during a first phase and then on the southern flank of the canyon, migrating towards the north.

4.4.2. Palaeoceanographic implications

The Pianosa CDS presents a continuous development since the Middle-Late Pliocene (this study; Roveri, 2002), after the progressive filling of the deep central part of the basin (units Y/X and lower part of U1). This continuity implies that over the long-term the intermediate waters have had a similar circulation pattern flowing northwards along the Pianosa Ridge since the Middle-Late Pliocene. The concordance of the present-day oceanographic regime with the stratigraphic evolution of the contourite drifts (Fig. 4.4) suggests that the general circulation at the Pianosa Ridge has been similar during the history of the Pianosa CDS. The drift morphology is stable over time, only presenting a small component of upslope progradation (Fig. 4.9). The formation of oblique chimneys in pockmarks can also be a good indicator of the dominant current direction. The interaction between bottom-currents and fluid escape favours the deflection of the gas plume and thus differential erosion/deposition on pockmark flanks, resulting in erosion downstream and deposition upstream (Riboulot et al., 2014). Fig. 4.4A shows that the mass transport deposit C3 is the origin of a pockmark that presents an oblique chimney. Since the MTD is a fixed source of fluid, the possible migration of pockmarks due to the migration or evolution of the fluid source can be rejected and therefore it can be argued that the formation of an oblique chimney is mainly linked to the effect of bottom currents on the sedimentation at the pockmark.

From the Middle-Late Pliocene to the Middle Pleistocene (U1) the Pianosa CDS had a continuous growth of small mounded drifts. Afterwards, a prominent erosional surface (reflection D1) marks the onset of better developed contourite mounded drifts (Fig. 4.8). The

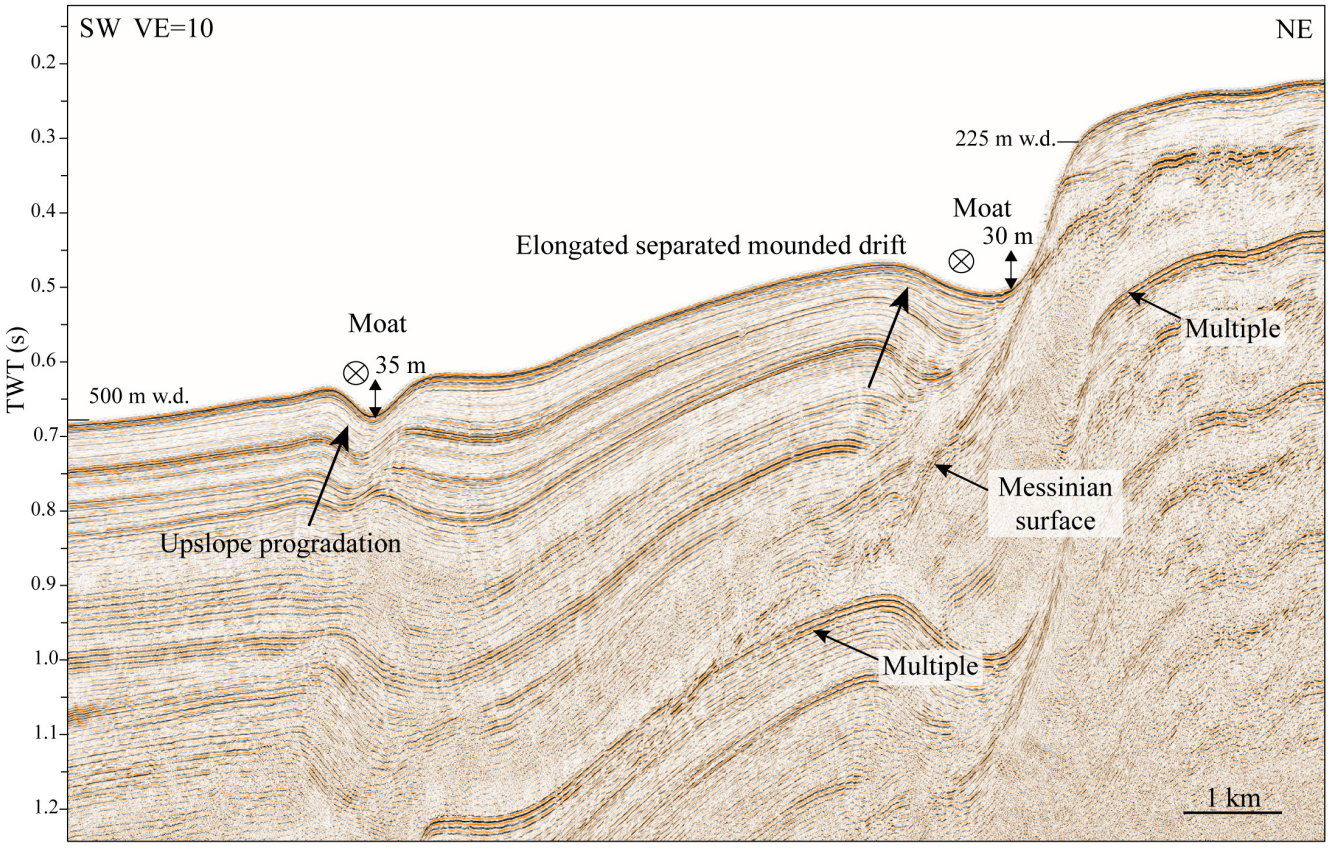

Fig. 4.14. ET93-P12B single-channel sparker seismic reflection profile showing two moats at 350 and 500 m water depth (w.d.) associated with an elongated separated mounded drift. See Fig. 4.2 for seismic profile location.

D1 reflection may correspond to the Middle Pleistocene Transition (MPT, 700–900 kyr). At that time, 100-kyr eccentricity cycles became dominant, resulting in longer glacial/interglacial cycles of higher amplitude, which might be related to the intensification of the Mediterranean Outflow Water (that is formed by the Mediterranean intermediate and deep waters) and the formation of a mid-Pleistocene discontinuity in the Gulf of Cadiz (Hernández-Molina et al., 2014). The onset of a stronger development of contourites in the Northern Tyrrhenian Sea coincides with the onset of the contourites along the Calabro-Tyrrhenian margin, in the Southern Tyrrhenian Sea (Amelio and Martorelli, 2008), suggesting that faster bottom currents in the depth range of the modern Levantine Intermediate Water impacted already the whole Tyrrhenian Sea.

4.4.3. Glacial-interglacial stratigraphic evolution

A model that describes the evolution of the sediment drifts in the Pianosa CDS is here proposed (Fig. 4.22). Contourite development in the Corsica Trough is mainly influenced by bottom-current velocity and sediment availability (that depends on the connection and disconnection of the turbidity systems), both directly influenced by climate changes. At present and since the beginning of the Holocene, the Golo Turbidite Network is disconnected (Calvès et al., 2013) and bottom currents are slow in the Corsica Trough (this study; Toucanne et al., 2012). Therefore, during sea level high-stands sedimentation rates are low in the contourites (step 1 in Fig. 4.22). During sea level falls bottom currents are faster (this study; Toucanne et al., 2012) and their core may be located deeper in the slope, eroding the crest of the sediment drift. Under these conditions, most of the Tuscan Shelf was exposed, likely providing additional and coarser sediment to the slope. During this period of enhanced currents, bioclastic sands are deposited on the crest of the contourite (step 2 in Fig. 4.22). The deposition of sand beds may take place in a short period of time and may be the result of downslope processes that transport coarse material from the Tuscan Shelf to the slope, later reworked and winnowed by slope-parallel currents. D6 is a good example for this case because two radiocarbon dates show the same age (30 kyr) under and above the 3-m-thick sandy layer, supporting a rapid formation of the deposit. In addition, the layer presents coarsening-up and posterior fining-up

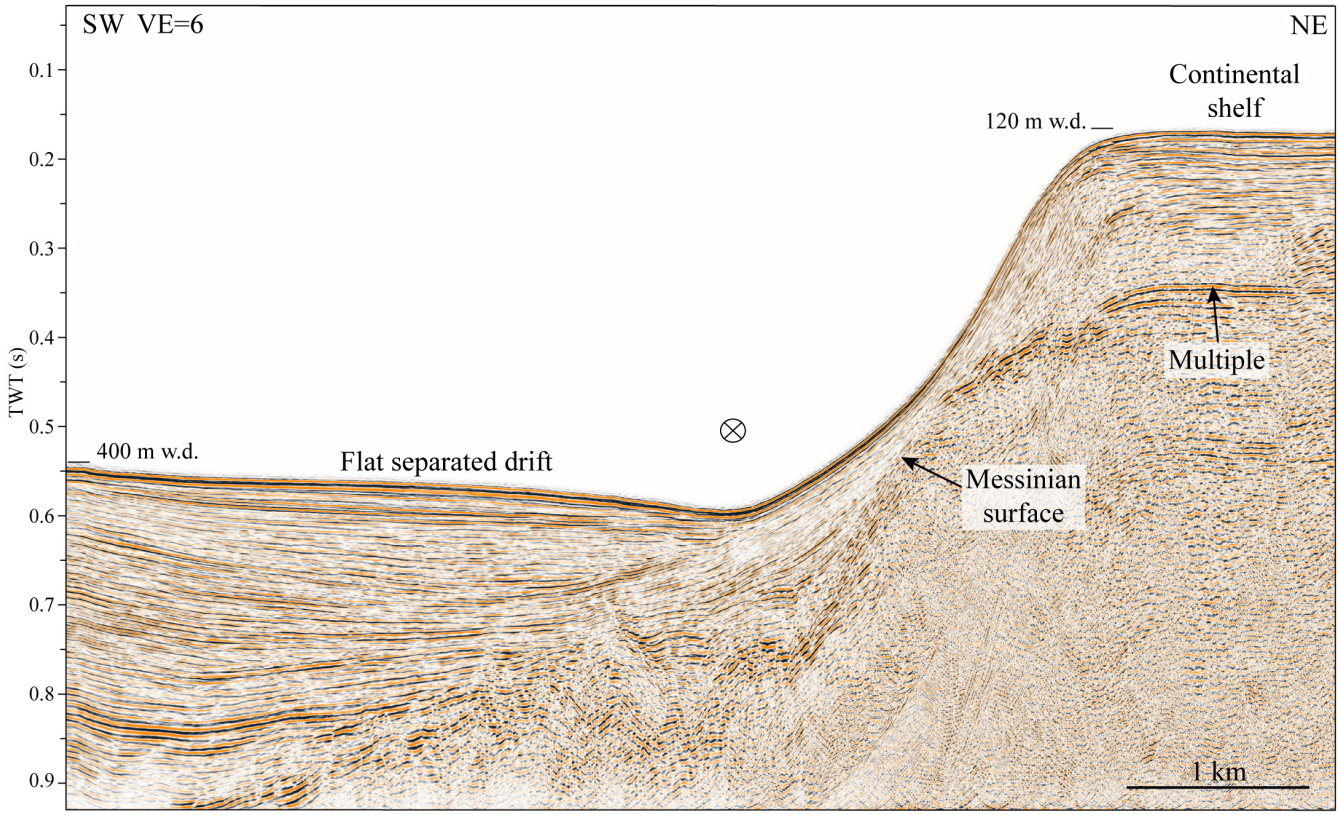

Fig. 4.15. ET93-P43 single-channel sparker seismic reflection profile showing a flat separated drift in zone 5 of the Pianosa CDS. See Fig. 4.2 for seismic profile location.

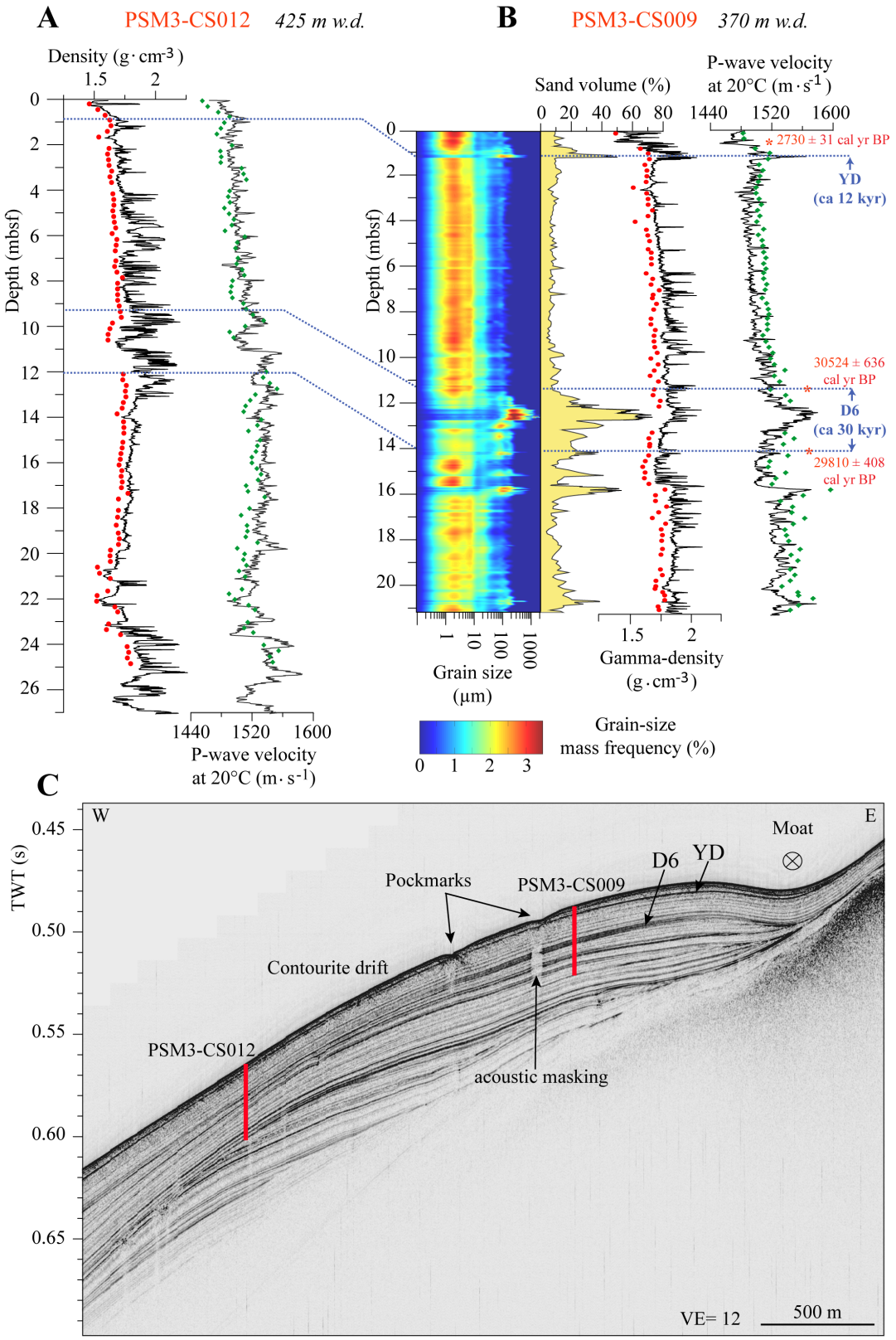

Fig. 4.16. (A) From left to right: Density from MSCL (black line) and water content (red dots) and P-wave velocity from MSCL (black lines) and celerimeter (green dots) of core PSM3-CS012. **(B)** From left to right: grain size distribution, percentage of sand volume, density from MSCL (black line) and water content (red dots) and P-wave velocity from MSCL (black lines) and celerimeter (green dots) of core PSM3-CS009. Red stars represent the location of radiocarbon dates. **(C)** PSM2-CH-064 SBP profile showing the location of cores PSM3-CS012 and PSM3-CS009 with red lines.

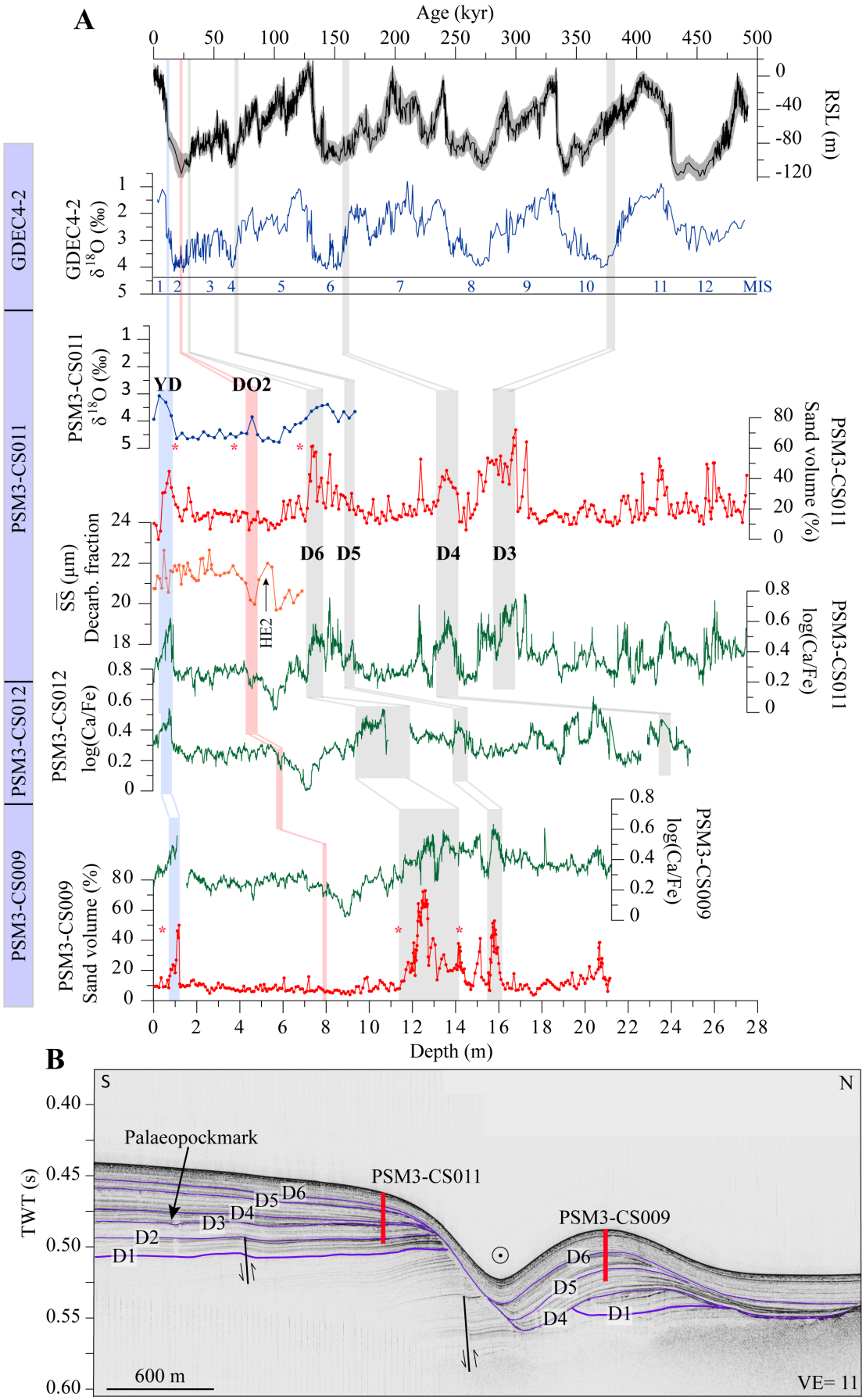
A
Age (kyr)
RSL (m)
GDEC4-2
GDEC4-2 δ18O (‰)
MIS
PSM3-CS011
PSM3-CS011 δ18O (‰)
YD
DO2
PSM3-CS011 Sand volume (%)
SS̄ (µm)
Decarb. fraction
HE2
D6 D5 D4 D3
PSM3-CS011 log(Ca/Fe)
PSM3-CS012
PSM3-CS012 log(Ca/Fe)
PSM3-CS009
PSM3-CS009 Sand volume (%)
PSM3-CS009 log(Ca/Fe)
Depth (m)
B
S
N
Palaeopockmark
PSM3-CS011
PSM3-CS009
D1
D2
D3
D4
D5
D6
TWT (s)
600 m
VE= 11

Fig. 4.17. (A) From the top to the bottom: relative sea level curve from Grant et al. (2014), $\delta^{18}O$ stack of benthic foraminifera (*Cibicides wuellerstorfi*, *Cibicidoides pachyderma* and *Cibicidoides kullenbergi*) from borehole GDEC4-2 showing in blue colour the corresponding Marine Isotope Stages (MIS), $\delta^{18}O$ stack of *Uvigerina peregrina* and *Uvigerina mediterranea* from core PSM3-CS011, percentage of sand volume from core PSM3-CS011, sortable silt mean grain size of the decarbonated fraction of core PSM3-CS011, XRF log(Ca/Fe) of core PSM3-CS011, XRF log(Ca/Fe) of core PSM3-CS012, XRF log(Ca/Fe) of core PSM3-CS009 and percentage of sand volume of core PSM3-CS009. The Younger Dryas (YD) is indicated with a blue band, the Dansgaard-Oeschger event 2 (DO2) with a red band and unit boundaries D6 to D3 with grey bands. Note that the higher mean sortable silt values are found during the YD and Heinrich Event 2 (HE2). Low mean sortable silt values are present at DO2. Differences in the $\delta^{18}O$ range between GDEC4-2 and PSM3-CS011 are caused by the use of different benthic foraminifera species (epifaunal foraminifera in GDEC4-2 and infaunal in PSM3-CS011). The log(Ca/Fe) curve of PSM3-CS012 is not entirely represented through D6 because this part of the core has been used for geotechnical analysis. Correlation was also done using seismic correlation with borehole GDEC4-2. Additional support for the correlation can be found with the good coherence between the XRF log(Ca/Fe) curves of this study and the XRF Calcium curves presented by Calvès et al. (2013) and Toucanne et al. (2012). Red stars represent the location of radiocarbon dates. (B) PSM2-CH-014 SBP profile showing the location of cores PSM3-CS011 and PSM3-CS009 with red lines and the seismic reflections that mark unit boundaries (D1 to D6).

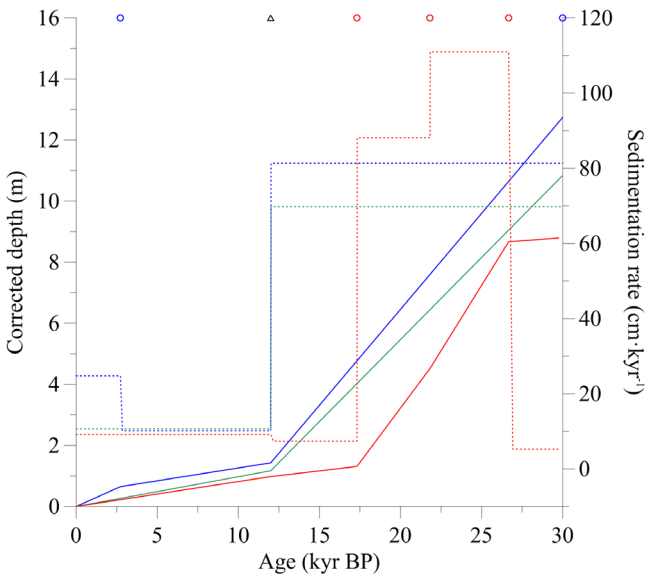

Fig. 4.18. Age models for cores PSM3-CS009 (blue line), PSM3-CS012 (green line) and PSM3-CS011 (red line), covering the last 30 kyr BP (Unit 7). Chronological tie points from borehole GDEC4-2 used for the three cores are represented with a black triangle, radiocarbon dates are represented as blue open circles for core PSM3-CS009 and red open circles for PSM3-CS011. Dashed lines are sedimentation rates for cores PSM3-CS009 (blue), PSM3-CS012 (green) and PSM3-CS011 (red). Core depths used for the calculation of sedimentation rates were corrected for coring perturbations and compaction.

sequences that suggest the rework by bottom-currents. The evolution of the drift above the sandy layer (Fig. 4.22) leads to two different scenarios of the growth of a mounded drift in zone 2 between MIS 2 and MIS 1 (Case A), and between MIS 4 and MIS 3 (Case B). During MIS 2, sea level low-stand and the onset of the following sea level rise, bottom currents were fast in the Pianosa Ridge, but slower than during the sea level fall. As a result, bottom currents could transport large amounts of sediment but would not be fast enough to produce erosion on the drift. In addition, the turbidite system was connected (Calvès et al., 2013) and provided sediment to the contourite system, resulting in a fast sedimentation of mud (step 3 for case A in Fig. 4.22), that sealed the sandy layer deposited during the sea level fall. This explanation is consistent with the heavy $\delta^{18}O$ values found between the Younger Dryas and D6 in core PSM3-CS011 (Fig. 4.17A), proving the formation of the contourite during a cold period. On the contrary, in case B, during MIS 4 sea level low-stand the slope-parallel current velocity was probably very high, preventing sediment deposition, even if the turbidite system was connected (Calvès et al., 2013), what would imply a sustained supply from the margin. This interpretation is sustained by the presence of light $\delta^{18}O$ values between D6 and D5 that could not be formed during MIS4 (Fig. 4.17A). Afterwards, during MIS3 the relative sea level remained in between -60 and -80 m (Fig. 4.17A), bottom currents likely slowed down but were still fast enough to transport large amounts of sediment, carried to the basin by recurrent

turbidity currents (Calvès et al., 2013). As a result, contourite drifts underwent a phase of accelerated growth during MIS 3 compared to MIS 4.

During the Younger Dryas, there was no major erosion, but enhanced bottom currents were evident by the deposition of coarse sediment in the contourite drifts, with higher contents in sand (up to 50% in cores PSM3-CS009 and PSM3-CS011; Figs. 4.16C, 4.17A and 4.19A) and higher sortable silt values in the basin floor (Figs. 4.17A and 4.19B; Toucanne et al., 2012; Mintoʾo et al., 2015). The deposition of sediment with higher sand contents during the Younger Dryas was also observed in the Gulf of Cadiz associated to the lower branch of the Mediterranean Outflow Water (Llave et al., 2006). The reduced tectonic activity in the Corsica Trough since the early Pliocene (Zitellini et al., 1986) permits to recover a sedimentary record of the contourite depositional system that is only influenced by climate changes, by inducing fluctuations in sediment supply and bottom current velocity. The proposed model could be applied to the margins where sediment supply and bottom current velocity are enhanced during cold periods, as observed for example in the Gulf of Cadiz (Llave et al., 2006) or in glacial margins (Laberg et al., 2001; Rebesco et al., 2002).

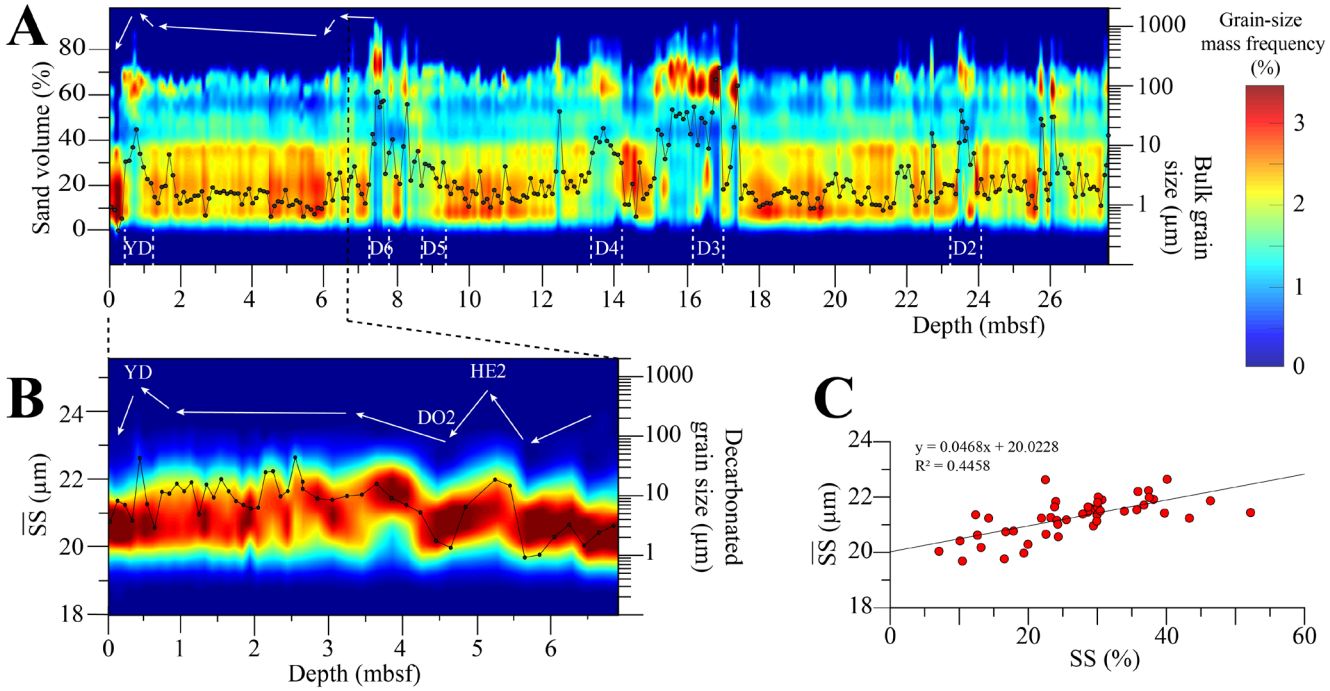

Fig. 4.19. (A) Bulk grain size distribution (colour graph) and sand volume percentage of the bulk sediment (black line and dots) of core PSM3-CS011. The Younger Dryas (YD) and the boundary units D6-D2 intervals are represented with dashed white lines. The white arrows show the general grain size tendency. **(B)** Decarbonated grain size distribution (colour graph) and mean sortable silt (black line and dots) of the decarbonated fraction of the upper 6.85 m of core PSM3-CS011. Note that most of the sand fraction disappears after removing carbonates from the sediment. The white arrows show the mean sortable silt tendency that can be interpreted in terms of palaeocurrent speed, suggesting faster bottom currents during the YD and the Heinrich Event 2 (HE2) and slower during the Dansgaard-Oeschger event 2 (DO2) and the Holocene. **(C)** Correlation of sortable silt (10-63 μm silt fraction) mean size with sortable silt percentage of the decarbonated fraction (right). The linear relationship between mean size of sortable silt and percentage of sortable silt, in a well sorted population, indicates a sorting processed controlled by current flow dynamics (McCave and Hall, 2006).

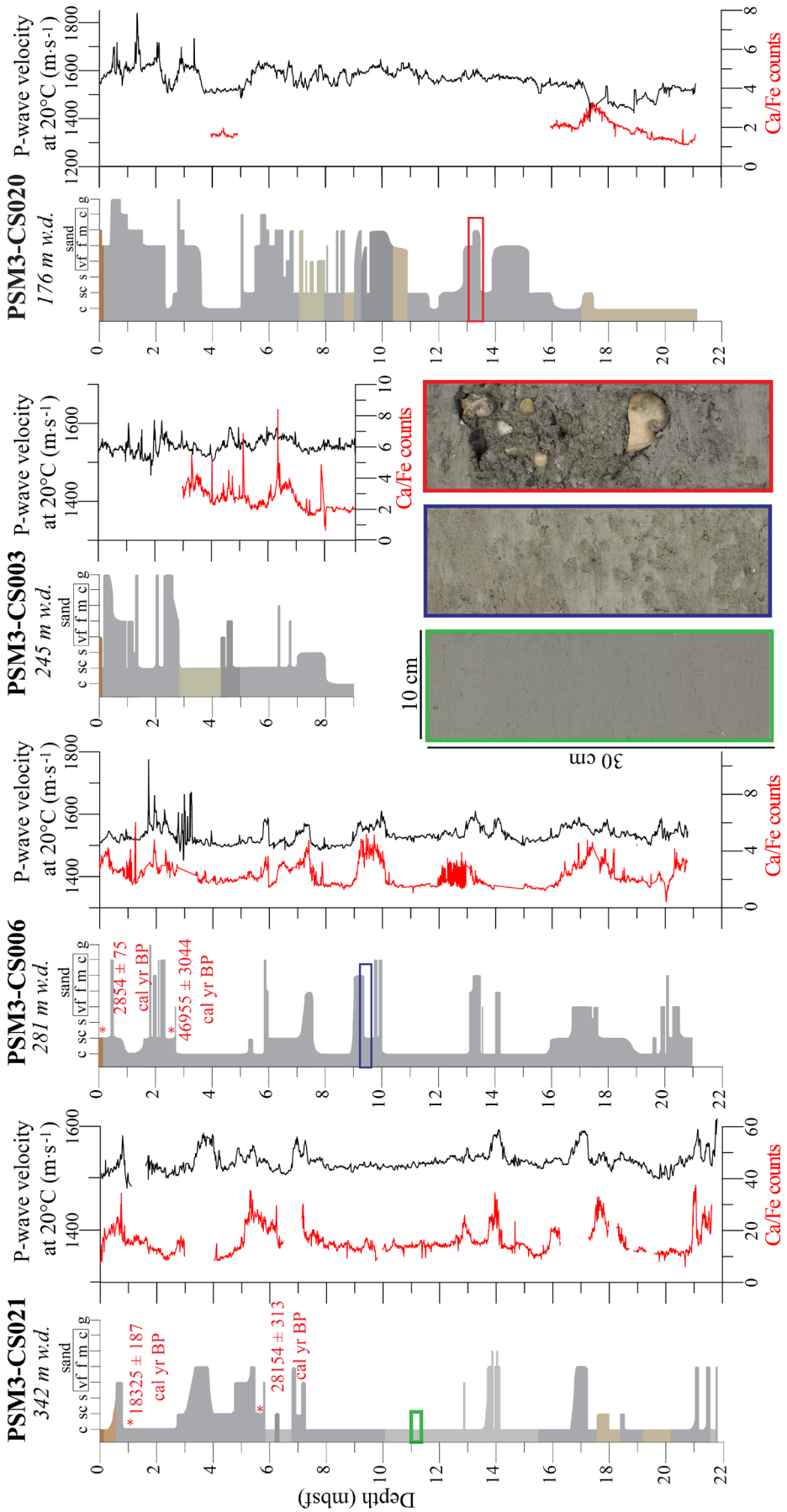

Fig. 4.20. Core log, P-wave velocity and XRF Ca/Fe curves of cores PSM3-CS021, PSM3-CS006, PSM3-CS003 and PSM3-CS020. Three photos show the main sedimentary facies, from left to right: mud, mottled mud with silty patches and a bioclastic sand interval with a sharp upper boundary. Colours in the logs represent the real colour of the sediment.

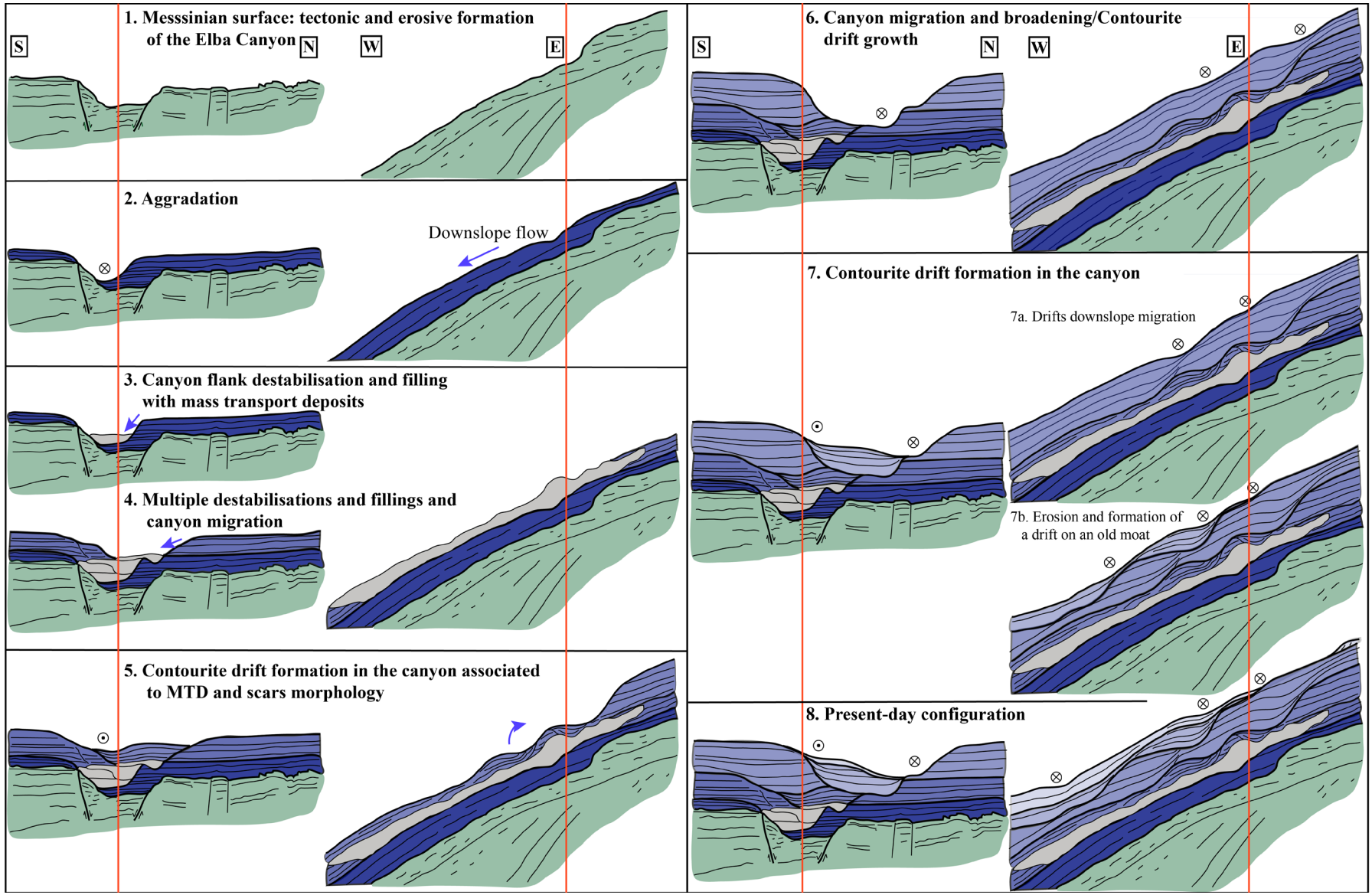

Fig. 4.21. Evolution of the Elba Canyon (profile N-S; Fig. 4.13) and the associated multicrested drift (profile E-W; Fig. 4.12) since the late Messinian. Note that the apparent complicated stacking pattern of the multicrested drifts is originated by the canyon migration and the interaction of a changing seafloor morphology with bottom currents.

	Case A (MIS 2-MIS 1)		*Case B (MIS 4 -MIS 3)*	
	Sediment availability	Bottom-currents velocity	Sediment availability	Bottom-currents velocity
1. Sea level high-stand	–	+	–	+
2. Sea level fall	–	+++	–	+++
3. Sea level low-stand	+	++	+	+++
4. Sea level high-stand	– (maximum RSL)	+	+ (medium RSL)	++

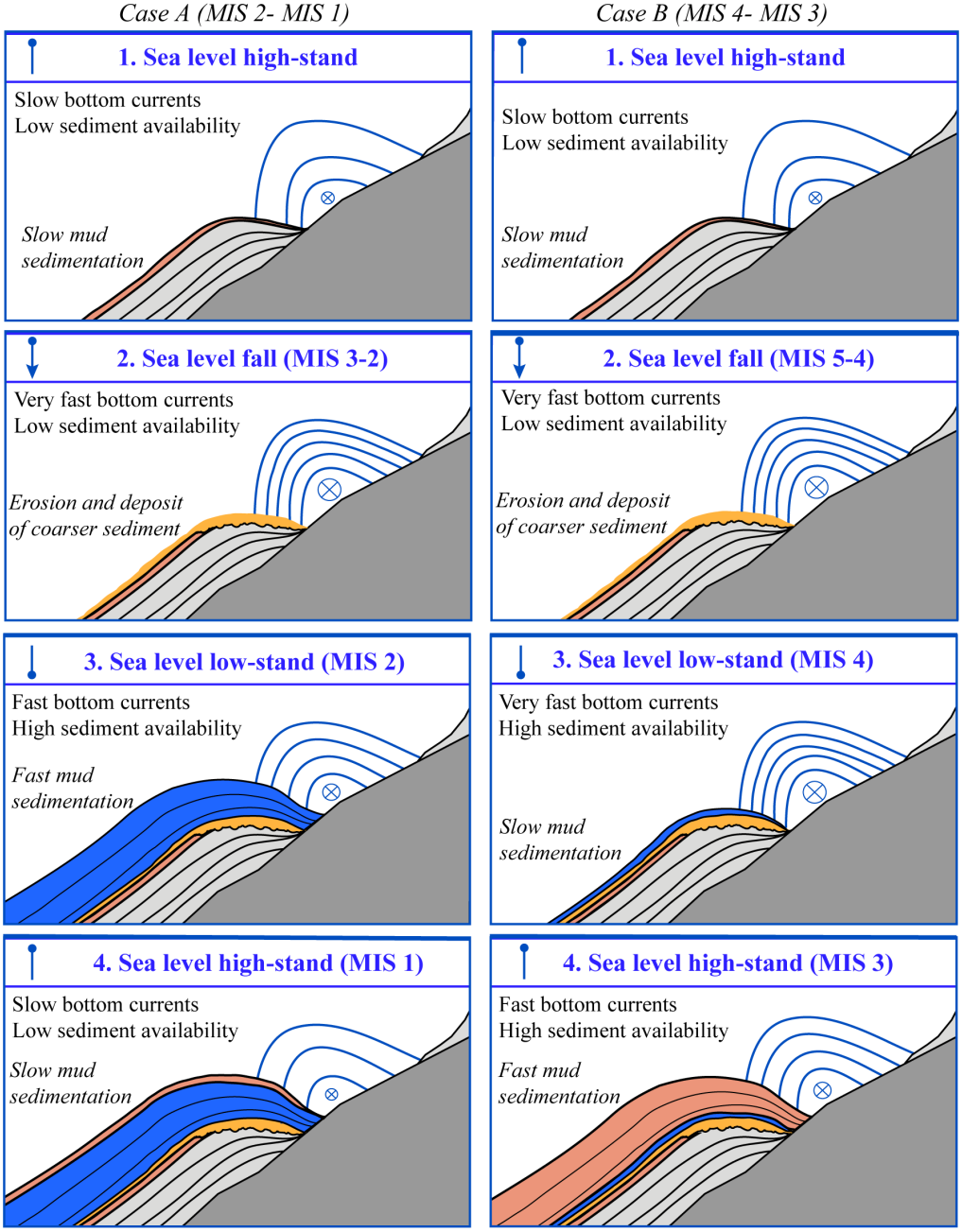

Fig. 4.22. Scheme explaining the evolution of a contourite drift during a single sea level cycle controlled by sediment availability (connection/disconnection of the turbidite system) and bottom-current velocity. Two different scenarios are proposed: high sediment accumulation due to fast bottom currents and high sediment availability during sea level low-stand (case A) or during periods of medium relative sea level (case B).

4.3. Conclusions

The Pianosa Contourite Depositional System (CDS) is located in the confined basin of the Corsica Trough (Northern Tyrrhenian Sea) and it extends between 170 and 850 m water depth along 120 km, with a maximum width of 10 km. Contourite drifts are mainly composed of bioturbated mud, although sandy bioclastic layers are also common, more frequent, thicker and formed by coarser material in the shallowest areas. The morphology of the contourites is strongly controlled by the physiography of the Pianosa Ridge, especially the development of sigmoid drifts in the area where the Pianosa Ridge forms a bulge. Other irregularities or depressions of the seafloor, such as the Elba Canyon, alter locally the hydrodynamic regime and may induce the upwelling of denser waters, allowing the formation of shallower contourites. Different types of contourites can be found in the Pianosa CDS: plastered drift, separated elongated mounded drift, sigmoid mounded drift and multicrested drift. The onset of the Pianosa CDS occurred in the Middle-Late Pliocene, although the development of the contourite drifts was enhanced after the Middle Pleistocene Transition (700-900 kyr). The evolution of the system is continuous and coherent with the present-day circulation pattern, with the Levantine Intermediate Water flowing northwards along the eastern margin of the Corsica Trough. However, its velocity changed in the past with faster bottom currents during cold periods. During sea level falls, very fast bottom currents produced erosional surfaces on the drifts (more evident in the middle and upper slope). The accumulation of coarse bioclastic material in the contourites during sea level falls was favoured by the fact that the material from the continental shelf was more easily transported to the slope. The accumulation of fine sediment was greater during sea level low-stands than during sea level high-stands because the turbidite system was connected (providing fine sediment to the basin) and the velocity of bottom currents was relatively high (pirating the fine sediment from the turbidites and transporting it along the Pianosa Ridge).

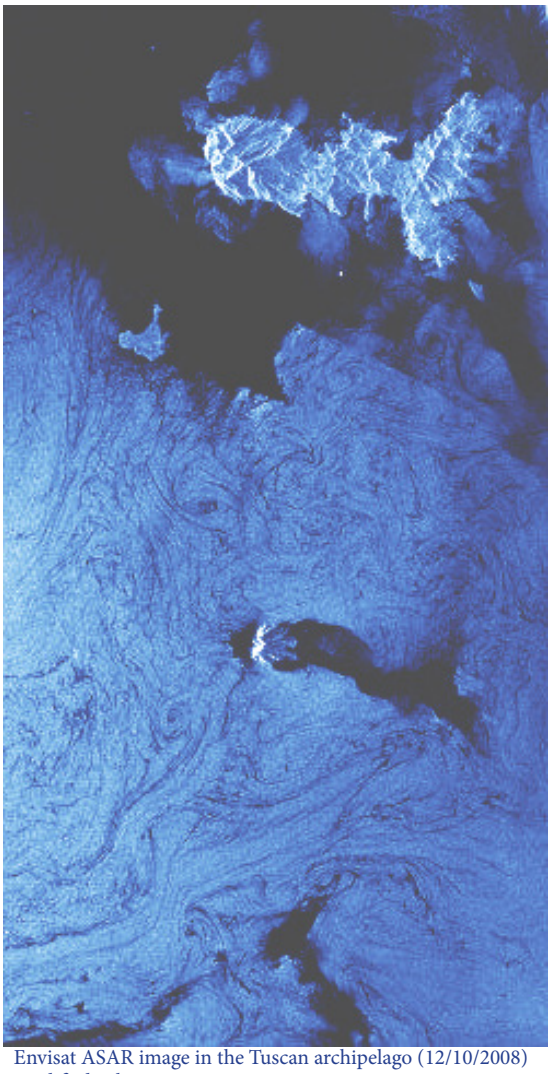

Envisat ASAR image in the Tuscan archipelago (12/10/2008) modified colours

CHAPTER 5. New insights on the formation of contourites from hydrodynamic modelling in the NW Mediterranean Sea

The effect of bottom currents on sediment deposition and erosion has been observed worldwide, including the Mediterranean Sea, however the oceanographic processes controlling the formation of contourites are still poorly constrained. In this study we couple the results of the MARS3D hydrodynamic model with geophysical and sedimentological data (multibeam bathymetry, seismic reflection profiles and grain size of surface sediment) that demonstrate the presence of contourites in the NW Mediterranean Sea. We modelled the circulation during winter and summer 2013 to represent extreme periods of high and low current intensity, respectively. The modelled bottom currents are coherent with the observed contourites and they show that the development of contourite depositional systems is mainly controlled by the extreme events of higher intensity. The heterogeneous distribution of bottom currents on continental slopes allows the development of the different types of contourite drifts. Plastered drifts grow in a zone of the slope with slow bottom currents comprised between two zones (upslope and downslope) with higher current velocities, while separated mounded drifts are formed at the foot of the slope when the bottom-current velocity is fast on the slope and slow at the foot of the slope. In contrast, no mounded morphologies develop when the current velocity is homogeneous across the slope, especially in margins with a direct sediment supply. In confined basins, current gyres may transport the suspended particles from a margin with a high sediment supply to a starved margin, favouring the development of contourites in the latter.

CHAPITRE 5. Nouvelles découvertes sur la formation de contourites à partir de modélisation hydrodynamique en Mer Méditerranée nord-occidentale

Les effets des courants de fond sur la sédimentation et l'érosion ont été observés en Mer Méditerranée comme dans tous les océans. Néanmoins les processus océanographiques qui contrôlent la formation des contourites ne sont pas encore bien contraintes. Dans cette étude les résultats du modèle hydrodynamique MARS3D sont confrontés avec les données géophysiques et sédimentologiques (bathymétrie multifaisceaux, profils de sismique de réflexion et granulométrie des sédiments de surface) qui attestent la présence de ces contourites en Mer Méditerranée nord-occidentale. La modélisation de la circulation a été réalisée en utilisant les conditions limites enregistrées pendant l'hiver et l'été 2013 afin de représenter les périodes respectives de forte et faible intensité des courants. Les courants de fond modélisés sont cohérents avec les contourites observées et ils démontrent que leur développement est principalement contrôlé par les événements extrêmes associés aux périodes « froides ». La distribution hétérogène de l'intensité des courants sur le fond permet la formation de différents types de dépôts contouritiques. Les « plastered drifts » pourraient se développer sur la pente continentale dans une zone de courants faibles encadrée par deux zones de courants plus forts. Les « separated mounded drifts » se forment en pied de pente quand les vitesses des courants sont importantes sur la pente et faibles en pied de pente. Par contre, le développement des morphologies linéaires est conditionné par des vitesses de courant homogènes sur la pente continentale associées à un apport sédimentaire direct. Enfin, les modélisations contribuent à prouver que les gyres dans ce bassins confinés sont capables de transporter les particules en suspension d'une marge alimentée en apport sédimentaire continentaux vers une marge isolée des apports clastiques ; ce transfert de matière par les courants favorise le développement des contourites dans des zones déconnectées des apports directs.

CAPíTULO 5. Nuevos conocimientos sobre la formación de contornitas a partir de modelización hidrodinámica en el NO del Mar Mediterráneo

El efecto de las corrientes sobre la sedimentación y la erosión ha sido observado en todos los océanos, incluido el Mar Mediterráneo. Sin embargo, todavía no se conocen bien los procesos oceanográficos que controlan la formación de contornitas. En este estudio acoplamos les resultados del modelo hidrodinámico MARS3D con datos geofísicos y sedimentológicos (batimetría multihaz, perfiles de sísmica de reflexión y medidas del tamaño de grano del sedimento superficial) que evidencian la presencia de contornitas en el NO del Mar Mediterráneo. Modelizamos la circulación durante el invierno y el verano de 2013 para representar periodos extremos de alta y baja intensidad respectivamente. Las corrientes de fondo modelizadas son coherentes con las contornitas observadas y muestran que el desarrollo de los sistemas deposicionales contorníticos está controlado principalmente por los eventos extremos de mayor intensidad. La distribución heterogénea de la intensidad de las corrientes de fondo sobre los taludes permite el desarrollo de diferentes tipos de depósitos contorníticos. Los "plastered drifts" crecen en la zona de corrientes débiles situada entre dos zonas de corrientes más fuertes, mientras que los depósitos contorníticos monticulares separados se forman al pie del talud cuando la velocidad de las corrientes es alta en todo el talud y baja al pie del talud. Por el contrario, no se desarrollan morfologías monticulares cuando la velocidad de la corriente es homogénea a través el talud, sobre todo en márgenes que tienen un aporte sedimentario directo. En cuencas confinadas los giros oceánicos pueden transportar las partículas en suspensión desde un margen con aportes sedimentarios altos hasta un margen con bajos aportes directos, favoreciendo la formación de contornitas en este último.

5.1. Introduction

Oceanic currents play a major role in controlling the morphological and sedimentary evolution of continental margins (Rebesco and Camerlenghi, 2008). Currents near the seafloor, also known as bottom currents, can winnow fine-grained sediment, mobilise the sediment, generate large scale erosion and focus the sediment accumulation in some areas (Hernández-Molina et al., 2008; Stow et al., 2009). The sediment deposited or substantially reworked by bottom currents is known as contourite and the contourite drifts are the major accumulations of this type of sediment bodies (Stow et al., 2002; Rebesco and Camerlenghi, 2008; Rebesco et al., 2014).

Although many intermittent oceanic processes may affect the seafloor (for example eddies, internal waves, deep sea storms, rogue waves or tsunami related currents; Shanmugam, 2013; Rebesco et al., 2014), contourites are commonly associated with persistent bottom currents related to the thermohaline circulation. However, the oceanic circulation is very variable at seasonal (Astraldi and Gasparini, 1992), interannual (Pinardi et al., 2015) and geological scale (Cacho et al., 2000). Therefore, it is not clear in the literature if contourite depositional systems, i.e. the erosional and depositional features created by bottom currents, are mainly formed by episodic extreme events of intense circulation or by constant bottom currents of moderate intensity. Furthermore, bottom currents can also rework and/or redistribute sediment from turbidity currents while they flow towards deep basin areas, redistributing sediment alongslope (Mulder et al., 2008). This lateral extraction of sediment from across-slope gravity flows may be the cause of unbalanced source-to-sink budgets where sediment accumulation in the basin is lower than the continental sediment production.

Sedimentation rates in contourite drifts can be up to one order of magnitude higher than in pelagic sediments, making contourite drifts advantageous targets for high resolution palaeoceanographic and palaeoclimatic studies (Knutz, 2008; McCave, 2008). Although contourites are frequently used for palaeoreconstructions, the physical processes that control their formation are still poorly understood (Hunter et al., 2007; Hernández-Molina et al., 2016), preventing a more effective exploitation of the paleoenvironmental information that they might convey. For example, bottom currents may control the particulate matter distribution (Durrieu de Madron et al., 1992; Puig and Palanques, 1998), influencing the transfer from the continent to the marine system and thus the biogeochemical cycles and the marine ecosystems (Asper et al., 1992).

The oceanic circulation in the western Mediterranean Sea has been widely studied from measurements and numerical modelling (Pinardi et al., 2015 and references therein) and it is a region where many contourites were identified: in the Balearic Sea (Velasco et al., 1996; Vandorpe et al., 2011), in the Tyrrhenian Sea (Roveri, 2002; Cattaneo et al., 2014; Miramontes et al., 2016b), in the Adriatic Sea (Verdicchio and Trincardi, 2008a,b; Pellegrini et al., 2015), and in the Alboran Sea (Ercilla et al., 2016; Juan et al., 2016).

Coupling physical oceanographic modelling with seafloor morphology implies the availability of similar spatial resolution when comparing the two independent datasets to reconstruct the origin of contourite formation. This is the reason why we focused in three areas of the NW Mediterranean Sea with the best available datasets: (1) the Catalan Sea (Minorca Basin or Valencia Trough), (2) the Ligurian Sea (offshore the Portofino Promontory) and (3) the Northern Tyrrhenian Sea (Corsica Trough and a seamount off southeast Corsica; Fig. 5.1). We use the terms Catalan Sea, Ligurian Sea and Tyrrhenian Sea when we refer to the general water circulation and water masses properties; but Minorca Basin, Minorca Margin, Catalan Margin, Ligurian Margin or Corsica Trough, when we refer to the seafloor or current-seafloor interaction.

For the present study, we use the MARS3D hydrodynamic model in the MENOR configuration, that covers the NW Mediterranean Sea (0°E 39.5°N-16°E 44.5°N), to model the oceanic circulation during winter and summer 2013. The studied contourites developed during the Plio-Quaternary and did not change their position during this period. Therefore, we assume that the main current patterns remained similar during the Plio-Quaternary, but with changes in intensity. The present-day winter period is assumed to represent intense circulation that could be similar during the glacial intervals. We used the 90th percentile of the bottom shear stress to estimate the seafloor erosion in order to remove the extreme events considered not representative. By coupling the results of hydrodynam-

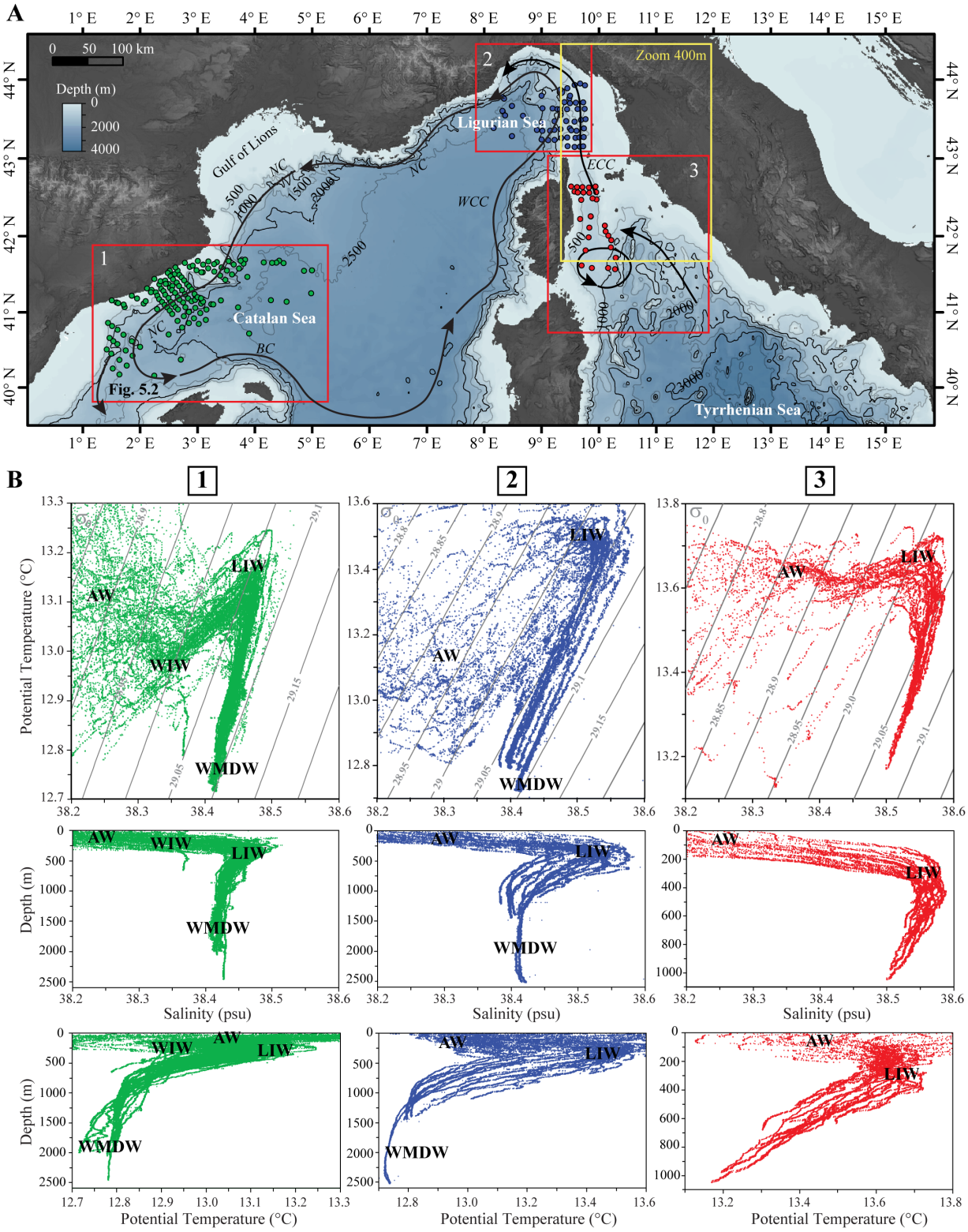

Fig. 5.1. (A) Bathymetry of the NW Mediterranean Sea (GEBCO) showing the main circulation structures at 200-300 based on Pinardi et al. (2015), and location of representative CTD stations of the three study areas: 1-Catalan Sea/Minorca Basin, 2-Ligurian Sea, 3-Northern Tyrrhenian Sea/Corsica Trough. The CTDs correspond to the spring season in the Catalan Sea (April-May), to avoid the periods of dense water formation, and to the winter season in the Ligurian and Tyrrhenian Seas (February-March). **(B)** From top to bottom: θ-S diagrammes, salinity-depth profiles and potential temperature-depth profiles from CTD stations acquired in the winter season (January-February and March) that are representative of the three study areas (from the NOAA database).

ic modelling with geophysical and sedimentological data from the NW Mediterranean Sea, we aim to understand: (i) the current velocities and bottom shear stresses associated to the formation of contourites, (ii) whether contourite drifts are mainly controlled by constant currents of moderate intensity or rather by extreme events, and (iii) how currents redistribute the sediment from a margin with high sediment supply to a starved margin.

5.2. Regional oceanographic setting

5.2.1. Mediterranean water masses

The Mediterranean Sea is a semi-enclosed sea connected with the Atlantic Ocean through the Strait of Gibraltar. It is divided in two sub-basins, the western and the eastern basins, separated by the Strait of Sicily. The Mediterranean Sea has an anti-estuarine circulation (inflow of low-salinity surface water and outflow of a deep denser water with high salinity) forced by wind stress and buoyancy fluxes (Pinardi et al., 2015). The negative heat and fresh water budgets of the Mediterranean Sea are balanced in a multidecadal time scale by the entrance of Atlantic Water (AW) through the Strait of Gibraltar (Pinardi et al., 2015). The AW is a fresher water mass that characterises the upper 100-200 m of the water column (Millot and Taupier-Letage, 2005; Millot, 2009). It overlies the Levantine Intermediate Water (LIW), which is formed in the Levantine Basin by a process of evaporation during the summer and a winter cooling (Lascaratos et al., 1993; 1999).

The deep water masses are different in the eastern and western basins due to the depth limitation of the Strait of Sicily (maximum water depth of 500 m). The Eastern Mediterranean Deep Water is mainly formed in the southern Adriatic Sea (Chiggiato et al., 2016), but also in the Aegean Sea (Bellacicco et al., 2016), in the Rhodes gyre (Levantine Deep Water; Gertman et al., 1994) and in the Sea of Crete (Cretan Deep Water; Tsimplis et al., 1999). When the EMDW and the LIW flow through the Strait of Sicily, they cascade into the Tyrrhenian Sea, with the upper part basically composed of LIW and the deeper part composed of the cooler and denser Tyrrhenian Dense Water (TDW; Millot, 1999; Millot and Taupier-Letage, 2005; Millot, 2009). However, the limit between the LIW and the TDW is not well defined (Millot, 1999). The Western Mediterranean Deep Water (WMDW) is mainly formed in the Gulf of Lions by surface cooling and evaporation due to cold and dry northern winds and open-sea convection (Durrieu de Madron et al., 2013). This deep water mass is present in the deep basins of the Western Mediterranean Sea, including the deepest part of the Tyrrhenian Sea, but not in the Corsica Trough due to its limited depth (max. 430-880 m; Millot, 1999). The Western Intermediate Water (WIW) is formed seasonally in the NW Mediterranean Sea due to the winter cooling of the surface AW and is characterised by a lower temperature than the AW and the LIW (Millot, 1999). When present, it is located above the LIW (Millot, 2009), deflecting the LIW to a deeper zone (Monserrat et al., 2008).

5.2.2. Study areas

5.2.2.1. Catalan Sea (Minorca Basin)

The Northern part of the NW Mediterranean Sea is dominated by the Northern Current (NC), that closes cyclonically in the Catalan Sea, flowing along the northern Balearic margin as the Balearic Current (BC; Pinot et al., 2002), and forming part of the Gulf of Lions gyre (Pinardi et al., 2006). In this area, the water column is usually composed of AW in the upper 200 m, WIW at 200-400 m (when it is present), LIW at 400-700 m and WMDW below 700 m (Salat and Font, 1987; Font et al., 1988). Contourites in the Minorca Basin are located at about 2300 m water depth and are thus under the influence of the WMDW (Fig. 5.1).

5.2.2.2. Ligurian Sea

The Ligurian margin is also affected by the previously mentioned Northern Current which presents a marked seasonal variability. In winter it is more intense, narrower and deeper (Albérola et al., 1995). WIW can also be formed in the Ligurian margin, like in the Catalan Sea and in the Gulf of Lions, when during winter the northern winds increase the density of the AW and it is then equilibrated above the LIW (Gasparini et al., 1999). In the Ligurian Sea the upper 150 m are characterised by the AW (Millot, 1999), with the LIW below this depth when the WIW is not present. The WMDW is on average present below 1000 m depth (Houpert, 2013). The identified contourite in this area is located at 900 m w.d., mainly under the influence of the LIW as part of the Northern Current (Fig. 5.1).

5.2.2.3. Northern Tyrrhenian Sea (Corsica Trough)

The AW flows northwards in the northern Tyrrhenian Sea as the East Corsica Current (ECC) and joins the

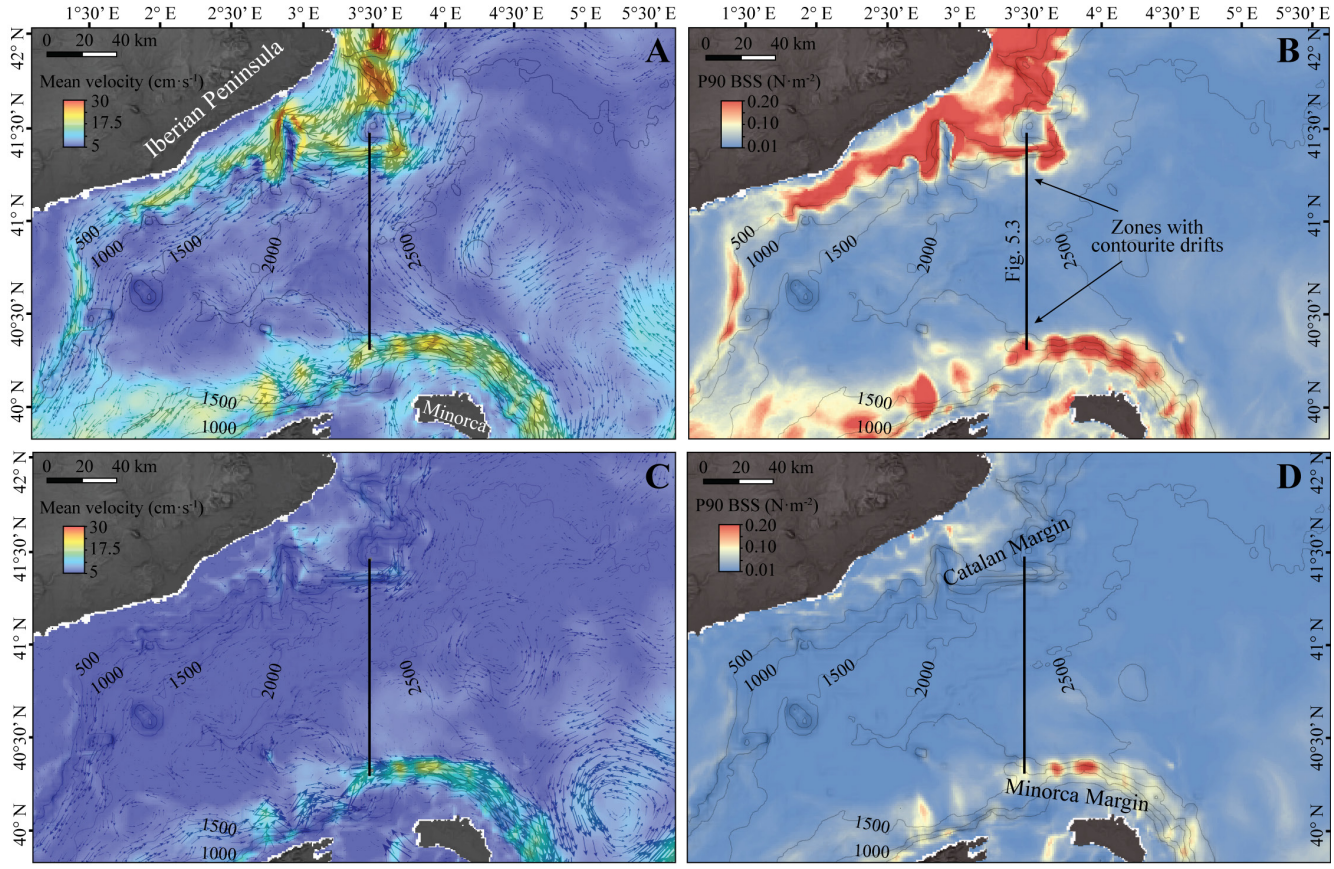

Fig. 5.2. Results of the MENOR model (cell size of 1.2 km) in the Catalan Sea: **(A)** Mean velocity and vectors of the mean velocity during the winter period 2013 (January, February and March). **(B)** 90th percentile of the Bottom Shear Stress (P90 BSS) during the winter period 2013 (January, February and March). **(C)** Mean velocity and vectors of the mean velocity during the summer period 2013 (July, August and September). **(D)** 90th percentile of the Bottom Shear Stress (P90 BSS) during the summer period 2013 (July, August and September).

West Corsica Current in the Ligurian Sea after crossing the Corsica Trough, forming the Northern Current (Astraldi et al., 1990; Fig. 5.1). The ECC presents mainly a barotropic structure flowing towards the north, with a maximum flux during winter, although some episodes of inversed current towards the south were registered in the deep part of the Corsica Trough (Astraldi et al., 1990). A large cyclonic gyre is present at the south of the Corsica Trough between Corsica and the mainland of Italy (Vetrano et al., 2010; Pinardi et al., 2015). The gyre has a barotropic signature, affecting both surface and intermediate layers (Vetrano et al., 2010). Only part of the LIW can flow northwards through the Corsica Trough to the Ligurian Sea, the rest flows back southwards along the margin of Sardinia (Millot, 1999; Millot and Taupier-Letage, 2005). The deep water mass present in the Tyrrhenian Sea is the TDW that results from the mixing of the WMDW and the EMDW (Astraldi et al., 1996; Sparnocchia et al., 1999). Part of the LIW coming from the eastern basin into the Tyrrhenian Sea mixes with the surrounding water masses and forms part of the TDW (Astraldi and Gasparini, 1994). The TDW flows northwards along the Italian margin and then back southwards along the margin of Sardinia (Millot, 1999; Millot and Taupier-Letage, 2005).

The contourite drifts in the Northern Tyrrhenian Sea are mainly under the influence of the LIW: in the Corsica Trough they are located at 170-850 m w.d. and in the seamount south of the Corsica Trough at 820-900 m w.d.

5.3. Results and interpretations

5.3.1. Catalan Sea (Minorca Basin)

The Catalan Sea is located between the north of the Balearic Islands and the Iberian Peninsula, with depths that decrease westwards from 2500 m to 1000 m (Fig. 5.1). The modelled circulation shows the same gener-

al patterns during winter and summer 2013: currents near the seafloor (bottom currents) flow westwards along the Catalan margin and turn cyclonically due to the bathymetric constrain, flowing back eastwards along the northern Balearic margin (Fig. 5.2). The results of the three months of winter 2013 (January, February and March) show shelf dense waters from the Gulf of Lions cascading downslope the Catalan margin and resulting in high mean velocities (20-30 cm·s^{-1}; Fig. 5.2A) in the Catalan continental slope and high P90 BSS (90th percentile of the Bottom Shear Stress), higher than 0.2 N·m^{-2} in great part of the Catalan margin (Fig. 5.2B). During winter, bottom currents are relatively fast along the continental slope of the Minorca Basin, especially in the lower slope at 1000-2000 m w.d., with mean velocities ranging between 15 and 25 cm·s^{-1} and P90 BSS 0.1-0.2 N·m^{-2}. Bottom currents remain relatively active along the Minorca Margin also in summer, with mean velocities of 10-20 cm·s^{-1} (Fig. 5.2C) and P90 BSS of 0.07-0.2 N·m^{-2} (Fig. 5.2D). In contrast, in the Catalan margin the circulation near the seafloor is much weaker during the summer with mean velocities below 10 cm·s^{-1} (Fig. 5.2C) and P90 BSS below 0.03 N·m^{-2}. It is the fastest at the foot of the slope between 1000 and 2000 m w.d. (Fig. 5.2D).

Bottom currents control the sedimentation in the Minorca Basin and are responsible of the formation of two separated mounded drifts along the Minorca and the Catalan margins at 2200-2400 m w.d (Fig. 5.3), and thus under the influence of the WMDW (Fig. 5.1). They are separated from the continental slope by moats that are about 4 km wide. The continental slopes of both margins are strongly eroded and are thus characterised by bedrock outcropping at the seafloor, coherent with the high modelled P90 BSS (Fig. 5.3). The separated mounded drifts develop in the zone where bottom currents are weak even during winter, with mean velocities below 7 cm·s^{-1} and P90 BSS below 0.03 N·m^{-2} (Table 5.1).

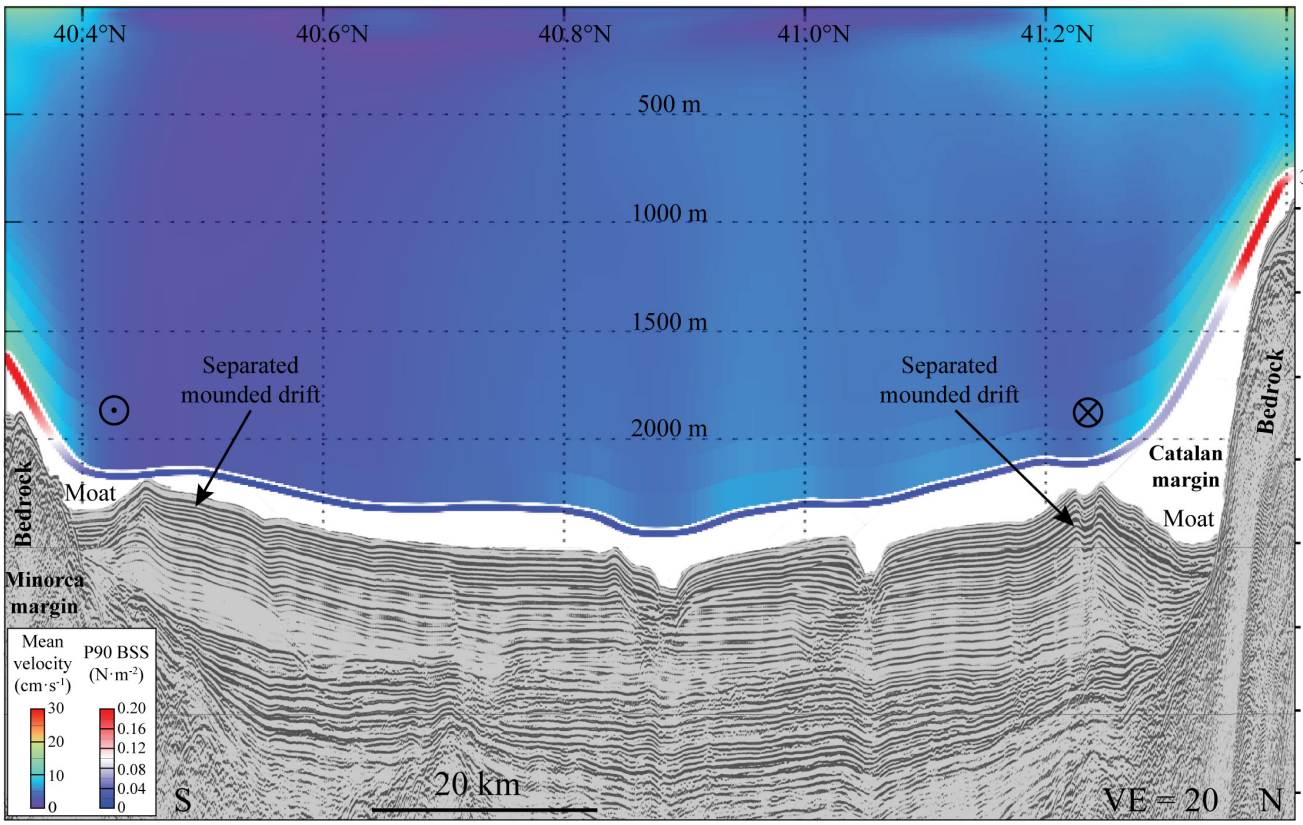

Fig. 5.3. Seismic reflection profile VALS88-808 and transect at the same position of the mean velocity and 90th percentile of the BSS from the MENOR model during the three months of the winter period. Note that the bathymetry used for the hydrodynamic model is a simplified bathymetry with a 1.2 km resolution and thus it does not fit perfectly with the seismic profile. The transect of the model and the seismic profile are not represented at the same depth to avoid overlapping between the images.

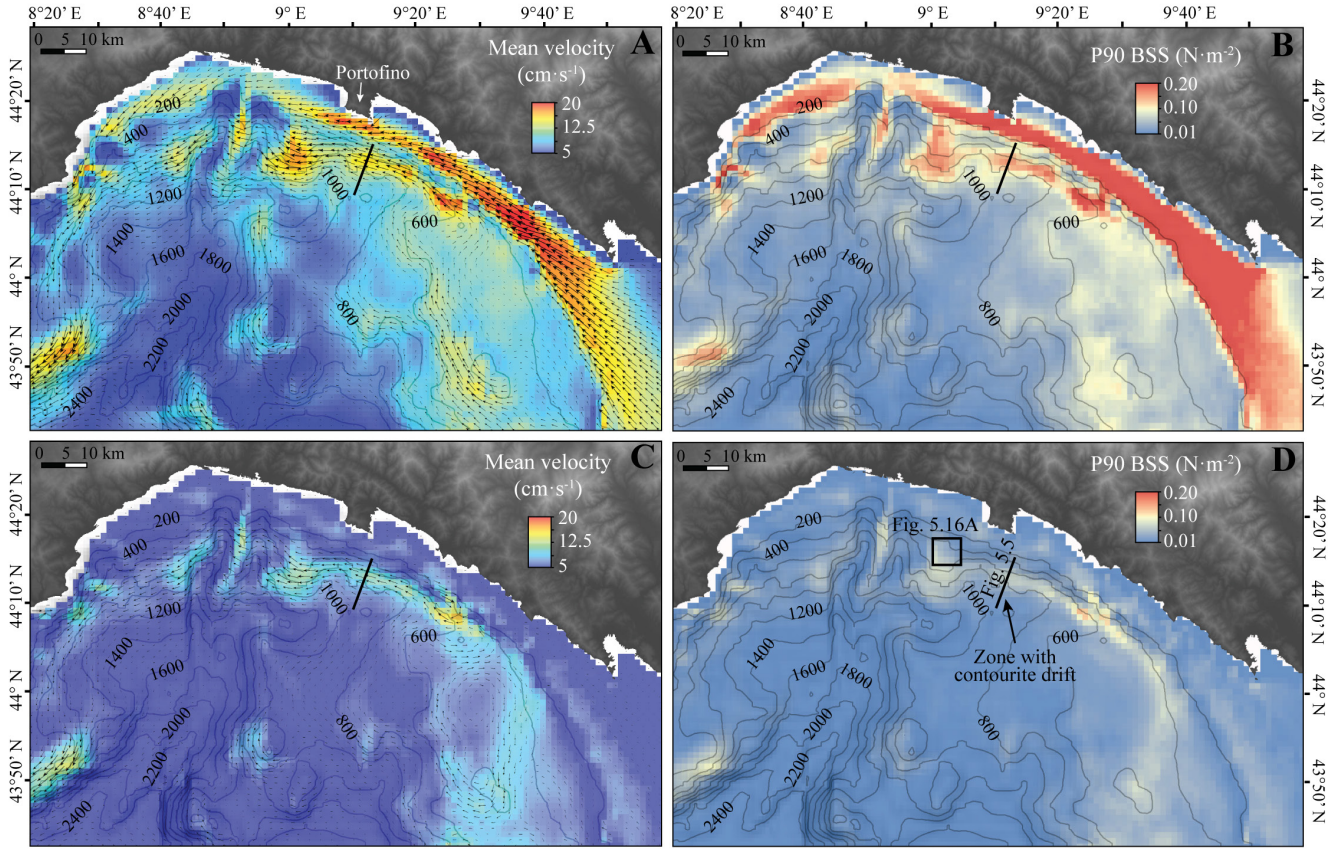

Fig. 5.4. Results of the MENOR model (cell size of 1.2 km) in the Ligurian Sea: **(A)** Mean velocity and vectors of the mean velocity during the winter period 2013 (January, February and March). **(B)** 90th percentile of the Bottom Shear Stress (BSS) during the winter period 2013 (January, February and March). **(C)** Mean velocity and vectors of the mean velocity during the summer period 2013 (July, August and September). **(D)** 90th percentile of the Bottom Shear Stress (BSS) during the summer period 2013 (July, August and September).

5.3.2. Ligurian Sea

Bottom currents flow northwards and westwards following the bathymetric contours along the Ligurian margin during winter and summer 2013. During winter currents are fast on the continental shelf (related to the AW) with mean velocities ranging between 15 and 20 cm·s^{-1} (Fig. 5.4A) and P90 BSS of 0.2-0.4 N·m^{-2} (Fig. 4B). Similar values are found related to the LIW at 600-800 m w.d. offshore Portofino, although in this area P90 BSS are lower between 0.1 and 0.2 N·m^{-2} (Fig. 5.4B). In summer the surface currents become less active, with mean velocities below 7 cm·s^{-1} (Fig. 5.4C) and P90 BSS below 0.04 N·m^{-2} (Fig. 5.4D). During summer the strongest currents near the seafloor are found on the continental slope at 400-1000 m w.d. with mean velocities between 10 and 15 cm·s^{-1} (Fig. 5.4C) and P90 BSS between 0.06 and 0.13 N·m^{-2} (Fig. 5.4D). Contourites are related to this zone of faster currents and the drifts develop in the adjacent deeper zone with lower currents at about 900 m w.d. (Fig. 5.5).

5.3.3. Northern Tyrrhenian Sea

The near seafloor circulation in the Corsica Trough is mainly dominated by two cyclonic gyres in the middle of the basin, one off the Elba Island and one off the Montecristo Island, as well as alongslope currents flowing northwards along the eastern margin (Pianosa Ridge) and southwards along the western margin (Fig. 5.6). Bottom currents are weak on the continental shelf, on the central part of the basin and on the Pianosa Ridge during summer, but they increase along the Corsican continental slope due to an enhanced entrance of water from the Ligurian Sea southwards into the Corsica Trough (Fig. 5.6C). The modelled strong currents flowing southwards along the western margin are coherent with the high percentages of sand found at the present-day seafloor that can reach up to 63% in this area (Fig. 5.6B). These currents are related to the entrance of cooler and less salty LIW from the Ligurian Sea, resulting in an asymmetric distribution of the LIW properties in the lower slope along the eastern

(saltier and warmer) and the western margins (cooler and less salty; Figs. 5.7 and 5.8). During March 2013 the core of the LIW carrying warmer water is very well defined at 150-300 m, forming two thermoclines, one at 100-150 m w.d. and another one at 300-500 m w.d. (Figs. 5.7A, 5.8A).

Contourites have been identified in the Corsica Trough along the eastern margin, in the upper slope of the western margin and at the north of the Corsica Sill (Fig. 5.6). All these deposits are found in areas where bottom currents are low in winter and in summer compared to other areas in this basin, i.e. contourites develop in areas where slower currents favour the preferential accumulation of sediment. The Pianosa Rigde presents a wide range of drift morphologies. The southern slope, between the Pianosa and the Montecristo Islands, is mainly dominated by a plastered drift, a convex-shaped sediment deposit that extends between 150 and 700 m w.d. (Figs. 5.9, 5.10). The plastered drift is characterised by a sedimentary terrace in the upper part with lower sediment accumulation and lower slope gradients and a zone of highest accumulation in the middle slope (Fig. 5.10). The circulation

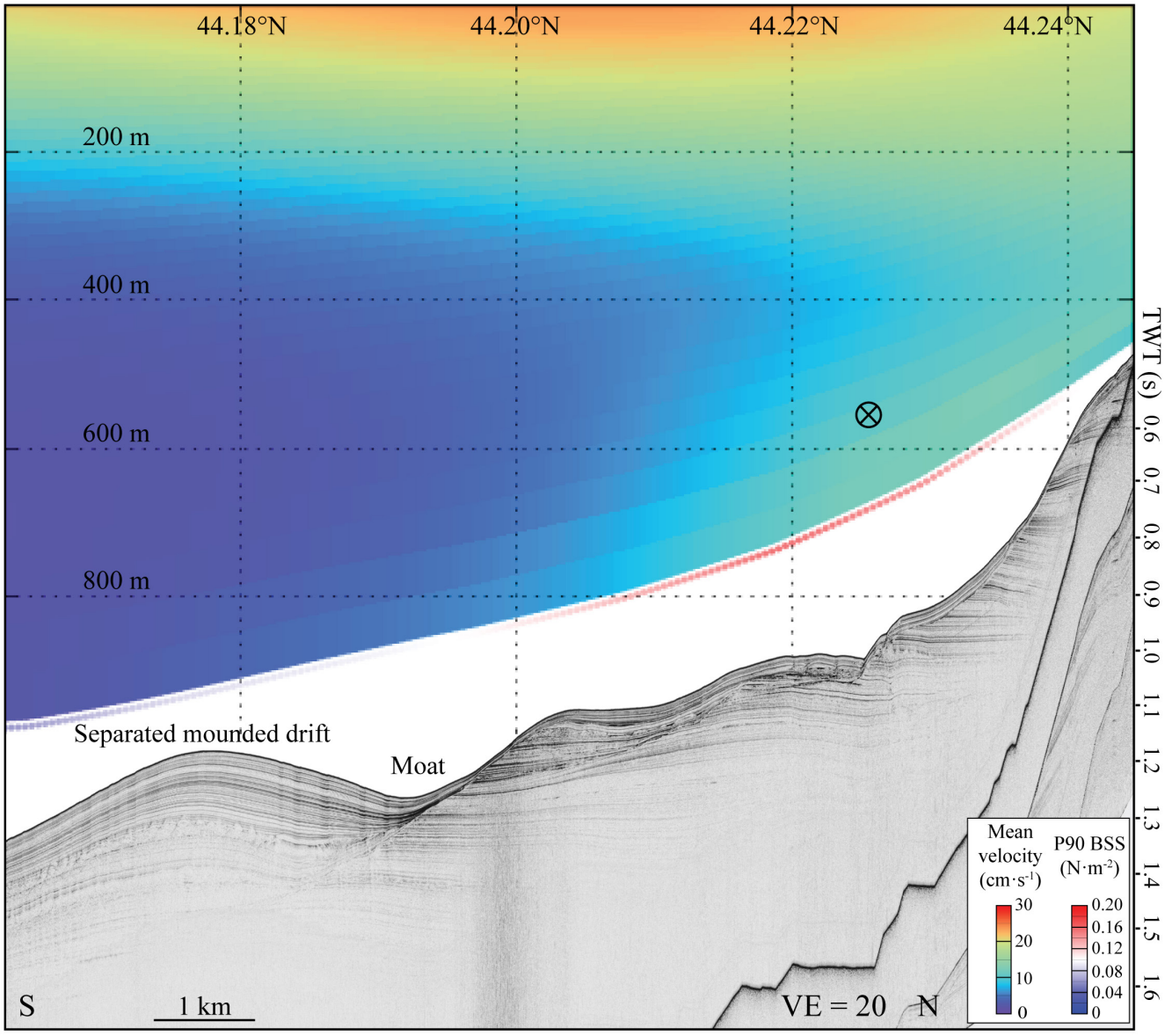

Fig. 5.5. Deep-towed SYSIF seismic reflection profile PSM2-15B-PL07-PR01 and transect at the same position of the mean velocity and 90th percentile of the BSS from the MENOR model during the three months of the winter period. Note that the bathymetry used for the hydrodynamic model is a simplified bathymetry with a 1.2 km resolution and thus it does not fit perfectly with the seismic profile. The transect of the model and the seismic profile are not represented at the same depth to avoid overlapping between the images.

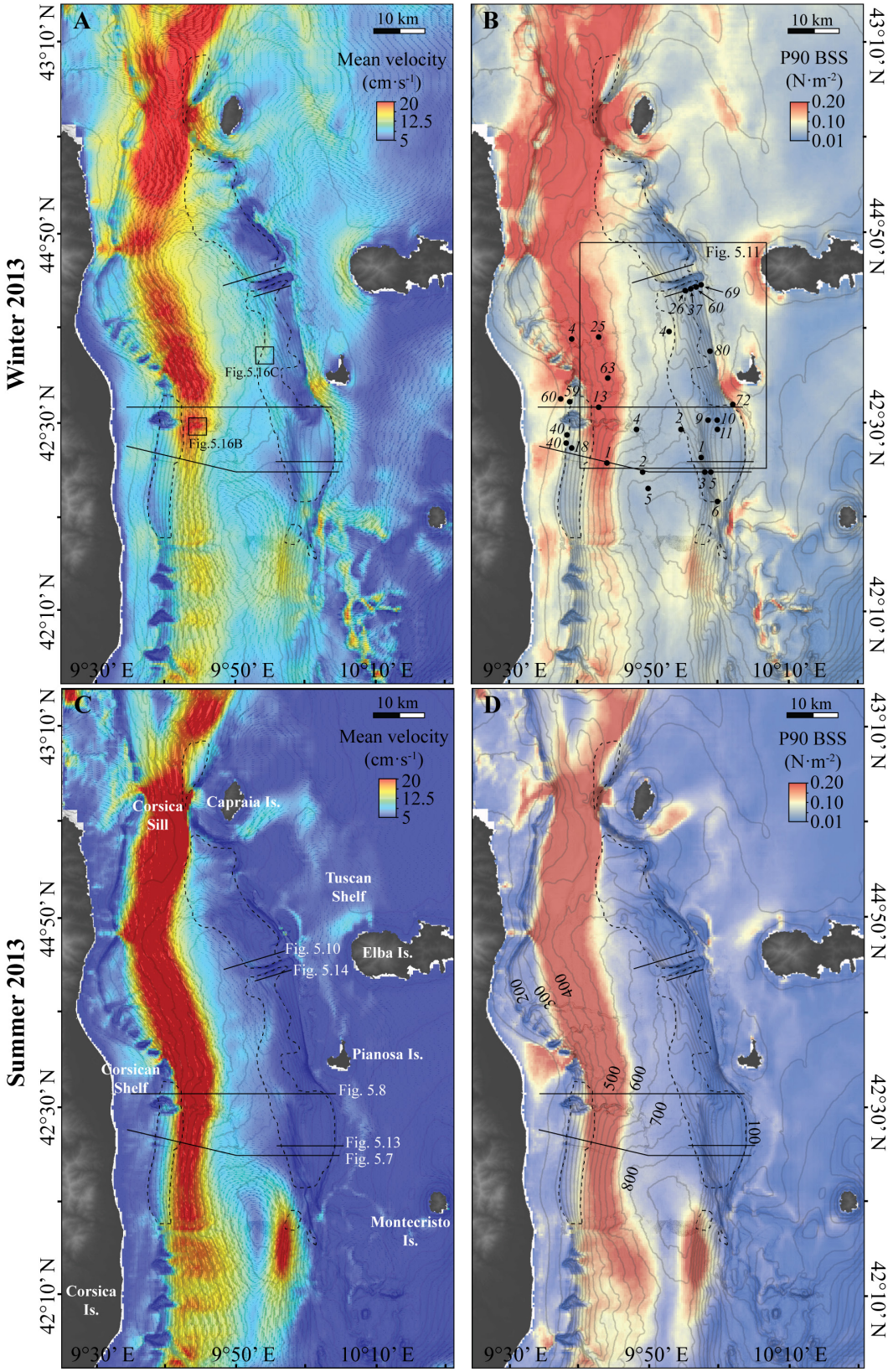

Fig. 5.6. Results of the MENOR model (zoom with cell size of 400 m) in the Corsica Trough: **(A)** Mean velocity and vectors of the mean velocity during the winter period 2013 (January, February and March). **(B)** 90th percentile of the Bottom Shear Stress (BSS) during the winter period 2013 (January, February and March) and sand volumes (in percentage) of the superficial sediment. **(C)** Mean velocity and vectors of the mean velocity during the summer period 2013 (July, August and September). **(D)** 90th percentile of the Bottom Shear Stress (BSS) during the summer period 2013 (July, August and September).

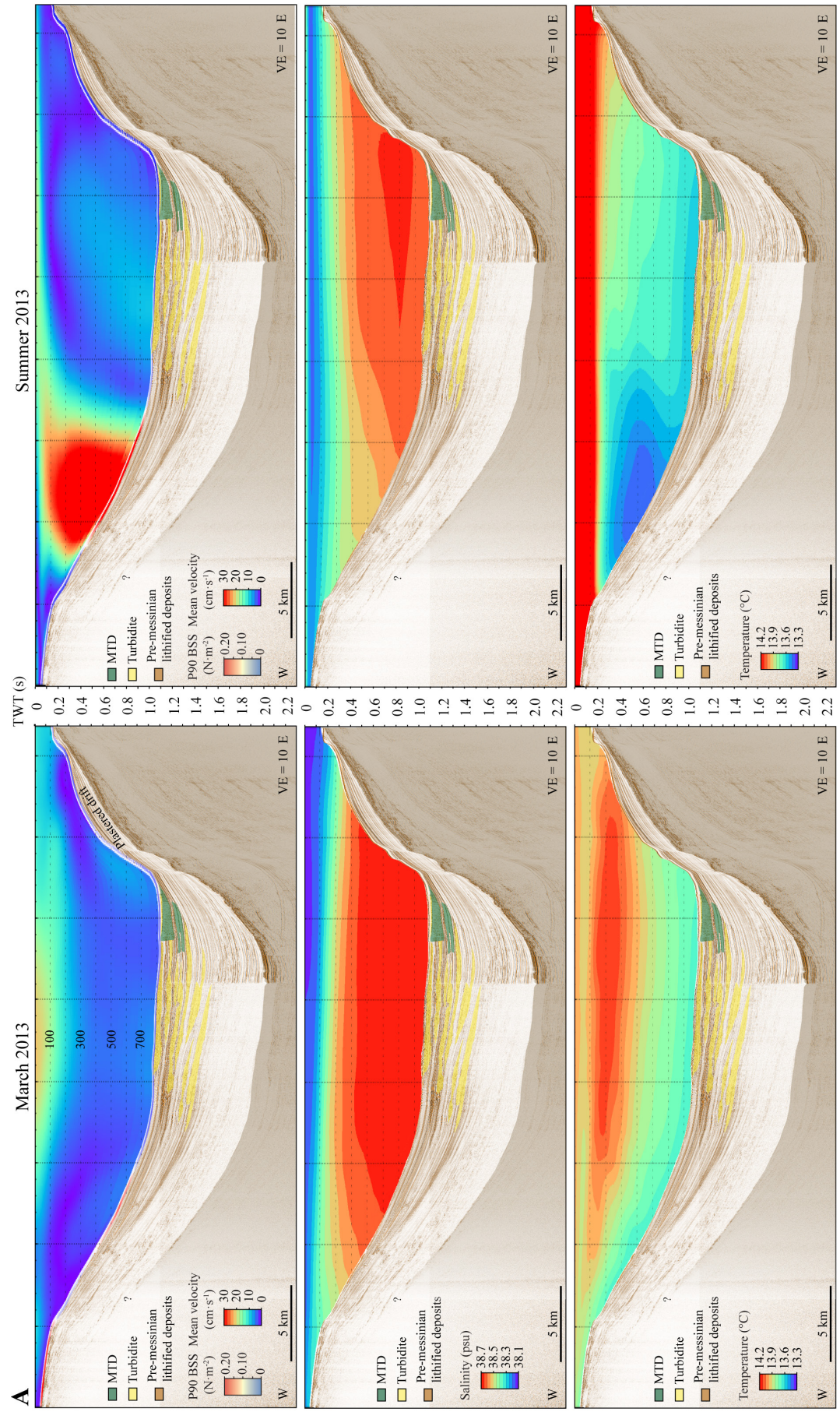

Fig. 5.7. Composite of multi-channel high resolution mini GI gun seismic reflection profiles Sigolo-MC069, Sigolo-MC054 and PSM2-HR033 coupled with a transects at the same position from the MENOR model (zoom 400 m): from top to bottom, mean velocity and 90th percentile of the BSS, salinity and temperature (**A**) during March 2013 and (**B**) during the summer (July, August and September).

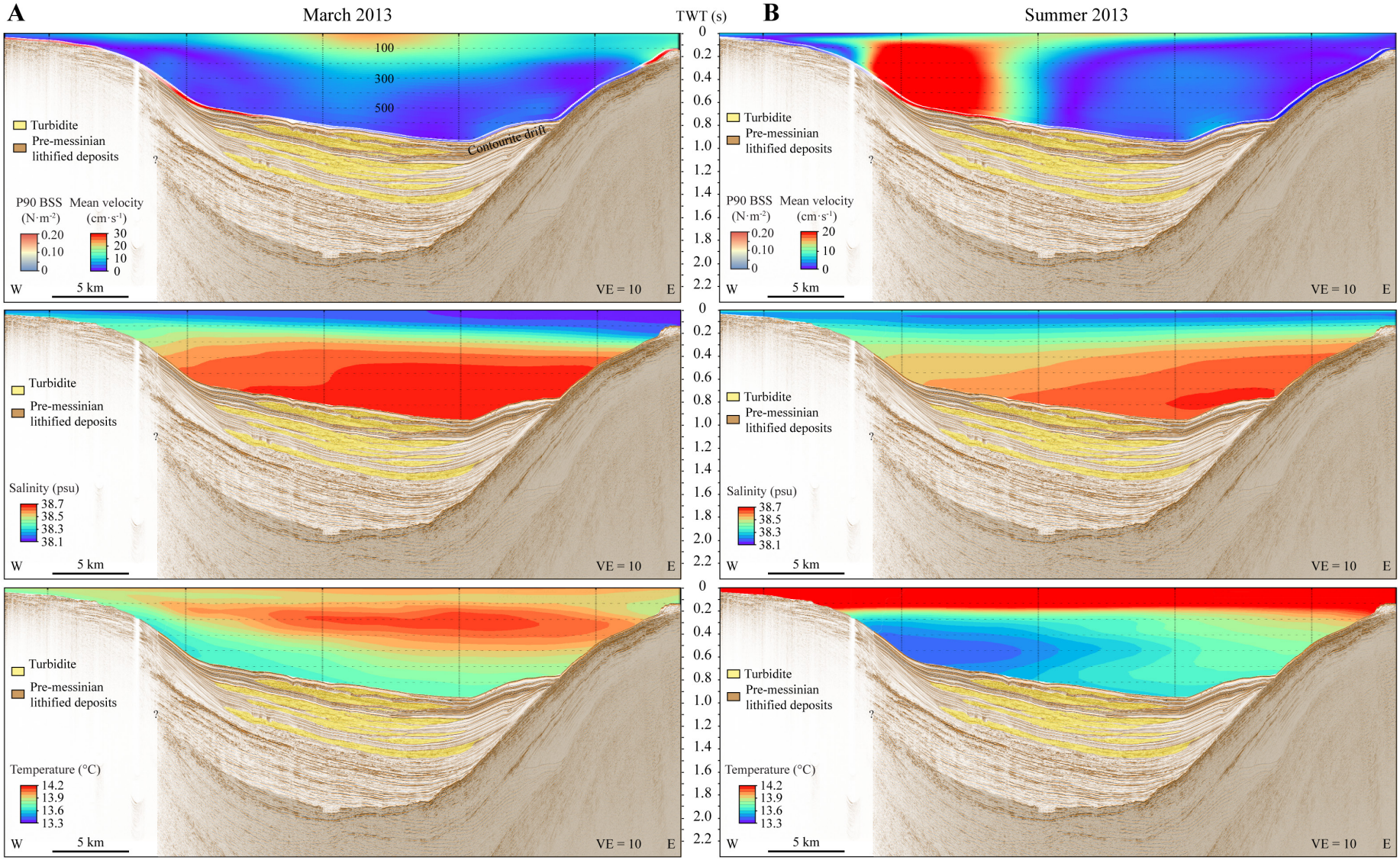

Fig. 5.8. Composite of multi-channel high resolution mini GI gun seismic reflection profiles Sigolo-MC036 and PSM2-HR037 coupled with a transects at the same position from the MENOR model (zoom 400 m): from top to bottom, mean velocity and 90th percentile of the BSS, salinity and temperature **(A)** during March 2013 and **(B)** during the summer (July, August and September).

model shows that during winter, and especially during the month of March 2013, bottom currents are weaker (mean velocity of 7 cm·s^{-1} and P90 BSS of 0.04 N·m^{-2}) in the upper and middle slope than in the lower slope, foot of the slope and shelf edge (Fig. 5.9), corresponding to the zone of the plastered drift development. In the lower slope and below 400 m w.d. bottom currents are faster during the same period, with mean velocity of 10 cm·s^{-1} and P90 BSS of 0.08 N·m^{-2}. Similar values are found at the shelf edge, so the plastered drift develops in an area of weaker currents constrained upslope and downslope by two areas of stronger currents. Besides the differences in absolute velocity, the direction of the currents is also different in the zone of the

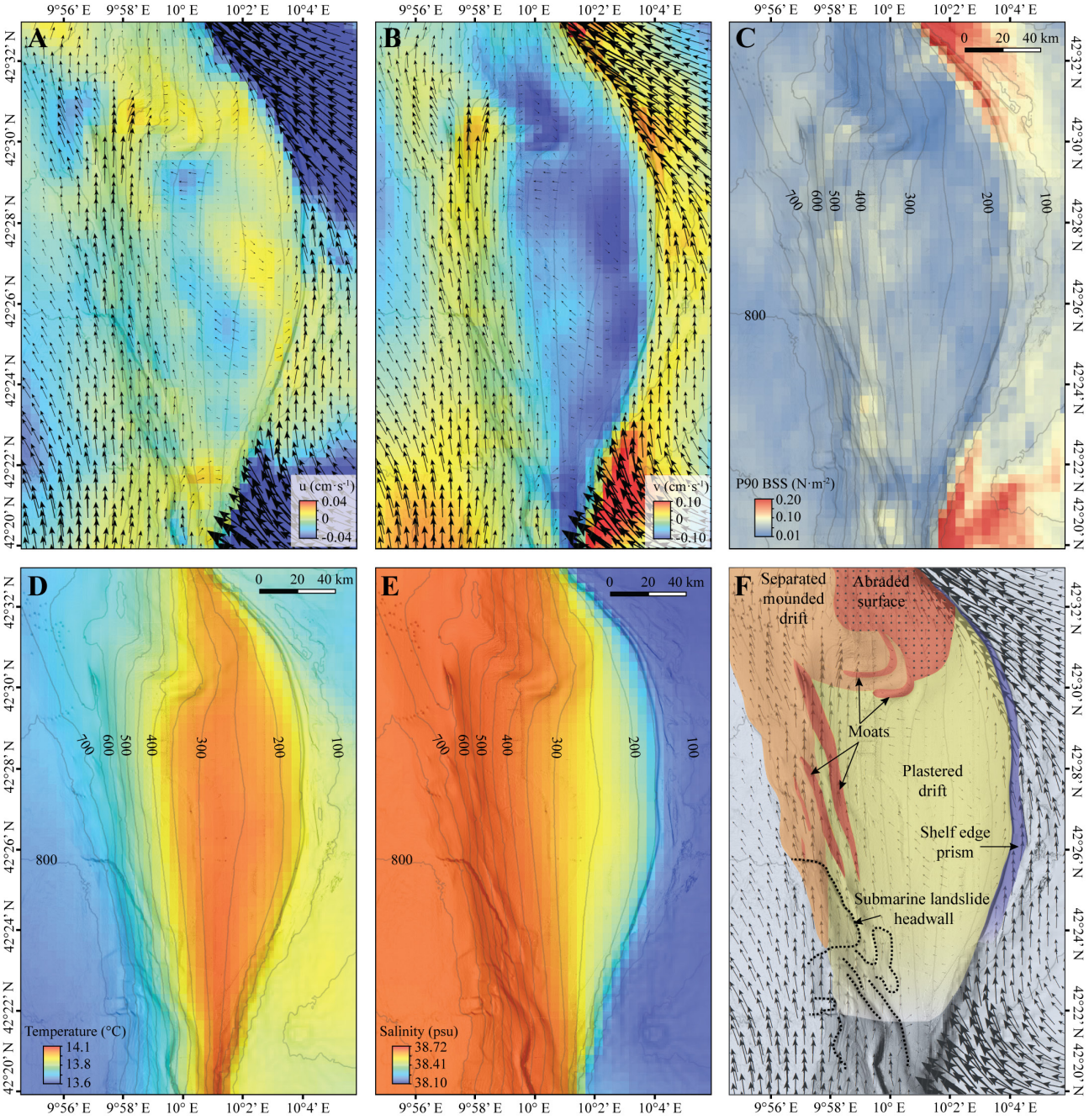

Fig. 5.9. Zoom on the southern part of the Pianosa Ridge showing the results of the 400 m zoom of the MENOR model during March 2013: **(A)** Zonal component of the mean velocity and vectors of the mean velocity current. **(B)** Meridional component of the mean velocity and vectors of the mean velocity current. **(C)** 90th percentile of the BSS. **(D)** Mean temperature. **(E)** Mean salinity. **(F)** Morphosedimentary map showing the location of the main depositional and erosive features and vectors of the mean velocity current.

plastered drift. At the shelf edge and at the lower slope bottom currents flow northwards along slope, and thus presenting a higher meridional (N-S) than zonal (E-W) component of the velocity (Fig. 5.9). On the contrary, on the plastered drift bottom currents show mainly an across slope direction: west-northwestwards in the middle slope and southeastwards in the upper slope (Fig.5.9).

In the lower slope, bottom currents generated moats, these incisions are oriented in plan view with an angle of about 10° at the left of the bathymetric contours. The moats mark the limit between the plastered drift and the separated mounded drift located at the foot of the slope (Fig. 5.9F). North of the plastered drift, the separated mounded drift is separated from the shelf by an abraded surface, a zone almost devoid of Plio-Quaternary sediment (Fig. 5.9F). The model shows that this area is at present under the influence of weak currents, with mean velocities of 5-6 $cm{\cdot}s^{-1}$ in winter and 3-4 $cm{\cdot}s^{-1}$ in summer, and P90 BSS of 0.02 $N{\cdot}m^{-2}$ in winter and 0.01 $N{\cdot}m^{-2}$ in summer (Figs. 5.6, 5.8, 5.9). The modelled bottom currents are consistent with the presence in this area of a thin layer of Holocene muddy sediment, deposited directly on the Messinian surface (Fig. 5.8). Therefore, the present-day currents in this area are low but this zone was often under erosive conditions in the past.

The area with the strongest bottom currents during winter at the shelf and shelf edge is located off the Pianosa Island, with mean velocities comprised between 10 and 20 $cm{\cdot}s^{-1}$ and P90 BSS between 0.1 and 0.3 $N{\cdot}m^{-2}$ (Fig. 5.11). According to Shields (in Soulsby, 1997) the critical shear stress for erosion of fine sand is 0.1 $N{\cdot}m^{-2}$, so this area would be eroded during winter according to the model results. This erosion could explain the absence of a shelf edge prism off the Pianosa Island and also the presence of gullies on the upper slope. The gullies could be formed when the eroded sands of the shelf edge prism fall downslope in a zone with steep slope gradients, triggering small scale gravity flows and generating incisions on the slope.

Further north, between the Pianosa Island and the Elba Canyon, the drift morphology changes and the slope is dominated by multicrested drifts that are separated from the shelf edge by an eroded zone (Fig. 5.12). The crests have variable orientations, to the south there

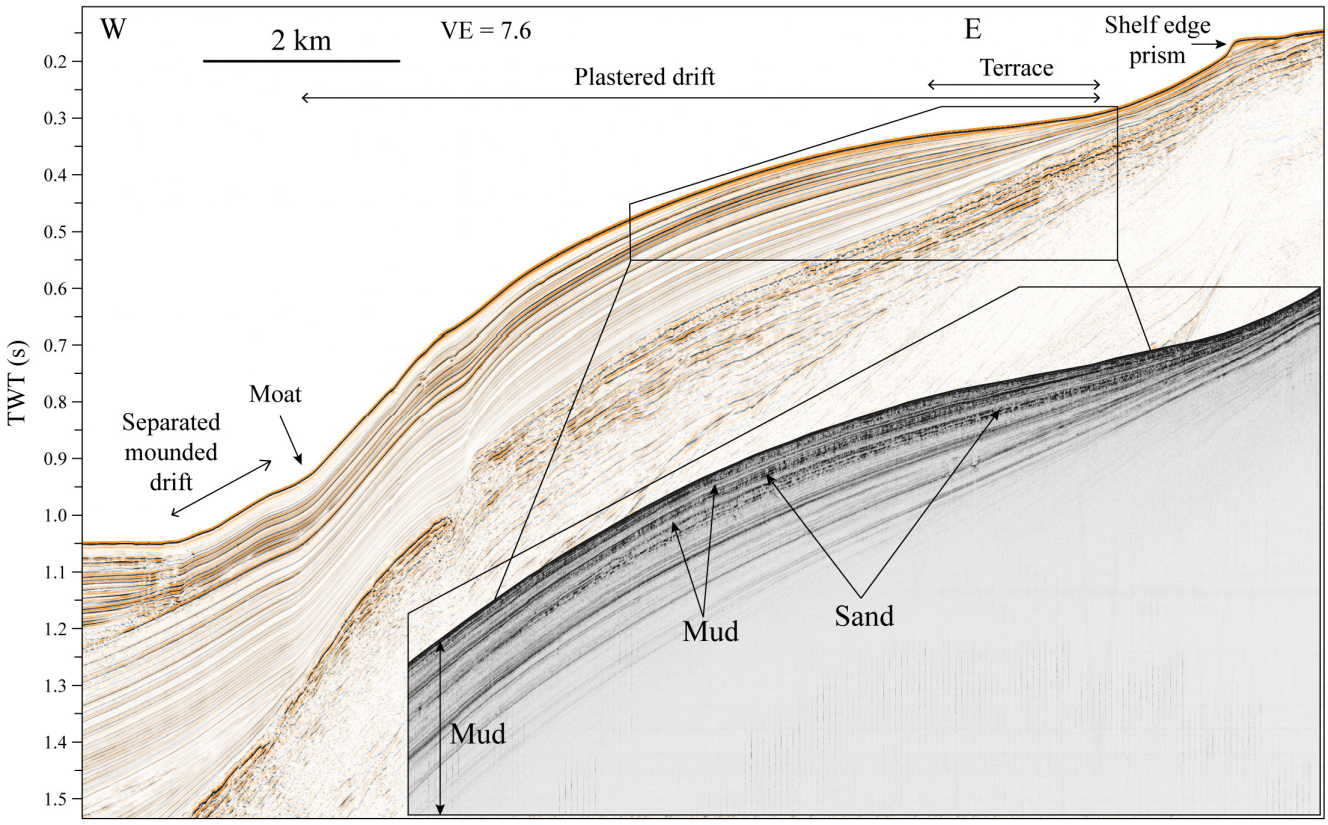

Fig. 5.10. PSM2-HR-068 multi-channel high resolution mini GI gun seismic reflection profile and PSM2-CH-068 SBP profile showing a plastered drift characterised by sandy material in the upper part and muddy sediment in the lower part.

is a single crest with NE orientation, while to the north the crests are smaller, multiple and parallel, presenting a NW orientation. The moats that separate these crests have an NW orientation and form an angle of about 10° with the bathymetric contours. The variable crest orientation can be explained with the circulation pattern near the seafloor during winter. In the central part of the basin there is a cyclonic gyre that affects the lower slope and forms the crest with the NE orientation (Fig. 5.12). The alongslope currents flowing towards the north at 500-700 m w.d. constrain the NE crest in its eastern part. Therefore, the drift crest with a NE orientation is the result of the enhanced sediment deposition in a zone of lower currents between a cyclonic gyre and alongslope currents (Fig. 5.12). The multicrested drifts with a NW orientation are related to the alongslope bottom currents. In the upper slope, where geophysical data show a zone of erosion, the

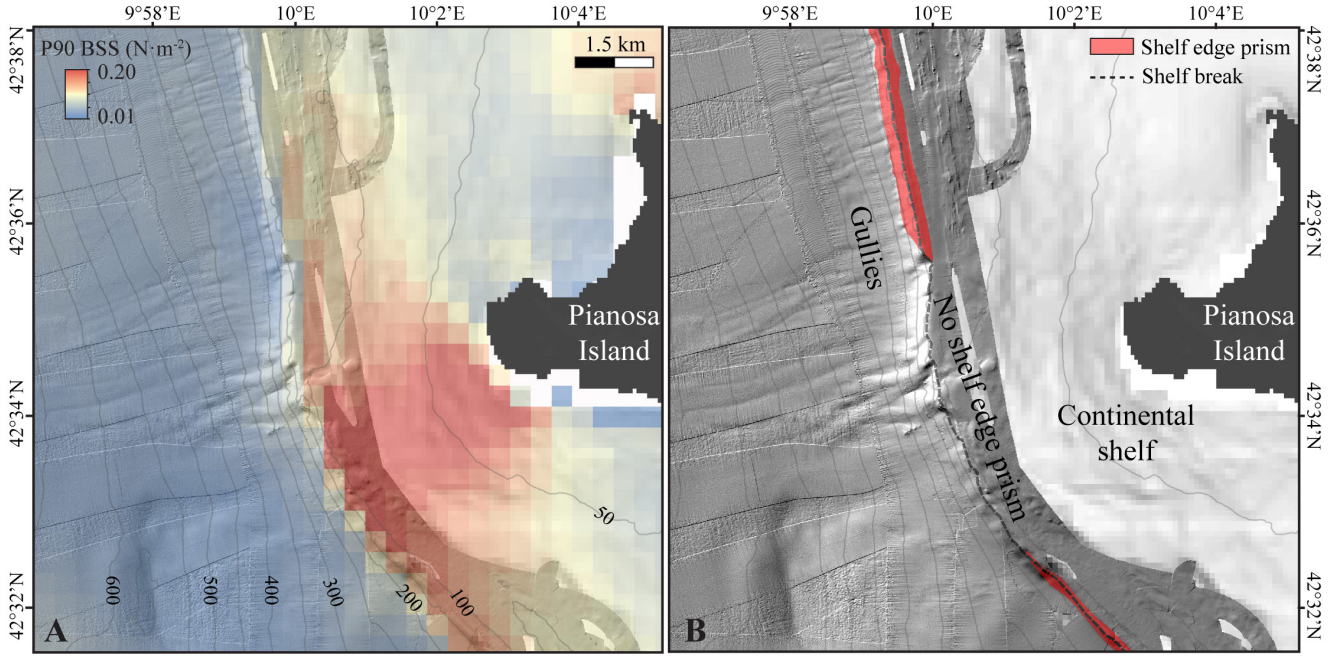

Fig. 5.11. Zoom on the northern part of the Pianosa Ridge showing the results of the 400 m zoom of the MENOR model during March 2013: **(A)** 90th percentile of the BSS. **(B)** Shaded image of the seafloor showing the presence of gullies in the upper slope related to a zone of fast bottom currents on the continental shelf and an eroded shelf edge prism.

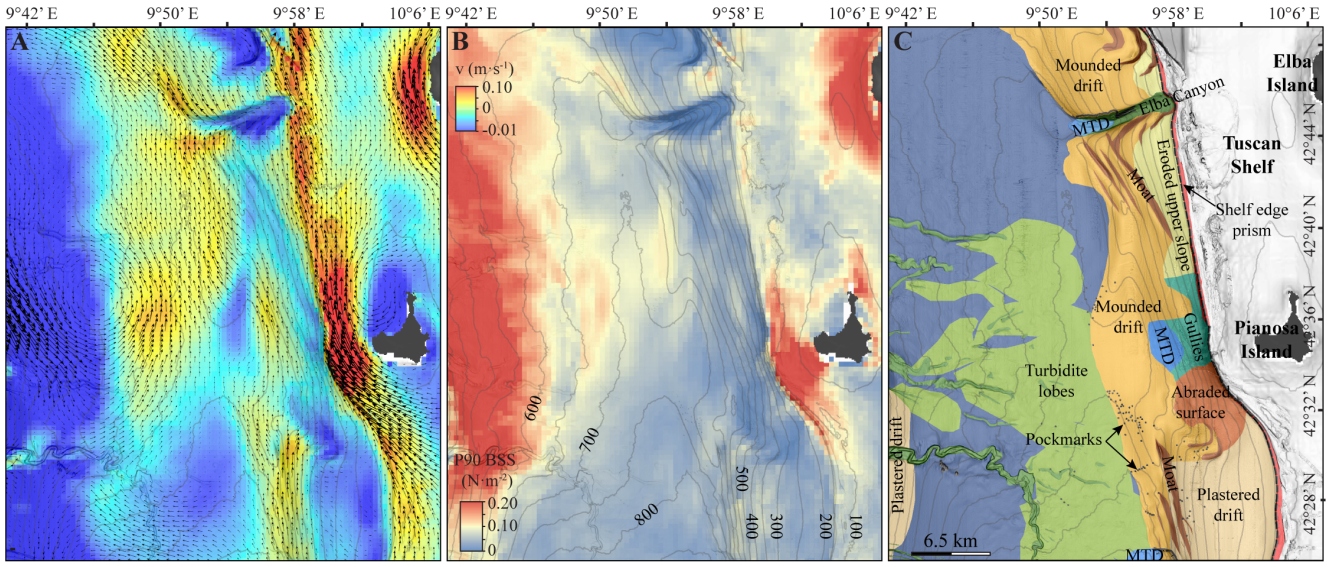

Fig. 5.12. Zoom on the northern part of the Pianosa Ridge showing the results of the 400 m zoom of the MENOR model during March 2013: **(A)** Meridional component of the mean velocity and vectors of the mean velocity current. **(B)** 90th percentile of the BSS. **(C)** Morphosedimentary map showing the location of the main depositional and erosive features.

model provides fast currents during the winter of 7-10 cm·s^{-1} and P90 BSS of 0.05-0.1 N·m^{-2} (Fig. 5.12). Taking into account that the critical shear stress for erosion of unconsolidated mud usually ranges between 0.02 and 0.05 N·m^{-2} (Schaaff et al., 2002), the mud could be eroded in this zone. This is in coherency with the high sand content in the sediment at the present seafloor (up to 80% of sand; Fig. 5.6B).

North of the Elba canyon the foot of the slope presents high slope gradients and an abrupt transition to

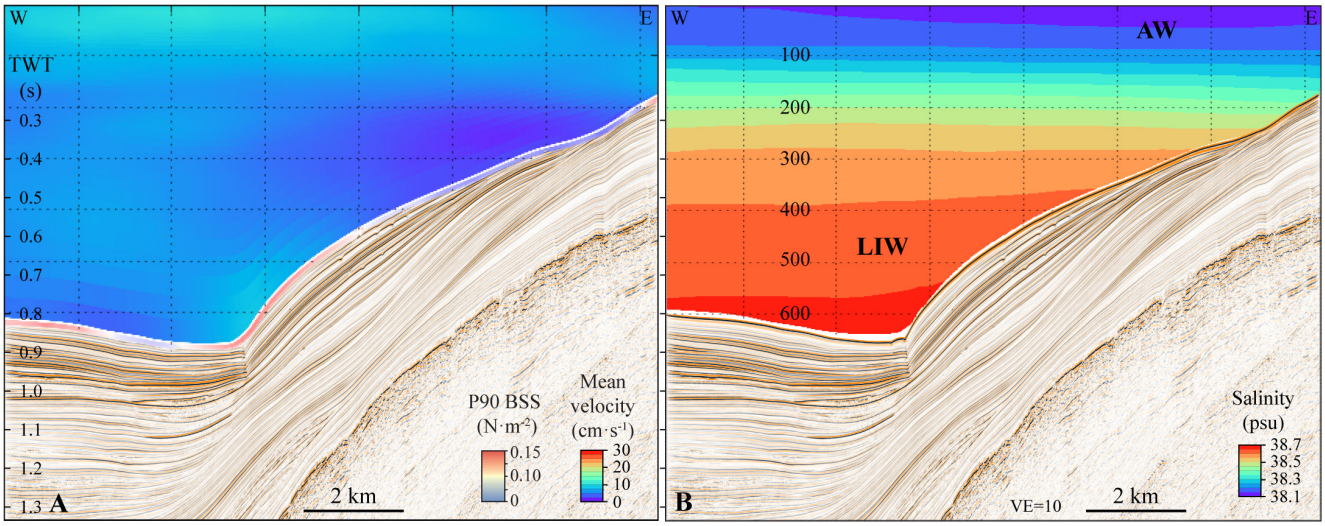

Fig. 5.13. Multi-channel high resolution seismic reflection profile PSM2-HR-043 coupled with a transect calculated with the 400 m zoom of the MENOR model during winter 2013 showing: **(A)** Mean velocity and 90th percentile of the BSS. **(B)** Salinity. Water depth in meters is shown in B.

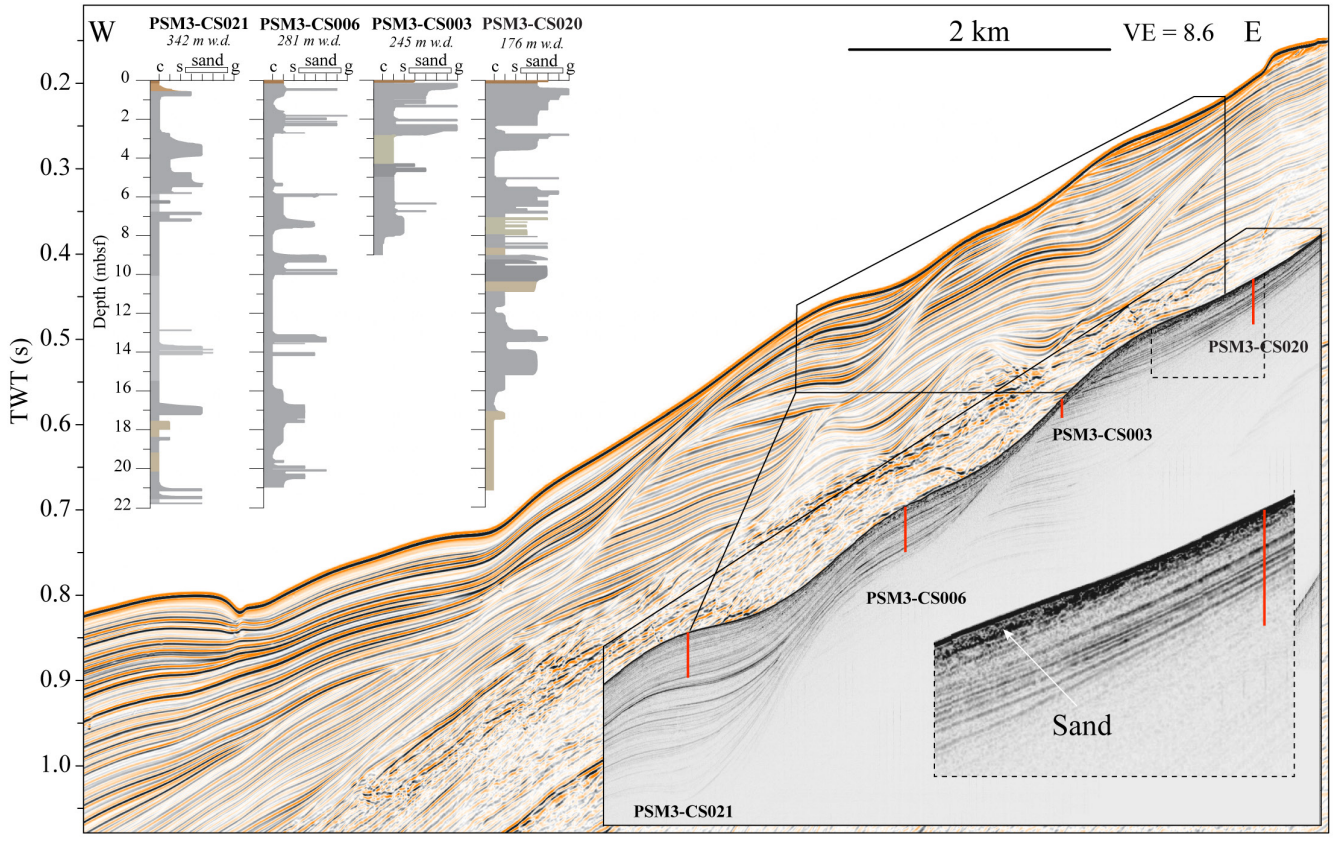

Fig. 5.14. PSM2-HR-054 multi-channel high resolution mini GI gun and PSM2-CH-054 SBP seismic reflection profiles showing muticrested mounded drifts, sampled by 4 Calypso piston cores. Note that the sediment is coarser in the upper slope.

the deepest part of the basin (Figs. 5.12 and 5.13). It corresponds to an area where the model shows strong bottom currents during winter with mean velocities of 12 cm·s^{-1} and P90 BSS of 0.10-0.12 N·m^{-2} (Figs. 5.12 and 5.13). This BSS would be enough to erode unconsolidated mud (and even fine sand), explaining the observed erosion at the foot of the slope.

Faster bottom currents at the shelf edge and at the upper slope favour the transport of sandy material from the shelf to the upper slope and the winnowing of fine material from the latter. Therefore, in the zone of the multicrested drifts, the grain size and the abundance of sediment layers with coarse material decrease with depth (Figs. 5.6B and 5.14). The sandy sediment is characterised by particular acoustic seismic Sub-Bottom Profiler (SBP) facies that are chaotic and granular (Fig. 5.14). The same seismic facies can be found in the upper and middle part of the plastered drift. The terrace located in the upper part of the plastered drift is mainly composed of sand, while in the middle part the sandy layers are interbedded with muddy sediment and in the lower part the plastered drift is mainly composed of mud (Figs. 5.6B and 5.10).

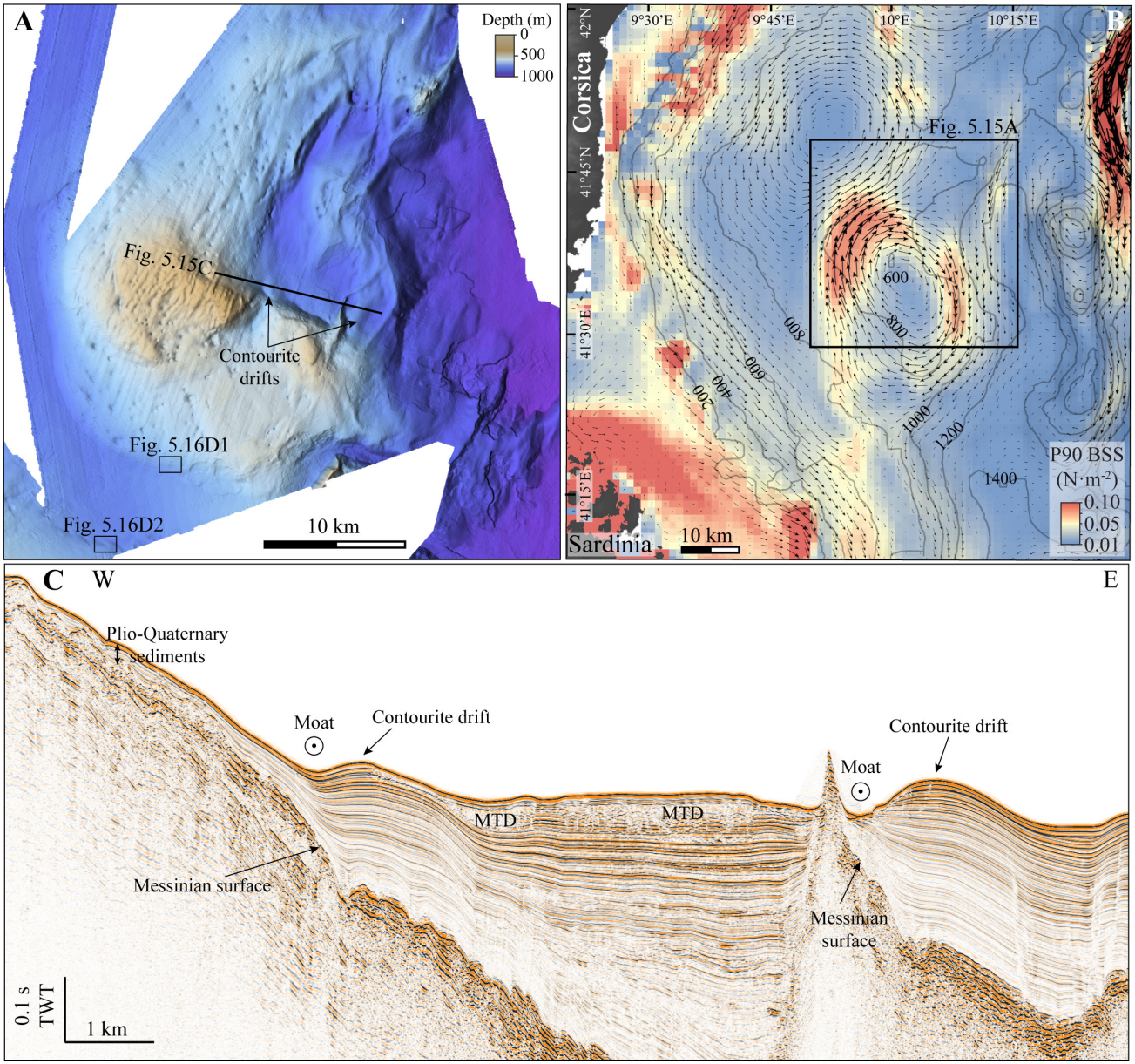

Fig. 5.15. **(A)** Multibeam bathymetry of a seamount in the Northern Tyrrhenian Sea with associated contourite drifts. **(B)** 90th percentile of the BSS and vectors of the mean velocity during winter 2013 from the MENOR model. **(C)** Multi-channel high resolution seismic reflection profile showing two contourite drifts.

In the Northern Tyrrhenian Sea, contourites are also found related to a submarine seamount located at the south of the Corsica Trough, off southeast Corsica (Fig. 5.15). The contourite drifts are situated at the east of the seamount (Fig. 5.15A), where the results of the model show southwards bottom currents. A clockwise bottom circulation is present around the seamount, that can be intense in winter, reaching up to 0.05-0.1 $N{\cdot}m^{-2}$ (Fig. 5.15B) and resulting in a low sedimentation on the seamount of only 20-50 m during the last 5.3 million years (Fig. 5.15C).

5.3.4. Pockmarks as bottom-current indicators

The effect of bottom currents on the surface morphology of pockmarks has been observed in the Ligurian margin and in the Northern Tyrrhenian Sea. The pockmarks affected by bottom currents show an elongated shape (Fig. 5.16). They usually present a steep flank upstream and a flat eroded flank downstream. A mounded sediment deposit, separated from the pockmark flanks by incisions, can be observed in the central part of the pockmarks in the Ligurian margin and in the western flank of the Corsica Trough (Fig. 5.15A,B). The deformation, elongation and erosion in all the observed pockmarks is consistent with the current direction provided by the hydrodynamic model: bottom currents flow westwards along the slope along the Ligurian margin (Fig. 5.4), southwards along the western flank of the Corsica Trough (Fig. 5.6A), and towards the northwest in the zone of pockmarks on the eastern flank of the Pianosa Ridge (Fig. 5.6A) and in the southern part of a seamount in the Northern Tyrrhenian Sea (Fig. 5.15A).

5.4. Discussion

5.4.1. The role of currents in sediment redistribution

Contourites along the Pianosa Ridge are a good case to study sediment transport and sediment redistribution controlled by currents because the Pianosa Ridge is a starved slope, with little direct sediment supply, located offshore the Tuscan continental shelf. This shelf separates the Corsica Trough from the Italian mainland and trapps most of the sediment transported by the Italian rivers (Roveri et al., 2002). In contrast, the morphology and sedimentary structure of the western flank of the Corsica Trough is dominated by turbiditic processes (Gervais et al., 2006) and presents mainly a prograding structure (Figs. 5.6, 5.7, 5.8). The sandy lobes of the turbidites are deposited in the central part of the basin and in the lower western slope during sea level low-stands (Figs. 5.7, 5.8, 5.12; Deptuck et al., 2008). As a consequence of this asymmetric arrangement of sediment transport pathways in the Corsica Trough, there is no possible confusion between contourtitic and turbiditic deposits at the Pianosa Ridge (Miramontes et al., 2016b). Therefore, most sediment deposited along the Pianosa Ridge that forms the contourites probably comes from the Corsica Island, and the fine sediment transported in suspension by the turbiditic currents may be retransported by the oceanic circulation to other zones of the basin. At present, the turbidite system is not active and the flux of terrigenous particles to the basin is thus lower than during sea level low-stands (Calvès et al., 2013; Toucanne et al., 2015).

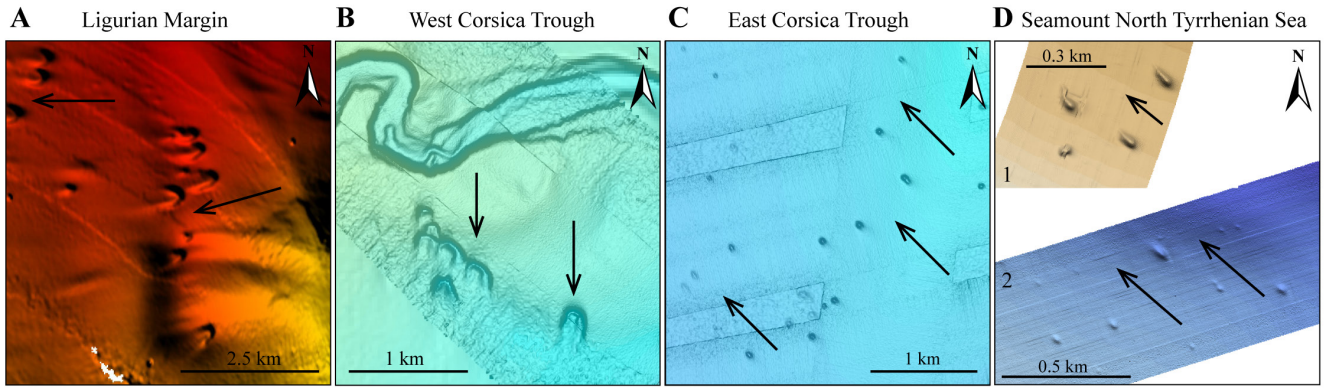

Fig. 5.16. Multibeam bathymetry of elongated pockmarks due to bottom currents in **(A)** the Ligurian Margin, **(B)** in the western flank of the Corsica Trough, **(C)** in the eastern flank of the Corsica Trough and (D) at the south of the seamount in the Northern Tyrrhenian Sea.

The MENOR hydrodynamic model shows the presence of two cyclonic gyres in the Corsica Trough that affect the whole water column, one is located between the latitudes 42°30'N and 42°50'N, and the other one is located between 42°N and 42°30'N (Fig. 5.17). These cyclonic gyres could transport the fine sediment in suspension from the western flank to the eastern flank of the Corsica Trough, that could be finally deposited on the contourites of the Pianosa Ridge.

A comparable setting to the Corsica Trough is the Gulf of Valencia, where the geostrophic circulation is commonly characterised by eddies (Pinot et al., 2002; Ribó et al., 2013; 2015). Ribó et al. (2013) found a continuous nepheloid layer at the surface and internal nepheloid layers coinciding with the base of the LIW, the latter mainly composed of terrigenous suspended particles. By analogy, a similar situation could be expected in the Corsica Trough, with suspended particles in a superficial nepheloid layer being transported by

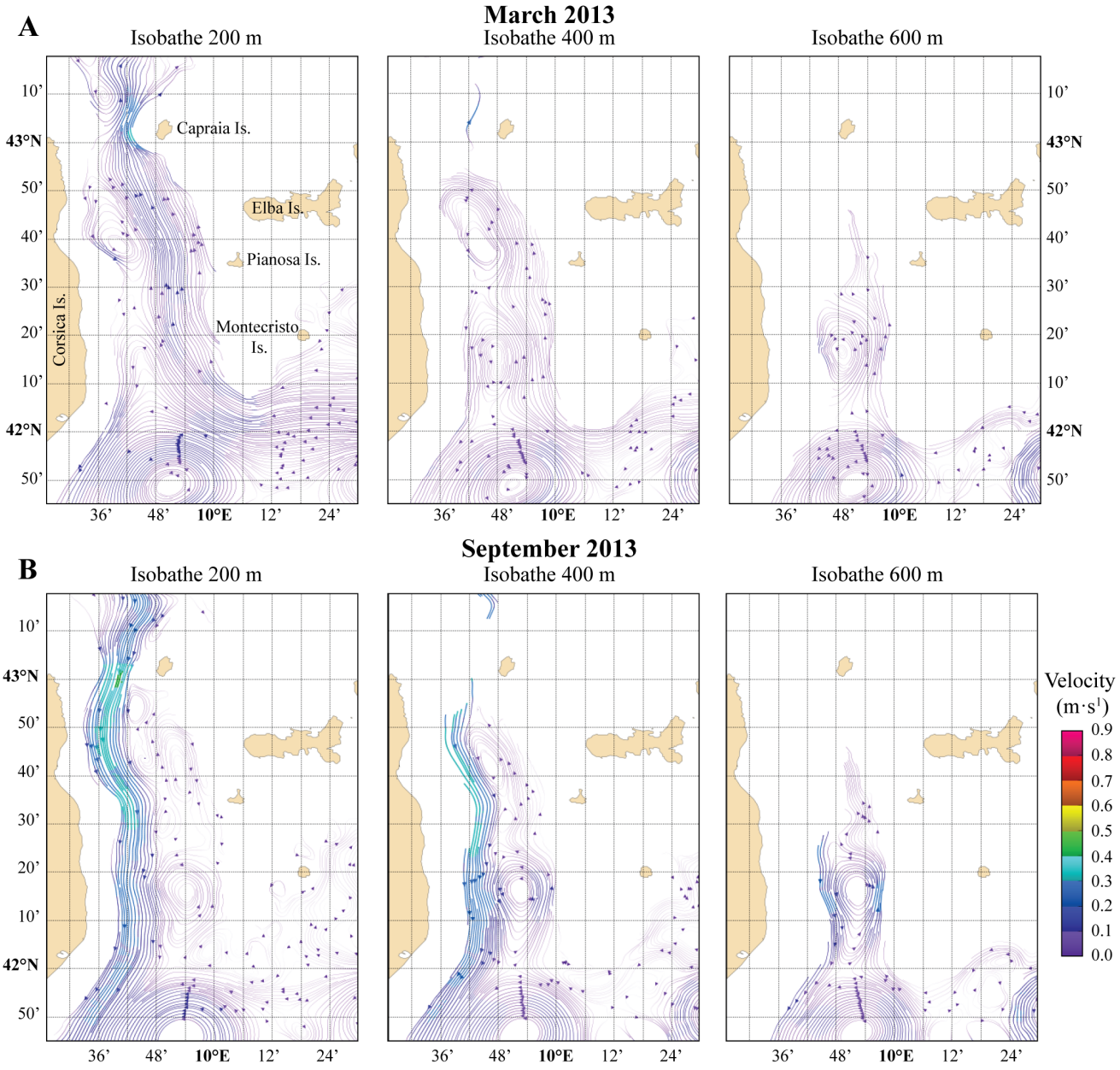

Fig. 5.17. Stream lines of the mean currents at three different depths: 200, 400 and 600 m calculated with the 400 m zoom of the MENOR model during **(A)** March 2013 and **(B)** September 2013. Note the presence of cyclonic gyres in the basin at all depths and seasons.

the gyres to the Pianosa Ridge and being finally deposited on the upper slope, forming the plastered drift (Figs. 5.9 and 5.10). Another nepheloid layer, associated to the deeper pycnocline at the base of the LIW (Fig. 5.7 and 5.8), could be deposited as a separated mounded drift at the foot of the slope (Figs. 5.9 and 5.10).

5.4.2. Seasonal variability in circulation

The results of the model show that all the zones of erosion (such as moats and eroded continental slopes identified from geophysical data) present P90 BSS higher than the critical shear stress of erosion of unconsolidated mud (above 0.05 N·m^{-2}; Schaaff et al., 2002), and in some cases even higher than the critical shear stress of erosion of fine sand (above 0.1 N·m^{-2}; according to Shields (in Soulsby, 1997)). In contrast, during summer these areas present much lower P90 BSS and they may not be under erosive conditions in some cases (Table 5.1; Fig. 5.18). Therefore, the eroded features observed in the geophysical data may be the result of erosion due to faster bottom currents during the winter season. Although sediments may be deposited in summer in these areas, they are eroded in winter, resulting in a net erosion throughout the year.

The Minorca slope is under strong currents that can even erode sand during the whole year (Table 5.1; Figs.

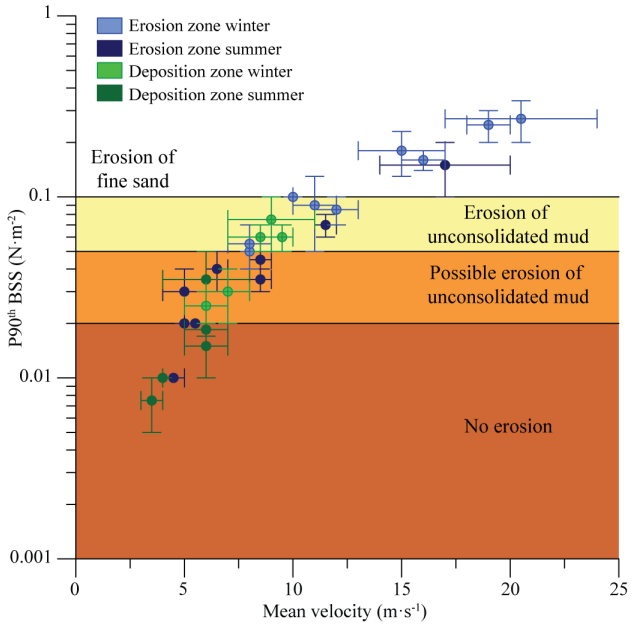

Fig. 5.18. Plot of the mean velocity and 90th percentile of the Bottom Shear Stress (BSS) calculated with the MENOR model for the period of winter and summer 2013 in the zones previously classified according the geophysical data as zones of erosion or sediment deposition, detailed in Table 5.1. The critical shear stress for erosion are based on a critical BSS for unconsolidated mud ranging between 0.02 and 0.05 N·m^{-2} (Schaaff et al., 2002) and a critical BSS for fine sand of 0.1 N·m^{-2} according to Shields (in Soulsby, 1997).

Table 5.1. Mean velocity and 90th percentile of the Bottom Shear Stress (P90 BSS) computed during winter and summer 2013 in the three study areas: (1) Catalan Sea/Minorca Basin; (2) Ligurian Sea; (3) Northern Tyrrhenian Sea/Corsica Trough. The areas classified as depositional environments according to geophysical data are in orange colour, while the erosive environments are in yellow colour.

Zone	Environment	Mean velocity winter (cm·s^{-1})	P90 BSS winter (N·m^{-2})	Mean velocity summer (cm·s^{-1})	P90 BSS summer (N·m^{-2})
1	Minorca moat	10	0.10	8-9	0.03-0.06
1	Minorca slope	17-24	0.20-0.34	14-20	0.10-0.20
1	Minorca drift	5-7	0.02-0.03	6-7	0.01-0.02
1	Catalan moat	11-13	0.07-0.1	5-6	0.02
1	Catalan slope	18-20	0.20-0.30	8-9	0.03-0.04
1	Catalan drift	5-7	0.02-0.03	3-4	0.005-0.01
2	Portofino moat	15-17	0.14-0.18	11-12	0.06-0.08
2	Portofino drift	9-10	0.05-0.07	5-7	0.017-0.02
3	Pianosa moats	8-10	0.05	5	0.02-0.04
3	Shelf edge-plastered drift	10-12	0.05-0.13	4	0.01
3	Shelf edge-offshore Pianosa	13-17	0.13-0.23	4-6	0.02-0.04
3	Plastered drift	6-8	0.03-0.05	4	0.01
3	Separated mounded drift	7-10	0.05-0.07	5-7	0.02-0.03
3	Multicrested drift	7-11	0.05-0.10	4-8	0.02-0.05
3	Upper slope multicrested drift	7-9	0.04-0.07	4-5	0.01
3	Foot of the slope north Elba Canyon	10	0.10	6-7	0.03-0.05

5.2, 5.3, 5.18), coherent with a slope characterised by the bedrock outcrop at the seafloor (Fig. 5.3). The zones of deposition are always present in zones of lower current velocity, but the unconsolidated mud can be also eroded during winter enhanced bottom circulation. Probably, the sediment follows multiple cycles of deposition resuspension until the particles are definitively incorporated into the sediment record.

The studied contourites in the NW Mediterranean Sea are Pliocene-Quaternary deposits that have not changed their position since their onset. This observation suggests that the direction and location of bottom currents have not significantly changed during the time of formation of these sedimentary bodies. Although the general circulation pattern in the NW Mediterrean Sea may not have dramatically changed since the Pliocene, the intensity of the bottom currents did change cyclically. The circulation near the seafloor in the Mediterranean Sea is known to be more intense during sea level low-stands than during sea level high-stands (Cacho et al., 2000; Toucanne et al., 2012; Mintoʻo et al., 2015) and to have affected the contourite depositional systems by having induced erosion and the formation of coarser deposits (Miramontes et al., 2016b). Modelling past oceanic circulation is very difficult because of the lack of valid boundary conditions. Therefore, we modelled the oceanic circulation during the winter and the summer seasons of 2013 as two representations of intense (winter) and weak (summer) oceanic circulation. Therefore, as a first approximation we could argue that the circulation pattern during sea level low-stands could be similar to the present-day winter season and thus the moats would be continuously under erosion during sea level low-stands.

5.4.3. New conceptual model of contourite drift formation

Three main type of margins can develop in zones where the whole water column flows in the same direction, depending on the amount of sediment supply and on the distribution of the bottom-current velocities (Fig. 5.19). We identified: 1) separated mounded drifts; 2) even (regular) seafloor; 3) plastered drifts and separated mounded drifts.

A separated mounded drift develops at the foot of the slope when bottom currents are strong on the slope and they become weaker basinwards, allowing the formation of a drift. Enhanced bottom currents at the foot of the slope generate a moat and may induce the formation of a mounded shape, such as in the Minorca Basin (Fig. 5.3). This sediment configuration is characteristic of starved margins with little direct sediment supply. Moreover, strong bottom currents on the slope can easily erode and prevent sediment deposition in this area (Fig. 5.19A). Contourites formed at the seamount of the Northern Tyrrhenian Sea are developed in similar conditions; they are related to escarpments with little sediment accumulation on the slope and the drifts grow in a zone of lower bottom currents at the foot of the slope (Fig. 5.15). These drifts have a small size compared to the Minorca drift because they are related to obstacles and they are confined in the irregularities of the seafloor, while in the case of Minorca the contourites develop all along the margin.

In a margin with direct sediment supply and strong bottom currents across all the slope, the resulting morphology is a straight regular seafloor mainly with a prograding structure, such as the western flank of the Corsica Trough (Figs. 5.7 and 5.8). A similar configuration would be generated if the bottom currents would be weak across all the slope. The most important factor in the generation of mounded sedimentary morphologies is the heterogeneous distribution of bottom currents. If bottom currents are homogeneous across the slope, then the sediment will be transported in a similar way in all the zones of the slope and the margin morphology will be mainly controlled by the location and quantity of the sediment supply (Fig. 5.19B).

Contourites develop more clearly on starved margins, where no canyons and no downslope gravity flows can destroy the sediment morphologies generated by bottom currents. Plastered drifts are typically convex-shaped sedimentary bodies that have an oval shape in plan view, like in the Pianosa Ridge (Figs. 5.9 and 5.10). They develop in a zone of weak bottom currents confined in between two zones of faster bottom currents in the upper and in the lower slope, resulting in the formation of a terrace on the top and a moat on the bottom (Fig. 5.19C). Moreover, the direction of bottom currents on the plastered drift is mainly across slope, favouring the sediment accumulation in this area. Related to a zone of slower bottom currents at the foot of the slope, a separated mounded drift can develop in a similar way to case "1" (Fig. 5.19A).

The formation of plastered drifts can be explained by the distribution of geostrophic currents on the slope.

If pycnoclines are located on the terrace, the action of internal waves could enhance sediment erosion on the terrace, at the top of the plastered drift (Pomar et al., 2013, Shamugham, 2013, Ercilla et al., 2016). However, internal waves are probably not at the origin of the terrace formation and the geostrophic currents are likely the main factor controlling the general morphology of the margin.

5.5. Conclusions

The results of the MARS3D hydrodynamic model in the MENOR configuration are consistent with the morphology of contourites obseved in 3 areas of the Northwestern Mediterranean Sea: the Catalan Sea, the Ligurian Sea and the Northern Tyrrhenian Sea. By coupling the model results of winter 2013 and summer 2013 with the geophysical and sedimentological data, we could deduce that the extreme events of more intense circulation control the formation of moats and erosive features on the seafloor. During summer, fine-grained sediment could be deposited in some of these areas, but the fast winter currents would generate erosion, resulting in an annual net erosion.

The morphology of the margins can be intensely controlled by geostrophic currents, especially in starved margins where the sediment is transported alongslope by the oceanic circulation. The presence of gyres in confined basins with asymmetric sediment input causes the redistribution of sediment from the margin with a direct sediment supply to the opposite starved margin.

The development of mounded sedimentary morphologies is favoured by heterogeneous bottom current distributions. Plastered drifts are formed in zones of relative low current velocity, mainly with an across-slope direction, confined between zones of high alongslope current velocity. These morphologies are commonly observed in starved margins not affected by frequent downslope gravity flows. Separated mounded drifts are formed in zones of low bottom currents at the foot of the slope associated with fast currents on the slope. In contrast, when bottom currents are homogeneous across the margin (either fast or slow), no mounded shapes can develop and the seafloor morphology is flat.

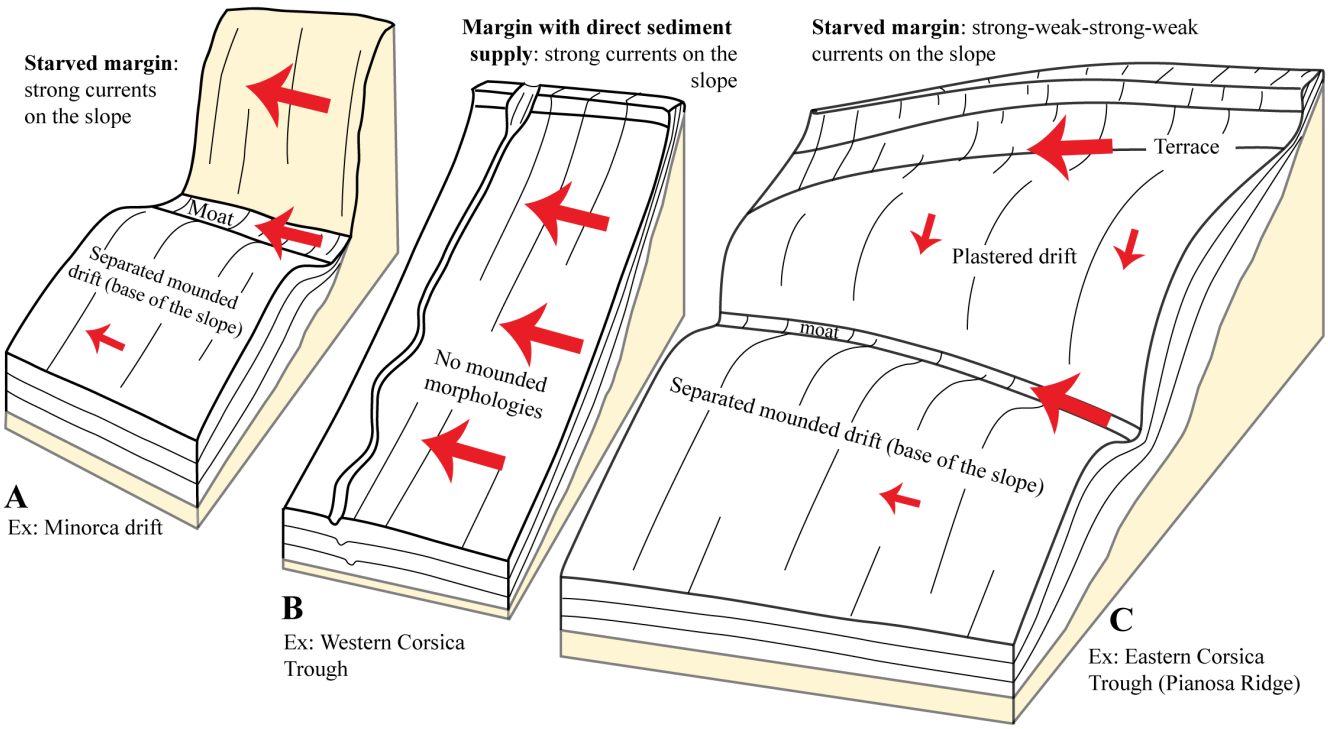

Fig. 5.19. 3D sketches showing three different types of margins: **(A)** a starved margin with an eroded continental slope and a separated mounded drift at the foot of the slope; **(B)** a margin with direct sediment supply and a homogeneous bottom-current distribution; **(C)** a starved margin with heterogeneous bottom current distribution, resulting in the formation of a plastered drift on the slope and a separated mounded drift at the foot of the slope. The arrows indicate bottom current direction and intensity according to their size.

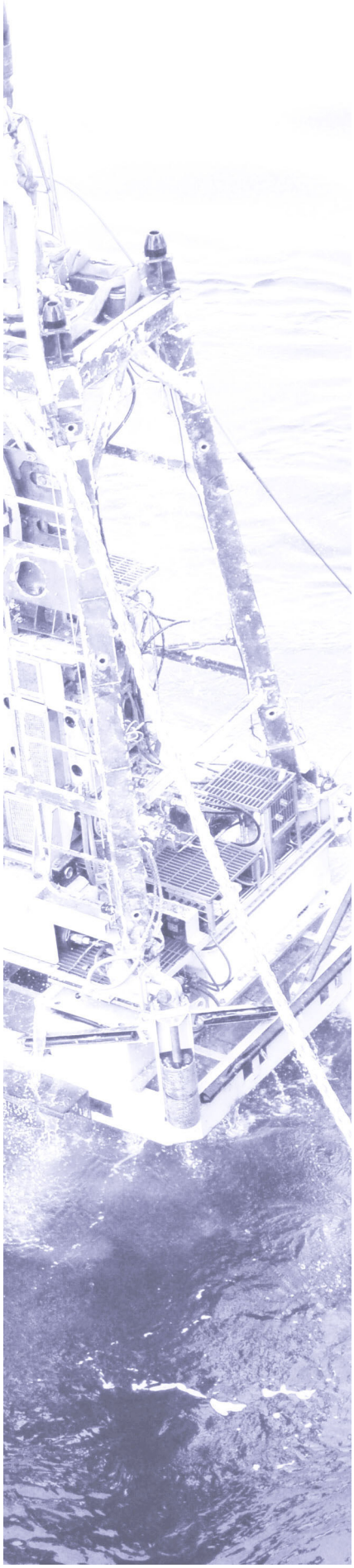

CHAPTER 6. Morphological control of slope instability in contourites: A geotechnical approach

Contourites are sediment deposits related to bottom currents that are commonly formed along continental margins. They are often affected by slope failure, but little information is available about whether they have special properties that make them more susceptible to slope instability. In this study we did a comparison of the sedimentological and geotechnical properties of contouritic and hemipelagic sediments in the Corsica Trough (Northern Tyrrhenian Sea) using a complete data set composed of Calypso piston cores, boreholes, cone penetration tests with pore pressure measurements and in situ P-wave velocity measurements.

Sedimentological and geotechnical analyses show some differences between the properties of contourites and hemipelagites. The plastered drift presents finer material, lower density and lower undrained shear strength than hemipelagites. Contourites have a higher compressibility than hemipelagites but a similar permeability. Mounded drifts are a type of contourites that present poorly sorted sandy layers. Liquefaction potential assessment using CPTU data show that these layers may not liquefy under seismic loading. Although sedimentation rates can be high in contourites (up to 1.15 $m{\cdot}kyr^{-1}$), 1D consolidation modelling results show that sedimentation alone cannot generate enough overpressure to influence slope instability in the Corsica Trough. After a geomorphological and a slope stability analysis, we found that the main factor controlling the location of submarine landslides in a contouritic environment is the morphology of the drifts. Plastered drifts are convex-shaped deposits formed on continental slopes that present steep slopes in the lower part, where the factor of safety and the stability is the lowest. Moreover, erosion is common at the foot of the plastered drifts and it may trigger a submarine landslide by undercutting the slope.

CHAPITRE 6. Contrôle morphologique de l'instabilité de pente en contourites : Une approche géotechnique

Les contourites sont des dépôts sédimentaires formés par les courants de fond le long des marges continentales. Même si elles sont fréquemment affectées par des glissements sous-marins, il n'a pas encore été démontré que les contourites aient des propriétés particulières qui les rendent plus susceptibles d'être déstabilisées. Dans cette étude, nous comparons les propriétés sédimentologiques et géotechniques des sédiments contouritiques et hémipélagiques dans le Canal de Corse (Mer Tyrrhénienne septentrionale) à l'aide d'un jeu de données complet composé de prélèvements sédimentaires issus de carottes de type Calypso et des forages et des mesures in situ de pression interstitielle et de vitesse des ondes P obtenues grâce au pénétromètre PENFELD.

Les analyses sédimentologiques et géotechniques montrent des différences entre les propriétés des contourites vaseuses et des sédiments hémipélagiques. Les « plastered drifts » présentent du matériel plus fin avec une densité plus basse et une résistance au cisaillement plus faible que les sédiments hémipélagiques. Les contourites ont une compressibilité plus forte que les hémipélagites, mais avec une perméabilité identique. Les « mounded drifts » présentent des couches sableuses mal triées et l'estimation du potentiel de liquéfaction à partir de mesures de CPTU montre que ces niveaux grossiers ne peuvent pas se liquéfier sous une charge sismique. Même si les taux de sédimentation dans les contourites peuvent être importants (jusqu'à 1,15 $m \cdot ka^{-1}$), les résultats de la modélisation 1D de consolidation montrent que la sédimentation seule ne peut pas engendrer de surpressions suffisantes pour déclencher les instabilités de pente dans ce secteur. Suite à une analyse géomorphologique et de stabilité de pente, nous démontrons que le facteur principal qui contrôle la localisation des glissements sous-marins au sein de ce complexe contouritique est la morphologie des dépôts contouritiques. Les «plastered drifts » ont une morphologie convexe avec des gradients de pente plus forts dans la partie avale, qui combinée à une érosion fréquente en pied de pente, en font des structures plus sujettes à l'instabilité.

CAPíTULO 6. Control morfológico de la inestabilidad de talud en contornitas: Un enfoque geotécnico

Las contornitas son depósitos sedimentarios creados bajo la acción de las corrientes de fondo, comunes a lo largo de los márgenes continentales. Aunque suelen estar afectadas por deslizamientos submarinos, existe poca información acerca de si las contornitas tienen propiedades particulares que las hacen más susceptibles a la inestabilidad de talud. En este estudio hicimos una comparación de las propiedades sedimentológicas y geotécnicas de sedimentos contorníticos y hemipelágicos en el Canal de Córcega (Mar Tirreno Septentrional) usando un conjunto de datos completo formado por testigos de pistón Calypso, perforaciones sedimentarias, penetrómetros con medidas de presión intersticial y medidas in situ de velocidad de las ondas P.

Los análisis sedimentológicos y geotécnicos muestran algunas diferencias entre las propiedades de las contouritas y del sedimento hemipelágico. El "plastered drift" presenta material más fino, una densidad más baja y una resistencia a la cizalla más baja que el sedimento hemipelágico. Las contornitas tienen una compresibilidad más alta que el sedimento hemipelágico pero la permeabilidad es similar. Los depósitos monticulares contorníticos son un tipo de contornitas que continenen abundantes capas de arena mal seleccionadas. La estimación del potencial de licuefacción a partir de medidas de CPTU muestra que estas capas de arena no se licuefactan bajo carga sísmica. Aunque las tasas de sedimentación pueden ser altas en las contornitas (hasta 1,15 $m \cdot ka^{-1}$), los resultados de la modelización 1D de la consolidación muestran que la sedimentación por sí sola no puede generar suficiente sobrepresión para influir en la inestabilidad de talud en este sector. Tras un análisis geomorfológico y de estabilidad de talud, descubrimos que el principal factor que controla la localización de los deslizamientos submarinos en los ambientes contorníticos es la morfología de los depósitos. Los "plastered drifts" son depósitos contorníticos que se forman en taludes continentales y que tienen una morfología convexa con pendientes más altas en la parte baja, donde el factor de seguridad y la estabilidad son los más bajos. Además, la erosión al pie del "plastered drift" es común y puede desencadenar un deslizamiento submarino al socavar la parte baja del talud.

6.1. Introduction

Contourites are sediment deposits related to the interaction of bottom currents and seafloor morphology that are commonly formed along continental margins (Stow and Faugères, 2008). They are often affected by slope failure, but little information is available about whether they have particular properties that make them especially susceptible to slope instability. Bryn et al. (2005a) and Laberg et al. (2002) reported that the basal failure surfaces of the Storegga and the Trænadjupet Slides (offshore Norway) were located within contourite deposits. The fine-grained contourites offshore Norway were found to be weaker and more sensitive (with a post-peak strength loss) than the glacigenic sediments (Baeten et al., 2014; Laberg et al., 2016). Laberg and Camerlenghi (2008) suggested that muddy contourites often present good sorting and high moisture content, and they are thus weak.

Submarine landslides initiated in contourites have been identified worldwide in many different oceanic settings: (i) in the Mediterranean Sea: in the Alboran Sea (Ercilla et al., 2016), offshore Mallorca (Lüdmann et al., 2012), in the Gela Basin (Verdicchio and Trincardi, 2008), offshore Israel (Frey-Martínez et al., 2006); (ii) in the Atlantic: offshore Uruguay and Argentina (Krastel et al., 2011; Preu et al., 2013; Hernández-Molina et al., 2016), along the Svalbard margin (Vanneste et al., 2006), off the Shetland Islands (Wilson et al., 2004), as well as offshore Norway, where some of the largest submarine landslides in the world took place (Laberg et al., 2001; Laberg et al., 2005; Bryn et al., 2005a,b). Slope failures at the lower part of convex-shaped contourites (plastered drifts) were also observed in carbonate systems, such as along the slope of the Bahamas (Principaud et al., 2015; Tournadour et al., 2015). Most of the slope failures that affected plastered drifts have been identified in the Atlantic Ocean and in the Mediterranean Sea, probably because these areas have been the most extensively studied zones by the scientific community that is sensitive to contouritic processes.

Submarine landslides are common features along continental margins, both in contouritic environments (dominated by alongslope currents) and non-contouritic environments (dominated by vertical hemipelagic sedimentation or downslope turbiditic processes). It has never been shown if contouritic sediments have different geotechnical properties than hemipelagites that could result in a preferential formation of slope failures within contourites. Actually, muddy contourites and hemipelagites are difficult to differentiate only from a standard sedimentological analysis, since both types of sediments tend to be homogeneous, poorly bedded, badly sorted and highly bioturbated (Stow and Tabrez, 1998; Stow and Faugères, 2008). On seismic reflection and multibeam bathymetric data, contourites are often characterised by a mounded shape (Hernández-Molina et al., 2008). In this study, we consider as a contourite, the sediment bodies that clearly show a mounded shape induced by bottom currents. In the Corsica Trough (Northern Tyrrhenian Sea), contourites are present along the Pianosa Ridge and in the upper slope of the Corsican margin (Fig. 6.1). The seafloor with no mounded shape is classified as hemipelagite.

The aim of this study is to compare the geotechnical characteristics of contourite drifts and non-contouritic deposits of the same area in order to investigate whether

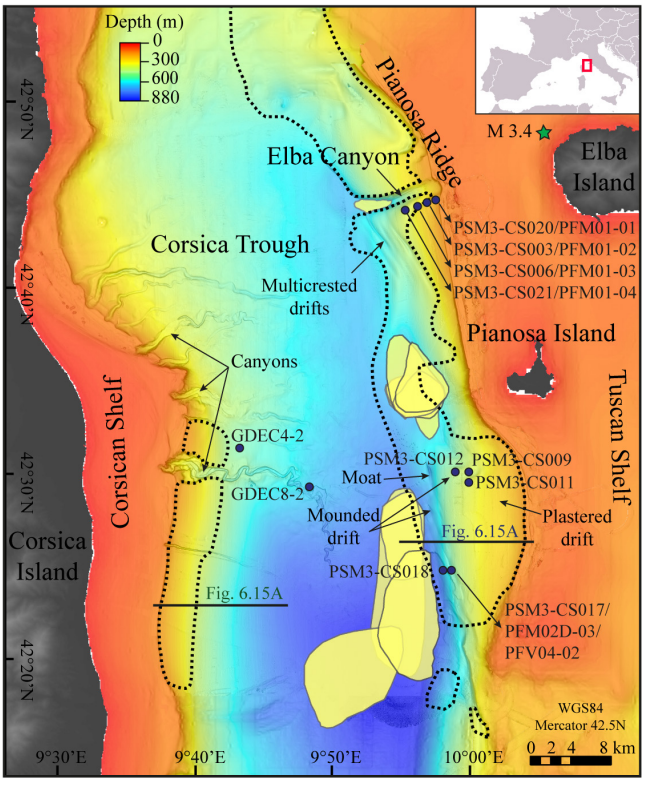

Fig. 6.1. Bathymetric map of the Corsica Trough with the location of contourites (outlined with dashed lines), mass transport deposits (represented with yellow polygons), Calypso piston cores, boreholes, CPTU measurements and in situ P-wave velocity measurements (blue dots). The green star shows the location of a 3.4 magnitude earthquake from the seismic record (RENASS catalogue).

contourites have intrinsic or inherited properties that make them susceptible to slope failure.

6.2. Regional setting

The Corsica Trough is a confined basin located in the Northern Tyrrhenian Sea, between Corsica and the Tuscan Shelf (Fig. 6.1). It is an asymmetric basin in terms of morphology and sediment processes. The eastern flank is formed by the Pianosa Ridge and has relative steep slopes that range between 3° and 10°, reaching 20° locally (Miramontes et al., 2016a). The Plio-Quaternary sedimentation along this flank is dominated by contouritic deposits (Marani et al., 1993; Roveri, 2002; Cattaneo et al., 2014; Miramontes et al., 2016b) and mass-wasting processes that resulted in the formation of 11 Mass Transport Depostis (MTDs), identified at the foot of the slope (Fig. 6.1; Miramontes et al., 2016a). South of the Pianosa Island, the continental slope is formed by a convex-shaped plastered drift. It is separated from a mounded drift by an incision (moat) located at the lower slope (Fig. 6.1; Miramontes et al., 2016b). The moat is a zone where faster bottom currents prevent sediment deposition and may also induce erosion. Offshore the Elba Island, south of the Elba Canyon, multicrested drifts are present on the continental slope. The crests of the drifts are parallel to each other and separated by moats. These drifts are oblique to the continental slope (Fig. 6.1; Miramontes et al., 2016b).

In contrast, the western flank of the basin has a gentle slope (mean values comprised between 2° and 3°) and its sediment is mainly composed of hemipelagites and turbidites (Gervais et al., 2004; 2006; Deptuck et al., 2008; Calvès et al., 2013). The turbidite system was connected to the continental shelf through submarine canyons, that are still evident on the seafloor (Fig. 6.1), and it was active during sea level low-stands (Calvès et al., 2013). Some contourite deposits (plastered drifts) are also present on the upper part of the Corsican continental slope (Fig. 6.1).

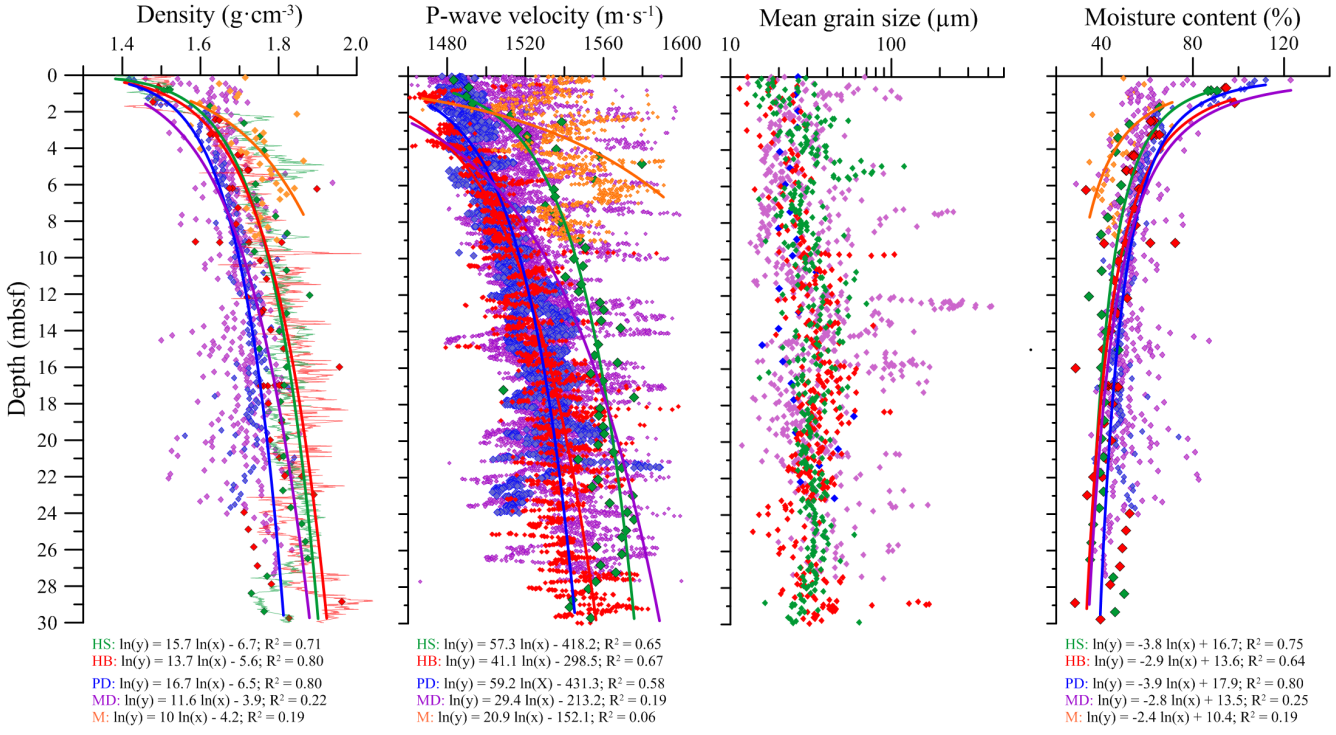

Fig. 6.2. From left to right: Density obtained from moisture content (diamonds) and MSCL (lines), P-wave velocity from MSCL (moat, plastered drift, mounded drift and hemipelagite-basin) and celerimeter (hemipelagite-slope), mean grain size and moisture content. HS: Hemipelagite Slope (GDEC4-2), HB: Hemipelagite Basin (GDEC8-2); PD: Plastered Drift (PSM3-CS017 and PSM3-CS018); MD: Mounded Drift (PSM3-CS006, PSM3-CS009, PSM3-CS012 and PSM3-CS021); M: Moat (PSM3-CS003). Fit curves and equations are displayed for each type of sediment. See Fig. 6.1 for core and borehole location.

Table 6.1. Physical and sedimentological properties of cores from the Pianosa CDS (PSM3 cores) and of boreholes from the basin (GDEC8-2) and from the western flank of the Corsica Trough (GDEC4-2).

Sample name	Type of sediment	Density ($g \cdot cm^{-3}$)	P-wave velocity ($m \cdot s^{-1}$)	Mean grain size (μm)	Clay volume (%, <6.2 μm)	Silt volume (%, 6.2-63 μm)	Sand volume (%, 63-2000 μm)	Moisture content (%)
PSM3 cores	Contourite	1.4-1.85	1460-1580	13-17 (excluding sandy layers)	Muddy plastered drift: 45-64 Muddy mounded drifts: 35-60 Sandy layers mounded drifts: 14-24	Muddy plastered drift: 31-39 Muddy mounded drifts: 26-50 Sandy layers mounded drifts: 15-34	Muddy plastered drift: 6-16 Muddy mounded drifts: 7-19 Sandy layers mounded drifts: 45-70	40-64 (max at the seafloor 123% and some layers up to 80-89%)
GDEC8-2	Hemipelagite (basin)	1.4-2.0	1460-1580	55-130	26-62	28-61	10-15	32-48 (max at the seafloor 95%)
GDEC4-2	Hemipelagite (western slope)	1.4-2.0	1460-1580	20-43	27-56	38-55	11-14	32-48 (max at the seafloor 95%)

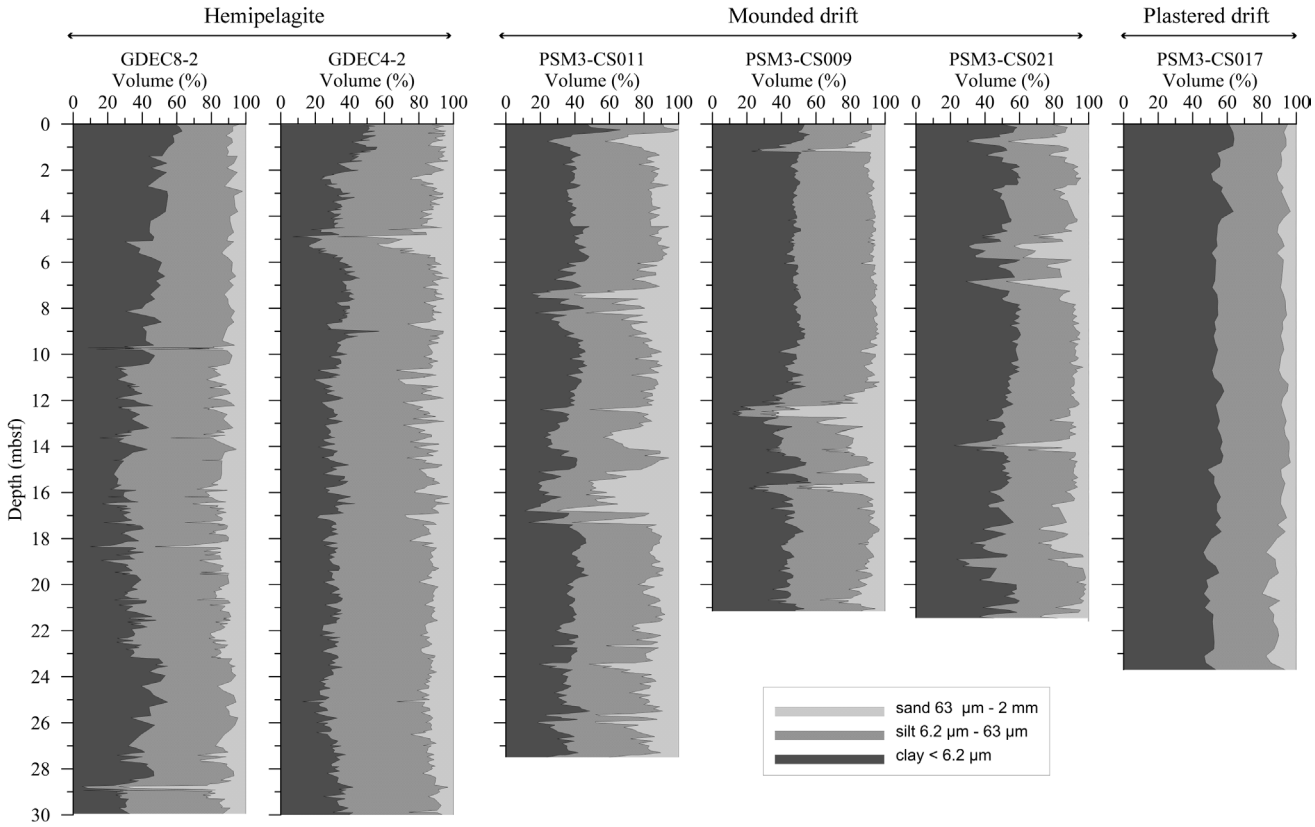

Fig. 6.3. Percent volumes of sand, silt and clay of boreholes GDEC8-2 and GDEC4-2 and Calypso piston cores PSM3-CS011, PSM3-CS009, PSM3-CS021 and PSM3-CS017. Note that core PSM3-CS017 (plastered drift) is very homogeneous compared to the other three sediment cores from mounded drifts, it is mainly composed of mud with clay contents between 45 and 64 %.

6.3. Results and interpretations

6.3.1. Geotechnical properties from core and borehole samples

6.3.1.1. Physical and sedimentological properties

Density and P-wave velocity values present a higher variability in mounded drifts and in the moat than in hemipelagites and plastered drifts, resulting in a low coefficient of determination (R^2; Fig. 6.2). Density values range between 1.4 and 1.85 g·cm^{-3} in contourites and between 1.4 and 2.0 g·cm^{-3} in hemipelagites. The general trends of both mounded and plastered drifts are slightly lower than the trends of the hemipelagites (Fig. 6.2). P-wave velocity values are similar in both types of sediment and typically increase from 1460 m·s^{-1} at the seabed to 1580 m·s^{-1} at 30 mbsf. The mounded drifts and the hemipelagites from the slope present slightly higher values that are very scattered and with many high peaks in the mounded drift (Fig. 6.2). In the moat (core PSM3-CS003; Fig. 6.1) the sediment presents higher P-wave velocity values that are very scattered and range between 1505 and 1585 m·s^{-1} within the upper 9 mbsf (Fig. 6.2).

Contouritic muddy sediments are slightly finer-grained than hemipelagic sediments, with a mean grain size of 15-30 μm, in contrast to the mean grain size values of GDEC4-2 and GDEC8-2, which range between 20 and 45 μm (Fig. 6.2). The analysed contouritic and hemipelagic sediments are mostly muddy, although the mounded drifts contain sandy layers, where the sand volume can reach up to 70 %, for instance at 12.5 m in core PSM3-CS009 (Fig. 6.3). The abundant sandy layers in the mounded drifts can explain the high peaks in P-wave velocity in this environment (Fig. 6.2). GDEC8-2 is composed of 26-62 % of clay (size fraction below 6.2 μm), 28-61 % of silt (size fraction 6.2-63 μm) and 10-15 % of sand (size fraction 63-2000 μm). GDEC4-2 contains between 27 and 56% of clay, 38-55 % of silt and 11-14% of sand (Table 6.1; Fig. 6.2). In the plastered drift the sediment is homogeneous, without sediment layers dominated by sand because the core PSM3-CS017 was located in the lower part of the plastered drift far from the shelf edge that is the source of the sandy material. The clay contents ranging between 45 and 64 %, 31-39% of silt and 6-16 % of sand (Table 6.1; Fig. 6.3). PSM3-CS009, PSM3-CS011 and PSM3-CS021 are located in mounded drifts, in the crest of the contourite, close to the moat. The muddy sections of these cores are composed of 35-

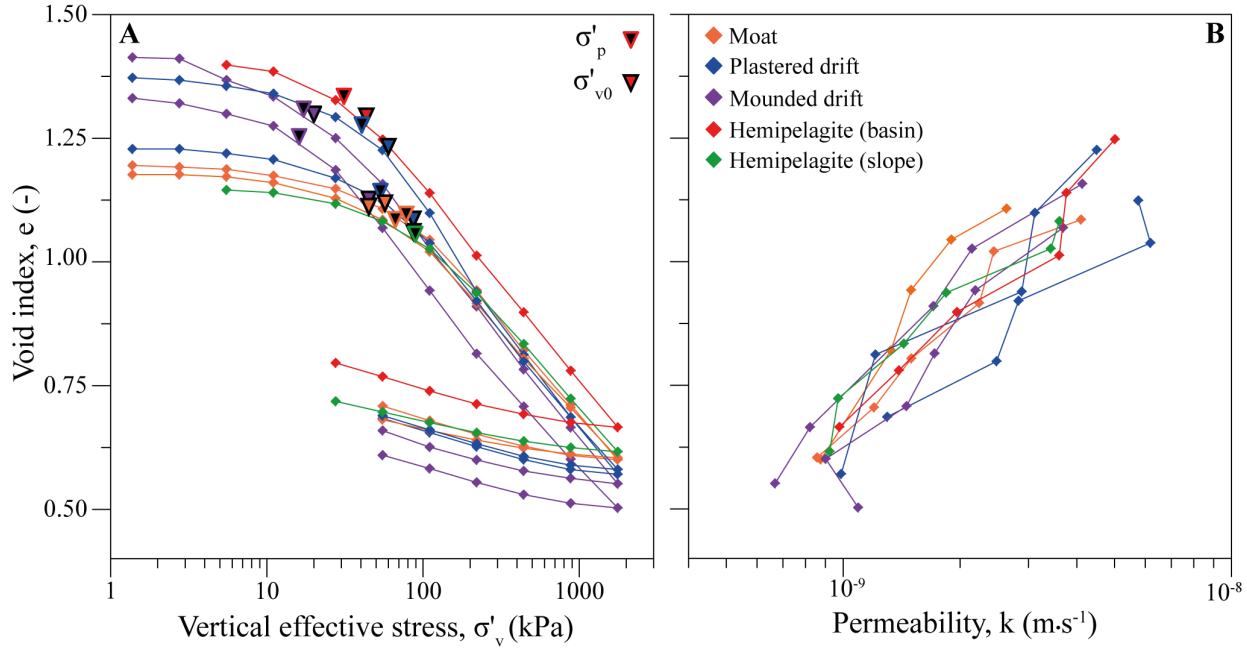

Fig. 6.4. (A) Void ratio - vertical effective stress plot obtained from oedometer tests. The initial vertical effective stress (σ'_{v0}) and the preconsolidation stress (σ'_p) are represented with triangles for each sample. **(B)** Void ratio - permeability plot obtained with the falling head permeameter. The samples chosen for the representation of each type of sediment are: PSM3-CS003-6.96 m and PSM3-CS003-7.97 m for the moat, PSM3-CS018-11.86 m and PSM3-CS017-9.73 m for the plastered drift, PSM3-CS009-5.21 m and PSM3-CS021-3.08 m for the mounded drift, GDEC8-2-8.14 m for hemipelagites in the basin and GDEC4-2-14.93 m for hemipelagites in the slope. See legend for colour details.

60 % of clay, 26-50 % of silt and 7-19% of sand (Table 6.1; Fig. 6.3).

Moisture content in hemipelagites decreases from 95 % at the seabed to 45 % within the upper 2 mbsf (Fig. 6.2). Below 2 mbsf moisture contents decrease gradually, remaining between 32 and 48 %. Contourites present a higher variability in moisture content, oscillating between 123 and 49 % at the seafloor. In general contouritic sediments tend to have slightly higher moisture contents than hemipelagites and are very scattered in the mounded drifts (Fig. 6.2). Mounded drifts present very high moisture content at about 14 mbsf and 20-24 mbsf, resulting in a lower density of the sediment and lower P-wave velocity values. It corresponds with a particular sediment layer that will be characterised and discussed in detail in Chapter 7. Overall the sediment at the moat presents the lowest moisture contents, that are very scattered and range between 35 and 60 % (Fig. 6.2). Mounded and plastered drifts present moisture content values mainly ranging between 40 and 64 %, very similar to hemipelagites (Fig. 6.2).

6.3.1.2. Consolidation state, permeability and compressibility

The oedometer tests carried out on samples from 7 cores in the Pianosa CDS showed that sediment drifts are generally normally to underconsolidated, with overconsolidation ratios (OCR) ranging between 0.5 and 1.1 (Figs 6.4A and 6.5). Higher OCR values (1.3-2.2), found within the upper 2 mbsf (Fig 6.5), can be ascribed to an apparent overconsolidation commonly measured in surface sediments (Sultan et al., 2000). OCR in core PSM3-CS003, located in a moat (Fig. 6.1), ranges between 1.2 and 2.1 (Fig. 6.5), corresponding to a slightly overconsolidated sediment. The hemipelagites sampled in boreholes are estimated to be normally consolidated (GDEC4-2) to underconsolidated (GDEC8-2) with OCR values around 0.7 (Fig. 6.5).

The permeability of hemipelagites is comprised within the same range as that of contourites (Figs. 6.4B, 6.5). In contourites, natural permeability values (k_i) are estimated to range between $5{\cdot}10^{-8}$ m·s^{-1} (extreme high values at the surface) and 3·10-9 m·s^{-1}, although most of the samples present k_i values between $4{\cdot}10^{-9}$ and $9{\cdot}10^{-9}$ m·s^{-1}. k_i values of the sediment from the moat are lower than in the sediment from the contourite drifts at the same depth below the seafloor. In hemipelagites, the natural permeability ranges between $9{\cdot}10^{-9}$ and $2{\cdot}10^{-8}$ m·s^{-1}. The permeability calculated from the log$k$-σ'_v curve at a σ'_v value of 1 kPa (k_0) is more scattered in mounded drifts, ranging between $2.5{\cdot}10^{-11}$ and $3.6{\cdot}10^{-10}$ m·s^{-1}. Hemipelagites and the plastered drift present lower variability in the k_0 values, comprised between $9{\cdot}10^{-11}$ and $1.8{\cdot}10^{-10}$ m·s^{-1} (Fig. 6.5).

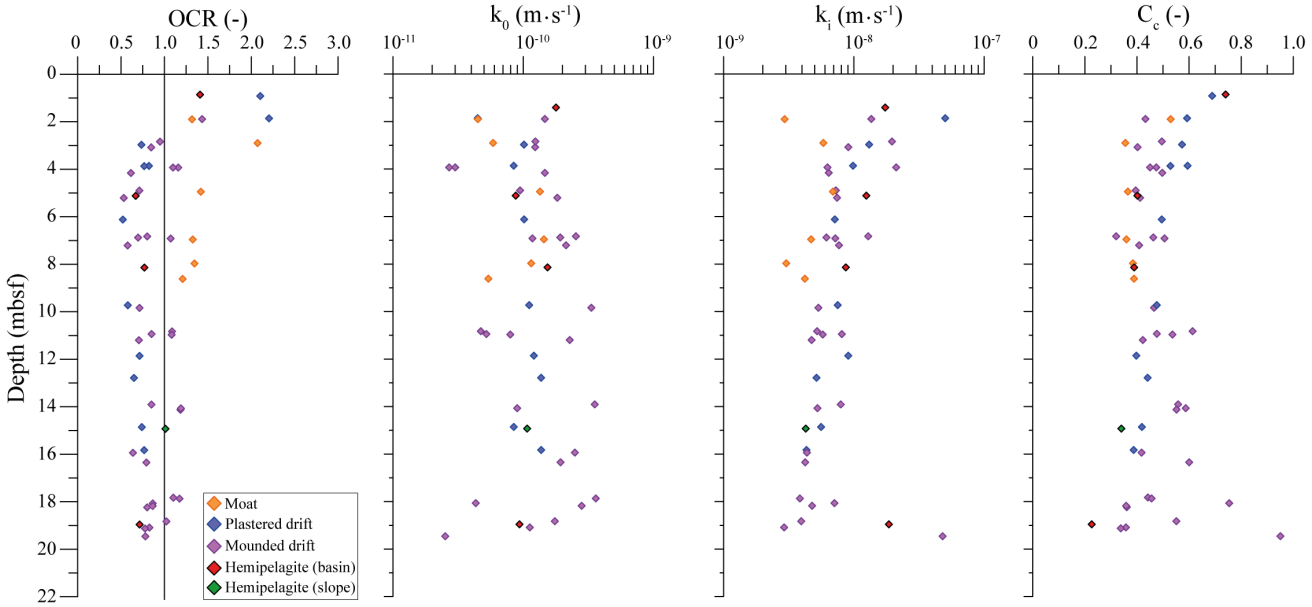

Fig. 6.5. Overconsolidation ratio (*OCR*), initial permeability (k_0) calculated at σ'_v of 1 kPa, natural permeability (k_i) and compression index (C_c) of 7 cores from the Pianosa CDS (1 from a moat, 2 from a plastered drift and 4 from mounded drifts) and of hemipelagites (from the slope and the basin). *OCR* values have been calculated using the Pacheco-Silva method (Pacheco Silva, 1970).

The high C_c and k_i values found in the mounded drifts between 16 and 20 mbsf correspond to a particular sediment layer that will be analysed in detail in Chapter 7. The sediment from the moat is less compressible than the sediment from the contourite drifts (Fig. 6.5). In hemipelagites compression indices are slightly lower than in most of the contouritic samples and range between 0.2 and 0.4 (apart from a sample at about 1 mbsf that presents higher C_c; Fig. 6.5). The compression curves shown in Fig. 6.4A correspond with the same samples as the permeability plots (Fig. 6.5B), but they are not representative of all the samples that are represented in Fig. 6.5.

The sediment from the moat (PSM3-CS003, see Fig. 6.1 for core location) is slightly overconsolidated and presents lower *in situ* permeability. Both properties suggest that the moat is an environment dominated by erosive processes. No major differences are found between hemipelagites and contourites, although contourites seem to be slightly more compressible than hemipelagites.

6.3.1.3. Undrained and effective shear strengths

The peak shear strength (Su_p) obtained from laboratory vane shear tests tend to increase with depth in a similar fashion in both hemipelagic and contouritic sediments. In general, it increases linearly from 3 kPa at the seafloor to 40 kPa at 30 mbsf. This trend is punctuated by strong oscillations in the range of 10 and 50 kPa from 14 to 28 mbsf. The sediment from the moat presents higher peak undrained shear strengths. Su_p values in the plastered drift are lower than in most of the analysed samples from hemipelagites and mounded drifts (Fig. 6.6).

Consolidated Undrained (CU) triaxial tests carried out on fine-grained sediment samples from the plastered drift (cores PSM3-CS017 and PSM3-CS018) show that this sediment presents an internal friction

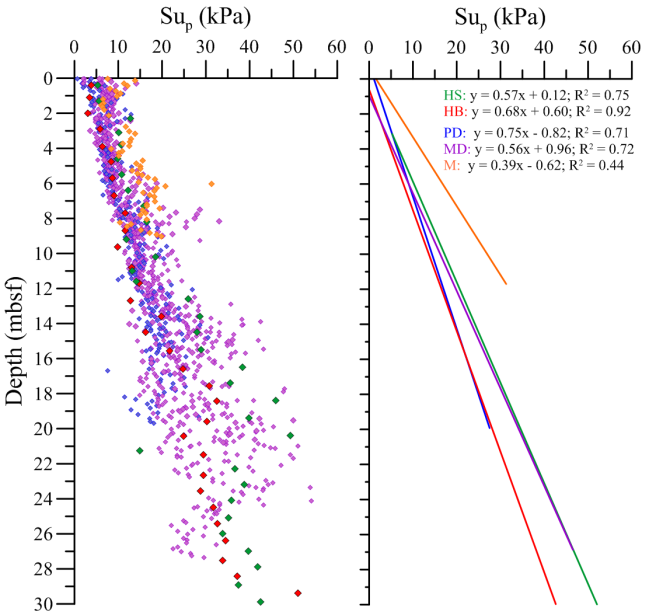

Fig. 6.6. Peak shear strength of hemipelagites (HS: Hemipelagite Slope; HB: Hemipelagite Basin) and contourites (PD: Plastered Drift; MD: Mounded Drift; M: Moat) obtained using laboratory vane shear tests. The linear fits to the vane shear test data are presented in the right graph.

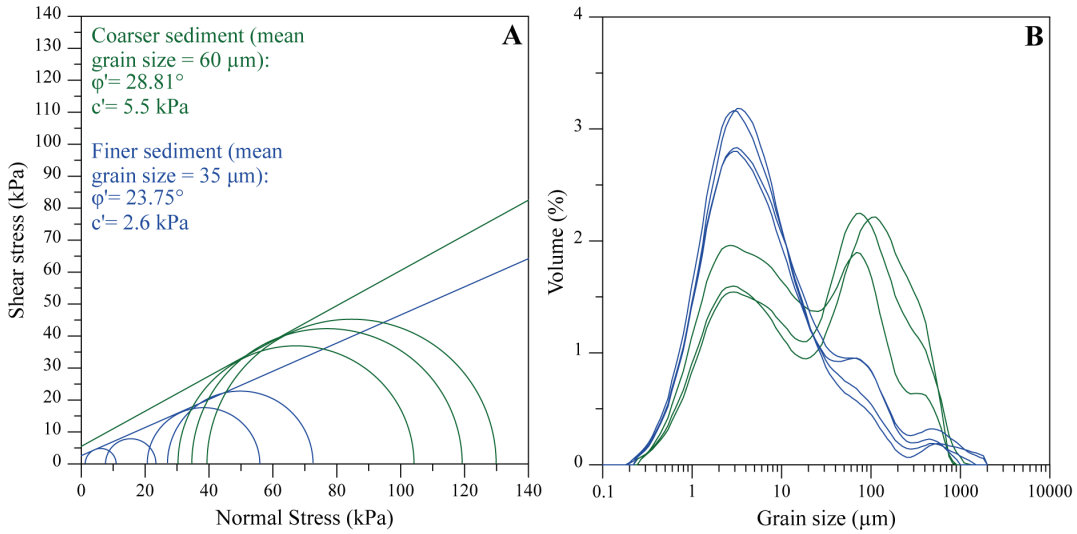

Fig. 6.7. (A) Coulomb failure lines and Mohr circles obtained from Consolidated Undrained (CU) triaxial tests on samples of a finer (blue) and coarser sediment of contourites (green). **(B)** Grain size distribution of the sediment samples used for the triaxial tests.

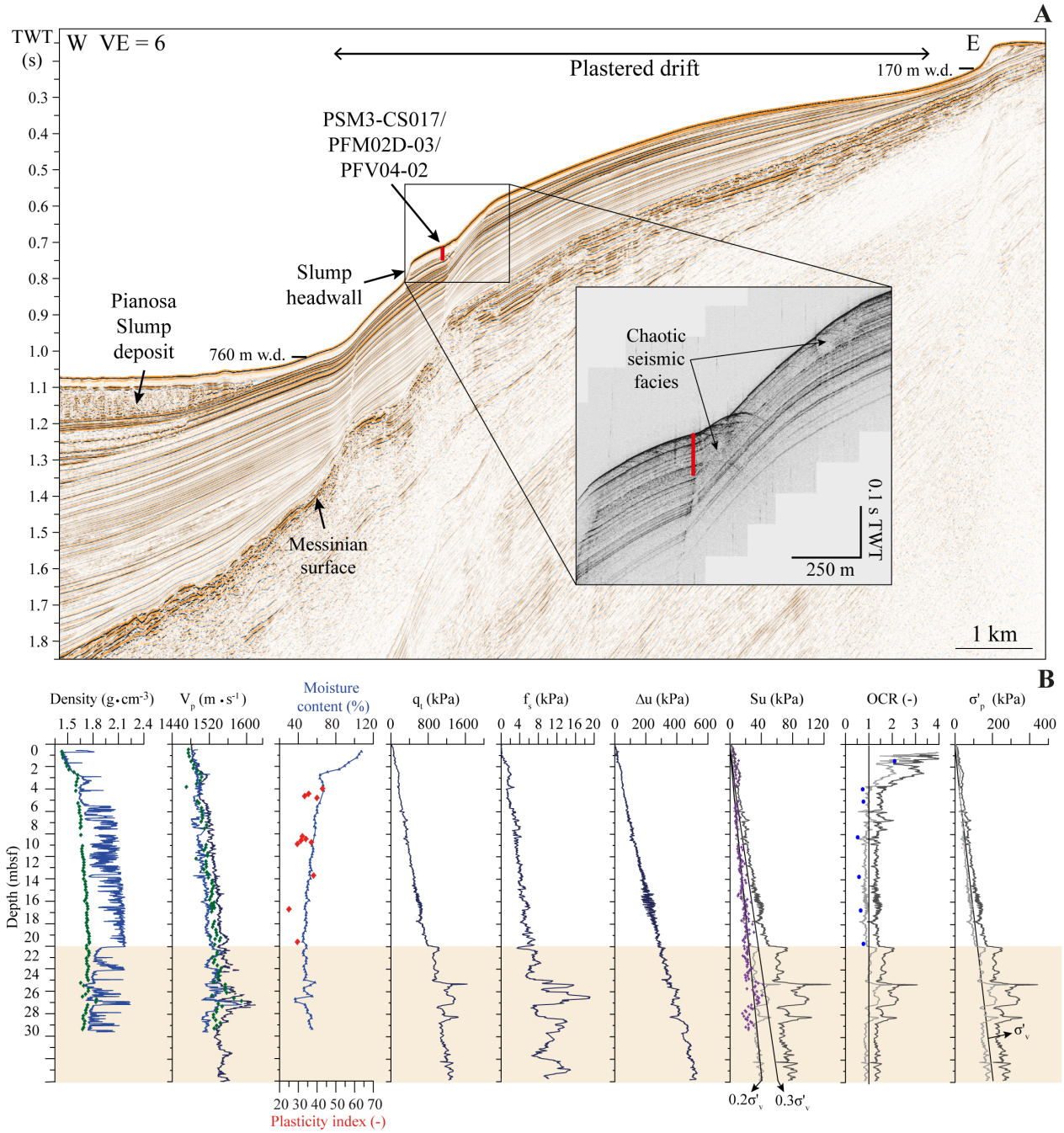

Fig. 6.8. (A) PSM2-HR-033 multi-channel high resolution seismic reflection profile showing the plastered drift on the Pianosa Ridge and the headwall related to the Pianosa Slump. The location of Calypso piston core PSM3-CS017, CPTU site PFM02D-03 and in situ P-wave velocity measurement PFV04-02 are indicated in more detail in the zoom of the SBP profile PSM2-CH-033. **(B)** From left to right: density from MSCL (blue line) and moisture content (green diamonds), P-wave velocity obtained using a MSCL (light blue line), a laboratory celerimeter (green diamonds) and from *in situ* measurement (dark blue line), moisture content (blue line) and plasticity index (red diamonds); CPTU data: corrected cone resistance (q_t), sleeve friction (f_s), excess pore pressure (Δu), peak undrained shear strength from CPTU (grey lines) and laboratory vane shear test on core PSM3-CS021 (purple diamonds), Overconsolidation Ratio (*OCR*) from CPTU (grey lines) and oedometer tests on core PSM3-CS017 (blue dots), and preconsolidation pressure (σ'_p). The undrained shear strength (*Su*) is calculated using N_{kt}=20 (light grey line) and N_{kt}=10 (dark grey line), max. and min. values after Low et al. (2010). *OCR* and σ'_p are calculated using $N_{\sigma t}$=4.5 (light grey) and $N_{\sigma t}$=2.9 (dark grey), max. and min. values after Demers and Leroueil (2002). The zone between 18-30 mbsf in salmon colour corresponds to deformed sediment.

angle (φ') of 23.75° and an effective cohesion (c') of 2.6 kPa. The mean grain size of this type of sediment is 35 μm. A coarser layer in the contourite sampled in the mounded drift by core PSM3-CS012 with a mean grain size of 60 μm has a φ' of 28.81° and a c' of 5.5 kPa (Fig. 6.7).

6.3.2. Geotechnical properties from in situ measurements

Five CPTU were carried out in three different environments of the Pianosa CDS to provide information on the mechanical properties of different sedimentary bodies present in the contourite depositional system: plastered drift, multicrested mounded drift and moat.

- The CPTU **PFM02D-03** was performed at 534 m w.d. in a plastered drift located in the southern zone of the Pianosa Ridge (Fig. 6.8A), where mass-wasting processes have been the most extensive (Miramontes et al., 2016a). Deformed sediment can be found between 18 and 30 mbsf (zone in salmon colour in Fig. 6.8B), characterised by higher values of corrected cone resistance (q_t), sleeve friction (f_s), P-wave velocity, as well as a higher variability in excess pore pressure (Δu; Fig. 6.8B). Values of overconsolidation ratios (OCR) and preconsolidation pressures (σ'_p) are higher in the deformed zone than in overlying sediments, probably due to compression during shearing (contractant behaviour) (Fig. 6.8B). In the undeformed sediments, q_t, f_s and Δu tend to increase linearly with depth. OCR values obtained from oedometers and from CPTU (calculated using $N_{\sigma t}$ equal to 4.5) show that the sediment is slightly underconsolidated to normally consolidated. This observation is coherent with the Su vales provided by the vane shear test and by the CPTU (with a N_{kt} factor of 20) that are close to the line corresponding to 0.2 σ'_v, suggesting normally consolidation (Chandler, 2000).
- The CPTUs **PFM01-04** and **PFM01-03** were conducted in a multicrested mounded drift south of the Elba Canyon (Figs. 6.1 and 6.9). PFM01-04 is situated at 342 m water depth (w.d.) and PFM01-03 at 281 m w.d. in a less developed drift crest, with lower sediment accumulation (Fig. 6.9). The two crests are separated by a moat. In contrast with measurements from the plastered drift at the site of PFM02D-03, in the multicrested mounded drifts CPTU measurements revealed a high variability

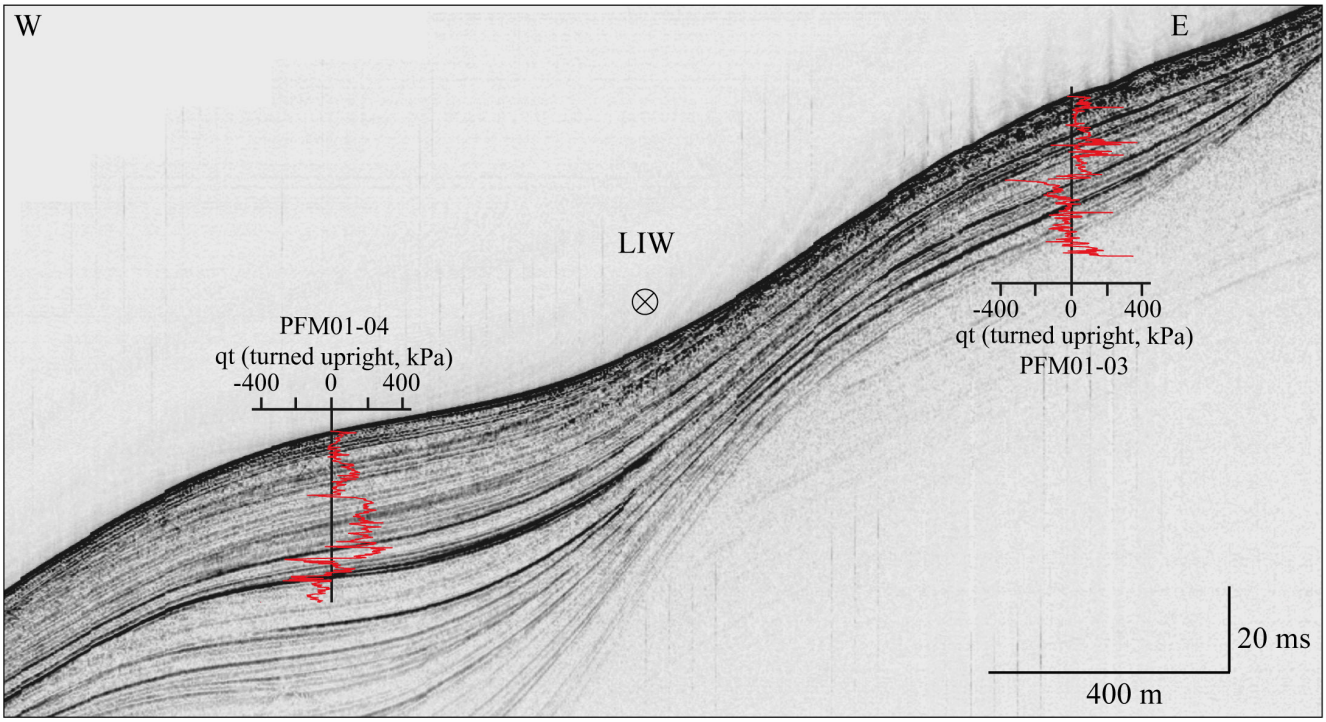

Fig. 6.9. PSM2-CH-054 SBP profile of the multicrested mounded drifts located south of the Elba Canyon, where bottom currents associated to the Levantine Intermediate Water (LIW) flow towards the north. For an easier correlation of the changes in corrected cone resistance (q_t) in PFM01-04 and PFM01-03 with the seismic reflections, the q_t curves have been turned upright by subtracting q_t to a mean linear trend of q_t (straight lines in the first graphs of Fig. 6.10).

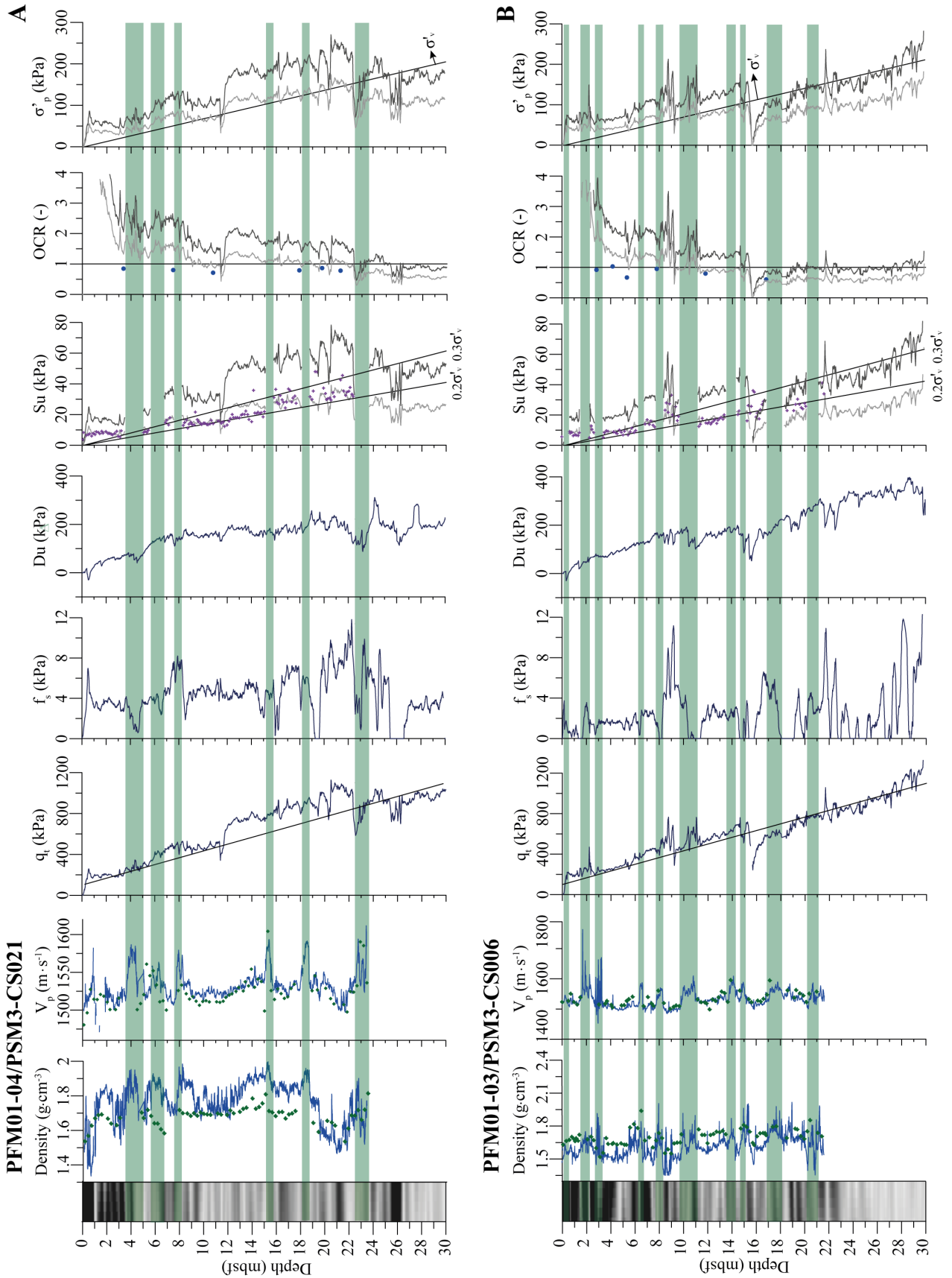
A
B
PFM01-04/PSM3-CS021
PFM01-03/PSM3-CS006
σ'p (kPa)
OCR (-)
Su (kPa)
Du (kPa)
fs (kPa)
qt (kPa)
Vp (m·s-1)
Density (g·cm-3)
σ'v
0.2σ'v 0.3σ'v
Depth (mbsf)

Fig. 6.10. (A) From left to right: SBP seismic facies at the site of CPTU PFM01-04 and core PSM3-CS021; core data: density from MSCL (blue line) and moisture content (green diamonds), P-wave velocity obtained using a MSCL (blue line) and a celerimeter (green diamonds); CPTU data: corrected cone resistance (q_t) and mean linear trend of q_t (straight line), sleeve friction (f_s), excess pore pressure (Δu), peak undrained shear strength (Su) from CPTU (grey lines) and from laboratory vane shear test on core PSM3-CS021 (purple diamonds), Overconsolidation Ratio (OCR) from CPTU (light and dark grey lines) and oedometer tests on core PSM3-CS021 (blue dots) and preconsolidation pressure (σ'_p). Undrained shear strength (Su) is obtained from the relation using N_{kt}=20 (light grey line) and N_{kt}=10 (dark grey line), max. and min. values after Low et al. (2010). OCR and σ'_p are calculated using $N_{\sigma t}$=4.5 (light grey line) and $N_{\sigma t}$=2.9 (dark grey line), max. and min. values after Demers and Leroueil (2002). **(B)** Same as **(A)** but at CPTU site PFM01-03 and core PSM-CS006. The green bands show sandy layers.

(Fig. 6.10). High P-wave velocity values obtained from Calypso piston cores PSM3-CS021 (at the site of PFM01-04) and PSM3-CS006 (at the site of PFM01-03) correspond to sandy layers (Fig. 6.10), with about 50 % of muddy material (Fig. 6.3) and the rest mainly composed of bioclasts (Miramontes et al., 2016b). These sandy layers are not easily identified by CPTU data alone, since they do not always present peaks in q_t values, although they do present a decrease in Δu values (Fig. 6.10). The studied crests of the multicrested drift are in general slightly underconsolidated to normally consolidated (OCR ranging between 0.7 and 1), except for some intervals that seem more underconsolidated: between 15 and 16 mbsf at site PFM01-03 (Fig. 6.10B), and below 22.5 mbsf at site PFM01-04 (Fig. 6.10A). These underconsolidated layers show σ'_p values that are lower than σ'_v, suggesting the presence of overpressure (Fig. 6.10).

- The CPTU **PFM01-02** was conducted in a moat at 245 m w.d., while **PFM01-01** was performed in the upper slope at 176 m w.d. near the shelf edge prism south of the Elba Canyon (Figs. 6.1 and 6.11). The moat is the zone of the contourite system where bottom currents are faster, preventing sediment deposition and even generating erosion in some cases. At the site of PFM01-02 the SBP

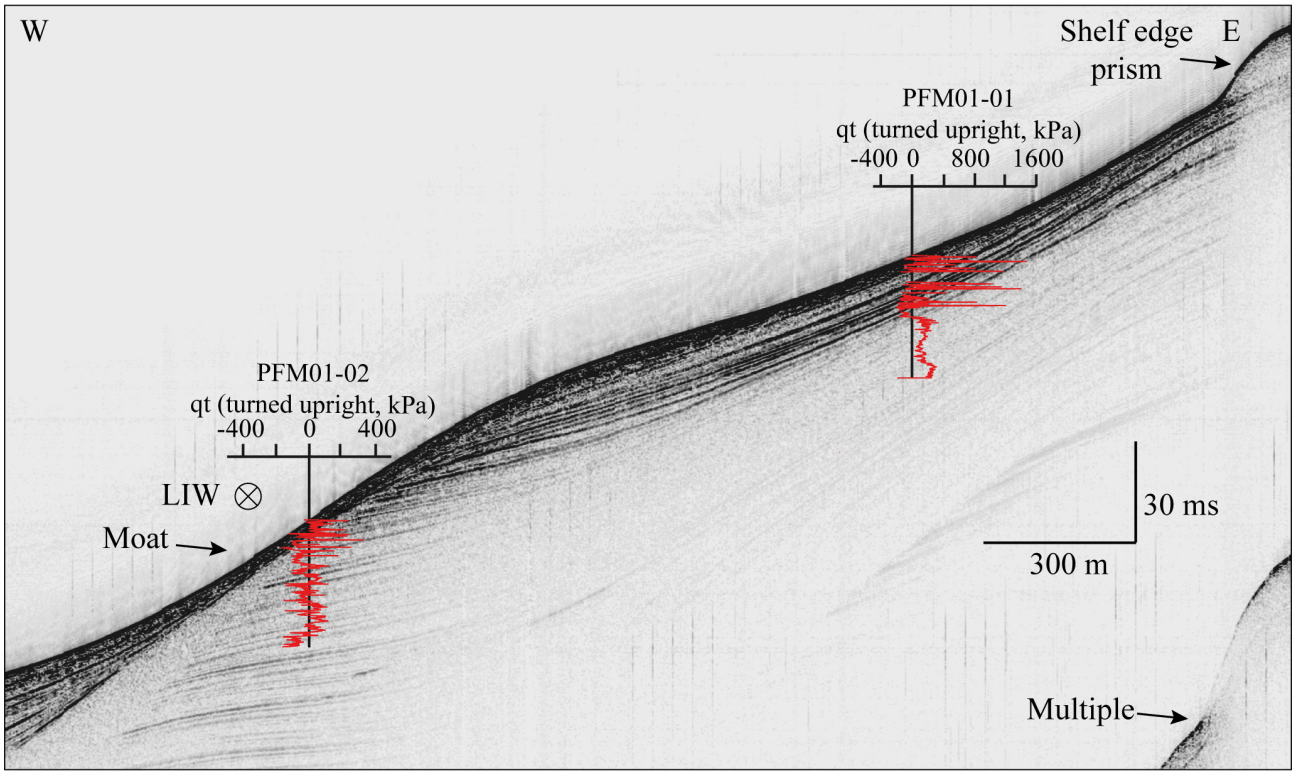

Fig. 6.11. PSM2-CH-054 SBP profile of the moat and the upper slope south of the Elba Canyon. For an easier correlation of the changes in corrected cone resistance (q_t) of PFM01-02 and PFM01-01 with the seismic reflections, the q_t curves have been turned upright by subtracting q_t to a mean linear trend of q_t (Fig. 6.12).

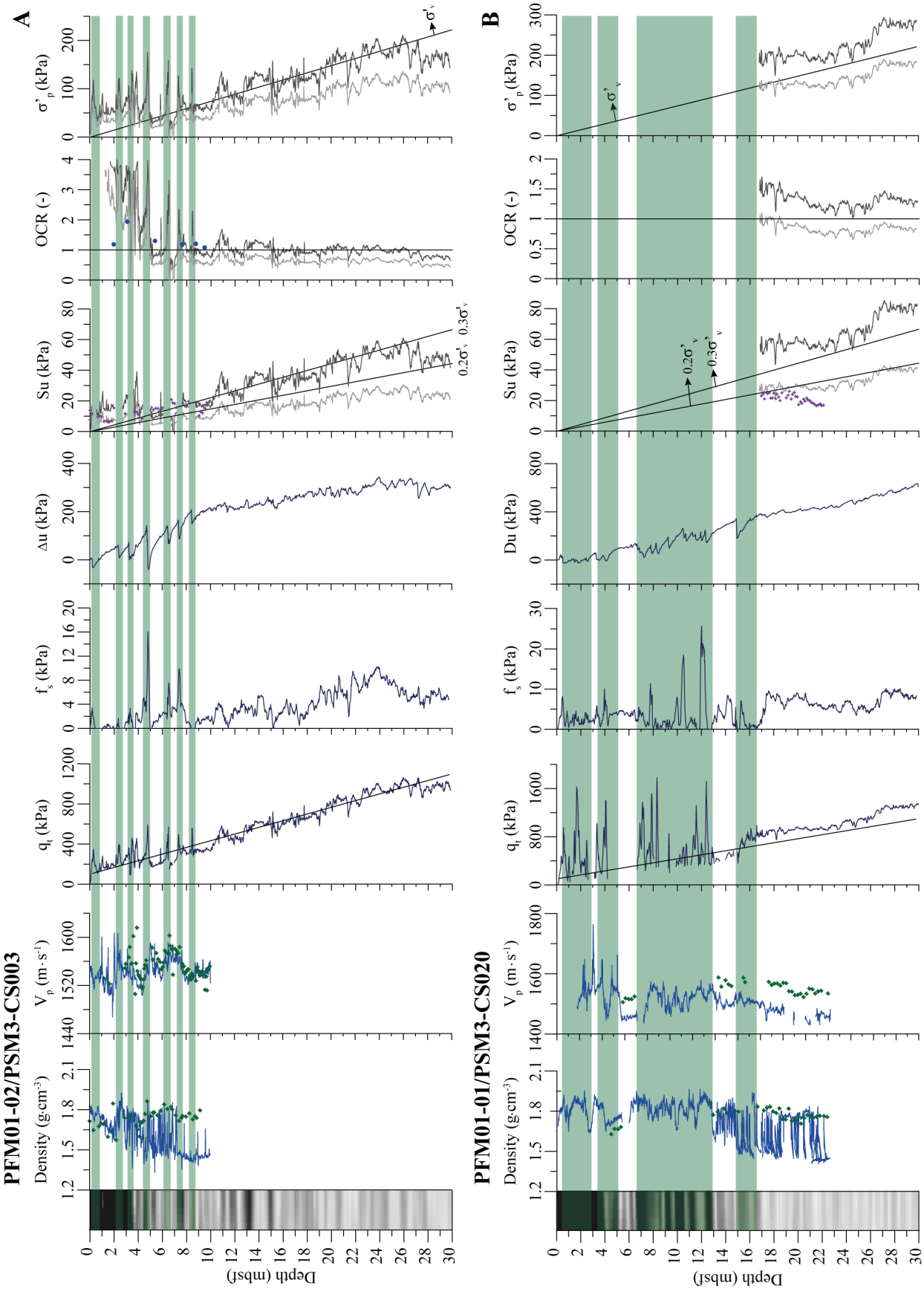
A
B
PFM01-02/PSM3-CS003
PFM01-01/PSM3-CS020
σ'p (kPa)
OCR (-)
Su (kPa)
Δu (kPa)
Du (kPa)
fs (kPa)
qt (kPa)
Vp (m·s-1)
Density (g·cm-3)
σ'v
0.2σ'v
0.3σ'v
Depth (mbsf)

Fig. 6.12. (A) From left to right: SBP seismic facies at the site of CPTU PFM01-02 and core PSM3-CS003; core data: density from MSCL (blue line) and moisture content (green diamonds), P-wave velocity obtained using a MSCL (blue line) and a celerimeter (green diamonds); CPTU data: corrected cone resistance (q_t) and mean linear trend of q_t (straight line), sleeve friction (f_s), excess pore pressure (Δu), peak undrained shear strength (Su) from CPTU (light and dark grey lines) and laboratory vane shear test (purple diamonds), Overconsolidation Ratio (OCR) from CPTU (red and grey lines) and oedometer tests (blue dots) and preconsolidation pressure (σ'_p). Undrained shear strength (Su) is calculated using N_{kt}=20 (light grey line) and N_{kt}=10 (dark grey line), max. and min. values after Low et al. (2010). OCR and σ'_p are calculated using $N_{\sigma t}$=4.5 (light grey line) and $N_{\sigma t}$=2.9 (dark gey line), max. and min. values after Demers and Leroueil (2002). **(B)** Same as **(A)** but at CPTU site PFM01-01 and core PSM-CS020. The green bands show sandy layers.

seismic profile shows truncated reflections under a seismic discontinuity (Fig. 6.11). Above this discontinuity, the seismic reflections pinch out in the zone of the moat due to the development of a sediment drift that decreases in thickness towards the moat. From seismic evidence alone, it could be argued that there was first a process of erosion that generated the discontinuity and then, mainly a process of non-deposition that created a zone of lower sediment accumulation at the moat (zone of high amplitude reflections within the first 4 mbsf in Figs. 6.11 and 6.12). The analysis of the geotechnical data provides more information to reconstruct the stress history of the site. The upper 8 mbsf are characterised by high amplitude reflections correlating with local increases in q_t and decreases in Δu, indicating the presence of coarse material (Fig. 6.12). The sediment core PSM3-CS003 located at the same site presents layers of bioclastic sand and gravel that are more abundant within the first 3 mbsf (Miramontes et al., 2016b). The upper 4 mbsf correspond with the sediment deposited after the discontinuity. This sediment layer is slightly overconsolidated with OCR values ranging between 1.3 and 2.0 (Fig. 6.12A), suggesting that the moat underwent erosion. The oedometer test at 3 mbsf provided a σ'_p of 41 kPa, almost twice σ'_v for this depth (21 kPa). At this depth the Overconsolidation Difference ($OCD = \sigma'_v - \sigma'_p$; Locat et al. (2003)) is 20 kPa, that is equivalent to the σ'_v of the uppermost 3 m (Fig. 6.12A). This suggests that erosive processes can remove up to 3 m of sediment from the moat. Below the seismic discontinuity the sediment is slightly overconsolidated with OCR values close to 1.5 and below 7 m, it is normally consolidated to slightly overconsolidated with OCR values mainly ranging between 1.0 and 1.3, increasing in some layers up to 1.8 (between 10 and 15 mbsf; Fig. 6.12A).

Site PFM01-01 is the shallowest CPTU site, located at 176 m w.d. on the upper continental slope, near the shelf edge prism. The upper 15 mbsf are characterised on the SBP profile by the presence of high amplitude reflections in the SBP profile (Figs. 6.11 and 6.12B), correlating with peaks of very high cone resistance (up to 1770 kPa), high sleeve friction (maximum values of 25 kPa) and low excess pore pressure (Fig. 6.12B). The Calypso piston core PSM3-CS020, collected at site PFM01-01, shows the presence of abundant bioclastic sandy to gravely layers (Miramontes et al., 2016b) within the first 15 m. Below 15 mbsf the sediment is muddy (Miramontes et al., 2016b) and the q_t and Du values tend to increase linearly with depth (Fig. 6.12B). The stepped increases in f_s observed at 17 and 27 mbsf may be related to slight lithological changes (Fig. 6.12B).

6.3.3. Liquefaction potential assessment

The present-day seismic activity in the Corsica Trough is low, 3.4 is the highest and closest detected magnitude (RENASS catalogue; Fig. 6.1). The maximum horizontal acceleration (a_{max}) or Peak Ground Acceleration (PGA) given for the Corsica Trough for a 475 year return period by the Global Seismic Hazard Assessment Program is lower than 0.04 g (Slejko et al., 1999). The potential for cyclic liquefaction was first evaluated using the method proposed by Robertson (2004) and CPTU measurements from sites PFM01-01, PFM01-02, PFM01-03 and PFM01-04 by considering a PGA of 0.04 g for and earthquake of magnitude 3.4. The high computed Factors Of Safety (FOS higher than 4; Fig. 6.13A) predict that the sediment has likely no liquefaction potential. Two more tests were performed by increasing PGA and earthquake magnitude in order to identify under which conditions sediment in contourites may liquefy. The PGA was calculated using the Idriss (1993) approach for an earthquake located at a dis-

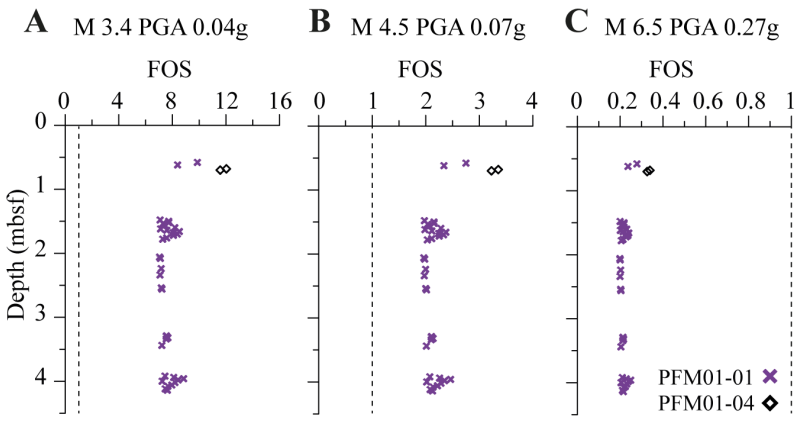

Fig. 6.13. Factor Of Safety (FOS) calculated for three different Magnitudes (M) and Peak Ground Accelerations (PGA): **(A)** M 3.4 and PGA 0.04 g; **(B)** M 4.5 and PGA 0.07 g; **(C)** M 6.5 and PGA 0.27 g. The calculation was done with all available CPTUs, but no results are shown for the sediment that may not liquefy.

tance of 15 km from the CPTU sites and considering two different magnitudes of 4.5 and 6.5. This distance was chosen because it corresponds to the distance between the CPTU and the nearest earthquake of the historical record (RENASS catalogue; Fig. 6.1). It was thus estimated that a magnitude 4.5 earthquake, generating a PGA of 0.07 g, could not produce liquefaction at any site, since the calculated FOS is always higher than 1 (Fig. 6.13B). A 6.5 magnitude earthquake and 0.27 g PGA would induce liquefaction only within a sediment layer at 0.7 mbsf at site PPFM01-04 (Fig. 6.13C). In contrast, at site PFM01-01 several layers would liquefy between above 4.5 mbsf (Fig. 6.13C).

This analysis shows that the poorly sorted sandy layers composed of more than 50 % of mud typical of the mounded drifts may not liquefy under seismic loading. No liquefaction could be possible in the plastered drift because no sandy layers are present in the lower part of this sedimentary body, where the Pianosa Slump was originated.

6.3.4. Effect of sedimentation rate on pore pressure generation

The Pianosa CDS has recorded the highest sedimentation rates during sea level low-stands, from about 0.8 m·kyr^{-1} in the mounded drift to 1.15 m·kyr^{-1} in the plastered drift where the Pianosa Slump occurred (Miramontes et al., 2016b). In order to test if this sedimentation rate was enough to generate excess pore pressure, we modelled the evolution of the pore pressure following the deposition of the layer corresponding to the basal surface of the Pianosa Slump (about 150 kyr BP) with the SeCo software (Sultan et al., 2004). The input parameters (initial void ratio, compressibility and permeability; Table 6.3) were derived from oedometer tests in core PSM3-C017, located in the plastered drift (Fig. 6.1). The sedimentation rates used to calculate excess pore pressure with the SeCo software are based in the chronology proposed by Miramontes et al. (2016b). The maximum sedimentation rate of 1.15 m·kyr^{-1} calculated for the plastered drift during MIS2 is also used for previous sea level low-stands (65-70 and 133-150 kyr BP; Table 6.3). For sea level high-stands (46-65 and 70-133 kyr BP) we used a sedimentation rate of 0.2 m·kyr^{-1} (Table 6.4). During sea level low-stands high sedimentation rates can generate an overpressure of up to 0.55 kPa, and it decreases fast when sedimentations rates are reduced down to 0.2 m·kyr^{-1} during sea level high-stands (Fig. 6.14). Therefore, no overpressure would be affecting the upper 35 mbsf of the plastered drift at the time of the Pianosa Slump formation (≈ 46 kyr BP). Even during the periods of high sedimentation rates the calculated excess pore pressure values are too low to influence slope stability at 35 mbsf, where the vertical effective stress is about 240 kPa.

Table 6.2. Input parameters for the excess pore pressure calculation using the SeCO software, corresponding to the minimum permeability values obtained from core PSM3-CS017 located at the plastered drift. e_0 is the void ratio at a reference vertical effective stress of 0.01 kPa, λ is the compression index of the sediment, σ'_{v0} the reference vertical effective stress, υ the viscosity, and a and b are permeability parameters obtained from the expression k=exp(ae+b), where k is the permeability and e is the void ratio.

e_0 (-)	λ	σ'_{v0} (kPa)	υ (kPa·s)	a	b
3.05	0.17	$1{\cdot}10^{-3}$	$1.15{\cdot}10^{-6}$	2.8805	-22.7092

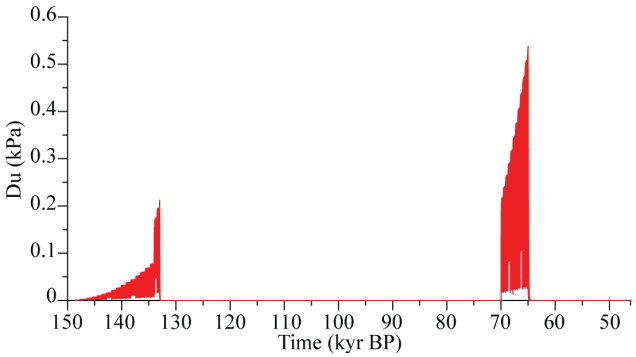

Fig. 6.14. Excess pore pressure generated due to sedimentation between 150 kyr BP (time of the formation of the Pianosa Slump basal failure surface) and 46 kyr BP (approximate time of the Pianosa Slump formation) using the SeCO software (Sultan et al., 2004).

Table 6.3. Sedimentation rates used to model excess pore pressure with the SeCO software.

Time period (kyr BP)	Sedimentation rate ($m \cdot kyr^{-1}$)
150-133	1.15
133-70	0.20
70-65	1.15
65-46	0.20

6.3.5. Slope stability analysis

The comparison of the geotechnical properties of hemipelagic and contouritic sediment shows that hemipelagites from the slope (GDEC4-2) present higher density (Fig. 6.2) and higher undrained shear strength (Fig. 6.6) than the sediment from the plastered drift. These two types of sediments characterise different flanks of the basin. The eastern flank is dominated by contourites, while the western flank is mainly composed of hemipelagic and turbiditic deposits (Fig. 6.1; Gervais et al., 2004; Gervais et al., 2006; Deptuck et al., 2008; Calvès et al., 2013; Cattaneo et al., 2014). Distinct sedimentation processes shaped in different ways the two flanks of the basin. The western flank presents in general a gentle slope of 2-3°, with a zone of higher slope gradient (5°) at 300-400 m w.d., that is related to a small plastered drift (Fig. 6.15A). The bathymetric profile of this margin is mainly straight (Fig. 6.15A). In contrast, the eastern flank in the southern part of the Pianosa Ridge presents steeper slope gradients, caused by the presence of convex-shaped contourites (plastered drift) and the moats generated by bottom currents at the foot of the slope (Fig. 6.15A). In the upper part of the plastered drift the slope gradient is low 1-3°, but it becomes much steeper in the middle and lower slope, reaching 11° in the moat (Fig. 6.15A).

We did a 1D slope stability analysis using the properties of the hemipelagic sediment from the slope and the properties of the plastered drift with different slope angles in order to investigate which factor has a more important role in slope stability: the seafloor morphology or the sediment properties. The calculation was carried out assuming infinite slope in undrained conditions because the development of catastrophic failure, that is the most critical scenario, is expected to occur very rapidly and will thus mobilise the undrained parameters of the sediment (Puzrin et al., 2016). Using the available data of undrained shear strength and unit weight (Fig. 6.15B), the Factor Of Safety (FOS) was calculated for hemipelagites (down to 50 mbsf) and plastered drift (down to 25 mbsf).

The slope stability assessment shows that both the hemipelagic and contouritic sediment are stable (FOS>1) for slope angles lower than 5° (Fig. 6.16), that are the typical values found in slopes mainly composed of hemipelagites (Fig. 6.15A). On the contrary, both hemipelagites and plastered drift would be unstable (FOS<1) for slope angles higher than 8° (Fig. 6.16). The zone upslope the moat in a plastered drift usually presents steep slopes that can be higher than 11° (Fig. 6.15A). Therefore, this zone is the most critical one independently of the type of sediment.

6.4. Discussion

6.4.1. Sedimentological and geotechnical properties of contourites and hemipelagites

The present study in the Corsica Trough shows some differences in the intrinsic sedimentological and geotechnical properties of contourites and hemipelagites, especially between the plastered drift and hemipelagites from the slope. The plastered drift has finer sediment (more abundant clay; Fig. 6.3), lower density (Fig. 6.2), higher moisture content, higher compressibility (also the mounded drift; Fig. 6.5) and lower undrained shear strength (Fig. 6.6). However, no major differences in *Su* were observed between the plastered drift and the hemipelagites from the bottom of the basin. All the analysed sediments present similar permeabilities (Figs. 6.4B, 6.5).

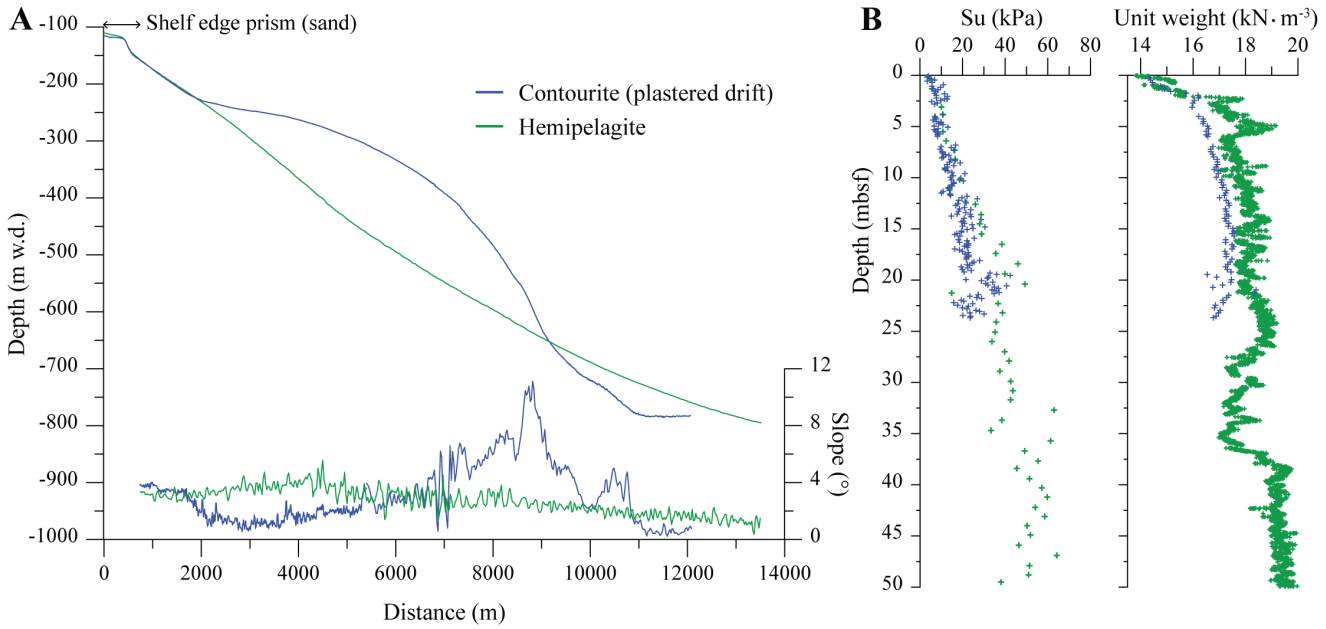

Fig. 6.15. (A) Bathymetric profiles and slope gradients of a contouritic margin (blue) and a hemipelagic margin (green). **(B)** Undrained shear strength (*Su*) and unit weight of the sediment used for the slope stability analysis: in blue a contourite (PSM3-CS017) and in green a hemipelagic deposit (GDEC4-2).

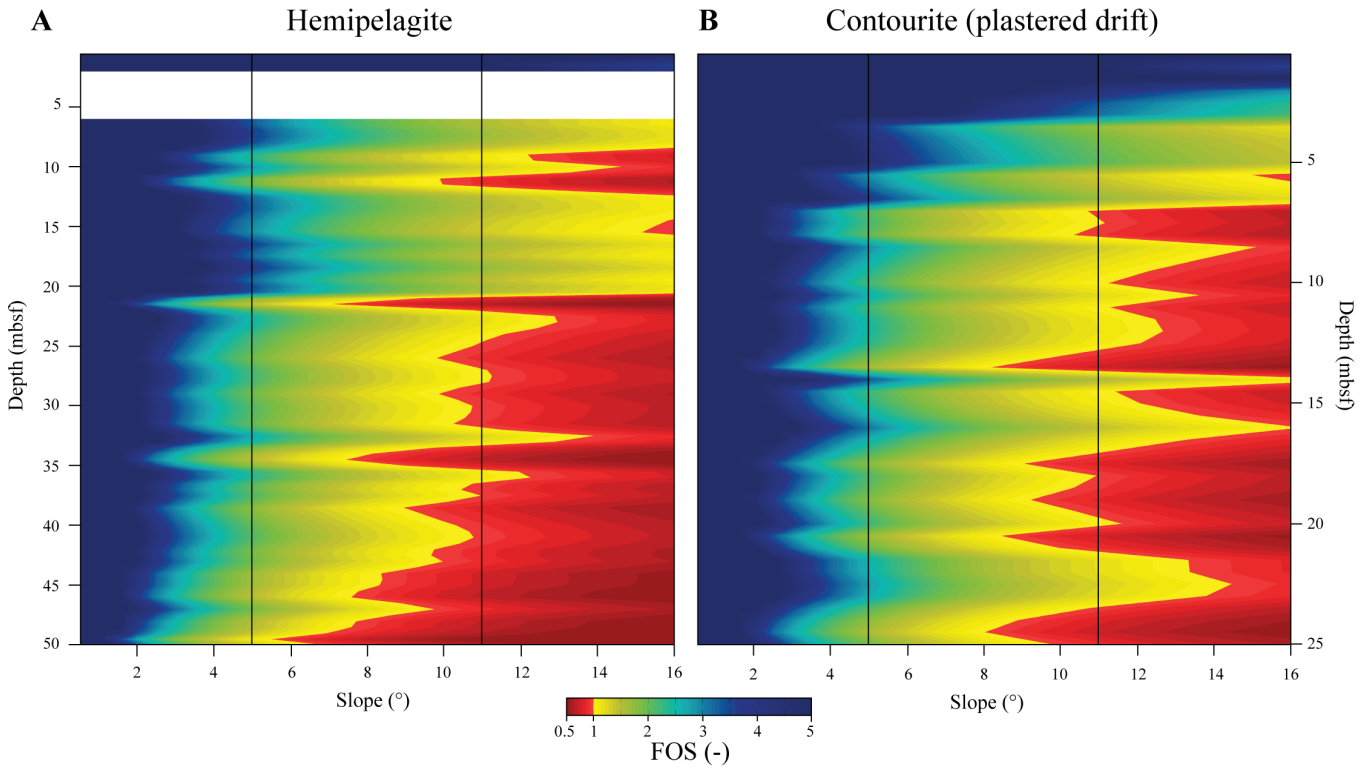

Fig. 6.16. Slope stability analysis showing the Factor Of Safety (FOS) as function of slope angle and depth under undrained conditions in a hemipelagic deposit **(A)** and in a plastered drift **(B)**. The black vertical lines show the maximum slope gradients found in the bathymetric profiles of Fig. 6.15A in hemipelagites (5°) and in the plastered drift (11°). FOS was not calculated in a sandy layer of GDEC4-2 and it was left blank. Note that both types of sediments present FOS>1 with the typical slopes of hemipelagic margins (slope <5°).

Contourite depositional systems may contain different types of sediments with distinct geotechnical properties. For instance, mounded drifts present abundant poorly sorted sandy layers, while they are absent in the lower part of the plastered drift (Fig. 6.2). The moat is the environment of the contourite depositional system that differs the most from the contourite drifts and the hemipelagites. It is composed of coarser material and due to erosive processes it presents different inherited properties: sediments are overconsolidated, with low moisture content, low permeability (Fig. 6.5) and high undrained shear strength (Fig. 6.6).

6.4.2. Potential causal factors of slope instability in contourites

Laberg and Camerlenghi (2008) argued that excess pore pressure and underconsolidation generated by gas charging and/or rapid sedimentation may favour slope instability in contouritic environments. Contourites in the Corsica Trough are slightly underconsolidated and recorded high sedimentation rates of up to 1.15 $m \cdot kyr^{-1}$ during sea level low-stands. However, the results obtained with the consolidation model for the plastered drift show that such a sedimentation rate was not high enough to have generated significant increases in pore pressure, even if the sediment is very fine with a relatively low permeability (Table 6.3).

Wilson et al. (2004) suggested that well-sorted sandy layers within a contourite drift could have liquefied under seismic loading and thus have acted as a failure surface for submarine landslides. Nevertheless, sandy layers in contourites are commonly poorly sorted (Stow and Faugères, 2008; Figs. 6.2, 6.3). The coarse layers of contourites in the Pianosa Ridge are poorly sorted, composed of sand and more than 40 % of mud (Fig. 6.3). Moreover, we found that in the Corsica Trough , the poorly sorted sandy layers in contourites may not liquefy under seismic loading (Fig. 6.13). Only the zone with abundant coarse material at site PFM01-01 and a shallow sandy layer (0.7 mbsf) at site PFM01-04 may liquefy under an earthquake of magnitude 6.5 and PGA of 0.27 g (Fig. 6.13). Therefore, we could conclude that the typical poorly sorted sandy layers found within muddy contourites are not susceptible to liquefaction.

Although contourites generally grow on gentle slopes (<1°; Laberg and Camerlenghi, 2008), they can also be formed on steep slopes and generate, due to their particular sediment pattern, zones with high slope angles (Fig. 6.15A). Plastered drifts commonly develop on continental slopes and they can be located right below the continental shelf edge or below a terrace (Hernández-Molina et al., 2016). When the evolution of continental slopes is mainly controlled by hemipelagic and turbiditic sedimentation (like the western flank of the Corsica Trough), it results in a linear bathymetric cross-section profile (Fig. 6.15A). On the contrary, in contourite systems bottom currents can induce preferential sediment deposition at mid slope, forming a plastered drift and generating a zone of steeper gradients in the lower slope (Fig. 6.15A). This convex slope profile is, independently of the sediment properties, potentially more unstable than the typical slope profile observed where hemipelagic and turbiditic sedimentation dominate (Fig. 6.16). Despite the observed differences in the geotechnical properties of hemipelagites from the slope and the plastered drift, the slope stability analysis shows that the main factor controlling the development of submarine landslides in contourites is the morphology of the plastered drift.

The plastered drift of the Pianosa Ridge was affected by four submarine landslides during the Plio-Quaternary period that were the largest mass failures in the area (Fig. 6.1; Miramontes et al., 2016a). Bottom currents play a very important role in shaping continental slopes and in creating convex seafloor morphologies that are more susceptible to failure. Therefore, the generation of a plastered drift can be a predisposing factor of slope instability. Moreover, it is common to find moats, channels and evidences of erosion at the foot of the plastered drifts (Hernández-Molina et al., 2016; Miramontes et al., 2016b), where undercutting processes could trigger a submarine landslide in the lower part of the plastered drift, as observed in many different settings such as the Uruguayan margin (Hernández-Molina et al., 2016), the Argentinean margin (Preu et al., 2013) or the Alboran Sea (Ercilla et al., 2016).

6.5. Conclusions

The Corsica Trough is a confined basin in the Northern Tyrrhenian Sea that presents an eastern margin dominated by contouritic and mass transport processes and a western margin dominated by turbiditic and hemipelagic processes. This asymmetry allowed a comparison between the sedimentological and geotechnical properties of contourites and hemipelagites, as well as between the seafloor morphologies and stability of the two margins.

In the Corsica Trough, the contourite drifts could be separated in two main groups with different properties: mounded drifts and plastered drifts. The mounded drifts contain more sandy layers related to periods of faster bottom currents. These sandy layers are more developed in zones close to the moat (incision created by bottom currents). The moat differs from the muddy contourite drifts and hemipelagites because it is dominated by erosive processes, it is slightly overconsolidated, it has coarser material, a lower permeability and a lower compressibility. The plastered drift is the contourite type that differs the most from the hemipelagites found in the slope. The sediment of the plastered drift has lower density, finer material, higher compressibility (like the mounded drift) and lower undrained shear strength than hemipelagites.

The poorly sorted sandy layers of the mounded drifts (with mud contents above 40 %) are not susceptible to liquefaction according to a liquefaction assessment performed using CPTU data. Moreover, no sandy layers were identified in the lower part of the plastered drift, where the largest submarine landslides took place. The 1-D consolidation modelling results showed that sedimentation alone could not generate significant overpressure in this area.

The main factor controlling slope instability in contourites is therefore the seafloor morphology, i.e. the steep slopes present in the lower part of the plastered drifts. The slope stability analysis shows that the western flank of the Corsica Trough is stable using either the properties of hemipelagites or the properties of contourites. On the contrary, both types of sediment are unstable in the lower part of the plastered drift, where the slope angle is about 11°. Moreover, bottom currents often generate erosion at the foot of the plastered drift and may trigger submarine landslides by undercutting the slope. Slope failures at the lower part of plastered drifts have been observed along many continental margins. A better understanding on the formation and evolution of this type of drifts could provide very valuable information about submarine geohazards.

CHAPTER 7. Altered volcanic deposits as basal failure surfaces of submarine landslides

One of the key features in the study of submarine landslides is the identification of potential weak layers responsible for the location of basal failure planes, thus for the position, size and causal mechanisms of the landslide. In spite of numerous studies on this subject, potential weak layers remain elusive. In the present study we identified the role of a weak layer in the eastern margin of the Corsica Trough (northern Tyrrhenian Sea) that originated the Pianosa Slump at 42-50 kyr BP. This layer is characterised by high moisture content, low density, high plasticity, high compressibility and a post-peak strain softening behaviour (i.e. strength loss with increasing strain).

Zeolites of analcime type with a concentration of 2-4 % in the muddy sediment are at the origin of the observed altered sedimentological and mechanical properties. Zeolites are minerals commonly formed by the alteration of volcanic rocks that were probably transported from the Tuscan magmatic province during a sea level low stand.

The coupling effect of observed undercutting erosion and the presence of zeolites on slope instability was tested numerically using an elastic-perfectly plastic model with an approximated strain softening approach. Modelling shows that an erosion of 3 m at the foot of the slope would create enough strain to reduce the shear strength of the zeolitic layer and focus here the failure surface. We propose that the strain softening behaviour of muddy zeolitic sediment plays an important role in predisposing submarine landslides on continental slopes.

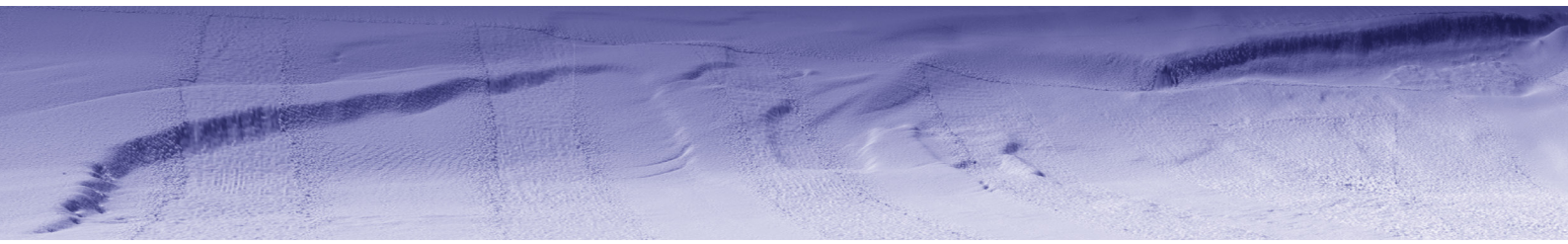

CHAPITRE 7. Influence de dépôts volcaniques altérés dans la surface de rupture de glissements sous-marins

Un des facteurs clé de l'étude de glissements sous-marins est l'identification de couches potentielles de faiblesse, responsables de la localisation des surfaces de rupture dans la stratigraphie, et donc de la position, de la taille et des mécanismes de formation de ces glissements. Malgré les nombreuses études sur ce sujet, ces surfaces de glissement ne sont pas réellement identifiées. Dans cette étude, nous avons pu mettre en évidence le rôle d'une couche de faiblesse dans la colonne stratigraphique du Canal de Corse à l'origine du glissement de Pianosa (Pianosa Slump) autour de 42-50 ka BP. Cette interface est caractérisée par une teneur en eau, une plasticité et une compressibilité importantes et une faible densité associées à un comportement mécanique caractérisé par du radoucissement (perte de résistance avec le cisaillement).

Les zéolites de type analcime avec une concentration de 2-4 % dans le sédiment vaseux sont à l'origine des propriétés sédimentologiques et mécaniques altérées. Ces minéraux formés généralement par l'altération des roches volcaniques ont probablement été transportés de la province magmatique de la Toscane pendant les périodes de bas niveau marin.

L'effet couplé de l'érosion basale et de la présence de zéolites sur la stabilité de pente a été testé numériquement en utilisant un modèle élastique-parfaitement plastique avec une approche approximative du comportement mécanique de radoucissement (perte de résistance avec le cisaillement). Les résultats du modèle montrent qu'une érosion de 3 m en pied de pente pourrait créer assez de contraintes de cisaillement pour réduire la résistance au cisaillement de la couche de zéolites et concentrer la surface de rupture au sein de la couche de zéolites. On propose que le comportement de radoucissement du sédiment vaseux zéolitique joue un rôle important prédisposant aux glissements sous-marins sur les pentes continentales.

CAPÍTULO 7. Depósitos volcánicos alterados como superficies basales de ruptura de deslizamientos submarinos

Uno de los factores clave en el estudio de deslizamientos submarinos es la identificación de potenciales capas débiles, responsables de la localización de las superficies basales de ruptura y por lo tanto de la posición, el tamaño y los mecanismos causales del deslizamiento. A pesar de los numerosos estudios sobre este tema, las características de las potenciales capas débiles siguen estando poco claras. En el presente estudio identificamos el papel de una capa débil en el margen este del Canal de Córcega (Mar Tirreno Septentrional) que originó el « Pianosa Slump » en 42-50 ka BP. Esta capa se caracteriza por tener un alto contenido en agua, una densidad baja, una plasticidad elevada, una compresibilidad elevada y un comportamiento de « strain softening » tras el pico de resistencia (es decir, una pérdida de la resistencia al cizallamiento cuando aumenta el esfuerzo aplicado).

Las zeolitas de tipo analcima con una concentración de 2-4 % en sedimento fangoso son la causa de las observadas alteraciones en la propiedades sedimentológicas y mecánicas. Las zeolitas son minerales que se suelen formar por la alteración de las rocas volcánicas, y en este caso probablemente fueron transportados desde la provincia magmática de la Toscana durante el nivel del mar bajo.

El efecto de la suma de la observada erosión al pie del talud y de la presencia de zeolitas en la estabilidad del talud fue analizado numéricamente con un modelo elástico-perfectamente plástico con una aproximación de « strain softening ». El modelo muestra que una erosión de 3 m al pie del talud produciría suficiente tensión para reducir la resistencia de la capa de zeolitas y focalizar en ella la superficie de ruptura. Proponemos que el comportamiento de «strain softening» del sedimento fangoso zeolítico juega un papel importante en predisponer deslizamientos submarinos en taludes continentales.

7.1. Introduction

The large size of submarine landslides compared to terrestrial landslides is related, among other factors, to the presence of extended weak layers within marine sediments accumulated along continental slopes (Puzrin et al., 2016). Weak layers can be induced when a process, such as the development of a strain softening behaviour, reduces the strength of the sediment (Locat et al., 2014). Marine sediments with a strain softening behaviour present a loss in strength with increasing strain and can thus develop progressive or catastrophic failure along large surfaces of rupture (Dey et al., 2016), as demonstrated for the Storegga slide (Kvalstad et al., 2005; Andresen and Jostad, 2007). Understanding the mechanical and sedimentological properties of weak layers is the key to identifying the potential failure surface of submarine landslides and to modelling their lateral propagation (Germanovich et al., 2016; Puzrin et al., 2016). In this work, we demonstrate how zeolites, the product of volcanic rock alteration (Chipera and Apps, 2001), influence the sedimentological and geotechnical properties of fine marine sediment and contribute to the development of slope failures. This finding has potentially broad impact, since many regions in the world present abundant volcanic material that can be a potential source of zeolites (Fig. 7.1).

7.2. A zeolite-rich weak layer

The Plio-Quaternary sedimentation along the Pianosa Ridge (Northern Tyrrhenian Sea) is composed of muddy contourites that were affected by multiple mass-wasting processes (Fig. 7.2A; Miramontes et al., 2016a,b). The Pianosa Slump (PS) is the youngest submarine landslide of the southern Pianosa Ridge, originated at 42-50 kyr BP in a convex-shaped contourite, flanked by zones of focused erosion (moats) at the foot of the slope, where slope gradients reach 10-16° (Fig. 2A; Miramontes et al., 2016a). During sea level falls bottom currents were faster and could erode sediment at the moats (Miramontes et al., 2016b). Between 52 and 48 kyr BP the sea level dropped 50 m (from -40 to -90 m below the present-day sea level; Rohling et al., 2008), coinciding within the interval of the Pianosa Slump formation. Therefore, a more intense bottom current circulation is expected to have occurred during this time.

The PS headwall is located at 500-670 m water depth and the scar is at present day covered by 20 m of sediment (Fig. 7.2B). Multi-channel high resolution seismic reflection profiles, acquired with a mini GI gun (50–250 Hz) during the PRISME2 cruise in 2013, show that the basal failure surface of the PS follows a stratigraphic horizon marked on seismic profiles by

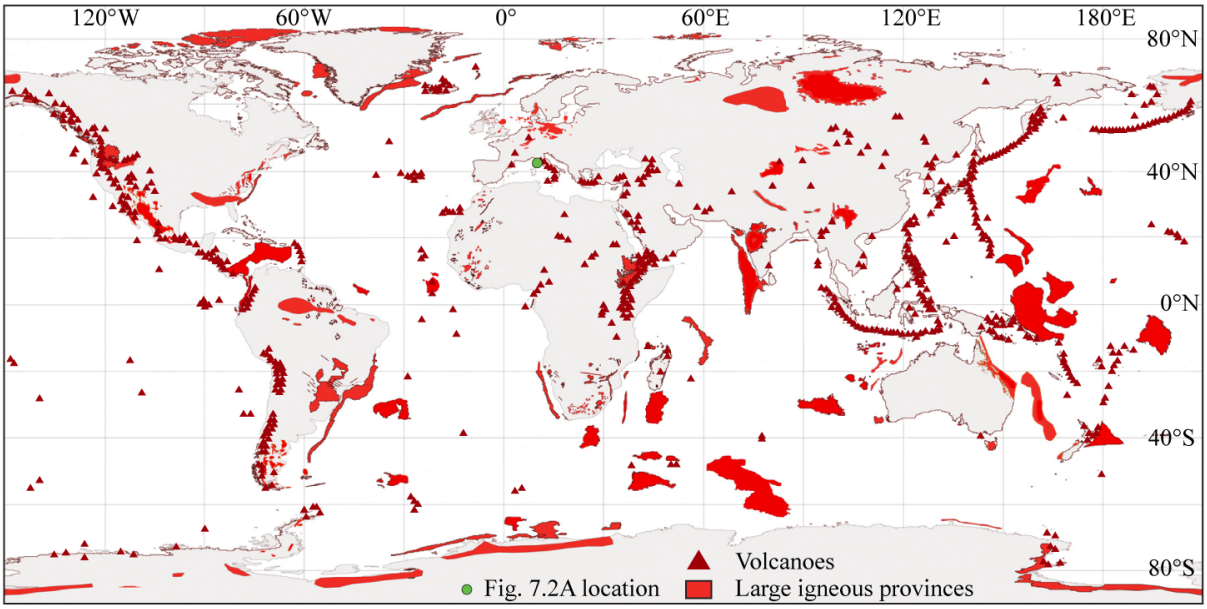

Fig. 7.1. World distribution of the large igneous provinces (Bryan and Ferrari, 2013) and volcanoes (Global Volcanism Program, 2013) as potential sources of zeolites. The green dot shows the location of the study area.

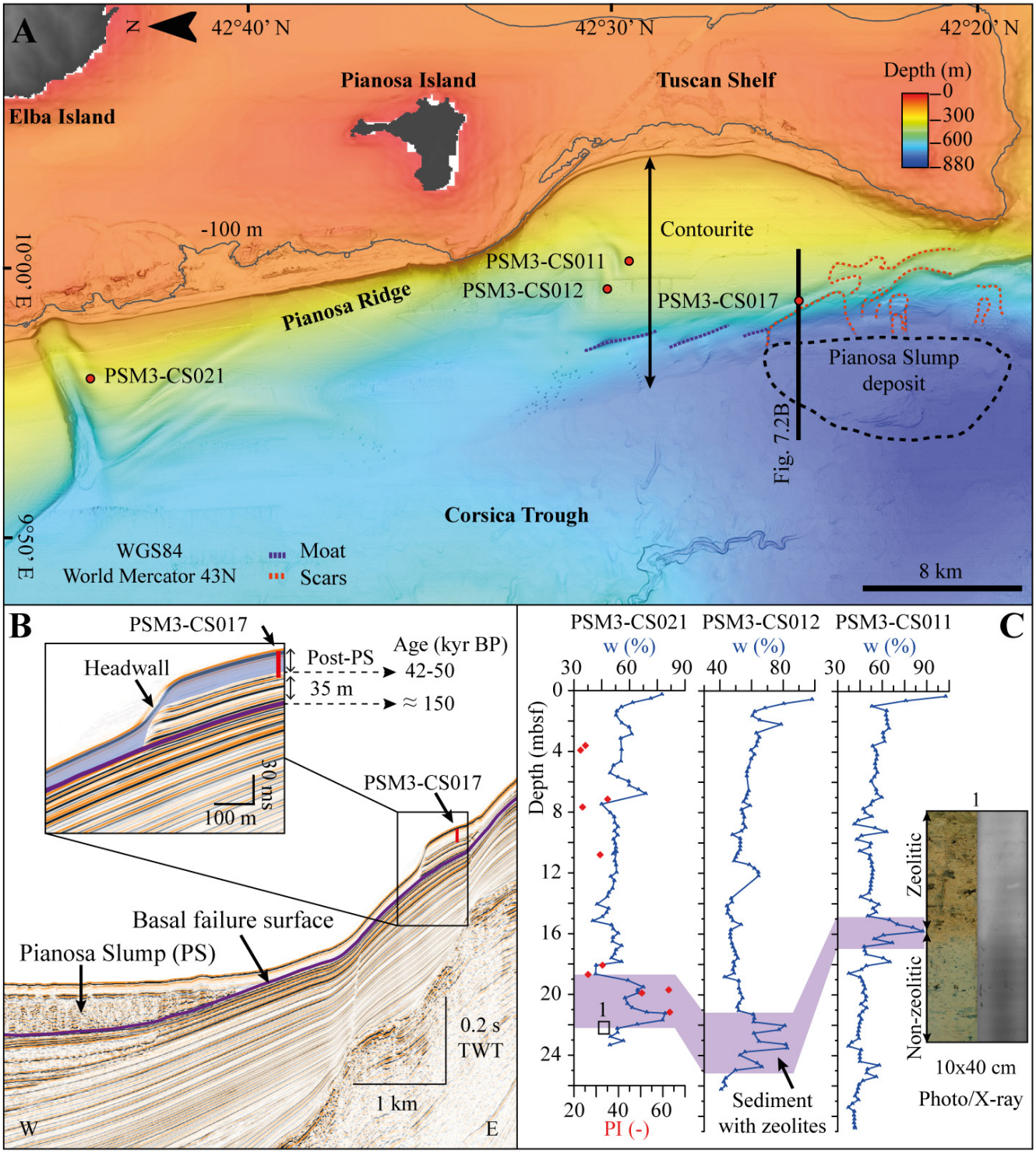

Figure 7.2. (**A**) Multibeam bathymetry of the Pianosa Ridge with the location of the contourites on the slope, the moats, the Pianosa Slump deposit and the failure scars. (**B**) PSM2-HR-033 multi-channel high resolution mini GI gun seismic reflection profile showing the Pianosa Slump deposit, headwall and basal failure surface. (**C**) Moisture content (*w*) of the three sediment cores that sampled the zeolitic sediment layer and plasticity index (*PI*) of core PSM3-CS021. The photo and the X-ray image show that the sediment with zeolites has a brownish colour, a spongy texture and a lower density.

Table 7.1. Mineralogical composition obtained with X-ray Diffraction (XRD) of common muddy contouritic samples and sediment samples that present different physical properties (lower density, lower P-wave velocity values and higher water contents; represented with bold font). The core depth was corrected using the software CINEMA[2] (Woerther et al., 2012). Note that the main difference is that the particular layer marked in bold font contains zeolites of analcime type.

Core	Depth (m)	Corrected depth (m)	Quartz (%)	Plagioclase (%)	K-feldspar (%)	Clay/Mica (%)	Zeolite (Analcime, %)	Halite (%)	Pyrite (%)	Calcite (%)	Dolomite (%)	Aragonite (%)	Mg-Calcite (%)
PSM3-CS012	10.92	12.49	14	3	3	44	0	1	1	20	3	5	6
PSM3-CS012	13.98	15.51	17	7	4	40	0	1	0	19	4	3	5
PSM3-CS012	**20.80**	**22.23**	**13**	**9**	**2**	**34**	**3**	**1**	**1**	**24**	**4**	**3**	**6**
PSM3-CS012	**21.88**	**23.30**	**15**	**7**	**4**	**43**	**3**	**2**	**1**	**14**	**3**	**3**	**5**
PSM3-CS012	**22.20**	**23.61**	**14**	**6**	**4**	**40**	**4**	**2**	**1**	**16**	**3**	**3**	**7**
PSM3-CS012	22.25	23.66	16	6	5	47	0	1	1	14	2	4	4
PSM3-CS017	3.14	4.18	15	6	4	44	0	1	0	19	4	3	6
PSM3-CS017	6.59	8.69	19	7	4	43	0	1	0	17	4	3	3
PSM3-CS021	10.03	10.96	17	7	4	43	0	1	<1	21	3	4	0
PSM3-CS021	16.60	18.12	17	7	4	36	0	1	<1	17	3	6	9
PSM3-CS021	**18.22**	**19.88**	**16**	**5**	**2**	**28**	**2**	**2**	**1**	**28**	**2**	**6**	**10**
PSM3-CS021	**19.32**	**21.08**	**17**	**8**	**3**	**40**	**2**	**1**	**1**	**14**	**4**	**2**	**6**

Table 7.2. Clay mineralogical composition obtained with X-ray Diffraction (XRD) of common muddy contouritic samples and sediment samples that present different physical properties (lower density, lower P-wave velocity values, higher moisture contents and containing zeolites; represented with bold font). The clay mineralogy is similar in all the samples. Only two out of five samples of the zeolitic layer (in bold) present higher smectite content. Therefore, the observed differences in the geotechnical properties cannot be explained by a change in the clay mineralogical composition.

Core	Depth (m)	Corrected depth (m)	Smectite (%)	Illite (%)	CWI	Cristalinity	Kaolinite (%)	Chlorite (%)
PSM3-CS012	10.92	12.49	7	53	0.26	0.50	15	26
PSM3-CS012	13.98	15.51	<5	52	0.24	0.45	12	33
PSM3-CS012	**20.80**	**22.23**	**16**	**53**	**0.23**	**0.44**	**10**	**20**
PSM3-CS012	**21.88**	**23.30**	**<5**	**59**	**0.25**	**0.43**	**12**	**27**
PSM3-CS012	**22.20**	**23.61**	**<5**	**63**	**0.25**	**0.46**	**10**	**27**
PSM3-CS012	22.25	23.66	8	56	0.22	0.46	12	24
PSM3-CS017	3.14	4.18	2	56	0.26	0.55	17	26
PSM3-CS017	6.59	8.69	<5	58	0.21	0.55	11	27
PSM3-CS021	10.03	10.96	<5	54	0.25	0.48	11	30
PSM3-CS021	16.60	18.12	5	54	0.26	0.48	11	26
PSM3-CS021	**18.22**	**19.88**	**25**	**45**	**0.25**	**0.39**	**9**	**21**
PSM3-CS021	**19.32**	**21.08**	**4**	**58**	**0.25**	**0.45**	**16**	**23**

high amplitude reflections (Fig. 7.2B). At the time of the failure this horizon was at about 35 m below the seafloor (mbsf; Fig. 7.2B), and its age has been estimated at about 150 kyr BP based on the chronology proposed by Miramontes et al. (2016b).

Three Calypso piston cores sampled this 2-4-m thick layer, during the PRISME3 cruise in 2013, in areas of lower sediment accumulation (Fig. 7.2). This layer is characterized by spongy texture and brownish colour (Fig. 7.2C). Mineralogical composition analyses of 12 samples from cores PSM3-CS012, PSM3-CS017 and PSM3-CS021 using X-ray Diffraction revealed that, in contrast to the adjacent sediment, the particular layer contains zeolitic minerals of analcime type in a concentration of 2-4% (Table 7.1). This difference in bulk mineralogy is not associated with a significantly different clay mineralogical composition (Table 7.2). The zeolitic layer also presents peculiar geotechnical properties. The moisture content is higher (up to 89%, similar to surface sediment values), resulting in a sediment with a lower density (Fig. 2C). This is not related to a rapid sedimentation that would result in underconsolidation, but to the presence of zeolites in the sediment. The liquid limit of the zeolitic sediment is very high (up to 100%), compared to liquid limits in the non-zeolitic sediment that are always below 77% (Fig. 7.3). Therefore, despite its high moisture content, the zeolitic layer is not in a state of potential flow. Plasticity indices, derived from fall cone tests, show high values within the zeolitic layer (50-70), twice the values obtained from the adjacent sediment (Fig. 7.2C). Based on oedometer tests the high plasticity indices of the zeolitic layers are associated with a higher compressibility (Fig. 7.4).

In order to test the mechanical behaviour during shearing of the zeolitic and non-zeolitic material, eight Consolidated Anisotropic Undrained Compression (CAUC) triaxial tests were performed on samples from cores PSM3-CS012 and PSM3-CS021 (Fig. 7.5A). These tests revealed that

the zeolitic layer reaches peak undrained shear strength earlier than the adjacent sediment: at 2% of axial strain in contrast to 8% for the non-zeolitic sediment, both tested at a mean effective stress of 151 kPa. Moreover, the zeolitic sediment presents an enhanced post-peak strain softening behavior (Fig. 7.5A). The adjacent sediment tested at a mean effective stress below or equal to 52 kPa shows a strain hardening behavior, with the undrained shear strength increasing slightly with strain. In contrast, the undrained shear strength of zeolite sediment is reduced by 33% at 15% strain and by 48% at 30% strain (Fig. 7.5A).

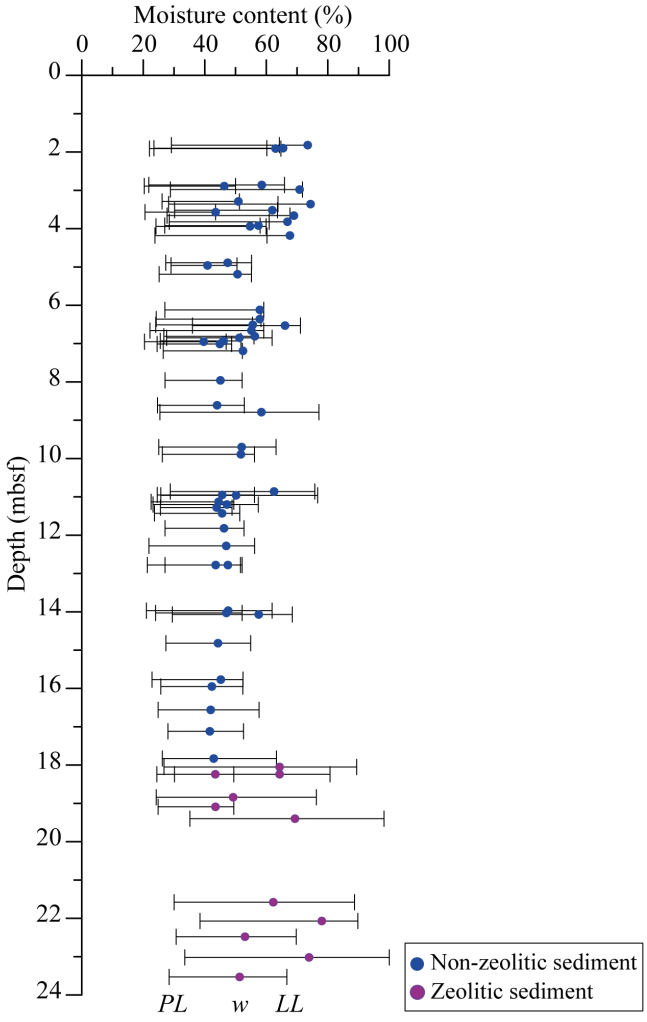

Fig. 7.3. Atterberg limits of non-zeolitic (blue dots) and zeolitic (purple dots) sediment samples: Plastic Limit, *PL*; natural moisture content, *w*; Liquid Limit, *LL*. Note that because the zeolitic samples present natural moisture contents similar to surface sediments but much higher liquid limits, they are not in a state of behaving as a viscous liquid.

7.3. Slope stability modelling

The effect of a zeolitic layer with strain softening behaviour on slope instability is modeled with the commercial software Plaxis 2D (Brinkgreve et al., 2012). The slope geometry is divided into 12 sedimentary layers 5-m thick, except for the zeolitic layer that is 3-m thick (at 35-38 mbsf) and the deepest layer that is 7-m thick (at 53-60 mbsf; Fig. 7.7A; Table 7.3). The initial slope angle in the zone of the moat used for the model is 10.5° (Fig. 7.7A). The sediment layers are modelled as a Mohr-Coulomb material. The zeolitic layer is also modelled as an elastic-perfectly plastic material, but an approximated strain-softening approach is used to simulate the post-peak shear strength loss by applying the method proposed by Lobbestael et al. (2013), based on Lo and Lee (1973) and Potts et al. (1990). The approach consists in tracking the plastic strains and reducing the shear strength accordingly, using the strength-strain curve obtained from the CAUC triaxial test carried out on a zeolitic sediment sample at an initial vertical effective stress of 151 kPa (Fig. 7.5A). The zeolitic layer is

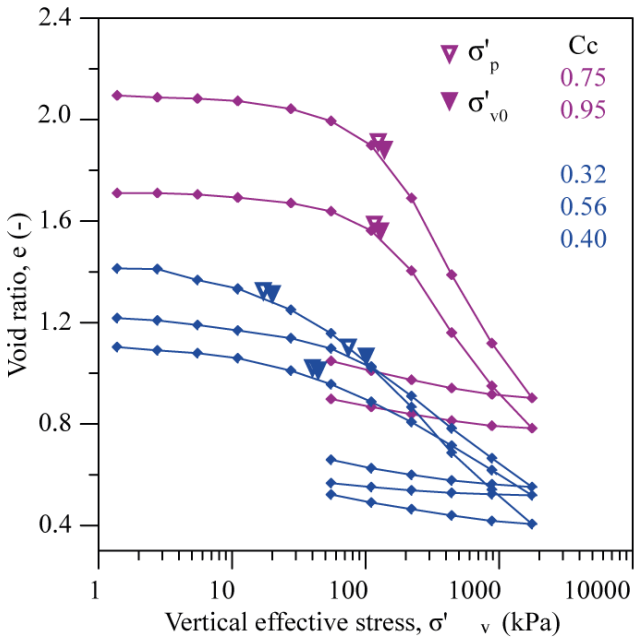

Fig. 7.4. Void ratio - vertical effective stress plot obtained from oedometer tests on zeolitic sediment (purple line) and non-zeolitic sediment (blue line) from cores PSM3-CS012 and PSM3-CS021. The initial vertical effective stress (σ'_{v0}) and the preconsolidation stress (σ'_{p}) are represented for each sample with filled and open triangles, respectively. Note that the zeolitic samples present higher compression indices (*Cc*) and are normally consolidated ($\sigma'_{p} \approx \sigma'_{v0}$).

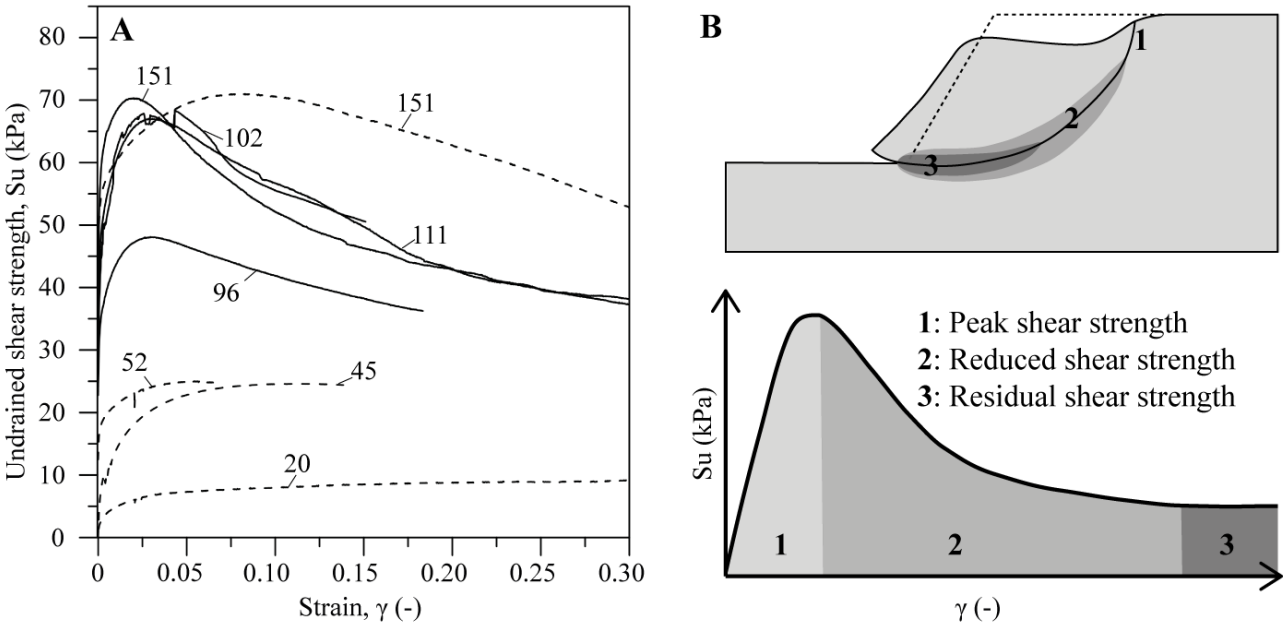

Fig. 7.5 (A) Undrained shear strength obtained from Consolidated Anisotropic Undrained Compression (CAUC) triaxial tests performed on samples from cores PSM3-CS021 and PSM3-CS012 in non-zeolitic sediment (dashed line) and in zeolitic sediment (solid line). The mean effective stress (kPa) after saturation and consolidation applied in each test is marked in the figure. See Fig. 7.2A for core location. **(B)** Scheme explaining the strain softening behaviour: and failure surface propagation with post-peak undrained shear strength reduction with increasing strains.

divided into small lateral sections (50 m long and 3 m high) to locally reduce the strength parameters in successive steps. The initial stresses are generated using the K_0 procedure, in which the *in situ* horizontal effective stresses are calculated using the vertical effective stress. The undrained shear strength (*Su*) used for slope stability modelling was obtained from laboratory vane shear tests on core PSM3-CS017 and extrapolated below 25 mbsf (Fig. 7.6). This core was selected as a reference for the model due to its localization near the Pianosa Slump headwall (Fig. 7.2A). Although the core PSM3-CS017 did not reach the zeolitic layer, cores PSM3-CS011, PSM3-CS012 and PSM3-CS021 could sample this regional layer in zones with lower sedimentation rates. *Su* was considered to increase constantly with depth, even in the zeolitic layer, because CAUC triaxial tests provide the same *Su* value on zeolitic and non-zeolitic material at the same mean effective stress (151 kPa) after saturation and consolidation (Fig. 7.5A). The shear strain degradation curve defined from the CAUC triaxial test at 151 kPa in the zeolitic material was used as a reference for modelling the strain softening behaviour. We did not use its absolute strength value because the sample was consolidated at a higher mean effective stress than in the natural conditions. Therefore, we use the *Su* values obtained from vane shear tests that are also more abundant and located at the site of the slope failure.

In order to reproduce the observed slope geometry, we simulate three phases, each one with an instantaneous erosion of 1 m at the central part of the moat, resulting in a final 3-m erosion. Polygons are 1 m thick in the central part of the moat and thin progressively

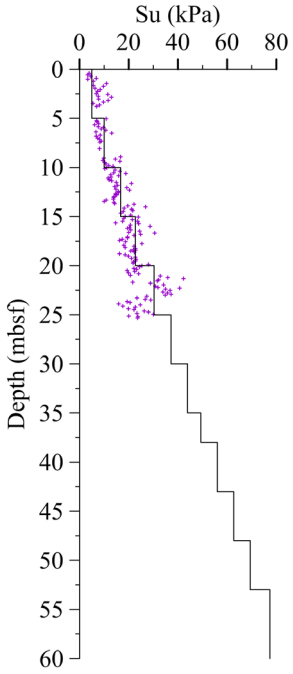

Fig. 7.6. Undrained shear strength (*Su*) used for slope stability modelling (solid line), obtained from laboratory vane shear tests on core PSM3-CS017 and extrapolated below 25 mbsf.

Table 7.3. Sediment parameters used in the slope stability model. The hydraulic conductivity was obtained with the falling head method.

Type of sediment	Depth top (mbsf)	Depth bottom (mbsf)	Unit weight ($kN \cdot m^{-3}$)	Void ratio (-)	Hydraulic conductivity ($m \cdot s^{-1}$)	Effective Young's modulus (kPa)	Undrained Poisson ratio (-)	Undrained shear strength (kPa)
Normal	0	5	15.6	1.86	$1.31 \cdot 10^{-8}$	1099	0.374	5.0
Normal	5	10	16.8	1.45	$7.31 \cdot 10^{-9}$	1099	0.374	10.0
Normal	10	15	17.2	1.16	$5.16 \cdot 10^{-9}$	1099	0.374	16.7
Normal	15	20	17.6	1.20	$3.85 \cdot 10^{-9}$	1099	0.374	22.7
Normal	20	25	18.0	1.14	$3.85 \cdot 10^{-9}$	1099	0.374	30.3
Normal	25	30	18.4	1.00	$3.85 \cdot 10^{-9}$	1099	0.374	37.2
Normal	30	35	18.8	0.90	$3.85 \cdot 10^{-9}$	1099	0.374	43.9
Zeolitic	35	38	15.8	2.10	$4.80 \cdot 10^{-8}$	1099	0.374	49.3
Normal	38	43	19.2	0.90	$3.85 \cdot 10^{-9}$	1099	0.374	56.0
Normal	43	48	19.2	0.90	$3.85 \cdot 10^{-9}$	1099	0.374	62.7
Normal	48	53	19.2	0.90	$3.85 \cdot 10^{-9}$	1099	0.374	69.4
Normal	53	60	19.2	0.90	$3.85 \cdot 10^{-9}$	1099	0.374	77.4

over a distance of 200 m upslope and downslope of the central part of the moat. The slope stability calculation is performed under undrained conditions since the development of catastrophic failure, which is the most critical scenario, is expected to occur very rapidly and will thus mobilise the undrained parameters of the sediment (Puzrin et al., 2016).

The application of a 3 m-erosion increases the slope angle at the moat to 11.3° and generates in the zeolitic layer a total deviatoric strain of 0.14 (Fig. Fig. 7.7B). Based on the CAUC triaxial tests, at this strain level the peak undrained shear strength is reduced by 33% (Fig. 7.5A). The slope stability analysis performed before the erosion phases provides a Factor Of Safety (FOS) of 1.10 with a shallow potential failure surface (Fig. 7.7A). After the last erosion phase and the induced strain softening within the zeolitic layer, the FOS remains comparable (=1.09) but the failure surface is enlarged and deepened crossing the sensitive layer (Fig. 7.7B). FOS values lower or equal to 1 indicate that the slope is unstable. The FOS values close to 1 here presented suggest that the slope is only marginally stable.

7.4. Discussion and conclusion

7.4.1. Role of zeolites in slope instability

The presence of zeolitic sediments with a strain softening behaviour may have an important impact on slope stability. Indeed, a pre-failure slope movement induces localised strain along a potential failure surface. For strain-softening materials, the development of high localized shear strains at the toe and mid-slope area will cause the degradation of the material properties since the post-peak undrained shear strength decreases with increasing strains (Fig. 7.5B). The degradation of the shear strength will also favour the retrogressive propagation of the strain accumulations and therefore

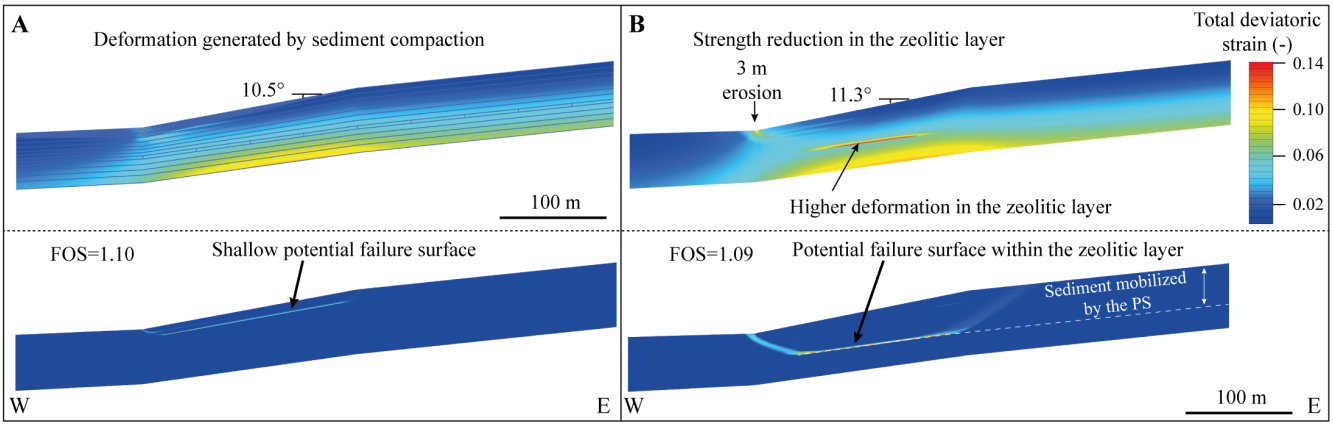

Fig. 7.7. Total deviatoric strain after sediment consolidation **(A)** and after strength reduction in the zeolitic layer caused by 3 m of erosion in the moat **(B)**. The lower contour plots show the critical failure surface at stages **(A)** and **(B)**. The observed failure surface of the Pianosa Slump is marked with a dashed white line.

accelerate the strength degradation along the weak plane while the rest of the body preserves its original strength (Leroueil, 2001).

Undercut has been widely proven to generate slope instability on land (Troncone, 2005), as well as in submarine canyons (Sultan et al., 2007). In the present study, the erosion would not have played such an important role without the presence of a potential weak layer with strain softening behaviour. Zeolites, even in low quantities (2-4%), can drastically change the sedimentological and mechanical properties of the sediment. The results of the slope stability analysis show that a 3-m erosion in the moat, located at the foot of the slope, would generate enough strain to reduce the strength of the zeolitic layer at a depth of 35 m below the seafloor due to its strain softening behaviour (Fig. 7.7). As a consequence, this process could trigger a submarine landslide without any additional external factor. The predicted failure surface does not extend upslope as much as the observed PS failure surface (Fig. 7.7B). The reason may be that the predicted failure surface may correspond to the first stage of a retrogressive process with several landslide stages that would lead to a much larger mass movement. Kvalstad et al. (2005) and Dey et al. (2016) demonstrated through numerical modelling that in sensitive sediment large landslides could be formed by the propagation of shear bands and retrogressive failure. Our findings concerning the mechanism of weak layer formation in fine-grained marine sediment with altered volcanic deposits could be applicable to all continental margins close to zones with volcanic material (Fig. 7.1). The strength of a zeolitic layer could be reduced by erosion, as it was shown for the present study area, but it could be also reduced by other external processes such as earthquake, overloading, sedimentation and steepening.

7.4.2. Origin and distribution of zeolites in marine sediments

The origin of zeolites in the Pianosa Ridge is probably not linked to the burial metamorphism of volcanic ashes since it was at only 35 mbsf at the time of the mass failure and this type of alteration usually happens at hundreds of meters below the surface (Di Roberto et al., 2012). Moreover, no volcanic ashes were found in the Corsica Trough. Zeolites were probably produced in the Tuscan magmatic province (in Italy; Fig. 7.1) and then transported to the continental slope. At the time of the zeolitic layer formation (150 kyr BP), the sea level was about 100 m below the present-day sea level (Rohling et al., 2014) and the shoreline was almost at the shelf edge (Fig. 7.2A), favouring the transport and accumulation of zeolites in the eastern flank of the Corsica Trough (Fig. 7.2). Zúñiga et al. (2007) identified a fine-grained turbidite rich in zeolites in the Balearic abyssal plain, probably originated on the Sardinian continental margin and also characterised by high moisture contents. This finding evidences that zeolites can be transported and deposited at hundreds of kilometers away from their formation site.

The presence of zeolites has been widely documented in volcanic settings, where mass failures are also common processes (Watt et al., 2014): in the Circum-Pacific arc (Machiels et al., 2014), in the Antilles volcanic arc (Jolly et al., 2001), in the Mediterranean Sea (Altaner et al., 2013) and in volcanic islands such as the Canary Islands (Donoghue et al., 2008), Cape Verde (Barker et al., 2009), Hawaii (Morgan and Clague, 2003), Iceland (Weisenberger and Selbekk, 2009) or Reunion (Bachèlery et al., 2003). The formation of sediment layers rich in zeolites can be extended in time and is not only restricted to the period of the zeolitic minerals formation, since they can be stocked onshore or on the continental shelf and later transported to the continental slope. Detecting the presence of zeolites in marine sediments can help understand the preconditioning conditions of submarine landslides on continental margins close to volcanic zones.

CHAPTER 8. Conclusions and perspectives

CHAPITRE 8. Conclusions et perspectives

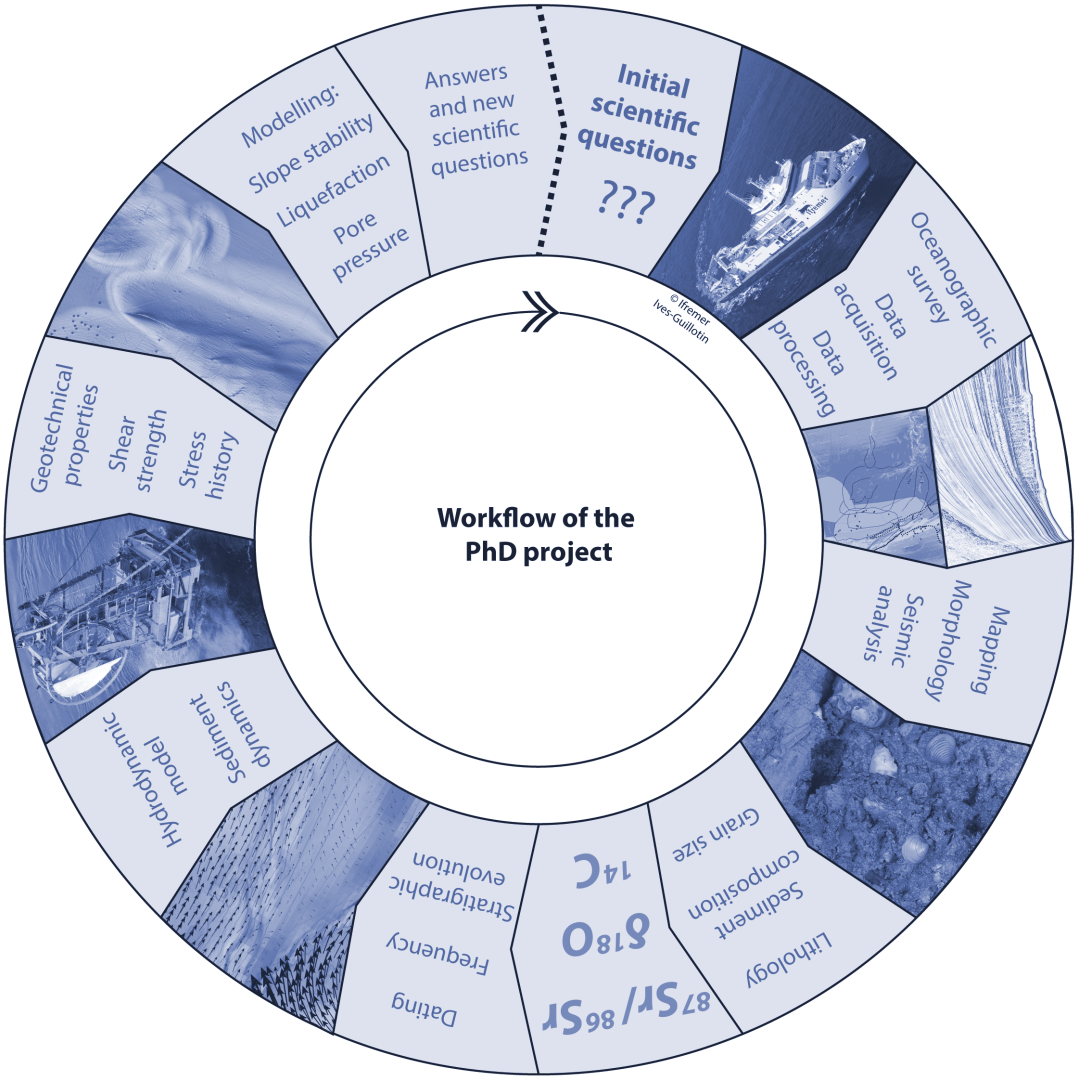

The objectives of this thesis were to identify the controlling parameters of seafloor instability and the nature of the main sedimentary processes generating contourite deposits in the Pianosa Ridge (Northern Tyrrhenian Sea). In this chapter the main conclusions of this work are summarised as the answers to the questions proposed in the introduction that were motivated by the present-day scientific discussions in the fields of submarine landslides and contourites, explained in detail in Chapter 1. The new questions and the perspectives of future work arisen from the present PhD project are explained at the end of Chapter 8.

8.1. What is the size of the landslides along the Pianosa Ridge? Is it related to the slope gradient?

Most compilations of submarine landslides consider Mass Transport Deposits (MTDs) large when their volume exceeds 1 km^3 (Urgeles and Camerlenghi, 2013; Urlaub et al., 2013; Talling et al., 2014; Pope et al., 2015). Only two out of the 11 MTDs identified in the Pianosa Ridge have volumes larger than 1 km^3 (C1 and C4 with 2.62 and 1.86 km^3 respectively). The other submarine landslides are smaller and their volume range between 0.04 and 0.67 km^3.

Remarkable differences in MTD size have been observed in the Pianosa Ridge associated to different types of slopes. In area B the mean slope gradient is higher and the MTDs are smaller than in area C. This difference is related to the slope gradient and to a higher sediment accumulation in area C (Fig. 8.1).

8.2. What is the frequency of the submarine landslides? Is there a climatic control of slope instability along the Pianosa Ridge?

At least nine submarine landslides took place along the Pianosa Ridge during the last 500 kyr, resulting in a frequency of 1.8 submarine landslides every 100 kyr. Only MTD C1 could be directly dated using radiocarbon isotopes. The age of the other MTDs was obtained by seismic correlation with borehole GDEC4-2, resulting in large age uncertainties that make difficult the interpretation of any climatic control for this group of MTDs (Fig. 8.2). The youngest MTDs in areas B and C (B1-C1 and B2-C2) seem to have occurred approximately at the same time in both areas. C1 could be analysed in more detail and it has been found that it was formed during a sea level fall, a period of faster bottom currents.

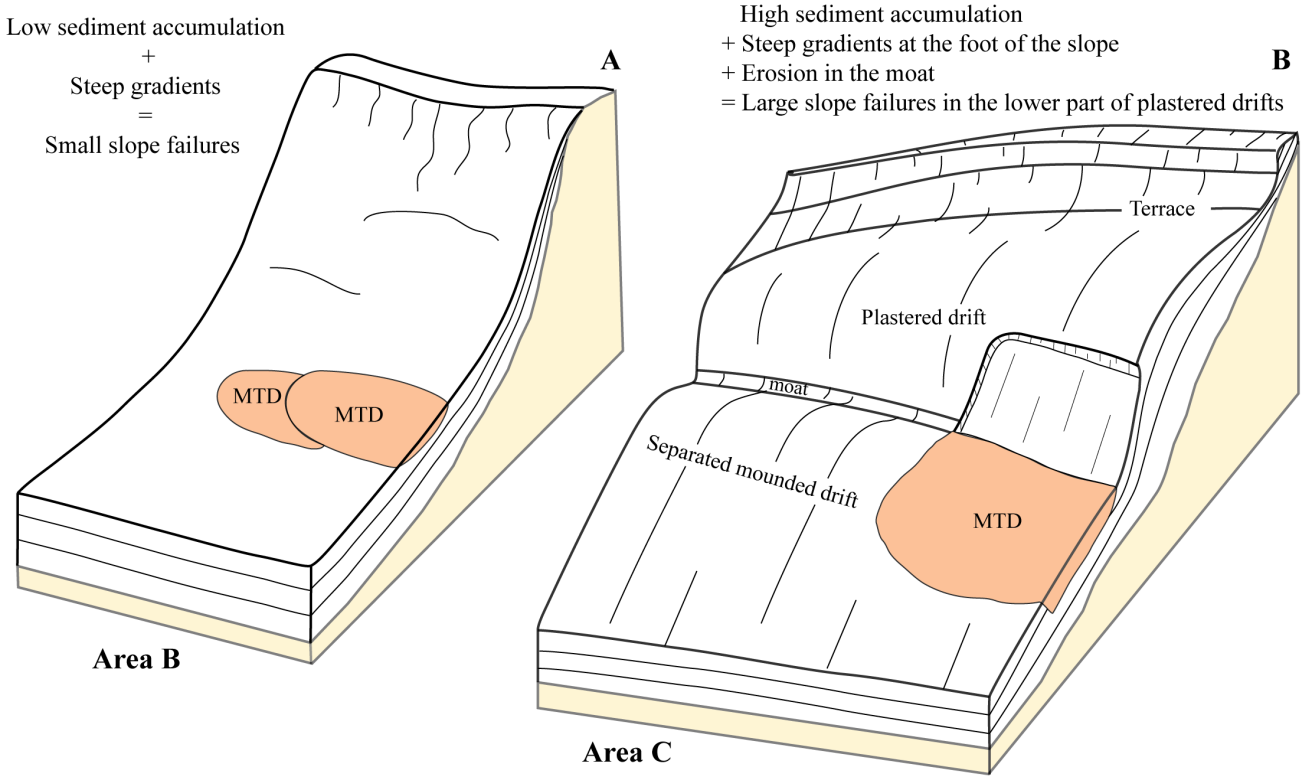

Fig. 8.1. 3D sketches showing two different types of slopes where mass-wasting processes took place, corresponding to area B in central part of the Pianosa Ridge **(A)** and area C, located at the south of the Pianosa Ridge **(B)**.

8.3. What are the predisposing and triggering factors of submarine landslides in the Corsica Trough?

The main predisposing factors are steep slopes in area B and A, the latter a canyon flank, and the particular convex morphology of the plastered drift in area C that generates steep slopes in the lower part of the drift. Another predisposing factor is the presence of a weak layer with strain softening behaviour (strength loss with increasing strain) caused by the zeolites (alteration product of volcanic rocks) in the muddy sediment. This weak layer formed the basal failure surface of C1. We found no evidences for other predisposing factors such as gas charging or overpressure generation due to rapid sediment accumulation.

The triggering factor could be for most of the cases undercutting by bottom currents, as proven for C1. Although it cannot be deduced from our chronological framework whether there is a climatic control of slope failure, we know that undercutting generated by enhanced bottom currents is an important triggering factor in this sector and since bottom currents were faster during sea level falls and sea level low stands (Toucanne et al., 2012; Mintoʾo et al., 2015), we expect a higher occurrence of submarine landslides during these periods. The tectonic activity in the Corsica Trough is very low since late Messinian (Pascucci et al., 1999) and the present-day seismicity is also considered to be very low (Scisciani and Calamita, 2009). Moreover, the absence of sandy layers susceptible to seismic liquefaction in the plastered drift where the main submarine landslides took place, suggests that earthquakes did not play a major role in triggering slope failures in this area.

8.4. Is there a high geological risk for the Corsica island and the Tuscan archipelago?

The geological hazard and therefore associated risk at present could be considered low since most of the MTDs are old (age > 42 kyr). Only one MDT (A) is of Holocene age, although its age could not have been precisely determined. It has been shown that MTDs in the Pianosa Ridge may have been triggered by undercutting during periods of strong bottom currents (i.e. during sea level falls). According to the circulation results, the seafloor in the Pianosa Ridge would not be eroded during the whole year and therefore, mass wasting processes are not expected to occur at present, unless human activities undercut the slope.

8.5. Do contourites have intrinsic or inherited properties that make them susceptible to slope failure?

Muddy contourites have slightly different sedimentological and geotechnical properties from hemipelagites in the Corsica Trough. The plastered drift presents finer material, lower density and lower undrained shear strength than hemipelagites. However, these differences are not so important as the morphology of contourites for slope instability. Plastered drifts are convex-shaped drifts located on the continental slope that present higher slope gradients in the lower part (due to the action of bottom currents), making this zone potentially more unstable. This zone is usually affected by submarine landslides in the Pianosa Ridge and in many other margins (Fig. 8.1; Preu et al., 2013; Ercilla et al., 2016; Hernández-Molina et al., 2016).

8.6. What is the origin of the sediment?

The eastern flank of the Corsica Trough is a starved margin with no direct connection to the continent. Moreover, multiple basins in the Tuscan shelf trap most of the sediment carried by the Italian rivers to the Tyrrhenian Sea (Roveri, 2002). Therefore, the main source of fine-grained sediment to the Pianosa Ridge is the Corsican rivers. This sediment could be

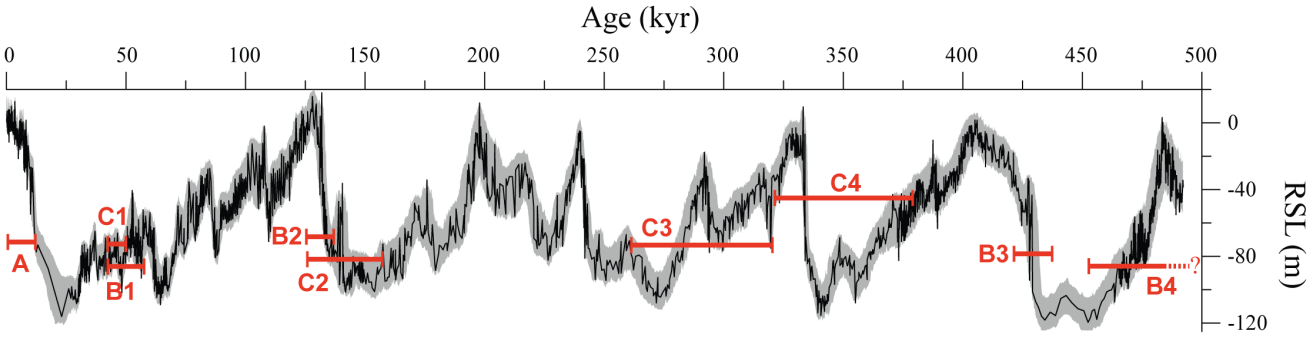

Fig. 8.2. Age of the MTDs of the Pianosa Ridge plotted over the sea level curve (Grant et al., 2014).

redistributed by the oceanic gyres present in the Corsica Trough. The bioclastic sand is probably originated in the Tuscan shelf or in the shelf edge prism and mainly transported to the slope during sea level falls.

8.7. What are the sedimentation rates in contourties?

The sediment accumulation in the contourites of the Pianosa Ridge depends on the sediment supply and thus on the activity of the turbidity currents from the Corsican margin. Turbidites are mainly formed during sea level low-stands and during these periods sedimentation rates can be up to 115 cm·kyr^{-1}. When the turbidite system is disconnected during sea level high-stands, sedimentation rates decrease in contourites down to 10 cm·kyr^{-1}.

8.8. How is the morphology and geological evolution of the contourites?

Despite being a relatively small study area with relatively small-scale contourite drifts, the morphology of contourites is very varied and we can find most of the typical drift forms: plastered drift, separated mounded drift, multicrested drift and the peculiar sigmoid drift.

Erosive processes are enhanced during cold periods, they more intense during sea level falls. During sea level low-stands contourites present the fastest growth due to the high sediment availability through the connected turbidite system. Although at present contourites grow slowly because of the low sediment availability, the contourite morphology is preserved due to enhanced bottom currents during winter that may induce erosion in the moat. This seasonal erosion in the Corsica Trough may not be very strong since no evidences have been observed in the seismic data. Therefore, we do not expect strong undercutting that could trigger a submarine landslide at present.

8.9. What is the intensity and variability of the currents that control the formation of contourites?

At present bottom currents are in general faster during winter than during summer and they were also fast in the past during cold periods (Toucanne et al., 2012; Mintoʾo et al., 2015). Contourite drifts develop in zones that present slow bottom currents (mean velocity<10 cm·s^{-1}) during the whole year, even during the cold season. On the contrary, the erosive environments of the contourite depositional systems are commonly under erosion during winter and usually present mean velocity values higher than 10 cm·s^{-1} in winter.

PERSPECTIVES

In this study we have demonstrated that low amounts of zeolites can change the physical and mechanical properties of fine-grained marine sediments. This has notably led to the inference that the strain softening behaviour associated with the presence of zeolites participated in the development of the failure surface of the Pianosa Slump. However, the precise mechanism by which zeolites tend to promote strain softening remains to be unravelled. Yukselen-Aksoy (2010) showed that natural zeolitic soils containing 70-90 % of zeolites and small quantities of sand are mechanically strong and do not show a pronounced strain softening behaviour. Besides Newson et al. (2006) showed that minerals with high ion exchange capacities like zeolite tend to cement or bind finer-grained particles together with no evidence of strain softening. Therefore, further investigation needs to be carried out to evaluate whether or not, when the content of zeolites is low, as in our case, sediment particles are effectively cemented together and if the breakdown of the cemented/aggregated structure during shearing is the reason behind sediment strain softening.

Further comparison of the sedimentological and geotechnical properties between contourites and hemipelagites needs to be done to better prove, confirm or deny their similarities. For that purpose, it would be necessary to compare more cores and in situ measurements from other geological settings, as well as to perform a statistical analysis.

Furthermore, to better understand the role of contourites in slope instability, we need to improve the basic knowledge about contourites since it is still a topic in development, as demonstrated by 3 special issues in Marine Geology (vol. 375, 377 and 378) dedicated to contourites and/or bottom currents in 2016. The criteria most commonly used to identify contourites are based on seismic data and the identification from sedimentary facies only from cores or outcrops remains challenging with the current knowledge. Contourites are defined as the sediments deposited or substantially reworked by the persistent action of bottom currents (Stow et al.,2002; Rebesco, 2005, 2014). This definition includes a large variety of sediments: sandy contourites formed by the winnowing of hemipelagites or turbidites, reworked turbidites, sand dunes, muddy mounded drifts, muddy sheeted drifts... Stow and Tabrez (1998)

state that hemipelagites are deposited by a combination of vertical settling and slow lateral advection. But how strong has to be the lateral advection to consider the deposit as a contourite? It is very problematic especially for the identification of muddy contourites because, as we have shown in this study, muddy sediment drifts mainly develop in the zones of low bottom currents. Mounded sediment morphologies are formed because of a heterogeneous distribution of the bottom currents that results in a preferential sediment accumulation in the zone of minimum currents. The oceans are in continuous movement, so it is difficult to imagine that the sedimentation could not be affected by the currents. The calculated mean current velocities near the seafloor for the NW Mediterranean Sea are mostly above 3 $cm \cdot s^{-1}$ and often above 10 $cm \cdot s^{-1}$ even in the deepest parts of the basin in summer and in winter (Fig. 8.3). Continental margins are more affected by intense bottom currents in winter, with mean velocities commonly above 10 $cm \cdot s^{-1}$ (Fig. 8.3B). A particle of coarse silt has a settling velocity of 0.1 $cm \cdot s^{-1}$ according to Gibbs et al. (1971). If it settles down in a zone of the ocean with weak currents of 3 $cm \cdot s^{-1}$ through the whole water column, it would take 11 days until the particle reaches 1000 m water depth and it would be deflected by 30 km from its origin. If the particle is fine silt with a settling velocity of 0.01 $cm \cdot s^{-1}$ (Gibbs et al., 1971) it would need almost 4 months to reach 1000 m and it would be deflected from its origin by 300 km. The sediment suffers always lateral advection while settling down. Therefore, we need to make more effort in quantifying sediment transport in deep settings using measurements and modelling in order to understand the strength of oceanic currents in shaping continental margins.

The effect of currents in deep-settings has been probably underestimated because the continuous effects of relatively weak currents are overwhelmed in the continental margins where down-slope gravitational processes dominate. In my opinion we also need to refocus the term contourite because the definition "sediments deposited or substantially reworked by the persistent action of bottom currents" could be applied to the whole oceanic seafloor since all the sediment is deposited under the effect of currents, apart from gravity flows. As used for this study, I suggest to restrict the use of the term "muddy contourite drifts" to the mounded morphologies of fine-grained sediment, unless we accept that all the seafloor is a contourite and that the term hemipelagite is restricted to the composition of the sediment and not to the process of pure vertical settling.

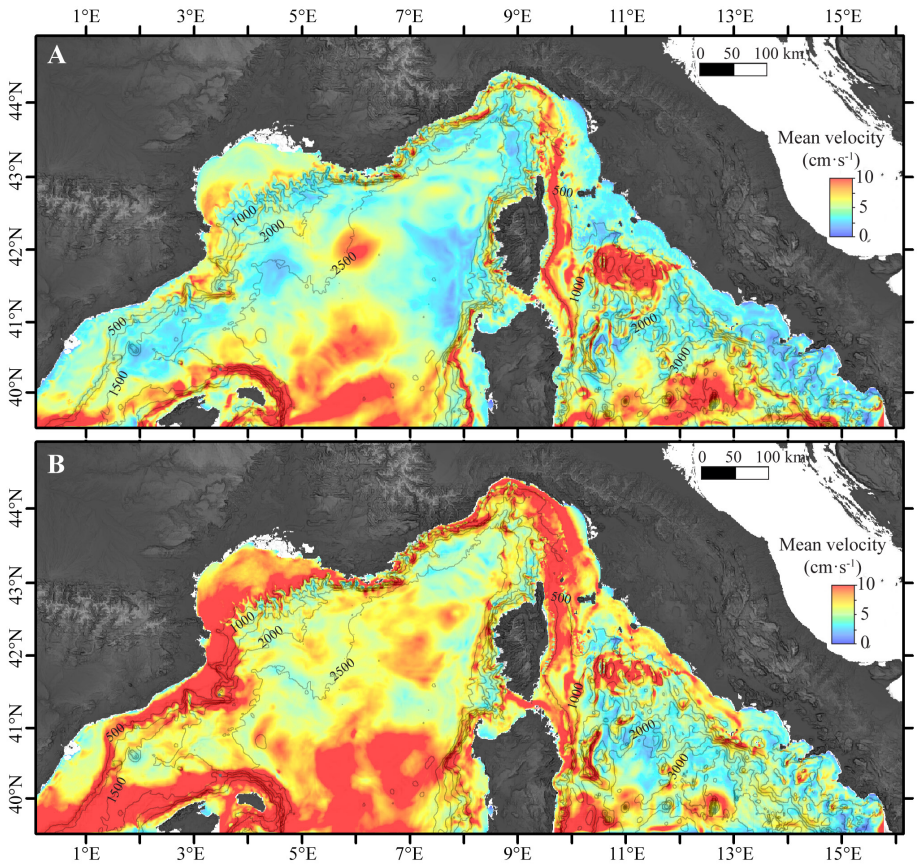

Fig. 8.3. Mean velocity near the seafloor calculated using the MARS3D model in the MENOR configuration during **(A)** summer 2013 (July, August and September) and **(B)** winter 2013 (January, February and March). Note that mean velocity values are mostly above 3 $cm \cdot s^{-1}$ and often above 10 $cm \cdot s^{-1}$ even in the deepest parts of the basin. The bathymetric contours are represented every 500 m.

Les objectifs de cette thèse étaient d'identifier les paramètres contrôlant l'instabilité des pentes, ainsi que la nature des processus sédimentaires générant des dépôts contouritiques le long de la Ride de Pianosa (Mer Tyrrhénienne septentrionale). Dans ce chapitre les conclusions principales de ce travail sont résumées sous la forme de réponses aux questions posées dans l'introduction. Ces questions ont été motivées par les discussions scientifiques actuelles dans les domaines des glissements sous-marins et des contourites- détaillées dans le Chapitre 1. Les nouvelles questions découlant de ce travail ainsi que les perspectives sont présentées à la fin de ce chapitre.

8.1. Quelle est la taille des glissements sous-marins le long de la Ride de Pianosa ? Est-elle liée au gradient de pente ?

La plupart des compilations de glissements sous-marins considèrent comme glissements de grande taille ceux dont le volume est supérieur à 1 km^3 (Urgeles and Camerlenghi, 2013 ; Urlaub et al., 2013 ; Talling et al., 2014 ; Pope et al., 2015). Seulement deux des 11 glissements identifiés le long de la Ride de Pianosa appartiennent à cette catégorie (C1 et C4 avec 2,62 et 1,86 km^3 respectivement). Les autres glissements sous-marins son plus petits avec des volumes compris entre 0,04 et 0,67 km^3.

Des différences notables quant à la taille des glissements ont été observées le long de la Ride de Pianosa selon la pente sur laquelle ils se sont produits. Dans la zone B où la pente moyenne est plus élevée que dans les autres zones, les glissements sont de plus petite dimension que ceux de la zone C. Cette différence est attribuée au gradient de pente mais aussi à une accumulation de sédiments plus importante dans la zone C (Fig. 8.1).

8.2. Quelle est la fréquence des glissements sous-marins ? Existe-il un contrôle climatique de l'instabilité de pente le long de la Ride de Pianosa ?

Au moins neuf glissements sous-marins se sont mis en place le long de la Ride de Pianosa pendant les derniers 500 ka, ce qui suggère une fréquence de 1,8 glissements sous-marins tous les 100 ka. Néanmoins, seul le glissement C1 a pu être daté directement par des âges radiocarbone. L'âge des autres glissements a

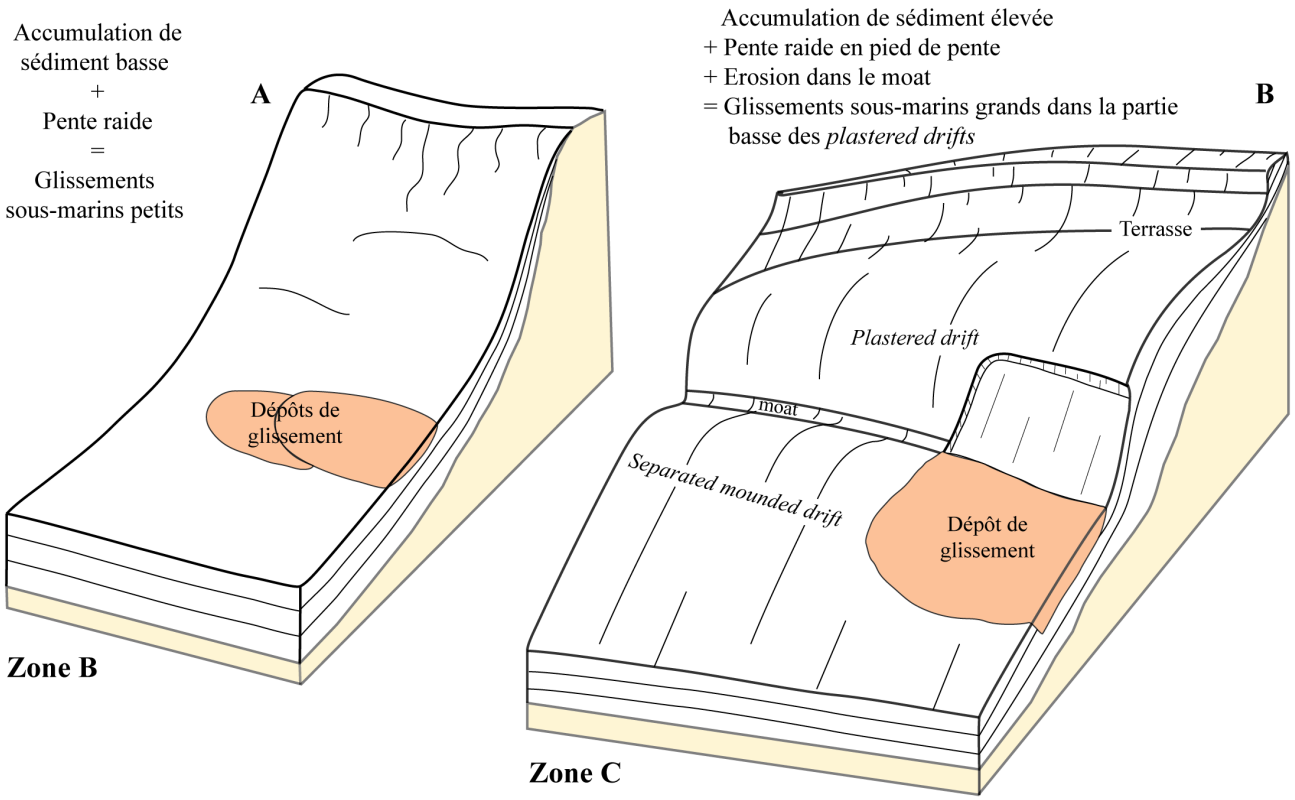

Fig. 8.1. Modèles 3D montrant pour deux morphologies et pentes différentes les glissements sous-marins associés. **(A)** Zone B dans la partie centrale de la Ride de Pianosa et **(B)** zone C, localisée dans la partie sud de la Ride de Pianosa.

été obtenu à partir d'une corrélation sismique avec le forage GDEC4-2, ce qui est implicitement associé à une importante incertitude ne permettant pas de tirer de conclusions fermes quant à un possible contrôle climatique pour les glissements de ce groupe (Fig. 8.2). D'après la stratigraphie sismique, il semble que les glissements les plus jeunes des zones B et C (B1-C1 et B2-C2) se soient produits à la même époque. D'après les analyses détaillées réalisés pour C1, ce glissement se serait formé pendant une chute du niveau marin correspondant à une période où les courants sont supposés plus rapides.

8.3. Quels sont les facteurs prédisposants et déclenchants des glissements sous-marins dans le Canal de Corse?

Les analyses morphologiques et numériques concourent à démontrer que les pentes raides constituent le principal facteur prédisposant dans les zones A et B. Une conclusion similaire ressort pour la zone C où les pentes raides se localisent dans la partie basse des dépôts contouritiques où sont observés les morphologies convexes du « plastered drift ».

L'autre facteur prédisposant mis en évidence est la faiblesse d'une couche dont le comportement mécanique se caractérise par du radoucissement (perte de résistance avec le cisaillement) du fait de la présence de zéolites (produits de l'altération des roches volcaniques) dans du sédiment vaseux. C'est dans cette couche que s'est notamment développé le plan de rupture du glissement C1 (*Pianosa Slump*).

Il n'y a pas d'évidences concrètes quant au rôle qu'ont pu jouer l'accumulation rapide de sédiment où le chargement en gaz en tant que facteur prédisposant des instabilités observées.

Comme cela a pu être mis en évidence pour le glissement C1, l'érosion en pied de pente générée par les courants de contour ressort comme le facteur déclenchant principal dans la zone d'étude. Même si l'analyse chronologique n'a pu démontrer l'existence d'un contrôle climatique sur les instabilités observées, on peut suspecter une relation avec les variations du niveau marin dans la mesure où ceux-ci influencent les courants de contour et de fait l'érosion sur le fond. A ce titre, plusieurs auteurs (Toucanne et al., 2012 ; Minto'o et al., 2015) ont montré que les courants étaient bien plus puissants dans la zone d'étude pendant les périodes de baisse du niveau marin. Cela tend à indiquer que les périodes de baisse du niveau marin sont les plus favorables au déclenchement d'instabilité dans la zone.

L'activité tectonique dans le Canal de Corse est demeurée faible depuis le Messinien tardif (Pascucci et al., 1999) jusqu'à l'actuel (Scisciani and Calamita, 2009). De plus, l'absence de couches de sable susceptibles de se liquéfier dans la zone étudiée suggère que les séismes n'ont pas participé au déclenchement de glissements dans cette zone.

8.4. Existe-il un risque géologique élevé pour l'Île de Corse et pour l'archipel de la Toscane ?

L'aléa géologique actuel et le risque associé pourraient être considérés assez faibles puisque la plupart des glissements sous-marins identifiés sont anciens (âge > 42 ka). Seul le glissement (A) s'est produit durant l'Holocène, même si son âge précis demeure incertain. Il a été démontré que les glissements sous-marins de la ride de Pianosa ont pu être déclenchés par l'érosion basale pendant des périodes où les courants de fond étaient particulièrement forts (c'est-à-dire pendant la baisse du niveau de la mer et le bas niveau marin).

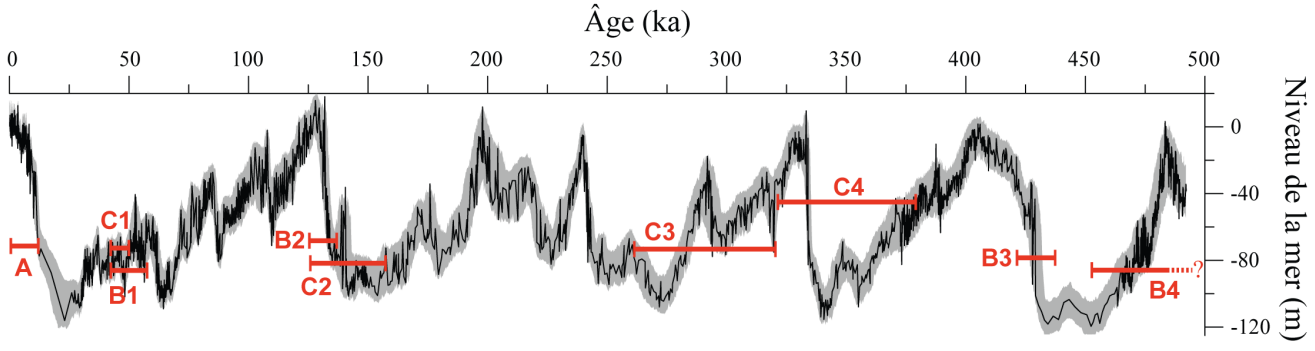

Fig. 8.2. Âge des glissements sous-marins de la Ride de Pianosa représentée sur la courbe du niveau de mer relatif (Grant et al., 2014).

On ne s'attend donc pas à la formation de glissements sous-marins avec l'intensité actuelle des courants de fond, à moins que des activités humaines provoquent de l'érosion basale.

8.5. Est-ce que les contourites ont des propriétés intrinsèques ou héritées qui les rendent susceptibles à l'instabilité de pente ?

Les analyses sédimentologiques et géotechniques montrent des différences entre les propriétés des contourites vaseuses et des sédiments hémipélagiques dans le canal de Corse. Les « plastered drifts » présentent du matériel plus fin avec une densité plus basse et une résistance au cisaillement plus faible que les sédiments hémipélagiques. Il ressort néanmoins de cette étude que les contourites sont plus susceptibles de se déstabiliser du fait de la morphologie des dépôts. Les « plastered drifts » sont des dépôts contouritiques avec une forme convexe qui se forment le long des pentes continentales et qui présentent une pente plus raide dans la partie basse (à cause des courants). Cette zone est celle qui est la plus fréquemment affectée par les glissements sous-marins sur la Ride de Pianosa au même titre que sur d'autres marges (Fig. 8.1; Preu et al., 2013; Ercilla et al., 2016; Hernández-Molina et al., 2016).

8.6. Quelle est l'origine du sédiment ?

Le flanc est du Canal de Corse n'enregistre que de faibles apports sédimentaires provenant indirectement du continent. De plus, plusieurs bassins du plateau de Toscane piègent la plupart des sédiments transportés vers la Mer Tyrrhénienne par les fleuves italiens. Par conséquent, les fleuves corses sont la source principale de sédiment alimentant la ride de Pianosa. Le sédiment peut être redistribué par les gyres présents dans le canal de Corse.

8.7. Quels sont les taux d'accumulation des contourites ?

L'accumulation de sédiment dans les contourites de la Ride de Pianosa dépend de l'apport sédimentaire et donc de l'activité des courants de turbidité. Les turbidites se forment principalement pendant les périodes de bas niveau marin avec des taux de sédimentation des contourites qui peuvent atteindre 115 $cm{\cdot}ka^{-1}$. Quand le système turbiditique est déconnecté pendant les périodes de haut niveau marin, les taux de sédimentation des contourites diminuent jusqu'à 10 $cm{\cdot}ka^{-1}$.

8.8. Quelle est la morphologie des contourites et comment évolue-t-elle ?

Malgré la relativement faible emprise géographique de la zone d'étude et la faible extension des dépôts contouritiques, la morphologie des contourites varie selon la plupart des types reconnus dans la littérature: «plastered drift», «separated mounded drift», «multicrested mounded drift» et le particulier «sigmoid drift».

Les processus érosifs sont plus intenses pendant les périodes froides, avec une intensité maximale pendant les baisses du niveau marin. Pendant les périodes de bas niveau marin, les contourites présentent une croissance rapide à cause d'une disponibilité élevée des sédiments à travers la connexion du système turbiditique. Même si à présent les contourites ne croissent que lentement à cause d'une disponibilité sédimentaire faible, la morphologie des contourites est préservée grâce aux courants de fond intenses pendant l'hiver qui peuvent induire l'érosion du moat. Aucune évidence soulignant des érosions actuelles dans le canal de Corse n'a été observée dans les données sismiques. Par conséquent, il est peu probable que les courants actuels puissent générer suffisamment d'érosion pour déclencher des glissements actuellement.

8.9. Quelle est l'intensité et la variabilité des courants contrôlant la formation des contourites ?

A présent, les courants de fond sont généralement plus forts pendant l'hiver que pendant l'été et ils ont été aussi plus rapides pendant les dernières périodes froides (Toucanne et al., 2012 ; Mintoʾo et al., 2015). Les dépôts contouritiques se développent dans les zones de courants de fond faibles (normalement vitesse moyenne < 10 $cm{\cdot}s^{-1}$) pendant toute l'année, même pendant la saison froide. Au contraire, les environnements érosifs des systèmes contouritiques sont généralement sujets à des pertes de sédiment plus fortes en hiver lorsque les vitesses moyennes des courants de fond sont supérieures à 10 $cm{\cdot}s^{-1}$.

PERSPECTIVES

Dans cette étude, nous avons démontré que des quantités faibles de zéolites peuvent engendrer de forts changements des propriétés physiques et mécaniques du sédiment marin fin. Cela a notamment conduit à déduire que le radoucissement associé à la présence de zéolite a participer au développement de la surface de rupture du glissement de Pianosa (*Pianosa Slump*). Yukselen-Aksoy (2010) a montré que les sols naturels zéolitiques contenant 70-90 % de zéolites et peu de sable sont mécaniquement très résistants et ne montrent pas de radoucissement. De plus, Newson et al. (2006) ont montré que les minéraux avec de fortes capacités d'échange d'ions comme les zéolites tendent à cimenter où lier les particules entre elles sans que du radoucissement ne se manifeste. De plus amples investigations semblent donc nécessaires pour évaluer si lorsque les teneurs en zéolites sont faibles, comme dans notre cas, la présence de zéolite cimente ou non les particules et si la perte de cimentation lors du cisaillement est la cause du radoucissement.

Il est nécessaire de mieux développer la comparaison entre les propriétés sédimentologiques et géotechniques des contourites et des sédiments hémipélagiques afin de confirmer ou d'infirmer les similarités observées dans le présent travail. Pour accomplir cet objectif, il faudrait comparer les données d'un plus grand nombre de carottes sédimentaires ainsi que les mesures in situ réalisées dans d'autres cadres géologiques. Une analyse statistique pourrait ainsi nous aider à mieux définir le degré de similarité entre les deux types de dépôts.

Afin de mieux comprendre le rôle des contourites sur la stabilité des pentes sous-marines, il est aujourd'hui primordial d'améliorer notre compréhension basique des courants de contour et les contourites, une thématique qui semble aujourd'hui en phase de développement. Les critères les plus souvent utilisés pour identifier les contourites se basent sur des données sismiques. L'identification à partir de facies sédimentaires seulement de carottes ou affleurements reste un défi avec les connaissances actuelles. Les contourites se définissent comme les sédiments déposés ou remobilisés par l'action persistante des courants de fond (Stow et al., 2002 ; Rebesco, 2005 ; 2014). Cette définition inclue une variété de sédiments très large : les contourites sableuses formées par le vannage d'hémipélagites ou de turbidites, les turbidites remobilisées, les dunes de sable, « les separated mounded drifts », « sheeted drifts»... Le postulat de Stow et Tabrez (1998) quant au fait que le sédiment hemipelagique se dépose sous les effets combinés d'une décantation verticale et d'advection latérale pose la question du seuil à partir duquel l'advection latérale commence à former des contourites. Cette problématique est au cœur du sujet de l'identification des contourites vaseuses puisque, comme l'a montré cette étude, les dépôts contouritiques se forment principalement dans les zones où le courant est le plus faible. Les morphologies monticulaires se développent du fait d'une distribution hétérogène des courants de fond avec une accumulation sédimentaire préférentielle dans la zone où les courants sont les plus faibles. Les océans sont en mouvement continu, il est donc difficile d'imaginer que la sédimentation pourrait ne pas être affectée par les courants. Les vitesses moyennes calculées près du fond pour la Mer Méditerranée nord-occidentale sont principalement supérieures à 3 $cm{\cdot}s^{-1}$ et fréquemment supérieures à 10 $cm{\cdot}s^{-1}$, même dans les zones les plus profondes du basin en été et en hiver (Fig. 8.3). Les marges continentales sont plus affectées par des courants de fond intenses en hiver, avec des vitesses moyennes généralement supérieures à 10 $cm{\cdot}s^{-1}$ (Fig. 8.3B). Une particule de silt grossier a une vitesse de décantation de 0,1 $cm{\cdot}s^{-1}$ selon Gibbs et al. (1971). Si elle décante dans une zone de l'océan où les courants sont aussi faibles que 3 $cm{\cdot}s^{-1}$ dans toute la colonne d'eau, il faudra attendre 11 jours jusqu'à ce que la particule arrive à 1000 m de profondeur et elle aura été déviée de 30 km de son point d'origine. Si la particule est du silt fin avec une vitesse de décantation de 0,01 $cm{\cdot}s^{-1}$ (Gibbs et al., 1971), elle aura besoin de presque de 4 mois pour arriver à 1000 m et elle sera déviée 300 km de son origine. Le sédiment est donc toujours sujet à l'advection latérale pendant la décantation. Nous avons besoin de faire plus d'effort de quantification du transport sédimentaire dans le domaine profond à l'aide de mesures et de modèles numériques, afin de comprendre la force des courants océaniques dans le modelage des marges continentales.

L'effet des courants en contextes profonds a été probablement sous-estimé parce que ces effets continus sont effacés sur les marges continentales où les processus gravitaires dominent. À mon avis, nous avons aussi besoin d'une simplification du terme contourite parce que la définition « sédiments déposés

ou remaniés considérablement par l'action persistante des courants de fond » pourrait êtree appliqué à tout le fond des océans, sauf aux dépôts générés par les écoulements gravitaires. De la même façon qu'on l'a utilisé dans cet étude, je propose de restreindre le terme «dépôt contouritique vaseux» aux morphologies monticulaires de sédiment fin, à moins d'accepter que tout le fond des océans soit contouritique et que le terme sédiment hémipélagique ne se réfère qu'à la composition du sédiment et à un processus de décantation purement.

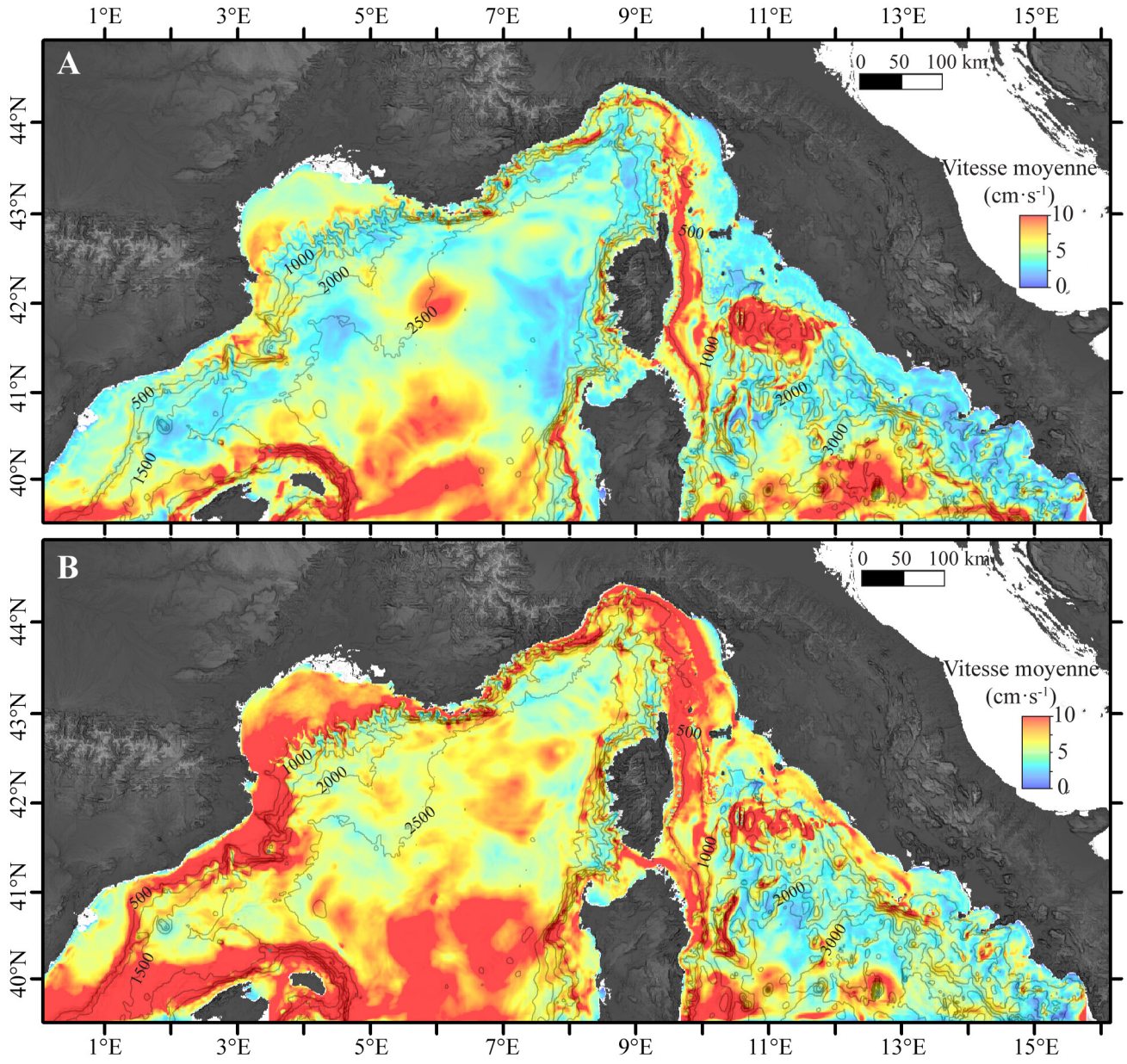

Fig. 8.3. Vitesse moyenne près du fond calculée avec le modèle MARS3D en configuration MENOR pendant **(A)** l'été 2013 (juillet, août et septembre) et **(B)** l'hiver 2013 (janvier, février et mars). Il faut noter que la plus part des valeurs sont supérieures à 3 cm·s^{-1} et souvent même supérieures à 10 cm·s^{-1}, même dans les zones les plus profondes du basin.

REFERENCES

Agrawal, Y.C., McCave, I.N., Riley, J.B. (1991). In: Syvitski, J.P.M. (Ed.) Principles, methods, and application of particle size analysis. Cambridge University Press 9, 119-129.

Albérola, C., Millot, C., Font, J. (1995). On the seasonal and mesoscale variabilities of the Northern Current during the PRIMO-0 experiment in the Western Mediterranean Sea. Oceanologica Acta 18(2),163–192

Altaner, S., Demosthenous, C., Pozzuoli, A., Rolandi, G. (2013). Alteration history of Mount Epomeo Green Tuff and a related polymictic breccia, Ischia Island, Italy: evidence for debris avalanche: Bulletin of Volcanology, 75(5).

Amelio, M., and Martorelli, E. (2008). Seismo-stratigraphic characters of paleocontourites along the Calabro-Tyrrhenian margin (Southern Tyrrhenian Sea). Marine Geology, 252, 141-149.

Andresen, L., and Jostad, H.P. (2007). Numerical modelling of failure mechanisms in sensitive soft clay - application to offshore geohazards. In Conference, O.T.(Ed.), Offshore Technology Conference, OTC, Houston, Texas, 18650.

Artale, M., and Gasparin,i G.P. (1990). Simultaneous temperature and velocity measurements of the internal wave field in the Corsican Channel (Eastern Ligurian Sea). Journal of Geophysical Research, 95(C2),1635-1645.

Asper, V.L., Deuser, W.G., Knauer, G.A., Lohrenz, S.E. (1992). Rapid coupling of sinking particle fluxes between surface and deep ocean waters. Nature 357, 670–672.

Astraldi, M., and Gasparini, G.P. (1992). The seasonal characteristics of the circulation in the north Mediterranean basin and their relationship with the atmospheric-climatic conditions. Journal of Geophysical Research: Oceans (1978–2012), 97, 9531-9540.

Astraldi, M., and Gasparini, G.P. (1994). The seasonal characteristics of the circulation in the Tyrrhenian Sea. In La Violette, P.E. (Ed.) Seasonal and interannual variability of the Western Mediterranean Sea, Coastal and Estuarine Studies, 46, 115–134.

Astraldi, M., Gasparini, P., Manzella, G.M.R., Hopkins, T.S. (1990). Temporal variability of currents in the eastern Ligurian Sea. Journal of Geophysical Research 95, 1515-1522.

Astraldi, M., Gasparini, G.P., Sparnocchia, S., Moretti, M., Sansone, E. (1996). The characteristics of the water masses and the water transport in the Sicily Strait at long time scales. Bulletin-Institut Oceanographique Monaco-Numero special, 17, 95–115.

Bachèlery, P., Robineau, B., Courteaud, M., Savin, C. (2003). Avalanches de débris sur le flanc occidental du volcan-bouclier Piton des Neiges (Réunion): Bulletin de la Société Géologique de France, 174 (2), 125-140.

Baeten, N.J., Laberg, J.S., Vanneste, M., Forsberg, C.F., Kvalstad, T.J., Forwick, M., Vorren, T.O., Haflidason, H. (2014). Origin of shallow submarine mass movements and their glide planes-Sedimentological and geotechnical analyses from the continental slope off northern Norway, Journal of Geophysical Research-Earth Surface, 119(11), 2335-2360.

Barker, A. K., Holm, P. M., Peate, D. W., Baker, J. A. (2009). Geochemical stratigraphy of submarine lavas (3–5 Ma) from the Flamengos Valley, Santiago, southern Cape Verde islands: Journal of Petrology, 50(1), 169-193.

Bartole, R. (1995). The North Tyrrhenian-Northern Apennines post-collisional system: constraints for a geodynamic model. Terra Nova, 7, 7-30.

Bellacicco, M., Anagnostou, C., Falcini, F., Rinaldi, E., Tripsanas, K., Salusti, E. (2016). The 1987 Aegean dense water formation: A streamtube investigation by comparing theoretical model results, satellite, field, and numerical data with contourite distribution. Marine Geology, 375, 120-133.

Brackenridge, R.E., Hernández-Molina, F.J., Stow, D.A.V., Llave, E. (2013). A Pliocene mixed contourite-turbidite system offshore the Algarve Margin, Gulf of Cadiz: Seismic response, margin evolution and reservoir implications. Marine and Petroleum Geology, 46, 36-50.

Brinkgreve, R. B. J., Engin, E., Swolfs, W. M. (2012). PLAXIS 2D 2012 Manual. Delft University of Technology and PLAXIS bv, Delf, The Netherlands.

Bryan, S. E., and Ferrari, L. (2013). Large igneous provinces and silicic large igneous provinces: Progress in our understanding over the last 25 years. Geological Society of America Bulletin, 125(7-8), 1053-1078.

Bryn, P., Berg, K., Stoker, M.S., Haflidason, H., Solheim, A. (2005a). Contourites and their relevance for mass wasting along the Mid-Norwegian Margin. Marine and Petroleum Geology, 22(1), 85-96.

Bryn, P., Berg, K., Forsberg, C.F., Solheim, A., Kvalstad, T.J. (2005b). Explaining the Storegga Slide, Marine and Petroleum Geology, 22(1), 11-19.

Bondevik, S., Lovholt, F., Harbitz, C., Mangerud, J.,. Dawson, A., Svendsen, J.I. (2005). The Storegga Slide tsunami - comparing field observations with numerical simulations. Marine and Petroleum Geology, 22(1-2), 195-208.

Boulanger, R.W., and Idriss, I.M. (2006). Liquefaction susceptibility criteria for silts and clays. Journal of Geotechnical and Geoenvironmental Engineering, 132 (11), 1413-1426.

Cacho, I., Grimalt, J.O., Sierro, F.J., Shackleton, N., Canals, M. (2000). Evidence for enhanced Mediterranean thermohaline circulation during rapid climatic coolings. Earth and Planetary Science Letters, 183, 417-429.

Calvès, G., Toucanne, S., Jouet, G., Charrier, S., Thereau, E., Etoubleau, J., Marsset, T., Droz, L., Bez, M., Abreu, V. (2013). Inferring denudation variations from the sediment record; an example of the last glacial cycle record of the Golo Basin and watershed, East Corsica, western Mediterranean sea. Basin Research, 25, 197-218.

Carter, L., Gavey, R., Tailing, P.J., Liu, J.T. (2014). Insights into Submarine Geohazards from Breaks in Subsea Telecommunication Cables. Oceanography, 27(2), 58-67.

Casagrande, A. (1936). The determination of the pre-consolidation load and its practical significance. In Proceedings of 1st International Soil Mechanics and Foundation Engineering Conference, Cambridge, Mass., 22–26 June 1936. Edited by A. Casagrande. Graduate School of Engineering, Harvard University, Cambridge, Mass. 3, 60–64.

Cattaneo, A., Jouet, G., Charrier, S., Thereau, E., Riboulot, V. (2014). Submarine Landslides and Contourite Drifts Along the Pianosa Ridge (Corsica Trough, Mediterranean Sea). In Krastel, S., Behrmann, J.-H., Vølker, D., Stipp, M., Berndt, C., Urgeles, R., Chaytor, J., Huhn, K., Strasser, M., and Harbitz, C.B. (Eds.), Submarine Mass Movements and Their Consequences, Dordrecht, The Netherlands, Advances in Natural Hazard Research, Springer, 37, 435-445.

Chandler, R.J. (2000). The Third Glossop Lecture Clay Sediments in Depositional Basins: the Geotechnical Cycle. Quarterly Journal of Engineering Geology and Hydrogeology, 33(1), 7-39.

Chiggiato, J., Schroeder, K., Trincardi, F. (2016). Cascading dense shelf-water during the extremely cold winter of 2012 in the Adriatic, Mediterranean Sea: Formation, flow, and seafloor impact. Marine Geology, (375), 1-4.

Chipera, S. J., and Apps, J. A. (2001). Geochemical stability of natural zeolites: Natural Zeolites. Occurrence, Properties, Applications, 45, 117-161.

Clare, M.A., Talling, P.J., Challenor, P.,Malgesini, G., Hunt, J.E. (2014). Distal turbidites reveal a common distribution for large (>0.1 km^3) submarine landslide recurrence. Geology, 42, 263–266.

Clementino, R. (2005). Discussion of "An oedometer test study on the preconsolidation stress of glaciomarine clays". Canadian Geotechnical Journal, 40, 857-872.

Coakley, J.P,. and Sytvitski, J.P.M. (1991). In: Syvitski, J.P.M. (Ed.) Principles, methods, and application of particle size analysis. Cambridge University Press 10, 129-143.

Dalla Valle, G., Gamberi, F., Rocchini, P., Minisini, D., Errera, A., Baglioni, L., Trincardi, F. (2013). 3D seismic geomorphology of mass transport complexes in a foredeep basin: Examples from the Pleistocene of the Central Adriatic Basin (Mediterranean Sea). Sedimentary Geology, 294.

Dalla Valle, G., Gamberi, F., Foglini, F., Trincardi, F. (2015). The Gondola Slide: A mass transport complex controlled by margin topography (South-Western Adriatic Margin, Mediterranean Sea). Marine Geology, 366, 97-113.

Demers, D., and Leroueil, S. (2002). Evaluation of preconsolidation pressure and the overconsolidation ratio from piezocone tests of clay deposits in Quebec. Canadian Geotechnical Journal 39, 174-192.

Deptuck, M.E., Piper, D.J.W., Savoye, B., Gervais, A. (2008). Dimensions and architecture of late Pleistocene submarine lobes off the northern margin of East Corsica. Sedimentology, 55, 869-U834.

Dey, R., Hawlader, B., Phillips, R., Soga, K. (2016). Numerical modeling of submarine landslides with sensitive clay layers. Géotechnique, 66, 454-468.

Di Roberto, A., Del Carlo, P., Rocchi, S., Panter, K. S. (2012). Early Miocene volcanic activity and paleoenvironment conditions recorded in tephra layers of the AND-2A core (southern McMurdo Sound, Antarctica). Geosphere, 8(6), 1342-1355.

Dini, A., Innocenti, F., Rocchi, S., Tonarini, S., Westerman, D. S. (2002). The magmatic evolution of the late Miocene laccolith-pluton-dyke granitic complex of Elba Island, Italy. Geological Magazine, 139(3), 257-279.

Donoghue, E., Troll, V. R., Harris, C., O'Halloran, A., Walter, T. R., Perez Torrado, F. J. (2008). Low-temperature hydrothermal alteration of intra-caldera tuffs, Miocene Tejeda caldera, Gran Canaria, Canary Islands. Journal of Volcanology and Geothermal Research, 176(4), 551-564.

Duhaut, T., Honnorat, M., Debreu, L. (2008). Développements numériques pour le modèle MARS, INRIA, Rapport pour le projet PREVIMER.

Durrieu de Maddron, X., Nyffeler, F., Balopoulos, E.T., Chronis, G. (1992). Circulation and distribution of suspended matter in the Sporades Basin (northwestern Aegean Sea). Journal of Marine Systems 3, 237–248.

Durrieu de Madron, X., Houpert, L., Puig, P., Sanchez-Vidal, A., Testor, P., Bosse, A., Estournel, C., Somot, S., Bourrin, F., Bouin, M.N., Beauverger, M., Beguery, L., Calafat, A., Canals, M., Cassou, C., Coppola, L., Dausse, D., D'Ortenzio, F., Font, J., Heussner, S., Kunesch, S., Lefevre, D., Le Goff, H., Martín, J., Mortier, L., Palanques, A., Raimbault, P. (2013). Interaction of dense shelf water cascading and open-sea convection in the northwestern Mediterranean during winter 2012. Geophysical Research Letters, 40(7), 1379-1385.

Ercilla, G., Juan, C., Hernández-Molina, F. J., Bruno, M., Estrada, F., Alonso, B., Casas, D., Farran, M., Llave, E., García, M., Vázquez, J. T., D'Acremont,E., Gorini, C., Palomino, D., Valencia, J., El Moumni, B., Ammar A. (2016). Significance of bottom currents in deep-sea morphodynamics: an example from the Alboran Sea. Marine Geology, 378, 157-170.

Fell, R., Corominas, J., Bonnard, C., Cascini, L., Leroi, E., Savage, W.Z. (2008). Guidelines for landslide susceptibility, hazard and risk zoning for land-use planning. Engineering Geology, 102, 85-98.

Finlay, P. J., Mostyn, G. R., Fell, R. (1999). Landslide risk assessment: prediction of travel distance. Canadian Geotechnical Journal, 36(3), 556-562.

Font, J., Salat, J., Tintoré, J. (1988). Permanent features of the circulation in the Catalan Sea. Oceanography, 51–57.

Fontanier, C., Mackensen, A., Jorissen, F.J., Anschutz, P., Licari, L., Griveaud, C. (2006). Stable oxygen and carbon isotopes of live benthic foraminifera from the Bay of Biscay: microhabitat impact and seasonal variability. Marine Micropaleontology, 58, 159–183.

Freslon, N. (2015). Etude des changements climatiques et de l'érosion en Corse au cours du Quaternaire à l'aide de nouveaux traceurs isotopiques et moléculaires. PhD thesis, Université de Bretagne Occidentale.

Frey-Martínez, J., Cartwright, J., James, D. (2006). Frontally confined versus frontally emergent submarine landslides: a 3D seismic characterisation, Marine and Petroleum Geology, 23(5), 585-604.

Gaspar P, Grégoris, Y., Lefevre, J.M. (1990). A simple eddy kinetic energy model for simulations of the oceanic vertical mixing: test at station Papa and long-term upper ocean study site. Journal of Geophysical Research 95, 16179–16193.Gasparini, G.P., Zodiatis, G., Astraldi, M., Galli, C., Sparnochia, S. (1999). Winter intermediate water lenses in the Ligurian Sea. Journal of Marine Systems. 20, 319–332.

Gennesseaux, M., Mauffret, A., Pautot, G. (1980). Les glissements sousmarins de la pente continentale niçoise et la rupture des câbles en mer Ligure (Méditerranée occidentale). Comptes Rendus de l'Académie des Sciences Paris, 290.

Germanovich, L. N., Kim, S., Puzrin, A. M. (2016). Dynamic growth of slip surfaces in catastrophic landslides. Proceedings Royal Society A, 472, 20150758.

Gertman, I., Ovchinnicov, I., Popov, Y. (1994). Deep convection in the eastern basin of the Mediterranean Sea. Oceanology 34.

Gervais, A. (2002). Analyse multi-échelles de la morphologie, de la géométrie et de l'architecture d'un système turbiditique sableux profond (système du Golo, marge Est-corse, mer Méditerranée), PhD thesis, Université Bordeaux 1.

Gervais, A., Savoye, B., Piper, D.J.W., Mulder, T., Cremer, M., Pichevin, L. (2004). Present morphology and depositional architecture of a sandy confined submarine system: the Golo turbidite system (eastern margin of Corsica). Confined Turbidite Systems, 222, 59-89.

Gervais, A., Savoye, B., Mulder, T., Gonthier, E. (2006). Sandy modern turbidite lobes: A new insight from high resolution seismic data. Marine and Petroleum Geology, 23, 485-502.

Gibbs, R.J., Matthews, M.D., Link, D.A. (1971). The relationship between sphere size and settling velocity. Journal of sedimentary research, 41(7), 7-18.

Global Volcanism Program (2013). Volcanoes of the World, v. 4.5.0. Venzke, E, ed., Smithsonian Institution. Downloaded 02 Jul 2016. http://dx.doi.org/10.5479/si.GVP.VOTW4-2013

Grant, K.M., Rohling, E.J., Ramsey, C.B., Cheng, H., Edwards, R.L., Florindo, F., Heslop, D., Marra, F., Roberts, A.P., Tamisiea, M.E. (2014). Sea-level variability over five glacial cyces. Nature communications, 5.

Haflidason, H., Lien, R., Sejrup, H.P., Forsberg, C.F., Bryn, P. (2005). The dating and morphometry of the Storegga Slide. Marine and Petroleum Geology, 22 (1–2), 123–136.

Hampton, M.A., Lee, H.J., Locat, J. (1996). Submarine landslides, Reviews of geophysics, 34(1), 33-59.

Harris, P.T., and Beaman, R.J. (2003). Processes controlling the formation of the Mertz Drift, George Vth continental shelf, East Antarctica: evidence from 3.5 kHz sub-bottom profiling and sediment cores. Deep Sea Research Part II: Topical Studies in Oceanography, 50, 1463-1480.

Harris, P.T., Domack, E., Manley, P.L., Gilbert, R., Leventer, A. (1999). Andvord drift: A new type of inner shelf, glacial marine deposystem from the Antarctic Peninsula. Geology, 27, 683-686.

Heezen, B.C., and Hollister, C. (1964). Deep-sea current evidence from abyssal sediments. Marine Geology, 1, 141-174.

Hernández-Molina, F.J., Somoza, L., Vázquez, J.T., Lobo, F., Fernández-Puga, M.C., Llave, E., Díaz-del Rio, V. (2002). Quaternary stratigraphic stacking patterns on the continental shelves of the southern Iberian Peninsula: their relationship with global climate and palaeoceanographic changes. Quaternary International, 92, 5-23.

Hernández-Molina, F.J., Llave, E., Stow, D.A.V., García, M., Somoza, L., Vázquez, J.T., Lobo, F.J., Maestro, A., del Río, V.D., León, R. (2006). The contourite depositional system of the Gulf of Cadiz: a sedimentary model related to the bottom current activity of the Mediterranean outflow water and its interaction with the continental margin. Deep Sea Research Part II: Topical Studies in Oceanography, 53, 1420-1463.

Hernández-Molina, F.J., Llave, E., Stow, D.A.V. (2008). Continental slope contourites. In: Rebesco, M., Camerlenghi, A. (Eds.), Contourites Developments in Sedimentology 60. Elsevier, 379–408.

Hernández-Molina, F.J., Stow, D.A.V., Alvarez-Zarikian, C.A., Acton, G., Bahr, A., Balestra, B., Ducassou, E., Flood, R., Flores, J.-A., Furota, S., Grunert, P., Hodell, D., Jimenez-Espejo, F., Kim, J.K., Krissek, L., Kuroda, J., Li, B., Llave, E., Lofi, J., Lourens, L., Miller, M., Nanayama, F., Nishida, N., Richter, C., Roque, C., Pereira, H., Goni, M.F.S., Sierro, F.J., Singh, A.D., Sloss, C., Takashimizu, Y., Tzanova, A., Voelker, A., Williams, T., Xuan, C. (2014). Onset of Mediterranean outflow into the North Atlantic. Science, 344, 1244-1250.

Hernández-Molina, F. J., Soto, M., Piola, A. R., Tomasini, J., Preu, B., Thompson, P., Badalini, G., Creaser, A., Violante, R.A., Morales, E., Paterlini, M., De Santa Ana, H. (2016). A contourite depositional system along the Uruguayan continental margin: Sedimentary, oceanographic and paleoceanographic implications. Marine Geology, 378, 333-349.

Hickey, B.M. (1997). The response of a steep-sided, narrow canyon to time-variable wind forcing. Journal of Physical Oceanography, 27, 697-726.

Houpert, L. (2013). Contribution to the study of transfer processes from the surface to the deep ocean in the Mediterranean sea using in situ measurements, PhD thesis, Univ. de Perpignan, Perpignan, France.

Hühnerbach, V., and Masson, D.G. (2004). Landslides in the North Atlantic and its adjacent seas: An analysis of their morphology, setting and behaviour. Marine Geology, 213, 343–362.

Hunter, S., Wilkinson, D., Louarn, E., McCave, I. N., Rohling, E., Stow, D. A., Bacon, S. (2007). Deep western boundary current dynamics and associated sedimentation on the Eirik Drift, Southern Greenland Margin. Deep Sea Research Part I: Oceanographic Research Papers, 54(12), 2036-2066.

Idriss, I.M. (1993). Procedures for Selecting Earthquake Ground Motions at Rock Sites. US Department of Commerce, National Institute of Standards and Technology.

Jaky, J. (1948). Pressure in silos. Proc. 2nd ICSMFE, Rotterdam, 1, 103-107.

Jolly, W. T., Lidiak, E. G., Dickin, A. P., Wu, T. W. (2001). Secular geochemistry of central Puerto Rican island arc lavas: Constraints on Mesozoic tectonism in the eastern Greater Antilles. Journal of Petrology, 42(12), 2197-2214.

Juan, C., Ercilla, G., Hernández-Molina, F. J., Estrada, F., Alonso, B., Casas, D., Garcia, M., Farran, M., Llave, E., Palomino, D., Vazquez, J.- T., Medialedea, T., Gorini, C., D'Acremont, E., El Moumni, B., Ammar, A. (2016). Seismic evidence of current-controlled sedimentation in the Alboran Sea during the Pliocene and Quaternary: Palaeoceanographic implications. Marine Geology, 378, 292-311.

Jouet, G., Charrier, S., Calves, G., Dennielou, B., Droz., L., Dupouy, M., Jorry, S., Lericolais, G., Marches, E., Marsset, T., Montferrand, M., Roubi, A., Toucanne, S., the Golo Program Team (2012). GoloDrill Program: Report of the Golo Program Phase 2. Ifremer-Exxon Mobil-Total-Fugro, Dec. 2011, Brest, 6, p. 1541.

Ker, S., Marsset, B., Garziglia, S., Le Gonidec, Y., Gibert, D., Voisset, M., Adamy, J. (2010). High-resolution seismic imaging in deep sea from a joint deep-towed/OBH reflection experiment: application to a Mass Transport Complex offshore Nigeria. Geophysical Journal International, 182(3), 1524-1542.

Klinck, J.M. (1996). Circulation near submarine canyons: A modeling study. Journal of Geophysical Research: Oceans (1978–2012), 101, 1211-1223.

Knutz, P.C. (2008). Paleoceanographic Significance of Contourite Drifts. In Rebesco, M., Camerlenghi, A. (Eds.), Contourites Developments in Sedimentology 60. Elsevier, 457–516.

Koumoto, T., and Houlsby, G. T. (2001). Theory and practice of the fall cone test. Géotechnique, 51(8), 701-712.

Krastel, S., Wefer, G., Hanebuth, T.J., Antobreh, A.A.,. Freudenthal, T., Preu, B., Schwenk, T. Strasser, M., Violante, R., Winkelmann, D. and M78/3 shipboard scientific party (2011). Sediment dynamics and geohazards off Uruguay and the la Plata River region (northern Argentina and Uruguay), Geo-Marine Letters, 31(4), 271-283..

Kvalstad, T. J., Andresen, L., Forsberg, C. F., Berg, K., Bryn, P., Wangen, M. (2005). The Storegga slide: evaluation of triggering sources and slide mechanics. Marine and Petroleum Geology, 22(1), 245-256.

La Violette, P.E. (1994). Overview of the major forcings and water masses of the Western Mediterranean Sea. Seasonal and Interannual Variability of the Western Mediterranean Sea, 1-11.

Laberg, J. S., and Camerlenghi, A. (2008). The significance of contourites for submarine slope stability. Developments in Sedimentology, 60, 537-556.

Laberg, J.S., Dahlgren, T., Vorren, T.O., Haflidason, H., Bryn, P. (2001). Seismic analyses of Cenozoic contourite drift development in the Northern Norwegian Sea. Marine Geophysical Researches, 22, 401-416.

Laberg, J. S., Vorren, T.O., Mienert, J., Evans, D., Lindberg, B., Ottesen, D., Kenyon, N.H., Henriksen, S. (2002). Late Quaternary palaeoenvironment and chronology in the Traenadjupet Slide area offshore Norway. Marine Geology, 188(1-2), 35-60.

Laberg, J. S., Baeten, N.J., Vanneste, M., Forsberg, C.F., Forwick, M., Haflidason, H. (2016). Sediment Failure Affecting Muddy Contourites on the Continental Slope Offshore Northern Norway: Lessons Learned and Some Outstanding Issues. In: Lamarche, G., Mountjoy, J. (Eds.), Submarine mass movements and their consequences 30. Springer, Dordrecht, 281-289.

Lafuerza, S., Sultan, N., Canals, M., Lastras, G., Cattaneo, A., Frigola, J., Costa, S., Berndt, C. (2012). Failure mechanisms of Ana Slide from geotechnical evidence, Eivissa Channel, Western Mediterranean Sea. Marine Geology, 307-310, 1-21.

Lambe, T.W., and Whitman, R.V. (1979). Soil Mechanics S.I. version. second ed. Wiley, New York.

Lascaratos, A., Williams, R.G., Tragou, E. (1993). A mixed-layer study of the formation of levantine intermediate water. Journal of Geophysical Research 98 (C8), 14 739–14 749.

Lascaratos, A., Roether, W., Nittis, K., Klein, B. (1999). Recent changes in deep water formation and spreading in the eastern Mediterranean Sea: a review. Progress in Oceanography, 44, 5-36.

Lazure, P., and Dumas, F. (2008). An external-internal mode coupling for a 3D hydrodynamical model for applications at regional scale (MARS), Advances in Water Resources, 31, 233-250.

Lee, H.J. (2009). Timing of occurrence of large submarine landslides on the Atlantic Ocean margin: Marine Geology, 264, 53–64.

Leroueil, S. (2001). Natural slopes and cuts: movement and failure mechanisms. Geotechnique, 51(3), 197-243.

Leynaud, D., Sultan, N., Mienert, J. (2007). The role of sedimentation rate and permeability in the slope stability of the formerly glaciated Norwegian continental margin: the Storegga slide model. Landslides, 4(4), 297-309.

Leynaud, D., Mienert, J., Vanneste, M. (2009). Submarine mass movements on glaciated and non-glaciated European continental margins: a review of triggering mechanisms and preconditions to failure. Marine and Petroleum Geology, 26, 618-632

Llave, E., Schonfeld, J., Hernández-Molina, F.J., Mulder, T., Somoza, L., del Rio, V.D., Sanchez-Almazo, I. (2006). High-resolution stratigraphy of the Mediterranean outflow contourite system in the Gulf of Cadiz during the-late Pleistocene: The impact of Heinrich events. Marine Geology, 227, 241-262.

Lo, K. Y., and Lee, C. F. (1973). Stress analysis and slope stability in strain-softening materials. Geotechnique, 23(1).

Lobbestael, A. J., Athanasopoulos-Zekkos, A., Colley, J. (2013). Factor of Safety Reduction Factors for Accounting for Progressive Failure for Earthen Levees with Underlying Thin Layers of Sensitive Soils: Mathematical Problems in Engineering, doi: http://dx.doi.org/10.1155/2013/893602.

Locat, J., Tanaka, H., Tan, T.S., Dasari, G.R., Lee, H. (2003). Natural soils: geotechnical behavior and geological knowledge. Characterisation and Engineering Properties of Natural Soils, 1, 3-28.

Locat, J., Leroueil, A., Locat, A., Lee, H.J. (2014).Weak layers: Their definition and classification from a geotechnical perspective. In Krastel, S., Behrmann, J.-H., Vølker, D., Stipp, M., Berndt, C., Urgeles, R., Chaytor, J., Huhn, K., Strasser, M., and Harbitz, C.B. (Eds.), Submarine Mass Movements and Their Consequences, Dordrecht, The Netherlands, Advances in Natural Hazard Research, Springer, 37, 61–74.

Low, H. E., Lunne, T., Andersen, K. H., Sjursen, M. A., Li, X., Randolph, M. F. (2010). Estimation of intact and remoulded undrained shear strengths from penetration tests in soft clays. Géotechnique, 60(11), 843-859.

Lüdmann, T., Wiggerhaus, S., Betzler, C., Hübscher, C. (2012). Southwest Mallorca Island: A cool-water carbonate margin dominated by drift deposition associated with giant mass wasting, Marine Geology, 307, 73-87.

Lunne, T., Robertson, P.K., Powell, J.J.M. (1997). Cone Penetration Testing in Geotechnical Practice. Blackie Academic and Professional, New York.

Machiels, L., Garces, D., Snellings, R., Vilema, W., Morante, F., Paredes, C., Elsen, J. (2014). Zeolite occurrence and genesis in the Late-Cretaceous Cayo arc of Coastal Ecuador: Evidence for zeolite formation in cooling marine pyroclastic flow deposits: Applied Clay Science, 87, 108-119.

Marani, M., Argnani, A., Roveri, M., Trincardi, F. (1993). Sediment drifts and erosional surfaces in the central Mediterranean-seismic evidence of bottom-current activity. Sedimentary Geology, 82, 207-220.

Marches, E., Mulder, T., Gonthier, E., Cremer, M., Hanquiez, V., Garlan, T., Lecroart, R. (2010). Perched lobe formation in the Gulf of Cadiz: Interactions between gravity processes and contour currents (Algarve Margin, Southern Portugal). Sedimentary Geology, 229, 81-94.

Marsset, T., Marsset, B., Ker, S., Thomas, Y., Le Gall, Y. (2010). High and very high resolution deep-towed seismic system: Performance and examples from deep water Geohazard studies. Deep-sea Research Part I-oceanographic Research Papers, 57(4), 628-637.

Marsset, B., Menut, E., Ker, S., Thomas, Y., Regnault, J.-P., Leon, P., Martinossi, H., Artzner, L., Chenot, D., Dentrecolas, S., Spychalski, B., Mellier, G., Sultan, N. (2014). Deep-towed High Resolution multichannel seismic imaging. Deep-sea Research Part I-oceanographic Research Papers, 93, 83-90.

Maslin, M., Mikkelsen, N., Vilela, C., Haq, B. (1998). Sea-level- and gas-hydrate controlled catastrophic sediment failures of the Amazon Fan. Geology 26 (12), 1107e1110.

Maslin, M., Owen, M., Day, S., Long, D. (2004). Linking continental-slope failures and climate change: testing the clathrate gun hypothesis. Geology 32, 53e56.

Masson, D. G., Wynn, R. B., Talling, P. J. (2010). Large Landslides on Passive Continental Margins: Processes, Hypotheses and Outstanding Questions. In Mosher, D.C., Shipp, R.C., Moscardelli, L., Chaytor, J.D., Baxter, C.D.P., Lee, H.J., and Urgeles, R. (Eds.), Submarine Mass Movements and Their Consequences, Dordrecht, The Netherlands, Advances in Natural Hazard Research, Springer, 28, 153-165.

Mayne, P.W. (2007). Cone penetration testing: A synthesis of highway practice. Project 20-5. Transportation Research board, Whashington, D.C. NCHRP synthesis 368.

McCave, I.N. (2008). Size sorting during transport and deposition of fine sediments: Sortable silt and flow speed. In: Rebesco, M., Camerlenghi, A. (Eds.), Contourites Developments in Sedimentology 60. Elsevier 121–142.

McCave, I.N., and Hall, I.R. (2006). Size sorting in marine muds: Processes, pitfalls, and prospects for paleoflow-speed proxies. Geochemistry Geophysics Geosystems, 7.

Millot, C. (1999). Circulation in the Western Mediterranean Sea. Journal of Marine Systems, 20, 423-442.

Millot, C. (2009). Another description of the Mediterranean Sea outflow. Progress in Oceanography, 82(2), 101-124.

Millot, C. (2013). Levantine Intermediate Water characteristics: an astounding general misunderstanding! Scientia Marina, 77, 217-232.

Millot, C., and Taupier-Letage, I. (2005). Circulation in the Mediterranean sea, The Mediterranean Sea. Springer, 29-66.

Minisini, D., and Trincardi, F. (2009). Frequent failure of the continental slope: The Gela Basin (Sicily Channel). Journal of Geophysical Research-Earth Surface, 114.

Minisini, D., Trincardi, F., Asioli, A., Canu, M., Foglini, F. (2007). Morphologic variability of exposed mass-transport deposits on the eastern slope of Gela Basin (Sicily channel). Basin Research, 19(2), 217-240.

Mintoʾo, C.M.A., Bassetti, M.A., Morigi, C., Ducassou, E., Toucanne, S., Jouet, G., Mulder, T. (2015). Levantine intermediate water hydrodynamic and bottom water ventilation in the northern Tyrrhenian Sea over the past 56,000 years: New insights from benthic foraminifera and ostracods. Quaternary International, 357, 295-313.

Miramontes, E., Cattaneo, A., Jouet, G., Garziglia, S. (2016a). Implications of sediment dynamics in mass transport along the Pianosa Ridge (Northern Tyrrhenian Sea). In Lamarche, G., Mountjoy, J., Bull, S., Hubble, T., Krastel, S., Lane, E., Micallef, A., Moscardelli, L., Mueller, C., Pecher, I., Woelz, S. (Eds.)., Submarine mass movements and their consequences, Dordrecht, The Netherlands, Advances in Natural Hazard Research, Springer, 30, 301–309.

Miramontes, E., Cattaneo, A., Jouet, G., Théreau, E., Thomas, Y., Rovere, M., Cauquil, E., Trincardi, F., (2016b). The Pianosa Contourite Depositional System (Northern Tyrrhenian Sea): Drift morphology and Plio-Quaternary stratigraphic evolution: Marine Geology, 378, 20-42.

Monserrat, S., López-Jurado, J.L., Marcos, M. (2008). A mesoscale index to describe the regional circulation around the Balearic Islands. Journal of Marine Systems 71, 413–420.

Morgan, J. K., and Clague, D. A. (2003). Volcanic spreading on Mauna Loa volcano, Hawaii: Evidence from accretion, alteration, and exhumation of volcaniclastic sediments: Geology,31(5), 411-414.

Morley, C.K. (2009). Growth of folds in a deep-water setting. Geosphere, 5 (2), 59-89

Mulder, T., Faugères, J.C., Gonthier, E. (2008). Mixed turbidite–contourite systems. Developments in Sedimentology, 60, 435-456.

Newson, T., Dyer, T., Adam, C., Sharp, S. (2006). Effect of structure on the geotechnical properties of bauxite residue. Journal of geotechnical and geoenvironmental engineering, 132(2), 143-151.

Onitsuka, K., Hong, Z., Hara, Y., and Shigeki, Y. (1995). Interpretation of oedometer test data for natural clays. Journal of the Japanese Geotechnical Society, Soils and Foundations, 35(3), 61–70.

Owen, M., Day, S., Maslin, M. (2007). Late Pleistocene submarine mass movements: occurrence and causes. Quaternary Science Reviews, 26, 958e978.

Pacheco Silva (1970). A new graphical construction for determination of the pre-consolidation stress of a soil sample. Proceedings of the 4th Brazilian Conference on Soil Mechanics and Foundation Engineering, Rio de Janeiro, Brazil, 2(1), 225–232.

Pandeli, E., Bartolini, C., Dini, A., Antolini, E. (2010). New data on the paleogeography of Southern Tuscany (Italy) since Late Miocene time. International Journal of Earth Sciences, 99(6), 1357-1381.

Pascucci, V. (2002). Tyrrhenian Sea extension north of the Elba Island between Corsica and western Tuscany (Italy). Bollettino della Società geologica italiana, 121, 819-828.

Pascucci, V., Merlini, S., Martini, I.P. (1999). Seismic stratigraphy of the Miocene-Pleistocene sedimentary basins of the Northern Tyrrhenian Sea and western Tuscany (Italy). Basin Research, 11, 337-356.

Pascucci, V., Martini, I.P., Sagri, M., Sandrelli, F., Nichols, G., Paola, C., Williams, E.A. (2007). Effects of transverse structural lineaments on the Neogene–Quaternary basins of Tuscany (inner Northern Apennines, Italy). Sedimentary Processes, Environments and Basins: A Tribute to Peter Friend, 155-183.

Pellegrini, C., Maselli, V., Trincardi, F. (2015). Pliocene–Quaternary contourite depositional system along the south-western Adriatic margin: changes in sedimentary stacking pattern and associated bottom currents. Geo-Marine Letters, 1-13.

Pinardi, N., Zavatarelli, M., Arneri, E., Crise, A., Ravaioli, M. (2006). The physical, sedimentary and ecological structure and variability of shelf areas in the Mediterranean Sea. In: Robinson, A., Brink, K. (Eds.), THE GLOBAL The Global Coastal Ocean: Interdisciplinary Regional Studies and Syntheses, vol. 14. Harvard University Press, The Sea (Chapter 32).

Pinardi, N., Zavatarelli, M., Adani, M., Coppini, G., Fratianni, C., Oddo, P., Simoncelli, S., Tonani, M., Lyubarstsev, V., Dobrici, S., Bonaduce, A. (2015). Mediterranean Sea large-scale low-frequency ocean variability and water mass formation rates from 1987 to 2007: A retrospective analysis. Progress in Oceanography, 132, 318-332.

Pinot, J.-M., López-Jurado, J.L., Riera, M. (2002).The CANALES experiment (1996–1998). Interannual, seasonal, and mesoscale variability of the circulation in the Balearic Channels. Progress in Oceanography 55, 335–370.

Pomar, L., Morsilli, M., Hallock, P., Bádenas, B. (2012). Internal waves, an under-explored source of turbulence events in the sedimentary record. Earth-Science Reviews, 111(1), 56-81.

Pope, E. L., Talling, P. J., Urlaub, M., Hunt, J. E., Clare, M. A., Challenor, P. (2015). Are large submarine landslides temporally random or do uncertainties in available age constraints make it impossible to tell?. Marine Geology, 369, 19-33.

Potts, D. M., Dounias, G. T., Vaughan, P. R. (1990). Finite-element analysis of progressive failure of Carsington embankment, Geotechnique, 40(1), 79-101.

Preu, B., Hernández-Molina, F. J., Violante, R., Piola, A. R., Paterlini, C. M., Schwenk, T., Voigt, I., Krastel, S., Spiess, V. (2013). Morphosedimentary and hydrographic features of the northern Argentine margin: the interplay between erosive, depositional and gravitational processes and its conceptual implications. Deep Sea Research Part I: Oceanographic Research Papers, 75, 157-174.

Pricipaud, M., Mulder, T., Gillet, H., Borgomano, J. (2015). Large-scale carbonate submarine mass-wasting along the northwestern slope of the Great Bahama Bank (Bahamas): Morphology, architecture, and mechanisms, Sedimentary Geology, 317, 27-42.

Puig, P., and Palanques, A. (1998). Nepheloid structure and hydrographic control on the Barcelona continental margin, northwestern Mediterranean.Marine Geology 149, 39–54.

Puzrin, A. M., Germanovich, L. N., Friedli, B. (2016). Shear band propagation analysis of submarine slope stability. Geotechnique, 66(3),)188-201.

Rebesco, M. (2005). Contourites. In Selley, R.C., Cocks, L.R.M., Plimer, I.R. (Eds.), Encyclopedia of Geology. Elsevier, Oxford, 513–527.

Rebesco, M. (2014). Contourites. In: Elias, S.A. (Ed.), Reference Module in Earth Systems and Environmental Sciences. Elsevier. http://dx.doi.org/10.1016/B978-0-12-409548- 9.02964-X.

Rebesco, M., and Camerlenghi, A. (2008). Contourites. Developments in Sedimentology, 60. Elsevier 663.

Rebesco, M., Pudsey, C.J., Canals, M., Camerlenghi, A., Barker, P.F., Estrada, F., Giorgetti, A. (2002). Sediment drifts and deep-sea channel systems, Antarctic Peninsula Pacific Margin. Geological Society, London, Memoirs, 22, 353-371.

Rebesco, M., Camerlenghi, A., Van Loon, A.J. (2008). Contourite Research: A Field in Full Development. Developments in Sedimentology, 60, 3-10.

Rebesco, M., Hernández-Molina, F.J., Van Rooij, D.,Wåhlin, A. (2014). Contourites and associated sediments controlled by deep-water circulation processes: State-of-the-art and future considerations. Marine Geology 352, 111-154.

Reimer, P.J., Bard, E., Bayliss, A., Beck, J.W., Blackwell, P.G., Ramsey, C.B., Buck, C.E., Cheng, H., Edwards, R.L., Friedrich, M., Grootes, P.M., Guilderson, T.P., Haflidason, H., Hajdas, I., Hatte, C., Heaton, T.J., Hoffmann, D.L., Hogg, A.G., Hughen, K.A., Kaiser, K.F., Kromer, B., Manning, S.W., Niu,M., Reimer, R.W., Richards, D.A., Scott, E.M., Southon, J.R., Staff, R.A., Turney, C.S.M., van der Plicht, J. (2013). IntCal13 and Marine13 radiocarbon age calibration curves 0–50,000 years cal BP. Radiocarbon, 55, 1869–1887.

Ribó, M., Puig, P., Salat, J., Palanques, A. (2013). Nepheloid layer distribution in the Gulf of Valencia, northwestern Mediterranean. Journal of Marine Systems 111, 130-138.

Ribó, M., Puig, P., van Haren, H. (2015). Hydrodynamics over the Gulf of Valencia continental slope and their role in sediment transport. Deep Sea Research Part I: Oceanographic Research Papers 95, 54-66.

Riboulot, V., Thomas, Y., Berne, S., Jouet, G., Cattaneo, A. (2014). Control of Quaternary sea-level changes on gas seeps. Geophysical Research Letters ,41, 4970-4977.

Robertson, P. K. (2004). Evaluating soil liquefaction and post-earthquake deformations using the CPT. Proceedings of ISC-2 on Geotechnical and Geophysical Site Caracterization, 233-249.

Rohling, E. J., Grant, K., Hemleben, C., Kucera, M., Roberts, A. P., Schmeltzer, I., Schulz, H., Siccha, M., Siddall, M., and Trommer, G. (2008). New constraints on the timing of sea level fluctuations during early to middle marine isotope stage 3. Paleoceanography, 23(3).

Rohling, E. J., Foster, G. L., Grant, K. M., Marino, G., Roberts, A. P., Tamisiea, M. E., Williams, F. (2014). Sea-level and deep-sea-temperature variability over the past 5.3 million years. Nature, 508(7497), 477-482.

Roveri, M. (2002). Sediment drifts of the Corsica Channel, northern Tyrrhenian Sea, in: Stow, D.AV., Pudsey, C.J., Howe, J.A., Faugères, J.-C., Viana, A.R. (Eds.), Deep-Water Contourite Systems: Modern Drifts and Ancient Series, Seismic and Sedimentary Characteristics. Geological Society, London, Memoirs, 22, 191-208.

Roveri, M., Flecker, R., Krijgsman, W., Lofi, J., Lugli, S., Manzi, V., Manzi, V., Sierro, F.J., Bertini, A., Camerlenghi, A., De Lange, G., Govers, R., Hilgen, F.J., Hübscher, C., Meijer, P.T., Stoica (2014). The Messinian Salinity Crisis: past and future of a great challenge for marine sciences. Marine Geology, 352, 25-58.

Salat, J., and Font, J. (1987). Water mass structure near and offshore the Catalan coast during the winters of 1982 and 1983. In Annales geophysicae. Series B. Terrestrial and planetary physics, 5, 49–54.

Schaaff, E., Grenz, C., Pinazo, C. (2002). Erosion of particulate inorganic and organic matter in the Gulf of Lion. Comptes Rendus Geoscience, 334 (15), 1071–1077.

Shanmugam, G. (2013). Modern internal waves and internal tides along oceanic pycnoclines: Challenges and implications for ancient deep-marine baroclinic sands. AAPG bulletin, 97(5), 799-843.

Schmiedl, G., Pfeilsticker, M., Hemleben, C., Mackensen, A. (2004). Environmental and biological effects on the stable isotope composition of recent deep-sea benthic foraminifera, from the western Mediterranean Sea. Marine Micropaleontology, 51, 129–152.

Scisciani, V., and Calamita, F. (2009). Active intraplate deformation within Adria: Examples from the Adriatic region. Tectonophysics, 476, 57-72.

Seed, H. B., and Idriss, I.M. (1971). Simplified procedure for evaluation soil liquefaction potential. Journal of the Soil Mechanics and Foundations Division, ASCE (SM9), 97, 1249-1273.

Skempton, A. W. (1954). The pore-pressure coefficients A and B. Géotechnique, 4(4), 143-147.

Slejko, D., Camassi, R., Cecic, I., Herak, D., Herak, M., Kociu, S., Kouskouna, V., Lapajne, J., Makropoulos, K., Meletti, C., Muço, B., Papaioannou, C., Peruzza, L., Rebez, A., Scandone, P., Sulstarova, E., Voulgaris, N., Živčić, M., Zupančič, P. (1999). Seismic hazard assessment for Adria. Annali di Geofisica, 42 (6), 1085-1107.

Smagorinsky, J. (1963). General circulation experiments with the primitive equation. I. The basic experiment. Monthly Weather Review 91(3): 99–164.

Sobarzo, M., Figueroa, M., Djurfeldt, L. (2001). Upwelling of subsurface water into the rim of the Biobio submarine canyon as a response to surface winds. Continental Shelf Research, 21, 279-299.

Sømme, T.O., Piper, D.J.W., Deptuck, M.E., Helland-Hansen, W. (2011). Linking onshore-offshore sediment dispersal in the Golo source-to-sink system (Corsica, France) during the late Quaternary. Journal of Sedimentary Research, 81, 118–137

Soulsby, R.L. (1997). Dynamics of marine sands. A manual for practical applications. Thomas Telford, London, 249.

Sparnocchia, S., G. P. Gasparini, M. Borghini, and P. Pistek (1999). Dynamics and mixing of the eastern Mediterranean outflow in the Thyrrhenian Sea, Journal of Marine Systems, 20, 301–332.

Stow, D.A.V., and Tabrez, A.R. (1998). Hemipelagites: processes, facies and model, Geological Society, London, Special Publications, 129(1), 317-337.

Stow, D. A. V., and J. C. Faugères (2008). Contourite facies and the facies model, Developments in Sedimentology, 60, 223-256.

Stow, D.A.V., Kahler, G., Reeder, M. (2002). Fossil contourites: type example from an Oligocene palaeoslope system, Cyprus. In: Stow, D.A.V., Pudsey, C.J., Howe, J.A., Faugères, J.-C., Viana, A.R. (Eds.), Deep-water Contourite Systems: Modern Drifts and Ancient Series, Seismic and Sedimentary Characteristics. Geological Society, London, Memoir, 22, pp. 443–455.

Stow, D.A.V., Hernández-Molina, F.J., Llave, E.,Sayago-Gil, M., Díaz del Río, V., Branson, A. (2009). Bedform-velocity matrix: the estimation of bottom current velocity from bed form observations. Geology 37(4), 327–330.

Sultan, N., Cochonat P., Dennielou, B., Bourillet,J.-F., Savoye, B., Colliat, J.L. (2000). Surconsolidation apparente et pression osmotique dans un sédiment marin. Comptes Rendus de l'Académie des Sciences-Series / /A-Earth and Planetary Science, 331(5), 379-386.

Sultan, N., Cochonat, P., Canals, M., Cattaneo, A., Dennielou, B., Haflidason, H., Laberg, J.S., Long, D., Mienert, J., Trincardi, F., Urgeles, R., Vorren,T.O., and Wilson, C. (2004). Triggering mechanisms of slope instability processes and sediment failures on continental margins: a geotechnical approach, Marine Geology, 213(1), 291-321.

Sultan, N., Gaudin, M., Berne, S., Canals, M., Urgeles, R., Lafuerza, S.(2007). Analysis of slope failures in submarine canyon heads: An example from the Gulf of Lions: Journal of Geophysical Research-Earth Surface, 112(F1).

Sumner, E.J., Siti, M.I., McNeill, L.C., Talling, P.J., Henstock, T.J., Wynn, R.B., Djajadihardja, Y.S., Permana, H. (2013). Can turbidites be used to reconstruct a paleoearthquake record for the central Sumatran margin?: Geology, 41, 763–766.

Talling, P., Clare, M., Urlaub, M., Pope, E., Hunt, J., Watt, S. (2014). Large submarine landslides on continental slopes: geohazards, methane release, and climate change. Oceanography, 27(2), 32-45.

Tappin, D.R., (2010). Submarine mass failures as tsunami sources: their climate control. Philosophical Transactions of the Royal Society 368, 2417-2434.

Tappin, D. R., Watts, P., McMurtry, GM., Lafoy, Y., Matsumoto, T. (2001). The Sissano, Papua New Guinea tsunami of July 1998 - offshore evidence on the source mechanism, Marine Geology, 175(1-4), 1-23.

Thinon, I., Guennoc, P., Serrano, O., Maillard, A., Lasseur, E., Réhault, J. P. (2016). Seismic markers of the Messinian Salinity Crisis in an intermediate-depth basin: data for understanding the Neogene evolution of the Corsica Basin (Northern Tyrrhenian Sea). Marine and Petroleum Geology, 77, 1274-1296.

Toucanne, S., Jouet, G., Ducassou, E., Bassetti, M.A., Dennielou, B., Minto'o, C.M.A., Lahmi, M., Touyet, N., Charlier, K., Lericolais, G., Mulder, T. (2012). A 130,000-year record of Levantine Intermediate Water flow variability in the Corsica Trough, western Mediterranean Sea. Quaternary Science Reviews, 33, 55-73.

Toucanne, S., Angue Minto'o, C.M., Fontanier, C., Bassetti, M.A., Jorry, S.J., Jouet, G. (2015). Tracking rainfall in the Northern Mediterranean borderlands during sapropel deposition. Quaternary Science Reviews 129, 178–195.

Tournadour, E., Mulder, T., Borgomano, J., Hanquiez, V., Ducassou, E., Gillet, H. (2015). Origin and architecture of a mass transport complex on the northwest slope of Little Bahama Bank (Bahamas): relations between off-bank transport, bottom current sedimentation and submarine landslides. Sedimentary Geology, 317, 9-26.

Troncone, A. (2005). Numerical analysis of a landslide in soils with strain-softening behaviour. Geotechnique, 55(8), 585-596.

Tsimplis, M., Velegrakis, A., Drakopoulos, P., Theocharis, A., Collins, M. (1999). Cretan deep water outflow into the eastern mediterranean. Progress In Oceanography 44 (4), 531–551.

Urgeles, R., and Camerlenghi, A. (2013). Submarine landslides of the Mediterranean Sea: Trigger mechanisms, dynamics, and frequency-magnitude distribution. Journal of Geophysical Research: Earth Surface, 118(4), 2600-2618.

Urlaub, M., Talling, P.J., Masson, D.G. (2013). Timing and frequency of large submarine landslides: implications for understanding triggers and future geohazard. Quaternary Science Reviews. 72, 63–82.

Van Paassen, L.A., Gareau, L. F. (2004). Effect of pore fluid salinity on compressibility and shear strength development of clayey soils. In Engineering Geology for Infrastructure Planning in Europe. Springer Berlin Heidelberg, 327-340.

Vandorpe, T.P., Van Rooij, D., Stow, D.A.V., Henriet, J.-P. (2011). Pliocene to Recent shallow-water contourite deposits on the shelf and shelf edge off south-western Mallorca, Spain. Geo-Marine Letters 31, 391-403.

Vanneste, M., Mienert, J., Bunz, S. (2006). The Hinlopen Slide: A giant, submarine slope failure on the northern Svalbard margin, Arctic Ocean. Earth and Planetary Science Letters, 245(1-2), 373-388.

Velasco, J.P.B., Baraza, J., Canals, M., Balón, J. (1996). La depression periférica y el lomo contourítico de Menorca: evidencias de la actividad de corrientes de fondo al N del talud Balear. Geogaceta 20, 359–362.

Verdicchio, G., and Trincardi, F. (2008a). Mediterranean shelf-edge muddy contourites: examples from the Gela and South Adriatic basins. Geo-Marine Letters, 28, 137-151.

Verdicchio, G., and Trincardi, F. (2008b). Shallow-water contourites. Developments in Sedimentology, 60, 409-433.

Vetrano, A., Napolitano, E., Iacono, R., Schroeder, K., Gasparini, G. P. (2010). Tyrrhenian Sea circulation and water mass fluxes in spring 2004: Observations and model results. Journal of Geophysical Research: Oceans, 115(C6).

Viana, A.R., Faugeres, J.C., Kowsmann, R.O., Lima, J.A.M., Caddah, L.F.G., Rizzo, J.G. (1998). Hydrology, morphology and sedimentology of the Campos continental margin, offshore Brazil. Sedimentary Geology 115, 133-157.

Vignudelli, S., Gasparini, G.P., Astraldi, M., Schiano, M.E. (1999). A possible influence of the North Atlantic Oscillation on the circulation of the Western Mediterranean Sea. Geophysical Research Letters, 26, 623-626.

Vignudelli, S., Cipollini, P., Astraldi, M., Gasparini, G.P., Manzella, G. (2000). Integrated use of altimeter and in situ data for understanding the water exchanges between the Tyrrhenian and Ligurian Seas. Journal of Geophysical Research-Oceans, 105, 19649-19663.

Völker, D., Scholz, F., Geerson, J. (2011). Analysis of submarine landsliding in the rupture area of the 27 February 2010 Maule earthquake, Central Chile. Marine Geology, 288, 79–89.

Watt, S. F. L., Talling, P. J., Hunt, J. E. (2014). New Insights into the Emplacement Dynamics of Volcanic Island Landslides. Oceanography, 27(2), 46-57.

Weisenberger, T., and Selbekk, R. S. (2009). Multi-stage zeolite facies mineralization in the Hvalfjordur area, Iceland: International Journal of Earth Sciences, 98(5), 985-999.

Wheeler, S.J. (1988). The undrained shear strength of soils containing large gas bubbles. Géotechnique 38, 399-413.

Wilson, C. K., Long, D., Bulat, J. (2004). The morphology, setting and processes of the Afen Slide, Marine Geology, 213(1), 149-167.

Woerther, P., Bourillet, J.-F., Damy, G., Dussud, L., Sultan, N. (2012). Improving in piston coring quality with acceleration and pressure measurements and new insights on quality of the recovery. 8th International Marine Technicians Symposium, INMARTECH 2012, 25 and 28 September 2012, Texel, The Netherlands.

Wright, S.G., and Rathje, E.M. (2003). Triggering mechanisms of slope instability and their relationship to earthquakes and tsunamis. Pure Applied Geophysics 160, 1865–1877.

Yukselen-Aksoy, Y., 2010, Characterization of two natural zeolites for geotechnical and geoenvironmental applications: Applied Clay Science, 50(1), 130-136.

Yukselen-Aksoy, Y., Kaya, A., Hakan Ören, A. (2008). Seawater effect on consistency limits and compressibility characteristics of clays. Engineering Geology, 102, 54-61.

Zitellini, N., Trincardi, F., Marani, M., Fabbri, A. (1986). Neogene tectonics of the northern Tyrrhenian Sea. Giornale di Geologia, 48, 2.

Zúñiga, D., Garcia-Orellana, J., Calafat, A., Price, N. B., Adatte, T., Sanchez-Vidal, A., Canals, M., Sanchez-Cabeza, J. A., Masque, P., and Fabres, J. (2007). Late Holocene fine-grained sediments of the Balearic Abyssal Plain, Western Mediterranean Sea. Marine Geology, 237(1), 25-36.

APPENDICES

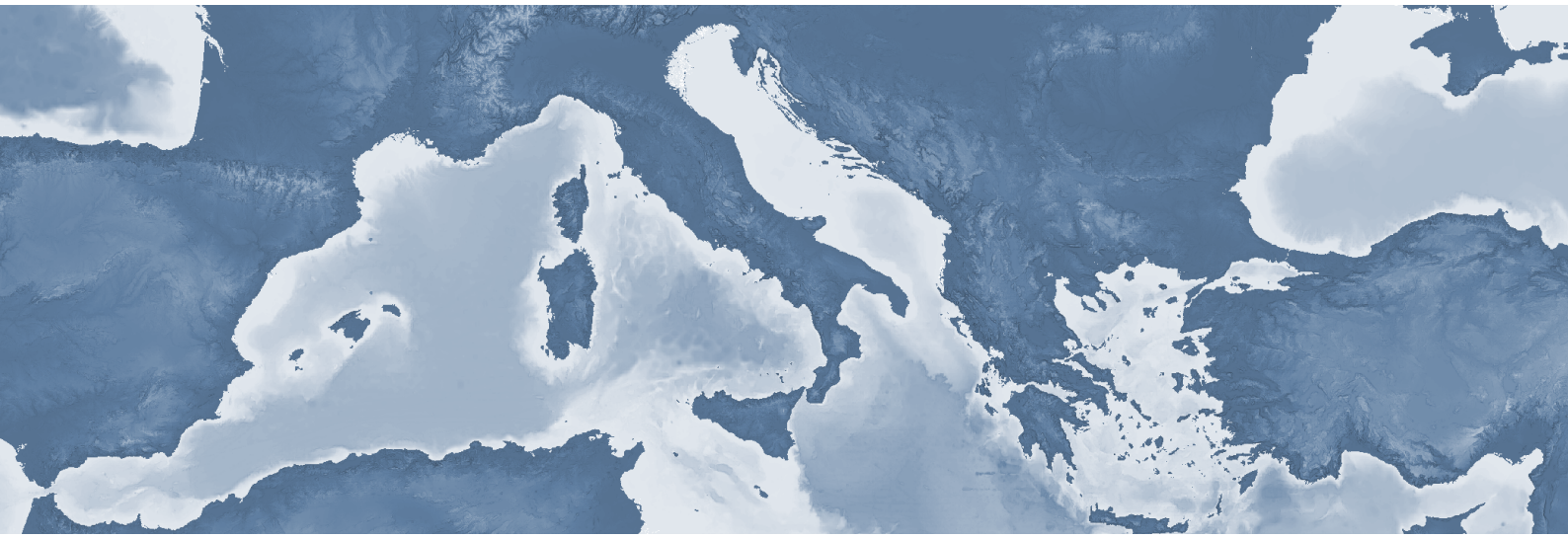

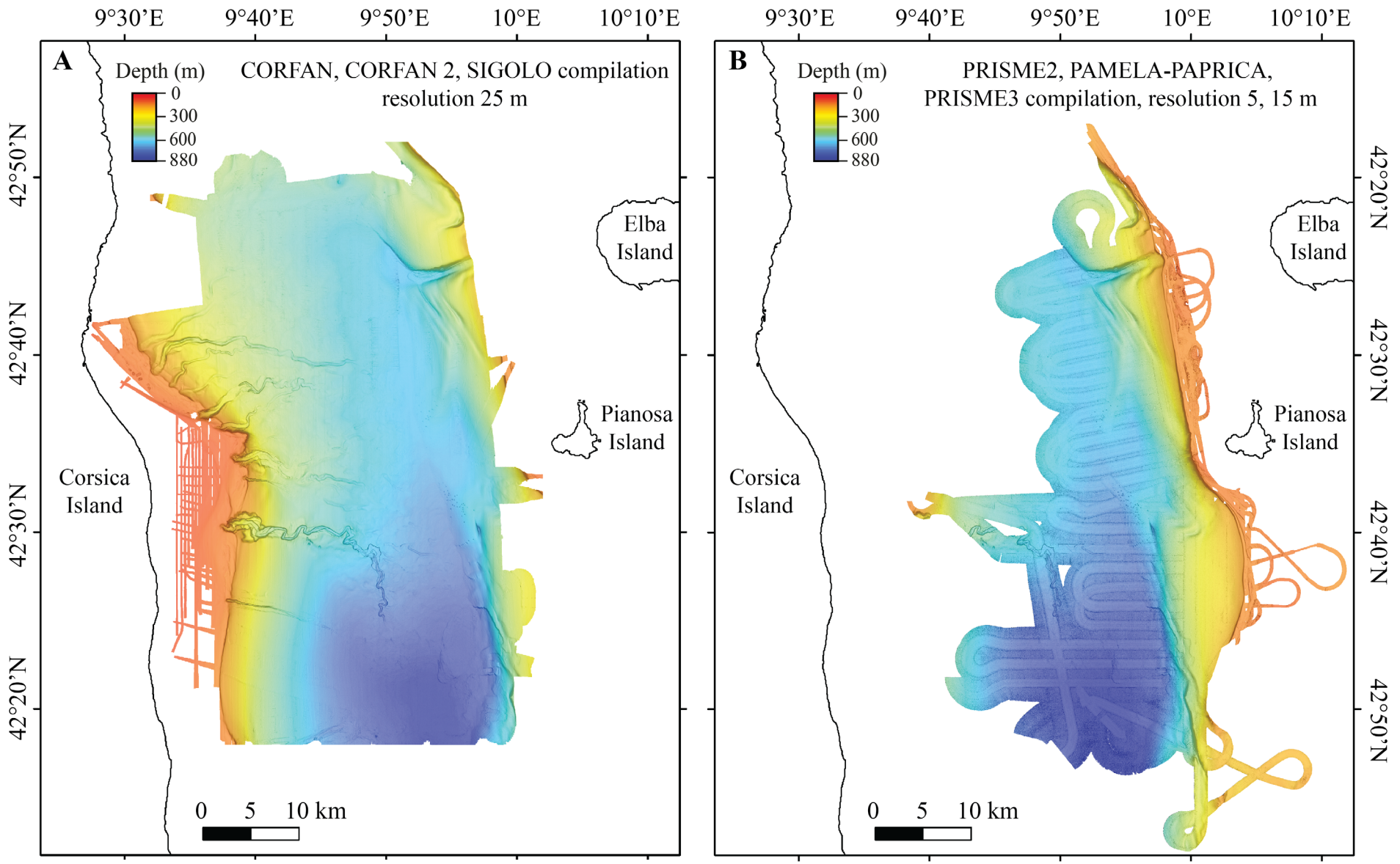

Fig. A.1. Multibeam bathymetry of the Corsica Trough acquired during: **(A)** CORFAN, CORFAN2 and SIGOLO surveys (25 m resolution); and **(B)** PRISME2, PAMELA-PAPRICA and PRISME3 surveys (5 and 15 m resolution).

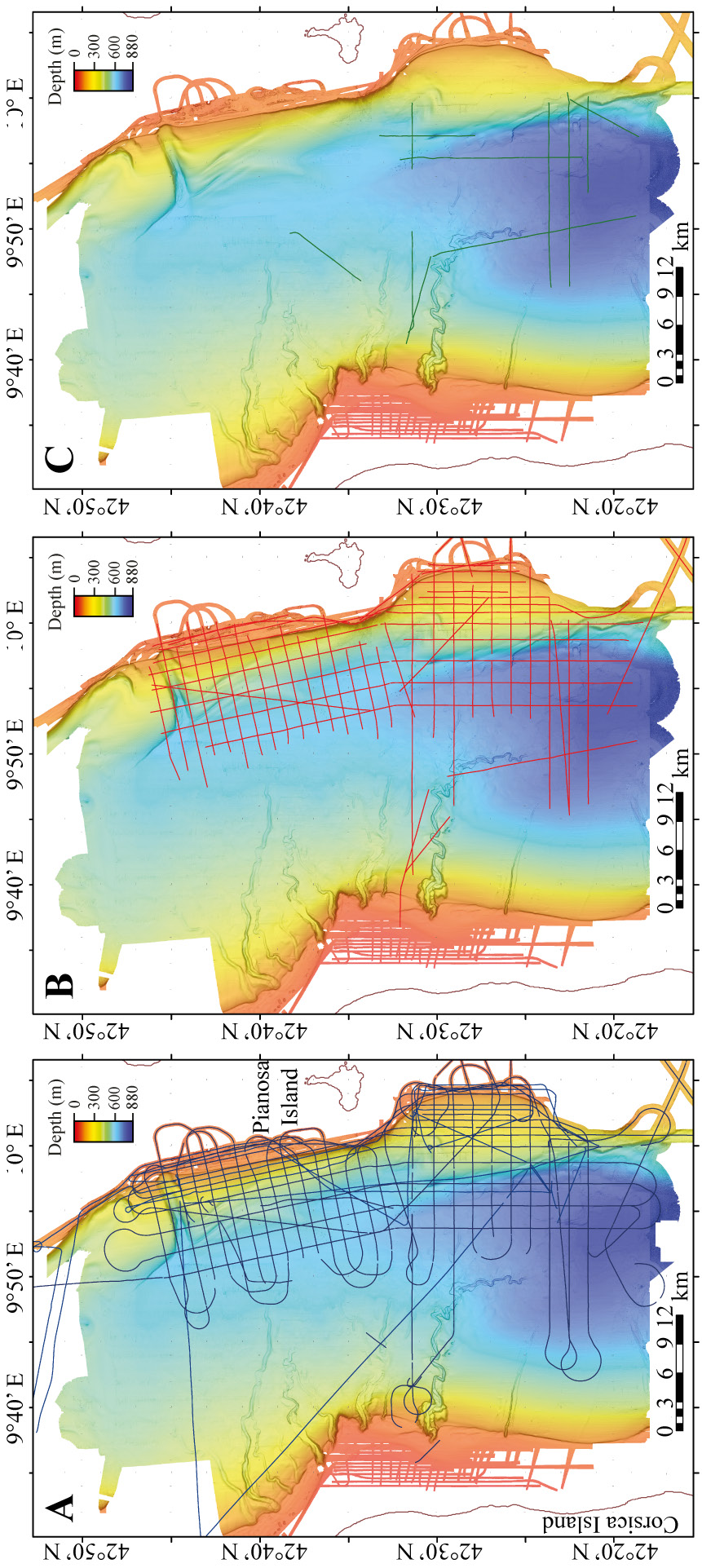

Fig. A.2. Multibeam bathymetry of the Corsica Trough with the location of the seismic profiles: (**A**) Hull-mounted sub-bottom profiler acquired during PRISME2, PAMELA-PAPRICA and PRISME3 cruises; (**B**) Multi-channel high resolution mini GI gun acquired during PRISME2 and PAMELA-PAPRICA cruises; (**C**) Deep-towed SYSIF acquired during the PRISME2 cruise.

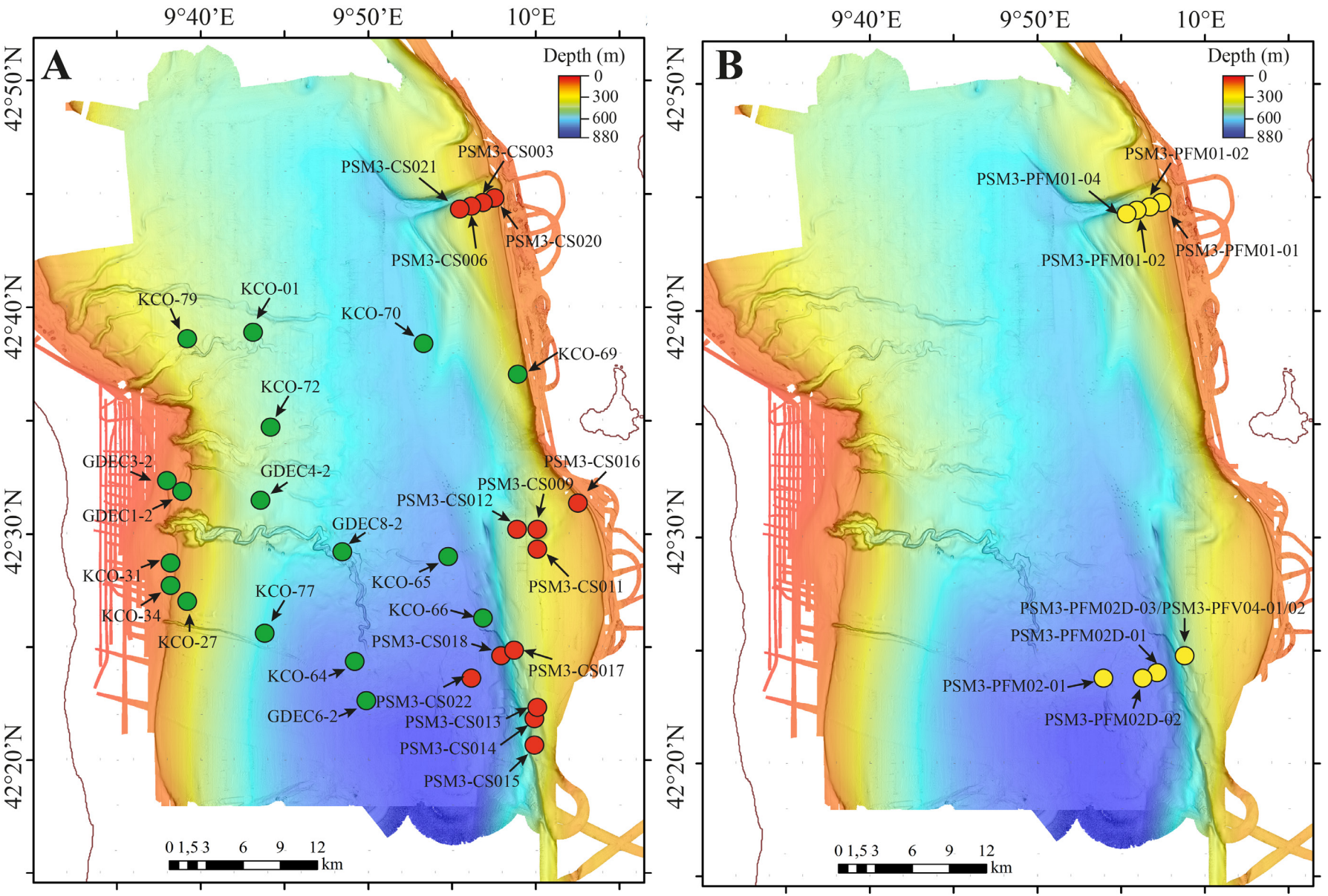

Fig. A.3. Multibeam bathymetry of the Corsica Trough with the location and names of: **(A)** sediment cores collected during the PRISME3 cruise in red and in green the complementary sediment cores and boreholes analysed in previous studies; **(B)** *In situ* geotechnical measurements (CPTU and P-wave velocity) acquired with the Penfeld penetrometer during the PRISME3 cruise.

Table A.1. Calypso piston cores collected along the Pianosa Ridge during the PRISME3 survey in 2013. See Fig. A.3A in the appendices for core location.

Core name	Latitude	Longitude	Water depth (m)	Length (m)
PSM3-CS003	42.741602°N	9.946704°E	245	9.14
PSM3-CS006	42.740227°N	9.938869°E	281	20.91
PSM3-CS009	42.503177°N	9.998834°E	370	21.23
PSM3-CS011	42.492267°N	9.999239°E	349	27.60
PSM3-CS012	42.503334°N	9.983666°E	425	26.96
PSM3-CS013	42.367498°N	9.998666°E	410	23.70
PSM3-CS014	42.363470°N	9.998663°E	434	20.60
PSM3-CS015	42.346669°N	9.998837°E	431	5.04
PSM3-CS016	42.523503°N	10.043666°E	171	9.10
PSM3-CS017	42.411721°N	9.976764°E	534	23.89
PSM3-CS018	42.412231°N	9.970599°E	594	19.83
PSM3-CS020	42.743169°N	9.956997°E	176	21.60
PSM3-CS021	42.738332°N	9.926891°E	342	20.69
PSM3-CS022	42.393883°N	9.941500°E	820	28.09

Table A.2. In situ measurements with the PENFELD penetrometer carried out along the Pianosa Ridge during the PRISME3 survey in 2013. See Fig. A.3B in the appendices for location.

Name	Latitude	Longitude	Tool (PENFELD)	Length (m)
PSM3-PFM01-01	42.74317°N	9.95701°E	Mechanic	30
PSM3-PFM01-02	42.7407°N	9.946358°E	Mechanic	30
PSM3-PFM01-03	42.74035°N	9.938228°E	Mechanic	30
PSM3-PFM01-04	42.738166°N	9.927166°E	Mechanic	30
PSM3-PFM02-01	42.393997°N	9.900844°E	Mechanic	23.47
PSM3-PFM02D-01	42.398842°N	9.95168°E	Mechanic	30
PSM3-PFM02D-02	42.393883°N	9.941506°E	Mechanic	30
PSM3-PFM02D-03	42.411723°N	9.976764°E	Mechanic	30
PSM3-PFV04-01	42.41164°N	9.976804°E	Velocity	8.53
PSM3-PFV04-02	42.411582°N	9.976875°E	Velocity	30

Chapter 30
Implications of Sediment Dynamics in Mass Transport along the Pianosa Ridge (Northern Tyrrhenian Sea)

Elda Miramontes, Antonio Cattaneo, Gwenael Jouet, and Sebastien Garziglia

Abstract The Pianosa Ridge forms the eastern flank of the Corsica Trough in the Northern Tyrrhenian Sea: it is the site of preferential accumulation of contourites and Mass Transport Deposits (MTDs). Along the Pianosa Ridge, 11 MTDs with a total volume of 6.5 km^3 were identified. These MTDs are distributed in three areas: (A) one small MTD associated to canyon flank destabilisation in the northern part of the study area; (B) six intermediate size MTDs in the central area; (C) four MTDs of larger size (up to 2.62 km^3) to the south, including the Pianosa Slump, which is the most recent MTD in this area (aged at 42–50 kyr BP) and analysed in more detail. The main factor controlling the formation of MTDs in areas A and B seems to be steep slopes associated to erosion and heterogeneous sedimentation caused by bottom currents, respectively. In contrast, multiple factors may control slope instability in the zone where the largest MTDs took place (area C): the incision generated by contour currents, the presence of coarser layers in contourite drifts that may accumulate gas and the location of normal faults near the headwall.

30.1 Introduction

The Corsica Trough is located between Corsica and the Tuscan Shelf in the Northern Tyrrhenian Sea. It has a maximum depth of 900 m and connects the Tyrrhenian and Ligurian Seas. The eastern flank of the Corsica Trough is formed by the Pianosa Ridge, a tectonic structure with typical slopes between 3 and 10°, reaching 20° locally (Fig. 30.1). This area is characterised by several submarine landslides and contourite deposits (Cattaneo et al. 2014; Fig. 30.1). Contourite drifts are formed by the Levantine Intermediate Water (LIW), flowing northwards (Artale and Gasparini 1990) and generating stronger bottom currents on the Pianosa

E. Miramontes (✉) • A. Cattaneo • G. Jouet • S. Garziglia
IFREMER, Géosciences Marines-EDROME, Centre de Brest, BP70, CS10070, 29280 Plouzané, France
e-mail: elda.miramontes.garcia@ifremer.fr

G. Lamarche et al. (eds.), *Submarine Mass Movements and their Consequences*, Advances in Natural and Technological Hazards Research 41,
DOI 10.1007/978-3-319-20979-1_30

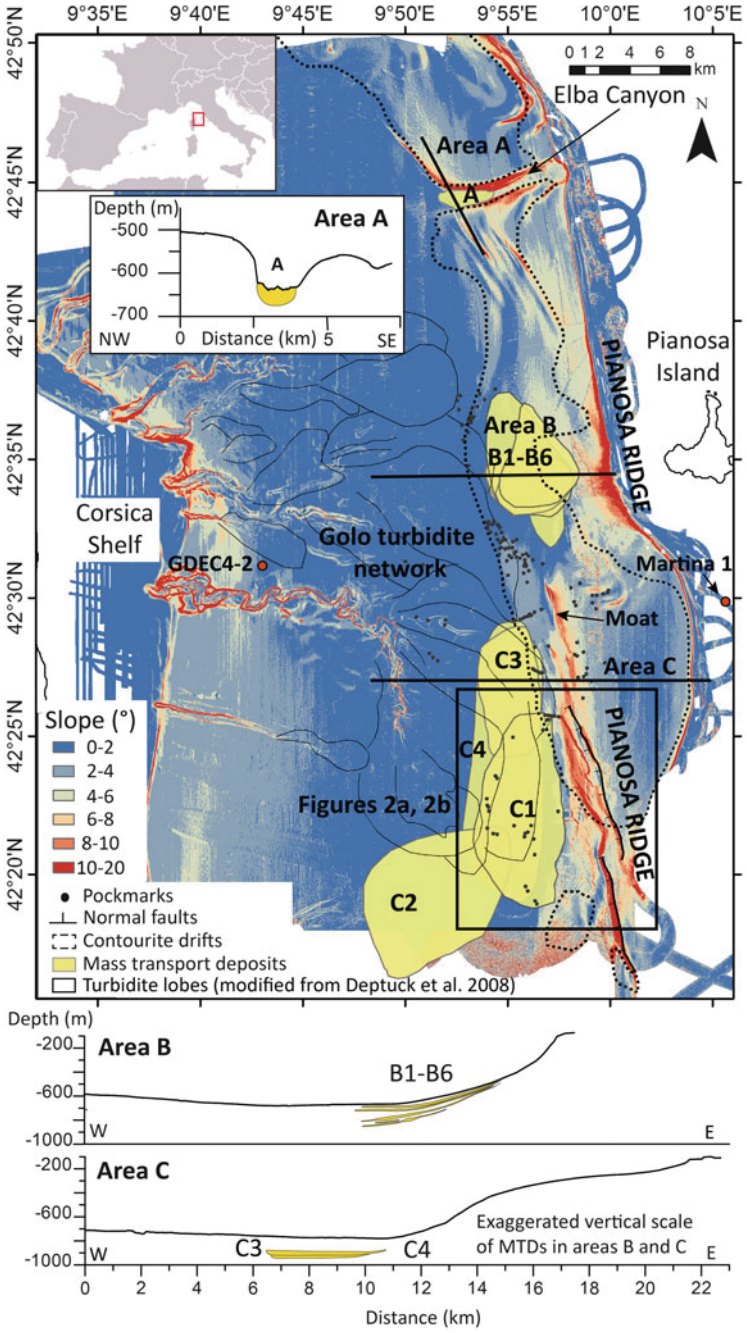

Fig. 30.1 Seafloor gradient map of the Corsica Trough with superposed location of morpho-sedimentary features: Mass Transport Deposits (MTDs), contourite drifts and turbidite lobes (see legend). Three bathymetric cross-sections across areas A, B and C show the location of MTDs

Ridge due to the Coriolis force. The sediment input from the Tuscan Shelf is low since sediment from Italian rivers is mostly trapped in the shelf and cannot reach the Corsica Trough (Roveri 2002). Most of the sediment deposited in the Corsica Trough is transported from the Corsica shelf by the Golo turbidite network (Deptuck et al. 2008; Fig. 30.1).

The aims of this study are to present the size and the stratigraphic distribution of Mass Transport Deposits (MTDs) along the Pianosa Ridge, and to analyse their relationship with the pre-existing seabed morphology.

30.2 Material and Methods

In 2013 two cruises, PRISME2 and PRISME3 onboard the R/V Atalante and R/V Pourquoi pas?, respectively, took place along the Pianosa Ridge. Multibeam bathymetry, 72-channel high-resolution mini GI gun (50–250 Hz) and CHIRP (1800–5300 Hz) seismic reflection profiles, and Calypso piston cores were collected along the Pianosa Ridge. P-wave velocity was measured on whole core sections using a Geotek Multi-Sensor Core Logger (MSCL). The bulk sediment semi-quantitative geochemical composition was measured with an Avaatech X-ray fluorescence (XRF) core scanner on split cores. Radiocarbon dating was obtained from bulk planktonic foraminifera at the Poznan radiocarbon laboratory. Radiocarbon ages were corrected for a marine reservoir effect of 400 years and calibrated using Calib 7.0.2 radiocarbon calibration software and the IntCal13 calibration curve (Reimer et al. 2013). MTDs were identified by seismic facies validated by the analysis of equivalent coring samples. MTD volume was calculated using the Kingdom Suite ® software by quantifying the time interval between the top and the bottom of the MTD from the seismic profiles. The velocity applied for time-depth conversion (1550–1560 m/s) was obtained from the velocity analysis calculated with the ProMAX ® Seismic Processing Software.

30.3 Results

Along the Pianosa Ridge 11 MTDs were identified in the Quaternary sediment record. Differences in location, volume and morphology were used to distinguish three areas of MTDs: A, B and C (Table 30.1). Seismic correlation with the borehole GDEC4-2 (Fig. 30.1; Angue Minto'o 2014) provided information about the stratigraphy in the region.

Area A shows a small submarine landslide associated to the destabilisation of the northern flank of the Elba Canyon (west of the Elba Island), where the slope is 8–20°. The headwall scarp and the deformation features of the MTD are clear in the bathymetry (Fig. 30.1). MTD A is of Holocene age, since it affects a regional reflector dated at 12 kyr.

Table 30.1 Characterisation of mass transport deposits in areas A, B and C

Area	Name	Volume (km^3)	Maximum runout (km)	Maximum length (km)	Maximum width (km)	Width/ length ratio	Age (kyr BP)
A	A	0.10	1.5	1.2	3.6	3.0	<12
B	B1	0.19	7.0	5.7	7.6	1.3	42–59
	B2	0.09	8.0	5.6	4.6	0.8	125–137
	B3	0.26	7.5	5.9	7.2	1.2	420–437
	B4	0.15	4.2	2.5	7.4	3.0	452->542
	B5	0.05	6.0	3.4	4.4	1.3	>542
	B6	0.04	6.2	3.6	4.4	1.2	>542
C	C1	2.62	9.0	6.0	13.5	2.3	42–50
	C2	0.47	16.0	10.0	7.8	0.8	125–160
	C3	0.67	6.0	4.0	8.7	2.2	265–321
	C4	1.86	10.4	5.3	18.6	3.5	321–380

Six small to intermediate size MTDs (B1 to B6) are observed in area B (Table 30.1). They are located west of the Pianosa Island, where the Pianosa Ridge forms an edge, generating in this zone high slope gradients (8–10°). The MTDs have an oval shape in plan view. B1, B2, B3 and B4 have a mean thickness of about 10 m; B5 and B6 mean thickness is 5 m. The continental slope in area B is starved during Pliocene and Quaternary. Pre-Messinian deposits (age deduced by correlation with the well Martina 1; Fig. 30.1; Pascucci et al. 1999) crop out in patches on the upper slope. Despite the reduced size of these MTDs, their thickness corresponds to about 30 % of the Pliocene-Quaternary deposits in the lower continental slope. B6 and B5 MTDs are older than 542 kyr, while the sediment covering B4 was deposited at 452 kyr, based on correlation to the bottom of borehole GDEC4-2. B3 is close in time to B4 but separated by 300 kyr from B2 (Table 30.1). B1 is the most recent MTD (42–59 kyr) in area B, it took place about 80 kyr after B2. The frequency of MTDs in area B is irregular and it was higher during the Middle Pleistocene than during the Upper Pleistocene.

Four MTDs (C1 to C4) are located in area C, in the southern zone of the study area. Their volume ranges from 0.67 to 2.62 km^3 and they are characterised by a high width/length ratio, except for C2 that has a ratio lower than 1 (Table 30.1). Between 265 and 380 kyr BP C3 and C4 were formed, followed by C2 at 125–160 kyr (Table 30.1). The Pianosa Slump (C1) is the most recent MTD of area C and it was analysed in more detail than the other MTDs since it was sampled by the Calypso piston core PSM3-CS022 (Figs. 30.2 and 30.3). The top of C1 (i.e. the bottom of the post-slide hemipelagic sediment; Fig. 30.3) is dated at 42,326 cal year BP and Cattaneo et al. (2014) report that the MTD disrupted sediments as old as 50,000 cal year BP. C1 is overlain by about 17–20 m of sediment (Fig. 30.3). However, various morphological features related to MTD C1 can still be appreciated at the present seafloor (Fig. 30.2).

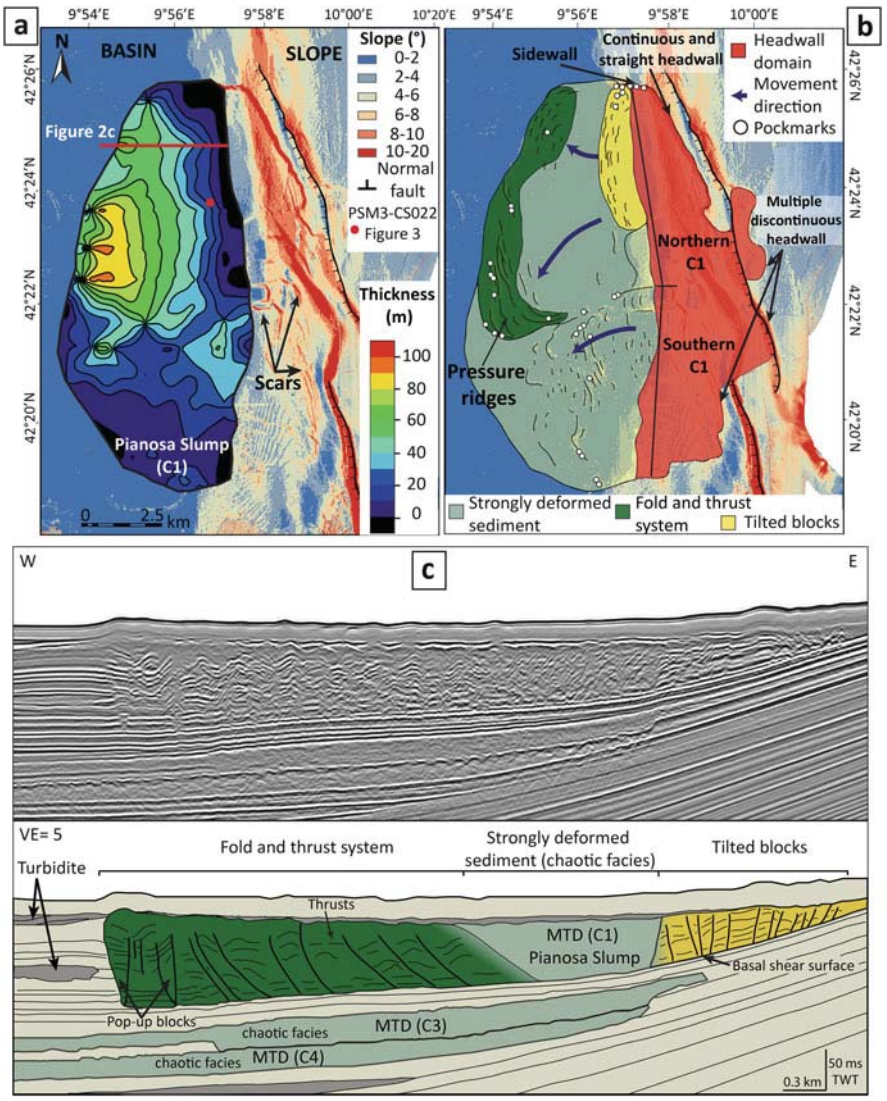

Fig. 30.2 (**a**) Isopach map of the Pianosa Slump (C1) overlaying the present seafloor gradient map with the location of Calypso piston core PSM3-CS022. (**b**) Morphological interpretation of C1. (**c**) Multichannel high-resolution mini GI gun seismic reflection profile across MTDs C1, C3 and C4 and line drawing with the interpretation

The headwall domain of C1 has the same lateral extent as the Pianosa Slump deposit. However, the headwall morphology is rather irregular. In the northern part, the headwall is continuous, parallel to a normal fault (Fig. 30.2b). It is connected to the MTD by a sidewall that is 30 m high at the present seafloor. South of this zone, the slope is cut by multiple discontinuous headwalls and scarps. C1 is composed of

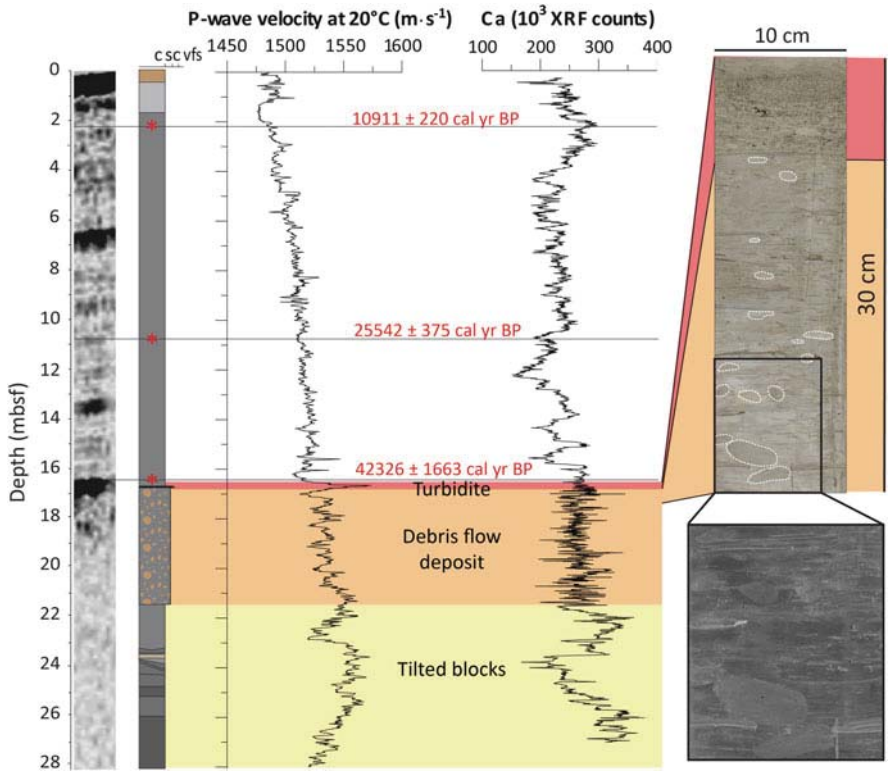

Fig. 30.3 From *left* to *right*: CHIRP seismic facies, core log, P-wave velocity and Calcium curves of Calypso piston core PSM3-CS022. Photo of the core and zoom with inverted colour. The *red* area shows a turbidite (peak in P-wave velocity), the *orange* area a debris flow deposit and the *yellow* area tilted blocks. Three calibrated radiocarbon ages are represented with red stars

three main parts (Fig. 30.2b, c) deduced from seismic profiles, bathymetry and Calypso piston core PSM3-CS022 (Fig. 30.3): (1) strongly deformed sediment, (2) fold and thrust system and (3) tilted blocks. The strongly deformed sediment corresponds to chaotic seismic facies that are present in the central northern part and in the southern part of C1, where the headwall is discontinuous. In this area the surface morphology shows lobate shapes and crests that indicate a movement towards the west that turned slightly to the southwest, in the direction of increasing depth. The MTD thickness of the southern part shows that there is a deposit at the foot of the slope up to 50 m thick and a thicker zone (50–70 m) in the central distal part.

In the northern part of C1 the internal structure of the deposit is more complex than in the southern part. In this area the toe domain of the MTD is formed by a fold and thrust system. The frontal part of C1 is composed of hemipelagites and turbidites that are deformed and compressed forming a system of thrusts, folds and pressure ridges, with individual pop-up blocks apparent in the frontal part of the

MTD (Fig. 30.2). The greatest thickness of C1 deposits (up to 100 m) is found in the central zone of C1 where the pressure ridges are higher (up to 10 m high) and larger (up to 2 km long) (Fig. 30.2a). The proximal part consists of tilted blocks (Fig. 30.2b) that become more deformed towards the south. Tilted blocks are identified in seismic profiles where reflectors dip in different directions. Moreover, tilted blocks form crests that are apparent in the seafloor. Groundtruthing evidence of the presence of tilted blocks comes from the bottom of Calypso piston core PSM3-CS022 (Fig. 30.3). This core shows that a 4.7-m-thick debris flow deposit composed of mud with clay pebbles lies on top of the tilted blocks. These distinct seismic and lithological facies correspond to different degrees of deformation, which can be identified in the Calcium curve. When the degree of deformation is very high (debris flow deposit), the Calcium signal is very noisy (Fig. 30.3). Between the compressed frontal zone and the zone of tilted blocks, the sediment is strongly deformed, characterised by chaotic seismic facies and by a relatively smooth upper surface (Fig. 30.2). Since the pressure ridges and the crests are perpendicular to the mass movement, they provide information on the direction of the transport. The northern part of the Pianosa Slump comes from the area of the straight headwall parallel to the fault. The northernmost part moved slightly towards the northwest, while most of the sediment was transported in a southwest direction, towards the deepest part of the basin.

Multibeam bathymetry reveals the presence of many pockmarks located in the contourite drifts between areas B and C and close to MTDs in zone C (Fig. 30.1). The fluid escape paths over the Pianosa Slump are mainly found in the pressure ridges, in the crests and in the sidewall (Fig. 30.2b).

30.4 Discussion and Conclusions

Slope instability has been a recurrent process along the Pianosa Ridge, although the origin and the control factors could vary according to the location of the submarine landslides. The differences in size and volume between MTDs in area B and C are linked to an uneven sedimentation along the Pianosa Ridge related to the basement morphology and to bottom currents. Sediment accumulation on the slope in area C is much higher compared to area B. Therefore, more sediment could be potentially mobilised by mass transport during a single event, generating larger submarine landslides. In area B bottom currents are accelerated due to the higher slope gradient, preventing sediment deposition.

Group B and C present some similarities in the time intervals of slope failure, since B1-C1 and B2-C2 are in similar ranges of age. In contrast, the other MTDs are not synchronous. When C3 and C4 were formed, area B was in stable conditions (Table 30.1).

The main predisposing factor in areas A and B seems to be the steep slopes (8–20° and 8–10°, respectively) (Fig. 30.1). Within the Elba Canyon, due to the Coriolis effect, bottom currents could produce a stronger erosion on the northern

flank of the canyon, generating the observed canyon asymmetry with a steeper northern flank (Fig. 30.1). Incisions and oversteepening on the northern flank might have contributed to the formation of MTD A. In area B, six MTDs are stacked, and represent a relevant percentage (30 %) of the Pliocene-Quaternary deposit in the lower slope, suggesting that an important proportion of the sediment accumulated on the middle and upper slope was affected by mass transport. The formation of submarine landslides in area C (Fig. 30.1) seems to be much more complex. Multiple factors may predispose slope instability in this area. Bottom currents may have an important role since they provide sediment and generate incisions with higher slopes, corridors of non deposition or slight erosion (moat with slope of 15°; Fig. 30.1). In addition, layers of coarser sediment in contourite drifts seem to influence the location of failure planes (Miramontes et al. 2014) and could potentially stock more gas than the overlying mud. Numerous pockmarks affect the present day seafloor on top of the MTDs and contourite drifts (Figs. 30.1 and 30.2). Some of these pockmarks are clearly rooted on buried MTDs and turbidite lobes (Fig. 30.1). Such a configuration suggests that the emplacement of these sedimentary bodies might have influenced subsequent instability.

In the Pianosa Ridge the present-day seismicity is considered to be very low (Scisciani and Calamita 2009), while the area entered in a post-rift phase from the late Messinian (Pascucci et al. 1999). However, the location of the headwall of the Pianosa Slump next to a normal fault that affects the Pliocene-Quaternary record (Fig. 30.3) raises questions about the possible relationship between faulting and slope instability.

Acknowledgments We thank the Captain and the crew of the PRISME2 and PRISME3 cruises (2013) onboard R/V Atalante and R/V Pourquoi pas?, respectively. We are grateful to reviewers M. Rovere and C. Campbell for their valuable suggestions that improved the manuscript. The thesis of Elda Miramontes is co-funded by TOTAL and Ifremer as part of the scientific project TOTAL-Ifremer PAMELA. We thank projects LabexMER ANR-10-LABX-19-01 Axis 4 for lab support.

References

Angue Minto'o CM (2014) Enregistrements sédimentaires des changements climatiques et environnementaux pendant le quaternaire terminal sur la marge Est-Corse. PhD Thesis, Université de Perpignan, Perpignan, 309

Artale M, Gasparini GP (1990) Simultaneous temperature and velocity measurements of the internal wave field in the Corsican Channel (Eastern Ligurian Sea). J Geophys Res 95(C2):1635–1645

Cattaneo A, Jouet G, Charrier S, Thereau E, Riboulot V (2014) Submarine landslides and contourite drifts along the Pianosa Ridge (Corsica Trough, Mediterranean Sea). In: Submarine Mass Movements and Their Consequences: 6th International Symposium 37:435–445

Deptuck ME, Piper DJW, Savoye B, Gervais A (2008) Dimensions and architecture of late Pleistocene submarine lobes off the northern margin of East Corsica. Sedimentology 55:869–898

Miramontes E, Cattaneo A, Jouet G, Garziglia S, Thereau E, Gaillot A, Roubi A, Rovere M (2014) The Pianosa Contourite Depositional System (Corsica Trough, North Tyrrhenian Sea): stratigraphic evolution and possible role in slope instability. In: Van Rooij D, Rüggeberg A (eds). 2014. Book of abstracts. 2nd deep-water circulation congress: the contourite log-book. Ghent, Belgium, 10–12 Sept 2014. VLIZ Special Publication 69:15–16

Pascucci V, Merlini S, Martini IP (1999) Seismic stratigraphy of the Miocene-Pleistocene sedimentary basins of the Northern Tyrrhenian Sea and Western Tuscany (Italy). Basin Res 11:337–356

Reimer PJ et al (2013) IntCal13 and Marine13 radiocarbon age calibration curves 0–50,000 years cal BP. Radiocarbon 55:1869–1887

Roveri M (2002) Sediment drifts of the Corsica Channel, northern Tyrrhenian sea. In: Stow DAV, Pudsey CJ, Howe JA, Fauge'res J-C, Viana A (eds) Deep-water contourite systems: modern drifts and ancient series, seismic and sedimentary characteristics, vol 22. Geological Society of London, London, Memoirs, pp 191–208

Scisciani V, Calamita F (2009) Active intraplate deformation within Adria: examples from the Adriatic region. Tectonophysics 476:57–72

Marine Geology 378 (2016) 20–42

Contents lists available at ScienceDirect

Marine Geology

journal homepage: www.elsevier.com/locate/margo

The Pianosa Contourite Depositional System (Northern Tyrrhenian Sea): Drift morphology and Plio-Quaternary stratigraphic evolution

E. Miramontes [a,*], A. Cattaneo [a], G. Jouet [a], E. Théreau [a], Y. Thomas [a], M. Rovere [b], E. Cauquil [c], F. Trincardi [b]

[a] IFREMER, Géosciences Marines-EDROME, Centre de Brest, BP70, 29280 Plouzané, France
[b] ISMAR-CNR, Via P. Gobetti 101, 40129 Bologna, Italy
[c] TOTAL SA, 92400 Paris La Défense, France

ARTICLE INFO

Article history:
Received 25 May 2015
Received in revised form 20 October 2015
Accepted 9 November 2015
Available online 10 November 2015

Keywords:
Sediment drift
Bottom current
Levantine Intermediate Water
Modified Atlantic Water
Mediterranean Sea
Sea level

ABSTRACT

The Pianosa Contourite Depositional System (CDS) is located in the Corsica Trough (Northern Tyrrhenian Sea), a confined basin dominated by mass transport and contour currents in the eastern flank and by turbidity currents in the western flank. The morphologic and stratigraphic characterisation of the Pianosa CDS is based on multibeam bathymetry, seismic reflection data (multi-channel high resolution mini GI gun, single-channel sparker and CHIRP), sediment cores and ADCP data. The Pianosa CDS is located at shallow to intermediate water depths (170 to 850 m water depth) and is formed under the influence of the Levantine Intermediate Water (LIW). It is 120 km long, has a maximum width of 10 km and is composed of different types of muddy sediment drifts: plastered drift, separated mounded drift, sigmoid drift and multicrested drift. The reduced tectonic activity in the Corsica Trough since the early Pliocene permits to recover a sedimentary record of the contourite depositional system that is only influenced by climate fluctuations. Contourites started to develop in the Middle–Late Pliocene, but their growth was enhanced since the Middle Pleistocene Transition (0.7–0.9 Ma). Although the general circulation of the LIW, flowing northwards in the Corsica Trough, remained active all along the history of the system, contourite drift formation changed, controlled by sediment influx and bottom current velocity. During periods of sea level fall, fast bottom currents often eroded the drift crest in the middle and upper slope. At that time the proximity of the coast to the shelf edge favoured the formation of bioclastic sand deposits winnowed by bottom currents. Higher sediment accumulation of mud in the drifts occurred during periods of fast bottom currents and high sediment availability (i.e. high activity of turbidity currents), coincident with periods of sea level low-stands. Condensed sections were formed during sea level high-stands, when bottom currents were more sluggish and the turbidite system was disconnected, resulting in a lower sediment influx.

1. Introduction

Contour currents are strictly defined as bottom currents flowing alongslope, parallel to a bathymetric contour, and driven by the thermohaline circulation or by the wind (Rebesco et al., 2008). The sediment deposits related to persistent contour currents, named contourites, were first recognised in deep sea environments (Heezen and Hollister, 1964). Numerous cases of contourite drifts controlled by the activity of long-lasting bottom currents have been later identified on the continental shelves (Harris et al., 1999; Harris and Beaman, 2003; Vandorpe et al., 2011) and the upper slope (Marani et al., 1993; Viana et al., 1998; Verdicchio and Trincardi, 2008a) in oceanic settings and along Mediterranean margins. Contourites in the Mediterranean Sea are typically of smaller size compared to drifts found in oceanic settings (Verdicchio and Trincardi, 2008b) and tend to be confined in settings constrained by local morphology such as straits or channels (Pellegrini et al., 2015 and references therein).

Shallow and intermediate depth contourites are more directly affected by sea level fluctuations, since during sea level low-stands, even if they remain in submerged conditions, the sediment flux from the continental shelf is usually enhanced and downslope transport is more frequent. In addition, the upper continental slope may be more influenced by wind-driven currents and the depth range of the superficial and intermediate water masses may change and thus the current regime affecting the seafloor.

Mixed turbidite–contourite systems are common along continental margins where contour currents rework and/or redistribute gravity deposits (Mulder et al., 2008). The interaction between downslope gravity currents and alongslope contour currents is often recognised when both processes take place along the same margin (Rebesco et al., 2002; Hernández-Molina et al., 2006; Marches et al., 2010; Brackenridge et al., 2013). In the Corsica Trough, turbidity and contouritic processes have occurred in opposite margins of the basin. This physical separation of along- and downslope processes avoids problems associated with the

* Corresponding author.
E-mail address: elda.miramontes.garcia@ifremer.fr (E. Miramontes).

http://dx.doi.org/10.1016/j.margeo.2015.11.004
0025-3227/

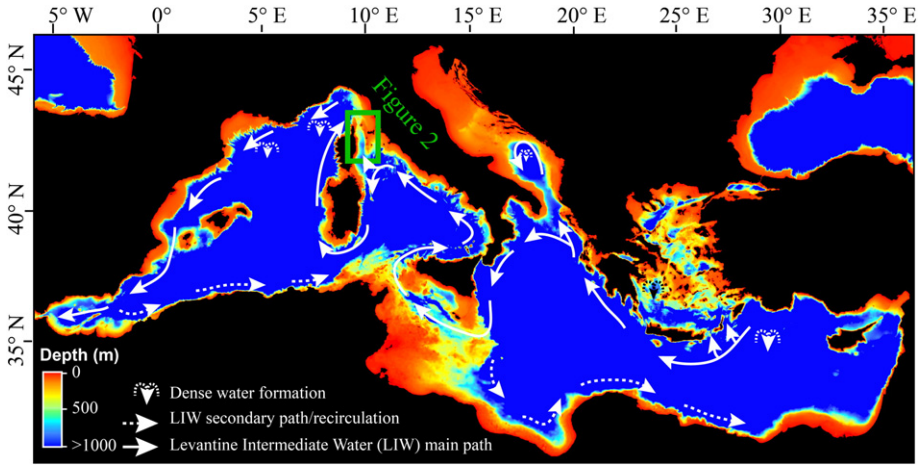

Fig. 1. Bathymetry of the Mediterranean Sea with the circulation of the Levantine Intermediate Water (adapted from Millot and Taupier-Letage (2005)).

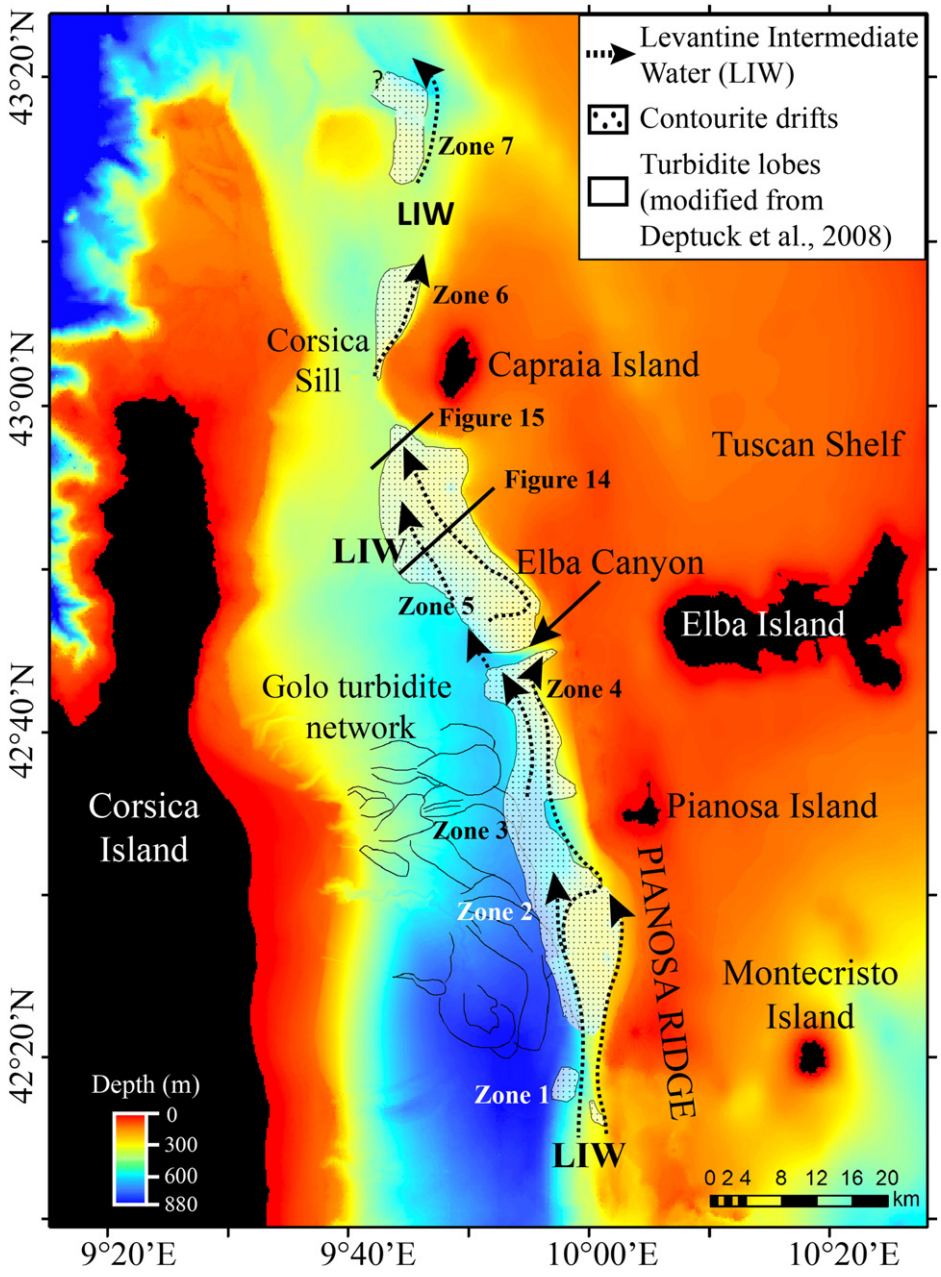

Fig. 2. Bathymetry of the Corsica Trough and cartography of the contourite drifts that form the Pianosa Contourite Depositional System and of the turbidite lobes of the Golo turbidite network.

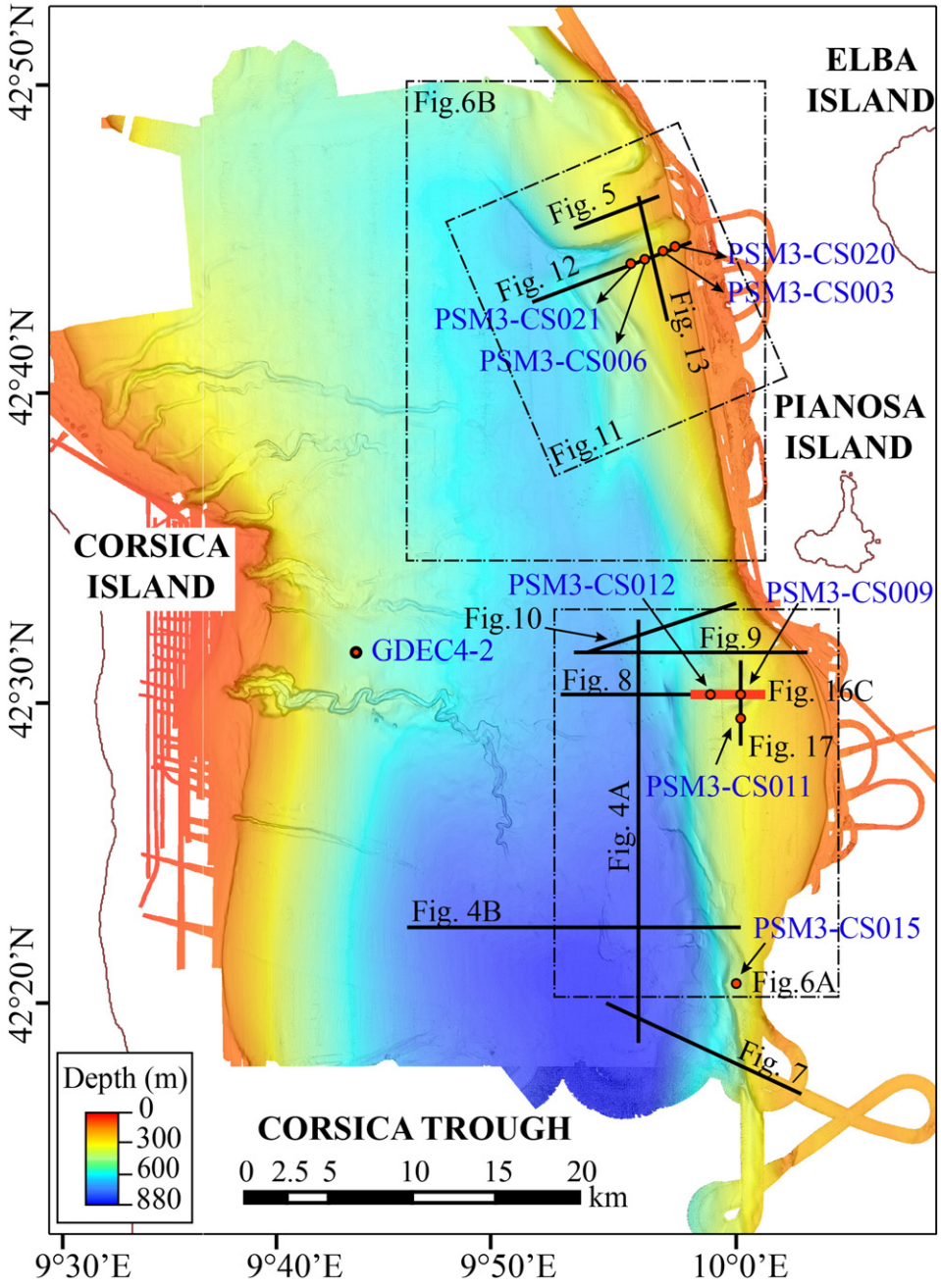

Fig. 3. Multibeam bathymetric map of the Corsica Trough with the location of the seismic profiles, sediment cores and the borehole used in this study. The location of Fig. 16C is represented by a red line superposed on the black line of Fig. 8. The location of Figs. 6 and 11 is represented with dashed squares.

Table 1
Radiocarbon ages of cores PSM3-CS009, PSM3-CS011, PSM3-CS006 and PSM3-CS021. The age dates were corrected for a marine reservoir effect of 400 years and calibrated using Calib 7.0.2 and the IntCal13 calibration curve (Reimer et al., 2013).

Core number	Zone	Depth (cm)	Material	Lab code	Cal BP age (year)
PSM3-CS009	2	41	Bulk planktonic	Poz-63392	2730 ± 31
PSM3-CS009	2	1126	Bulk planktonic	Poz-63393	30,524 ± 636
PSM3-CS009	2	1400	Bulk planktonic	Beta-394859	29,810 ± 408
PSM3-CS011	2	104	Bulk planktonic	Beta-394860	17,311 ± 193
PSM3-CS011	2	380	Bulk planktonic	Beta-394861	21,820 ± 221
PSM3-CS011	2	709	Bulk planktonic	Beta-394862	26,668 ± 366
PSM3-CS006	4	7	Bulk planktonic	Poz-63394	2854 ± 75
PSM3-CS006	4	250	Bulk planktonic	Poz-63395	46,955 ± 3044
PSM3-CS021	4	100	Bulk planktonic	Beta-394864	18,325 ± 187
PSM3-CS021	4	550	Bulk planktonic	Beta-394865	28,154 ± 313

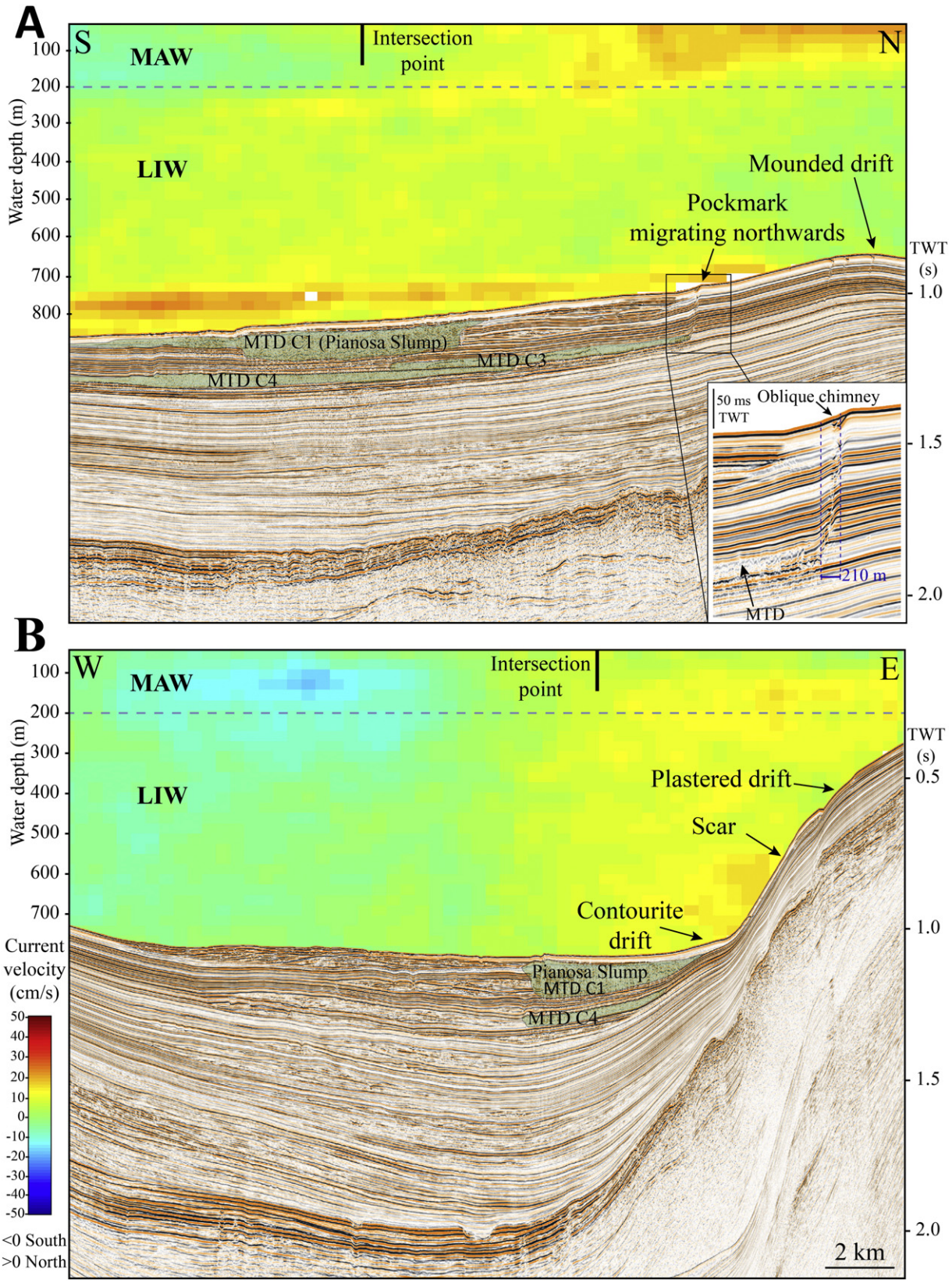

Fig. 4. Current velocity in north–south direction (positive towards the north and negative towards the south) from hull-mounted ADCP, coupled with multi-channel high resolution mini GI gun seismic reflection profiles. (A) North–South profile PSM2-HR-009 and zoom showing the presence of a pockmark with an oblique chimney rooted in MTD C3. (B) East–West profile PSM2-HR-061. The horizontal dashed blue line shows the general interphase between the Modified Atlantic Water (MAW) and the Levantine Intermediate Water (LIW) (Astraldi and Gasparini, 1992; La Violette, 1994; Millot, 1999; Toucanne et al., 2012). Mass Transport Deposits (MTDs) are outlined by green polygons. See Fig. 3 for seismic profile location.

identification and differentiation of sediment bodies related to contour or turbidity currents, and permits to better constrain the influence of the activity of turbidity currents on the development of contourites.

The purpose of this study is to present an accurate morphologic and stratigraphic characterisation of the contourite depositional system located on the eastern flank of the Corsica Trough, named here the Pianosa Contourite Depositional System (CDS). Thanks to the confined setting and the available stratigraphic control, the Pianosa CDS provides a unique opportunity to achieve a high resolution reconstruction of the spatial and chronological contourite evolution and to infer their relationship to the activity of the turbidite system and sea level fluctuations.

2. Regional setting

2.1. Geology and morphology

The Corsica Trough is a narrow basin located in the Northern Tyrrhenian Sea (Fig. 1), flanked by the Corsica Island to the west and by the Pianosa Ridge and the Tuscan Shelf to the east (Fig. 2). It is a N–S trending basin, about 100 km long and 10–35 km wide at depth of the shelf edge. This basin connects the Ligurian and Tyrrhenian Seas. It has a maximum depth of 880 m in the southern part, becoming shallower towards the north. The narrowest and shallowest zone is found offshore the Capraia Island, where the Tuscan and Corsican continental shelves are separated by the Corsica Sill, that is 9.5 km wide between opposite shelf edges (Fig. 2).

The Corsica Trough developed during the opening of the Northern Tyrrhenian Sea, between the late Burdigalian and Langhian (Zitellini et al., 1986), resulting in the formation of a half graben (Pascucci, 2002). The Pianosa Ridge corresponds to a tilted block of the half graben, with the master fault located on the Corsican side of the basin (Pascucci, 2002) and separates the Corsica Trough from the Tuscan Shelf. Several N–S and NW–SE trending basins can be found in the Tuscan Shelf (Pascucci et al., 2007), trapping a great part of the sediment from Italy (Roveri, 2002). They developed on a thrust substrate locally dissected by normal faults (Bartole, 1995).

The asymmetry of the Corsica Trough is the result of tectonic processes and is still evident at the present seafloor (Fig. 2). The western flank of the basin has a gentle slope (mean values between 2° and 3°), while the eastern flank, formed by the Pianosa Ridge, has steeper slopes (between 3° and 10°, reaching 20° locally). The western part of the Corsica Trough is dominated by downslope gravity-driven depositional processes that resulted in the formation of the Golo turbidite network (Fig. 2; Gervais et al., 2004; Gervais et al., 2006; Deptuck et al., 2008; Calves et al., 2013). On the other side, the Pianosa Ridge is characterised by both alongslope processes, resulting in contourite drifts (Marani et al., 1993; Roveri, 2002; Cattaneo et al., 2014), and downslope mass-wasting processes (Cattaneo et al., 2014; Miramontes et al., 2016).

2.2. Oceanography

The limited depth of the Corsica Trough (max. 880 m) does not allow the transit of the Mediterranean Deep Water, being the Levantine Intermediate Water (LIW) the only water mass in contact with the seafloor. The Western Intermediate Water formed in the Liguro-Provençal subbasin is not present in the Tyrrhenian Sea. Therefore, the LIW is in general located just below the Modified Atlantic Water (MAW) (Millot, 2013). The MAW is found at water depths ranging from 0 to 200 m

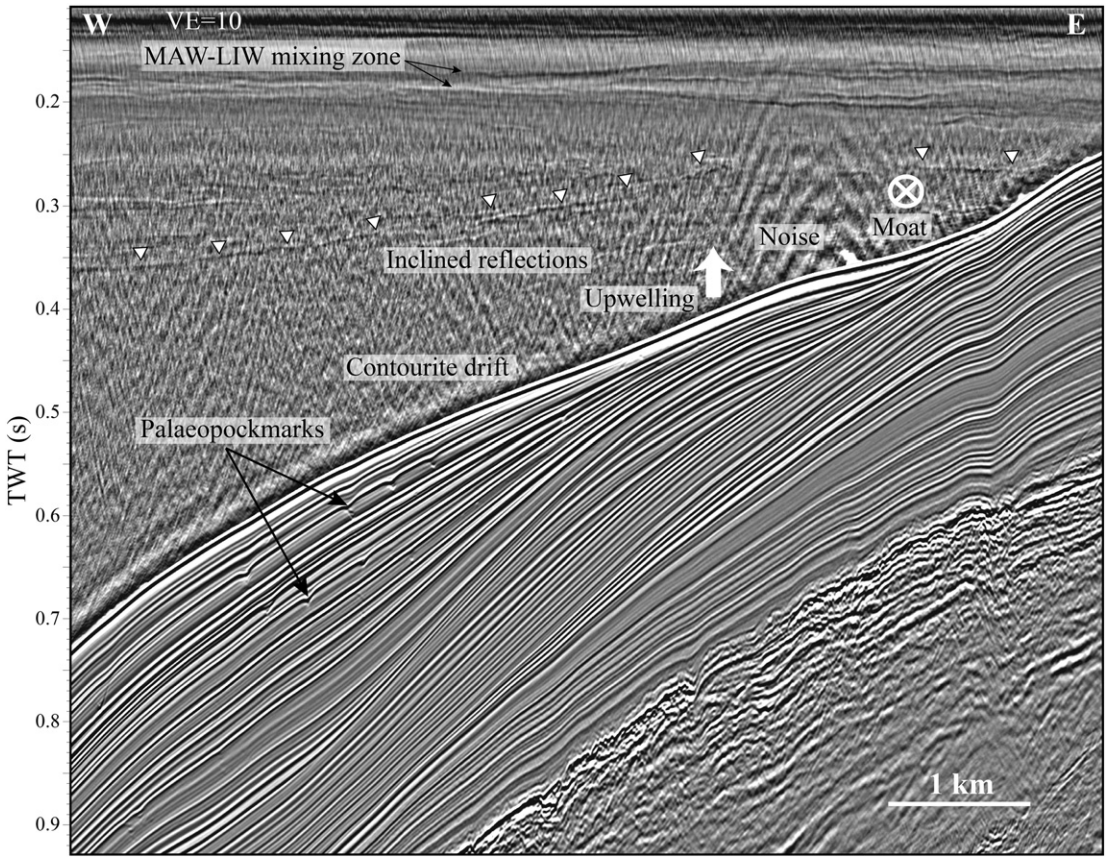

Fig. 5. PSM2-HR-043 multi-channel high resolution mini GI gun seismic reflection profile of the water column and sedimentary succession located at the north of the Elba Canyon. The horizontal reflections located at 0.16–0.20 s TWT (120–150 m w.d.) are interpreted as the mixing zone between the Modified Atlantic Water (MAW) and the Levantine Intermediate Water (LIW). Inclined reflections in the water column located at 0.30–0.36 s TWT (225–270 m w.d.) and marked with white triangles show the upwelling of deeper and denser water on the slope, where a moat and a mounded drift are formed. See Fig. 3 for seismic profile location.

(Astraldi and Gasparini, 1992; La Violette, 1994; Millot, 1999; Toucanne et al., 2012). The LIW is formed in the Rhodes cyclonic gyre in the NW of the Levantine Basin (Fig. 1) by a process of evaporation during the summer, resulting in a warm and salty surface water mass, and a later winter cooling that increases its density. As a consequence, the water sinks inside the Rhodes cyclone during February and March (Lascaratos et al., 1999). The LIW formation presents interannual variability: the formation area is enlarged during very cold winters, covering the whole north Levantine Basin (Lascaratos et al., 1999). After its formation, the LIW flows westwards through the Strait of Sicily, then it continues northwards in the Tyrrhenian Sea. A branch of the LIW keeps the same direction crossing the Corsica Trough, while another branch turns to the south and flows along eastern Sardinia (Fig. 1; Millot and Taupier-Letage, 2005).

The circulation along the eastern part of the Corsica Trough is characterised by northward flowing currents that change significantly with seasons, being stronger during the cold seasons (reaching 10–40 cm s^{-1} from late autumn to early spring) (Astraldi and Gasparini, 1992; Vignudelli et al., 1999) and resulting in a higher water transport through the Corsica Trough during this period (Vignudelli et al., 2000). The seasonal variability is in part caused by a climatological steric difference in sea level between the Ligurian and the Tyrrhenian Seas because of the formation of colder and saltier water masses in the Ligurian Sea during the winter (Vignudelli et al., 2000). These changes in circulation are related to large-scale atmospheric patterns, such as the North Atlantic Oscillation (Vignudelli et al., 1999). Similar processes have likely occurred in the past. During cold periods bottom water masses were better ventilated (Cacho et al., 2000; Minto'o et al., 2015) and faster (Toucanne et al., 2012) in the Mediterranean Sea. More arid and cold climatic conditions during cold intervals could favour the production of denser LIW (Cacho et al., 2000).

3. Materials and methods

The present study is based on the analysis of seismic reflection and sedimentological data acquired in the Corsica Trough since 1990 (Marani et al., 1993; Roveri, 2002; Gervais et al., 2004; Deptuck et al., 2008; Toucanne et al., 2012; Calves et al., 2013; Angue Minto'o, 2014; Toucanne et al., 2015). The multibeam bathymetry from the Corsica Trough was acquired during the SIGOLO survey in 2008 (Calves et al., 2013) and completed with the zone of the Pianosa Ridge during surveys PRISME2-PAPRICA and PRISME3 carried out by IFREMER in 2013 onboard the R/V Atalante and the R/V Pourquoi pas?, respectively. The outer bathymetric data were retrieved from the EMODnet Bathymetry compilation (http://portal.emodnet-bathymetry.eu/). The seismic data used for the study are 2D seismic reflection profiles: single-channel 1 kJ sparker (50–60 Hz) profiles collected during cruises ET91 (N/O Bannock), ET93 and ET95 (N/O Urania) carried out by the former Istituto di Geologia Marina of Bologna of the Italian National Research Council (CNR), now ISMAR-CNR (Roveri, 2002); CHIRP (Compressed High Intensity Radar Pulse, 1800–5300 Hz) profiles and 72-channel high-resolution profiles sourced by a mini GI gun (50–250 Hz) were acquired in 2013 during cruises PRISME2-PAPRICA and PRISME3 (Figs. 2 and 3). Seismic data from surveys ET91 and ET95 were interpreted from analogical profiles and used for the mapping of the contourites. Current velocity was acquired with the hull-mounted Acoustic Doppler Current Profiler (ADCP) OS38 of R/V Atalante during the cruise PRISME2-PAPRICA in August 2013. The data were processed with the CASCADE

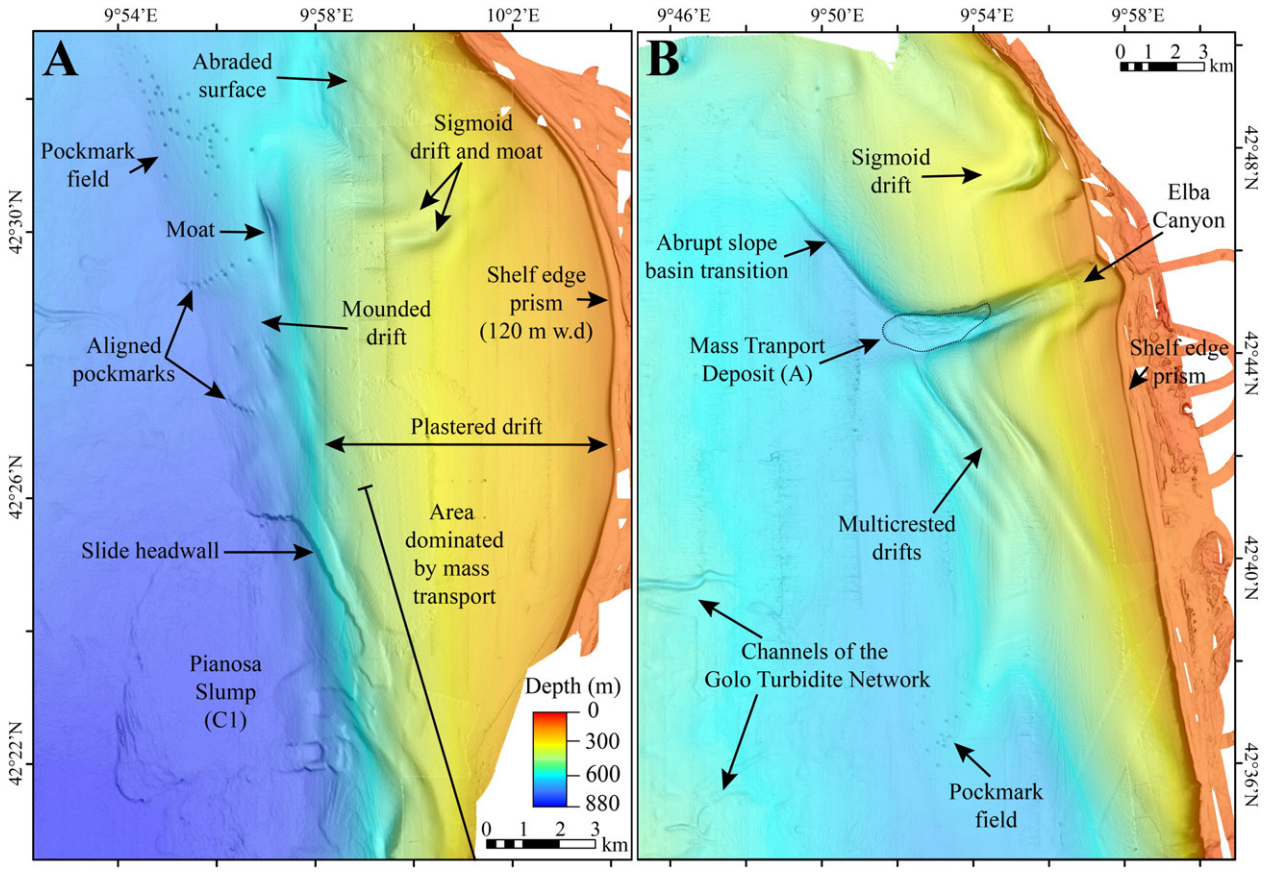

Fig. 6. (A) Multibeam bathymetry zoom of the southern area of the system evidencing the presence of sigmoid drifts, a separated mounded drift, a plastered drift, numerous pockmarks, a mass transport deposit (Pianosa Slump, C1) and an area of the slope very affected by mass-wasting processes. (B) Multibeam bathymetry zoom of the area around the Elba Canyon revealing the surface morphology of multicrested and sigmoid drifts, a pockmark field and a mass transport deposit (A) at the toe of the Elba Canyon.

V6.1 software developed by IFREMER. Tide corrections and a linear filter were applied.

The seven Calypso piston cores used for this study were collected during the cruise PRISME3 along the Pianosa Ridge in 2013. P-wave velocity and gamma-density were measured on whole core sections using a Geotek Multi-Sensor Core Logger (MSCL) at IFREMER laboratories. The bulk sediment semi-quantitative geochemical composition was measured with an Avaatech X-ray fluorescence (XRF) core scanner at IFREMER on split cores, except on intervals of coarse sediment, that were skipped due to methodological constraints. Cores PSM3-CS009 and PSM3-CS011 were sampled for grain size analysis with variable spacing ranging from 10 cm (in the homogeneous muddy facies) to 2 cm (in the sandy areas and mud-sand transitions). Grain size measurements were performed using a Coulter LS200 laser microgranulometer with no chemical pre-treatment of the bulk sediment. Further grain size measurements were performed on the carbonate-free fraction of the upper 6.85 m

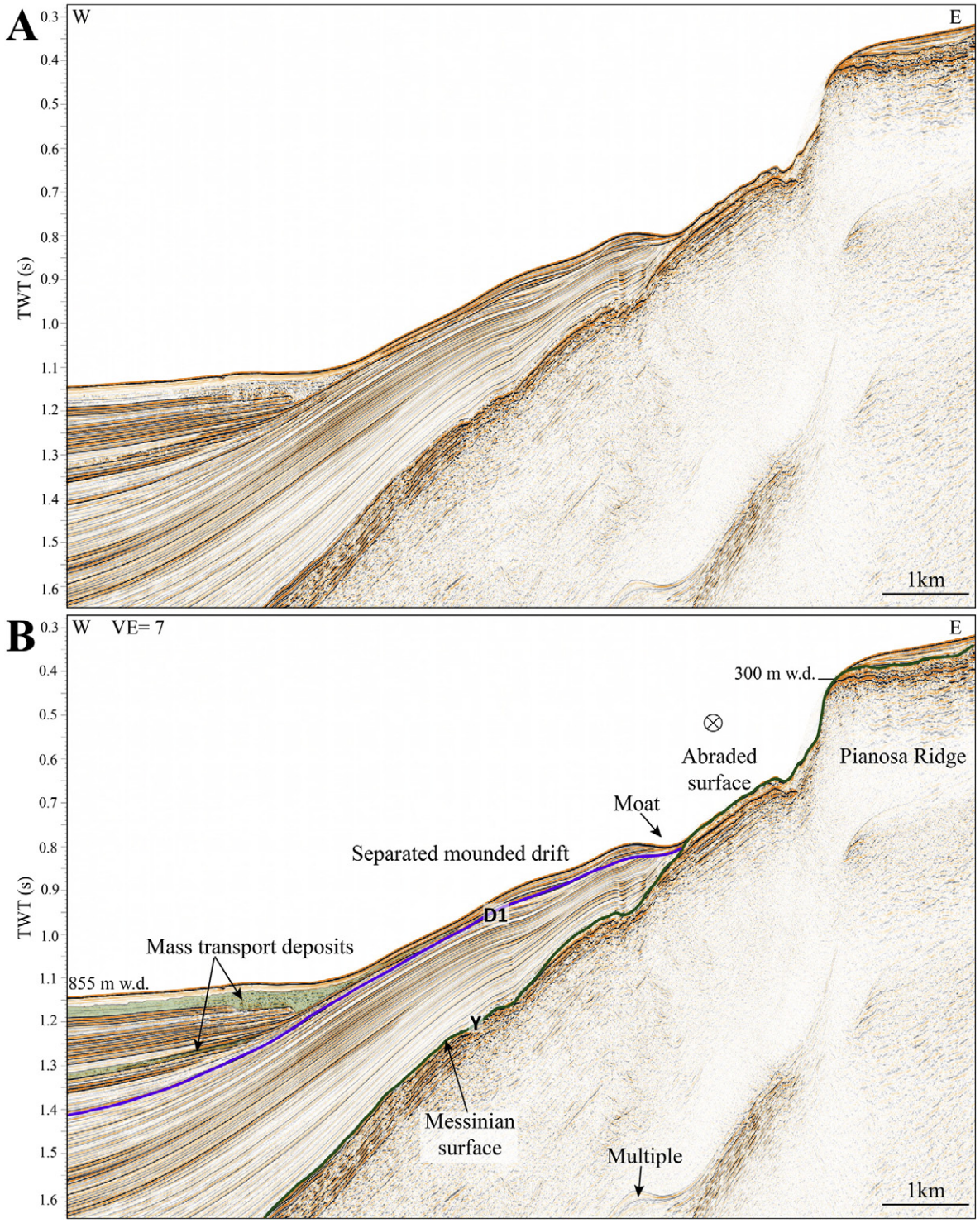

Fig. 7. (A) Uninterpreted and (B) interpreted PSM2-HR-074 multi-channel high resolution mini GI gun seismic reflection profile showing the main seismic unit boundaries in zone 1 of the Pianosa CDS. The mounded drift is separated from the escarpment by an abraded surface. See Fig. 3 for seismic profile location.

of core PSM3-CS011 using a Malvern Mastersizer 3000 laser microgranulometer. The sortable silt (SS) mean size (the mean value of the 10–63 μm grain size fraction) was used as a proxy for palaeobottom flow speed (McCave et al., 1995; McCave and Hall, 2006).

Radiocarbon dating measurements were performed on bulk planktonic foraminifera and carried out by the Beta Analytic and the Poznan radiocarbon laboratories (Table 1). Radiocarbon ages were corrected for a marine reservoir effect of 400 years and calibrated using Calib 7.0.2 radiocarbon calibration software and the IntCal13 calibration curve (Reimer et al., 2013). Stable isotope (oxygen) measurements were carried out on samples from core PSM3-CS011 using specimens of benthic foraminifera (*Uvigerina peregrina* and *Uvigerina mediterranea*) from the size fraction higher than 150 μm. Isotope analyses were done at the laboratories of the Leibniz Institute of Marine Sciences of the University of Kiel. A correction factor of −0.25‰ for $\delta^{18}O$ was applied to the isotope values from *U. mediterranea* to take into account the common differences in isotope values recorded between *U. peregrina* and *U. mediterranea* related to their different vital and habitat preferences

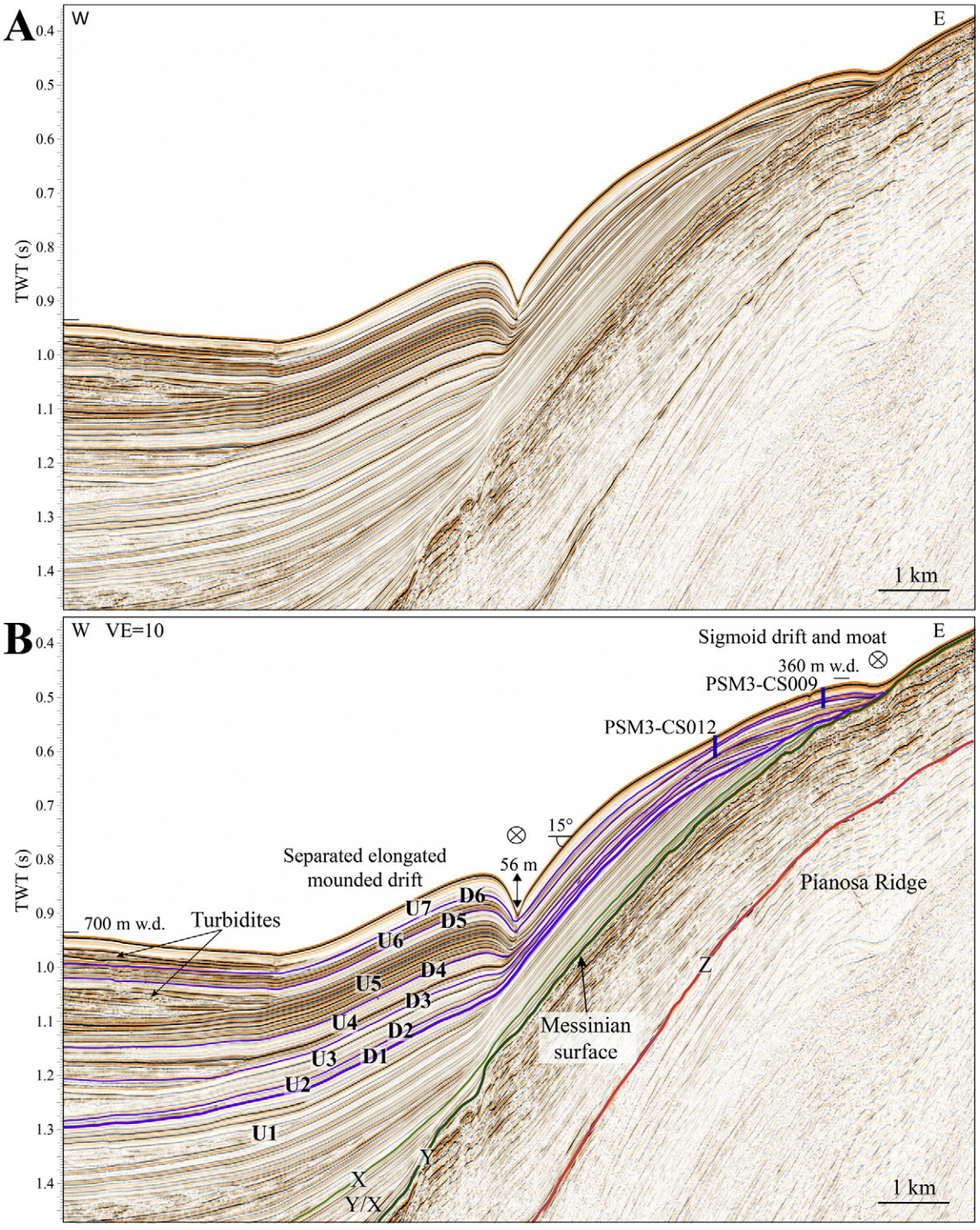

Fig. 8. (A) Uninterpreted and (B) interpreted PSM2-HR-064 multi-channel high resolution mini GI gun seismic reflection profile of zone 2 showing the main seismic unit boundaries and units of the Pianosa CDS. The location of Calypso piston cores PSM3-CS009 and PSM3-CS012 is indicated with blue lines. See Fig. 3 for cores and seismic profile locations.

(Schmiedl et al., 2004; Fontanier et al., 2006). The $\delta^{18}O$ curve of borehole GDEC4-2 (western slope of the Corsica Trough; Fig. 3; Angue Minto'o, 2014; Toucanne et al., 2015) was used as a reference for the construction of the age model with the $\delta^{18}O$ values of core PSM3-CS011 (eastern slope of the Corsica Trough, Pianosa Ridge). Cores PSM3-CS012 and PSM3-CS009 were correlated with PSM3-CS011 using the Ca/Fe ratio obtained from the XRF. The chronology is supported by multiple radiocarbon dates (Table 1) and by seismic correlation with borehole GDEC4-2. Carbonates recovered at the bottom of PSM3-CS015 (Fig. 3) were dated by SEDISOR using Strontium isotopes.

The depth below the seafloor of the cores was corrected using the software CINEMA[2] that measures the space for sampling during the penetration between the bottom of the piston and the bottom of the core catcher and permits to know the in situ depth that corresponds

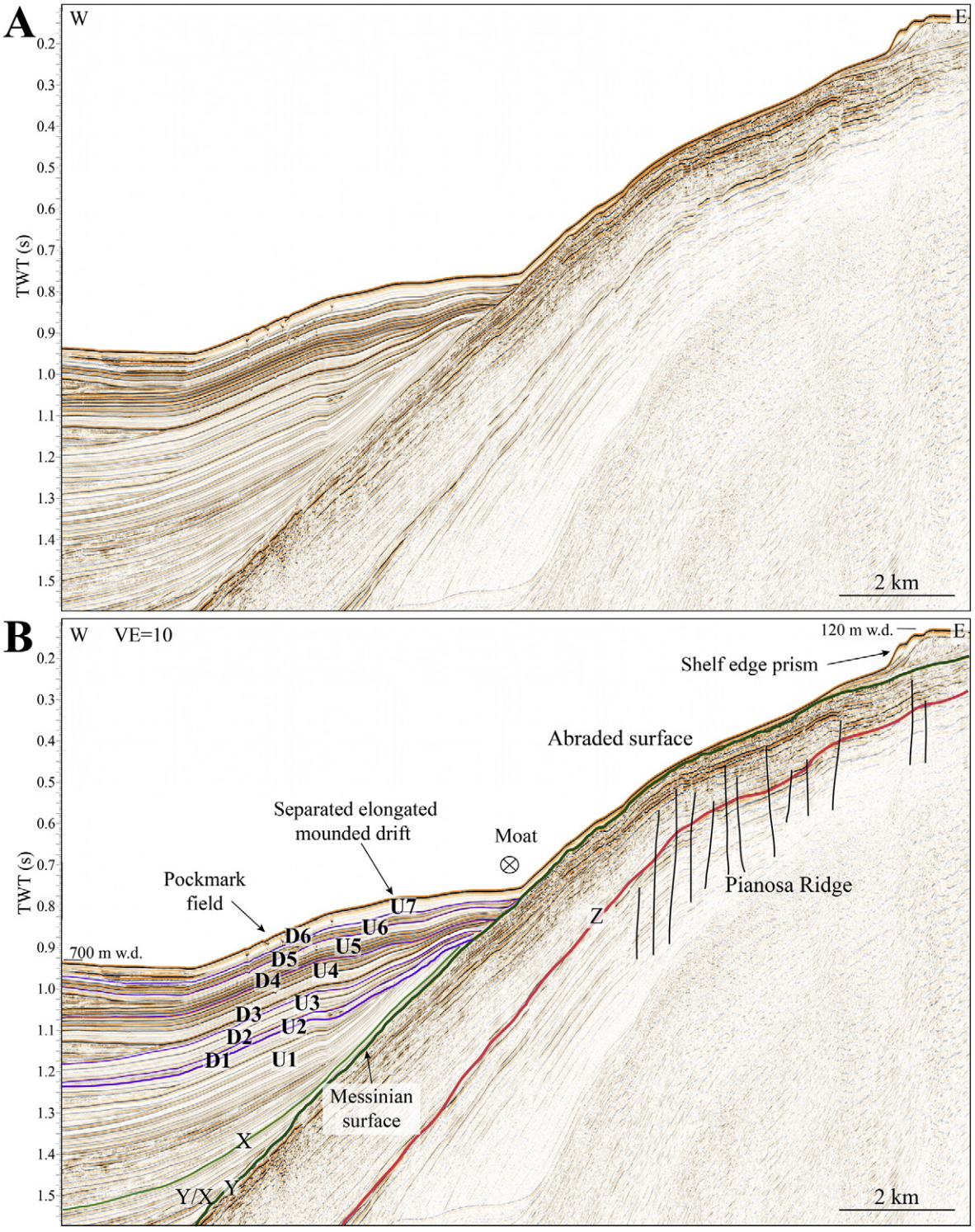

Fig. 9. (A) Uninterpreted and (B) interpreted PSM2-HR-037 multi-channel high resolution mini GI gun seismic reflection profile of zone 3 showing the main seismic unit boundaries and units of the Pianosa CDS. The contourite drift is separated from the shelf edge prism by an abraded surface. See Fig. 3 for seismic profile location.

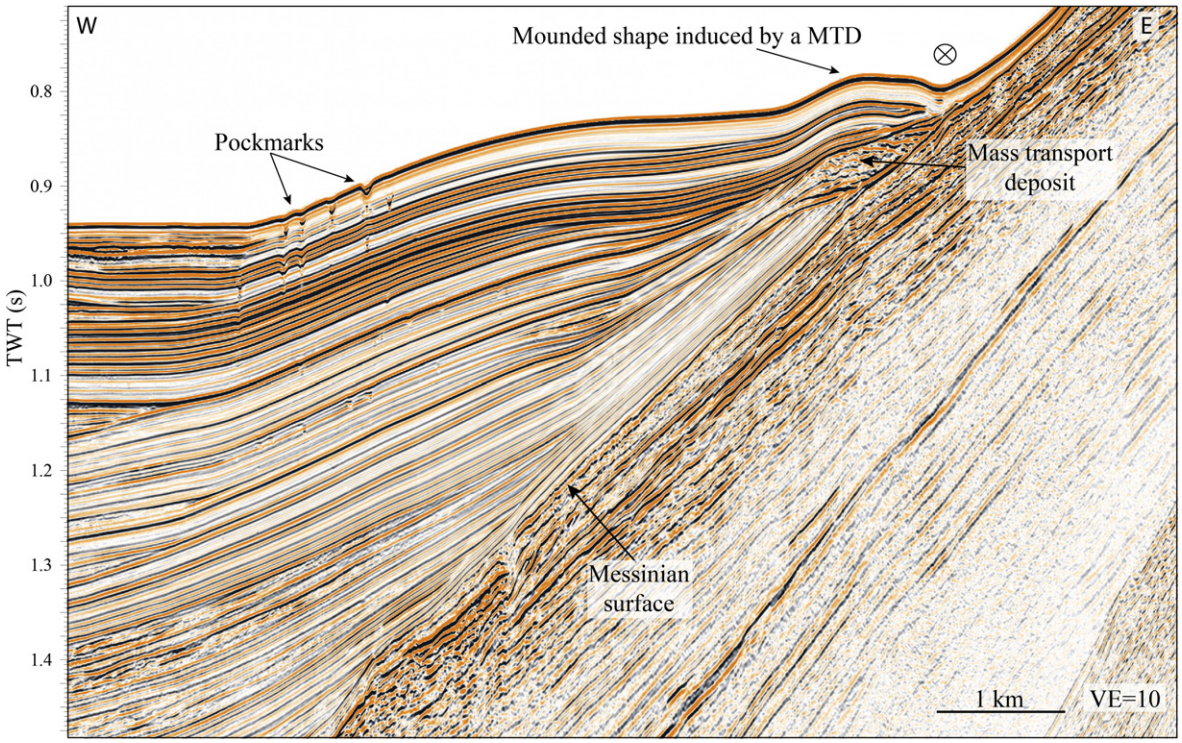

Fig. 10. PSM2-HR-063 multi-channel high resolution mini GI gun seismic reflection profile, showing the formation of a mounded shape induced by a mass transport deposit. See Fig. 3 for seismic profile location.

to the position in the core (Woerther et al., 2012). Corrected depths were used to estimate sedimentation rates.

Compression indexes obtained from oedometer tests, carried out on cores PSM3-CS009 and PSM3-C012, were used to correct the effect of compaction on the sediment thickness and thus to calculate sedimentation rates, by applying the compressibility equation that links the void ratio (e) with the vertical effective stress (σ'_v) (Lambe and Whitman, 1979; Nygard et al., 2004; Garziglia, 2010):

$$e = e_0 - \lambda \cdot \ln\left(\frac{\sigma'_v}{\sigma'_{v0}}\right) \quad (1)$$

where e_0 is a reference void ratio at a reference vertical effective stress σ'_{v0} of 1 kPa and λ is the compression index. The e-$\ln(\sigma'_v)$ plots obtained from the oedometer test provide the values of e_0 as the intersection of the virgin compression line and the reference value $\sigma'_v = 1$ kPa. The compression index (λ) is the slope of this line. The values used for core PSM3-CS009 are $\lambda = 0.180$ and $e_0 = 1.921$; and for core PSM3-CS012 $\lambda = 0.204$ and $e_0 = 2.111$. They correspond to the mean λ and e_0 values obtained from 5 oedometer tests on samples from core PSM3-CS012 and 4 oedometer tests on samples of PSM3-CS009 located in between 2 and 11 mbsf. Decompaction in core PSM3-CS011 was carried out using λ and e_0 values obtained from core PSM3-CS009.

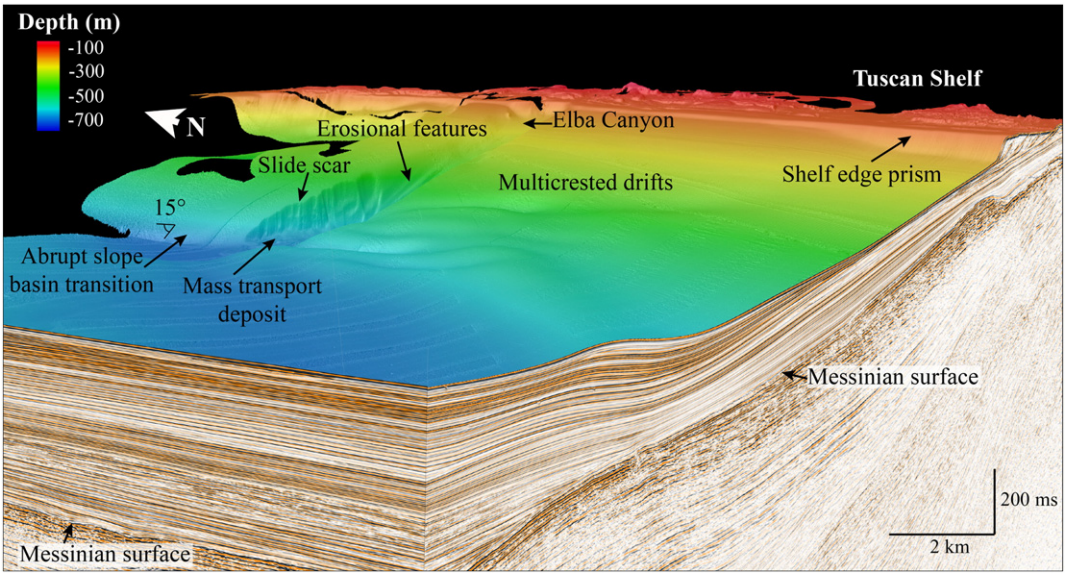

Fig. 11. 3D-rendered image composed of PSM2-HR-046 (E-W) and PSM2-HR-004 (N-S) multi-channel high resolution mini GI gun seismic reflection profiles and multibeam bathymetry of zone 4 in the Pianosa CDS showing the Elba Canyon and multicrested drifts. Note that the number of crests of the contourite drifts increases towards the north, while the size of the crests decreases in the same direction. See Fig. 3 for location.

The change in thickness (Δh) of a sediment layer of thickness h, created by the increment of the lithostatic stress, depends directly on the change in void ratio (Δe), according to:

$$\frac{\Delta h}{h} = \frac{\Delta e}{1+e_0} = -\frac{\lambda}{1+e_0}\ln\left(\frac{\sigma'_v}{\sigma'_{v0}}\right). \quad (2)$$

Then, the decompacted thickness h_d can be calculated following the equation:

$$h_d = h\left[1+\frac{\lambda}{1+e_0}\ln\left(\frac{\sigma'_v}{\sigma'_{v0}}\right)\right]. \quad (3)$$

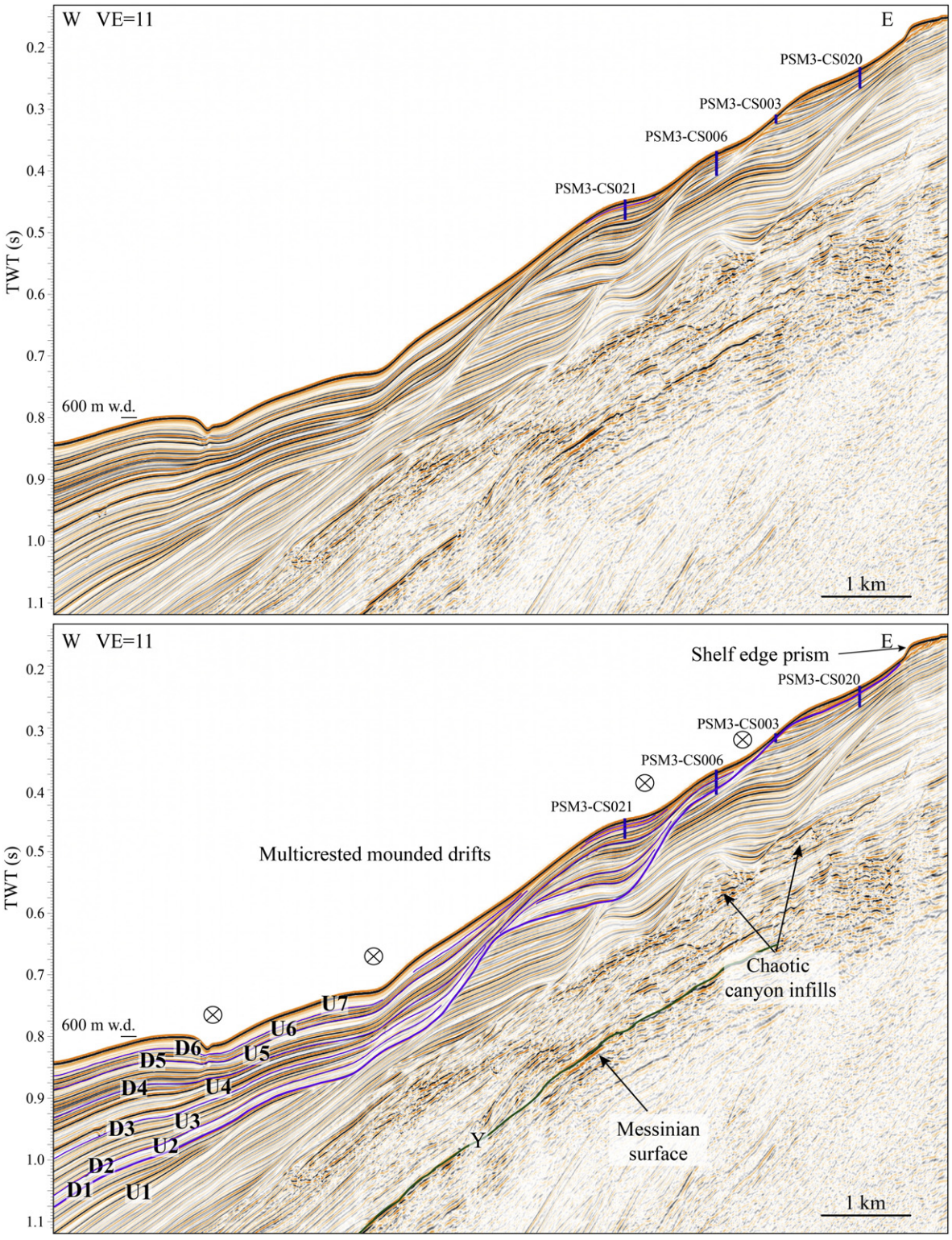

Fig. 12. (A) Uninterpreted and (B) interpreted PSM2-HR-054 multi-channel high resolution mini GI gun seismic reflection profile of zone 4 showing the main seismic unit boundaries and units of the Pianosa CDS in the zone of multicrested drifts. See Fig. 3 for seismic profile location.

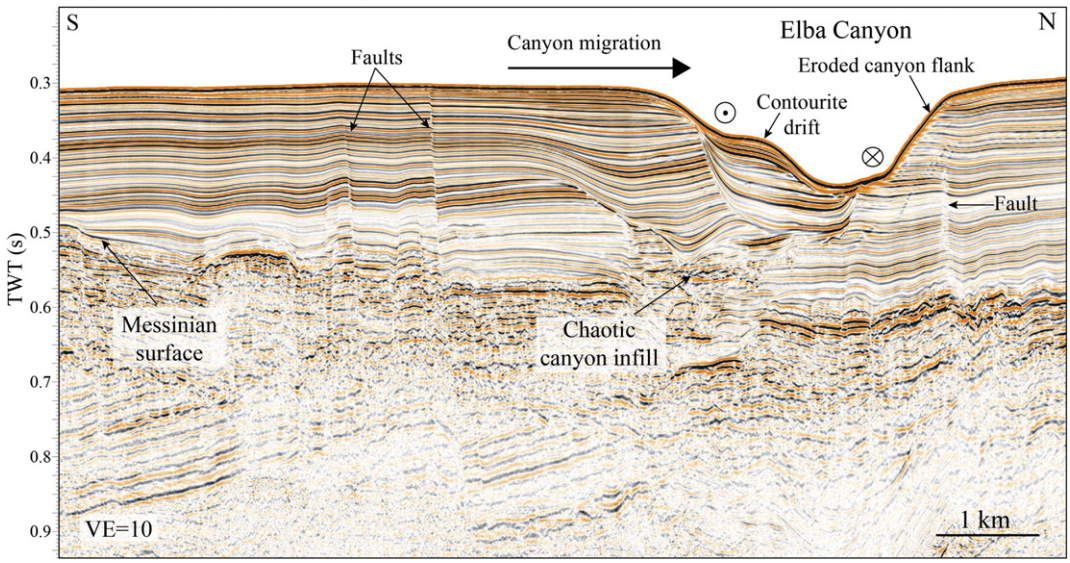

Fig. 13. PSM2-HR-015 multi-channel high resolution mini GI gun seismic reflection profile across the Elba canyon showing the northwards migration of the canyon and the formation of a contourite drift on the southern flank. See Fig. 3 for seismic profile location.

4. Results

4.1. Evidences of present-day bottom-current activity

Current velocity obtained from hull-mounted ADCP shows two main zones with northward currents and higher velocities (25–30 cm s^{-1}), found at 50–200 m and at 700–850 m in the eastern part of the basin (Fig. 4A). The whole water column flows northwards in the eastern part of the Corsica Trough at about 10 cm s^{-1}, while the central-western part of the basin has a preferential velocity of about 5 cm s^{-1} towards the south, with maximum values of 10 cm s^{-1} at 100–200 m water depth (Fig. 4B).

The coupling of ADCP data and the seafloor reflections provides a better understanding of how currents influence the seafloor morphology. Fig. 4A shows a faster (25–30 cm s^{-1}) pathway of the LIW in northern direction at about 800 m water depth (w.d.) that decreases in velocity towards the north, at the place where the separated, elongated, mounded drift starts to develop. Higher velocities are found at the lower

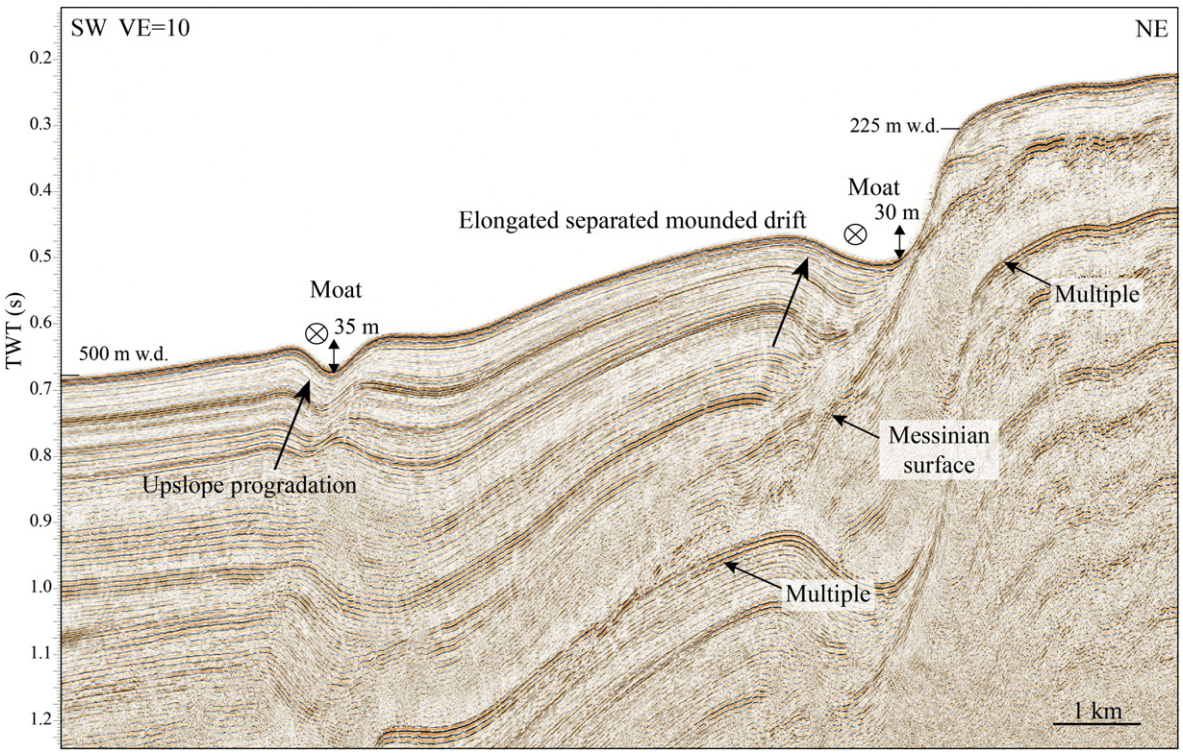

Fig. 14. ET93-P12B single-channel sparker seismic reflection profile showing two moats at 350 and 500 m water depth (w.d.) associated to an elongated separated mounded drift. See Fig. 2 for seismic profile location.

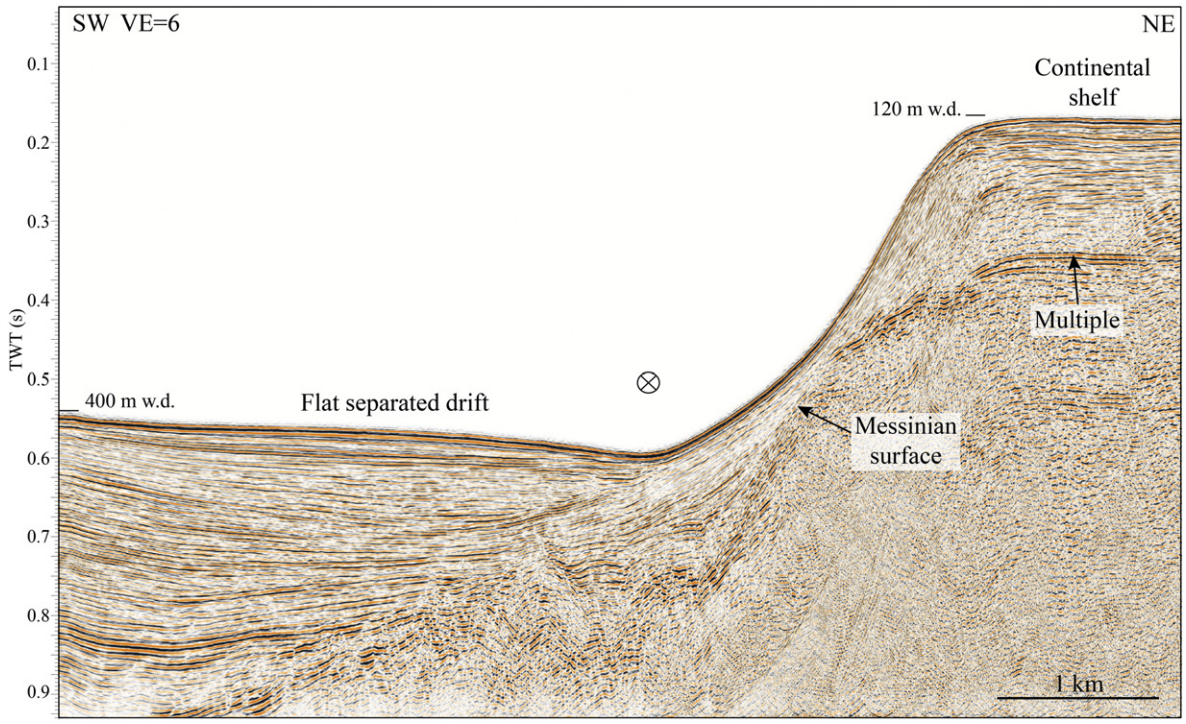

Fig. 15. ET93-P43 single-channel sparker seismic reflection profile showing a flat separated drift in zone 5 of the Pianosa CDS. See Fig. 2 for seismic profile location.

slope, at the bottom of the Pianosa Slump scar, where the present-day seafloor gradient is 13° (Fig. 4B).

The LIW pathway is strongly affected by the presence of a seafloor depression, that we define as the Elba Canyon (Fig. 2), in the short-term by inducing an upwelling to the north of the canyon (Fig. 5) and in the long-term by forming sigmoid drifts at the north of the canyon (Fig. 6B). Although the multi-channel high resolution mini GI seismic data were acquired and calibrated to image the sediment below the seabed, some reflections are apparent in the upper water column (Fig. 5). The horizontal reflections located at 120–150 m w.d. are interpreted as the mixing zone between the Modified Atlantic Water (MAW) and the Levantine Intermediate Water. Other minor changes in salinity and/or temperature of the Levantine Intermediate Water may have formed the deeper reflections found between 225 and 270 m w.d. (Fig. 5).

4.2. Distribution and morphology of the Pianosa Contourite Depositional System

The Pianosa CDS is 120 km long and has a maximum width of 10 km, extending along the Pianosa Ridge, also known as Elba Ridge (Roveri, 2002) or Elba-Pianosa Ridge (Pascucci et al., 1999), from the southernmost part (west of Montecristo Island; Fig. 2) to the north of the Corsica Sill, that connects the Ligurian and the Tyrrhenian Seas at the north of the Capraia Island (Fig. 2). The drift size and morphology present remarkable changes along the system due to the variations in depth and physiography of the basin and the Pianosa Ridge. For a better understanding, the system has been divided in seven zones (zone 1 at the south and zone 7 at the north; Fig. 2).

Table 2
Stratigraphic framework of the Pianosa Ridge. MIS: Marine Isotope Stage. MPT: Middle Pleistocene Transition. The name of unit boundaries in red colour is the original name used by Zitellini et al. (1986).

Age (kyr)	Unit boundaries (this study; Zitellini et al. (1986))	Units	Tectonic phases
		U7	Post–rift
MIS 2 (30)	D6		
		U6	
MIS 4	D5		
		U5	
MIS 6	D4		
		U4	
MIS 10	D3		
		U3	
MIS 14–MPT	D2		
		U2	
MPT (700– 900)	D1		
		U1	
	X		
Late Messinian to Early Pliocene		Y/X	Syn–rift
Messinian salinity crisis	Y		
Tortonian to Early Messinian		Z/Y	
	Z		
Early to Middle Miocene			Pre–rift

Fig. 16. (A) From left to right: density from MSCL (black line) and water content (red dots) and P-wave velocity from MSCL (black lines) and celerimeter (green dots) of core PSM3-CS012. (B) From left to right: grain size distribution, percentage of sand volume, density from MSCL (black line) and water content (red dots) and P-wave velocity from MSCL (black lines) and celerimeter (green dots) of core PSM3-CS009. Red stars represent the location of radiocarbon dates. (C) PSM2-CH-064 CHIRP profile showing the location of cores PSM3-CS012 and PSM3-CS009 with red lines.

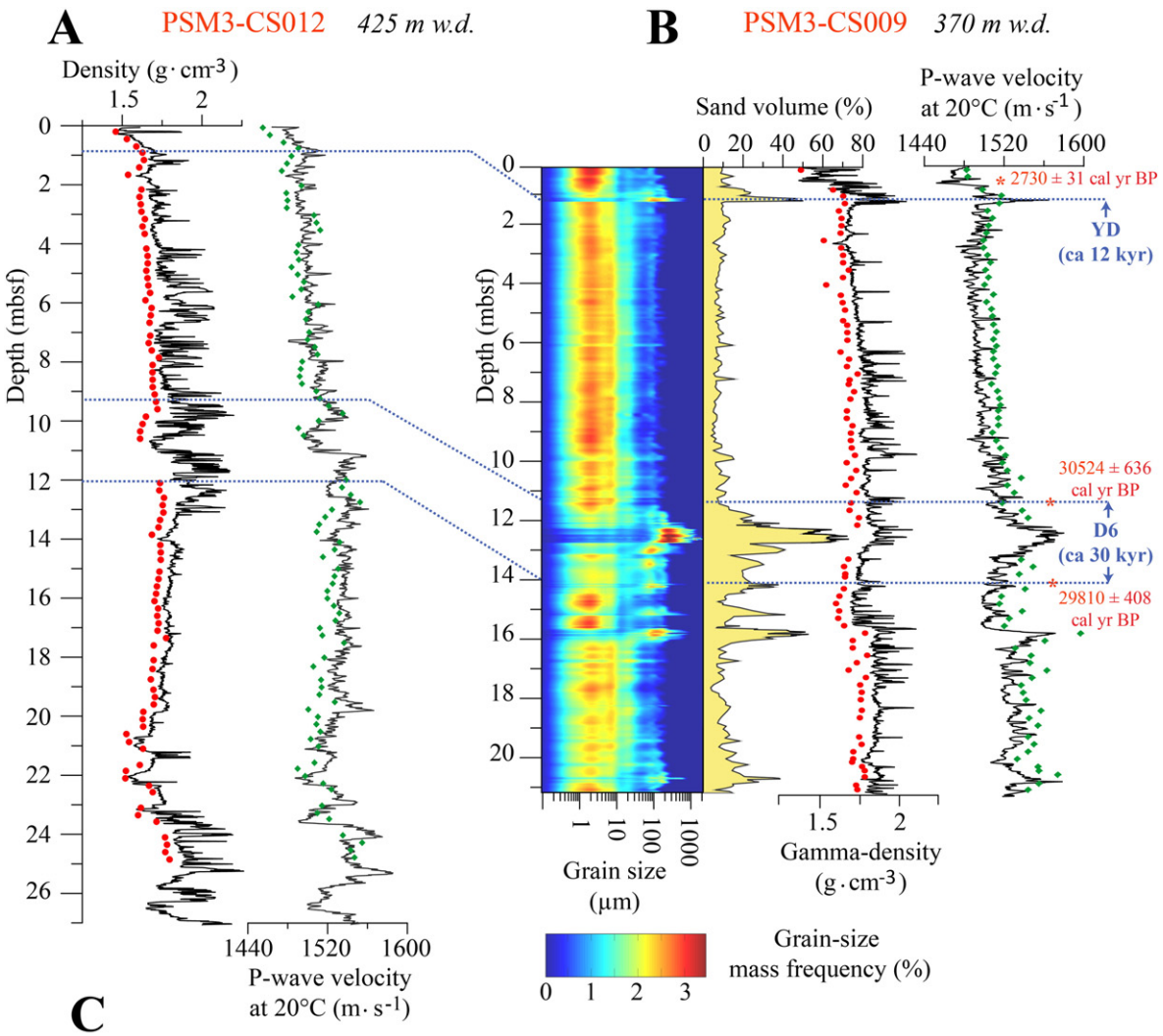
A
PSM3-CS012
425 m w.d.
Density (g·cm-3)
1.5
2
Depth (mbsf)
0
2
4
6
8
10
12
14
16
18
20
22
24
26
1440
1520
1600
P-wave velocity
at 20°C (m·s-1)
B
PSM3-CS009
370 m w.d.
Sand volume (%)
0
20
40
60
80
P-wave velocity
at 20°C (m·s-1)
1440
1520
1600
2730 ± 31 cal yr BP
YD
(ca 12 kyr)
30524 ± 636
cal yr BP
D6
(ca 30 kyr)
29810 ± 408
cal yr BP
Depth (mbsf)
1
10
100
1000
Grain size
(μm)
1.5
2
Gamma-density
(g·cm-3)
0
1
2
3
Grain-size
mass frequency (%)

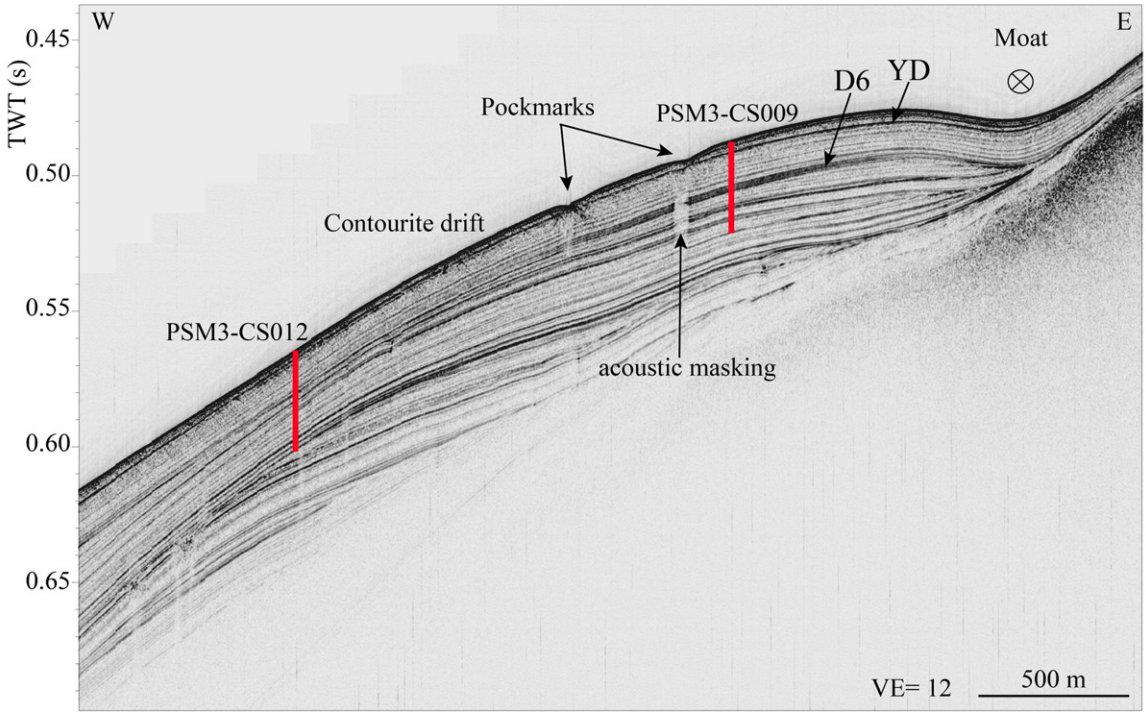
C
W
E
Moat
TWT (s)
0.45
0.50
0.55
0.60
0.65
D6
YD
Pockmarks
PSM3-CS009
Contourite drift
PSM3-CS012
acoustic masking
VE= 12
500 m

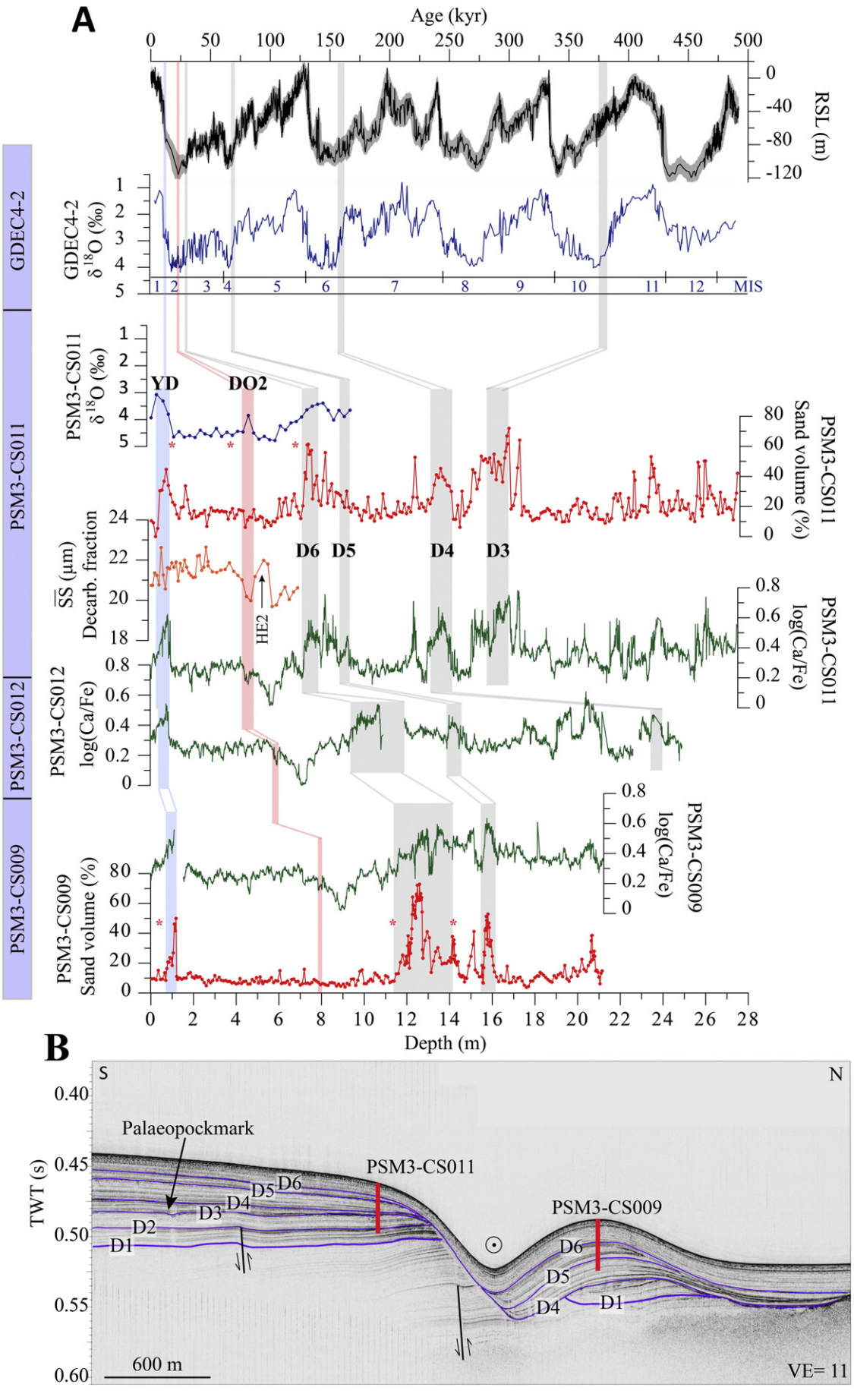
A
Age (kyr)
RSL (m)
GDEC4-2
GDEC4-2 δ18O (‰)
MIS
PSM3-CS011
PSM3-CS011 δ18O (‰)
YD
DO2
PSM3-CS011 Sand volume (%)
D6 D5 D4 D3
SS (μm) Decarb. fraction
HE2
PSM3-CS011 log(Ca/Fe)
PSM3-CS012
PSM3-CS012 log(Ca/Fe)
PSM3-CS009
PSM3-CS009 Sand volume (%)
PSM3-CS009 log(Ca/Fe)
Depth (m)
B
S
N
Palaeopockmark
PSM3-CS011
PSM3-CS009
D1
D2
D3
D4
D5
D6
TWT (s)
600 m
VE= 11

Two separated mounded drifts have been identified in the southernmost part of the CDS (zone 1; Fig. 2). An escarpment generates a local acceleration of bottom currents, maintaining an abraded surface where the Messinian surface outcrops at the seafloor, and forming adjacent contourite drifts (Fig. 7). North of this zone, a plastered drift is found in the continental slope between 230 and 700 m w.d., bounded in the upper part by faster bottom currents formed at the interphase between the MAW and the LIW (Fig. 4B). The southern part of the plastered drift was affected by multiple mass-wasting processes that formed scars on the slopes and mass transport deposits on the basin (Figs. 4B and 6A). A small mounded drift was formed at the bottom of the scar of the Pianosa Slump, related to faster bottom currents at the foot of the slope (Fig. 4B).

Faster bottom currents present along the lower slope at about 600–650 m depth (Fig. 4B) are coincident with the location of a deep moat (up to 56 m deep) in zone 2 (Fig. 2), that creates a corridor with steeper slopes, up to 15° (Fig. 8). West of the moat, an elongated separated drift is formed, with the western limit marked by an inflexion in the slope: turbidites and hemipelagites dip eastwards, while contourite drifts dip westwards (Fig. 8). Offshore the Pianosa Island (zone 2) the Pianosa Ridge is retreated towards the east, forming a bulge on the slope (Fig. 6A). This morphological structure induced a change in the LIW pathway. While the mentioned deeper LIW branch continues northwards, another branch of the current flows at about 400 m depth contouring the slope edge and forming sigmoid moats and sigmoid separated mounded drifts (Figs. 6A and 8).

North of the bulge in the Pianosa Ridge (zone 3; Fig. 2) the continental slope is relatively steep with slope values between 8° and 10°. An abraded surface extends from the bottom of the prograding shelf edge prism at 225 m depth, that was formed during the last sea level low-stand, to the mounded drift, until 560 m water depth (Figs. 6A and 9). In this zone the moat is flat and the crest is not very well developed. The separated elongated mounded drift presents multiple undulations and a pockmark field (Figs. 6A and 9). Slightly to the north, the same contourite drift has a more developed mounded shape at the crest next to the moat, which is about 1 km wide and was originated by an obstacle created by a buried mass transport deposit (Fig. 10).

North of the Pianosa Island (zone 4; Fig. 2) the slope becomes gentler (2–6°) and contourite drifts develop from 650 to 200 m water depth (Figs. 11 and 12). The deeper LIW branch flows in northeast direction until it converges with the shallowest branch that flows northwards parallel to the ridge (Fig. 2). As a result, and probably also due to the interaction with the Elba Canyon, multiple branches with north-east direction are formed, resulting in the deposition of multicrested drifts (Figs. 6B, 11 and 12).

The Elba Canyon is located offshore the Elba Island and it is the only canyon that crosses the Pianosa Ridge. Neither channel-levee systems nor turbidite lobes have been found associated with this canyon, and a low-stand shelf edge prism was deposited on the top of the canyon head (Fig. 11). Bottom currents have modelled its morphology in three different ways:

1: A contourite drift extends into the inner southern flank of the canyon (Fig. 13).
2: Downslope bottom currents through the canyon are accelerated towards the north, eroding the northern flank and forming an asymmetric canyon. The slope in the northern eroded flank is steeper (up to 20°) than in the southern flank, that is dominated by drift deposits (up to 15°) (Fig. 13).
3: Downslope bottom currents are deflected towards the north when they flow out of the canyon toe, creating an abrupt transition with high seafloor gradients (up to 15°) between the basin and the lower slope (Figs. 6B and 11).

In zone 5 (Fig. 2), the LIW pathway is affected by the presence of the canyon and it is separated by two branches (Fig. 2). The first branch continues flowing northwards at about 650 m w.d. The second shallowest branch is deflected towards the east, upwelling until about 150 m w.d. (Figs. 5 and 6B), where it becomes stabilised and continues flowing northwards, constrained by the steep morphology of the continental slope. The shallowest branch forms a sigmoid separated mounded drift similar to the drift located at the south of the Pianosa Island (zone 2). Northwards, these two LIW pathways run parallel, the shallowest one forms a 30-m-deep moat located parallel to the ridge at about 350 m w.d.; and the deepest pathway forms a 35-m-deep moat at 500 m w.d. (Fig. 14). These mounded drifts become flatter towards the north, at the same time that the basin becomes shallower and narrower, favouring erosion and non-deposition (Fig. 15).

The northernmost part of the system is characterised by patchy mounded drifts related to obstacles. North of the Corsica Sill, the basin opens in a funnel shape. Consequently, the LIW likely decelerates, favouring the sediment deposition and the formation of a drift (zone 6; Fig. 2). Finally, in the middle of the funnel-shaped basin (zone 7), a contourite drift is formed, associated with a mounded elevation (Fig. 2).

4.3. Stratigraphy of the Pianosa Contourite Depositional System

4.3.1. Seismic stratigraphy and age model

The Corsica Trough entered in a rifting phase during the Middle Miocene (Zitellini et al., 1986). Horizon Z (name used by Zitellini et al., 1986) corresponds to the seismic reflection that marks the lower boundary of the syn-rift deposits (Figs. 8, 9; Zitellini et al., 1986). Reflection Y (name used by Zitellini et al., 1986) is the erosional surface formed during the Messinian salinity crisis (Table 2). It corresponds to a very high amplitude reflection that marks a strong increase in sound velocity, since it separates the Plio-Quaternary sediment from the Miocene carbonates. Core PSM3-CS015 sampled the carbonates that form this surface in the Pianosa Ridge (Fig. 3), dated at 9.25 ± 0.27 Myr (Tortonian age, Late Miocene) through Strontium isotopic stratigraphy. This result suggests that no Messinian material is preserved in the Pianosa Ridge. Reflection X (name used by Zitellini et al., 1986) is the base of the post-rift deposits, of Middle Pliocene age (Table 2; Zitellini et al., 1986). Unit Y/X was deposited during the early Pliocene and it is mainly located in the deeper part of the basin. It usually onlaps the flanks of the basin, but in some zones it forms a thin layer concordant to the lower slope (Figs. 8 and 9).

Fig. 17. (A) From the top to the bottom: relative sea level curve from Grant et al. (2014), $\delta^{18}O$ stack of benthic foraminifera (*Cibicides wuellerstorfi*, *Cibicidoides pachyderma* and *Cibicidoides kullenbergi*) from borehole GDEC4-2 showing in blue colour the corresponding Marine Isotope Stages (MIS), $\delta^{18}O$ stack of *Uvigerina peregrina* and *Uvigerina mediterranea* from core PSM3-CS011, percentage of sand volume from core PSM3-CS011, sortable silt mean grain size of the decarbonated fraction of core PSM3-CS011, XRF log(Ca/Fe) of core PSM3-CS011, XRF log(Ca/Fe) of core PSM3-CS012, XRF log(Ca/Fe) of core PSM3-CS009 and percentage of sand volume of core PSM3-CS009. The Younger Dryas (YD) is indicated with a blue band, the Dansgaard-Oeschger event 2 (DO2) with a red band and unit boundaries D6 to D3 with grey bands. Note that the higher mean sortable silt values are found during the YD and Heinrich Event 2 (HE2). Low mean sortable silt values are present at DO2. Differences in the $\delta^{18}O$ range between GDEC4-2 and PSM3-CS011 are caused by the use of different benthic foraminifera species (epifaunal foraminifera in GDEC4-2 and infaunal in PSM3-CS011). The log(Ca/Fe) curve of PSM3-CS012 is not entirely represented through D6 because this part of the core has been used for geotechnical analysis. Correlation was also done using seismic correlation with borehole GDEC4-2. Additional support for the correlation can be found with the good coherence between the XRF log(Ca/Fe) curves of this study and the XRF Calcium curves presented by Calves et al. (2013) and Toucanne et al. (2012). Red stars represent the location of radiocarbon dates. (B) PSM2-CH-014 CHIRP profile showing the location of cores PSM3-CS011 and PSM3-CS009 with red lines and the seismic reflections that mark unit boundaries (D1 to D6).

The sediment deposited in the Corsica Trough from the Middle Pliocene (reflection X) to the present-day, is composed of 7 main units: U1, U2, U3, U4, U5, U6 and U7 (Figs. 8 and 9). Unit 1 is bounded between seismic reflection X (Middle Pliocene) and D1. The seismic discontinuity D1 is proposed to be related to the Middle Pleistocene Transition (MPT, 700–900 kyr) by analogy with the Quaternary stratigraphic pattern suggested by Hernández-Molina et al. (2002) for the Gulf of Cadiz and the Alboran Sea (Table 2). Reflections in unit 1 onlap the lower part of the continental slope and are concordant to the middle slope. The upper boundary of unit 1 is the erosional surface D1. This regional erosion removed most of the sediment deposited on the middle slope, forming erosional truncations on the easternmost part of unit 1 (Figs. 7, 8 and 9). Mounded reflections can be found in unit 1, evidencing the presence of mounded drifts in all the system, more developed in the vicinity of the Elba Canyon (Fig. 12). Unit 2 is bounded by erosional seismic reflection D1 and D2, both characterised by being of high amplitude (Figs. 8, 9, 12, 16C and 17B). D2 is deeper than the bottom of borehole GDEC4-2 (western side of the Corsica Trough) that was dated at 550 kyr BP.

Units 3 to 7 are separated by seismic reflections of high amplitude that correspond to coarser sediment layers (Figs. 8, 9, 12 and 17). All the units present similar characteristics: they alternate packages of low amplitude reflections with packages of high amplitude reflections (Fig. 9). Unit 7 is the most recent one, it is characterised by low amplitude reflections that follow the same morphology as the previous units, but it drapes the shallowest moat in zones 2 and 3, as well as part of the middle slope, thinning upslope (Figs. 8, 9 and 16C). Seismic and oxygen isotope correlation with borehole GDEC4-2 allowed the more precise chronology of units 3 to 7 (Fig. 17A). Unit 3 extends until MIS 10, unit 4 from MIS 10 to MIS 6, unit 5 from MIS 6 to MIS 4, unit 6 from MIS 4 to MIS 2 (30 kyr) and unit 7 from 30 kyr to the present (Table 2).

Sedimentation rates (SR) were calculated for unit 7 in contourite drifts of zone 2 (Fig. 18). The core depths used for the estimation of sedimentation rates were corrected for coring perturbations (Woerther et al., 2012) and mechanical compaction effects. SR on the crest of the mounded contourite drift in the middle slope from core PSM3-CS009 (Figs. 6, 14 and 15) resulted in a mean SR value corrected for compaction and core sampling perturbations of 13 cm kyr^{-1} for the last 12 kyr. (non-corrected SR would be 9.5 cm kyr^{-1}) and 81 cm kyr^{-1} between 12 and 30 kyr (non-corrected SR is 63 cm kyr^{-1}) (Fig. 18). Core PSM3-CS012 is located in a deeper zone of the contourite, farther from the moat, where sediment accumulation is slightly lower, with mean corrected SR values of 11 cm kyr^{-1} for the last 12 kyr BP (non-corrected SR would be 6 cm kyr^{-1}) and 70 cm kyr^{-1} between 12 and 30 kyr BP (non-corrected SR is 47 cm kyr^{-1}). Core PSM3-CS011 shows a similar pattern in sedimentation rates, with lower values during the last 17.3 kyr (9 cm kyr^{-1}, 6 cm kyr^{-1} non-corrected) and higher SR between 17.3 and 26.7 kyr (88–111 cm kyr^{-1}, 61–68 cm kyr^{-1} non-corrected). PSM3-CS011 presents low SR (5 cm kyr^{-1}, 3 cm kyr^{-1} non-corrected) between 26.7 and 30 kyr BP (Fig. 18).

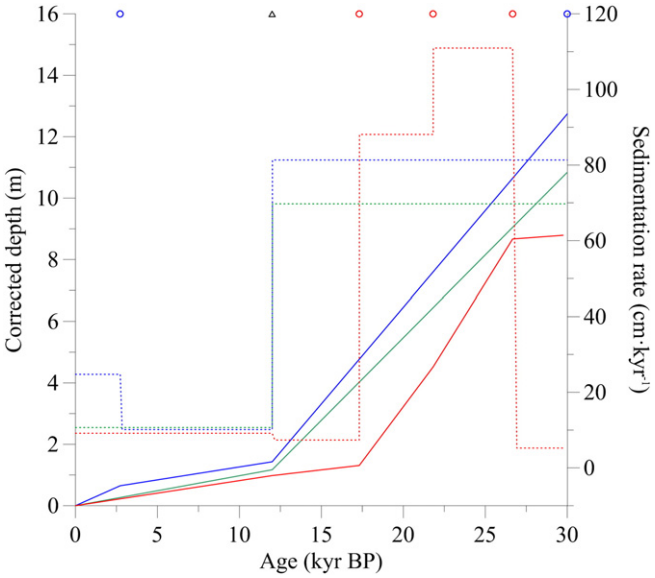

Fig. 18. Age models for cores PSM3-CS009 (blue line), PSM3-CS012 (green line) and PSM3-CS011 (red line), covering the last 30 kyr BP (Unit 7). Chronological tie points from borehole GDEC4-2 used for the three cores are represented with a black triangle, radiocarbon dates are represented as blue open circles for core PSM3-CS009 and red open circles for PSM3-CS011. Dashed lines are sedimentation rates for cores PSM3-CS009 (blue), PSM3-CS012 (green) and PSM3-CS011 (red). Core depths used for the calculation of sedimentation rates were corrected for coring perturbations and compaction.

4.3.2. Sedimentological characterisation

Contourite drifts in the Pianosa CDS are mainly composed of bioturbated mud without lamination, although it is also common to find layers of bioclastic muddy sand. The abundance, grain size and bed thickness of these sandy layers changes along and across the Pianosa Ridge. Three Calypso piston cores sampled the sigmoid drift of zone 2: PSM3-CS011, PSM3-CS009 and PSM3-CS012, recovering information from units 2 to 7. In general, contourites are muddy with sand contents around 10% of the total bulk volume (Figs. 16B and 17A). The sand is mainly composed of bioclasts. Decarbonated samples of core PSM3-CS011 (between 0 and 6.85 mbsf) present sand contents between 0.2 and 3% of the total volume in the range 63–150 μm. Bulk grain size analysis of the same samples showed sand volumes oscillating between 5 and 45% of the total volume in the range 63–1000 μm (Fig. 19). Some layers have higher sand contents (up to 70%; Figs. 16B and 17A) and correspond to high amplitude reflections in the multi-channel and CHIRP seismic profiles and to increased P-wave velocities (Figs. 16 and 17B). The granulometry of PSM3-CS009 shows that D6 corresponds to a sandy layer coarsening-up until it reaches a maximum sand content of 70% and, then fining-up (Fig. 16B). Two radiocarbon analyses were carried out on planktonic foraminifera in core PSM3-CS009 on the muddy sediment over the sandy layer (at 11.26 mbsf) and under it (14.00 mbsf), resulting in approximately the same age: 30,000 cal yr. BP (Table 1). Sand content in the contourite drift decreases with depth and with the distance to the moat. Therefore, PSM3-CS012 has a finer grain size than PSM3-CS009, especially remarkable in the coarser layers. For instance, the peak in P-wave velocity that corresponds to D6 in PMS3-CS012 (Fig. 16A) is less marked than in PSM3-CS009 (Fig. 16B). Another layer of coarser material can be found at 1.14 mbsf in core PSM3-CS009 and at 0.76 mbsf in core PSM3-CS012 that was deposited during the Younger Dryas (Fig. 16). PSM3-CS011 also shows coarser grain size at D6 and the Younger Dryas (Fig. 19A) and finer sediment during MIS2 (between YD and D6). Mean sortable silt values obtained from decarbonated samples of PSM3-CS011 between 0 and 6.85 mbsf increase during Heinrich Event 2 (HE2) and then a decrease during Dansgaard–Oeschger Event 2 (DO2; Figs. 17A and 19B). During MIS 2 mean sortable silt values tend to increase, reaching higher values in the Younger Dryas and, finally decreasing during the Holocene (Figs. 17A and 19B).

The multicrested mounded drifts of zone 4 were sampled by four Calypso piston cores along an east–west profile located at the south of the Elba Canyon (Figs. 12 and 20): PSM3-CS021, PSM3-CS006, PSM3-CS003, PSM3-CS020 (from the deepest to the shallowest core in water depth). These cores are between 9 and 22 m long and penetrated sediment from units from 1 to 7. In zone 4 there is an evident decrease in grain size with water depth, sandy layers become less abundant, thinner and finer

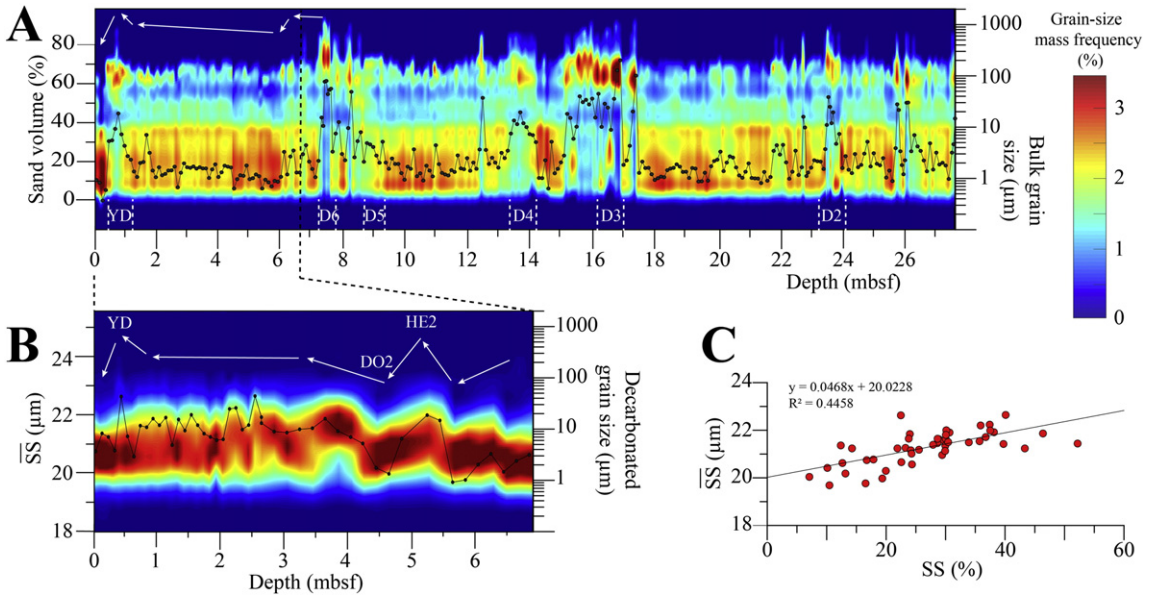

Fig. 19. (A) Bulk grain size distribution (colour graph) and sand volume percentage of the bulk sediment (black line and dots) of core PSM3-CS011. The Younger Dryas (YD) and the boundary units D6-D2 intervals are represented with dashed white lines. The white arrows show the general grain size tendency. (B) Decarbonated grain size distribution (colour graph) and mean sortable silt (black line and dots) of the decarbonated fraction of the upper 6.85 m of core PSM3-CS011. Note that most of the sand fraction disappears after removing carbonates from the sediment. The white arrows show the mean sortable silt tendency that can be interpreted in terms of palaeocurrent speed, suggesting faster bottom currents during the YD and the Heinrich Event 2 (HE2) and slower during the Dansgaard-Oeschger event 2 (DO2) and the Holocene. (C) Correlation of sortable silt (10–63 μm silt fraction) mean size with sortable silt percentage of the decarbonated fraction (right). The linear relationship between mean size of sortable silt and percentage of sortable silt, in a well sorted population, indicates a sorting processed controlled by current flow dynamics (McCave and Hall, 2006).

grained with depth (Fig. 20). The coarser layers are mainly composed of coarse grained bioclasts and mud, with abundant shells of bivalves, brachiopods (*Gryphus vitreus*) and fragments of the bryozoan *Myriapora truncata*. Some of the transitions between the sandy and the muddy layers are gradual, while others form sharp contacts (Fig. 20). The gradual transitions and the muddy layers located between two proximal sandy areas are commonly mottled mud with silty patches. The sandy layers are easily identified in the P-wave velocity and in the Ca/Fe curves since they correspond to faster P-wave velocities in sand and higher calcium content because of the bioclastic content.

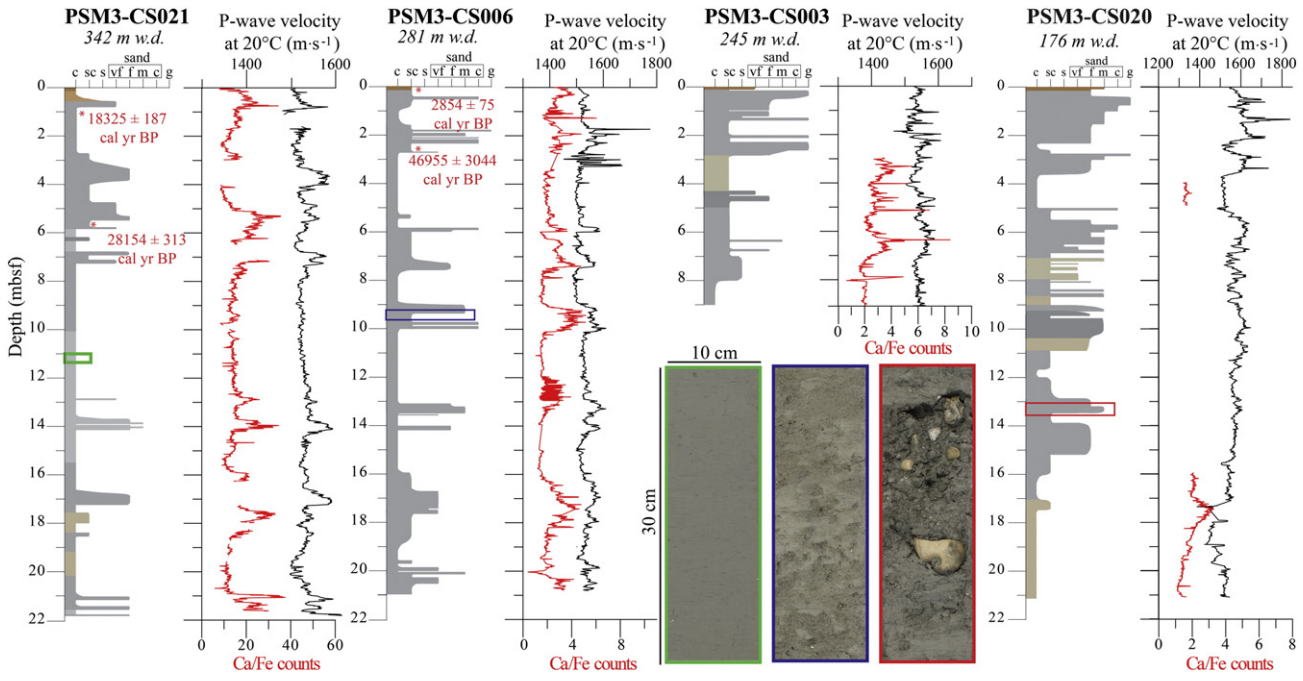

Fig. 20. Core log, P-wave velocity and XRF Ca/Fe curves of cores PSM3-CS021, PSM3-CS006, PSM3-CS003 and PSM3-CS020. Three photos show the main sedimentary facies, from left to right: mud, mottled mud with silty patches and a bioclastic sand interval with a sharp upper boundary. Colours in the logs represent the real colour of the sediment.

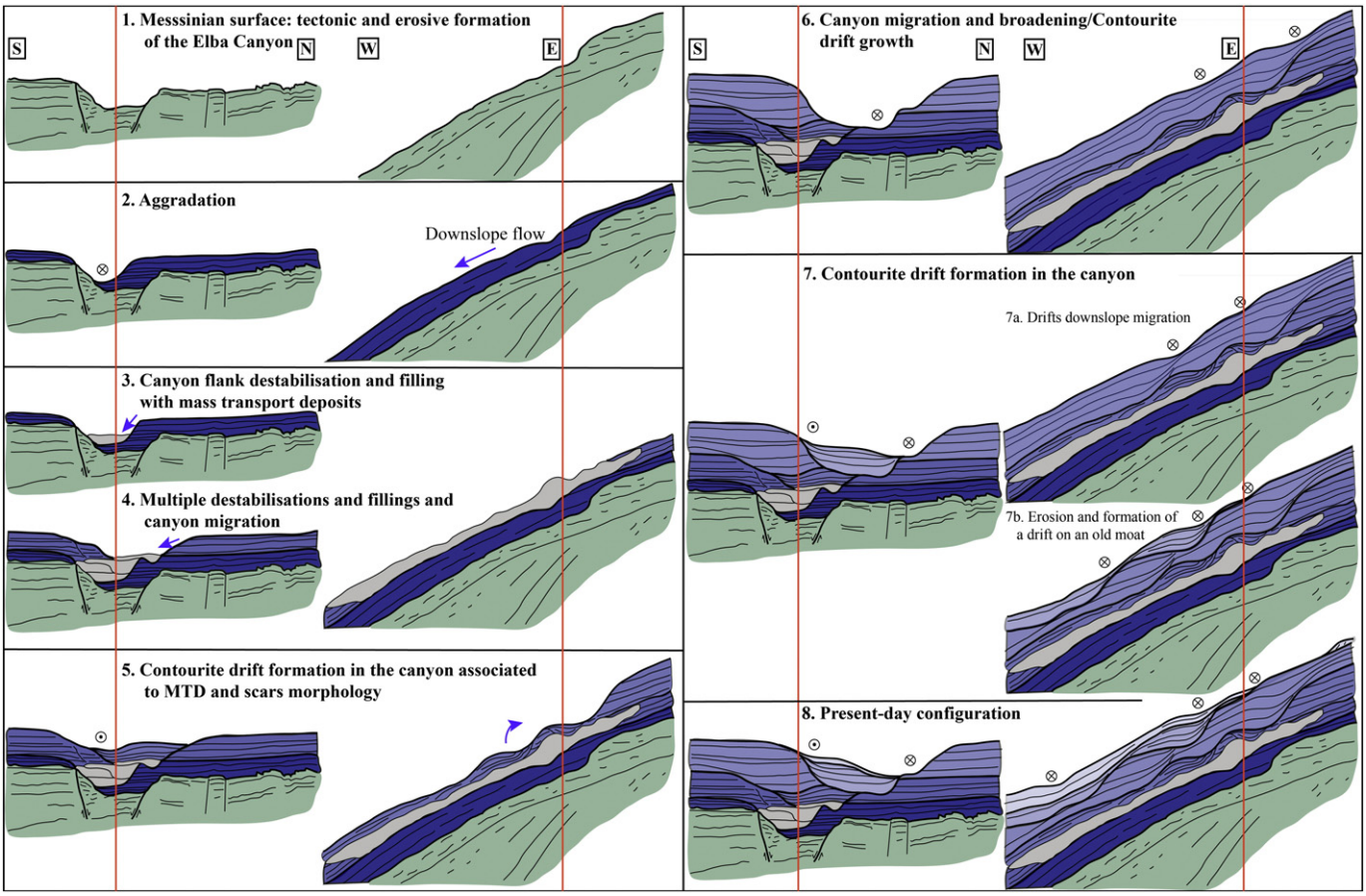

Fig. 21. Evolution of the Elba Canyon (profile N–S; Fig. 13) and the associated multicrested drift (profile E-W; Fig. 12) since the late Messinian. Note that the apparent complicated stacking pattern of the multicrested drifts is originated by the canyon migration and the interaction of a changing seafloor morphology with bottom currents.

5. Discussion

5.1. Influence of seafloor morphology on contourite drift structure

The evolution of contourite deposits is directly linked to water circulation influenced by the seafloor morphology. In the Pianosa CDS the effect of locally increased slopes and the occurrence of bulges clearly impacts the bottom-current pathways, and consequently the growth of the sediment drifts. For instance, a sigmoid drift is related to a bulge in the Pianosa Ridge at the south of the Pianosa Island (Fig. 6A).

The Elba Canyon seems to be a morphological depression originated as a graben in the basement and developed by sedimentation altered by bottom currents (Figs. 13 and 21). There are no evidences of active turbidity activity through this canyon since neither channel-levees system nor turbidite lobes have been observed related to this canyon. In addition, a shelf edge prism blocks the head of the canyon. This prism extends almost all along the Pianosa Ridge. Downslope processes probably exist all along the margin. They may transport coarser bioclastic material from the Tuscan Shelf to the contourite drifts. However, they do not seem to be high density flows saturated of sediment recurrent in time that result in the formation of turbidite lobes in the basin. The Elba Canyon does not seem to be a typical canyon of mixed turbidite-contourite processes that can be found for example in the Gulf of Cadiz (Hernández-Molina et al., 2006; Marches et al., 2010; Brackenridge et al., 2013) or in Antarctica (Rebesco et al., 2002). It is most probably a depression modelled mainly by bottom currents, by processes of differential erosion and deposition. It is an important difference because this is a continuous process, while in mixed turbidite–contourite canyons the effect of turbidity currents is only caused by discrete events separated in time.

Bottom-current circulation is more dynamic in the zone around the Elba Canyon. Firstly, the branches of the current are slightly deflected towards the NE and enter into the canyon. Secondly, part of the water may flow downslope along the canyon, eroding the northern flank and forming longitudinal incisions on it (Fig. 6B). At the end of the canyon, bottom currents may turn to the right and erode the bottom of the slope (Fig. 6B). Thirdly, the inclination of the reflections in the seismic profile of the water column located at the north of the Elba Canyon (Fig. 5) suggests the upwelling of deeper denser water to the upper slope that could be induced by the effect of the canyon on an alongslope current (Klinck, 1996; Hickey, 1997; Sobarzo et al., 2001). The development of the multicrested contourite drifts (Fig. 12), located at the south of the Elba Canyon at the present-day seafloor, is strongly subjected to the migration and evolution of the latter. Fig. 12 registers the first aggradation in the centre of the canyon (step 2 in Fig. 21), followed by

Fig. 22. Scheme explaining the evolution of a contourite drift during a single sea level cycle controlled by sediment availability (connection/disconnection of the turbidite system) and bottom-current velocity. Two different scenarios are proposed: high sediment accumulation due to fast bottom currents and high sediment availability during sea level low-stand (case A) or during periods of medium relative sea level (case B).

	Case A (MIS 2-MIS 1)		*Case B (MIS 4 -MIS 3)*	
	Sediment availability	Bottom-currents velocity	Sediment availability	Bottom-currents velocity
1. Sea level high-stand	–	+	–	+
2. Sea level fall	–	+++	–	+++
3. Sea level low-stand	+	++	+	+++
4. Sea level high-stand	– (maximum RSL)	+	+ (medium RSL)	++

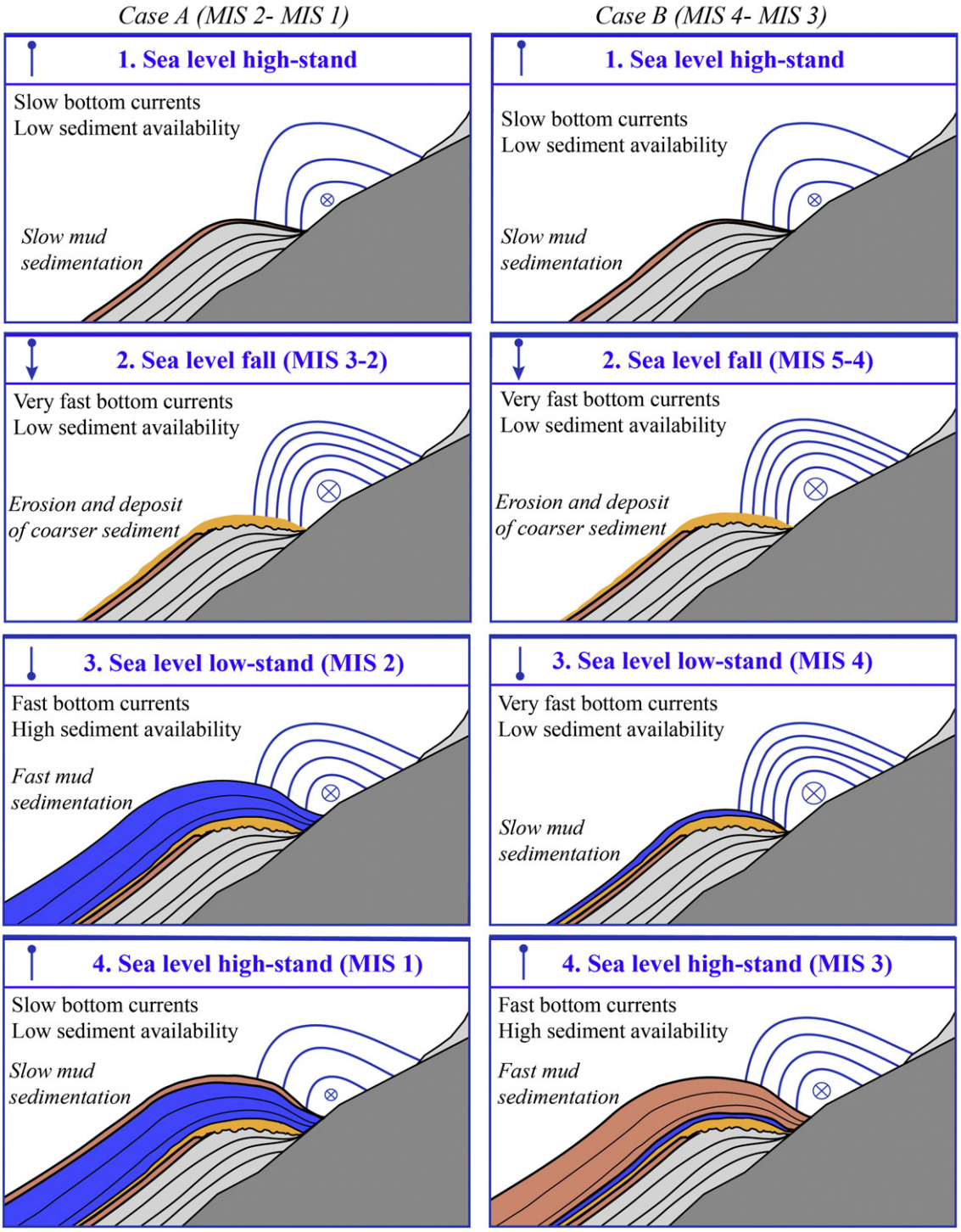

multiple destabilisations of the canyon flanks deposited on the axis of the canyon (steps 3–4 in Fig. 21). During this period, the canyon starts to migrate towards the north; later, a contourite drift is formed in the centre of the canyon (step 5 in Fig. 21). Afterwards, the canyon migrates farther north and contourites grow on its southern flank (step 6 in Fig. 21). Finally, a drift enters from the south into the canyon axis (steps 7–8 in Fig. 21). In summary, Fig. 12 documents the apparent complicated morphology of the sediment drifts because it was positioned in the middle of the canyon during a first phase and then on the southern flank of the canyon, migrating towards the north.

5.2. Palaeoceanographic implications

The Pianosa CDS presents a continuous development since the Middle–Late Pliocene (this study; Roveri, 2002), after the progressive filling of the deep central part of the basin (units Y/X and lower part of U1). This continuity implies that over the long term the intermediate waters have had a similar circulation pattern flowing northwards along the Pianosa Ridge since the Middle–Late Pliocene. The concordance of the present-day oceanographic regime with the stratigraphic evolution of the contourite drifts (Fig. 4) suggests that the general circulation at the Pianosa Ridge has been similar during the history of the Pianosa CDS. The drift morphology is stable over time, only presenting a small component of upslope progradation (Fig. 9). The formation of oblique chimneys in pockmarks can also be a good indicator of the dominant current direction. The interaction between bottom currents and fluid escape favours the deflection of the gas plume and thus differential erosion/deposition on pockmark flanks, resulting in erosion downstream and deposition upstream (Riboulot et al., 2014). Fig. 4A shows that the mass transport deposit C3 is the origin of a pockmark that presents an oblique chimney. Since the MTD is a fixed source of fluid, the possible migration of pockmarks due to the migration or evolution of the fluid source can be rejected and therefore it can be argued that the formation of an oblique chimney is mainly linked to the effect of bottom currents on the sedimentation at the pockmark.

From the Middle–Late Pliocene to the Middle Pleistocene (U1) the Pianosa CDS had a continuous growth of small mounded drifts. Afterwards, a prominent erosional surface (reflection D1) marks the onset of better-developed contourite mounded drifts (Fig. 8). The D1 reflection may correspond to the Middle Pleistocene Transition (MPT, 700–900 kyr). At that time, 100-kyr eccentricity cycles became dominant, resulting in longer glacial/interglacial cycles of higher amplitude, which might be related to the intensification of the Mediterranean Outflow Water (that is formed by the Mediterranean intermediate and deep waters) and the formation of a mid-Pleistocene discontinuity in the Gulf of Cadiz (Hernández-Molina et al., 2014). The onset of a stronger development of contourites in the Northern Tyrrhenian Sea coincides with the onset of the contourites along the Calabro-Tyrrhenian margin, in the Southern Tyrrhenian Sea (Amelio and Martorelli, 2008), suggesting that faster bottom currents in the depth range of the modern Levantine Intermediate Water impacted already the whole Tyrrhenian Sea.

5.3. Glacial-interglacial stratigraphic evolution

A model that describes the evolution of the sediment drifts in the Pianosa CDS is here proposed (Fig. 22). Contourite development in the Corsica Trough is mainly influenced by bottom-current velocity and sediment availability (that depends on the connection and disconnection of the turbidity systems), both directly influenced by climate changes. At present and since the beginning of the Holocene, the Golo Turbidite Network is disconnected (Calves et al., 2013) and bottom currents are slow in the Corsica Trough (this study; Toucanne et al., 2012). Therefore, during sea level high-stands sedimentation rates are low in the contourites (step 1 in Fig. 22). During sea level falls bottom currents are faster (this study; Toucanne et al., 2012) and their core may be located deeper in the slope, eroding the crest of the sediment drift. Under these conditions, most of the Tuscan Shelf was exposed, likely providing additional and coarser sediment to the slope. During this period of enhanced currents, bioclastic sands are deposited on the crest of the contourite (step 2 in Fig. 22). The deposition of sand beds may take place in a short period of time and may be the result of downslope processes that transport coarse material from the Tuscan Shelf to the slope, later reworked and winnowed by slope-parallel currents. Unit boundary D6 is a good example for this case because two radiocarbon dates show the same age (30 kyr) under and above the 3-m-thick sandy layer, proving a rapid formation of the deposit. In addition, the layer presents coarsening-up and then fining-up sequences that suggest the rework by bottom-currents. The evolution of the drift above the sandy layer (Fig. 22) leads to two different scenarios of the growth of a mounded drift in zone 2 between MIS 2 and MIS 1 (Case A), and between MIS 4 and MIS 3 (Case B). During MIS 2, with sea level low-stand and the onset of the following sea level rise, bottom currents were fast in the Pianosa Ridge, but slower than during the sea level fall. As a result, bottom currents could transport large amounts of sediment but would not be fast enough to produce erosion on the drift. In addition, the turbidite system was connected (Calves et al., 2013) and provided sediment to the contourite system, resulting in a fast sedimentation of mud (step 3 for case A in Fig. 22), that sealed the sandy layer deposited during the sea level fall. This explanation is consistent with the heavy $\delta^{18}O$ values found between the Younger Dryas and D6 in core PSM3-CS011 (Fig. 17A), proving the formation of the contourite during a cold period. On the contrary, in case B, during MIS 4 sea level low-stand, the slope-parallel current velocity was probably high, preventing sediment deposition, even if the turbidite system was connected (Calves et al., 2013), implying a sustained supply from the margin. This interpretation is sustained by the presence of light $\delta^{18}O$ values between D6 and D5 that could not be formed during MIS4 (Fig. 17A). Afterwards, during MIS3 the relative sea level remained in between −60 and −80 m (Fig. 17A), bottom currents likely slowed down but were still fast enough to transport large amounts of sediment, carried to the basin by recurrent turbidity currents (Calves et al., 2013). As a result, contourite drifts underwent a phase of accelerated growth during MIS 3 compared to MIS 4.

During the Younger Dryas there was no major erosion, but enhanced bottom currents were evident by the deposition of coarse sediment in the contourite drifts, with higher contents in sand (up to 50% in cores PSM3-CS009 and PSM3-CS011; Figs. 16C, 17A and 19A) and higher sortable silt values (Figs. 17A and 19B; Toucanne et al., 2012; Minto'o et al., 2015). The deposition of sediment with higher sand contents during the Younger Dryas was also observed in the Gulf of Cadiz associated to the lower branch of the Mediterranean Outflow Water (Llave et al., 2006).

The reduced tectonic activity in the Corsica Trough since the early Pliocene (Zitellini et al., 1986) permits to recover a sedimentary record of the contourite depositional system that is only influenced by climate changes, by inducing fluctuations in sediment supply and bottom current velocity. The proposed model could be applied to the margins where sediment supply and bottom current velocity are enhanced during cold periods, as observed for example in the Gulf of Cadiz (Llave et al., 2006) or in glacial margins (Laberg et al., 2001; Rebesco et al., 2002).

6. Conclusions

The Pianosa Contourite Depositional System (CDS) is located in the confined basin of the Corsica Trough (Northern Tyrrhenian Sea) and it extends between 170 and 850 m water depth along 120 km, with a maximum width of 10 km. Contourite drifts are mainly composed of bioturbated mud, although sandy bioclastic layers are also common, more frequent, thicker and formed by coarser material in the shallowest areas. The morphology of the contourites is strongly controlled by the physiography of the Pianosa Ridge, especially the development of sigmoid drifts in the area where the Pianosa Ridge forms a bulge. Other

irregularities or depressions of the seafloor, such as the Elba Canyon, alter locally the hydrodynamic regime and may induce the upwelling of denser waters, allowing the formation of shallower contourites. Different types of contourites can be found in the Pianosa CDS: plastered drift, separated elongated mounded drift, sigmoid mounded drift and multicrested drift. The onset of the Pianosa CDS occurred in the Middle–Late Pliocene, although the development of the contourite drifts was enhanced after the Middle Pleistocene Transition (700–900 kyr). The evolution of the system is continuous and coherent with the present-day circulation pattern, with the Levantine Intermediate Water flowing northwards along the eastern margin of the Corsica Trough. However, its velocity changed in the past with faster bottom currents during cold periods. During sea level falls, fast bottom currents produced erosional surfaces on the drifts (more evident in the middle and upper slope). The accumulation of coarse bioclastic material in the contourites during sea level falls was favoured by the fact that the material from the continental shelf was more easily transported to the slope. The accumulation of fine sediment was greater during sea level lowstands than during sea level high-stands because the turbidite system was connected (providing fine sediment to the basin) and the velocity of bottom currents was relatively high (pirating the fine sediment from the turbidites and transporting it along the Pianosa Ridge).

Acknowledgements

We thank the Captain and the crew of the PRISME2-PAPRICA and PRISME3 cruises (2013) onboard R/V Atalante and R/V Pourquoi pas?, respectively. We are grateful to ISMAR-CNR for allowing us to have access to the seismic data from surveys ET91, ET93 and ET95, to M. Ligi for the processing of the sparker seismic reflection data and to the Collège Doctoral International of the Université Européene de Bretagne and the Conseil Régional de Bretagne for having awarded E. Miramontes with a travel grant during her stay at ISMAR-CNR. We would like to thank P. Dupont for the processing of the multi-channel high resolution seismic reflection data; S. Garziglia, S. Toucanne, N. Sultan, M. Taviani, C. Pellegrini and V. Maselli for the insightful scientific discussion; A. Roubi and M. Rovere for the technical support and M. Payo Payo for helping with the visualisation of the grain size measurements. We are grateful to the guest editor C. Campbell and to the two anonymous reviewers for their valuable suggestions that improved the manuscript. The thesis of E. Miramontes and the cruise PRISME2-PAPRICA are co-funded by TOTAL and Ifremer as part of the scientific project TOTAL-Ifremer PAMELA. We thank projects LabexMER ANR-10-LABX-19-01 Axis 4 for lab support.

References

Amelio, M., Martorelli, E., 2008. Seismo-stratigraphic characters of paleocontourites along the Calabro-Tyrrhenian margin (Southern Tyrrhenian sea). Mar. Geol. 252, 141–149.

Angue Minto'o, C.M., 2014. Enregistrements sédimentaires des changements climatiques et environnementaux pendant le quaternaire terminal sur la marge Est-Corse PhD Thesis Université de Perpignan, Perpignan, p. 309.

Astraldi, M., Gasparini, G.P., 1992. The seasonal characteristics of the circulation in the north Mediterranean basin and their relationship with the atmospheric-climatic conditions. Journal of Geophysical Research: Oceans 97, 9531–9540 (1978–2012).

Bartole, R., 1995. The North Tyrrhenian–Northern Apennines post-collisional system: constraints for a geodynamic model. Terra Nova 7, 7–30.

Brackenridge, R.E., Hernández-Molina, F.J., Stow, D.A.V., Llave, E., 2013. A Pliocene mixed contourite-turbidite system offshore the Algarve Margin, Gulf of Cadiz: seismic response, margin evolution and reservoir implications. Mar. Pet. Geol. 46, 36–50.

Cacho, I., Grimalt, J.O., Sierro, F.J., Shackleton, N., Canals, M., 2000. Evidence for enhanced Mediterranean thermohaline circulation during rapid climatic coolings. Earth Planet. Sci. Lett. 183, 417–429.

Calves, G., Toucanne, S., Jouet, G., Charrier, S., Thereau, E., Etoubleau, J., Marsset, T., Droz, L., Bez, M., Abreu, V., 2013. Inferring denudation variations from the sediment record; an example of the last glacial cycle record of the Golo Basin and watershed, East Corsica, western Mediterranean sea. Basin Res. 25, 197–218.

Cattaneo, A., Jouet, G., Charrier, S., Thereau, E., Riboulot, V., 2014. Submarine landslides and contourite drifts along the Pianosa Ridge (Corsica Trough, Mediterranean Sea). In: Krastel, S. (Ed.), Submarine mass movements and their consequences 37. Springer, Dordrecht, pp. 435–445.

Deptuck, M.E., Piper, D.J.W., Savoye, B., Gervais, A., 2008. Dimensions and architecture of late Pleistocene submarine lobes off the northern margin of East Corsica. Sedimentology 55 (869-U834).

Fontanier, C., Mackensen, A., Jorissen, F.J., Anschutz, P., Licari, L., Griveaud, C., 2006. Stable oxygen and carbon isotopes of live benthic foraminifera from the Bay of Biscay: microhabitat impact and seasonal variability. Mar. Micropaleontol. 58, 159–183.

Garziglia, S., 2010. Typologie, phénoménologie et approche des facteurs déclenchants des glissements sous-marins: application aux deltas profonds du Nil et du Niger PhD Thesis Université de Nice, pp. 306–307.

Gervais, A., Savoye, B., Piper, D.J.W., Mulder, T., Cremer, M., Pichevin, L., 2004. Present morphology and depositional architecture of a sandy confined submarine system: the Golo turbidite system (eastern margin of Corsica). Confined Turbidite Systems 222, pp. 59–89.

Gervais, A., Savoye, B., Mulder, T., Gonthier, E., 2006. Sandy modern turbidite lobes: a new insight from high resolution seismic data. Mar. Pet. Geol. 23, 485–502.

Grant, K.M., Rohling, E.J., Ramsey, C.B., Cheng, H., Edwards, R.L., Florindo, F., Heslop, D., Marra, F., Roberts, A.P., Tamisiea, M.E., 2014. Sea-level variability over five glacial cyces. Nat. Commun. 5.

Harris, P.T., Beaman, R.J., 2003. Processes controlling the formation of the Mertz Drift, George Vth continental shelf, East Antarctica: evidence from 3.5 kHz sub-bottom profiling and sediment cores. Deep-Sea Res. II Top. Stud. Oceanogr. 50, 1463–1480.

Harris, P.T., Domack, E., Manley, P.L., Gilbert, R., Leventer, A., 1999. Andvord drift: a new type of inner shelf, glacial marine deposystem from the Antarctic Peninsula. Geology 27, 683–686.

Heezen, B.C., Hollister, C., 1964. Deep-sea current evidence from abyssal sediments. Mar. Geol. 1, 141–174.

Hernández-Molina, F.J., Somoza, L., Vázquez, J.T., Lobo, F., Fernández-Puga, M.C., Llave, E., Díaz-del Rio, V., 2002. Quaternary stratigraphic stacking patterns on the continental shelves of the southern Iberian Peninsula: their relationship with global climate and palaeoceanographic changes. Quat. Int. 92, 5–23.

Hernández-Molina, F.J., Llave, E., Stow, D.A.V., García, M., Somoza, L., Vázquez, J.T., Lobo, F.J., Maestro, A., del Río, V.D., León, R., 2006. The contourite depositional system of the Gulf of Cadiz: a sedimentary model related to the bottom current activity of the Mediterranean outflow water and its interaction with the continental margin. Deep-Sea Res. II Top. Stud. Oceanogr. 53, 1420–1463.

Hernández-Molina, F.J., Stow, D.A.V., Alvarez-Zarikian, C.A., Acton, G., Bahr, A., Balestra, B., Ducassou, E., Flood, R., Flores, J.-A., Furota, S., Grunert, P., Hodell, D., Jimenez-Espejo, F., Kim, J.K., Krissek, L., Kuroda, J., Li, B., Llave, E., Lofi, J., Lourens, L., Miller, M., Nanayama, F., Nishida, N., Richter, C., Roque, C., Pereira, H., Goni, M.F.S., Sierro, F.J., Singh, A.D., Sloss, C., Takashimizu, Y., Tzanova, A., Voelker, A., Williams, T., Xuan, C., 2014. Paleoceanography onset of Mediterranean outflow into the North Atlantic. Science 344, 1244–1250.

Hickey, B.M., 1997. The response of a steep-sided, narrow canyon to time-variable wind forcing. J. Phys. Oceanogr. 27, 697–726.

Klinck, J.M., 1996. Circulation near submarine canyons: a modeling study. J. Geophys. Res. 101, 1211–1223 (1978–2012).

La Violette, P.E., 1994. Overview of the major forcings and water masses of the Western Mediterranean Sea. Seasonal and Interannual Variability of the Western Mediterranean Sea, pp. 1–11.

Laberg, J.S., Dahlgren, T., Vorren, T.O., Haflidason, H., Bryn, P., 2001. Seismic analyses of Cenozoic contourite drift development in the Northern Norwegian Sea. Mar. Geophys. Res. 22, 401–416.

Lambe, T.W., Whitman, R.V., 1979. Soil Mechanics S.I. version. second ed. Wiley, New York.

Lascaratos, A., Roether, W., Nittis, K., Klein, B., 1999. Recent changes in deep water formation and spreading in the eastern Mediterranean Sea: a review. Prog. Oceanogr. 44, 5–36.

Llave, E., Schonfeld, J., Hernández-Molina, F.J., Mulder, T., Somoza, L., del Rio, V.D., Sanchez-Almazo, I., 2006. High-resolution stratigraphy of the Mediterranean outflow contourite system in the Gulf of Cadiz during the late Pleistocene: the impact of Heinrich events. Mar. Geol. 227, 241–262.

Marani, M., Argnani, A., Roveri, M., Trincardi, F., 1993. Sediment drifts and erosional surfaces in the central Mediterranean-seismic evidence of bottom-current activity. Sediment. Geol. 82, 207–220.

Marches, E., Mulder, T., Gonthier, E., Cremer, M., Hanquiez, V., Garlan, T., Lecroart, R., 2010. Perched lobe formation in the Gulf of Cadiz: interactions between gravity processes and contour currents (Algarve Margin, Southern Portugal). Sediment. Geol. 229, 81–94.

McCave, I.N., Hall, I.R., 2006. Size sorting in marine muds: processes, pitfalls, and prospects for paleoflow-speed proxies. Geochem. Geophys. Geosyst. 7.

McCave, I.N., Manighetti, B., Robinson, S.G., 1995. Sortable silt and fine sediment size/composition slicing: parameters for palaeocurrent speed and palaeoceanography. Paleoceanography 10, 593–610.

Millot, C., 1999. Circulation in the Western Mediterranean Sea. J. Mar. Syst. 20, 423–442.

Millot, C., 2013. Levantine intermediate water characteristics: an astounding general misunderstanding! Sci. Mar. 77, 217–232.

Millot, C., Taupier-Letage, I., 2005. Circulation in the Mediterranean sea, the Mediterranean sea. 29-66. Springer.

Minto'o, C.M.A., Bassetti, M.A., Morigi, C., Ducassou, E., Toucanne, S., Jouet, G., Mulder, T., 2015. Levantine intermediate water hydrodynamic and bottom water ventilation in the northern Tyrrhenian Sea over the past 56,000 years: new insights from benthic foraminifera and ostracods. Quat. Int. 357, 295–313.

Miramontes, E., Cattaneo, A., Jouet, G., Garziglia, S., 2016. Implications of sediment dynamics in mass transport along the Pianosa Ridge (Northern Tyrrhenian Sea). In: Lamarche, G., Mountjoy, J. (Eds.), Submarine mass movements and their consequences 30. Springer, Dordrecht, pp. 301–309.

Mulder, T., Faugères, J.C., Gonthier, E., 2008. Mixed turbidite–contourite systems. Dev. Sedimentol. 60, 435–456.
Nygard, R., Gutierrez, M., Gautam, R., Hoeg, K., 2004. Compaction behavior of argillaceous sediments as function of diagenesis. Mar. Pet. Geol. 21, 349–362.
Pascucci, V., 2002. Tyrrhenian Sea extension north of the Elba Island between Corsica and western Tuscany (Italy). Boll. Soc. Geol. Ital. 121, 819–828.
Pascucci, V., Merlini, S., Martini, I.P., 1999. Seismic stratigraphy of the Miocene–Pleistocene sedimentary basins of the Northern Tyrrhenian Sea and western Tuscany (Italy). Basin Res. 11, 337–356.
Pascucci, V., Martini, I.P., Sagri, M., Sandrelli, F., Nichols, G., Paola, C., Williams, E.A., 2007. Effects of Transverse Structural Lineaments on the Neogene–Quaternary Basins of Tuscany (Inner Northern Apennines, Italy). Sedimentary Processes, Environments and Basins—a Tribute to Peter Friend. Special Publication 37 pp. 155–183.
Pellegrini, C., Maselli, V., Trincardi, F., 2015. Pliocene–Quaternary contourite depositional system along the south-western Adriatic margin: changes in sedimentary stacking pattern and associated bottom currents. Geo-Mar. Lett. 1-13.
Rebesco, M., Pudsey, C.J., Canals, M., Camerlenghi, A., Barker, P.F., Estrada, F., Giorgetti, A., 2002. Sediment drifts and deep-sea channel systems, Antarctic Peninsula Pacific Margin. Geol. Soc. Lond. Mem. 22, 353–371.
Rebesco, M., Camerlenghi, A., Van Loon, A.J., 2008. Contourite research: a field in full development. Dev. Sedimentol. 60, 3–10.
Reimer, P.J., Bard, E., Bayliss, A., Beck, J.W., Blackwell, P.G., Ramsey, C.B., Buck, C.E., Cheng, H., Edwards, R.L., Friedrich, M., Grootes, P.M., Guilderson, T.P., Haflidason, H., Hajdas, I., Hatte, C., Heaton, T.J., Hoffmann, D.L., Hogg, A.G., Hughen, K.A., Kaiser, K.F., Kromer, B., Manning, S.W., Niu, M., Reimer, R.W., Richards, D.A., Scott, E.M., Southon, J.R., Staff, R.A., Turney, C.S.M., van der Plicht, J., 2013. IntCal13 and Marine13 radiocarbon age calibration curves 0–50,000 years cal BP. Radiocarbon 55, 1869–1887.
Riboulot, V., Thomas, Y., Berne, S., Jouet, G., Cattaneo, A., 2014. Control of Quaternary sea-level changes on gas seeps. Geophys. Res. Lett. 41, 4970–4977.
Roveri, M., 2002. Sediment drifts of the Corsica Channel, Northern Tyrrhenian Sea. In: Stow, D.A.V., Pudsey, C.J., Howe, J.A., Faugères, J.-C., Viana, A.R. (Eds.), Deep-Water Contourite Systems. Modern Drifts and Ancient Series, Seismic and Sedimentary Characteristics. Geological Society, London, Memoirs 22, pp. 191–208.
Schmiedl, G., Pfeilsticker, M., Hemleben, C., Mackensen, A., 2004. Environmental and biological effects on the stable isotope composition of recent deep-sea benthic foraminifera, from the western Mediterranean Sea. Mar. Micropaleontol. 51, 129–152.
Sobarzo, M., Figueroa, M., Djurfeldt, L., 2001. Upwelling of subsurface water into the rim of the Biobio submarine canyon as a response to surface winds. Cont. Shelf Res. 21, 279–299.
Toucanne, S., Jouet, G., Ducassou, E., Bassetti, M.A., Dennielou, B., Minto'o, C.M.A., Lahmi, M., Touyet, N., Charlier, K., Lericolais, G., Mulder, T., 2012. A 130,000-year record of Levantine intermediate water flow variability in the Corsica Trough, western Mediterranean Sea. Quat. Sci. Rev. 33, 55–73.
Toucanne, S., Angue Minto'o, C.M., Fontanier, C., Bassetti, M.A., Jorry, S.J., Jouet, G., 2015. Tracking rainfall in the Northern Mediterranean borderlands during sapropel deposition. Quat. Sci. Rev. 129, 178–195.
Vandorpe, T.P., Van Rooij, D., Stow, D.A.V., Henriet, J.-P., 2011. Pliocene to recent shallow-water contourite deposits on the shelf and shelf edge off south-western Mallorca, Spain. Geo-Mar. Lett. 31, 391–403.
Verdicchio, G., Trincardi, F., 2008a. Mediterranean shelf-edge muddy contourites: examples from the Gela and South Adriatic basins. Geo-Mar. Lett. 28, 137–151.
Verdicchio, G., Trincardi, F., 2008b. Shallow-water contourites. Dev. Sedimentol. 60, 409–433.
Viana, A.R., Faugeres, J.C., Kowsmann, R.O., Lima, J.A.M., Caddah, L.F.G., Rizzo, J.G., 1998. Hydrology, morphology and sedimentology of the Campos continental margin, offshore Brazil. Sediment. Geol. 115, 133–157.
Vignudelli, S., Gasparini, G.P., Astraldi, M., Schiano, M.E., 1999. A possible influence of the North Atlantic oscillation on the circulation of the Western Mediterranean Sea. Geophys. Res. Lett. 26, 623–626.
Vignudelli, S., Cipollini, P., Astraldi, M., Gasparini, G.P., Manzella, G., 2000. Integrated use of altimeter and in situ data for understanding the water exchanges between the Tyrrhenian and Ligurian Seas. J. Geophys. Res. Oceans 105, 19649–19663.
Woerther, P., Bourillet, J.-F., Damy, G., Dussud, L., Sultan, N., 2012. Improving in piston coring quality with acceleration and pressure measurements and new insights on quality of the recovery. 8th International Marine Technicians Symposium, INMARTECH 2012, 25 and 28 September 2012, Texel, The Netherlands.
Zitellini, N., Trincardi, F., Marani, M., Fabbri, A., 1986. Neogene tectonics of the northern Tyrrhenian sea. Giorn. Geol. 48, 2.

Submarine landslides in the Northern Tyrrhenian Sea and relationship with the turbiditic and contouritic deposits: morphology, stratigraphy, geotechnics and modelling

The Corsica Trough is an asymmetric confined basin located between the Corsica Island and the Tuscan Archipelago, with the western flank dominated by turbiditic and hemipelagic processes and the eastern flank by mass transport and contouritic processes. The present PhD project aims to develop our understanding of the mechanisms that control the formation of submarine landslides within muddy contourites (sediment deposits related to bottom currents) during the Plio-Quaternary. The broad data set available for this PhD project includes: multibeam bathymetry, seismic reflection data, sediment cores, *in situ* geotechnical measurements, current ADCP measurements and results of a hydrodynamic model.

The contourites of the Corsica Trough are mainly composed of mud with sandy layers formed by enhanced bottom currents during periods of sea level fall. The contourite drifts grow slowly during sea level high-stands and rapidly during sea level low-stands due to the high sediment availability provided by an active turbidite system. Bottom currents control the seafloor morphology and generate plastered drifts on the slope. This is a convex-shaped contourite with steep slope gradients in the lower part limited by a moat (incision created by bottom currents). The Pianosa Slump was initiated in this lower part of the plastered drift. The occurrence of continuous erosive processes during cold periods could undercut the slope and trigger submarine landslides. Another predisposing factor for slope instability identified is the presence of a potential weak layer with a post-peak strain softening behaviour (strength loss with increasing strain). This particular property is caused by the presence of zeolites (product of the alteration of volcanic rocks). This layer originated the basal failure surface of the Pianosa Slump.

In summary, the two main factors predispose the formation of submarine landslides in the Pianosa Ridge are: the morphology of the plastered drift with steep slopes in the lower part and a potential weak layer composed of zeolitic muddy sediment. The main triggering factor seems to be undercutting by bottom currents.

Keywords: Mass transport deposit, slope instability, zeolite, strain softening, weak layer, erosion, bottom currents, sediment drift, Mediterranean Sea, Corsica

Glissements sous-marins en Mer Tyrrhénienne septentrionale et relations avec les dépôts contouritiques et turbiditiques : morphologie, stratigraphie, géotechnique et modélisation

Le Canal de Corse est un bassin confiné asymétrique localisé entre l'Île de Corse et l'Archipel de la Toscane, dont le flanc ouest est dominé par des processus turbiditiques et hémipélagiques et le flanc est par des mouvements en masse et des processus contouritiques. Le présent projet de doctorat a pour objectif de comprendre plus précisément les mécanismes contrôlant la formation des glissements sous-marins dans les contourites vaseuses (dépôts sédimentaires formés par les courants) pendant la période Plio-Quaternaire. Le vaste jeu de données disponible pour ce projet de doctorat inclut : la bathymétrie multifaisceaux, la sismique réflexion, les mesures géotechniques *in situ*, les mesures de vitesse de courant et les résultats d'un modèle hydrodynamique.

Les contourites du Canal de Corse sont principalement composées de vase avec la présence de couches de sable formées par de forts courants de fond pendant les périodes de baisse du niveau marin. La croissance des dépôts contouritiques dépend de la disponibilité de sédiment fourni par le système turbiditique. Ainsi, cette croissance est lente pendant les périodes interglaciaires de haut niveau marin et rapide pendant les bas niveaux marins. Les courants contrôlent la morphologie du fond et génèrent les *plastered drifts* de forme convexe avec des pentes plus raides dans la partie avale, limités par une incision créée par les courants (*moat*). Le *Pianosa Slump* a été initié dans cette partie basse du plastered drift. Les moats pourraient être érodés préférentiellement pendant les périodes froides passées déclenchant ainsi certains glissements observés. Un autre facteur prédisposant l'instabilité de pente sur la Ride de Pianosa est la faiblesse d'une couche dont le comportement mécanique se caractérise par du radoucissement (perte de résistance avec le cisaillement). Cette propriété particulière est due à la présence de zéolites (produit de l'altération des roches volcaniques). Cette couche a formé la surface basale de rupture du Pianosa Slump.

En conclusion, les deux principaux facteurs prédisposant la formation de glissements sous-marins sur la Ride de Pianosa sont : la morphologie du plastered drift avec une pente plus raide en avale et la couche faible composée de sédiment vaseux riche en zéolites. Le principal facteur déclenchant semble être l'érosion basale.

Mots-clés : Masse glissée, instabilité de pente, zéolite, radoucissement, couche de faiblesse, érosion, courants de fond, contourite, Mer Méditerranée, Corse